Indonesian Journal of Chemistry
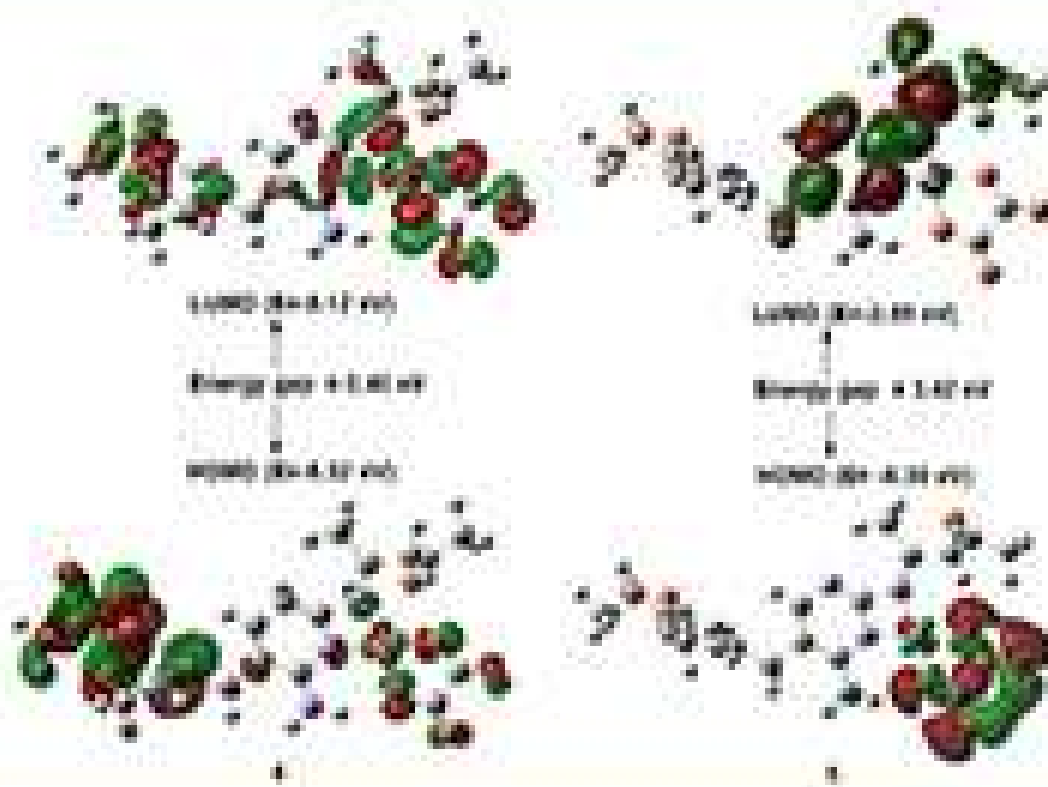
A Computational Design of siRNA in SARS-CoV-2 Spike Glycoprotein Gene and Its Binding Capability toward mRNA

Arli Aditya Parikesit[1*], Arif Nur Muhammad Ansori[2], and Viol Dhea Kharisma[3]

[1]*Department of Bioinformatics, School of Life Sciences, Indonesia International Institute for Life Sciences, Jakarta 13210, Indonesia*

[2]*Professor Nidom Foundation, Surabaya 60115, Indonesia*

[3]*Computational Virology Research Unit, Division of Molecular Biology and Genetics, Generasi Biologi Indonesia Foundation, Gresik 61171, Indonesia*

Abstract: *COVID-19 pandemic has no immediate ending in sight, and any significant increasing cases were observed worldwide. Currently, there are only two main strategies for developing COVID-19 drugs that predominantly use a proteomics-based approach, which are drug repurposing and herbal medicine strategies. However, a third strategy has existed, called small interfering RNA or siRNA, which is based on the transcriptomics approach. In the case of SARS-CoV-2 infection, it is expected to perform by silencing the viral gene, which brings the surface glycoprotein (S) gene responsible for SARS-CoV-2 viral attachment to the ACE2 receptor on the human host cell. This third approach applies a molecular simulation method comprising data retrieval, multiple sequence alignment, phylogenetic tree depiction, 2D/3D structure prediction, and RNA-RNA molecular docking. The expected results are the prediction of 2D and 3D structures of both siRNA and mRNA silenced S genes along with a complex as the result of a docking method formed by those silenced genes. An Insilco chemical interaction study was performed in testing siRNA and mRNA complex's stability with the confirmation result of a stable complex which is expected to be formed before mRNA reaches the ribosome for the translation process. Thus, siRNA from the S gene could be considered a candidate for the COVID-19 therapeutic agent.*

Keywords: *COVID-19; SARS-CoV-2; siRNA; S gene; molecular docking*

■ INTRODUCTION

COVID-19 is an upper respiratory tract disease caused by the SARS-CoV-2 virus [1-2]. COVID-19 pandemic has contributed to almost 520 million cases and more than 6 million mortalities to date (per 12th of May 2022). However, WHO has yet made any endorsement for anti-SARS-CoV-2 drugs. Any previously supported drugs, such as redeliver and hydroxychloroquine, are paused for further review [3]. In contrast, endorsement of interleukin blockers and dexamethasone as COVID-19 drugs are given only for severe or critical patients. Even though these drugs are not directly stated as antiviral, they ameliorate the overreaction of the immune system post-SARS-CoV-2 infection [4-5]. In this regard, there is room for improvement in designing anti-SARS-CoV-2 therapy.

Furthermore, the SARS-CoV-2 genome is considered larger compared to any other RNA virus, such as influenza and HIV [6]. Hence, it draws a complicated repertoire of protein-protein interactions encompassing various viral activities such as host attachment, infection, and replications [7]. Then, one of the focal points for COVID-19 drug design is by blocking the virulence of its viral particle [8]. SARS-CoV-2 virus' infectivity or virulence is mainly delivered by its spike protein located on the viral surface [9]. It plays an important role in viral penetration to the host cell by facilitating the attachment to ACE2 receptors [10]. Thus, it is logical in the sense of rational drug design that SARS-CoV-2 spike protein should be inhibited to ward off viral infection [11]. However,

although it is considered the primary paradigm for drug design, the proteomics-based approach currently does not confer any significant number of COVID-19 WHO-endorsed drugs [2-4,12]. In fact, until recently, there was no significant breakthrough in COVID-19 drug design studies. Even worse, the pandemic ravaged to the new escalation as the SARS-CoV-2 delta variant appeared (Pango Lineage: B.1.617.2) as the variant of concern (VOC) with much higher infection and hospitalization rate ever worldwide [13-15]. Furthermore, it is also known that the SARS-CoV-2 delta variant has 1000 times more viral loads than the original SARS-CoV-2 strain [16]. In this regard, the transcriptomics-based pipeline could be considered a breakthrough [17]. The transcriptomics-based drug works by leveraging RNA as a therapeutic agent [18]. Mainly, siRNA was deployed for deterring other upper respiratory tract viral infections, such as influenza and MERS, and SARS, as proven in the wet laboratory setting [19-23]. The very principle of siRNA deployment is so-called 'preemptive striking', which blocks the viral genes before upregulating the protein expression [24].

Meanwhile, structural bioinformatics, as the application of computational chemistry in the field of molecular biology, has played a pivotal role in the pipeline development for siRNA studies [25-28]. The basics of this approach are the chemical thermodynamics and kinetics theory working under the classical mechanic paradigm [29-32]. The occurring spontaneous reaction is the foundation of molecular docking and dynamics simulations, which become the pillars of drug design [33-35]. Molecular simulation methods which are commonly deployed in proteomics research, have been proven to be successfully applied for any RNA-RNA and/or RNA-Protein simulations with some adjustments [36-37]. Finally, RNA-based molecular simulation is applicable as well for the purpose of designing the COVID-19 drug. The objective of this research was to examine the chemical interaction of siRNA in silencing SARS-CoV-2 S gene mRNA. Lastly, this research would induce a siRNA design, the docking analysis of the siRNA-mRNA complex, and it would be concluded with the result of chemical interaction analysis.

■ EXPERIMENTAL SECTION

Computer Hardware

The research was carried out with a Macbook Pro Retina® computer with 8 GB RAM, Intel® Core™ i5, Intel graphics processor 1.5 GB VRAM, and 256 GB SSD. The deployed software was based on MacOSX 10.4.6 Mojave operating system.

Techniques

The procedure was inspired by the previously developed pipeline for RNA-RNA molecular simulation [38-39]. Specific parameters were added, as mentioned in the subsections below, if necessary. The procedure of subsections below should be followed consecutively for the consistency of the whole pipeline.

Data Retrieval

The NCBI virus website was accessed from https://www.ncbi.nlm.nih.gov/labs/virus/ [40]. Then, a Tabular view was selected, and the nucleotide tab was clicked. The following search criteria for the data annotation were applied: Virus (SARS-CoV-2, taxid: 2697049); Sequence length (100–1000 bp); Nucleotide completeness (partial); Proteins (Surface glycoprotein); Geographic region (Africa, Asia, and South America); Collection date (Nov 16, 2020, to May 18, 2021); Host (Homo sapiens, TaxId: 9605); and Sequence type (GenBank). Other parameters are left at default values.

MSA and Phylogenetic Tree

The default MSA (multiple sequence alignment) and phylogenetic tree of NCBI virus applets were deployed. The NCBI virus MSA method was built on the MUSCLE algorithm and previously deployed parameters [39]. ClustalX was employed for NCBI virus downloaded data for MSA annotation. The utilized parameters were Gap Opening: 15; Gap Extension 6.66; Delay Divergent Sequences (%): 30; DNA Transition Weight: 0.5; Use Negative Matrix: Off; Protein Weight Matrix: Gonnet series; and DNA Weight Matrix: IUB. The MSA conserved region was extracted with the default text editor. The parameters used for phylogenetic tree were: Bootstrap NJ tree annotation with Random number

generator seed 111 and number of bootstrap trials 1000.Ph format. The data was then saved as phylip tree format.

RNAxs Application of siRNA Design for Repressing the S Gene mRNA

RNAxs software was accessed through this link: http://rna.tbi.univie.ac.at/cgi-bin/RNAxs/RNAxs.cgi [41]. The conserved region of the MSA section was applied in this pipeline. The utilized parameters were set as follows: 8nt Accessibility Threshold: 0.01157; 16nt Accessibility Threshold: 0.001002; Self Folding Energy: 0.9022; Sequence Asymmetry: 0.5; Energy Asymmetry: 0.4655; Free End: 0.625; Custom Sequence Rules: NNNNNNNNNNNNNNNNNNN; and the maximal number of siRNAs: 3.

Locating siRNA Target's Conserved Region in MSA Results

The .aln file of the MSA result was forwarded to Jalview 2.11 to determine the siRNA target [42].

RNAalifold for Conserved Structure of S Gene's mRNA

RNAalifold software was accessed through the following link: http://rna.tbi.univie.ac.at/cgi-bin/RNA WebSuite/RNAalifold.cgi [43]. The conserved region of the MSA section was applied in this pipeline. The utilized parameters were as follows: RNAalifold version: new RNAalifold with RIBOSUM scoring; Fold algorithms and basic options: minimum free energy (MFE) and partition function; and avoiding any isolated base pairs.

RNAfold for both siRNA and mRNA's 2D Structures

RNAfold software was accessed from this link: http://rna.tbi.univie.ac.at/cgi-bin/RNAWebSuite/RNAfold.cgi [44]. The conserved region of the MSA section was applied in this pipeline. The employed parameters were as follows: Fold algorithms and basic options: minimum free energy (MFE) and partition function; and avoiding any isolated base pairs.

Barrier Server for Determining siRNA and mRNA 2D Structure Diversity

The barrier Server software was accessed at this link: http://rna.tbi.univie.ac.at/cgi-bin/RNAWebSuite/barriers.

cgi [45-46]. The Vienna dot-bracket annotation of 2D data annotation was applied in this pipeline. The utilized parameters were as follow: the maximal number of lowest local minima: 50; considered only minima with a barrier higher than: 0.1; avoiding any isolated base pairs; declining energies on both sides of a helix in any case; RNA parameters with Turner model; and rescaling the energy parameters to given temperature (C): 37.

iFoldRNA Iteration for both siRNA and mRNA's Sequences and 2D Structure

An iFoldRNA software was accessed from this link: https://dokhlab.med.psu.edu/ifoldrna/ [47-48]. The Vienna dot-bracket annotation of 2D data annotation and FASTA format was applied in this pipeline. The employed parameters were as follow: simulation time 20000; Replica 1 Temperature (DMD Units) 0.2; Replica 2 Temperature (DMD Units) 0.225; Replica 3 Temperature (DMD Units) 0.25; Replica 4 Temperature (DMD Units) 0.27; Replica 5 Temperature (DMD Units) 0.3; Replica 6 Temperature (DMD Units) 0.333; Replica 7 Temperature (DMD Units) 0.367; Replica 8 Temperature (DMD Units) 0.4; Replica Exchange Interval (DMD units): 1000; Heat Exchange Coefficient (Berendsen Thermostat, DMD Units): 0.1.

Validation of 3D RNA Structures

Molprobity server in http://molprobity.biochem.duke.edu/index.php was used in validating 3D RNA structures with parametric thresholds [49]. The designated parameters for RNA structure validation were all-atom contacts, nucleic acid geometry, and additional validations.

3D Structures' Energy Protonation and Minimization of mRNA and siRNA using AVOGADRO

AVOGADRO molecular editor software was downloaded from: https://avogadro.cc/ [50-51]. RNA data in PDB format was applied in this pipeline. The employed parameters were as follows: Select the 'add hydrogen' option. The tapping of the 'minimize energy' button was performed using the following parameters: force field: UFF; steps per update: 4; and algorithm: Steepest Descent Algorithm.

RNA-RNA Molecular Docking of siRNA and mRNA using HNADOCK

HNADOCK nucleic acid docking software was accessed here: http://huanglab.phys.hust.edu.cn/hnadock/ [52]. RNA data are optimized PDB format was applied in this pipeline. The utilized parameters were RNA secondary structure prediction method: RNAfold; RNA-RNA interaction prediction method: ab initio; and refining the top 10 complex models: yes (Longer molecular dynamic simulation would be provided).

Chemical Interaction Prediction of siRNA and mRNA Complex with IntaRNA

An IntaRNA software was accessed from the following link: http://rna.informatik.uni-freiburg.de/IntaRNA/Input.jsp [53-55]. The Vienna dot-bracket annotations from 2D data annotation and FASTA format were applied in this pipeline. The employed parameters were a number of interactions per RNA pair: 1; suboptimal interaction overlap: an overlap in query; no lonely base pairs; no GU at helix ends; minimum number of base pairs in seed: 7; and ignoring seeds with GU ends.

Prediction of siRNA-mRNA Complex's 3D Chemical Interactions using PLIP

PLIP software was accessed from this website: https://plip-tool.biotec.tu-dresden.de [56]. siRNA-mRNA complex in PDB file format was applied in this pipeline. The employed parameters for detecting macromolecule-ligand interactions were used by treating nucleic acid as a receptor and detecting interactions for 1 model. However, the detection of interactions between the rest of the macromolecule and chain(s) was also accomplished by treating nucleic acid as a receptor and detecting interactions for 1 model.

Data Analysis and Complex Visualization

The data annotation of the siRNA-mRNA complex was visualized with UCSF chimera software version 1.15 [57]. The visualization was focused on observing the chemical structure's integrity and feasibility.

■ RESULTS AND DISCUSSION

S gene entry in GenBank was dominated by DNA sequences from India, possibly due to the shifting COVID-19 pandemic epicenter at that time. Currently (per June 2021), even though with a declining tendency, India has the highest daily cases in the world [58]. Table 1 clearly presents that the delta variant started to dominate S gene annotations from the South Asia region and this condition was in line with the increased transmission of the variant. It also started to replace alpha variants as well in the recently annotated S gene data.

Table 1. The SARS-CoV-2 S gene nucleotide sequences retrieved from GenBank (https://www.ncbi.nlm.nih.gov/labs/virus/vssi)

No.	Accession	Geo location	SARS-CoV-2 variant (Pango lineage/WHO naming)	Collection date
1	MZ149959	India: Assam	B.1.617.2/Delta	23/04/21
2	MZ149960	India: Assam	B.1.617.2/Delta	25/04/21
3	MZ149961	India: Assam	B.1.617.2/Delta	23/04/21
4	MZ149962	India: Assam	B.1.617.2/Delta	22/04/21
5	MZ149963	India: Assam	B.1.617.2/Delta	23/04/21
6	MZ149964	India: Assam	B.1.617.2/Delta	24/04/21
7	MZ149965	India: Assam	B.1.617.2/Delta	23/04/21
8	MZ149966	India: Assam	B.1.617.2/Delta	23/04/21
9	MZ149967	India: Assam	B.1.617.2/Delta	23/04/21
10	MZ149968	India: Assam	B.1.617.2/Delta	23/04/21
11	MZ149973	India: Assam	B.1.617.2/Delta	23/04/21
12	MZ149974	India: Assam	B.1.617	01/05/21
13	MZ149975	India: Assam	B.1.617	16/04/21

No.	Accession	Geo location	SARS-CoV-2 variant (Pango lineage/WHO naming)	Collection date
14	MZ149976	India: Assam	B.1.617	16/04/21
15	MW897354	Iraq	NA	10/02/21
16	MW897355	Iraq	NA	23/03/21
17	MW897356	Iraq	NA	23/03/21
18	MW835152	Uzbekistan: Tashkent, M. Ulugbek district	NA	10/02/21
19	MW835153	Uzbekistan: Tashkent, M. Ulugbek district	NA	10/02/21
20	MW835154	Uzbekistan: Tashkent, Ynusabad district	NA	10/02/21
21	MW835155	Uzbekistan: Tashkent, Ynusabad district	NA	10/02/21
22	MW839583	Uzbekistan: Tashkent, Yunisabad district	NA	11/02/21
23	MW839584	Uzbekistan: Tashkent, Yunisabad district	NA	11/02/21
24	MW828609	Uzbekistan: Tashkent almazar district	NA	13/03/21
25	MW828610	Uzbekistan: Tashkent almazar district	NA	13/03/21
26	MW828611	Uzbekistan: Tashkent almazar district	NA	13/03/21
27	MW828612	Uzbekistan: Tashkent almazar district	NA	13/03/21
28	MW699627	India: Assam	B.1.1.7/Alpha	18/02/21
29	MW699628	India: Assam	B.1.1.7/Alpha	18/02/21
30	MW699629	India: Assam	B.1.1.7/Alpha	24/02/21
31	MW699630	India: Assam	B.1.1.7/Alpha	18/02/21
32	MW648379	India: Assam	B.1.1.7/Alpha	29/01/21
33	MW648380	India: Assam	B.1.1.7/Alpha	29/01/21
34	MW648381	India: Assam	B.1.1.7/Alpha	10/02/21
35	MW646466	Pakistan	NA	02/12/20
36	MW642506	Pakistan	NA	02/12/20
37	MW644688	Pakistan	NA	02/12/20
38	MW644689	Pakistan	NA	02/12/20
39	MW644690	Pakistan	NA	02/12/20
40	MW617293	Pakistan	NA	25/01/21
41	MW617298	Pakistan	NA	25/01/21
42	MW617306	Pakistan	NA	08/02/21
43	MW617312	Pakistan	NA	26/01/21
44	MW617321	Pakistan	NA	26/01/21
45	MW617324	Pakistan	NA	08/02/21
46	MW617325	Pakistan	NA	08/02/21

NOTE: NA, information is not available in the GenBank database

As exhibited in the table, the phylogenetic trees are categorized into three main clusters. Two clusters are dominated by Indian samples, while the others are dominated by Uzbek and Pakistani samples (Fig. 1(a)). Then, in Fig. 1(b), the radiated tree clearly depicts an S gene sample from Pakistan, which has formed an outlier from the clusters. However, the outlier seemed to be evolutionarily closer to the Indian cluster than the Pakistan one. This phenomenon might happen due to the extensive people exchange between the two countries causing both clusters to be closer.

Consequently, mRNA's conserved sequence has served as a siRNA target. Moreover, Fig. 2 illustrates both mRNA and siRNA sequences in the rightmost area of the box. Moreover, this box also displays siRNA as the best-annotated one in the database. Table 2 shows FASTA-formatted sequences for easier process and further annotation efforts.
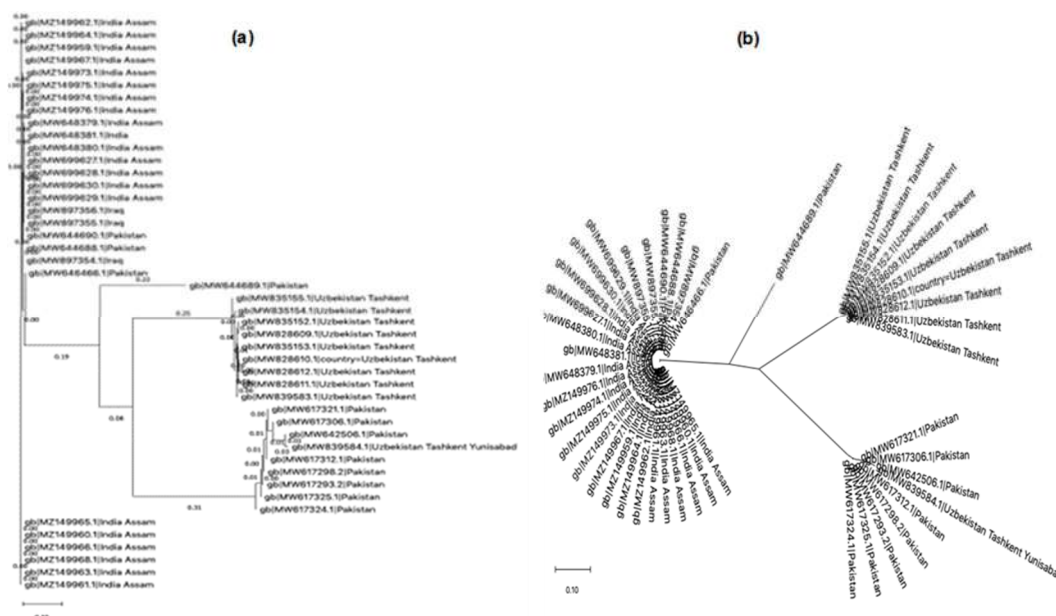
Fig 1. Phylogenetic tree of annotated SARS-CoV-2 S gene from South and Central Asia. (a) Rectangular tree, (b) Radiation tree
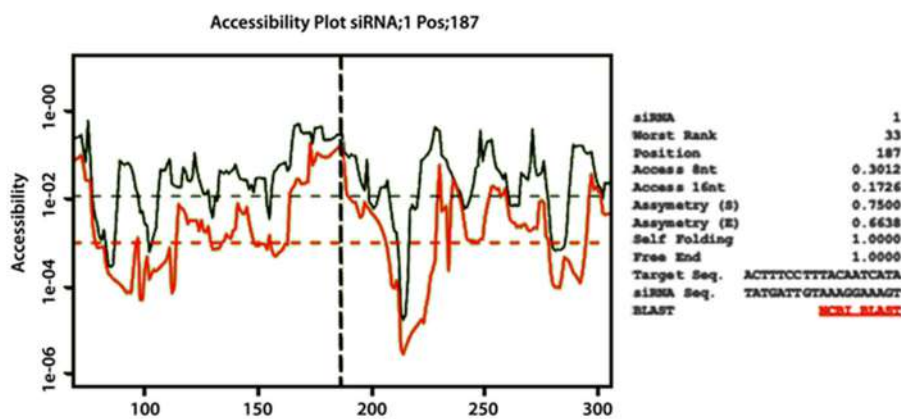
**Fig 2.** RNAxs output for siRNA of SARS-CoV-2 S gene

Table 2. Annotated ncRNA sequences from RNAxs run of SARS-CoV-2 S gene

| Indicator	Value
Rank	33
Position	187
Chosen the best target seq from RNAxs	ACUUUCCUUUACAAUCAUA
Chosen the best siRNA seq from RNAxs	UAUGAUUGUAAAGGAAAGU

Based on the target sequence from RNAxs output above, it is aligned with the consensus sequence of MSA results in Fig. 3. It triggers a significant coverage of consensus regions and exhibits a possibility of siRNA binding in the highlighted region. The consensus region would serve as a foundation for conducting a docking analysis toward the target sequence.

Fig. 4 displays the annotated 2-Dimensional structure of both siRNA's targeted mRNA and its conserved S gene mRNA. Fig. 4(a) is annotated from the
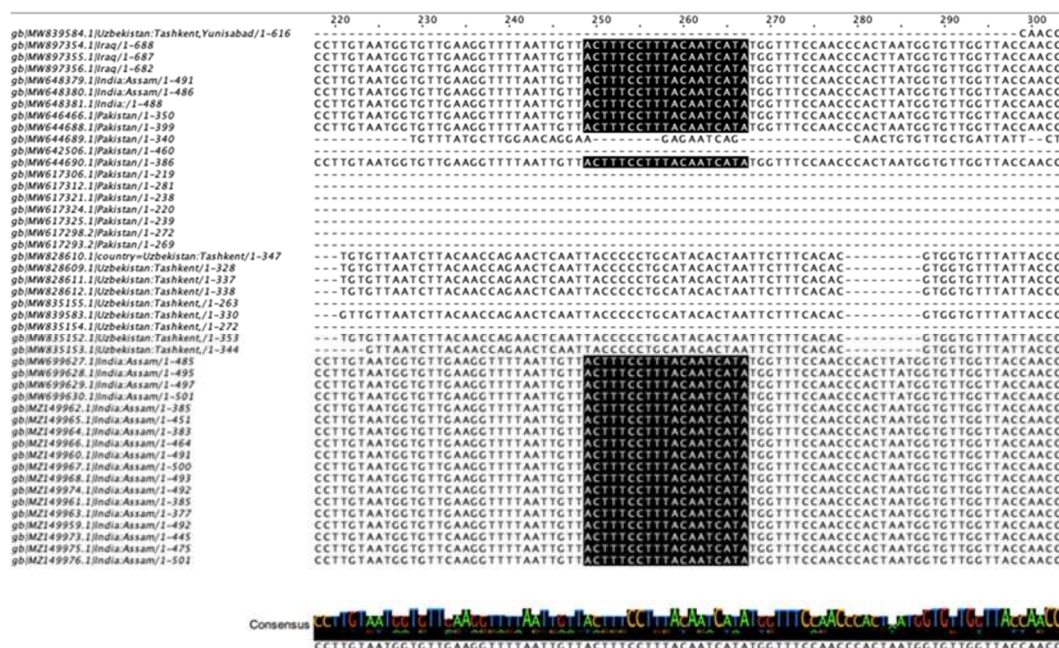
Fig 3. A conserved region of siRNA target in MSA result is highlighted in black. It corresponds to the consensus logo below, and it is the output of JALVIEW 2.11 software
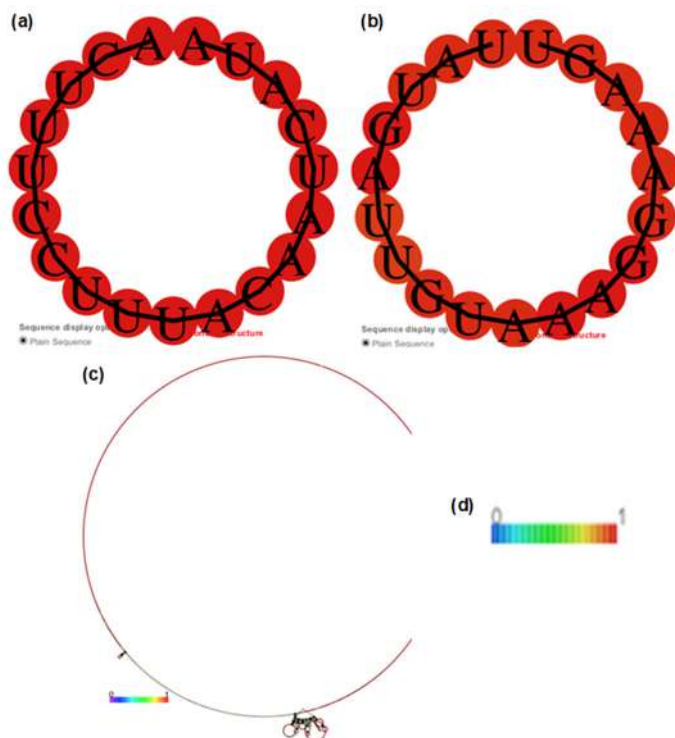
Fig 4. SARS-CoV-2 2D structures prediction (a) S gene mRNA from RNAfold, (b) S gene siRNA from RNAfold, (c) S gene mRNA conserved structure from RNAlifold, (d) A conservation legend, 0 means not conserved, 1 means the most conserved

targeted mRNA gene in Fig. 2. Notably, the minimum free energy prediction of the targeted mRNA is 0.00 kcal/mol; thus, the structure is not considered as spontaneously occurring (Fig. 4(a)). However, siRNA minimum energy is −0.06 kcal/mol indicating a spontaneous structure (Fig. 4(b)). Significantly, the conserved structure minimum energy of S gene mRNA is indicated at −18.62 kcal/mol (Fig. 4(c)). Although it is feasible in a structural manner, the structure has formed an overstretched bulge which is not intuitively feasible in a stereochemical manner. This kind of structure could only exist in a chemical reaction transition state.

Conclusively, it is known from our data that mRNA's structure is singular, not diverse. Thus, the animated structural transition is not feasible to be depicted. The structure of siRNA is more diverse and annotated with three possible conformations, as exhibited in Fig. 5. The very limited number of structural transitions might occur due to the possible steric effects arising from RNA's stereochemical conformation. Moreover, the barrier server only illustrates the transitional structure in a 2D trajectory, thereby limiting the conformational flexibility compared to the 3-dimensional one.
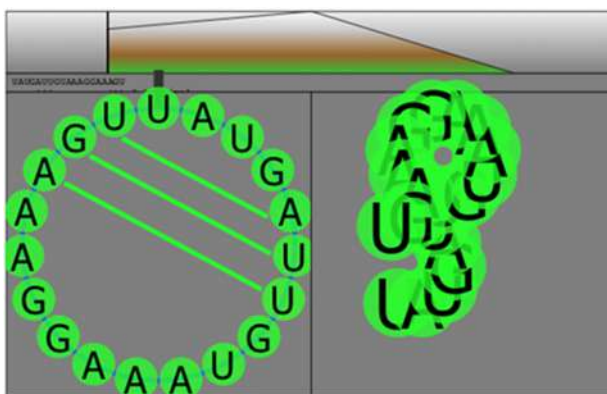
Fig 5. Barrier Server illustration of siRNA 2D conformations

Furthermore, the 3D de novo modeling method has obtained structures of both SARS-CoV-2 S gene conserved mRNA and siRNA (Fig. 6). It displays that both structures differ in their respective conformations. The structure of mRNA clearly expresses a solid loop conformation; therefore, its strand bind to each other (Fig. 6(a)). In contrast, siRNA structure shows a much loose loop conformation because some parts of its strand are not binding to each other (Fig. 6(b)). Regarding 3D structure validation, although they are considered in the warning threshold, both structures produce a near-optimal model that mostly still lies below the quality control threshold of 10% deviation standard from the standard plot (Table 3) [59]. Therefore, it is decided to still proceed with the docking protocol.

Fig. 7 presents the docking results of both mRNA

and siRNA structures which have successfully formed a complex. However, the complex visualization using the HNADOCK built-in visualizer is not vivid enough to
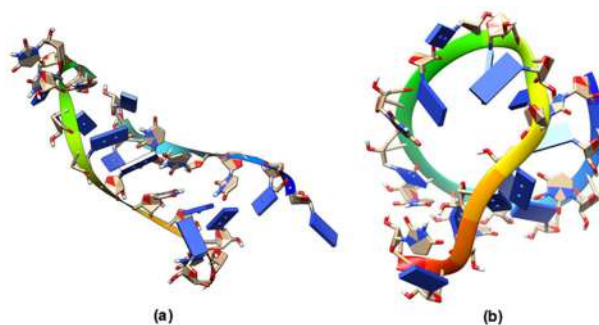

Fig 6. SARS-CoV-2 S gene 3D visualization (a) mRNA, (b) siRNA. Both are illustrated from the result of iFOLDRNA modelling
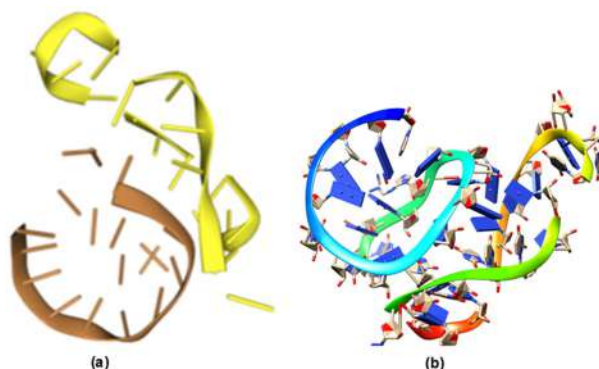

Fig 7. Docking result of SARS-CoV-2 S gene mRNA and siRNA complex (a) Complex visualization using HNADOCK, (b) Complex visualization using UCSF Chimera

Table 3. Molprobity Validation results for RNA 3D Structures. Green is good, yellow is cautious, and red is a warning sign [60]

Indicators	Parameters	siRNA 3D model		mRNA 3D model		Notes
All-atom contacts	Clashscore, all atoms:	206.35		210.72		0th percentile* (N = 1784, all resolutions)
	Clashscore is the number of serious steric overlaps (> 0.4 Å) per 1000 atoms					
Nucleic acid geometry	Probably wrong sugar puckers:	2	10.53%	0	0.00%	Goal: 0
	Bad bonds:	16/460	3.48%	17/434	3.92%	Goal: 0%
	Bad angles:	37/713	5.19%	25/668	3.74%	Goal: < 0.1%
Additional validations	Chiral volume outliers	0/95				
	Waters with clashes	0/0	0.00%			

* The 100th percentile is the best among structures of comparable resolution; the 0th percentile is the worst

Indones. J. Chem., 2022, 22 (5), 1163 - 1176

1171
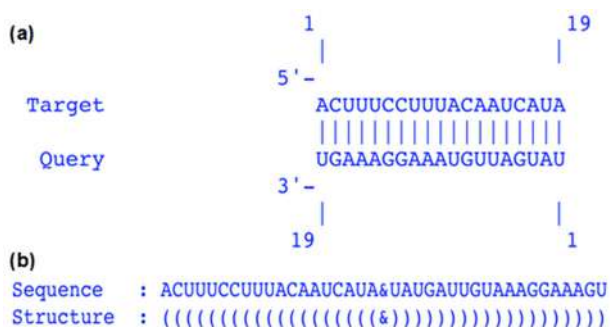
Fig 8. IntaRNA result of SARS-CoV-2 S gene siRNA (Query)-mRNA (Target) complex (a) 2D interactions, (b) Rendition of sequence in FASTA format and structure in Vienna dot-bracket format

observe the conformation (Fig. 7(a)). Thus, the UCSF Chimera visualizer was employed, and a vivid visualization was obtained accordingly (Fig. 7(b)).

The docking visualization has its own limitation in narrating the binding nature because there is no detailed explanation of the involved chemical interactions. Engaging common 2D chemical interactions visualizer such as ligplot+ and leview is not feasible due to their protein-specific scoring function [61-62]. Therefore, Fig. 8 expresses the predicted hydrogen bonds between mRNA and siRNA in a 2D fashion. The rendition of IntaRNA software toward the siRNA-mRNA complex could predict the hydrogen bonding of the pairs. However, the notable absence is other types of interactions, such as Van

der Waals and hydrophobic ones.

As IntaRNA could only provide a general repertoire of siRNA-mRNA chemical interactions, another software was employed to provide a fine-grained resolution of the bindings. PLIP, a package that is normally utilized for protein-ligand interactions, was applied for this matter. Therefore, as seen in Fig. 9, a higher resolution image of the complex's 3D chemical interactions is exposed accordingly. In the interface of siRNA-mRNA interaction, as seen in Fig. 9, a more specific interaction between Adenosine Triphosphate (ATP) and magnesium ion (Mg^{2+}) appears. In the blue box of Fig. 9, it portrays nine hydrogen bonds and π stacking interactions exposing the resonance between two phenyl groups also exist. These interactions, namely hydrogen bond, metal interaction, and π stacking, are the underlying path for siRNA-mRNA complex integrity.

■ CONCLUSION

It is concluded that based on the current S gene data annotation in the GenBank, the delta variant of SARS-CoV-2 has already gained ground throughout the South Asia region. As this variant has already become a dominant feature worldwide, it would serve as a useful blueprint for drug design. Then, this siRNA for SARS-CoV-2 S gene mRNA was designed from the conserved region annotated with significant numbers of delta variant sequences. Both siRNA and mRNA prediction
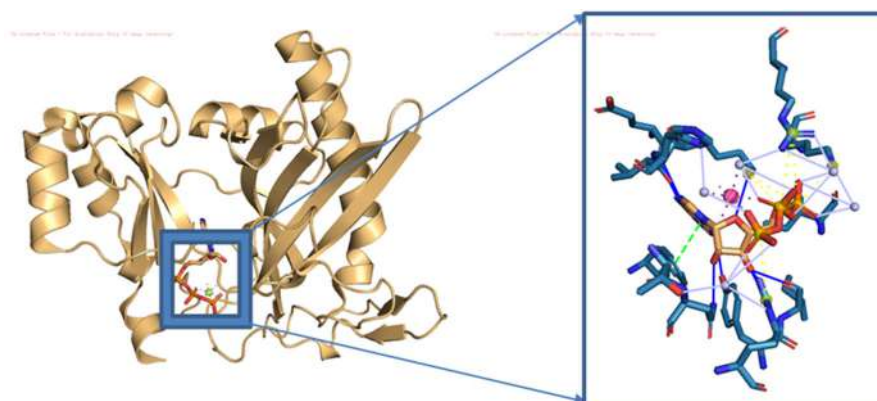
Fig 9. Illustrations of siRNA-mRNA complex with intermolecular siRNA-mRNA interaction, the blue box portray ATP-Mg^{2+} interaction along with the enlarged ATP-Mg^{2+} interactions inside the square. The green ball represents magnesium ions. The red ball represents magnesium ion, while the dashed line represents π-stack, and the straight connecting lines are hydrogen bonding

mechanisms have provided models that could be tested in docking and chemical interaction studies. The chemical interaction studies also produced a high possibility of solid siRNA-mRNA complex integrity. Finally, siRNA design should be elicited in the wet laboratory setting for further validation.

■ AUTHOR CONTRIBUTIONS

AAP conducted and supervised the experiment. AAP, ANMA, and VDK wrote and revised the manuscript. All authors agreed to the final version of this manuscript.

■ REFERENCES

[1] Ansori, A.N.M., Kharisma, V.D., Muttaqin, S.S., Antonius, Y., and Parikesit, A.A., 2020, Genetic variant of SARS-CoV-2 isolates in Indonesia: Spike glycoprotein gene, *J. Pure Appl. Microbiol.*, 14, 971–978.

[2] Turista, D.D.R., Islamy, A., Kharisma, V.D., and Ansori, A.N.M., 2020, Distribution of COVID-19 and phylogenetic tree construction of SARS-CoV-2 in Indonesia, *J. Pure Appl. Microbiol.*, 14, 1035–1042.

[3] Agarwal, A., Rochwerg, B., Lamontagne, F., Siemieniuk, R.A.C., Agoritsas, T., Askie, L., Lytvyn, L., Leo, Y.S., Macdonald, H., Zeng, L., Amin, W., Barragan, F.A.J., Bausch, F.J., Burhan, E., Calfee, C.S., Cecconi, M., Chanda, D., Dat, V.Q., De Sutter, A., Du, B., Freedman, F., Geduld, H., Gee, P., Gotte, M., Harley, N., Hashimi, M., Hunt, B., Jehan, F., Kabra, S.K., Kanda, S., Kim, Y.J., Kissoon, N., Krishna, S., Kuppalli, K., Kwizera, A., Castro-Rial, M.L., Lisboa, T., Lodha, R., Mahaka, I., Manai, H., Mino, G., Nsutebu, E., Preller, J., Pshenichnaya, N., Qadir, N., Relan, P., Sabzwari, S., Sarin, R., Shankar-Hari, M., Sharland, M., Shen, Y., Ranganathan, S.S., Souza, J.P., Stegemann, M., Swanstrom, R., Ugarte, S., Uyeki, T., Venkatapuram, S., Vuyiseka, D., Wijewickrama, A., Tran, L., Zeraatkar, D., Bartoszko, J.J., Ge, L., Brignardello-Petersen, R., Owen, A., Guyatt, G., Diaz, J., Kawano-Dourado, L., Jacobs, M., and Vandvik, P.O., 2020, A living WHO guideline on drugs for covid-19, *BMJ*, 370, m3379.

[4] Kharisma, V.D., and Ansori, A.N.M., 2020, Construction of epitope-based peptide vaccine against SARS-CoV-2: Immunoinformatics study, *J. Pure Appl. Microbiol.*, 14, 999–1005.

[5] Kharisma, V.D., Agatha, A., Ansori, A.N.M., Widyananda, M.H., Rizky, W.C., Dings, T.G.A., Derkho, M., Lykasova, I., Antonius, Y., Rosadi, I., and Zainul, R., 2022, Herbal combination from *Moringa oleifera* Lam. and *Curcuma longa* L. as SARS-CoV-2 antiviral via dual inhibitor pathway: A viroinformatics approach, *J. Pharm. Pharmacogn. Res.*, 10 (1), 138–146.

[6] Fernandes, J.D., Hinrichs, A.S., Clawson, H., Gonzalez, J.N., Lee, B.T., Nassar, L.R., Raney, B.J., Rosenbloom, K.R., Nerli, S., Rao, A.A., Schmelter, D., Fyfe, A., Maulding, N., Zweig, A.S., Lowe, T.M., Ares, M., Corbet-Detig, R., Kent, W.J., Haussler, D., and Haeussler, M., 2020, The UCSC SARS-CoV-2 genome browser, *Nat. Genet.*, 52 (10), 991–998.

[7] Parikesit, A.A., 2020, Protein domain annotations of the SARS-CoV-2 proteomics as a blue-print for mapping the features for drug and vaccine designs, *J. Mat. Sains*, 25, 26–32.

[8] Dai, W., Zhang, B., Jiang, X.M., Su, H., Li, J., Zhao, Y., Xie, X., Jin, Z., Peng, J., Liu, F., Li, C., Li, Y., Bai, F., Wang, H., Cheng, X., Cen, X., Hu, S., Yang, X., Wang, J., Liu, X., Xiao, G., Jiang, H., Rao, Z., Zhang, L.K., Xu, Y., Yang, H., and Liu, H., 2020, Structure-

based design of antiviral drug candidates targeting the SARS-CoV-2 main protease, *Science*, 368 (6497), 1331–1335.

[9] Mansbach, R.A., Chakraborty, S., Nguyen, K., Montefiori, D.C., Korber, B., and Gnanakaran, S., 2021, The SARS-CoV-2 spike variant D614G favors an open conformational state, *Sci. Adv.*, 7 (16), eabf3671.

[10] Fahmi, M., Kharisma, V.D., Ansori, A.N.M., and Ito, M., 2021, Retrieval and investigation of data on SARS-CoV-2 and COVID-19 using bioinformatics approach, *Adv. Exp. Med. Biol.*, 1318, 839–857.

[11] Ansori, A.N.M., Kharisma, V.D., Fadholly, A., Tacharina, M.R., Antonius, Y., and Parikesit, A.A., 2021, Severe acute respiratory syndrome coronavirus-2 emergence and its treatment with alternative medicines: A review, *Res. J. Pharm. Technol.*, 14 (10), 5551–5557.

[12] Beigel, J.H., Tomashek, K.M., Dodd, L.E., Mehta, A.K., Zingman, B.S., Kalil, A.C., Hohmann, E., Chu, H.Y., Luetkemeyer, A., Kline, S., Lopez de Castilla, D., Finberg, R.W., Dierberg, K., Tapson, V., Hsieh, L., Patterson, T.F., Paredes, R., Sweeney, D.A., Short, W.R., Touloumi, G., Lye, D.C., Ohmagari, N., Oh, M., Ruiz-Palacios, G.M., Benfield, T., Fätkenheuer, G., Kortepeter, M.G., Atmar, R.L., Creech, C.B., Lundgren, J., Babiker, A.G., Pett, S., Neaton, J.D., Burgess, T.H., Bonnett, T., Green, M., Makowski, M., Osinusi, A., Nayak, S., Lane, H.C., and ACTT-1 Study Group Members, 2020, Remdesivir for the treatment of Covid-19 - Final report, *N. Engl. J. Med.*, 383 (19), 1813–1826.

[13] O'Dowd, A., 2021, Covid-19: Cases of delta variant rise by 79%, but rate of growth slows, *BMJ*, 373, n1596.

[14] Torjesen, I., 2021, Covid-19: Delta variant is now UK's most dominant strain and spreading through schools, *BMJ*, 373, n1445.

[15] Kusumawati, R.L., Lubis, I., Kumaheri, M.A., Pradipta, A., Faksri, K., Mutiara, M., Shankar, A.H., and Tania, T., 2022, Clinical epidemiology of pediatric COVID-19 Delta variant cases from North Sumatra, Indonesia, *Front. Pediatr.*, 10, 810404.

[16] Burnett, J.C., and Rossi, J.J., 2012, RNA-based therapeutics: Current progress and future prospects, *Chem. Biol.*, 19 (1), 60–71.

[17] Reardon, S., 2021, How the Delta variant achieves its ultrafast spread, *Nature*, 10.1038/d41586-021-01986-w.

[18] Yu, A.M., Jian, C., Yu, A.H., and Tu, M.J., 2019, RNA therapy: Are we using the right molecules?, *Pharm. Ther.*, 196, 91–104.

[19] Pashkov, E.A., Faizuloev, E.B., Svitich, O.A., Sergeev, O.V., and Zverev, V.V., 2020, The potential of synthetic small interfering RNA-based antiviral drugs for influenza treatment, *Vopr. Virusol.*, 65 (4), 182–190.

[20] Qiu, M., Li, Y., Bloomer, H., and Xu, Q., 2021, Developing biodegradable lipid nanoparticles for intracellular mRNA delivery and genome editing, *Acc. Chem. Res.*, 54 (21), 4001–4011.

[21] Le, T.K., Paris, C., Khan, K.S., Robson, F., Ng, W.L., and Rocchi, P., 2021, Nucleic acid-based technologies targeting coronaviruses, *Trends Biochem. Sci.*, 46 (5), 351–365.

[22] Yu, A.M., Choi, Y.H., and Tu, M.J., 2020, RNA drugs and RNA targets for small molecules: Principles, progress, and challenges, *Pharmacol. Rev.*, 72, 862–898.

[23] Sohrab, S.S., El-Kafrawy, S.A., Mirza, Z., Kamal, M.A., and Azhar, E.I., 2018, Design and delivery of therapeutic siRNAs: Application to MERS-coronavirus, *Curr. Pharm. Des.*, 24 (1), 62–77.

[24] Hua, K., Jin, J., Zhao, J., Song, J., Song, H., Li, D., Maskey, N., Zhao, B., Wu, C., Xu, H., and Fang, L., 2016, miR-135b, upregulated in breast cancer, promotes cell growth and disrupts the cell cycle by regulating LATS2, *Int. J. Oncol.*, 48 (5), 1997–2006.

[25] Cruz, J.A., Blanchet, M.F., Boniecki, M., Bujnicki, J.M., Chen, S.J., Cao, S., Das, R., Ding, F., Dokholyan, N.V., Flores, S.C., Huang, L., Lavender, C.A., Lisi, V., Major, F., Mikolajczak, K., Patel, D.J., Philips, A., Puton, T., Santalucia, J., Sijenyi, F., Hermann, T., Rother, K., Rother, M., Serganov, A., Skorupski, M., Soltysinski, T., Sripakdeevong, P., Tuszynska, I., Weeks, K.M., Waldsich, C., Wildauer, M., Leontis, N.B., and Westhof, E., 2012, RNA-Puzzles: A CASP-like evaluation of RNA

three-dimensional structure prediction, *RNA*, 18 (4), 610–625.

[26] Hufsky, F., Beerenwinkel, N., Meyer, I.M., Roux, S., Cook, G.M., Kinsella, C.M., Lamkiewicz, K., Marquet, M., Nieuwenhuijse, D.F., Olendraite, I., Paraskevopoulou, S., Young, F., Dijkman, R., Ibrahim, B., Kelly, J., Le Mercier, P., Marz, M., Ramette, A., and Thiel, V., 2020, The international virus bioinformatics meeting 2020, *Viruses*, 12 (12), 1398.

[27] Marz, M., Beerenwinkel, N., Drosten, C., Fricke, M., Frishman, D., Hofacker, I.L., Hoffmann, D., Middendorf, M., Rattei, T., Stadler, P.F., and Töpfer, A., 2014, Challenges in RNA virus bioinformatics, *Bioinformatics*, 30 (13), 1793–1799.

[28] Li, B., Cao, Y., Westhof, E., and Miao, Z., 2020, Advances in RNA 3D structure modeling using experimental data, *Front. Genet.*, 11, 574485.

[29] Kang, Y., and Fortmann, C.M., 2013, An alternative approach to protein folding, *BioMed Res. Int.*, 2013, 583045.

[30] Wei, G., Xi, W., Nussinov, R., and Ma, B., 2016, Protein ensembles: How does nature harness thermodynamic fluctuations for life? The diverse functional roles of conformational ensembles in the cell, *Chem. Rev.*, 116 (11), 6516–6551.

[31] Smerlak, M., 2021, Quasi-species evolution maximizes genotypic reproductive value (not fitness or flatness), *J. Theor. Biol.*, 522, 110699.

[32] Li, C.Y., de Veer, S.J., Law, R.H.P., Whisstock, J.C., Craik, D.J., and Swedberg, J.E., 2019, Characterising the subsite specificity of urokinase-type plasminogen activator and tissue-type plasminogen activator using a sequence-defined peptide aldehyde library, *ChemBioChem*, 20 (1), 46–50.

[33] Seidel, T., Schuetz, D.A., Garon, A., and Langer, T., 2019, The pharmacophore concept and its applications in computer-aided drug design, *Prog. Chem. Org. Nat. Prod.*, 110, 99–141.

[34] Buglak, A.A., Samokhvalov, A.V., Zherdev, A.V., and Dzantiev, B.B., 2020, Methods and applications of in silico aptamer design and modeling, *Int. J. Mol. Sci.*, 21 (22), 8420.

[35] Wang, J., 2020, Fast identification of possible drug treatment of coronavirus disease-19 (COVID-19) through computational drug repurposing study, *J. Chem. Inf. Model.*, 60 (6), 3277–3286.

[36] Parikesit, A.A., and Ramanto, K.N., 2019, The binding prediction model of the iron-responsive element binding protein and iron-responsive elements, *Bioinf. Biomed. Res. J.*, 2 (1), 12–20.

[37] Ivan, J., Nurdiansyah, R., and Parikesit, A.A., 2020, Computational modeling of AGO-mediated molecular inhibition of ARF6 by miR-145, *Indones. J. Biotechnol.*, 25 (2), 102–108.

[38] Valeska, M.D., and Parikesit, A.A., 2020, Structural bioinformatics approach for the molecular models of miR-135b and its silencer as triple negative breast cancer (TNBC) biomarkers, *Horiz. Cancer Res.*, 77, 232–245.

[39] Parikesit, A.A., and Nurdiansyah, R., 2020, The predicted structure for the anti-sense siRNA of the RNA polymerase enzyme (RdRp) gene of the SARS-CoV-2, *Berita Biologi*, 19 (1), 97–108.

[40] Brister, J.R., Ako-Adjei, D., Bao, Y., and Blinkova, O., 2015, NCBI viral genomes resource, *Nucleic Acids Res.*, 43 (D1), D571–D577.

[41] Giulietti, M., Righetti, A., Cianfruglia, L., Šabanović, B., Armeni, T., Principato, G., and Piva, F., 2018, To accelerate the Zika beat: Candidate design for RNA interference-based therapy, *Virus Res.*, 255, 133–140.

[42] Procter, J.B., Carstairs, G.M., Soares, B., Mourão, K., Ofoegbu, T.C., Barton, D., Lui, L., Menard, A., Sherstnev, N., Roldan-Martinez, D., Duce, S., Martin, D.M.A., and Barton, G.J., 2021, Alignment of biological sequences with Jalview, *Methods Mol. Biol.*, 2231, 203–224.

[43] Velandia-Huerto, C.A., Yazbeck, A.M., Schor, J., and Stadler, P.F., 2022, Evolution and phylogeny of microRNAs — Protocols, pitfalls, and problems, *Methods Mol. Biol.*, 2257, 211–233.

[44] Ender, A., Stadler, P.F., Mörl, M., and Findeiß, S., 2022, RNA design principles for riboswitches that regulate RNase P-mediated tRNA processing, *Methods Mol. Biol.*, 2518, 179–202.

[45] Günzel, C., Kühnl, F., Arnold, K., Findeiß, S., Weinberg, C.E., Stadler, P.F., and Mörl, M., 2021, Beyond plug and pray: Context sensitivity and in silico design of artificial neomycin riboswitches, *RNA Biol.*, 18 (4), 457–467.

[46] Stadler, P.F., 2021, Alignments of biomolecular contact maps, *Interface Focus*, 11 (4), 20200066.

[47] Yuan, L., Guo, Z.H., Cao, W.J., Luo, Y., and Shi, Y.Z., 2021, An Integrated Tool for RNA 3D Structure Prediction and Analysis, *2021 33rd Chinese Control and Decision Conference (CCDC)*, 4293–4297.

[48] Krokhotin, A., Houlihan, K., and Dokholyan, N.V., 2015, iFoldRNA v2: Folding RNA with constraints, *Bioinformatics*, 31 (17), 2891–2893.

[49] Williams, C.J., Headd, J.J., Moriarty, N.W., Prisant, M.G., Videau, L.L., Deis, L.N., Verma, V., Keedy, D.A., Hintze, B.J., Chen, V.B., Jain, S., Lewis, S.M., Arendall, W.B., Snoeyink, J., Adams, P.D., Lovell, S.C., Richardson, J.S., and Richardson, D.C., 2018, MolProbity: More and better reference data for improved all-atom structure validation, *Protein Sci.*, 27 (1), 293–315.

[50] Hanwell, M.D., Curtis, D.E., Lonie, D.C., Vandermeersch, T., Zurek, E., and Hutchison, G.R., 2012, Avogadro: An advanced semantic chemical editor, visualization, and analysis platform, *J. Cheminf.*, 4 (1), 17.

[51] Avery, P., Ludowieg, H., Autschbach, J., and Zurek, E., 2017, Extended Hückel calculations on solids using the Avogadro molecular editor and visualizer, *J. Chem. Educ.*, 95 (2), 331–337.

[52] He, J., Wang, J., Tao, H., Xiao, Y., and Huang, S.Y., 2019, HNADOCK: A nucleic acid docking server for modeling RNA/DNA–RNA/DNA 3D complex structures, *Nucleic Acids Res.*, 47 (W1), W35–W42.

[53] Raden, M., Ali, S.M., Alkhnbashi, O.S., Busch, A., Costa, F., Davis, J.A., Eggenhofer, F., Gelhausen, R., Georg, J., Heyne, S., Hiller, M., Kundu, K., Kleinkauf, R., Lott, S.C., Mohamed, M.M., Mattheis, A., Miladi, M., Richter, A.S., Will, S., Wolff, J., Wright, P.R., and Backofen, R., 2018, Freiburg RNA tools: A central online resource for RNA-focused research and teaching, *Nucleic Acids Res.*, 46 (W1), W25–W29.

[54] Raden, M., Müller, T., Mautner, S., Gelhausen, R., and Backofen, R., 2020, The impact of various seed, accessibility and interaction constraints on sRNA target prediction- a systematic assessment, *BMC Bioinf.*, 21 (1), 15.

[55] Mann, M., Wright, P.R., and Backofen, R., 2017, IntaRNA 2.0: Enhanced and customizable prediction of RNA-RNA interactions, *Nucleic Acids Res.*, 45 (W1), W435–W439.

[56] Salentin, S., Schreiber, S., Haupt, V.J., Adasme, M.F., and Schroeder, M., 2015, PLIP: Fully automated protein-ligand interaction profiler, *Nucleic Acids Res.*, 43 (W1), W443–W447.

[57] Butt, S.S., Badshah, Y., Shabbir, M., and Rafiq, M., 2020, Molecular docking using Chimera and Autodock Vina software for nonbioinformaticians, *JMIR Bioinf. Biotechnol.*, 1, e14232.

[58] WHO, 2021, *Novel Coronavirus Disease (Covid-19): Situation Update Report - 50*, World Health Organization, New Delhi, India.

[59] Chen, V.B., Wedell, J.R., Wenger, R.K., Ulrich, E.L., and Markley, J.L., 2015, MolProbity for the masses– of data, *J. Biomol. NMR*, 631 (1), 77–83.

[60] Molprobity, 2021, *Molprobity Legend for Structural Validation*, http://molprobity.biochem.duke.edu/ help/validation_options/summary_table_guide.html.

[61] Laskowski, R.A., and Swindells, M.B., 2011, LigPlot+: Multiple ligand-protein interaction diagrams for drug discovery, *J. Chem. Inf. Model.*, 51 (10), 2778–2786.

[62] Caboche, S., 2013, LeView: Automatic and interactive generation of 2D diagrams for biomacromolecule/ligand interactions, *J. Cheminf.*, 5 (1), 40.

[63] Maladan, Y., Krismawati, H., Hutapea, H.M.L., Oktavian, A., Fatimah, R., and Widodo, W., 2019, A new *Mycobacterium leprae* dihydropteroate synthase variant (V39I) from Papua, Indonesia, *Heliyon*, 5 (3), e01279.

[64] Tüzün, B., and Kaya, C., 2018, Investigation of DNA–RNA molecules for the efficiency and activity of corrosion inhibition by DFT and molecular docking, *J. Bio- Tribo-Corros.*, 4 (4), 69.

[65] Yan, Y., and Huang, S.Y., 2020, Modeling protein–protein or protein–DNA/RNA complexes using the HDOCK webserver, *Methods Mol. Biol.*, 2165, 217–229.

[66] Parikesit, A.A., 2021, "Introductory Chapter: The Emerging Corner of the Omics Studies for Rational Drug Design" in *Drug Design - Novel Advances in the Omics Field and Applications*, IntechOpen, Rijeka, 4.

[67] Parikesit, A.A., 2018, "Introductory Chapter: The Contribution of Bioinformatics as Blueprint Lead for Drug Design" in *Molecular Insight of Drug Design*, IntechOpen, Rijeka, 7.

[68] Ivan, J., Agustriawan, D., Parikesit, A.A., and Nurdiansyah, R., 2021, MiRNA-regulated HspB8 as potent biomarkers in low-grade gliomas, *Res. J. Biotechnol.*, 16 (1), 17–25.

[69] Agustriawan, D., Parikesit, A.A., Nurdiansyah, R., Ivan, J., and Ramanto, K.N., 2021, Correlation and transcriptomic analysis revealing potential microRNA-gene interactions associated with breast cancer formation, *Res. J. Biotechnol.*, 16 (2), 16–23.

[70] Medeiros, I.G., Khayat, A.S., Stransky, B., Santos, S., Assumpção, P., and de Souza, J.E.S., 2021, A small interfering RNA (siRNA) database for SARS-CoV-2, *Sci. Rep.*, 11 (1), 8849.

[71] Donia, A., and Bokhari, H., 2021, RNA interference as a promising treatment against SARS-CoV-2, *Int. Microbiol.*, 24 (1), 123–124.

[72] Idris, A., Davis, A., Supramaniam, A., Acharya, D., Kelly, G., Tayyar, Y., West, N., Zhang, P., McMillan, C.L.D., Soemardy, C., Ray, R., O'Meally, D., Scott, T.A., McMillan, N.A.J., and Morris, K.V., 2021, A SARS-CoV-2 targeted siRNA-nanoparticle therapy for COVID-19, *Mol. Ther.*, 29 (7), 2219–2226.

[73] Khaitov, M., Nikonova, A., Shilovskiy, I., Kozhikhova, K., Kofiadi, I., Vishnyakova, L., Nikolskii, A., Gattinger, P., Kovchina, V., Barvinskaia, E., Yumashev, K., Smirnov, V., Maerle, A., Kozlov, I., Shatilov, A., Timofeeva, A., Andreev, S., Koloskova, O., Kuznetsova, N., Vasina, D., Nikiforova, M., Rybalkin, S., Sergeev, I., Trofimov, D., Martynov, A., Berzin, I., Gushchin, V., Kovalchuk, A., Borisevich, S., Valenta, R., Khaitov, R., and Skvortsova, V., 2021, Silencing of SARS-CoV-2 with modified siRNA-peptide dendrimer formulation, *Allergy*, 76 (9), 2840–2854.

[74] Tenda, E.D., Asaf, M.M., Pradipta, A., Kumaheri, M.A., and Susanto, A.P., 2021, The COVID-19 surge in Indonesia: What we learned and what to expect, *Breathe*, 17, 210146.

[75] Dyer, O., 2021, Covid-19: Indonesia becomes Asia's new pandemic epicentre as delta variant spreads, *BMJ*, 374, n1815.

[76] Kupferschmidt, K., and Wadman, M., 2021, Delta variant triggers new phase in the pandemic, *Science*, 372 (6549), 1375–1376.

Phase Transfer Catalyzed Preparation of 4-Methylbenzenesulfonyl Imidazole for Regioselective Synthesis of Mono-6-(4-methylbenzenesulfonyl)-β-cyclodextrin

I Wayan Muderawan[1*], I Wayan Mudianta[1], and Made Kurnia Widiastuti Giri[2]

[1]Department of Chemistry, Faculty of Mathematics and Natural Sciences, Ganesha University of Education, Singaraja 81117, Bali, Indonesia

[2]Study Program of Medicine, Faculty of Medicine, Ganesha University of Education, Singaraja 81117, Bali, Indonesia

Abstract: *The preparation of 4-methylbenzenesulfonyl imidazole by using triethylamine as an effective phase-transfer catalyst (PTC) under mild biphasic conditions has been studied intensively. The method can be used for large-scale preparation with high purity and high yield of 4-methylbenzene-sulfonyl imidazole. The result in 4-methylbenzenesulfonyl imidazole has been successfully applied for the regioselective synthesis of mono-6-(4-methylbenzenesulfonyl)-β-cyclodextrin in an aqueous medium. This synthetic methodology concept, together with the synthetic versatility of PTC, provides a general and reliable general strategy for the practical and industrial regioselective synthesis of highly valuable mono-6-(4-methylbenzenesulfonyl)-β-cyclodextrin as a key intermediate for the single functional isomer mono-substituted cyclodextrin derivatives. As characterized by FTIR, NMR and mass spectrometry, mono-6-(4-methylbenzenesulfonyl)-β-cyclodextrin was obtained in high purity.*

Keywords: *phase transfer catalysis; 4-methylbenzenesulfonyl imidazole; regioselective synthesis; mono-6-(4-methylbenzenesulfonyl)-β-cyclodextrin*

■ INTRODUCTION

Cyclodextrins (CDs) are naturally occurring cyclic oligosaccharides consisting of six, seven, and eight glucopyranose units, which are termed α-, β-, and γ-cyclodextrins, respectively [1-2]. These oligosaccharides consist of α-1,4-connection of each α-D-glucopyranose unit to form cyclic structures and they are shaped like truncated cones rather than perfect cylinders. Native cyclodextrins have limited aqueous solubility. In particular, β-cyclodextrin (β-CD) forms intramolecular hydrogen bonds between secondary OH groups at C-2 and C-3 positions which detract from hydrogen bond formation with surrounding water molecules, resulting in less negative heat of hydration and significant lowering of solubility, i.e., 18.5 g/L at 25 °C [2]. In order to improve the solubility of β-cyclodextrin in aqueous media, it is necessary to modify β-cyclodextrin by substituting one OH group at either 2- or 6-position with other groups to give functionalized CD derivatives which are more soluble in water [3-4].

Mono-6-(4-methylbenzenesulfonyl)-β-CD is the most important precursor to further functionalize the primary hydroxyl groups (C-6) of β-CD, since 4-methylbenzenesulfonylate is a good leaving group and can be easily substituted by other nucleophiles [5-6]. The most convenient procedure to prepare mono-6-(4-methylbenzenesulfonyl)-β-CD is by using 4-methylbenzenesulfonyl imidazole as an important reagent reacting with β-CD in a basic medium [7]. The reported procedure for preparation of 4-methylbenzenesulfonyl imidazole employs an excess amount of imidazole, a lot of organic solvents, including dichloromethane (500 mL), a mixture of ethyl acetate-*n*-hexane (500 mL), ethyl acetate (50 mL), *n*-hexane (500 mL), 3.5 h reaction, and complicated purification process [7]. The synthetic methodology, in particular, the purification steps was challenging, used a lot of solvents, produced many waste materials, and resulted

in a long and expensive procedure. These wastes should be destroyed, disposed, or regenerated thus consuming a lot of energy and creating a serious and heavy burden on the environment. Therefore, it is of great importance to develop, provide and use new synthetic methodologies of 4-methylbenzene-sulfonyl imidazole that minimize these problems. Perhaps one of the most general, efficient, and effective methodologies that fulfill this requirement is phase-transfer catalysis (PTC) [8-10]. This PTC synthetic methodology is applicable to a great variety of reactions in which organic substrates react with organic and inorganic anions. It consists of the use of heterogeneous two-phase systems - one phase being a reservoir of reacting base or anions for the generation of organic anions in an aqueous system, whereas catalyst and organic reactants as the source of lipophilic cations are present in the other (organic) phase [9].

Here, we report a convenient and economical method for the preparation of 4-methylbenzene-sulfonyl imidazole by using PTC on a high scale with high yields. Moreover, the use of 4-methylbenzene-sulfonyl imidazole as a precursor in synthesis with β-cyclodextrin is described to obtain a highly pure mono-6-(4-methylbenzene sulfonyl)-β-cyclodextrin with an acceptable yield in the aqueous media.

■ **EXPERIMENTAL SECTION**

Materials

Imidazole was purchased from Merck. Triethylamine, β-cyclodextrin, sodium bicarbonate, sodium hydroxide, anhydrous magnesium sulfate, dichloromethane, acetone, and *n*-hexane were purchased from Sigma-Aldrich. The 4-methylbenzenesulfonyl chloride and ammonium chloride were purchased from Fluka. All chemicals were directly used without further purification.

Instrumentation

Melting points were determined with Büchi Melting Point B-540 apparatus. Elemental analyses were performed with a Perkin Elmer 240C elemental analyzer for C, H, N, and S determination. UV-Vis spectra were recorded by using Double Beam Spectrophotometer Shimadzu UV-1800. Infrared spectra were recorded with a Perkin Elmer 1600 spectrometer and samples were prepared as KBr pellets. Electron spray ion mass spectrometry (ESI MS) was performed on a Finningan TSQ7000 mass spectrometer. The ^{1}H and ^{13}C-NMR spectra were recorded with a Bruker ACF 300 Spectrometer. Samples were dissolved in deuterated solvents and chemical shifts (δ) are reported in parts per million (ppm) according to tetramethylsilane (TMS) as the internal standard.

Procedure

Synthesis of 4-methylbenzenesulfonylimidazole (BsIm)

Imidazole (136.16 g, 2.0 mol) and 4-methylbenzenesulfonyl chloride (381.28 g, 2.1 mol) were dissolved in dichloromethane (1500 mL) in an Erlenmeyer. Sodium bicarbonate (176.421 g, 2.1 mol) was added to the water (1500 mL) and followed by the addition of triethylamine (20 mL) as a PTC. The two-layer mixtures, aqueous and organic layers, were stirred at room temperature. Carbon dioxide gas was released during the reaction and the mixture was continuously stirred for 4 h until no more gas formed. The organic layer was separated and the aqueous layer was extracted with dichloromethane (3 × 1000 mL). The organic phases were combined and dried with anhydrous MgSO$_4$, then filtered, concentrated to approximately 750 mL, and added with *n*-hexane (150 mL). The mixture was allowed overnight to form a white crystal and the crystal was filtered and dried under vacuum to give the desired product (425.62 g, 93.5%) with a melting point of 77.5–78.5 °C (lit. 78.0–79.0 °C) [7].

FTIR (cm^{-1}, KBr): 3159, 3103, 3032, 1595, 1516, 1383, 1151. ^{1}H-NMR (300 MHz, CDCl$_3$) δ: 2.42 (s, 3H, CH$_3$), 7.07 (s, 1H, =CH-4$_{im}$), 7.28 (s, 1H, =CH-5$_{im}$), 7.34 (d, 2H, *J* = 8.43 Hz, =CH$_{meta}$), 7.81 (d, 2H, *J* = 8.01 Hz, =CH$_{ortho}$), 7.99 (s, 1H, =CH-2$_{im}$). ^{13}C-NMR (75 MHz, CDCl$_3$) δ: 21.5 (CH$_3$), 117.4 (C4), 127.2 (C$_{meta}$), 130.3 (C$_{ortho}$), 131.2 (C5), 134.8 (C$_{para}$), 136.5 (C2), 146.2 (C$_{ipso}$). ESI-MS (*m/z*): 223.03 [M+H]$^+$, calc. 223.05.

Synthesis of mono-6-(4-methylbenzenesulfonyl)-β-cyclodextrin

In this study, a modified reported procedure was used to synthesize mono-6-(4-methylbenzenesulfonyl)-β-cyclodextrin [7]. The 4-methylbenzenesulfonyl imidazole (12.22 g, 0.055 mol) was added to a suspension of β-cyclodextrin hydrate (67.55 g, 0.05 mol) in water (500 mL). The mixture was allowed to be stirred for 2 h. A solution of sodium hydroxide (20 g in 100 mL, 0.5 mol) was added and stirred for 10 min. The insoluble solid was removed by filtration. The filtrate was neutralized to pH value was approximately 7.0 by adding ammonium chloride. The white solid formed was collected by filtration and washed with cold water to give the product (27.5 g, 42.5%) with a melting point of 173 °C slow dec., (lit. 163–168 °C (dec.) [11].

FTIR (cm^{-1}, KBr): 3400, 2935, 1647, 1367, 1159, 1080, 1031, 582. ^{1}H-NMR (300 MHz, DMSO-$_{d6}$) δ : 2.43 (s, 3H, CH$_3$), 3.22-3.40 (overlap with HDO, m, 14 H, H-2 and H-4), 3.46–3.65 (m, 28H, H-5, H-3, and H-6), 4.16–4.22 (m, 1H, OH-6), 4.31–4.40 (m, 1H, OH-6), 4.45–4.53 (m, 4H, OH-6), 4.77 (d, 2H, J = 3.21 Hz, H-1), 4.84 (d, 5H, J = 3.24 Hz, H-1), 5.64–5.83 (m, 14H, OH-3 and OH-2), 7.43 (d, 2H, J = 8.4 Hz, =CH$_{meta}$ aromatic), 7.75 (d, 2H, J = 8.4 Hz, =CH$_{orto}$ aromatic). ^{13}C-NMR (75 MHz, DMSO-$_{d6}$) δ: 21.2 (CH$_3$), 59.9 (C-6), 68.9 (C-6'), 69.7 (C-5'), 72.0 (C-5), 72.4 (C-3), 73.0 (C-2), 80.7 (C-4'), 81.5 (m, C-4), 101.9 (C-1), 101.2 (C-1'), 127.6 (C$_{meta}$), 129.9 (C$_{ortho}$), 132.7 (C$_{para}$), 144.8 (C$_{ipso}$). ESI-MS (m/z): 1311.2 [M+Na]$^+$, calc. 1311.38. Microanalysis (%): C 45.3, H 6.1, S 2.4; calc., C 45.7, H 5.9, S 2.5.

Determination of binding constant of BsIm/β-CD inclusion complex

The binding constant of the inclusion complex was determined according to the reported procedure [12] with slight modification. The standard solution of 4-methylbenzenesulfonyl imidazole (BsIm) in water (5 mL, 5×10^{-5} M) and a volume (5 mL) of a standard solution of β-CD solution (2, 4, 6, and 8×10^{-3} M) were placed in a volumetric flask (10 mL). The volume was adjusted with deionized water and the mixture was stirred for 30 min to allow the formation of the complex. The absorbance of resultant solutions was determined using a UV-Vis spectrophotometer.

RESULTS AND DISCUSSION

Synthesis of 4-Methylbenzenesulfonylimidazole

The 4-methylbenzenesulfonylimodazole has been prepared from the 4-methylbenzenesulfonyl chloride by reaction with 2.26 equivalents of imidazole and 1.0 equivalent of triethylamine in dichloromethane [7]. For high-scale preparation or industrial purpose, the method is not convenient because consuming a lot of imidazole as substrate, triethylamine as a catalyst, dichloromethane, ethyl acetate and n-hexane as solvents, as well as long purification processes. Hence, we developed a new synthetic method by using PTC, and this method has advantages for industrial manufacturing as it is more effective and efficient. PTC reactions of organic anions use the inorganic phase contains bases such as concentrated aqueous or solid NaOH or KOH or solid K$_2$CO$_3$ as aqueous solutions whereas the organic phase contains the anion precursor, an electrophilic reactant, and eventually a solvent [8-10].

This methodology is efficiently applicable for the preparation of 4-methylbenzenesulfonyl imidazole. The mixture of 4-methylbenzenesulfonyl chloride, imidazole and triethylamine in a catalytic amount was dissolved in dichloromethane. The mixture was added with a saturated solution of sodium bicarbonate to form immiscible two-phase systems – the organic and aqueous phases. Since both phases are mutually immiscible, the reaction does not proceed unless the catalyst, usually a trialkylamine, R$_3$N is present. In the organic phase, in the presence of triethylamine, 4-methylbenzene-sulfonyl chloride reacts with imidazole to produce 4-methylbenzenesulfonyl imidazole and hydrochloric acid (HCl). The HCl further reacts with triethylamine to give quaternary ammonium salt which is soluble and transfers into an aqueous layer. In the aqueous phase, the ammonium salt then reacts with sodium bicarbonate and produces water, sodium chloride, carbon dioxide (CO$_2$) gas, and triethylamine (Scheme 1). The regenerated triethylamine returns to
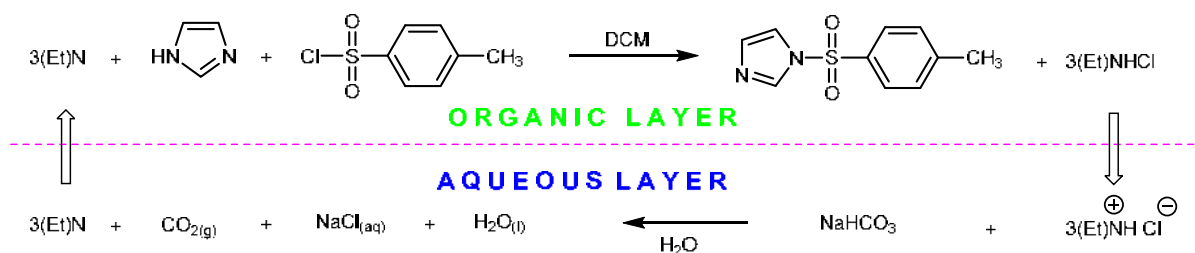
Scheme 1. Synthesis of 4-methylbenzenesulfonyl imidazole using phase transfer catalysis method

the organic layer and the cycle continues until all of 4-methylbenzenesulfonyl chloride completely reacts with imidazole. The end of the reaction can be monitored from the absence of CO_2 bubbles.

The method used triethylamine in catalytic amount and could be used for high-scale preparation and gives a high yield. In this study, the synthetic method used 0.1 to 2.0 mol of imidazole and 4-methylbenzenesulfonyl chloride with a yield in the range of 93–94%. The comparison of the quantities of reactants, catalysts, solvents and products obtained in the preparation of 4-methylbenzenesulfonyl imidazole is given in Table 1. A similar reaction has been performed without phase transfer catalyst and the yield was 75–78%. This yield is lower than the reaction with a phase transfer catalyst, which is probably due to an incomplete reaction or equilibrium reaction.

This new synthetic method of making 4-methylbenzenesulfonyl imidazoles which are more efficient and effective used 4-methylbenzenesulfonyl chloride and imidazole reagents, tertiary amine as phase transfer catalyst, organic solvents, dichloromethane, and water to form two liquid phases and do not dissolve in each other. Upon completion of the reaction, the organic phases, dichloromethane layers, which contain the pure product,

is separated by simple distillation and the product can be subsequently purified by crystallization. The dichloromethane obtained from distillation and aqueous phase upon separation of NaCl formed can be used again for another reaction process so the only waste is solid NaCl. Moreover, the 4-methylbenzenesulfonyl imidazole produced has been successfully used as a precursor in synthesis with β-cyclodextrin to obtain a highly pure mono-6-(4-methylbenzenesulfonyl)-β-cyclodextrin in an aqueous environment with an acceptable yield.

Synthesis of Mono-6-(4-methylbenzenesulfonyl)-β-cyclodextrin

Cyclodextrins are toroidal cyclic oligosaccharides with the primary C-6 hydroxyl group on the smaller open face and the secondary hydroxyls of glucose C-2 and C-3 on their more open face which can be modified with various functional groups. Chemical modifications of cyclodextrins influence the shape of the macrocyclic structure, the size of the molecular cavity, the ability to form hydrogen bonds, and in other physical properties. Therefore, the catalytic behavior and the binding properties can be controlled by the introduction of functional groups.

Table 1. The reactants ratio used and the yield of 4-methylbenzenesulfonyl imidazole

| Imidazole (mol)	4-Methylbenzene-sulfonyl chloride (mol)	Et₃N (mL)	DCM (mL)	NaHCO₃ (mol)	H₂O (mL)	Yield g (%)
0.10	0.10	1.00	100	0.11	100	20.89 (94.00)
0.20	0.20	2.00	200	0.21	200	42.02 (94.50)
0.30	0.30	3.00	250	0.32	250	62.88 (94.30)
0.40	0.40	4.00	300	0.42	300	84.05 (94.50)
0.50	0.50	5.00	400	0.53	400	103.68 (93.30)
1.00	1.00	10.00	750	1.05	750	206.48 (92.90)
1.50	1.50	15.00	1200	1.58	1200	311.72 (93.50)
2.00	2.00	20.00	1500	2.10	1500	415.62 (93.50)

Establishing the synthetic approach for mono sulfonylation of one of the C-6 primary hydroxyl groups of β-cyclodextrin is an important step in providing a suitable intermediate for the introduction of a variety of other substituents or coupling of β-cyclodextrin at its primary hydroxyl group [13-16]. The selective chemical modification of cyclodextrins is possible by using the differences in reactivity of the three types of hydroxyl groups. The primary hydroxyl groups of the cyclodextrins are the most basic compared to the C-2- and C-3-hydroxyls which are secondary alcohols. They are also the most nucleophilic, as a consequence of which they may be selectively modified through their reaction with electrophilic species. While different synthetic methods for selectively functionalization, one single primary (C-6) hydroxyl group of cyclodextrins were reported and several by-products may be formed, requiring extensive subsequent purification procedures [17]. The most common synthetic strategies employed either organic or aqueous solvent/base systems.

Among numerous β-cyclodextrin derivatives, of particular interest is mono-6-(4-methylbenzenesulfonyl)-β-cyclodextrin [17]. The known methods of synthesis of this compound include acylation of β-cyclodextrin with 4-methylbenzenesulfonic hydride [18] and with 4-methylbenzenesulfonyl chloride in DMF [19], pyridine [20], aqueous acetonitrile [21], or sodium hydroxide solution [11]. These procedures utilize toxic solvents and are multistep and time- and energy-consuming.

In this study, mono-6-(4-methylbenzenesulfonyl)-β-cyclodextrin was synthesized using 4-methylbenzenesulfonyl imidazole (Scheme 2) and the yield was given in Table 2. It should be noted that the obtained mono-6-(4-methylbenzenesulfonyl)-β-cyclodextrin is characterized by high purity, so it can be used without additional purification.

As indicated in Scheme 2, a β-cyclodextrin molecule contains three types of hydroxyl groups, each including seven hydroxyl groups, in positions C-2, C-3 and C-6. The molecular structure of β-cyclodextrin has the form of a truncated cone, and unlike hydroxyl groups attached to the C-3 and C-6, the hydroxyl group is attached to the second carbon atom (OH-2) is oriented into the cavity of the cone and is thus not available for substitution
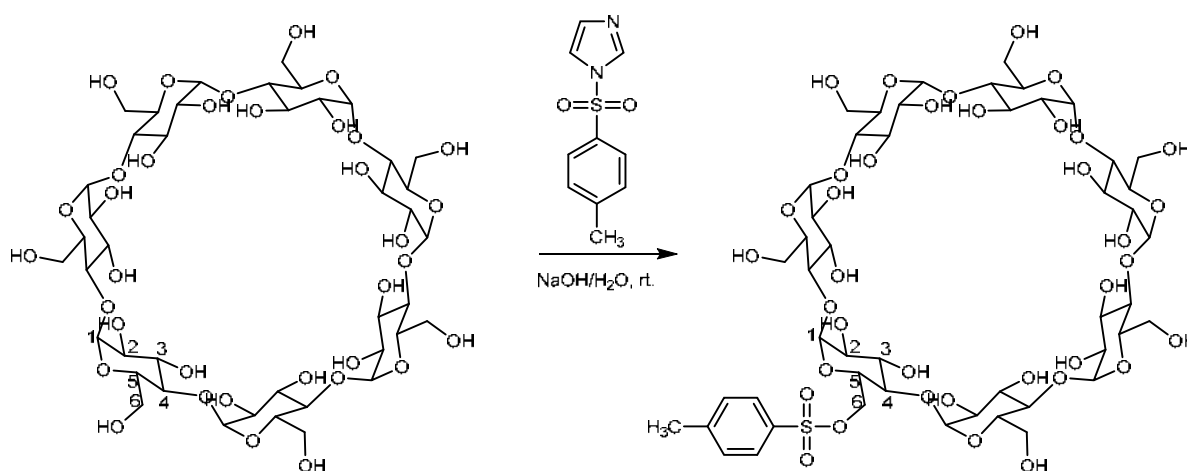
Scheme 2. Synthesis of mono-6-(4-methylbenzenesulfonyl)-β-cyclodextrin

Table 2. The yields and quantities of reactants and solvents used in the synthesis of mono-6-(4-methylbenzenesulfonyl)-β-cyclodextrin

No	β-CD	BsIm	Water	NaOH	Yield
1.	2.70 g (2 mmol)	0.47 g (2.10 mmol)	20 mL	0.80 g (20 mmol)	1.08 g (42.01%)
2.	13.51 g (0.01 mol)	0.47 g (0.01 mol)	100 mL	0.80 g (0.10 mol)	5.42 g (42.05%)
3.	27.02 g (0.02 mol)	4.90 g (0.02 mol)	200 mL	8.00 g (0.20 mol)	10.89 g (42.25%)
4.	67.55 g (0.05 mol)	12.22 g (0.05 mol)	500 mL	20.00 g (0.50 mol)	27.40 g (42.50%)

reactions with 4-methylbenzenesulfonyl imidazole. The mechanism of regioselective synthesis of mono-6-(4-methylbenzenesulfonyl)-β-cyclodextrin probably proceeds through the inclusion of complex formation between β-cyclodextrin and 4-methylbenzene-sulfonyl imidazole prior to sodium hydroxide addition. The β-cyclodextrin should form a 1:1 complex with 4-methylbenzenesulfonyl imidazole. This argument was supported by the observation of solid formation immediately when the solution of β-cyclodextrin was added with 4-methylbenzene-sulfonyl imidazole. This observation was consistent with the results obtained when mono-6-(4-methylbenzenesulfonyl)-β-cyclodextrin was made from β-cyclodextrin with 4-methylbenzenesulfonyl chloride [18] or 4-methylbenzenesulfonic anhydride [22].

In order to prove the inclusion of complex formation between 4-methylbenzenesulfonyl imidazole (BsIm) and β-CD, the BsIm/β-CD complex formed was isolated and the spectrometric experiment was performed. The UV absorption spectra of 4-methylbenzenesulfonyl imidazole and the BsIm/β-CD inclusion complex in aqueous solutions are shown in Fig. 1. A comparison of the UV spectra of BsIm and the BsIm/β-CD complex showed a distinct difference. The complexation of BsIm to β-CD causes a small red shift in the absorbance

maximum and a large increase in the molar absorption coefficient. The increase in the molar absorption is presumably caused by the BsIm being complexed in the hydrophobic interior of the β-CD cavity. Therefore, the broad absorption at around 235 nm in Fig. 1 must be caused by the complex formation of β-CD with BsIm and not benzylated β-CD (β-CD-OBs).

Moreover, the complex formation of β-CD with BsIm may be confirmed by the determination of the binding constant (K_a). On the basis of the reliable Benesi-Hildebrand method for the 1:1 host-guest complex the double reciprocal plots have been drawn using Eq. (1) [12].

$$\frac{[H]_o[G]_o}{\Delta A} = \frac{1}{\Delta\varepsilon b K_a} + \frac{[H]_o}{\Delta\varepsilon b} \qquad (1)$$

where $[H]_o$ and $[G]_o$ are the molar concentration of β-CD and BsIm, ΔA is the change in absorbance after the addition of β-CD, and $\Delta\varepsilon$ is the difference of the molar absorptivities for free and complexed BsIm. The binding constant for the 1:1 inclusion complex, K_a, can be calculated from Eq. (2).

$$Ka = \left(\frac{slope}{intercept}\right) \times 1000 \qquad (2)$$

The Benesi-Hildebrand plots for β-CD with BsIM gave a straight line, Fig. 2. The K_a value for the complexes
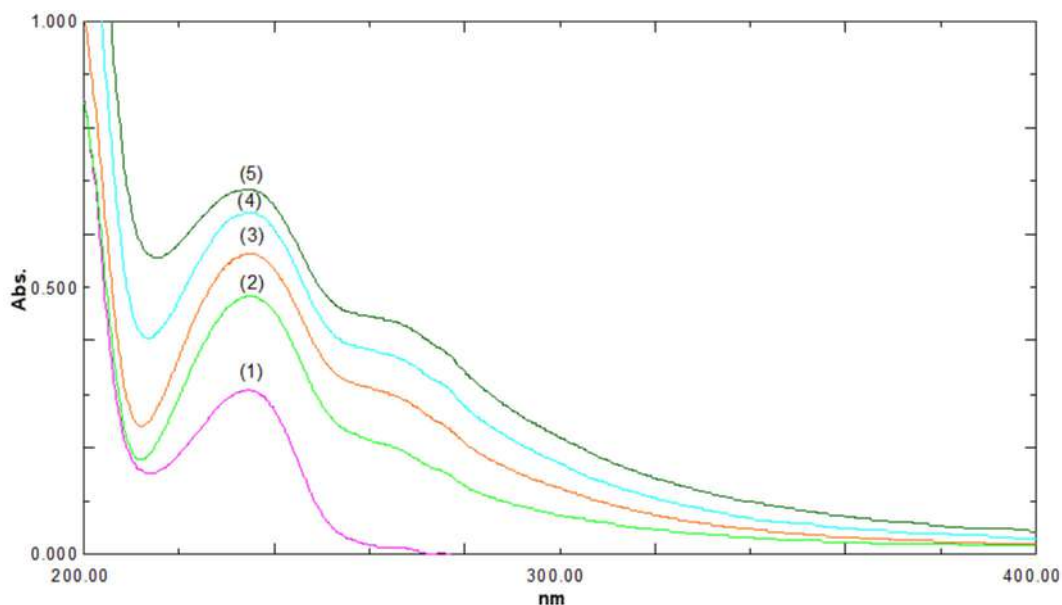
Fig 1. Spectrum of BsIm at varying β-CD concentration, aqueous, pH 7.0, 28 °C. [BsIm] is 2.5×10^{-4} M. [CD] is (1) 0 $\times 10^{-3}$, (2) 1×10^{-3}, (3) 2×10^{-3}, (4) 3×10^{-3}, (5) 4×10^{-3} M
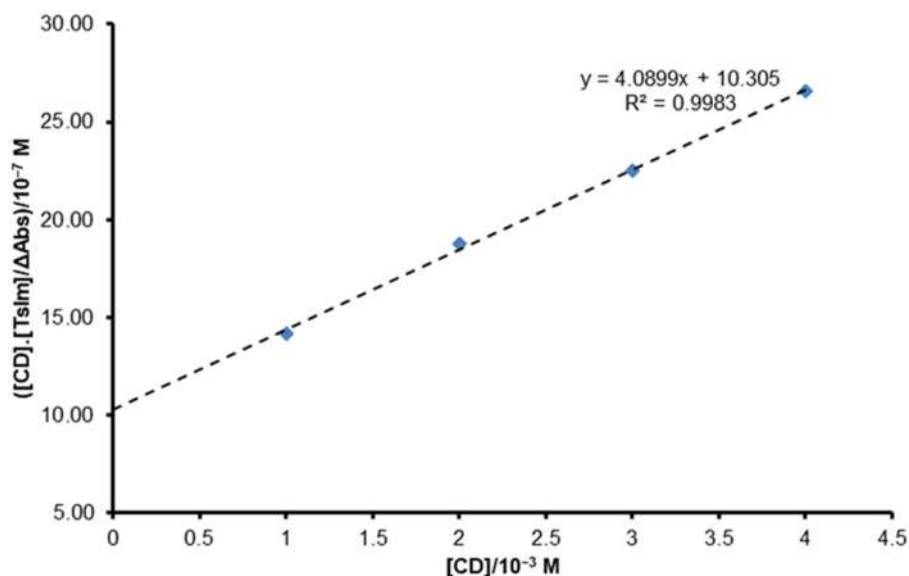
Fig 2. Benesi-Hildebrand plot for the mixture of β-CD and BsIm

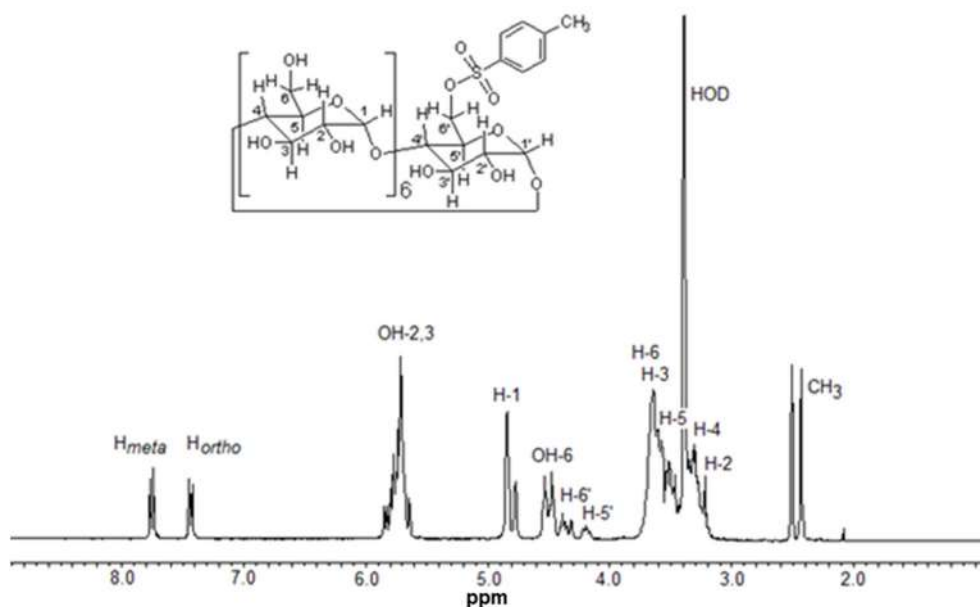**Fig 3.** ^{1}H-NMR spectrum of mono-6-(4-methylbenzenesulfonyl)-β-CD in DMSO-d_6

of β-CD with BsIM, as calculated from the slope and intercept of this line, is 396.885 M^{-1}. This suggested that the mechanism of regioselective synthesis of mono-6-(4-methylbenzenesulfonyl)-β-CD proceeds through the formation of an inclusion complex between β-CD and BsIm with the 1:1 ratio.

The FTIR, NMR, and MS studies were conducted to identify and prove the structure of mono-6-(4-methyl benzene sulfonyl)-β-cyclodextrin. The functionalization of β-cyclodextrin with 4-methylbenzenesulfonyl group was confirmed by FTIR based on the peaks at 1159 cm^{-1} (S-O-R), which were not present in β-cyclodextrin or 4-methylbenzene-sulfonyl imidazole and could be attributed to alkyl substituted sulfonyl group. In addition, the comparison of ^{1}H-NMR spectra for the starting β-cyclodextrin and the product of its reaction with 4-methylbenzenesulfonyl imidazole determine the structural orientation of the reaction. The ^{1}H-NMR spectrum (Fig. 3) shows the resonance signals at 7.75 ppm (d, J = 8.4 Hz, 2 H$_{ortho}$), 7.43 ppm (d, J = 8.4 Hz, 2 H$_{meta}$),

and 2.43 ppm (s, 3H) for characteristic peaks of aromatic and CH$_3$ protons. A molar amount of > 99% of 4-methylbenzenesulfonyl group in the mono-6-(4-methylbenzenesulfonyl)-β-CD was detected by comparing the integral of the anomeric protons (H$_1$) at 4.85–4.76 ppm with that of benzene protons (-C$_6$H$_4$-CH$_3$) at 7.77–7.74 and 7.45–7.42 ppm, which stresses the high purity of the obtained product.

Furthermore, based on the integral ratios of the anomeric proton and the multiplet signal at 4.53–4.45 ppm (OH-6), which were calculated to be 7:6, it was confirmed that only one of the seven primary hydroxyl groups (C6-OH) of β-CD was replaced by 4-methylbenzenesulfonyl group. The 4-methylbenzenesulfonyl substituent causing unshielded effects resulted in a downfield peak shift at 4.37 ppm for the two protons of the derivatized C-6' and at 4.20 ppm for the adjacent C-5' proton, respectively. These facts gave information and proved the binding of the 4-methylbenzenesulfonyl group to the C-6' carbon. This result is consistent with previously reported ^{1}H-NMR data for mono-6-(4-methylbenzenesulfonyl)-β-cyclodextrin [23].

Fig. 4 shows the ^{13}C-NMR spectrum of mono-6-(4-methylbenzenesulfonyl)-β-CD and the assignments of resonance signals for the cyclodextrin region are as in inset. The ^{13}C-NMR spectrum shows important resonance signals at 144.8, 132.6, 129.8, 127.5, and 21.1 ppm for C$_{ipso}$, C$_{para}$, C$_{ortho}$, C$_{meta}$ of the aromatic ring, and CH$_3$, respectively. The resonance signal for -CH$_2$- linked to 4-methylbenzenesulfonyl group is at 68.9 ppm. In the ^{13}C-NMR spectrum, peak shifts could be detected due to the functionalization of one (C-6') out of a total of seven C-6 carbons of β-cyclodextrin, namely, (i) a downfield shift of C-6' from 59.9 to 68.9 ppm, (ii) an upfield shift of adjacent C-5' from 71.8 to 69.6 ppm, and (iii) upfield shifts of C-4' (80.7 ppm) and C-1' (101.2 ppm). These values are consistence with Breslow's theory, which states that sulfonylation of the hydroxyl group causes a downward field shift of the carbon-carrying hydroxyl (the α-carbon), a small upward field shift of the β-carbon and a smaller upfield shift of the γ-carbon [24]. All ^{13}C-NMR peaks of non-functionalized carbon atoms showed the same chemical shift as the starting β-CD, supporting that a mono-functionalized product was obtained.

The mass spectrometry (MS) revealed a molecular weight of the molecular ion [M+Na]$^+$ of 1311.2 g mol^{-1}, which perfectly agreed with the calculated value (1311.38) for mono-6-(4-methylbenzenesulfonyl)-β-cyclodextrin. Importantly, compared to previous approaches to obtain mono-6-(4-methylbenzenesulfonyl)-β-cyclodextrin, the entire process, allowed to use of lower amounts of 4-methylbenzenesulfonyl imidazole and sodium hydroxide
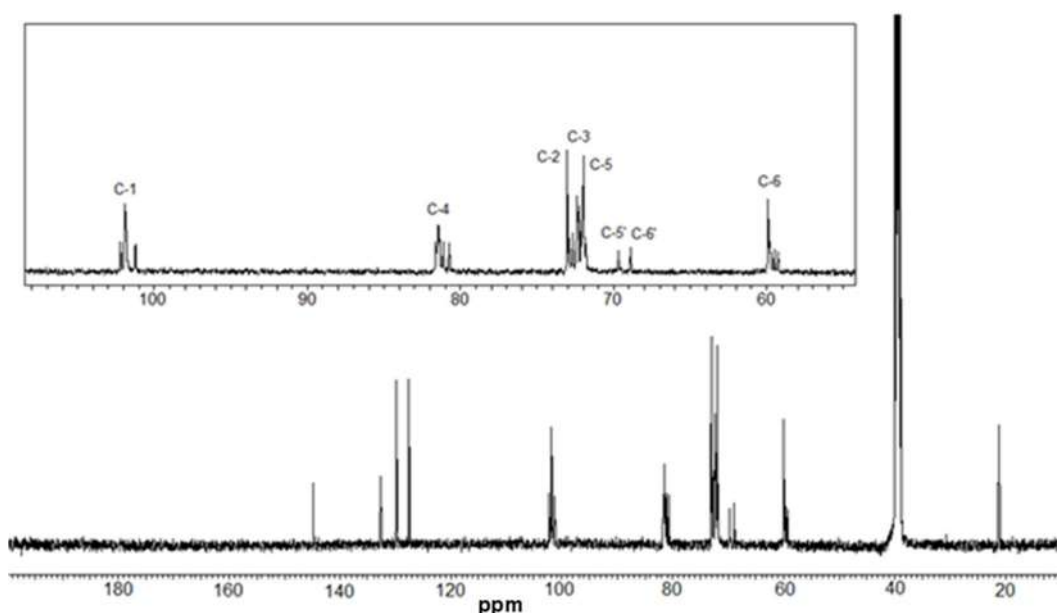

Fig 4. ^{13}C-NMR spectra of mono-6-(4-methylbenzenesulfonyl)-β-CD in DMSO-d_6

(molar ratio 4-methylbenzenesulfonylimidazole/β-cyclodextrin = 1.1 and NaOH/β-cyclodextrin = 10) in reasonable yield and high purity compared to the previously reported approach in NaOH/water environment [7].

■ CONCLUSION

The 4-methylbenzenesulfonyl imidazole has been prepared from the 4-methylbenzenesulfonyl chloride and imidazole by using phase transfer catalysis. This method can be used in the large-scale synthesis of 4-methylbenzenesulfonyl imidazole as it is easy to carry out and can produce a high percentage of yields. In addition, the method uses triethylamine in a catalytic amount and the solvent can be recycled and reused. It is a more effective and efficient synthetic methodology. Moreover, the 4-methylbenzene-sulfonyl imidazole produced has been successfully used as a precursor in regioselective synthesis with β-cyclodextrin to obtain a highly pure mono-6-(4-methylbenzenesulfonyl)-β-cyclodextrin in an aqueous environment with an acceptable yield. This synthetic methodology provides a reliable synthesis of mono-6-(4-methylbenzenesulfonyl)-β-cyclodextrin required for further synthesis of important single isomer mono-substituted β-cyclodextrin derivatives, containing just one substituent per β-CD molecule at the C-6 position.

■ ACKNOWLEDGMENTS

■ REFERENCES

[1] Crini, G., 2014, Review: A history of cyclodextrins, *Chem. Rev.*, 114 (21), 10940–10975.

[2] Kurkov, S.V., and Loftsson, T., 2013, Cyclodextrins, *Int. J. Pharm.*, 453 (1), 167–180.

[3] Jansook, P., Ogawa, N., and Loftsson, T., 2018, Cyclodextrins: Structure, physicochemical properties and pharmaceutical applications, *Int. J. Pharm.*, 535 (1-2), 272–284.

[4] Liu, J.Y., Zhang, X., and Tian, B.R., 2020, Selective modification at the different positions of cyclodextrins: A review of strategy, *Turk. J. Chem.*, 44 (2), 261–278.

[5] Kasal, P., and Jindřich, J., 2021, Mono-6-substituted cyclodextrins–Synthesis and applications, *Molecules*, 26 (16), 5065.

[6] Tang, W., Ng, S.C., and Sun, D., 2013, *Modified Cyclodextrins for Chiral Separation*, Springer-Verlag, Heidelberg, Berlin.

[7] Byun, H.S., Zhong, N., and Bittman, R., 2000, 6^A-O-*p*-Toluenesulfonyl β-cyclodextrin, *Org. Synth.*, 77, 225.

[8] Makosza, M., and Fedoryński, M., 2020, Interfacial processes–The key steps of phase transfer catalyzed reaction, *Catalysts*, 10 (12), 1436.

[9] Joshi, D.R., and Adhikari, N., 2019, Phase transfer catalysis in organic synthesis, *World J. Pharm. Res.*, 8 (8), 508–515.

[10] Senthamizh Selvi, R., Nanthini, R., and Sukanyaa, G., 2012, The basic principle of phase-transfer catalysis, some mechanistic aspects and important applications, *Int. J. Sci. Technol. Res.*, 1 (3), 61–63.

[11] Novokshonov, V.V., Xuan, N.T.T., and Shaglaeva, N.S., 2019, Synthesis of 6I-*O*-(4-methylbenzenesulfonyl)-β-cyclodextrin, *Russ. J. Org. Chem.*, 55 (10), 1616–1617.

[12] Srivastava, K.K., Srivastava, S., Alam, M.T., and Rituraj, R., 2014, Spectrometric determination of reliable association constant of weakly bounded charge transfer complex in solution, *Int. J. Curr. Res.*, 6 (3), 5481–5486.

[13] Popr, M., Hybelbauerová, S., and Jindřich, J., 2014, A complete series of 6-deoxy-monosubstituted tetraalkylammonium derivatives of α-, β-, and γ-cyclodextrin with 1, 2, and 3 permanent positive charges, *Beilstein J. Org. Chem.*, 10, 1390–1396.

[14] Poulson, B.G., Alsulami, Q.A., Sharfalddin, A., El Agammy, E.F., Mouffouk, F., Emwas, A.H., Jaremko, L., and Jaremko, M., 2022, Cyclodextrins: Structural, chemical, and physical properties, and applications, *Polysaccharides*, 3 (1), 1–31.

[15] Jouffroy, M., Armspach, D., Matt, D., and Toupet, L., 2013, Regioselective di- and tetra-functionalisation of γ-cyclodextrin using capping methodology, *Org. Biomol. Chem.*, 11 (22), 3699–3705.

[16] Xiao, S., Wang, Q., Yu, F., Peng, Y., Yang, M., Sollogoub, M., Sinaÿ, P., Zhang, Y., Zhang, L., and Zhou, D., 2012, Conjugation of cyclodextrin with fullerene as a new class of HCV entry inhibitors, *Bioorg. Med. Chem.*, 20 (18), 5616–5622.

[17] Lai, W.F., 2019, "Design of Cyclodextrin-Based Systems for Intervention Execution" in *Delivery of Therapeutics for Biogerontological Inventions*, Academic Press, Cambridge, US, 49–59.

[18] Raoov, M., Mohamad, S., and Abas, M.R., 2014, Synthesis and characterization of β-cyclodextrin functionalized ionic liquid polymer as a macroporous material for the removal of phenols and As(V), *Int. J. Mol. Sci.*, 15 (1), 100–119.

[19] Lai, X.H., and Ng, S.C., 2004, Convenient synthesis of mono-(6[A]-*N*-allylamino-6[A]-deoxy)permethylated β-cyclodextrin: A promising chiral selector for an HPLC chiral stationary phase, *Tetrahedron Lett.*, 45 (23), 4469–4472.

[20] Xiao, S., Wang, Q., Si, L., Zhou, X., Zhang, Y., Zhang, L., and Zhou, D., 2016, Synthesis and biological evaluation of novel pentacyclic triterpene α-cyclodextrin conjugates as HCV entry inhibitors, *Eur. J. Med. Chem.*, 124, 1–9.

[21] Yin, J.J., Sharma, S., Shumyak, S.P., Wang, Z.X., Zhou, Z.W., Zhang, Y., Guo, P., Li, C.Z., Kanwar, J.R., Yang, T., Mohapatra, S.S., Liu, W., Duan, W., Wang, J.C., Li, Q., Zhang, X., Tan, J., Jia, L., Liang, J., Wei, M.Q., Li, X., and Zhou, S.F., 2013, Synthesis and biological evaluation of novel folic acid receptor-targeted, β-cyclodextrin-based drug complexes for cancer treatment, *PLoS One*, 8 (5), e62289.

[22] Onozula, S., Kojima, M., Hattori, K., and Toda, F., 1980, The regiospecific mono tosylation of cyclodextrins, *Bull. Chem. Soc. Jpn.*, 53 (11), 3221–3224.

[23] Tripodo, G., Wischke, C., Neffe, A.T., and Lendlein, A., 2013, Efficient synthesis of pure monotosylated beta-cyclodextrin and its dimers, *Carbohydr. Res.*, 381, 59–63.

[24] Ueno, A., and Breslow, R., 1982, Selective sulfonation of a secondary hydroxyl group of β-cyclodextrin, *Tetrahedron Lett.*, 23 (34), 3451–3454.

Indones. J. Chem., 2022, 22 (5), 1187 - 1194

1187

Utilizing Organic Aromatic Melamine Moiety to Modify Poly(Vinyl Chloride) Chemical Structure and Micro CuO That Plays an Important Role to Enhance Its Photophysical Features

Mohammed Hussein Al-Mashhadani[1*], Ekhlas Abdulkhadiar Salman[1], Amani Ayad Husain[2], Mustafa Abdallh[1], Muna Bufaroosha[3], and Emad Yousif[1]

[1]*Department of Chemistry, College of Science, Al-Nahrain University, 64021, Baghdad, Iraq*

[2]*Polymer Research Unit, College of Science, Al-Mustansiriyah University, 10052, Baghdad, Iraq*

[3]*Department of Chemistry, College of Science, UAE University, 15551, Al-Ain, UAE*

Abstract: *Three arms Schiff base unit based on melamine moiety was synthesized and introduced to polyvinyl chloride (PVC) to produce a modified PVC polymer. The polymer composite of new modified PVC polymer was blended with micro copper oxide as a reflecting mirror of UV light to enhance the photostability of PVC. Three different concentrations of micro copper oxide (0.01–0.03 wt.%) were mixed with the modified PVC and cast as a thin film. The photostability test has shown high resistance to photodegradation upon exposure to UV light. In this work, different approaches were applied to examining doped modified PVC's thin film efficiency against photodegradation after exposure to UV light for 300 h in an ambient atmosphere. The exhibited studies, such as infrared spectroscopy and weight loss percentage, have demonstrated the improvement of photophysical properties for modified PVC and blended modified films in comparison to blank PVC polymeric films. These outcomes are so interesting as they could contribute to reducing the consumption of PVC around the world hence its waste causing huge environmental problems for the marine ecosystem.*

Keywords: *aromatic; photo-stabilizers; micro copper oxide; FTIR; melamine*

■ INTRODUCTION

Plastics have a wide range of chemical and physical qualities as well as inexpensive manufacturing costs. They are mass-produced and used in a variety of industrial applications [1-3]. However, in recent years, both academic and industrial companies have been under intense work to address issues arising from the usage of plastics. For example, the amount of trash produced, the composition of that waste, and its negative impact on the ecosystem. Another major challenge is how to enhance the characteristics of plastics for long-term usage [4-6]. Polyvinyl chloride (PVC) is a flexible thermoplastic used in various applications, from food wrapping to equipment used in medicine. PVC is an inexpensive polymer easy to make and has excellent features. On the other hand, it has low thermal and mechanical stability.

Furthermore, when irradiated by ultraviolet (UV) radiation for lengthy periods, especially at high temperatures, the most prevalent types of synthesized PVC undergo a specific de-hydrochlorination process [7-8]. Because of the HCl molecules released, such processes result in the making (C=C) double bonds inside the polymer structure, cracking, discoloration, deformation, and a defect in the mechanical qualities of polymeric films [9-11]. Furthermore, PVC degrades slowly in landfills in natural settings [12]. As a result, at the numerous disposal sites where PVC trash ends up, it must either be burnt or collected and recycled [13]. PVC incineration creates harmful by-products that damage the environment as well as soil and groundwater [14]. Thus, including different stabilizers in the polymeric chemical structures might be a way to improve PVC

characteristics and enhance its stability against heat and UV light [15-16]. The PVC stabilizers should be well-matched with the polymer and not change the product's color. The additives' main features are stability against harsh conditions, non-volatile, and inexpensive to manufacture [17-18]. Highly aromatic organic molecules, organometallic materials, inorganic nano-compounds, and Schiff bases are the most often used PVC stabilizers [19-22].

On the other hand, additives having heavy metals are not an amazing way to protect PVC for a long time because they have a propensity to leak out, generating ecosystem and human health issues. Because titanium dioxide is an efficient UV light absorber, it may be utilized as a PVC additive [23-24]. Nevertheless, titanium dioxide is a photocatalyst and speeds up the weathering and deterioration of PVC surfaces [25].

As a result, novel PVC stabilizers that are proficient, easy to manufacture, aromatic, and work as light stabilizers still have the potential to be developed. Melamine is a fragrant, odorless, low-cost, very stable material and not toxic. It is employed in a variety of industrial settings, including corrosion inhibitors [26-29]. Previous studies used copper oxide particles as photo stabilizers for paint media [30]. However, a new approach in this study was followed by using copper oxide microparticles as PVC additives. It used micro copper oxide, which should work as a reflecting mirror, which reflects the UV light from the surface of the polymeric films and prevents the chemical structure damage of it. Thus, the copper oxide was chosen because it is cheap and available. Also, it was used as an example to open the door for a new stabilization mechanism that could be expanded for many other metallic oxides.

■ EXPERIMENTAL SECTION

Materials

Petkim Petrokimya (Istanbul, Turkey) has supplied PVC generously for this work. The supplied PVC has a K value of 67. The copper oxide was purchased from Sigma-Aldrich company as a powder, with particle size < 10 μm and purity of 98% since it was used without any further purifications. All other chemicals are purchased from Sigma Aldrich (Gillingham, UK).

Instrumentation

The final PVC composite films have a thickness of about 40 μm measured via Digital Caliper DIN 862 micrometer (Germany). In order to run a photodegradation experiment, A QUV tester instrument was used to simulate the exposure to sunlight under laboratory conditions. The UV light was centered at 313 nm with an intensity of 6.43×10^{-9} ein dm^{-3} s^{-1}. UV rays irradiated all the samples for a maximum of 300 h irradiation time.

Procedure

Synthesis of three arms Schiff base unit based on melamine moiety (3)

Dimethylformamide (DMF) (40 mL) was used to dissolve (0.50 g, 4 mmol) of melamine under stirring at 120 °C completely. An excess of aromatic aldehyde (1.61 g, 13.2 mmol) dissolved in 5 mL DMF in addition to acetic acid (glacial) (0.2 mL) was mixed with the previous solution. The reaction was then heated up to refluxed (6 h). After cooling to ambient temperature, toluene was added to crash out the precipitate. The precipitate was filtrated and thoroughly rinsed with toluene and methanol. The pure target product was dried under a vacuum [19].

Synthesis of PVC/3 films

A 0.25 g of PVC polymer was dissolved in tetrahydrofuran (THF). A few drops of pyridine were then added to the above solution, followed by the addition of compound **3** (0.05 g) to the previous mixture. The solution was heated to reflux for 3 h and then cast on a glass mold. The solution was then kept in a dry place to let the solvent evaporate at room temperature. The resulted films have a thickness of about 40 μm.

Prepare PVC/3 micro copper oxide films

The modified PVC polymer with copper oxide composite was prepared by dissolving the PVC/3 polymer (0.3 g) in THF (5 mL) with different concentrations (0.01, 0.02, and 0.03 wt.%) of micro copper oxide. The solution was heated to reflux for 4 h to give the PVC-3/CuO composite. The solution was then kept dry to let the solvent evaporate at room temperature to give the final product.

Weight loss method

The weight alterations of the samples are calculated using Eq. (1). The changes in the weight of the samples pre (W1) and post (W2) illumination with ultraviolet light are used to determine the percentage of the change.

$$\text{Weight loss } \% = \frac{W1 - W2}{W1} \times 100 \qquad (1)$$

■ RESULTS AND DISCUSSION

Synthesis of Aromatic Melamine

The synthesis route of **3** is accomplished according to the procedure described by previous literature [19]. First, melamine was condensed with an excess of 4-hydroxybenzaldehyde in the existence of acetic acid, as shown in Fig. 1. Then, the final product **3** was obtained as a pale yellow powder in a 73% yield.

Modification of PVC Chemical Structure

In recent times many attempts have been tried to modify the chemical structure of PVC to enhance its properties [31-32]. This work used melamine as a highly aromatic moiety to modify the chemical structure of PVC

polymeric chains, as shown in Fig. 2. A very small amount of melamine was used compared to polymer; melamine molecules replaced a few chlorine atoms. The reaction has likely followed SN2 mechanisms due to the
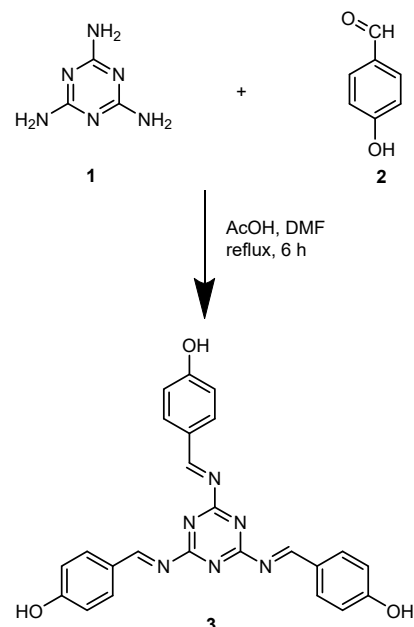

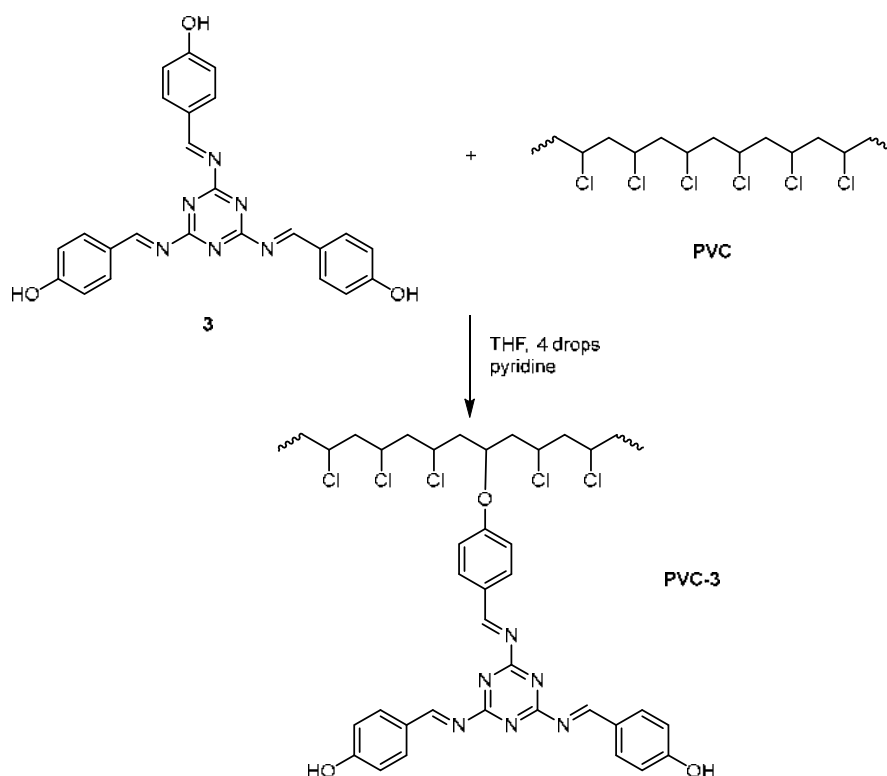**Fig 1.** Synthesis of melamine Schiff base **3**

Fig 2. Modification of PVC chemical structure

steric hindrance, as a slightly similar mechanism was described in previous research [33]. The product was identified using FTIR spectroscopy. Hence it noticed the Schiff base peak at 1776 cm^{-1} as well as the decreasing of the intensity of the OH band. It is clear evidence that almost all of the melamine was replaced by chlorine from one side. This is possible due to steric hindrance effects since the molecule prefers to react from one side rather than strictly hindrance situations with making cross-linking. However, there is a possibility that a very trace amount reacted from two or three sides, but the majority reacted from only one side. The idea is to use a very small amount of aromatic units so it does not affect the chemical or physical properties of the polymer; at the same time, it provides very good photoprotection for the polymer. Melamine in a small amount was not changing the features of PVC, and it works as an excellent UV absorber due to its high aromaticity. This work also used micro CuO particles to enhance the photo-stability of PVC films, proposing a new stabilization mechanism, as will be discussed in the next section.

The Blending of Modified PVC with a Trace Amount of Micro CuO

After that, the modified polymer was mixed with different percentages of micro copper oxide (0.01, 0.02, and 0.03 wt.%) to get a blend of modified PVC with micro copper oxide. It was thought that micro CuO could work as a reflecting mirror of sunlight and protect the polymer from degradation. Fig. 3 is an animated diagram that shows how melamine and micro copper oxide can protect the PVC from photodegradation.

Utilizing the FTIR Technique to Examine Modified PVC Stability

The prepared polymeric films described in the experimental section were irradiated by UV light for 300 h of blank and blended PVC films. The photodegradation of polymeric films was monitored using the FTIR technique (4000–400 cm^{-1}) because the PVC undergoes an elimination process by releasing HCl molecules when irradiated by UV light, which leads to the formation of alkene groups. Furthermore, it is possible
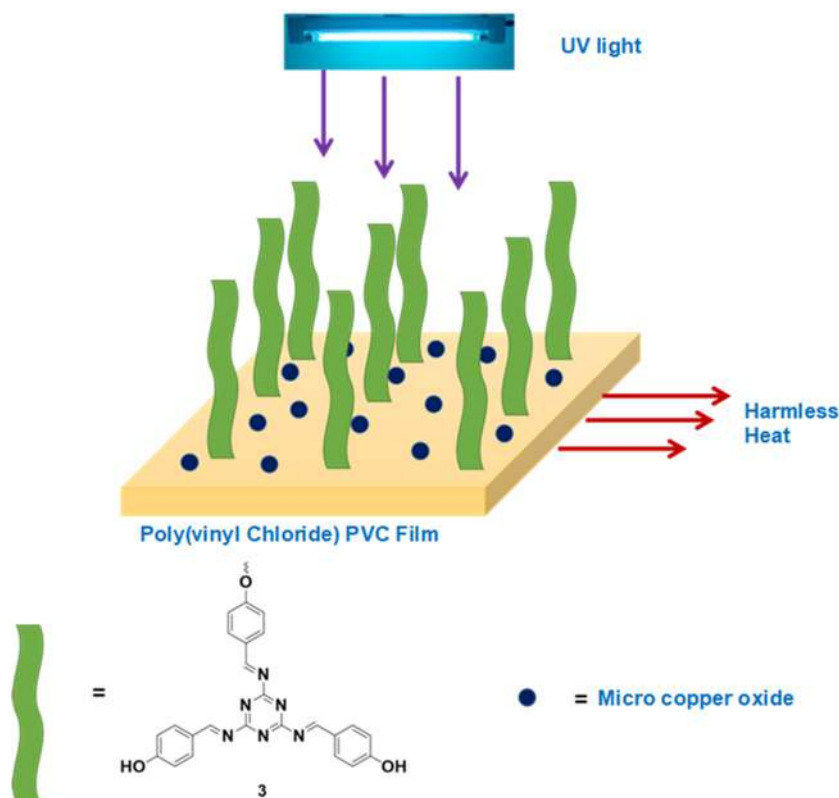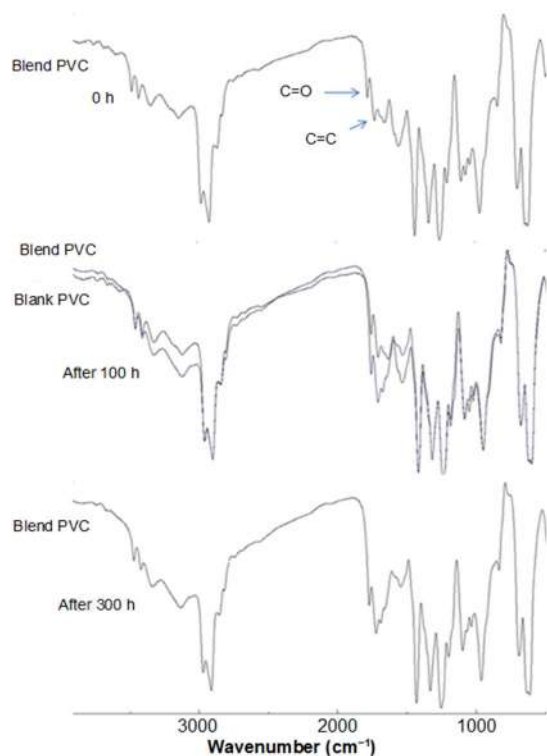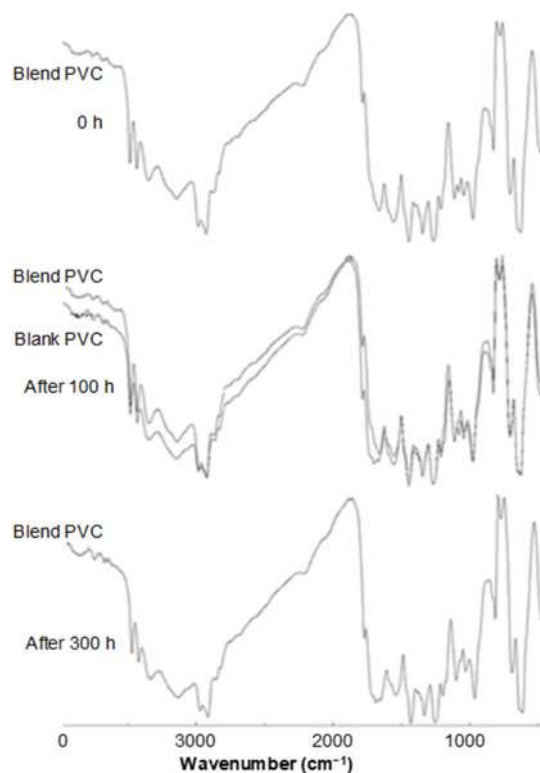

Fig 3. Animated diagram of photostability for modified PVC doped with CuO

Mohammed Hussein Al-Mashhadani et al.

Indones. J. Chem., 2022, 22 (5), 1187 - 1194

1191

Fig 4. Infrared spectrums of PVC blended with micro copper oxide (0.01 wt.%)


Fig 5. Infrared spectrums of PVC blended with micro copper oxide (0.03 wt.%)

to oxidize the polymeric chains and form carbonyl groups in the presence of oxygen. Therefore, both alkene (C=C) and carbonyl (C=O) groups could be monitored using FTIR, which shows peaks at 1660 and 1720 cm^{-1}, respectively. Fig. 4 and 5 clearly show that blend modified PVC has very good stability against UV light matched to blank PVC, as shown in Fig. 4 and 5 after 100 h irradiation.

Weight Loss Percentages Approach to Monitor the Stability of PVC

Another approach was utilized to exhibit the efficiency of blend modified PVC, which is the weight loss percentage against irradiation time, as shown in Fig. 6. In all cases, it is obvious that the weight loss percentage increases with increasing the irradiation time. This is because the PVC chemical structure has the ability to undergo an elimination reaction and release HCl molecules when irradiated by UV light. This leads to reducing the molecular weight of the polymer and increasing the weight loss as this is the main known defect of PVC materials. Hence, it was taken and weighed for both blank and blend PVC in an interval time of 50 h. Using micro CuO particles with modified polymer has enhanced the photostability of PVC. Another result was obtained from this study that increasing the percentage of micro copper oxide can decrease the degradation of polymeric film. Hence, micro copper oxide works as a reflecting mirror of UV light in this case. It is important to mention that modified
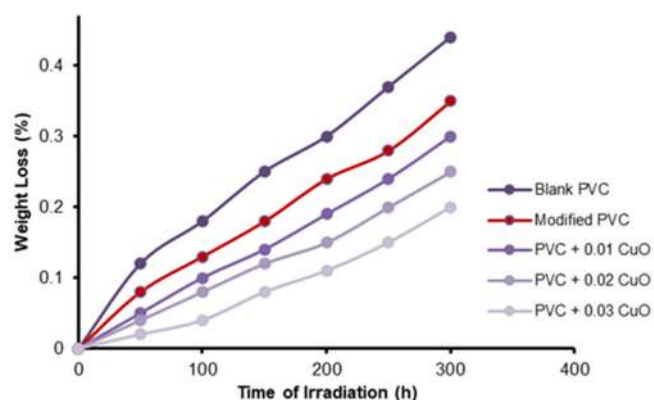
Fig 6. The loss of weight percentage of PVC mixed with different concentrations of micro copper oxide at 300 h of irradiation

PVC has provided good protection for PVC polymeric films compared to blank PVC. This is because melamine has a highly aromatic system, which absorbs UV light and works as a UV blocker. This protects the PVC chemical structure from photodegradation after exposure to UV light.

■ CONCLUSION

To summarize, this study used a highly aromatic organic molecule (melamine) to modify the chemical structure of PVC and utilized FTIR to identify the product. This modification was done to enhance the photophysical properties of PVC. Hence, melamine has a highly conjugated system and absorbs in the UV region. Copper oxide (CuO) was added to modified PVC in different concentrations. It is thought that CuO could work as a reflecting mirror of UV light and protect PVC films from degradation. Two approaches, FTIR spectra and weight loss were considered to examine the stability of blend PVC compared to blank PVC. Both studies were in agreement and proved that modifying the structure of PVC with a very small amount of aromatic molecules and blending it with micro CuO particles can improve the properties of the polymer and reduce its photodegradation.

■ ACKNOWLEDGMENTS

■ AUTHOR CONTRIBUTIONS

Conceptualization and experimental design were done by Mohammed H. Al-Mashhadani, and Ekhlas A. Salman. The experimental work and data analysis were done by Amani Ayad Husain and Mustafa Abdallh. Meanwhile, writing–original draft preparation was done by Muna Bufaroosha, and writing–review and editing by Emad Yousif.

■ REFERENCES

[1] Huang, Z., Ding, A., Guo, H., Lu, G., and Huang, X., 2016, Construction of nontoxic polymeric UV-absorber with great resistance to UV-photoaging, *Sci. Rep.*, 6 (1), 25508.

[2] Martins, L.M.D.R.S., Hazra, S., Guedes de Silva, M.F.C., and Pombeiro, A.J.L., 2016, A sulfonated Schiff base dimethyltin(IV) coordination polymer: Synthesis, characterization and application as a catalyst for ultrasound- or microwave-assisted Baeyer-Villiger oxidation under solvent-free conditions, *RSC Adv.*, 6 (81), 78225–78233.

[3] Najafi, V., Ahmadi, E., and Ziaee, F., 2018, Chemical modification of PVC by different nucleophiles in solvent/non-solvent system at high temperature, *Iran. Polym. J.*, 27 (11), 841–850.

[4] Allen, N.S., and Edge, M., 2021, Perspectives on additives for polymers. Part 2. Aspects of photostabilization and role of fillers and pigments, *J. Vinyl Addit. Technol.*, 27 (2), 211–239.

[5] Lu, L., Kumagai, S., Kameda, T., Luo, L., and Yoshioka, T., 2019, Degradation of PVC waste into a flexible polymer by chemical modification using DINP moieties, *RSC Adv.*, 9 (49), 28870–28875.

[6] Sabaa, M.W., Oraby, E.H., Abdel Naby, A.S., and Mohammed, R.R., 2005, Anthraquinone derivatives as organic stabilizers for rigid poly(vinyl chloride) against photodegradation, *Eur. Polym. J.*, 41 (11), 2530–2543.

[7] Yang, K., Zeng, H., Zhong, A., Yuan, H., Zeng, S, and Ma, Y., 2020, Effect of vinyl chloride copolymer elastomer on modification and properties of PVC, *Zhongguo Suliao*, 34 (9), 16–21.

[8] Sabaa, M.W., and Mohamed, R.R., 2007, Phenyl urea derivatives as organic stabilizers for rigid poly (vinyl chloride) against photo-degradation, *J. Appl. Polym. Sci.*, 103 (4), 2217–2226.

[9] Folarin, O.M., and Sadiku, E.R., 2011, Thermal stabilizers for poly(vinyl chloride): A review, *Int. J. Phys. Sci.*, 6 (18), 4323–4330.

[10] Abdrakhmanova, L.A., and Stroganov, V.F., 2019, Modification of polyvinyl chloride compositions by polymerizable epoxyallyl oligomers, *Polym. Sci., Ser. D*, 12 (2), 121–123.

[11] Khalaf, M., Fadhil, Z., Al-Mashhadani, M.H., Abdallh, M., Bufaroosha, M., Majeed, A., Salih N., and Yousif, E., 2020, PVC films performance

stabilized by dibutyltin(IV) complex for sustainable environment, *J. Phys.: Conf. Ser.*, 1664, 012072.

[12] Samuels, A., Rensing, K., Douglas, C., Mansfield, S., Dharmawardhana, D., and Ellis, B., 2002, Cellular machinery of wood production: Differentiation of secondary xylem in *Pinus contorta* var latifolia, *Planta*, 216 (1), 72–82.

[13] Bhuiyan, N.H., Selvaraj, G., Wei, Y., and King, J., 2009, Role of lignification in plant defense, *Plant Signaling Behav.*, 4 (2), 158–159.

[14] Sabaa, M.W., Oraby, E.H., Naby, A.S.A., and Mohamed, R.R., 2005, Anthraquinone derivatives as organic stabilizers for rigid poly(vinyl chloride) against photo-degradation, *Eur. Polym. J.*, 41 (11), 2530–2543.

[15] Hoffman, E., Guernsey, J.R., Walker, T.R., Kim, J.S., Sherren, K., and Andreou, P., 2017, Pilot study investigating ambient air toxics emissions near a Canadian kraft pulp and paper facility in Pictou County, Nova Scotia, *Environ. Sci. Pollut. Res.*, 24 (25), 20685–20698.

[16] Ahmed, D.S., Ibrahim, F.M., Bufaroosha, M., Al-Mashhadani, M.H., Jawad, A.H., Yusop, R.M., Salih, N., Mohammed, S.A., and Yousif, E., 2021, Polyphosphates as thermal stabilizers for poly(vinyl chloride), *Mater. Today: Proc.*, 42, 2680–2685.

[17] Zhao, X., and Liu, D., 2013, Kinetic modeling and mechanisms of acid-catalyzed delignification of sugarcane bagasse by aqueous acetic acid, *BioEnergy Res.*, 6 (2), 436–447.

[18] Hoffman, E., Bernier, M., Blotnicky, B., Golden, P.G., Janes, J., Kader, A., Kovacs-Da Costa, R., Pettipas, S., Vermeulen, S., and Walker, T.R., 2015, Assessment of public perception and environmental compliance at a pulp and paper facility: A Canadian case study, *Environ. Monit. Assess.*, 187 (12), 766.

[19] Qi, B., and Yang, Q., 2020, Application of PVC-melamine-formaldehyde resin composite in drug adsorption, *IOP Conf. Ser.: Mater. Sci. Eng.*, 892, 012016.

[20] Pi, H., Xiong, Y., and Guo, S., 2005, The kinetic studies of elimination of HCl during thermal decomposition of PVC in the presence of transition metal oxides, *Polym.-Plast. Technol. Eng.*, 44 (2), 275–288.

[21] Rodionova, A.P., Zemlyakova, E.O., Koryakova, O.V., Mekhaev, A.V., Azarova, Y.A., Bratskaya, S.Y., and Pestov, A.V., 2019, Chemical modification of polyvinyl chloride with thiourea, *Russ. Chem. Bull.*, 68 (6), 1248–1251.

[22] Hoffman, E., Lyons, J., Boxall, J., Robertson, C., Lake, C.B., and Walker, T.R., 2017, Spatiotemporal assessment (quarter century) of pulp mill metal (loid) contaminated sediment to inform remediation decisions, *Environ. Monit. Assess.*, 189 (6), 257.

[23] Ahmed, A., Abdallh, M., Al-Mashhadani, M.H., Ahmed, D.S., Bufaroosha, M., Jawad, A.H., and Yousif, E., 2021, Environmental stability of poly(vinyl chloride) modified by Schiff's base under exposure to UV, *Biointerface Res. Appl. Chem.*, 11 (5), 13465–13473.

[24] Hussein, S.S., Ibrahim, S.S., Toma, M.A., Alsalhy, Q.F., and Drioli, E., 2020, Novel chemical modification of polyvinyl chloride membrane by free radical graft copolymerization for direct contact membrane distillation (DCMD) application, *J. Membr. Sci.*, 611, 118266.

[25] Ahmed, A., Al-Mashhadani, M.H., Ahmed, D.S., Ahmed, A.A., Yousif, E., and Yusop, R.M., 2021, Preparation of polymeric films containing Schiff base as UV-absorber with good resistance against UV-photoaging, *Biointerface Res. Appl. Chem.*, 11 (5), 12743–12749.

[26] Moersilah, M., Siswanta, D., Roto, R., and Mudasir, M., 2017, PAN-immobilized PVC-NPOE membrane for environmentally friendly sensing of Cd(II) ions, *Indones. J. Chem.*, 17 (1), 1–6.

[27] Al-Mashhadani, M.H., Thamer, H., Adil, H., Ahmed, A., Ahmed, D.S., Bufaroosha, M., Jawad, A.H., and Yousif, E., 2021, Environmental and morphological behavior of polystyrene films containing Schiff base moiety, *Mater. Today: Proc.*, 42, 2693–2699.

[28] Visakh, P.M., and Darie-Nita, R.N., 2022, "Polyvinylchloride (PVC)-Based Blends: State of Art, New Challenges and Opportunities" in

1194

Indones. J. Chem., 2022, 22 (5), 1187 - 1194

Polyvinylchloride-based Blends: Preparation, Characterization and Applications, Springer International Publishing, Cham, Switzerland, 1–17.

[29] Shneshil, M.K., and Redayan, M.A., 2010, Photostabilization of PVC films by using some novel tetra Schiff's bases derived from 1,2,4,5-tetra-[5-amino-1,3,4-thiadiazole-2-yl]-benzene, *Diyala J. Pure Sci.*, 7 (1), 34–77.

[30] Rasti, F., and Scott, G., 1980, Mechanisms of antioxidant action: The role of copper salts in the photostabilization of paint media, *Eur. Polym. J.*, 16 (12), 1153–1158.

[31] Gaballah, S.T., El-Nazer, H.A., Abdel-Monem, R.A., El-Liethy, M.A., Hemdan, B.A., and Rabie, S.T., 2019, Synthesis of novel chitosan-PVC conjugates encompassing Ag nanoparticles as antibacterial polymers for biomedical applications, *Int. J. Biol. Macromol.*, 121, 707–717.

[32] Priya, A., Senthil, R.A., Selvi, A., Arunachalam, P., Senthil Kumar, C.K., Madhavan, J., Boddula, R., Pothu, R., and Al-Mayouf, A.M., 2020, A study of photocatalytic and photoelectrochemical activity of as-synthesized WO_3/g-C_3N_4 composite photocatalysts for AO_7 degradation, *Mater. Sci. Energy Technol.*, 3, 43–50.

[33] Bufaroosha, M., Salih, N., Hadi, A.G., Ahmed, D.S., Al-Mashhadani, M.H., and Yousif, E., 2020, The effect of UV aging on the structure of PVC in the presence of organotin(IV) compounds, *ANJS*, 23, 57–61.

Efficient Degradation of Methylene Blue Using La-PTC-HIna/Ti₃C₂Tₓ MXene: Adsorption and Photocatalytic Degradation

Agustino Zulys[1*], Adawiah Adawiah[2], and Nasruddin Nasruddin[3]

[1]Department of Chemistry, Faculty of Mathematics and Natural Sciences, Universitas Indonesia, Depok, 16424, Indonesia

[2]Integrated Laboratory Centre, Faculty of Science and Technology, UIN Syarif Hidayatullah Jakarta, Jl. Ir. H. Juanda No. 95, Ciputat 15412, Indonesia

[3]Department of Mechanical Engineering, Faculty of Engineering, Universitas Indonesia, Depok, 16424, Indonesia

Abstract: *Isonicotinic acid is a pyridine carboxylic compound that can be used as a linker to construct coordination complexes. Adding isonicotinic acid (HIna) to the metal-organic framework (MOF) enhanced the MOF surface area, pore volume, and pore size and increased its catalytic activity. Ti₃C₂Tₓ MXene nanosheet with excellent metal conductivity was also employed on MOF to optimize its functionality. This work aims to synthesize MOF modulated isonicotinic acid La-PTC-HIna and design the new materials: La-PTC/Ti₃C₂Tₓ MXene and La-PTC-HIna/Ti₃C₂Tₓ MXene hybrid, then apply them for methylene blue photodegradation. La-PTC-HIna, La-PTC/Ti₃C₂Tₓ MXene, and La-PTC-HIna/Ti₃C₂Tₓ MXene were synthesized by the sonochemical method. MOF La-PTC-HIna has the highest methylene blue photocatalytic degradation activity than MOF La-PTC, Ti₃C₂Tₓ MXene, La-PTC/Ti₃C₂Tₓ MXene, and La-PTC-HIna/Ti₃C₂Tₓ MXene with degradation efficiency of 99.48% in 20 ppm methylene blue under visible irradiation for 210 min. This study reveals the La-PTC-HIna and La-PTC-HIna/Ti₃C₂Tₓ MXene as a new material that has the potential to remove methylene blue from an aqueous solution.*

Keywords: *metal-organic framework; Ti₃C₂Tₓ MXene; La-PTC; La-PTC-Hina; La-PTC/Ti₃C₂Tx MXene; La-PTC-HIna/Ti₃C₂Tx MXene*

■ INTRODUCTION

The textile industry is one of the primary industrial sectors contributing to water pollution. The textile industry releases about 20% of organic dye waste worldwide [1]. These organic dyes are difficult to degrade, toxic, and disrupt aquatic ecosystems. In the last few decades, many nanomaterials have been used to treat dyes waste, i.e., modified bentonite [2], activated carbon [3], metal-organic frameworks (MOFs) [4], and MXene [5].

MOFs are nanoporous materials that consist of coordination bonds between transition-metal cations and multidentate organic linkers [6]. These materials have unique properties, such as large surface area and porosity [7], abundant active sites, redox ability, tunable structure, and pore size [8]. Therefore, MOFs can be used to eliminate dyes contaminant from water. Several researchers reported MOFs as a nanomaterial for photocatalytic dye degradation. Zulys et al. [9] reported MOFs La-PTC-based sodium perylene-3,4,9,10-tetracarboxylic as an organic linker and lanthanum metal ion. MOFs La-PTC degrade methylene blue at 67.02% for 240 min under visible light irradiation in the presence of hydrogen peroxide 0.2 M.

The photocatalytic activity of MOF was enhanced by adding modulator compounds like isonicotinic acid. Isonicotinic acid is a pyridine carboxylate compound that can be an excellent linker to construct coordination complexes [10]. Garibay et al. [11] reported that the addition of isonicotinic acid increases MOFs' size and pore volume and enhances their catalytic activity. Adawiah et al. [12] also reported that MOFs Cr-PTC-HIna has higher photocatalytic activity than Cr-PTC in methylene blue degradation.

MXene is a new type of two-dimensional (2D) material produced by etching a layer of "A" groups from MAX phases, where M is a transition metal like titanium, A is an IVA/IIA (e.g., H, Al, Ga, In, Si, Ge, Sn, Pb, P, or As), and X is nitrogen or carbon [13]. They are composed of transition metal carbides and nitrides with different functional groups like OH^-, O^-, and F^- attached to their surface. The general chemical formula of MXene is $M_{n+1}X_nT_x$, where M is the transition metal like titanium, X is carbon, and T_x is the termination group like OH^-, O^-, and F^- [14-17]. MXene can be applied for treating dyes wastewater because of its physicochemical properties, including high surface area, chemical stability, hydrophilicity, and structure [18]. Besides, the electrical conductivity of Ti_3C_2 MXene is 4600 ± 1100 S.cm^{-1} with highly anisotropic carrier mobility, favoring the capture and transfer of photogenerated electron-hole pairs in the photocatalysis process [19].

According to previous studies by other researchers, MOFs also are often combined with other materials to protect the MOFs from degradation and enhance their photocatalytic activity. Wang et al. [20] reported the synthesis of Ti_3C_2 MXene/MIL-100(Fe) composite for the photocatalytic oxidation of nitrogen fixation. Tian et al. [21] used $Ti_3C_2/TiO_2/UiO-66-NH_2$ hybrids for the photocatalytic reaction of hydrogen gas evolution. Jun et al. [18] reported $Ti_3C_2T_x$ MXene and Al-based metal-organic framework for methylene blue and acid blue 80 adsorptions.

Thus, it is reasonable for us to design new material-based MOFs La-PTC that are modulated by isonicotinic acid (HIna) and combined with $Ti_3C_2T_x$ MXene. This study aims to investigate their characteristics and performance for methylene blue photocatalytic degradation.

■ EXPERIMENTAL SECTION

Materials

All materials were purchased and used without any purification. $La(NO_3)_3 \cdot 6H_2O$ (Merck), dimethyl formamide (DMF) (Merck), sodium hydroxide (Merck), ethanol absolute (Merck), isonicotinic acid (IDN), and $Ti_3C_2T_x$ MXene (Nanochemazone).

Instrumentation

All materials were characterized by X-ray diffraction (PXRD) to determine crystallinity, Fourier transforms infrared (FT-IR) spectroscopy to investigate the functional groups, ultraviolet-visible diffusion reflectance spectroscopy (Shimadzu UV 2700) to measure the band gap, the Brunauer Emmett Teller (BET) surface area analyzer (Micromeritics, ASAP 2020) to evaluate the surface area, pore volume and pore size, and scanning electron microscope energy dispersive X-ray (EDX) spectroscopy to obtain the particle morphology.

Procedure

Preparation of sodium perylene-3,4,9,10-tetracarboxylate (Na₄PTC)

Perylene-3,4,9,10-tetracarboxylic dianhydride (PTCDA) (0.5 g, 1.27 mmol) was dissolved in distilled water (50 mL) on a beaker glass. NaOH (0.356 g, 8.9 mmol) was added to the mixture while stirring vigorously at 300 rpm for 1 h. The greenish-yellow solution was obtained and filtered. Then, excess ethanol was added to obtain a yellow sodium perylene-3,4,9,10-tetracarboxylic (Na₄PTC) precipitate. The yellow bulk powder of Na₄PTC was collected by filtration, washed with ethanol until a pH of 7 was reached, and dried at room temperature overnight.

Synthesis of MOF La-PTC

MOF La-PTC was synthesized according to the method in our previous research [9] $La(NO_3)_3 \cdot 6H_2O$ powder, Na₄PTC at a molar ratio of 1.0:0.5 in dimethyl formamide (DMF), and deionized water mixture (1:5 v/v) in a Teflon liner. After the mixture was stirred magnetically at 300 rpm for 60 min, the Teflon liner was sealed in a solvothermal reactor and heated at 170 °C for 24 h. After cooling to room temperature, the product was purified and washed with deionized water and DMF to remove residual Na₄PTC and other impurities. Finally, the orange powder product was centrifuged and dried at 70 °C overnight.

Synthesis of La-PTC-HIna

$La(NO_3)_3 \cdot 6H_2O$ powder, Na₄PTC, and isonicotinic acid were mixed at a molar ratio of 1.0:0.5:1.0 in DMF

and deionized water mixture (1:5 v/v) in a beaker glass. Then, the mixture was stirred magnetically at 300 rpm for 120 min and ultrasonically treated for 2 h. The bulk powder was filtrated and washed with deionized water and DMF to remove residual Na₄PTC and other impurities. Finally, the brown powder product was centrifuged and dried at 70 °C overnight.

Synthesis of La-PTC/Ti₃C₂Tₓ MXene

The La-PTC/Ti₃C₂Tₓ MXene nanocomposites were constructed by a facile synthetic method. MOF La-PTC and quantitative Ti₃C₂Tₓ MXene (20 wt.%) were put into ethanol absolute. The mixture was stirred for 24 h at 300 rpm, ultrasonically treated for 3 h, and then dried at 60 °C for 18 h. The product was then heated in a 300 °C furnace for 2 h. Finally, the Ti₃C₂Tₓ MXene nanosheets were coupled with MOF La-PTC after grinding.

Synthesis of La-PTC-HIna/Ti₃C₂Tₓ MXene

La(NO₃)₃·6H₂O powder, Na₄PTC, and isonicotinic acid were mixed at a molar ratio of 1.0:0.5:1.0 in DMF and deionized water mixture (1:5 v/v) in a beaker glass. Then a quantitative Ti₃C₂ MXene (20 wt.%) was added. Then, the mixture was stirred magnetically at 300 rpm for 120 min and ultrasonically treated for 2 h. The precipitate was filtrated and washed with deionized water and DMF to remove residual Na₄PTC and other impurities. Finally, the brown powder product was centrifuged and dried at 70 °C overnight.

Degradation of methylene blue analysis

The material (25 mg) was dispersed in 50 mL of methylene blue (MB) solution (20 ppm) in a Pyrex reactor. Subsequently, the sample was irradiated with the 250 W mercury lamp with stirring at 300 rpm and room temperature. The concentration of MB after the reaction was measured by a UV-Visible spectrophotometer at 665 nm. The methylene blue degradation efficiency is calculated using Eq. (1). A control experiment was carried out under dark condition.

$$DE(\%) = \frac{Co - Ct}{Co} \times 100\% \qquad (1)$$

where DE (%) is the degradation efficiency of methylene blue, Co is the initial concentration, and Ct is the final concentration.

■ RESULTS AND DISCUSSION

Characteristic of Photocatalysts

The XRD analysis showed the different diffraction spectrums of materials. Fig. 1 shows that La-PTC-HIna and La-PTC-HIna/Ti₃C₂Tₓ MXene have amorphous forms, while the other three have pretty good crystallinity. The XRD peaks of La-PTC were observed at $2\theta = 6.31°, 12.64°, 16.6°, 28.7°, 33.3°, 44.6°, 47.9°, 50.9°, 59.6°, 62.3°, 70°, 77.3°$ [9]. Peaks at $2\theta = 9.0°, 18.3°, 27.7°, 36.1°, 41.9°,$ and $60.7°$ correspond to the (002), (004), (006), (101), (105), and (110) reflections of Ti₃C₂Tₓ MXene [22]. Peaks at $2\theta = 5.7°, 8.4°, 12.1°, 18.5°, 20.9°, 22.9°, 26.9°,$ and $29.3°$ are characteristics of La-PTC/Ti₃C₂Tₓ MXene (Fig. 1). It shows a chemical interaction between Ti₃C₂Tₓ MXene and La-PTC compounds which looks at the difference in the spectrum of the three materials. Meanwhile, for La-PTC-HIna and La-PTC-HIna/Ti₃C₂Tₓ MXene, the spectral peaks cannot be determined because the resulting particles are amorphous.

FT-IR spectroscopy was employed to determine the functional groups in the five materials. The infrared spectrum of all materials can be seen in Fig. 2 and Table 1. The FTIR spectrum of La-PTC/Ti₃C₂Tₓ Mxene is very similar to La-PTC, and La-PTC-HIna/Ti₃C₂Tₓ Mxene is
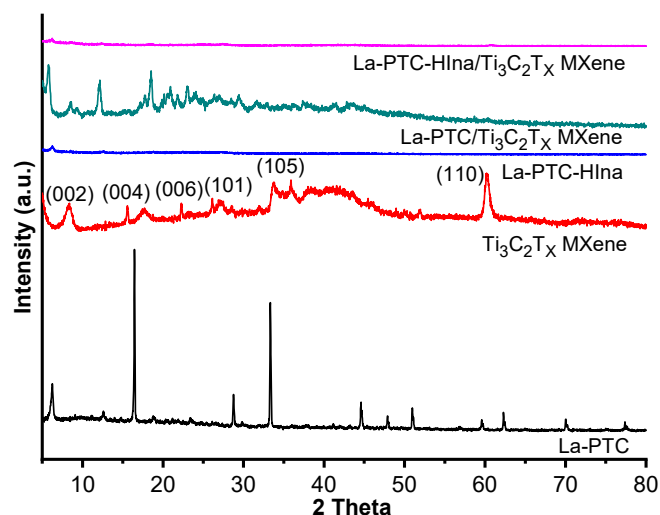
Fig 1. XRD pattern of MOF La-PTC, Ti₃C₂Tₓ MXene, La-PTC/Ti₃C₂Tₓ MXene, La-PTC-HIna, and La-PTC-HIna/Ti₃C₂Tₓ Mxene

Table 1. Wavenumber and functional group of materials

Wavenumber (cm⁻¹)					
Ti₃C₂Tₓ MXene	La-PTC	La-PTC-HIna	La-PTC/Ti₃C₂Tₓ MXene	La-PTC-HIna/Ti₃C₂Tₓ MXene	Description
425			421	424	the deformation vibration of the Ti–O bond
506			501	502	Ti-C vibration
	572	570	556	568	La-O vibration
	749	759	761	757	Out of plane C=C aromatic ring
	849, 808	849, 807	848, 807	858, 807	Bending vibration (C-H) out of plane aromatic ring
	1210	1207	1209	1233	Bending vibration (C-H) in plane aromatic ring
	1530	1585	1590	1591	asymmetric stretching vibration (-COO)
	1434	1526	1503	1537	symmetric stretching vibration (-COO)
3034		3356	3399	3117	Hydroxyl (OH)
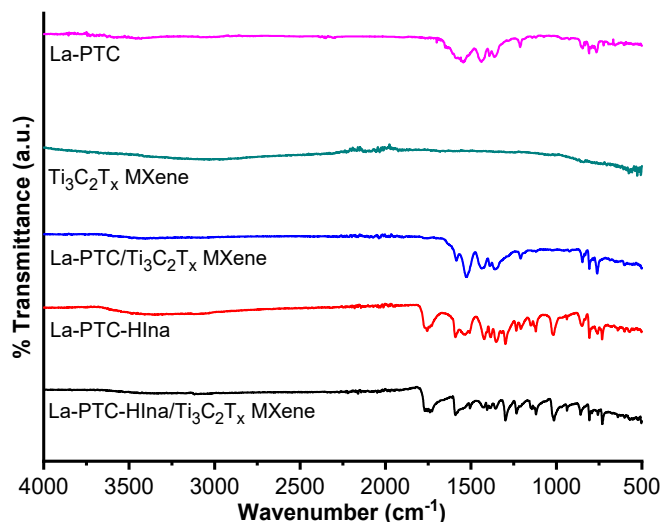
**Fig 2.** IR spectrum of MOF La-PTC, Ti₃C₂Tₓ MXene, La-PTC/Ti₃C₂Tₓ MXene, La-PTC-HIna, and La-PTC-HIna/Ti₃C₂Tₓ MXene

very similar to La-PTC-HIna. It indicates the functional group consistency of the La-PTC and La-PTC-HIna materials on the surface of the La-PTC/Ti₃C₂Tₓ Mxene and La-PTC-HIna/Ti₃C₂Tₓ Mxene hybrid.

A UV-Vis spectrophotometer was carried out to determine the band gap energy and visible light absorption capacity of the materials. Fig. 3 exhibits the absorption band edges for the La-PTC, Ti₃C₂Tₓ MXene, La-PTC-HIna, La-PTC/Ti₃C₂Tₓ MXene, and La-PTC-HIna/Ti₃C₂Tₓ MXene composite. The band gap energy of those materials was calculated using the Kubelka-Munk

equation ($\alpha h\nu = A(h\nu~Eg)^2$) [23]. The calculation results in the band gap energy of Ti₃C₂Tₓ MXene of 1.3 eV (Table 2) and does not show an absorption band because it is a metallic material [24]. La-PTC/Ti₃C₂Tₓ MXene hybrid band gap (2.3 eV) is higher than that of the La-PTC (2.21 eV). In contrast, the band gap energy of La-PTC-HIna/Ti₃C₂Tₓ MXene composite (1.9 eV) is less than La-PTC-HIna (2.02 eV). It confirmed that the Ti, C, and O doping process from Ti₃C₂Tₓ MXene to the surface of the La-PTC and La-PTC-HIna structure had been successfully carried out. This difference occurs because of the heterojunction formed by MOF La-PTC, La-PTC-HIna, and Ti₃C₂Tₓ MXene, forming a new material. On the other hand, the band gap energy of La-PTC-HIna (2.02 eV) is less than La-PTC. (2.2 eV) The factor that can affect the bandgap energy is particle size. Modulated isonicotinic acid in the La-PTC reduces its particle size. The decreased particle size generated the MOFs charge carriers to interact quantum mechanically. It leads to a discrete electrolytic state which increases bandgap energy and a shift in band edge.

Table 2. Band gap energy of materials

Material	Eₖ (eV)
Ti₃C₂Tₓ MXene	1.30
La-PTC	2.20
La-PTC-HIna	2.02
La-PTC/Ti₃C₂Tₓ MXene	2.30
La-PTC-HIna/Ti₃C₂Tₓ MXene	1.90

Indones. J. Chem., 2022, 22 (5), 1195 - 1204

1199
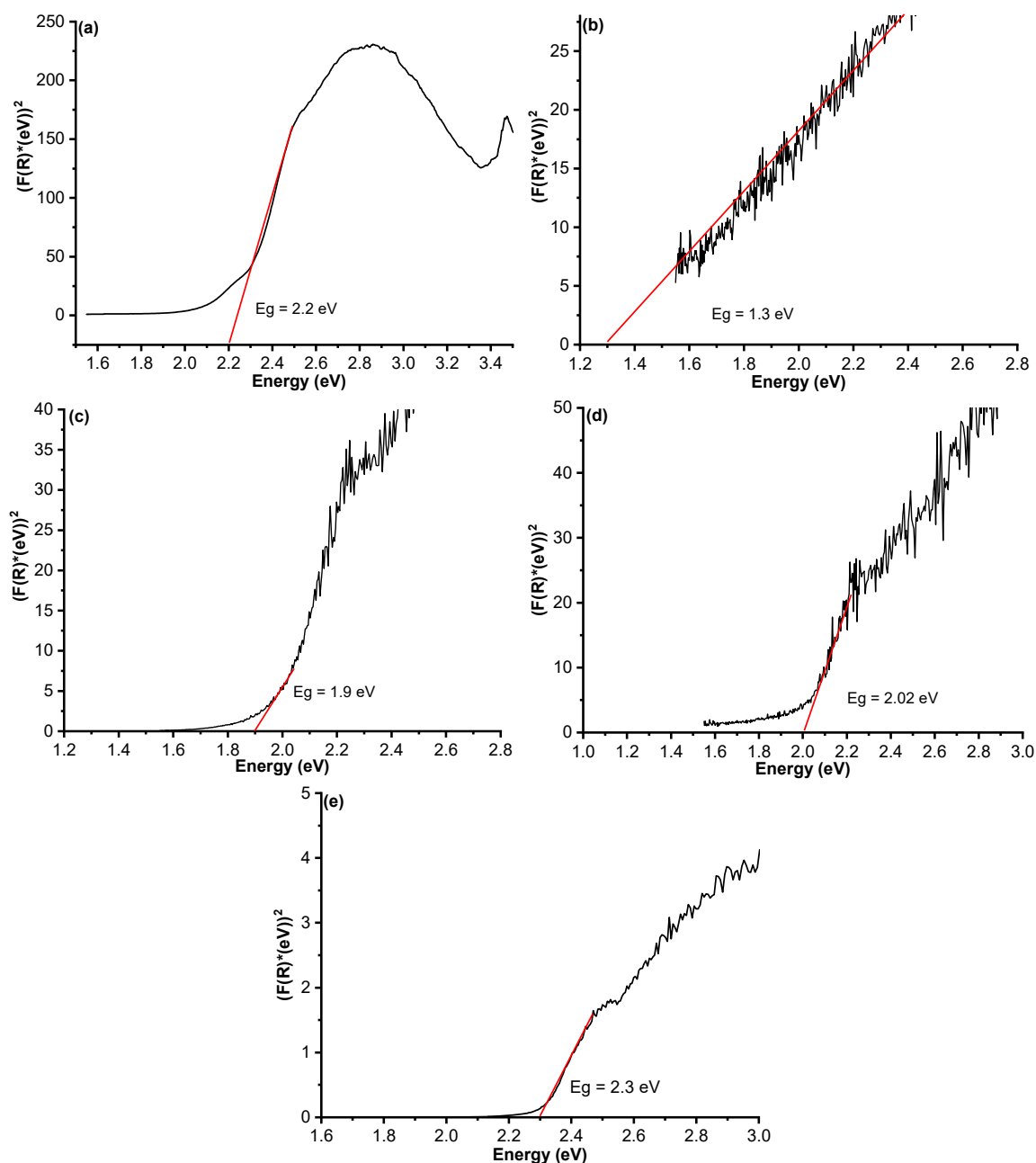
Fig 3. Band gap energy curves derived from UV-Vis diffuse reflectance spectroscopy (DRS) spectra for (A) MOF La-PTC; (B) $Ti_3C_2T_x$ MXene; (C) La-PTC-HIna; (D) La-PTC-HIna/$Ti_3C_2T_x$ MXene, and (E) La-PTC/$Ti_3C_2T_x$ MXene

The measured parameters of those five materials include the specific surface area (S_{BET}), the total pore volume (V_p), and the average pore size (D_p). Modulated isonicotinic acid (HIna) improved the surface area, pore volume, and pore size of La-PTC (Table 3). Table 3 exhibited that all materials have pore size distribution found in the 2–25 nm range. It is assumed that they were mesoporous materials groups, which have the advantage of being a photocatalyst that can provide a short distance to reduce the recombination of photo-excited electron and hole pairs [25]. Modulated isonicotinic acid (HIna) and loading of $Ti_3C_2T_x$ MXene on the MOF La-PTC do not destroy the MOF's mesoporosity.

The morphological features of all materials were determined by scanning electron microscopy (SEM). Fig. 4(a) shows the multilayer nanoflakes of $Ti_3C_2T_x$

1200

Indones. J. Chem., 2022, 22 (5), 1195 - 1204

MXene. It was produced when Ti_3AlC_2 released H_2 gas during the exothermic reaction of HF and the process of freeze-drying [26]. Fig. 4(b) shows that the La-PTC has a rod shape structure with various lengths and diameters. The structure of La-PTC has a good homogeneity, as indicated by the crystal structure having almost the same morphology at each observation point.

The EDS characterization in Table 4 exhibited that La-PTC/$Ti_3C_2T_x$ MXene and La-PTC/$Ti_3C_2T_x$ MXene contain elements derived from their constituents, namely $Ti_3C_2T_x$ MXene, La-PTC and La-PTC-HIna. It confirmed that combining the two compounds has succeeded in producing hybrid compounds that are different from their constituent precursors.

Table 3. Surface area, pore volume, and pore size of materials

Material	S_{BET} (m^2 g^{-1})	V_p (cm^3 g^{-1})	D_p (nm)
$Ti_3C_2T_x$ MXene	2.0892	0.0127	24.3011
La-PTC	22.2364	0.0685	12.3291
La-PTC-HIna	55.3904	0.1927	13.9166
La-PTC/$Ti_3C_2T_x$ MXene	34.8508	0.1033	11.8532
La-PTC-HIna/$Ti_3C_2T_x$ MXene	43.2119	0.1655	15.3235
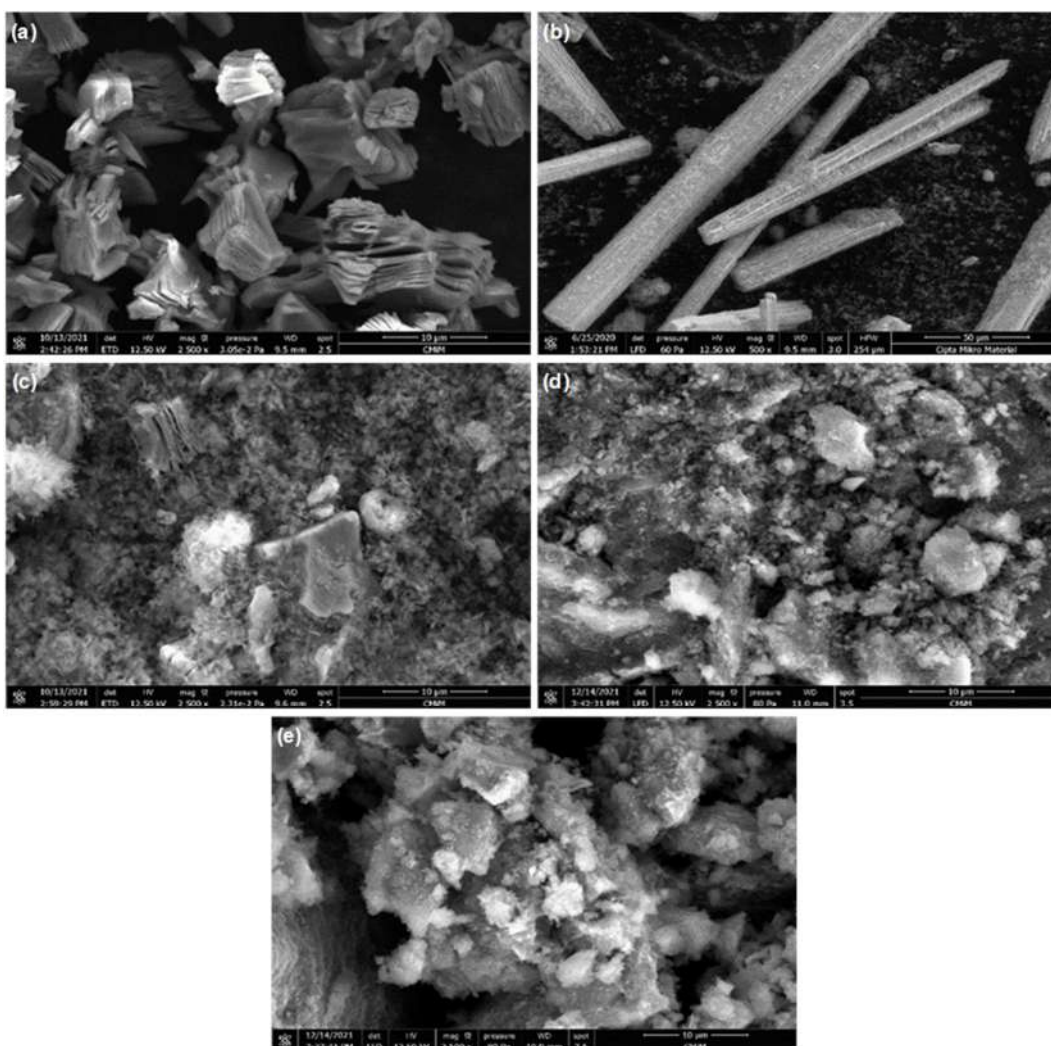
Fig 4. Scanning electron microscope (SEM) morphology of (a) $Ti_3C_2T_x$ MXene; (b) La-PTC; (c) La-PTC/$Ti_3C_2T_x$ MXene; (d) La-PTC-HIna; (e) La-PTC-HIna/$Ti_3C_2T_x$ MXene

Table 4. Element composition of materials

Element	Material				
	$Ti_3C_2T_x$ MXene	La-PTC	La-PTC-HIna	La-PTC/$Ti_3C_2T_x$ MXene	La-PTC-HIna/$Ti_3C_2T_x$ MXene
C	17.44	51.8	54.61	51.30	29.15
O	14.97	28.3	12.07	19.69	12.07
F	14.81			2.29	13.08
Al	1.26		4.41	0.34	0.94
Ti	51.52			9.35	19.78
La		19.9	23.97	17.05	24.27

Degradation of Methylene Blue

Fig. 5 shows the methylene blue degradation efficiency by La-PTC, $Ti_3C_2T_x$ MXene, La-PTC/$Ti_3C_2T_x$ MXene, La-PTC-HIna, and La-PTC-HIna/$Ti_3C_2T_x$ MXene for 210 min time reaction. Methylene blue degradation can be attained in dark and light conditions and occurs through surface adsorption and photocatalytic degradation mechanisms. Fig. 5 observed that La-PTC and La-PTC/$Ti_3C_2T_x$ MXene have no photocatalytic activity. Zulys et al. [9] explained that the photocatalytic activity of La-PTC depends on the electron-hole recombination process. The conduction band (CB) of La-PTC (-1.60 eV) which less negative than the lowest unoccupied molecular orbital (LUMO) of methylene blue (-0.25 eV), and the valence band (VB) of La-PTC (+0.61 eV) is less positive than highest occupied molecular orbital (HOMO) of MB (+1.66 eV). Thus, photoexcited electron-hole pairs do not oxidize the MB to produce the

MB radical (MB•). Then it will be recombined, and the formation of radical species was not produced. Therefore, it inhibited the methylene blue photocatalytic degradation. On the other hand, the degradation efficiency of methylene blue by $Ti_3C_2T_x$ MXene, La-PTC-HIna, and La-PTC-HIna/Ti_3C_2 MXene hybrid in the light condition was higher than in dark conditions. It confirmed that those materials have the photocatalytic activity to degrade methylene blue.

In dark conditions, $Ti_3C_2T_x$ MXene degrades methylene blue through an adsorption mechanism that was influenced by electrostatic interaction between the negative charge of both hydroxyl (-OH) and fluoride (F^-) termination group on the $Ti_3C_2T_x$ MXene surface and positive charge on sulfur (S) or nitrogen (N) on the methylene blue molecule [27]. These F^- and OH termination groups are developed to form negative charges on the $Ti_3C_2T_x$ MXene surface, such as [Ti-F]$^-$
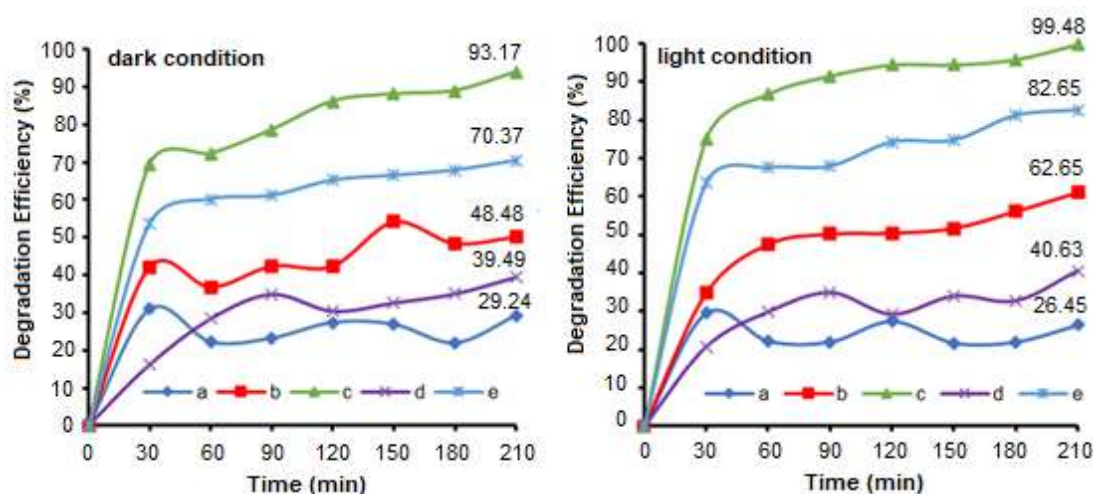
Fig 5. Degradation efficiency of methylene blue for different materials: (a) La-PTC, (b) $Ti_3C_2T_x$ MXene, (c) La-PTC-HIna, (d) La-PTC/$Ti_3C_2T_x$ MXene, and (e) La-PTC-HIna/$Ti_3C_2T_x$ MXene in the dark and light irradiation

and [TiO]⁻H⁺, which are acted as receptors to cationic species such as methylene blue [27]. The complex formation between methylene blue and $Ti_3C_2T_x$ MXene is given below.

[Ti-F]⁻ + MB → Ti-F-MB (1)
[Ti-O]⁻H⁺ → [Ti-O]⁻ + H⁺ (2)
[Ti-O]⁻ + MB → Ti-O-MB (1)
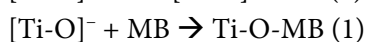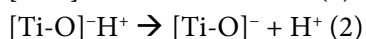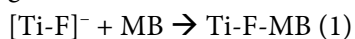
My Tran et al. [27] explained that the F⁻ terminated group on MXene plays a prominent role in the adsorption of MB. The adsorption capability of $Ti_3C_2T_x$ MXene on methylene blue decreased as the pH increased from 2 to 7 [27]. Increasing the pH causes a decrease in the number of F⁻ termination groups on the surface of the $Ti_3C_2T_x$ MXene because F⁻ terminated groups were replaced with OH⁻ ions from water. It also, the electronegativity of F is larger than O ($\chi F = 3.98$, $\chi O = 3.44$), leading to the remarkable ability of most F⁻ terminated $Ti_3C_2T_x$ to attract and absorb MB species. In addition, after the F⁻ group is replaced with an OH⁻ group, the degree of electrostatic attraction between O⁻ and MB⁺ decreases with H⁺ compensation [27]. Lim et al. [28] reported that increasing the pH solution explained the increase in the adsorption capacity of $Ti_3C_2T_x$ MXene to methylene blue. At the high pH level, $Ti_3C_2T_x$ MXene was more negatively charged. It is attributed to promoting the adsorption of cationic dyes like methylene blue via electrostatic attraction. Otherwise, the $Ti_3C_2T_x$ MXene surface becomes a relatively less negative charge at a low pH level because the hydroxyl group (OH⁻) is neutralized on the $Ti_3C_2T_x$ MXene surface by hydrogen ion (H⁺) in solution.

Hasan and Jhung [29] explained that the MB adsorption by MOF occurred through electrostatic, hydrophobic, acid-base, π-π, hydrogen attraction, or a combination of these interactions. In La-PTC, the electrostatic attraction occurs between the positive charge of MB and the negative charge of MOF La-PTC. π-π interaction occurred through π bonding in the aromatic ring in MB and the aromatic ring in the perylene linker contained in the La-PTC. The hydrogen attraction was constructed between the hydrogen of MB and the oxygen of perylene. In addition, the hydrogen interaction between hydrogen in MB and nitrogen from the pyridine ring of isonicotinic acid contributed to La-PTC-HIna.

Fig. 5 shows that under dark conditions, the five materials' adsorption ability is affected by their surface area, volume, and pore size. La-PTC-HIna has the highest adsorption ability, producing a degradation efficiency of 93.95% compared to the other four materials. It is because La-PTC-HIna has the highest surface area, pore volume, and pore size (except $Ti_3C_2T_x$ MXene and La-PTC-HIna/$Ti_3C_2T_x$ MXene pore size), which is 55.3904 m²/g, 0.1927 cm³/g and 13.9166 nm (Table 2). Although $Ti_3C_2T_x$ MXene has a lower surface area and pore volume than La-PTC and La-PTC/$Ti_3C_2T_x$ MXene, it has a higher adsorption capacity (48.48%) due to its pore size, which is twice the pore size of La-PTC and La-PTC/$Ti_3C_2T_x$ MXene (Table 2). The same thing was also proven by Gupta et al. [30], who succeeded in synthesizing Cu-BTC, Ag-Cu-BTC, and Ca-Cu-BTC with a surface area of 163.43, 187.64, and 17.08 m²/g, respectively. The total pore volume is 0.144, 0.113, and 0.299 cm³/g, and the pore size is 3.5, 2.4, and 70.1 nm. The adsorption activity of MOFs Cu-BTC, Ag-Cu-BTC, and Ca-Cu-BTC against methylene blue compounds was 12.7, 8.9, and 19.6 mg/g.

Fig. 5 also exhibits that under light irradiation, MOF La-PTC-HIna has the highest photocatalytic activity among other materials, with a degradation efficiency of 99.48%. The addition of isonicotinic acid as a modulator enhanced the photocatalytic activity of La-PTC. The isonicotinic acid in the La-PTC-HIna acts as a linker competitor. It competes with perylene to replace some of the perylene ligands in the La-PTC [31]. The perylene replacement by the isonicotinic acid formed a MOF with a smaller particle size [20]. The smaller particle size of the MOFs increases the surface area of MOFs. Therefore, the pores containing the active site will increase [32]. It generates an increasing number of active sites, and the photocatalytic activity will be higher.

■ CONCLUSION

La-PTC, $Ti_3C_2T_x$ MXene, La-PTC-HIna, La-PTC/$Ti_3C_2T_x$ MXene, and La-PTC-HIna/$Ti_3C_2T_x$ MXene were comparatively evaluated for their application as photocatalysts in the methylene blue degradation. La-PTC-HIna has the most significant degradation activity compared to La-PTC, $Ti_3C_2T_x$

MXene, La-PTC/Ti$_3$C$_2$T$_x$ MXene, and La-PTC-HIna/Ti$_3$C$_2$T$_x$ MXene hybrid with a degradation efficiency of 99.48% in 20 ppm methylene blue under visible irradiation for 210 min. The degradation of methylene blue by La-PTC-HIna occurs via the adsorption and photocatalytic mechanism. The methylene blue degradation by La-PTC-HIna/Ti$_3$C$_2$T$_x$ MXene hybrid is lower than La-PTC-HIna due to a decrease in surface area and pore volume in the material after the loading of Ti$_3$C$_2$T$_x$ MXene.

■ **ACKNOWLEDGMENTS**

■ **REFERENCES**

[1] Saeed, M., Usman, M., and ul Haq, A., 2018, "Catalytic Degradation of Organic Dyes in Aqueous Medium" in *Photochemistry and Photophysics – Fundamentals to Applications*, Eds. Saha, S., and Mundal, S., IntechOpen, Rijeka, Croatia, 197–211.

[2] Khelifi, S., and Ayari, F., 2019, Modified bentonite for anionic dye removal from aqueous solutions. Adsorbent regeneration by the photo-Fenton process, *C. R. Chim.*, 22 (2-3), 154–160.

[3] Saini, J., Garg, V.K., Gupta, R.K., and Kataria, N., 2017, Removal of Orange G and Rhodamine B dyes from aqueous system using hydrothermally synthesized zinc oxide loaded activated carbon (ZnO-AC), *J. Environ. Chem. Eng.*, 5 (1), 884–892.

[4] Fan, Y.H., Zhang, S.W., Qin, S.B., Li, X.S., and Qi, S.H., 2018, An enhanced adsorption of organic dyes onto NH$_2$ functionalization titanium-based metal-organic frameworks and the mechanism investigation, *Microporous Mesoporous Mater.*, 263, 120–127.

[5] Ibrahim, Y., Meslam, M., Eid, K., Salah, B., Abdullah, A.M., Ozoemena, K.I., Elzatahry, A., Sharaf, M.A., and Sillanpa, M., 2022, A review of MXenes as emergent materials for dye removal from wastewater, *Sep. Purif. Technol.*, 282, 120083.

[6] Lu, W., Wei, Z., Gu, Z.Y., Liu, T.F., Park, J., Park, J.,

[7] Tian, J., Zhang, M., Zhang, Q., Gentle III, T., Bosch, M., and Zhou, H.C., 2014, Tuning the structure and function of metalorganic frameworks via linker design, *Chem. Soc. Rev.*, 43 (16), 5561–5593.

[7] Alqadami, A.A., Naushad, M., Alothman, Z.A., and Ahamad, T., 2018, Adsorptive performance of MOF nanocomposite for methylene blue and malachite green dyes: Kinetics, isotherm and mechanism, *J. Environ. Manage.*, 223, 29–36.

[8] Gong, X., Zhao, R., Qin, J., Wang, H., and Wang, D., 2019, Ultra-efficient removal of NO in a MOFs-NTP synergistic process at ambient temperature, *Chem. Eng. J.*, 358, 291–298.

[9] Zulys, A., Adawiah, A., Gunlazuardi, J., and Yudhi, M.D.L., 2021, Light-harvesting metal-organic frameworks (MOFs) La-PTC for photocatalytic dyes degradation, *Bull. Chem. React. Eng. Catal.*, 16 (1), 170–178.

[10] Zhang, F.H., Wang, Y.Y., Lv, C., Li, Y.C., and Zhao, X.Q., 2019, Luminescent complexes associated with isonicotinic acid, *J. Lumin.*, 207, 561–570.

[11] Garibay, S.J., Iordanov, I., Islamoglu, T., DeCoste, J.B., and Farha, O.K., 2018, Synthesis and functionalization of phase-pure NU-901 for enhanced CO$_2$ adsorption: The influence of zirconium salt and modulator on topology and phase purity, *CrystEngComm*, 20 (44), 7066–7070.

[12] Adawiah, A., Oktavia, W., Saridewi, N., Azhar, F.M., Fitria, R.N., Gunawan, M.S., Komala, S., and Zulys A., 2022, Synthesis metal-organic framework (MOFs) Cr-PTC-HIna modulated isonicotinic acid for methylene blue photocatalytic degradation, *Bull. Chem. React. Eng. Catal.*, 17 (2), 383–393.

[13] Wang, H., Zhao, R., Qin, J., Hu, H., Fan, X., Cao, X., and Wang, D., 2019, MIL-100(Fe)/Ti$_3$C$_2$ MXene as a Schottky catalyst with enhanced photocatalytic oxidation for nitrogen fixation activities, *ACS Appl. Mater. Interfaces*, 11 (47), 44249–44262.

[14] Anasori, B., Xie, Y., Beidaghi, M., Lu, J., Hosler, B.C., Hultman, L., Kent, P.R.C., Gogotsi, Y., and Barsoum, M.W., 2015, Two-dimensional, ordered, double transition metals carbides (MXenes), *ACS Nano*, 9 (10), 9507–9516.

[15] Khazaei, M., Arai, M., Sasaki, T., Chung, C.Y., Venkataramanan, N.S., Estili, M., Sakka, Y., and Kawazoe, Y., 2013, Novel electronic and magnetic properties of two-dimensional transition metal carbides and nitrides, *Adv. Funct. Mater.*, 23 (17), 2185–2192.

[16] Naguib, M., Mochalin, V.N., Barsoum, M.W., and Gogotsi, Y., 2014, MXenes: A new family of two-dimensional materials, *Adv. Mater.*, 26 (7), 992–1005.

[17] Khazaei, M., Arai, M., Sasaki, T., Estili, M., and Sakka, Y., 2014, Two-dimensional molybdenum carbides, potential thermoelectric materials of the MXene family, *Phys. Chem. Chem. Phys.*, 16 (17), 7841–7849.

[18] Jun, B.M., Kim, S., Heo, J., Park, C.M., Her, N., Jang, M., Huang, Y., Han, J., and Yoon, Y., 2018, Review of MXenes as new nanomaterials for energy storage/delivery and selected environmental applications, *Nano Res.*, 12 (3), 471–487.

[19] Khazaei, M., Ranjbar, A., Arai, M., Sasaki, T., and Yunoki, S., 2017, Electronic properties and applications of MXenes: A theoretical review, *J. Mater. Chem. C*, 5 (10), 2488–2503.

[20] Wang, F., Guo, H., Chai, Y., Li, Y., and Liu, C., 2013, The controlled regulation of morphology and size of HKUST-1 by "coordination modulation method", *Microporous Mesoporous Mater.*, 173, 181–188.

[21] Tian, P., He, X., Zhao, L., Li, W., Fang, W., Chen, H., Zhang, F., Huang, Z., and Wang, H., 2019, Enhanced charge transfer for efficient photocatalytic H_2 evolution over UiO-66-NH_2 with annealed $Ti_3C_2T_x$ MXenes, *Int. J. Hydrogen Energy*, 44 (2), 788–800.

[22] Zhao, X., Liu, M., Chen, Y., Hou, B., Zhang, N., Chen, B., Yang, N., Chen, K., Li, J., and An, L., 2015, Fabrication of layered Ti_3C_2 with an accordion-like structure as a potential cathode material for high performance lithium-sulfur batteries, *J. Mater. Chem. A*, 3 (15), 7870–7876.

[23] Mu, X., Jiang, J., Chao, F., Lou, Y., and Chen, J., 2018, Ligand modification of UiO-66 with an unusual visible light photocatalytic behavior for RhB degradation, *Dalton Trans.*, 47 (6), 1895–1902.

[24] Lukatskaya, M.R., Mashtalir, O., Ren, C.E., Dall'Agnese, Y., Rozier, P., Taberna, P.L., Naguib, M., Simon, P., Barsoum, M.W., and Gogotsi, Y., 2013, Cation intercalation and high volumetric capacitance of two-dimensional titanium carbide, *Science*, 341 (6153), 1502–1505.

[25] Chang, S.S., Clair, B., Ruelle, J., Beauchêne, J., Di Renzo, F., Quignard, F., Zhao, G.J., Yamamoto, H., and Gril, J., 2009, Mesoporosity as a new parameter for understanding tension stress generation in trees, *J. Exp. Bot.*, 60 (11), 3023–3030.

[26] Alhabeb, M., Maleski, K., Anasori, B., Lelyukh, P., Clark, L., Sin, S., and Gogotsi, Y., 2017, Guidelines for synthesis and processing of two-dimensional titanium carbide ($Ti_3C_2T_x$ MXene), *Chem. Mater.*, 29 (18), 7633–7644.

[27] My Tran, N., Thanh Hoai Ta, Q., Sreedhar, A., and Noh. J.S., 2021, $Ti_3C_2T_x$ MXene playing as a strong methylene blue adsorbent in wastewater, *Appl. Surf. Sci.*, 537, 148006.

[28] Lim, S., Kim, J.H., Park, H., Kwak, C., Yang, J., Kim, J., Ryu, S.Y., and Lee, J., 2021, Role of electrostatic interactions in the adsorption of dye molecules by Ti_3C_2-MXenes, *RSC Adv.*, 11 (11), 6201–6211.

[29] Hasan, Z., and Jhung, S.H., 2015, Removal of hazardous organics from water using metal-organic frameworks (MOFs): Plausible mechanisms for selective adsorptions, *J. Hazard. Mater.*, 283, 329–339.

[30] Gupta, N.K., Bae, J., and Kim, K.S., 2022, Role of bimetallic solution in the growth and functionality of Cu-BTC metal-organic framework, *Materials*, 15 (8), 2804.

[31] Hasan, M.R., 2015, Pengaruh Penambahan Modulator Asam Asetat pada Sintesis Metal Organic Framework Tipe HKUST-1, *Undergraduate Thesis*, Intitute Teknologi Sepuluh Nopember, Surabaya, Indonesia.

[32] Tambun, R., Limbong, H.P., Pinem, C., and Manurung, E., 2016, Pengaruh ukuran partikel, waktu dan suhu pada ekstraksi fenol dari lengkuas merah, *Jurnal Teknik Kimia USU*, 5 (4), 53–56.

Role of Temperature and Exposure Time for Controlled and Accelerated Synthesis of Graphene Oxide Using Tour Method

Uswatul Chasanah[1], Wega Trisunaryanti[1*], Haryo Satriya Oktaviano[2],
Triyono Triyono[1], and Dyah Ayu Fatmawati[1]

[1]*Department of Chemistry, Faculty of Mathematics and Natural Sciences, Universitas Gadjah Mada,*
Sekip Utara, Yogyakarta 55281, Indonesia

[2]*Research & Technology Center, PT. Pertamina (Persero), Sopo Del Tower A, Floor 51,*
Jl. Mega Kuningan Barat III, Kawasan Mega Kuningan, Jakarta Selatan, DKI Jakarta, 12950, Indonesia

* *Corresponding author:*

email: wegats@ugm.ac.id

Abstract: *Synthesis of graphene oxide (GO) with the Tour method has been studied. In this procedure, phosphoric acid was mixed with sulfuric acid in the ratio of 1:9, and then potassium permanganate and graphite with the ratio of 6:1 was added in an ice bath at the variation of oxidation times of 1, 7 and 24 h and temperatures of 40, 50 and 60 °C. The GOs were characterized by UV–Visible spectroscopy, Fourier Transform InfraRed (FT-IR) spectroscopy, X-ray Diffraction (XRD), Scanning Electron Microscopy-Energy Dispersive X-Ray (SEM-EDX), and Transmission Electron Microscopy (TEM). The results show that the GO oxidized at 40 °C for 7 h (GO-7-40) has been successfully formed indicating that GO-7-40 is the most efficient GO. The GO-7-40 is characterized by a peak at $2\theta = 10.89°$ in the XRD diffractogram, resulting calculation of the average distance between graphene layer (d) of 0.81 nm. The average number of graphene layers (n) is 4, the oxidation level (C/O) is 1.50 according to EDX data, λ_{max} at 226 nm attributes to $\pi{\rightarrow}\pi^*$ transitions of C=C bond in UV-Vis spectrum, and the functional groups such as O-H, C=C, C-OH, and C-OC are observed in FT-IR spectrum.*

Keywords: *graphene oxide; oxidation time; temperature; Tour method*

■ INTRODUCTION

Graphene oxide (GO) is a single-layer graphene nanosheet bonded with functional groups containing oxygen and is part of carbon material derivatives [1]. Graphene oxide displays some outstanding properties, such as high thermal conductivity, specific surface area and electrical conductivity [2]. The high electrical conductivity of graphene is due to zero-overlap semimetal with electrons and holes as charge carriers. Each carbon atom has six electrons, and the four outermost electrons are available for chemical bonding, but in the 2-D plane, each atom is connected to three other carbon atoms, and one electron is freely available for electronic conduction in the 3-D space [3]. It has received much attention for use as an adsorption material and in catalytic applications, owing to its suitable adsorbents and photonic properties

for catalysis, which can improve the photocatalytic properties of materials [4]. Graphene oxide is usually also used as antibiotics [5], chemical sensors [6], and in the removal of organic dyes [7] as well as heavy metal ions [8].

Graphene oxide can be synthesized by the chemical vapor deposition (CVD) as one of the effective techniques for the preparation of low-defect density and enhanced large area monolayer or film-layer graphene films. However, the CVD technique consumes time, uses large amounts of high purity gases and demands high energy input. Plasma enhanced CVD utilizes lower processing temperature. However, producing high-quality graphene with enhanced surface area with fewer defects remains challenging [9]. The other choice, GO can be produced from the oxidation and exfoliation of

graphite, generally in an aqueous solution, yielding hydrophilic carbon-based sheets that are decorated with various oxygenated functional groups [10]. Synthesis of graphene with high quality from graphite can be done with the chemical exfoliation method [11]. This technique combines the oxidation of graphite followed by the reduction process to produce graphene nanosheets. The oxidation of graphite is spread over a long period. Benjamin Collins Brodie [12] has reported that the addition of potassium chlorate ($KClO_3$) to the graphitic compound in nitric acid (HNO_3) provides an increase in the weight of the sample due to the incorporation of hydrogen (H) and oxygen (O). Another method of graphite oxidation has been reported by Staudenmaier [13] with still emphasizing the use of sulfuric acid (H_2SO_4) and a high amount of potassium chlorate ($KClO_4$). Meanwhile, Hummers and Offeman [14] have proposed the use of potassium permanganate ($KMnO_4$) and sulfuric acid as reagents. The H_2SO_4 acts as an intercalation agent stabilizing the oxidant and solvent to transport the oxidant into the graphite interlayers [15]. This approach differs from Brodie method [12], particularly regarding to the reagents and the time of the reaction. Also, the Hummers method requires a step to remove the excess permanganate ions and stop the oxidation reaction using hydrogen peroxide [16]. In the Hummers method, $KMnO_4$ is used to replace $KClO_3$ to avoid spontaneous explosion during the oxidation process, while $NaNO_3$ replaced fuming HNO_3 to eliminate fog acid produced. This process takes just in few hours to produce high-quality GO. The Hummers method still has flaws, whereby it produces toxic gas such as NO_2 and N_2O_4 because of the use of $NaNO_3$ [17].

Marcano et al. [10] have completed the study on the differences among the Hummers method, modified Hummers method, and improved Hummers method without $NaNO_3$. In 2010, Tour et al. [18] reported an improvement in the Hummers method by excluding $NaNO_3$ to prevent the generation of toxic gases, using ice instead of liquid water to prevent the high-temperature rise, thus promoting better and easier control of the process, and also increasing the yield and degree of oxidation, together with promoting the retention of

carbon rings in the basal plane by introducing phosphoric acid (H_3PO_4) to the reaction media. The Tour method is based on the dispersing of graphite in a mixture of concentrated sulfuric and phosphoric acids in a volume ratio of 9:1 and further oxidation of graphite by potassium permanganate [19]. The Tour method eliminates the production of toxic gases and produces a more oxidized graphite oxide with a more regular carbon framework and larger sheet size [20]. Another advantage of the Tour method is to produce a higher yield of heavily oxidized hydrophilic GO [21-22].

According to researchers [23-25], various modifications of the Tour methods can be carried out using different amounts of graphite, oxidant concentrations, oxidation time, and temperature used. Temperature affects the formation of single-layer GO [26]. Many reports that provide a detailed procedure for the synthesis of GO were analyzed based on this perspective. For example, Olorunkosebi et al. [27] allowed this step to prolong with various oxidation times 11, 12, 13, and 14 h at 50 °C. Sali et al. [16] studied temperature of 30 °C but used oxidation time of 72 h. Habte and Ayele [28] maintained the temperature of the system at 50 °C for 12 h, while Benzait et al. [24] synthesized GO at temperature below 10 °C for 24 h. Ranjan et al. [29] concluded that good quality GO samples can be synthesized through Tour method at 65 °C with the oxidation time of 24 h This strategy did not have any Mn and spurious carbonaceous residues without the need for any sophisticated filtration protocol. Meanwhile, Kang et al. [30] adopted the Hummers method and investigated it with three time-variables (2, 4 and 8 h) and three temperature-variables (45, 70 and 95 °C) resulting in GO at 45 °C for 8 h.

There have been many studies on GO synthesis with various oxidation times and/or temperatures. The oxidation time used is quite long (above 8 h) and the temperature used is quite high. Therefore, this study suggests a new insight for studying temperature and oxidation time using the Tour method. Reducing oxidation time and temperature can improve the green chemistry aspect. This research is expected to get an effective and efficient method for producing more GO.

■ EXPERIMENTAL SECTION

Materials

Hydrochloric acid (37% HCl), sulfuric acid (98% H_2SO_4), graphite, phosphoric acid (85% H_3PO_4), potassium permanganate ($KMnO_4$), hydrogen peroxide (30% H_2O_2), silver nitrate ($AgNO_3$), barium chloride ($BaCl_2$), and ethanol were purchased from Merck. The deionized water was obtained from One-med, while bi-distilled water and phosphate-buffered saline (PBS) was utilized for the washing process.

Instrumentation

X-ray diffraction (XRD) measurement was performed on a Bruker D2 Phaser diffractometer using the Cu Kα as the irradiation (k = 0.15405 nm) at a 2θ scan range of 5–90° to detect the crystal size. The functional group of GO was characterized by Fourier transform infrared (FTIR) spectrophotometer (Shimadzu Prestige 21, FTIR impact 410) with a range of 400–4000 cm^{-1} using KBr pellets. The surface morphology of GO was examined by Scanning Electron Microscope (SEM, JEOL JSM-6510). Graphene nanosheet structure was determined by transmission electron microscopy (TEM, JEOL JEM-1400). The electronic transition condition of GO was measured by UV-Vis Spectrophotometer 1800 from Shimadzu Scientific.

Procedure

Our method was adapted from Benzait et al. [24] and Ranjan et al. [29] methods with certain crucial modifications (Fig. 1). Initially, graphite powder and $KMnO_4$ (1:6 %w/w) were mixed in a mortar and pestle for 5 min and kept at a temperature below 5 °C. A separate solution of H_2SO_4 and H_3PO_4 (9:1 %v/v) was prepared and also kept at a temperature below 5 °C. The acid solution was then added to the mixture of graphite powder and $KMnO_4$ with continuous stirring (using a magnetic stirrer). The solution obtained was heated at 65 °C and was left with variation times of 1, 7 and 24 h with continuous stirring denoted as GO-1-65, GO-7-65, and GO-24-65. After the stirring process, the solution was
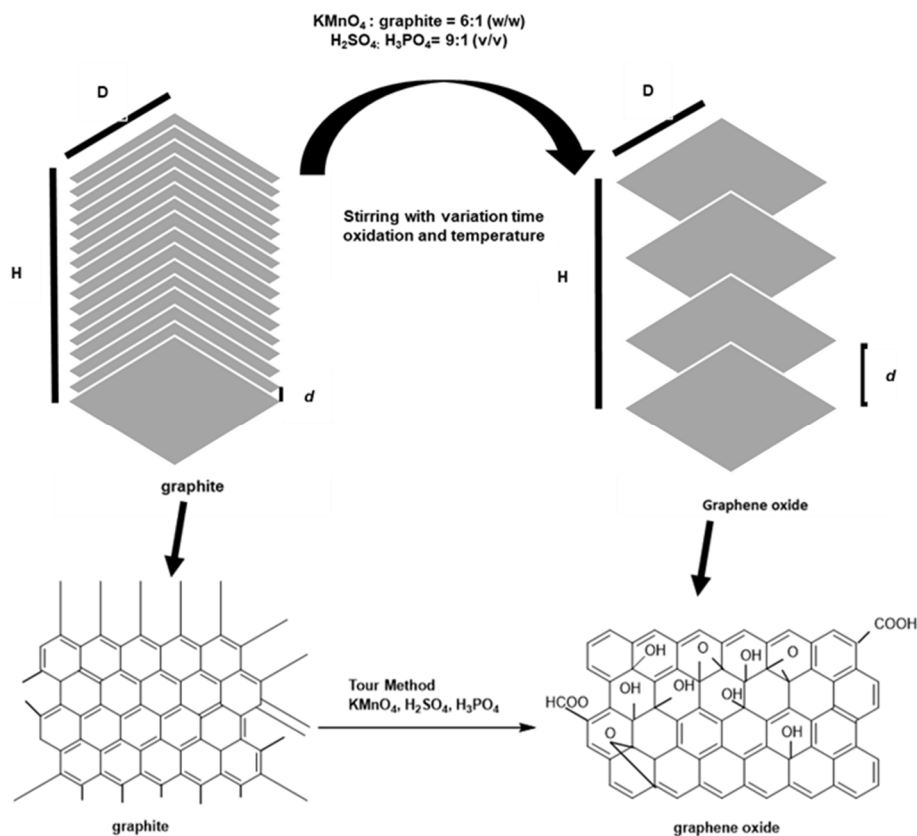

Fig 1. The illustration of Tour method

allowed to cool to room temperature. This was then added to a beaker containing 200 mL of deionized water and ice. Then, 4 mL of H_2O_2 was added while stirring the mixture with a glass rod. The purpose of H_2O_2 was to stop the oxidation reaction and to reduce the residual $KMnO_4$ to soluble manganese sulfate ($MnSO_4$) in an acidic medium, as described in Eq. (1) [28]:

$$2KMnO_4 + 5H_2O_2 + 3H_2SO_4 \rightarrow 2MnSO_4 + K_2SO_4 \\ + 8H_2O_{(steam)} + 5O_2 \quad (1)$$
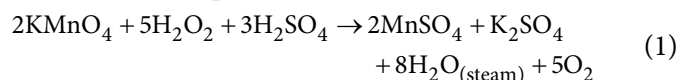
When H_2O_2 was added, bubbling occurred, and a bright yellow color was observed, indicating a high level of oxidation. The mixture was washed with HCl (2 times) and ethanol (2 times) with intermediate centrifugation (at 5,000 rpm for 5 min). The precipitate was washed with PBS until pH 7. The neutral solution was checked by $AgNO_3$ to detect the presence of SO_4^{2-} ion and $BaCl_2$ to detect the presence of Cl^- ion. The solution was rewashed using bi-distilled water until the solution was free of both ions. The precipitate formed was dried at 70 °C for 24 h. The step was repeated with variation temperatures at 40, 50 and 60 °C for 7 h, denoted as GO-7-40, GO-7-50, and GO-7-60.

■ **RESULTS AND DISCUSSION**

Diffractograms of graphite and all GO samples are shown in Fig. 2. The XRD pattern of graphite shows a peak at 2θ = 26.21° (hkl 002) according to the pattern of JCPDS standard graphite diffraction No.75-2078. Graphite has a sharp peak with high intensity, which

indicates that graphite has good crystallinity. It is in line with the structure of graphite, which is composed of carbon atoms bonded together and fully conjugated sp^2 to form honeycomb-like crystals [31]. However, after the graphite is oxidized, the crystal undergoes a structural change or defect due to oxygen functional groups from the permanganate oxidizing agent. As the consequence, there is a change in the conjugation of some carbons from sp^2 to sp^3, causing the crystallinity to decrease and the peak to be broader (amorphic of the material appears). The broadening effect of the peak is probably due to the formation of complex epoxidation of oxygenated unsaturated groups throughout the graphene layer, which distorts the lattice in the stacking order of the graphite [32]. The infiltration of oxygen functional groups between the graphene sheets in the graphite structure also resulted in an increase in the distance between the sheets from 0.34 to ~0.9 nm. Therefore, the 2θ angle seen in the XRD spectra also shifted from ~26° to ~9°. The peaks are associated with d = 0.8–0.9 nm due to the presence of chemical groups onto the graphene basal plane, so the d of GO depends on the degree of oxidation of graphite and the number of water molecules intercalation between the oxidized graphene layers [33].

Increasing the oxidation time, the XRD pattern of GO-1-65, GO-7-65, and GO-24-65 shows the intensity of the peak at 2θ of 9.78, 9.59, and 9.39°, respectively, but the interlayer spacing (d) does not significantly change
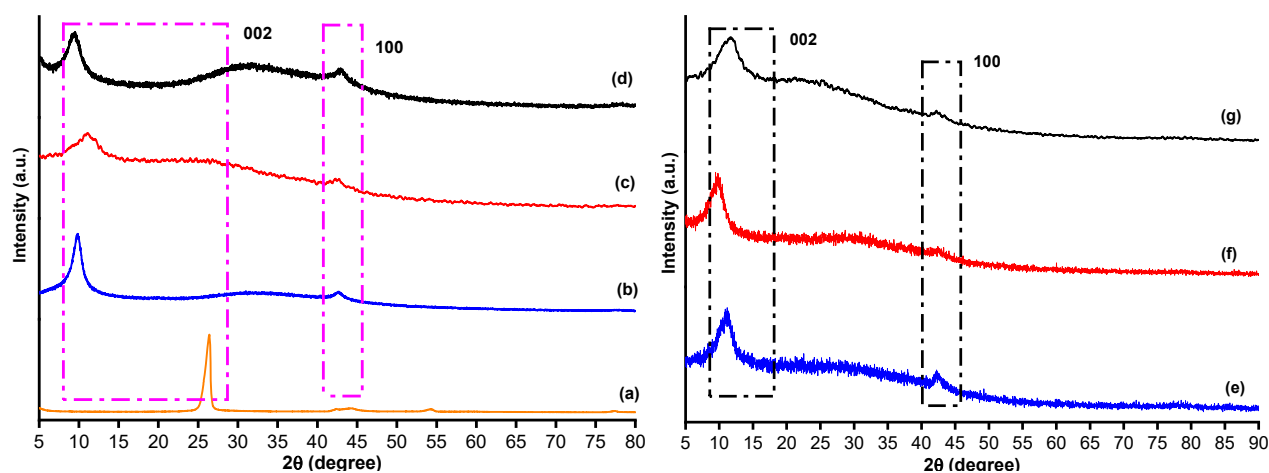
Fig 2. Diffractogram of (a) graphite, (b) GO-1-65, (c) GO-7-65, (d) GO-24-65, (e) GO-7-40, (f) GO-7-50, (g) GO-7-60

about 0.9 nm. Meanwhile, GO-7-40, GO-7-50, and GO-7-60 show peaks centered at 10.89, 9.64, and 11.39°, respectively, with d of 0.8–0.9 nm. The results show that the role of temperature can have more effect on the peak in the diffractogram than the oxidation time. Those are consistent with the range values of 9–12° reported in the literature [34-38]. The oxidation time of 7 h was chosen to evaluate the effect of temperature based on the results of UV-Vis analysis which will be described in the following explanation (Fig. 3).

The distance between graphene layers or interlayer spacing (d) from peak (002) reflection was calculated using Bragg equation. Meanwhile, the average height of stacking layers (H) was calculated using Scherrer equation with a constant equal to 0.9. The average diameter of stacking layers (D) was determined by using the Scherrer equation with a Warren constant of 1.84 [39]. The

graphite and GO have a nanostructure dimension size (D×H, see Table 1). The oxidation time of GO-24-65 can just exfoliate graphite until 5–6 layers, although the others GO from oxidation time GO-1-65 (7 layers) and GO-7-65 (6 layers), but from the oxidation temperature of GO-7-60 more can exfoliate graphite until 3 layers whereas GO-7-40 and GO-7-50 can exfoliate graphite just 4 layers, indicating that the oxidation temperature effect has more effect than the oxidation time. The ideal GO has 1 layer. In the other word, the production of GO with a few layers is more expected [40]. Therefore, GO-7-60 has the best graphite exfoliation.

The UV-Vis spectra for graphite and all GO samples in the range of 190–900 nm were investigated in water solution. As we can observe in Fig. 3, the region 400–900 nm is not affected by absorptions. The maximum absorbance for GO-7-65 and GO-24-65 is 243

Table 1. Calculation of H (the average height of samples GO stacking nanolayers), D (average diameter in stacking layers), n (the average number of graphene layers), and d (the average distance between graphene layers) of graphite and GO samples

| Sample	Peak (002)					Peak (100)		
	2θ (deg)	FWHM (deg)	H (nm)	d (nm)	n	2θ (deg)	FWHM (deg)	D (nm)
graphite	26.21	0.74	11	0.34	32	42.32	0.46	38
GO-1-65	9.78	1.38	6	0.90	7	42.64	1.09	17
GO-7-65	9.59	1.46	6	0.94	6	42.77	1.11	15
GO-24-65	9.39	1.71	4	0.94	5-6	42.95	1.25	14
GO-7-40	10.89	2.39	3	0.81	4	42.34	0.96	18
GO-7-50	9.64	2.04	4	0.92	4	41.47	6.67	13
GO-7-60	11.39	3.27	3	0.78	3	42.127	1.21	14
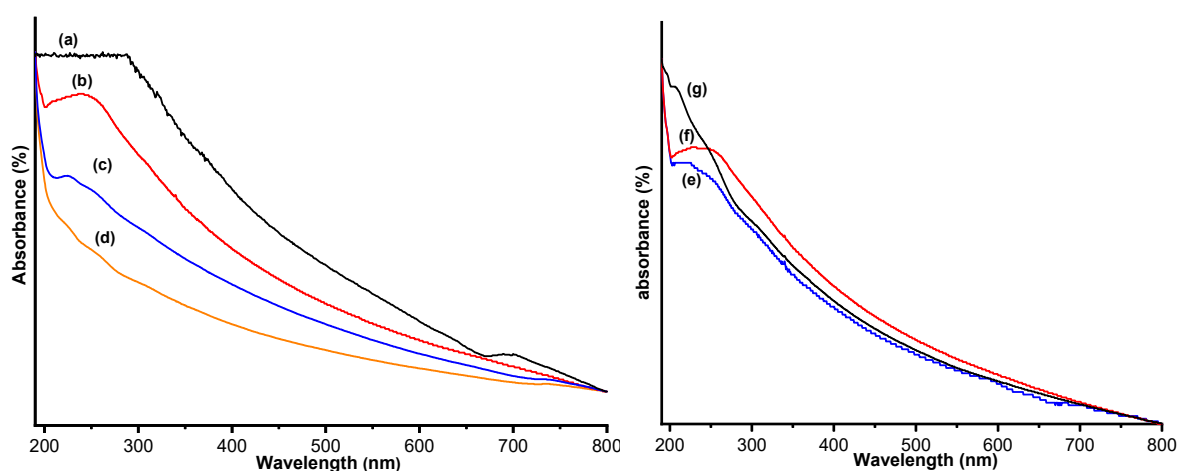
Fig 3. UV-Vis spectra of (a) graphite, (b) GO-1-65, (c) GO-7-65, (d) GO-24-65, (e) GO-7-40, (f) GO-7-50, (g) GO-7-60

and 226 nm, respectively. However, the peak of GO-1-65 at ~210–240 nm has not emerged yet (Fig. 3(b-d)), probably because the oxidation of 1h does not completely occur or only it was formed graphite oxide. The main difference between graphite oxide and graphene oxide is, thus, the number of layers. While graphite oxide is a multilayer system in graphene oxide (Fig. 4). Hence, the oxidation time of 7 was chosen for the variation of temperature. The maximum absorbance for GO-7-40, GO-7-50, and GO-7-60 (Fig. 3(e-g)) takes place at λ_{max} of 226, 228 and 210 nm, respectively. This band is attributed to $\pi \rightarrow \pi^*$ transitions of C=C bond in conjugated systems [41-42]. The lower the absorption peak, the more decreased delocalized electrons are, and it is considered that higher energy is required for the electronic transition. It indicates that the sample is more oxidized with more functional groups on the basal planes [42]. This blue shift in UV-Vis absorption is due to the hybridization of sp^3 carbon atoms and a decrease in the number of electrons [18].

The FTIR analysis (Fig. 5) was carried out to obtain information about the oxygen functionalities incorporated into the graphitic planes due to the oxidation. The IR absorbances are observed in the regions of 1210–1320, 1540–1675 and 1020–1075 cm⁻¹ corresponding to the vibrations of C-O from ether and ester, sp^2-hybridized C=C in-plane vibrations, C–O stretching of alcohol (C–OH), and carboxylic acid (C–OC) functional groups, respectively [43–45]. The vibration of the C–OH functional group indicated graphite has successfully oxidized [46]. The spectra still contain C=C vibration because these materials consist of almost sp^2-conjugated carbon, although they have few defects of sp^3-conjugated carbon. All spectra also show a broader IR absorbance in the range 3000–3720 cm⁻¹. The characteristic of O–H stretching modes supports the presence of hydroxyl and carboxyl groups [47]. When the oxidation time of graphite increased from 1 to 24 h, the positions of FTIR bands remains unchanged, indicating that the types of functional groups are independent of the
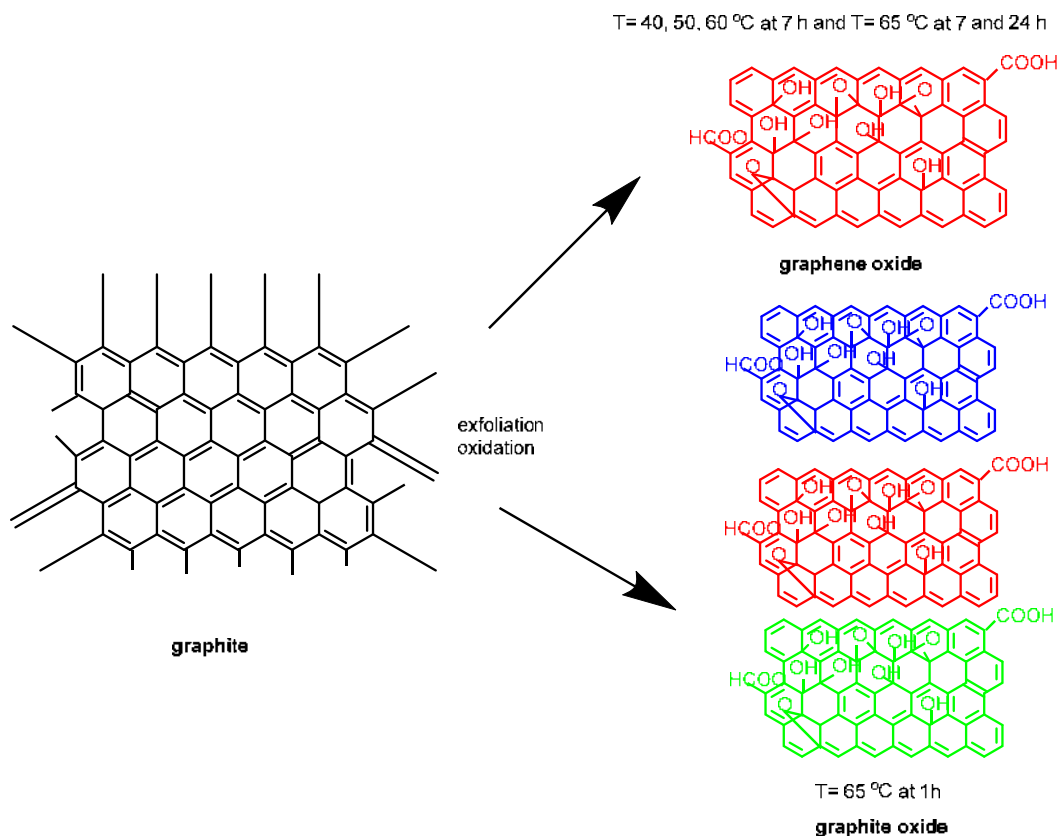
Fig 4. The mechanism of temperature and time oxidation oxide of graphene oxide synthesis
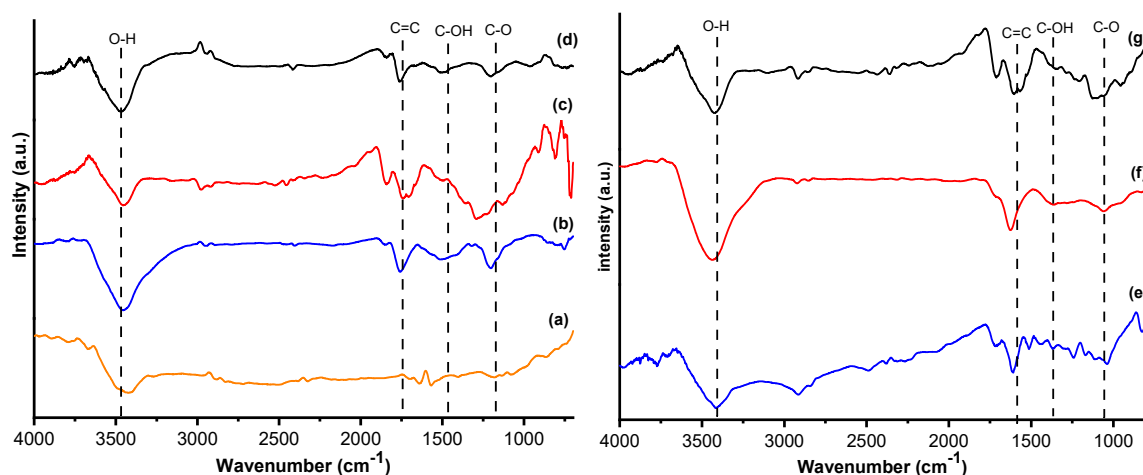
Fig 5. FT-IR spectra of (a) graphite, (b) GO-1-65, (c) GO-7-65, (d) GO-24-65, (e) GO-7-40, (f) GO-7-50, (g) GO-7-60

oxidation time [32]. Similar FTIR pattern is observed for the variation of temperature (40–60 °C). These types of functional groups cause the distance of the graphene layer in graphite structure to increase, confirming the previous XRD data. The presence of various oxygen-containing groups reveals that the graphite has been oxidized. The presence of the polar groups, especially the surface hydroxyl groups, leads to the formation of hydrogen bonds between the graphitic layer and water molecules. This further explains the hydrophilic nature of GO. The detail of absorption peak of O–H, C=C, C-OH, and C–OC functional groups formed analyzed by FTIR can be seen in Table 2.

The morphological aspects of graphite and all GO samples are investigated by using a scanning electron microscope (SEM), as shown in Fig. 6. Here, graphite (Fig. 6(a)) is displayed and exhibits large grains. Unlikely, GO-1-65, GO-7-65, GO-24-65, GO-7-40, GO-7-50, and GO-7-60 morphology consist of tightly packed layers, as

shown in Fig. 6b-g. The distinct morphology is related to the exfoliation process in the first step of synthesis and the re-packing of the material in the solid phase due to the oxygen domains on the graphene basal plane [26]. The micrograph of all GO materials has a porous sponge-like structure with the graphene sheet not well connected. It is an indication that graphite has been exfoliated during the oxidation process. It may be due to the distorted graphene sheets when oxygen and other functional groups are attached to graphene sheets to form GO [48–50]. Fig. 6(b-g) also describe the GOs as thin sheets with a few layered GOs that match the literature [51].

The elemental analysis is evaluated from energy dispersive X-ray (EDX) spectra. The spectrum shows peaks corresponding to C, O, S, Na, K, and Ca. Potassium, sodium, and sulfur were present due to H_2SO_4 and $KMnO_4$ being used as the oxidizing agent, and PBS was used during the washing process. The carbon-oxygen

Table 2. Absorption peaks of graphite and all GO samples

Sample	Functional groups (cm^{-1})			
	O–H	C=C	C–OH	C–OC
Graphite	3422			
GO-1-65	3421	1624	1369	1035
GO-7-65	3414	1609	1369	1044
GO-24-65	3421	1609	1356	1052
GO-7-40	3436	1603	1376	1031
GO-7-50	3422	1627	1368	1043
GO-7-60	3407	1613	1368	1031
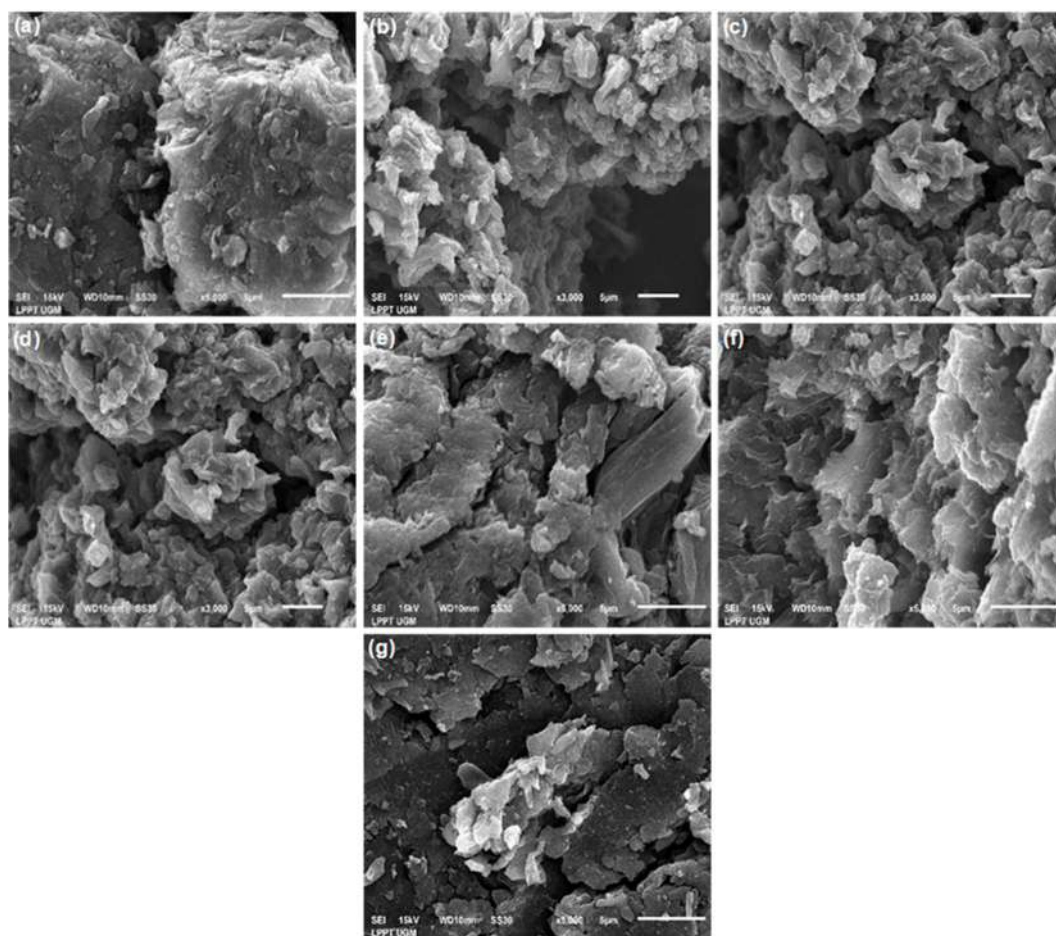
Fig 6. SEM images of (a) graphite, (b) GO-1-65, (c) GO-7-65, (d) GO-24-65, (e) GO-7-40, (f) GO-7-50, (g) GO-7-60

Table 3. The element contained in graphite and GO samples based on EDX

Material	% mass						
	C	O	K	Na	Cl	S	C/O
Graphite	100						∞
GO-1-65	51.72	42.07		4.75	0.17	1.29	1.23
GO-7-65	55.95	39.54		3.08	0.34	1.09	1.41
GO-24-65	52.39	44.86	2.29	3.41	0.32	0.14	1.13
GO-7-40	57.87	38.54	2.72	2.72	0.31	0.57	1.50
GO-7-50	57.32	39.81	0.57	0.34	0.52	1.14	1.44
GO-7-60	57.53	38.87	2.51	0.36		0.73	1.48

ratio (C/O) from GO using the Hummers method is 1.8–2.5 [48-49]. Meanwhile, in the modified Hummers or Tour method, the ratio is 0.7–1.3 [18]. In this work (Table 3), the C/O ratio of GO-7-65 and GO-24-65 are 1.41 and 1.13, respectively, and the C/O ratio of GO-7-40, GO-7-50, and GO-7-60 are 1.50, 1.44, and 1.48, respectively implying high oxidized graphene [50]. The increased temperature and oxidation time give more oxidized graphene, but there is an outlier datum (GO-1-65). The outlier datum is matched with UV-Vis data which does not appear to peak at 210–240 nm. Instead, from our data, fewer oxidized samples of GO-7-40 and GO-7-60 are found, and this affects the GO properties, e.g., a higher angle at 10.89 and 11.39° in comparison with the

Table 4. Comparison of GO yielding from Hummers method and Tour method

Method	Graphite	Material	Yield	Ref.
Hummers method	3 g	6 $KMnO_4$ H_2SO_4 0.5 $NaNO_3$	3.9 g	[18]
Tour method	3 g	6 $KMnO_4$ 9:1 (H_2SO_4:H_3PO_4)	5.3 g	

average value that is around 9° in XRD diffractogram [26], or the FTIR spectrum.

In contrast with all materials GO, the C/O ratio of graphite is ∞ indicating that graphite does not have impurity since graphite only has carbon element. The results also prove that the exfoliation from graphite to GO is successfully carried out because of the inhibition of the oxygenated groups. The results match with FTIR data.

The TEM micrograph of graphite (Fig. 7(a)) shows major dark areas. All GO samples (Fig. 7(b-g)) show the wrinkled and folded nature of GO sheets [54]. The dark area indicates the thick stacking nanostructure of several graphene layers. The higher transparency area is resulted from stacking nanostructure exfoliation because of the presence of a few amount of oxygen functional groups [55]. Since all GO materials have a light area, so exfoliation of graphite has been successfully conducted.

Table 4 shows that the Tour method has a higher yield GO than the Hummers method. The results match to the literature [21-22] and conclude that the Tour method is more effective and efficient method to produce GO than the Hummers method.

■ **CONCLUSION**

Facile low temperature and reducing the time of GO synthesis have been studied. In XRD data, the oxidation time does not significantly affect the d spacing value compared to oxidation temperature treatment. Both increasing oxidation time and temperature caused the average number of graphene (n) to decrease. The samples of GO-1-65, GO-7-65, GO-24-65, GO-7-40, GO-7-50, and
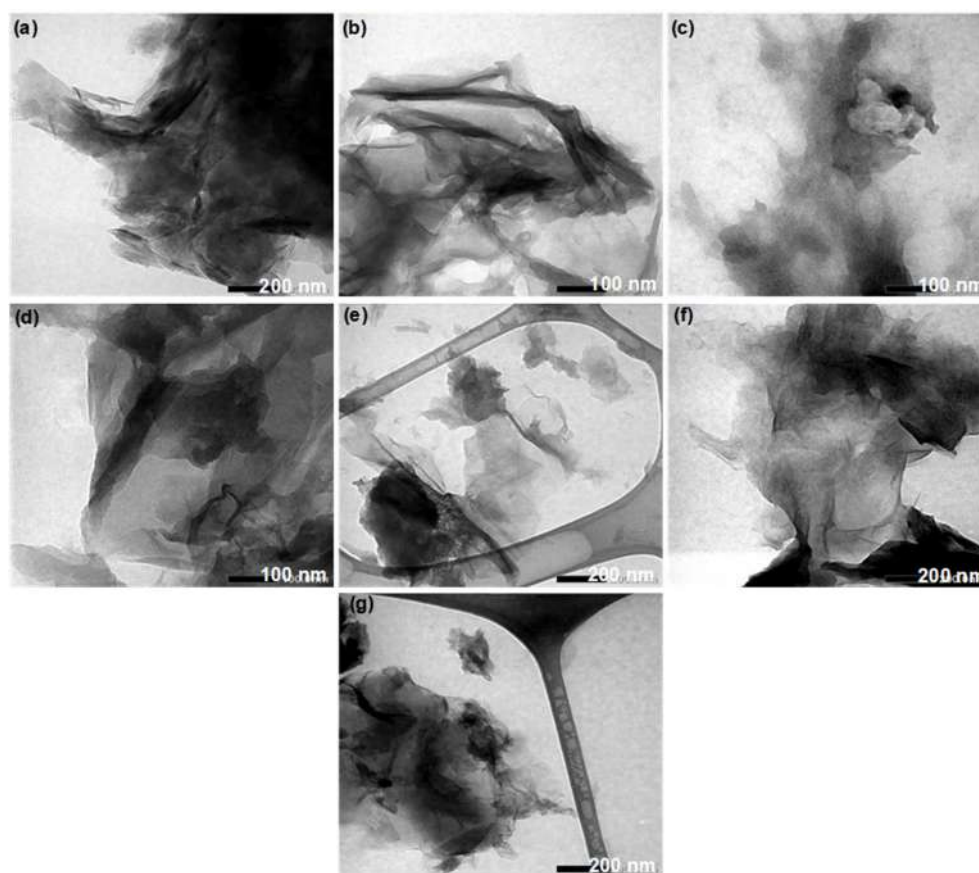
Fig 7. TEM images of (a) graphite, (b) GO-1-65, (c) GO-7-65, (d) GO-24-65, (e) GO-7-40, (f) GO-7-50 (g) GO-7-60

and GO-7-60 show the intensity of the peak at $2\theta = 9.78$, 9.59, 9.39, 10.89, 9.64, and 11.39°, respectively, with d of 0.8–0.9 nm. The sample of GO-7-60 can exfoliate graphite until 3 layers compared to others such as GO-24-65 which can just exfoliate graphite until 5-6 layers. Then, GO-1-65 (7 layers) and GO-7-65 exfoliate 6 layers, but from the oxidation temperature of GO-7-40 and GO-7-50 can just exfoliate graphite 4 layers. The peaks of UV-Vis spectra indicate all of the samples GO formed except GO-1-65 because the peak does not appear. The peaks of GO-7-65, GO-24-65, GO-7-40, GO-7-50, and GO-7-60 occur at λ_{max} of 243, 226, 226, 228, and 210 nm, respectively. These peaks correspond to $\pi \rightarrow \pi^\star$ transitions for the C=C aromatic from sp^2 bonding. According to UV-Vis spectra, the higher the oxidation time and temperature, the lower the wavelength formed. The FTIR analysis among all the samples contains the functional groups indicating the formation of GO. The SEM images show GO-1-65, GO-7-65, GO-24-65, GO-7-40, GO-7-50, and GO-7-60 morphology consist of tightly packed layers. The EDX resulted in the increasing oxidation time, and temperature lead the C/O ratio decrease. Based on all of the research results, GO-7-60 shows the best material characteristic among all synthesized GOs because it can exfoliate graphite until 3 layers, close to the ideal graphene, i.e., 1 layer. In addition, synthesis of GO-7-40 has been achieved under lower oxidation temperature, which is in line with the green chemistry principles. From that results, these GO from Tour method can be applied in the removal of organic dye, antibiotics, chemical sensors, and heavy metal ions.

■ ACKNOWLEDGMENTS

■ REFERENCES

[1] Thangavel, S., and Venugopal, G., 2014, Understanding the adsorption property of graphene-oxide with different degrees of oxidation levels, *Powder Technol.*, 257, 141–148.

[2] Georgakilas, V., Otyepka, M., Bourlinos, A.B., Chandra, V., Kim, N., Kemp, K.C., Hobza, P., Zboril, R., and Kim, K.S., 2012, Functionalization of graphene: Covalent and non-covalent approaches, derivatives and applications, *Chem. Rev.*, 112 (11), 6156–6214.

[3] Malik, R., Tomer, V.K., and Chaudhary, V., 2019, "Hybridized graphene for chemical sensing" in *Functionalized Graphene Nanocomposites and Their Derivatives*, Eds. Jawaid, M., Bouhfid, R., and Qaiss, A.K., Elsevier, Amsterdam, Netherlands, 323–338

[4] Gupta, K., and Khatri, O.P., 2017, Reduced graphene oxide as an effective adsorbent for removal of malachite green dye: Plausible adsorption pathways, *J. Colloid Interface Sci.*, 501, 11–21.

[5] Gao, Y., Wu, J., Ren, X., Tan, X., Hayat, T., Alsaedi, A., Cheng, C., and Chen, C., 2017, Impact of graphene oxide on the antibacterial activity of antibiotics against bacteria, *Environ. Sci.: Nano*, 4 (5), 1016–1024.

[6] Saleh, T.A., and Fadillah, G., 2019, Recent trends in the design of chemical sensors based on graphene–metal oxide nanocomposites for the analysis of toxic species and biomolecules, *TrAC, Trends Anal. Chem.*, 120, 115660.

[7] Tan, H.L., Denny, F., Hermawan, M., Wong, R.J., Amal, R., and Ng, Y.H., 2017, Reduced graphene oxide is not a universal promoter for photocatalytic activities of TiO_2, *J. Materiomics*, 3 (1), 51–57.

[8] Gopalakrishnan, A., Krishnan, R., Thangavel, S., Venugopal, G., and Kim, S.J., 2015, Removal of heavy metal ions from pharma-effluents using graphene-oxide nanosorbents and study of their adsorption kinetics, *J. Ind. Eng. Chem.*, 30, 14–19.

[9] Ajala, O.J., Tijani, J.O., Bankole, M.T., and Abdulkareem, A.S., 2022, A critical review on graphene oxide nanostructured material: Properties, synthesis, characterization and application in water and wastewater treatment, *Environ. Nanotechnol. Monit. Manage.*, 18, 100673.

[10] Marcano, D.C., Kosynkin, D.V., Berlin, J.M., Sinitskii, A., Sun, Z., Slesarev, A., Alemany, L.B., Lu, W., and Tour, J.M., 2010, Improved synthesis of graphene oxide, *ACS Nano*, 4 (8), 4806–4814.

[11] Alshamkhani, M.T., Teong, L.K., Putri, L.K., Mohamed, A.R., Lahijani, P., and Mohammadi, M., 2021, Effect of graphite exfoliation routes on the properties of exfoliated graphene and its photocatalytic applications, *J. Environ. Chem. Eng.*, 9 (6), 106506.

[12] Brodie, B.C., 1859, On the atomic weight of graphite, *Philos. Trans. R. Soc. London*, 149, 249–259.

[13] Staudenmaier, L., 1898, Verfahren zur darstellung der draphitsäure, *Ber. Dtsch. Chem. Ges.*, 31, 1481–1487.

[14] Hummers, W.S., and Offeman, R.E., 1958, Preparation of graphitic oxide, *J. Am. Chem. Soc.*, 80 (6), 1339.

[15] Zhu, Y., Kong, G., Pan, Y., Liu, L., Yang, B., Zhang, S., Lai, D., and Che, C., 2022, An improved Hummers method to synthesize graphene oxide using much less concentrated sulfuric acid, *Chin. Chem. Lett.*, 33 (10), 4541–4544.

[16] Sali, S., Mackey, H.R., and Abdala, A.A., 2019, Effect of graphene oxide synthesis method on properties and performance of polysulfone-graphene oxide mixed matrix membranes, *Nanomaterials*, 9 (5), 769.

[17] Zaaba, N.I., Foo, K.L., Hashim, U., Tan, S.J., Liu, W.W., and Voon, C.H., 2017, Synthesis of graphene oxide using modified Hummers method: Solvent influence, *Procedia Eng.*, 184, 469–477.

[18] Marcano, D.C., Kosynkin, D.V., Berlin, J.M., Sinitskii, A., Sun, Z., Slesarev, A.S., Alemany, L.B., Lu, W., and Tour, J.M., 2018, Correction to improved synthesis of graphene oxide, *ACS Nano*, 12 (2), 2078.

[19] Bychko, I., Abakumov, A., Didenko, O., Chen, M., Tang, J., and Strizhak, P., 2022, Differences in the structure and functionalities of graphene oxide and reduced graphene oxide obtained from graphite with various degrees of graphitization, *J. Phys. Chem. Solids*, 164, 110614.

[20] Romero, A., Lavin-Lopez, M.P., Sanchez-Silva, L., Valverde, J.L., and Paton-Carrero, A., 2018, Comparative study of different scalable routes to synthesize graphene oxide and reduced graphene oxide, *Mater. Chem. Phys.*, 203, 284–292.

[21] Chen, J., Li, Y., Huang, L., Li, C., and Shi, G., 2015, High-yield preparation of graphene oxide from small graphite flakes via an improved Hummers method with a simple purification process, *Carbon*, 81, 826–834.

[22] Lavin-Lopez, M.P., Romero, A., Garrido, J., Sanchez-Silva, L., and Valverde, J.L., 2016, Influence of different improved hummers method modifications on the characteristics of graphite oxide in order to make a more easily scalable method, *Ind. Eng. Chem. Res.*, 55 (50), 12836–12847.

[23] Park, J., Cho, Y.S., Sung, S.J., Byeon, M., Yang, S.J., and Park, C.R., 2018, Characteristics tuning of graphene-oxide-based-graphene to various end-uses, *Energy Storage Mater.*, 14, 8–21.

[24] Benzait, Z., Chen, P., and Trabzon, L., 2021, Enhanced synthesis method of graphene oxide, *Nanoscale Adv.*, 3 (1), 223–230.

[25] Boychuk, V.M., Kotsyubynsky, V.O., Bandura, K.V., Yaremiy, I.P., and Fedorchenko, S.V., 2019, Reduced graphene oxide obtained by Hummers and Marcano-Tour methods: Comparison of electrical properties, *J. Nanosci. Nanotechnol.*, 19 (11), 7320–7329.

[26] Pendolino, F., Armata, N., Masullo, T., and Cuttitta, A., 2015, Temperature influence on the synthesis of pristine graphene oxide and graphite oxide, *Mater. Chem. Phys.*, 164, 71–77.

[27] Olorunkosebi, A.A., Eleruja, M.A., Adedeji, A.V., Olofinjana, B., Fasakin, O., Omotoso, E., Oyedotun, K.O., Ajayi, E.O.B., and Manyala, N., 2021, Optimization of graphene oxide through various Hummers' methods and comparative reduction using green approach, *Diamond Relat. Mater.*, 117, 108456.

[28] Habte, A.T., and Ayele, D.W., 2019, Synthesis and characterization of reduced graphene oxide (rGO) started from graphene oxide (GO) using the Tour method with different parameters, *Adv. Mater. Sci. Eng.*, 2019, 5058163.

[29] Ranjan, P., Agrawal, S., Sinha, A., Rao, T.R., Balakrishnan, J., and Thakur, A.D., 2018, A low-cost non-explosive synthesis of graphene oxide for scalable applications, *Sci. Rep.*, 8 (1), 12007.

[30] Kang, J.H., Kim, T., Choi, J., Park, J., Kim, Y.S., Chang, M.S., Jung, H., Park, K.T., Yang, S.J., and Park, C.R., 2016, Hidden second oxidation step of Hummers method, *Chem. Mater.*, 28 (3), 756–764.

[31] Jara, A.D., and Kim, J.Y., 2020, Chemical purification processes of the natural crystalline flake graphite for Li-ion Battery anodes, *Mater. Today Commun.*, 25, 101437.

[32] Suhaimin, N.S., Hanifah, M.F.R., Jusin, J.W., Jaafar, J., Aziz, M., Ismail, A.F., Othman, M.H.D., Abd Rahman, M., Aziz, F., Yusof, N., and Muhamud, M., 2021, Tuning the oxygen functional groups in graphene oxide nanosheets by optimizing the oxidation time, *Phys. E*, 131, 114727.

[33] Meng, L.Y., and Park, S.J., 2012, Preparation and characterization of reduced graphene nanosheets via pre-exfoliation of graphite flakes, *Bull. Korean Chem. Soc.*, 33 (1), 209–214.

[34] Dimiev, A.M., and Tour, J.M., 2014, Mechanism of graphene oxide formation, *ACS Nano*, 8 (3), 3060–3068.

[35] Lee, D.W., De Los Santos V.L., Seo, J.W., Leon Felix, L., Bustamante D.A., Cole, J.M., and Barnes, C.H.W., 2010, The structure of graphite oxide: Investigation of its surface chemical groups, *J. Phys. Chem. B*, 114 (17), 5723–5728.

[36] Dubey, A., Bhavsar, N., Pachchigar, V., Saini, M., Ranjan, M., and Dube, C.L., 2021, Microwave assisted ultrafast synthesis of graphene oxide based magnetic nano composite for environmental remediation, *Ceram. Int.*, 48 (4), 4821–4828.

[37] Roy, O., Jana, A., Pratihar, B., Saha, D.S., and De, S., 2021, Graphene oxide wrapped Mix-valent cobalt phosphate hollow nanotubes as oxygen evolution catalyst with low overpotential, *J. Colloid Interface Sci.*, 610, 592–600.

[38] Shen, B., Lu, D., Zhai, W., and Zheng, W., 2013, Synthesis of graphene by low-temperature exfoliation and reduction of graphite oxide under ambient atmosphere, *J. Mater. Chem. C*, 1 (1), 50–53.

[39] Stobinski, L., Lesiak, B., Malolepszy, A., Mazurkiewicz, M., Mierzwa, B., Zemek, J., Jiricek, P., and Bieloshapka, I., 2014, Graphene oxide and reduced graphene oxide studied by the XRD, TEM and electron spectroscopy methods, *J. Electron Spectrosc. Relat. Phenom.*, 195, 145–154.

[40] Kumar, V., Kumar, A., Lee, D.J., and Park, S.S., 2021, Estimation of number of graphene layers using different methods: A focused review, *Materials*, 14 (16), 4590.

[41] Paredes, J.I., Villar-Rodil, S., Martínez-Alonso, A., and Tascón, J.M.D., 2008, Graphene oxide dispersions in organic solvents, *Langmuir*, 24 (19), 10560–10564.

[42] Ding, H., Zhang, S., Chen, J.T., Hu, X.P., Du, Z.F., Qiu, Y.X., and Zhao, D.L., 2015, Reduction of graphene oxide at room temperature with vitamin C for RGO-TiO$_2$ photoanodes in dye-sensitized solar cell, *Thin Solid Films*, 584, 29–36.

[43] Tammer, M., 2004, G. Sokrates: Infrared and Raman characteristic group frequencies: Tables and charts, *Colloid Polym. Sci.*, 283 (2), 235.

[44] Lotfi, M., Yari, H., Sari, M.G., and Azizi, A., 2022, Fabrication of a highly hard yet tough epoxy nanocomposite coating by incorporating graphene oxide nanosheets dually modified with amino silane coupling agent and hyperbranched polyester-amide, *Prog. Org. Coat.*, 162, 106570.

[45] Sahoo, P., Shubhadarshinee, L., Jali, B.R., Mohapatra, P., and Barick, A.K., 2021, Synthesis and characterization of graphene oxide and graphene from coal, *Mater. Today: Proc.*, 56, 2421–2427.

[46] Fadillah, G., Saleh, T.A., Wahyuningsih, S., Ninda Karlina Putri, E., and Febrianastuti, S., 2019, Electrochemical removal of methylene blue using alginate-modified graphene adsorbents, *Chem. Eng. J.*, 378, 122140.

[47] Cao, H., Wu, X., Yin, G., and Warner, J.H., 2012, Synthesis of adenine-modified reduced graphene oxide nanosheets, *Inorg. Chem.*, 51 (5), 2954–2960.

[48] Liu, F., Cao, Y., Yi, M., Xie, L., Huang, W., Tang, N., Zhong, W., and Du, Y., 2013, Thermostability, photoluminescence, and electrical properties of reduced graphene oxide-carbon nanotube hybrid materials, *Crystals*, 3 (1), 28–37.

[49] Geng, J., Liu, L., Yang, S.B., Youn, S.C., Kim, D.W., Lee, J.S., Choi, J.K., and Jung, H.T., 2010, A simple approach for preparing transparent conductive graphene films using the controlled chemical reduction of exfoliated graphene oxide in an aqueous suspension, *J. Phys. Chem. C*, 114 (34), 14433–14440.

[50] Eda, G., and Chhowalla, M., 2010, Chemically derived graphene oxide: Towards large-area thin-film electronics and optoelectronics, *Adv. Mater.*, 22 (22), 2392–2415.

[51] Fadillah, G., Wicaksono, W.P., Fatimah, I., and Saleh, T.A., 2020, A sensitive electrochemical sensor based on functionalized graphene oxide/SnO_2 for the determination of eugenol, *Microchem. J.*, 159, 105353.

[52] You, S., Luzan, S.M., Szabó, T., and Talyzin, A.V., 2013, Effect of synthesis method on solvation and exfoliation of graphite oxide, *Carbon*, 52, 171–180.

[53] Jung, I., Field, D.A., Clark, N.J., Zhu, Y., Yang, D., Piner, R.D., Stankovich, S., Dikin, D.A., Geisler, H., Ventrice, C.A., and Ruoff, R.S., 2009, Reduction kinetics of graphene oxide determined by electrical transport measurements and temperature programmed desorption, *J. Phys. Chem. C*, 113 (43), 18480–18486.

[54] Tambe, P., 2021, Synthesis and characterization of acid treated reduced graphene oxide, *Mater. Today: Proc.*, 49, 1294–1297.

[55] Chasanah, U., Trisunaryanti, W., Triyono, T., Oktaviano, H.S., and Fatmawati, D.A., 2021, The performance of green synthesis of graphene oxide prepared by modified Hummers method with oxidation time variation, *Rasayan J. Chem.*, 14 (3), 2017–2023.

Interaction Studies of Chlorpheniramine Maleate in Mono and Dihydric Alcohols by Density, Viscosity, and HPLC Methods

Zainab Khan[1], Summyia Masood[1*], Nighat Shafi[1], Rafia Azmat[1], Salman Khurshid[2], and Samreen Begum[1]

[1]Department of Chemistry, University of Karachi, Karachi-75270, Pakistan

[2]Southern-zone Agriculture Research Center, (PARC) Karachi University Campus, Karachi-75270, Pakistan

Abstract: *The examination of a drug in water and other aqueous systems gives insight into the chemistry of biological systems. This work aims to study the physico-chemical properties of chlorpheniramine maleate (drug) in water and aq-MeOH/EG (mono/dihydric alcohols) systems at different temperatures by using different techniques. Densities and viscosities of chlorpheniramine maleate in water and also in MeOH/EG aqueous solutions have been measured over a temperature range of 298.15 to 318.15 K. Number of several parameters, i.e., apparent molar volume (ϕ_v), partial molar volume (ϕ_v^o), Hepler's constant $(\partial C_P/\partial P)_T$, Falkenhagen coefficient (A), and Jones-Dole coefficient (B) have been calculated by using experimentally measured density and viscosity values. The mentioned calculated parameters were found to be valuable in perceiving drug-drug and drug-solvent interactions. Moreover, one of the liquid chromatographic techniques such as RP-HPLC has also been performed, and the outcomes supported the conclusion procured from the volumetric and viscometric studies. Drug interactions help to understand their behavior in different solvent systems during drug development.*

Keywords: *apparent molar volume; RP-HPLC; drug-solvent interactions; chlorpheniramine maleate*

■ INTRODUCTION

A drug is a chemical that produces a change in biological function through its chemical reaction and/or interaction. The proteins present inside the body interact with the drug, and the active ingredient of the drug consists of a chemical that can change a physiological function in the body. Chlorpheniramine maleate (CPM) is an anti-allergic drug and this drug is used to prevent the symptoms of allergic conditions like rhinitis and urticaria and against respiratory systems and hay fever. CPM has antidepressant and antianxiety effects as well. CPM is the maleate salt of chlorpheniramine (Fig. 1). It is a weak base having a pKa value of 9.2 [1]. CPM is easily soluble in water and alcohol due to the formation of salt between a carboxylic group of maleic acid and a tertiary amine group of chlorpheniramine by the process of proton transfer.

Volumetric and viscometric properties are very important to understand the various types of interactions (drug-solvent or drug-drug) that occur in solutions. The examination of drugs in water and other aqueous systems gives insight into the chemistry of biological systems [2]. A study of physicochemical properties like density and viscosity plays a major role in elucidating any compound's structural organization [3]. In different solutions, the nature and effect of solute in aqueous and non-aqueous solutions have been observed
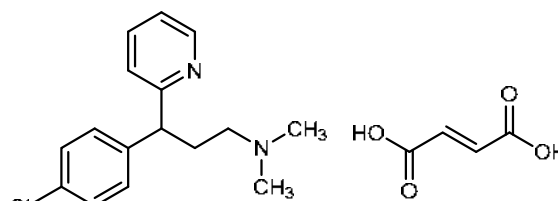

Fig 1. Structure of chlorpheniramine maleate

with the help of volumetric and viscometric parameters. Several researchers [4-6] worked on volumetric and viscometric properties and proved that these properties play an important role in investigating intermolecular interactions occurring in the solutions. Densities and viscosities of some vitamins (L-ascorbic acid, nicotinic acid, thiamine hydrochloride, and pyridoxine hydrochloride) in different concentrations of the aqueous media were investigated at different temperatures [7-9]. The properties of antidepressant drug (Escitalopram oxalate) in the aqueous and alcoholic media were also examined by volumetric and ultrasonic studies. The study of nicotinic acid in aqueous NaCl and dilute HCl solutions has been determined with the help of volumetric and viscometric parameters [10]. RP-HPLC with UV-Vis is of great importance for drug analysis in pharmaceuticals because of its high-resolution power, and sophisticated and sensitive technique. In literature, several research articles [11-13] have been published on drug analysis.

Literature survey shows that different interaction studies of chlorpheniramine maleate have been reported with a variety of techniques such as physical interaction of active ingredients as well as excipients in a dosage form has accomplished by the solubility test parameter, polarization microscope, powder X-ray diffraction, and FTIR [14]. Other researchers [15] have established an "*in-vivo*" and "*in-vitro*" drug-drug interaction in a simulated body environment as gastric and intestinal pH by UV-Visible spectrophotometry.

A lot of research data for drugs is available with ethanol [16-18], but no work has been published on methanol and ethylene glycol systems so far. Therefore, the present work aims to scrutinize the chlorpheniramine maleate in water, monohydric (methanol), and dihydric alcohol (ethylene glycol) systems through density and viscosity measurements. To explore the structure-breaking/promoting behavior in water and aq-alcoholic systems, volumetric and viscometric parameters have been investigated. Verification of these interactions in the said solvent systems was further supported by the more advanced technique RP-HPLC.

■ EXPERIMENTAL SECTION

Materials

Chlorpheniramine maleate was procured from Nabi Qasim (a pharmaceutical industry) and used without any purification (drugs purity near to 0.99 mol fraction). Methanol (CH_3OH) and ethylene glycol ($HOCH_2CH_2OH$) of BDH are 99% pure. Deionized water was used as a solvent for the experimental work.

To prepare the mobile phase, all reagents and water used for HPLC analysis were of HPLC grade. Methanol and phosphoric acid 85% were purchased from Merck, Germany. Stock and working solutions were prepared in the mobile phase. Before injection, all solutions were filtered by 0.45 μm filters and degassed using a sonicator.

Chromatographic Instrument and Conditions

Analysis was carried out on LC- 10 AT VP pump HPLC system (Shimadzu, Japan) equipped with a UV-Visible detector. Hypersil C_{18} column (4.6 mm × 15 cm, 5 μm) was used as a stationary phase. RP-HPLC system was connected via CBM-102 Shimadzu model to a P-IV computer loaded with CLASS-VP (Version 2.0) Shimadzu software for data acquirement and arithmetical calculations. Manual injector rheodyne with 20 μL fitted loop and DGU-14 AM sonicator was used as online degasser. Additionally, a microliter syringe and a micropore filtration assembly were utilized for the filtration purpose of the sample and mobile phase. Additionally, a VWP Scientific thermo state water bath model 1120m SER 9143791, weighing balance Shimadzu, AUW220, and Ostwald viscometer type Techniconominal constant 0.1 Cs/s capillaries, ASTMD 445 were also utilized in this work.

The chromatographic analysis was carried out according to the reported method [19]. Chromatographic condition is based on isocratic elution mode at ambient temperature. The mobile phase consisted of 0.1% orthophosphoric acid and acetonitrile (70:30 v/v) and was pumped at a flow rate of 1.5 mL min^{-1}. A sample volume of 20 μL was injected in triplicate onto the HPLC column, and effluents were screened over the dative UV region at 240 nm.

1220

Indones. J. Chem., 2022, 22 (5), 1218 - 1232

Table 1. Densities of CPM in aqueous, aq-MeOH, and aq-EG systems at different temperatures

10^2 [CPM] mol dm^{-3}	ρ (g cm^{-3}) at temperature (K)				
	298.15	303.15	308.15	313.15	318.15
aqueous system					
4.00	969.36	0.96795	0.96639	0.96453	0.96236
6.00	0.97141	0.96931	0.96759	0.96544	0.96347
8.00	0.97229	0.97061	0.96901	0.96710	0.96514
10.0	0.97433	0.97289	0.9709	0.96900	0.96710
12.0	0.97536	0.97376	0.97191	0.97014	0.96784
14.0	0.97765	0.97731	0.97641	0.97545	0.97484
aq-MeOH System (10% v/v)					
4.00	0.97921	0.97795	0.97715	0.97707	0.97701
6.00	0.97998	0.97869	0.97721	0.97712	0.97705
8.00	0.97875	0.97872	0.97817	0.97741	0.97735
10.0	0.97979	0.97893	0.97825	0.97782	0.97775
12.0	0.98085	0.97899	0.97829	0.97813	0.97809
14.0	0.98088	0.98011	0.97925	0.97921	0.97914
aq-EG System (10% v/v)					
4.00	0.98268	0.98013	0.97778	0.97596	0.97441
6.00	0.98397	0.98155	0.97897	0.97719	0.97542
8.00	0.98549	0.98224	0.98012	0.97813	0.97650
10.0	0.98652	0.98316	0.98112	0.97906	0.97756
12.0	0.98732	0.98405	0.98193	0.98025	0.97841
14.0	0.98857	0.98515	0.98311	0.98107	0.97926

Procedure

Grade A quality glassware (Pyrex) was used for solution preparation. The preparation of an aqueous solution of 10% v/v MeOH and EG was done by using a certain volume of MeOH and EG in deionized water. Stock solutions (0.14 mol dm^{-3}) of CPM were prepared individually in water and aq-MeOH/EG systems. Dilutions of different concentration ranges (0.04–0.12 ± 0.01 mol dm^{-3}) were made from a stock solution in water, aq-MeOH/EG systems. The density of solvents and solutions was measured at different temperatures by using a 10 cm^3 relative density bottle (R.D bottle) and a thermostatic water bath, which kept the temperature of solutions constant. The uncertainty in the experimental data of density was found to be ± 0.0001 g cm^{-3}, and that of the temperature is ± 0.01 K. The Ostwald viscometer (Techniconominal constant 0.1 Cs/s capillary, ASTMD 445) was used to measure the viscosity of liquids, and the results contain uncertainty of ± 0.0002 mPas. The reproducibility of obtained results was verified by doing

all the measurements thrice.

In RP-HPLC sets of experiments, appropriate amounts of the standard drug were transferred into individual 25 mL volumetric flasks and diluted with the mobile phase up to the mark having a concentration of 0.06 mol dm^{-3}. Similarly, for the interaction mixture, the drug was fully dissolved in all solvent systems individually and finally diluted with the mobile phase up to the mark. The portion of these solutions was filtered through a disposable 0.45 μm Millipore polytetrafluoroethylene (PTFE) filter membrane and then injected into the HPLC system.

■ RESULTS AND DISCUSSION

Volumetric Properties

Experimental data for the densities of chlorpheniramine maleate solutions within the concentrations range of 0.04–0.14 mol dm^{-3} are tabulated in Table 1, at various T = (298.15–318.15) K.

The obtained result unveils that the density values of

drug solutions escalate with the increase in concentration due to the addition of more solute (drug) in a solvent, and a decrease in magnitude was observed by raising the temperature because at higher temperatures faster-moving molecules go further apart causing the increase in volume resulting in a decrease in density. The procured density data was useful for the calculation of apparent molar volume (ϕ_v) by using the below-mentioned relation.

$$\phi_v = \frac{M}{\rho^\circ} - \frac{1000(\rho - \rho^\circ)}{C\rho^\circ} \tag{1}$$

where ρ is the density of the solution, ρ° is the density of the solvent, M is the molecular weight of solute (drug), and C (mol dm^{-3}) is the concentration of the drug solution. The calculated ϕ_v of binary and ternary solutions are tabulated in Table 2. In the studied systems, ϕ_v was showing a linear function with concentration and obeyed Masson's equation. The survey in Table 2 signifies that ϕ_v is positive in binary and ternary systems showing the existence of drug-solvent interaction, which decreases

from water to alcoholic systems at studied temperatures (298.15–318.15) K [6]. This behavior also indicates the presence of strong drug-solvent interactions.

The collective effect of drug-solvent interactions reflects the partial molar volume of the drug. The partial molar volume (ϕ_v°) and experimental slope S_v have been computed with the help of apparent molar volume by using the following Masson equation [20].

$$\phi_v = \phi_{v^\circ} + S_V C^{1/2} \tag{2}$$

where ϕ_v° is related to drug-solvent interaction, $C^{1/2}$ is the square root of drug concentration and S_v indicates drug-drug interaction. Representative graphs of ϕ_v versus $C^{1/2}$ in Fig. 2, were linear, and from the intercept and slope, ϕ_v°, and S_v respectively can be obtained. The values of ϕ_v°, and S_v are mentioned in Table 3.

The positive values of ϕ_v° for CPM in water were detected to be enhanced by the rise in temperature while a drop in values was observed in aq-MeOH/EG systems. The monitored ϕ_v° values were found to be the least in

Table 2. Apparent molar volume (ϕ_v) of CPM in aqueous, aq-MeOH, and aq-EG systems at different temperatures

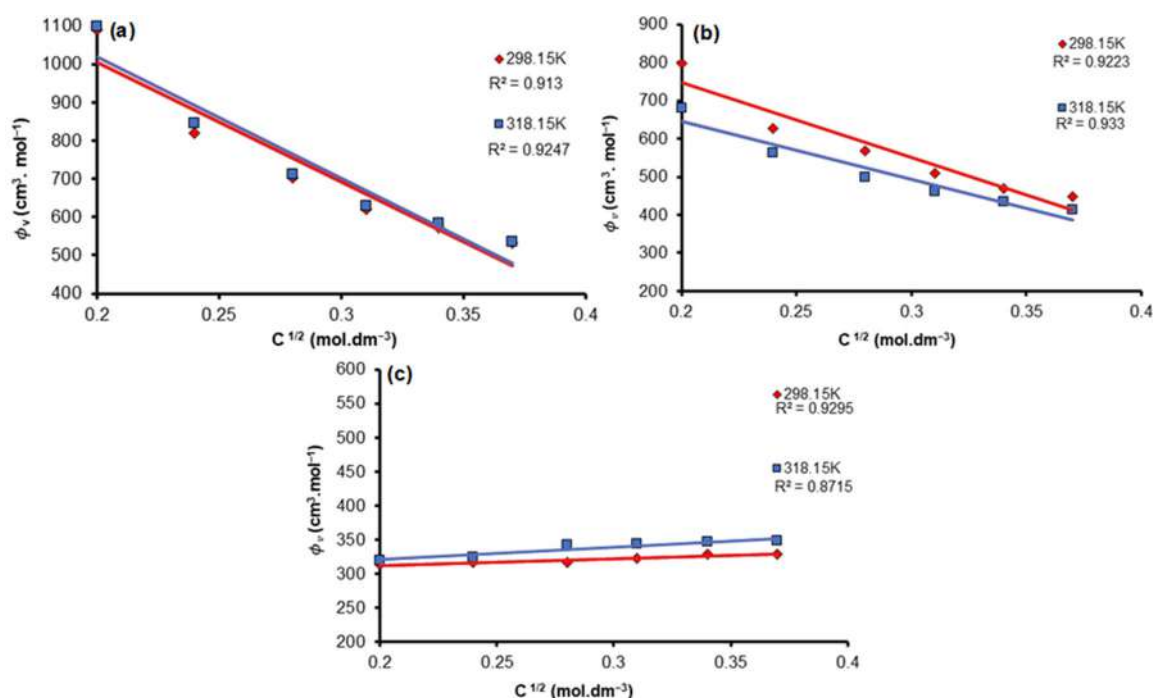| 10^2 [CPM] mol dm^{-3}	$10^{-2} \phi_v$ (cm^3 mol^{-1}) at temperature (K)				
	298.15	303.15	308.15	313.15	318.15
aqueous system					
4.00	10.907±0.000[a]	10.891±0.001[d]	10.916±0.001[b]	10.922±0.001[c]	10.985±0.001[e]
6.00	8.209±0.001[a]	8.339±0.001[b]	8.370±0.001[c]	8.442±0.001[d]	8.453±0.001[e]
8.00	7.036±0.001[a]	7.071±0.001[b]	7.082±0.001[c]	7.106±0.001[d]	7.115±0.001[e]
10.0	6.200±0.001[a]	6.214±0.001[b]	6.261±0.001[c]	6.281±0.001[d]	6.284±0.001[e]
12.0	5.734±0.001[a]	5.760±0.001[b]	5.788±0.001[c]	5.795±0.001[d]	5.832±0.001[e]
14.0	5.325±0.001[a]	5.333±0.001[b]	5.347±0.001[c]	5.362±0.001[d]	5.368±0.001[e]
aq-MeOH system (10 % v/v)					
4.00	7.980±0.001[e]	7.956±0.001[d]	7.768±0.001[c]	7.691±0.001[b]	6.801±0.001[a]
6.00	6.274±0.001[e]	6.265±0.001[d]	6.255±0.001[c]	6.205±0.001[b]	5.618±0.001[a]
8.00	5.672±0.001[e]	5.508±0.001[d]	5.385±0.001[c]	5.433±0.001[b]	4.994±0.001[a]
10.0	5.083±0.001[e]	5.036±0.001[d]	4.952±0.001[c]	4.957±0.001[b]	4.609±0.001[a]
12.0	4.689±0.001[e]	4.734±0.001[d]	4.666±0.001[c]	4.648±0.001[b]	4.358±0.001[a]
14.0	4.481±0.001[e]	4.442±0.001[d]	4.396±0.001[c]	4.372±0.001[b]	4.127±0.001[a]
aq-EG system (10 % v/v)					
4.00	3.131±0.001[a]	3.139±0.001[b]	3.155±0.001[c]	3.176±0.001[d]	3.193±0.001[e]
6.00	3.165±0.001[a]	3.286±0.001[d]	3.289±0.001[e]	3.211±0.001[b]	3.243±0.001[c]
8.00	3.172±0.001[a]	3.300±0.001[b]	3.322±0.001[c]	3.373±0.001[d]	3.431±0.001[e]
10.0	3.223±0.001[a]	3.346±0.001[b]	3.357±0.001[c]	3.406±0.001[d]	3.440±0.001[e]
12.0	3.285±0.001[a]	3.379±0.001[b]	3.396±0.001[c]	3.411±0.001[d]	3.464±0.001[e]
14.0	3.293±0.001[a]	3.388±0.001[b]	3.425±0.001[c]	3.433±0.001[d]	3.481±0.001[e]

Fig 2. Plot of apparent molar volume (ϕ_v) versus $C^{1/2}$ for CPM in (a) aqueous, (b) aq-MeOH, (c) aq-EG systems

Table 3. Partial molar volume (ϕ_v) and S_v of CPM in aqueous, aq-MeOH, and aq-EG systems at different temperatures

	$10^{-2} \phi_v$ (cm^3 mol^{-1}) at temperature (K)				
Solvent systems	298.15	303.15	308.15	313.15	318.15
aqueous system	16.308±0.002[a]	16.389±0.001[b]	16.421±0.000[c]	16.479±0.003[d]	16.559±0.001[e]
aq-MeOH system (10% v/v)	11.411±0.002[e]	11.336±0.000[d]	11.105±0.003[c]	10.996±0.001[b]	9.474±0.004[a]
aq-EG system (10% v/v)	2.916±0.002[e]	2.913±0.003[d]	2.899±0.000[c]	2.854±0.001[b]	2.843±0.001[a]
	$10^{-2} S_v$ (cm^2 dm$^{1/2}$ mol$^{-3/2}$) at temperature (K)				
aqueous system	-31.285±0.001[e]	-31.450±0.002[d]	-31.472±0.003[c]	-31.589±0.002[b]	-31.790±0.001[a]
aq-MeOH system (10% v/v)	-2.041±0.001[c]	-2.125±0.003[b]	-2.432±0.002[a]	-1.704±0.001[d]	-1.622±0.004[e]
aq-EG system (10% v/v)	1.017±0.002[a]	1.355±0.001[b]	1.465±0.003[c]	1.656±0.001[d]	1.830±0.000[e]

the aq-EG system as compared to water and aq-MeOH systems. The difference in values of ϕ_v^o for CPM in studied systems is because of the variance in solvation pattern around the solute. The S_v parameter characterizes the pair-wise interaction of solvated species in solution; this parameter is a volumetric coefficient. The interaction patterns among the drug species are determined with the help of the S_v parameter, which builds upon solution nature and temperature [21-22]. The data gathered for CPM at multiple temperatures displayed negative values of S_v in water and aq-MeOH systems, although positive in the aq-EG system. The negative S_v in water and aq-MeOH systems at T = (298.15–318.15 K) points out the very weak

solute-solute (drug-drug) interactions. The observed positive slope in the aq-EG system is due to the incomplete ionization of drug molecules that show the positive slope. Furthermore, at higher temperatures, low positive values were observed, which may be accredited to the decline in the solvation of ions by rising temperature.

The partial molar volume of transfer ($\phi_{v(tr)}^o$) is used to express valuable information regarding interactions between solute-solvent molecules in a solution. The following expression was used to manifest the standard transfer volume in ternary solutions.

$$\phi_{v(tr)}^o = \phi_{v(aq-MeOH)}^o - \phi_{v(aq)}^o \tag{3}$$

$$\phi_{v(tr)}^o = \phi_{v(aq-EG)}^o - \phi_{v(aq)}^o \tag{4}$$

Partial molar transfer volume data are presented in Table 4, as calculated by Eqs. (3) and (4). The magnitude of $\phi^o_{v(tr)}$ in ternary solutions (CPM+aq-MeOH/EG) is negative, demonstrating that ϕ^o_v values are higher in water at studied temperatures.

The combination of change in volume of solute after interaction with the solvent and innate volume of solute is defined as the standard partial molar volume of transfer [23]. Below-mentioned contributions are helpful in defining innate volume [24-25]

$$\phi^o_{v(int)} = V_{vw} + V_{void} \tag{5}$$

where V_{vw} is the volume occupied by the solute because of its van der Waals volume [24] and V_{void} is the volume related to the voids and empty spaces which are present thereto, including the involvement of a solute molecule to its standard partial molar volume.

$$\phi^o_{v(int)} = V_{vw} + V_{void} - n\sigma_s \tag{6}$$

where σ_s is used for the volume shrinkage which occurs due to the interaction of solute (Hydrogen bonding groups) with water molecules, and n is the number of potential hydrogen bonding groups inside the molecule. Hence, the composition of $\phi^o_{v(int)}$ is as follows.

$$\phi^o_{v(int)} = V_{vw} + V_{void} - V_{shrinkages} \tag{7}$$

In all types of aqueous solutions, the $\phi^o_{v(tr)}$ value depends on the $V_{Shrinkage}$ because V_{vw} and V_{void} are almost unchanged. The use of Eq. (7) that the increase in the values of $V_{Shrinkage}$ in the presence of aq-MeOH/EG systems is because of a rise in the number of interactions with water molecules which causes the decline in values of limiting apparent molar volume; therefore, negative $\phi^o_{v(tr)}$ values are procured [26].

The co-sphere overlap model, which is proposed by Friedman and Krishnan [27] helpful in the interpretation of obtained results. According to Friedman and Krishnan's proposed study [27], several interactions occur between solute (drug) and solvent systems (water, aq-MeOH/EG) such as ion-dipole, dipole-dipole, ion-hydrophobic, and hydrophobic-hydrophobic interactions. Dipole-dipole or ion-dipole interactions are types of hydrophilic-hydrophilic interactions. In consonance with the theory, the dominance of dipole-dipole interactions will lead to a positive $\phi^o_{v(tr)}$, whereas the hydrophobic–hydrophobic interactions lead to a negative $\phi^o_{v(tr)}$.

The results in Table 4, depicted the supremacy of hydrophobic-hydrophobic interactions over dipole-dipole interactions in studied systems [28]. Hydrophobic and charge contributions are the indication of the solution properties of drug molecules. The polar groups are hydrated in water, and in drug molecules, the intermolecular aggregation through their hydrophobic parts, which favors their limited aqueous solubilization, is anticipated to happen in a way practically equivalent to micellization. However, this solubilization inclination is influenced by the addition of non-aqueous components. Hydrophobic tails and hydrophilic groups are both present in alcohol molecules. This interesting quality leads to an aqueous environment to complex self-association behavior that is not exhibited in non-aqueous solvents. Through the phenomenon of polar hydrophobic hydration in the water region, the solution behavior of alcohol molecules is largely established [4]. An overall result of several drug-drug and drug-solvent interactions in solutions is pronounced as electrostatic interactions between the local charge on the drug, co-solutes or its ions and the dipole moment of H_2O, interlocking packing interactions of the ions, solutes, or co-solutes with H_2O which causes caging and also solvation and another polar-ionic group (H-bonding) interactions between different polar and non-polar groups of drugs and different solvent systems; overall state

Table 4. Partial molar transfer volume of ($\phi^o_{v(tr)}$) of CPM in aq-MeOH and aq-EG systems at different temperatures

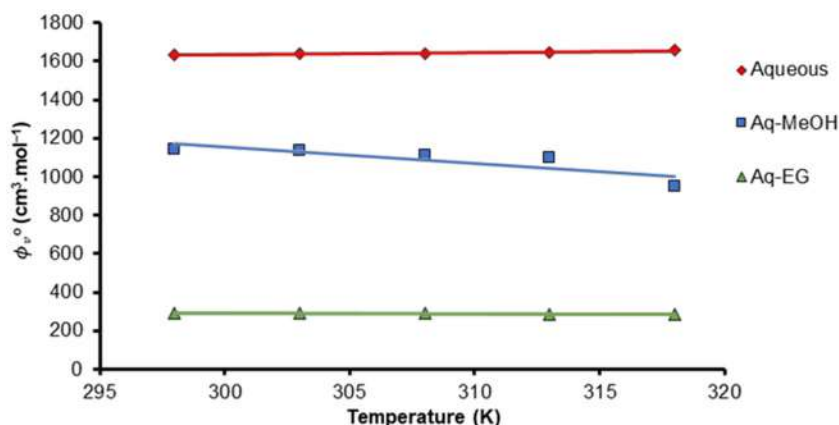|	$10^{-2}\ \phi^o_{v(tr)}$ (cm³ mol⁻¹) at temperature (K)				
Solvent systems	298.15	303.15	308.15	313.15	318.15
aq-MeOH system (10% v/v)	-04.986±0.002[e]	05.030±0.001[d]	-05.316±0.003[c]	-05.483±0.002[b]	07.084±0.001[a]
aq-EG system (10% v/v)	-13.390±0.000[e]	13.475±0.001[d]	-13.522±0.002[c]	-13.624±0.003[b]	13.715±0.004[a]

Fig 3. The plot of ϕ_v^o versus temperature for CPM in aqueous, aq-MeOH, and aq-EG systems

Table 5. Values of coefficients (α_0, α_1, α_2) for CPM in aqueous, aq-MeOH and aq-EG systems

Polynomial Coefficients			
Solvent systems	α_0 (cm^3 mol^{-1} K^{-1})	α_1 (cm^3 mol^{-1} K^{-1})	α_2 (cm^3 mol^{-1} K^{-2})
aqueous system	1928.6	-3.0400	0.0069
aq-MeOH system (10% v/v)	-71373	479.20	-0.7916
aq-EG System (10% v/v)	-7338.1	46.649	-0.0709

of the studied solutions can characterize all these interactions with the help of the standard partial molar volume of a solute [29].

The variation of apparent molar volume at infinite dilution ϕ_v^o, with the temperature can be expressed by the following general polynomial equation, which is presented in Fig. 3.

$$\phi_v^o = \alpha_0 + \alpha_1 T + \alpha_2 T_2 \tag{8}$$

The values of coefficients α_0, α_1, α_2 for CPM are determined over the temperature ranges under investigation and are tabulated in Table 5. The calculation of partial molar expansibilities can be done through the differentiation of Eq. (8) with temperature.

$$\phi_E^o = (\partial\phi_v^o / \partial T)p = \alpha_1 + 2\alpha_1 T \tag{9}$$

The increase and decrease in values with the variation in temperature are used to describe the presence and absence of caging and packing effects, respectively. The magnitude of partial molar expansibilities for CPM in water, aq-MeOH/EG systems are observed to be amplified by the rise in temperature, which expresses the presence of caging effect as described in Fig. 4 and data displayed in Table 6.

The below-mentioned thermodynamic expression was established by Hepler [30], which shows the behavior
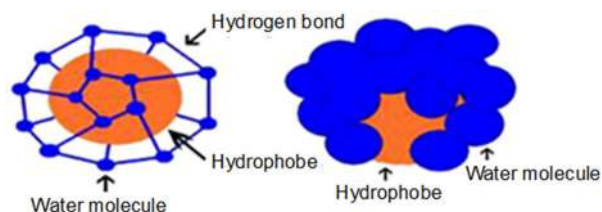
Fig 4. Caging effect of water

of solute in solvent systems (structure promoter or structure breaker) [31].

$$(\partial C_p / \partial_p)_T = (\partial 2\phi_v^o / \partial T^2)p = 2\alpha_2 \tag{10}$$

The sign of $(\partial^2\phi_v^o/\partial T^2)_p$ with respect to temperature $(\partial^2\phi_v^o/\partial T^2)_p$ was used to determine the structure-making/breaking effect with the help of ϕ_v. Based on Hepler's criterion, it can be evaluated that the sign of $(\partial^2\phi_v^o/\partial T^2)_p$ will be positive for structure promoting solute, whereas the negative sign 2 is the structure breaking behavior of solute. According to Hepler's criterion, the positive is used for structure promoter, whereas the negative sign corresponds to structure breaking property. The data tabulated in our investigation (Table 6), indicated the structure-making behavior in the water while the negative sign of $(\partial C_P/\partial P)_T$ was observed in aq-alcoholic systems, which is the indication of structure-breaking behavior. The basis

Indones. J. Chem., 2022, 22 (5), 1218 - 1232

1225

Table 6. Partial molar expansibility (ϕ_E^o) and $(\partial^2\phi_v^o/\partial T^2)_P$ of CPM in aqueous, aq-MeOH, and aq-EG systems

|	ϕ_E^o (cm³ mol⁻¹) at temperature (K)					
Solvent systems	298.15	303.15	308.15	313.15	318.15	$(\partial^2\phi_v^o/\partial T^2)_P$
aqueous system	1.072±0.002[b]	1.141±0.001[c]	1.210±0.001[d]	1.279 ±0.004[e]	1.348±0.003[a]	0.0138
aq-MeOH system (10% v/v)	7.406±0.002[e]	-0.509±0.001[d]	-8.425±0.003[c]	-16.341±0.001[b]	-24.257±0.000[a]	-1.5832
aq-EG system (10% v/v)	-0.167±0.001[e]	-2.297±0.002[b]	-2.427±0.001[a]	-0.557±0.002[d]	-0.687±0.003[c]	-0.0260

of structure promoting behavior of CPM in water is due to the presence of different interacting groups (hydrophilic, hydrophobic, and ionic) in the surroundings, which causes relaxation in hydrated and electro-strict molecules of water, resulting dominance of solute-co-solute interaction. The observed structure-breaking behavior in aq-MeOH/EG systems is due to the formation of a hexa-atomic ring between alcohols (MeOH and EG) and water [32] as presented in Fig. 5. The formation of a hexa-atomic ring between water and alcohols weakens the interaction of hydrogen bonding of alcohols around CPM.

Viscometric Properties

The data for viscosity measurement is tabulated in Table 7, and escalation in viscosity values was observed with increasing concentration of CPM in studied systems, while a decline was observed with the rise in temperature because the kinetic energy of molecules increased, which enhanced the fluidity of solutions [33].

The detected data of CPM in aq-alcoholic system showed greater viscosity values as compared to water because MeOH and EG contain both hydrophilic and hydrophobic groups, which are responsible for stronger hydrogen bonding and cause disruption in the structure of water with other possible interactions as well; therefore, the overall viscosity of the solution increased.
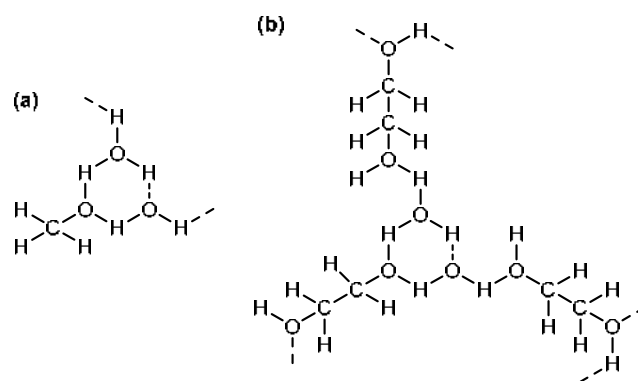
Fig 5. Hexa-atomic ring of (a) MeOH and (b) EG with water

Table 7. Viscosities of CPM in aqueous, aq-MeOH, and aq-EG systems at different temperatures

	η (mPa s) at temperature (K)				
10² [CPM] (mol dm⁻³)	298.15	303.15	308.15	313.15	318.15
aqueous system					
4.00	0.8937	0.7995	0.7212	0.6554	0.5996
6.00	0.9144	0.8598	0.7452	0.6769	0.6205
8.00	0.9387	0.8815	0.7859	0.6985	0.6313
10.0	0.9624	0.9129	0.8067	0.7299	0.6529
12.0	1.0115	0.9348	0.8182	0.7407	0.6742
14.0	1.0526	0.9467	0.8391	0.7618	0.6951
aq-MeOH system (10% v/v)					
4.00	0.9079	0.8496	0.7747	0.7239	0.6789
6.00	0.9242	0.8703	0.7958	0.7429	0.6912
8.00	0.9459	0.8823	0.8175	0.7556	0.7126
10.0	0.9677	0.9146	0.8395	0.7763	0.7343
12.0	1.0117	0.9367	0.8615	0.8178	0.7561
14.0	1.0530	0.9674	0.8884	0.8295	0.7785

Table 7. Viscosities of CPM in aqueous, aq-MeOH, and aq-EG systems at different temperatures (*Continued*)

10² [CPM] (mol dm⁻³)	η (mPa s) at temperature (K)				
	298.15	303.15	308.15	313.15	318.15
aq-EG system (10% v/v)					
4.00	0.9217	0.8424	0.7555	0.6977	0.6613
6.00	0.9458	0.8536	0.7564	0.7042	0.6686
8.00	0.9656	0.8682	0.7766	0.7198	0.6829
10.0	0.9915	0.9081	0.7983	0.7480	0.7266
12.0	1.0018	0.9196	0.8501	0.7539	0.7408
14.0	1.0208	0.9313	0.8529	0.8152	0.7904

The Jones–Dole relation was used to determine A and B coefficients for CPM in studied systems by applying the least square fitting method [34].

$$\eta_{sp}/C^{1/2} = A + BC^{1/2} \qquad (11)$$

where η_{sp} stands for specific viscosity, A is solute-solute and B is used for solute-solvent interactions. The representation of curves between $\eta_{sp}/C^{1/2}$ and $C^{1/2}$ are presented in Fig. 6, and the data are listed in Table 8. The data prophesied that A values are negative, indicating weak drug-drug interaction, but the negative values decreased by increasing temperature in aq-MeOH/aq-EG systems which shows weaker drug-drug interactions at higher temperatures, while in water, the values increased with the rise of temperature indicating drug-drug interaction got strengthen at high temperatures.

On the other hand, the B values of binary and ternary systems are positive, indicating that drug-solvent interactions exist in studied systems [35]. The derivative of viscosity B coefficient with respect to temperature, i.e., dB/dT can provide a direct indication of structure promoting/breaking nature of solute (drug) in solution. The sign of dB/dT is positive for structure-breaking groups while the value becomes negative for promoting groups. The enumerated data show negative

Table 8. Values of A and B coefficients of Jones-Dole parameters and dB/dT for CPM in aqueous, aq-MeOH, and aq-EG systems at different temperatures

Temp (K)	A (m³/² mol⁻½)	B (m³ mol⁻¹)	10² dB/dT
aqueous system			
298.15	-0.556±0.003[a]	2.768±0.001[d]	
303.15	-0.416±0.002[e]	2.697±0.002[e]	
308.15	-0.466±0.001[c]	2.606±0.003[c]	-1.680
313.15	-0.476±0.003[b]	2.583±0.002[b]	
318.15	-0.440±0.000[d]	2.405±0.004[a]	
aq-MeOH system (10% v/v)			
298.15	-0.314±0.002[e]	2.183±0.003[a]	
303.15	-0.437±0.002[c]	2.192±0.002[b]	
308.15	-0.421±0.001[d]	2.255±0.004[c]	1.240
313.15	-0.464±0.004[b]	2.376±0.002[d]	
318.15	-0.486±0.003[a]	2.401±0.001[e]	
aq-EG system (10% v/v)			
298.15	-0.228±0.001[e]	1.554±0.004[a]	
303.15	-0.302±0.002[d]	1.745±0.001[b]	
308.15	-0.324±0.003[c]	2.097±0.002[c]	4.040
313.15	-0.391±0.001[b]	2.254±0.004[d]	
318.15	-0.342±0.002[a]	2.309±0.000[e]	
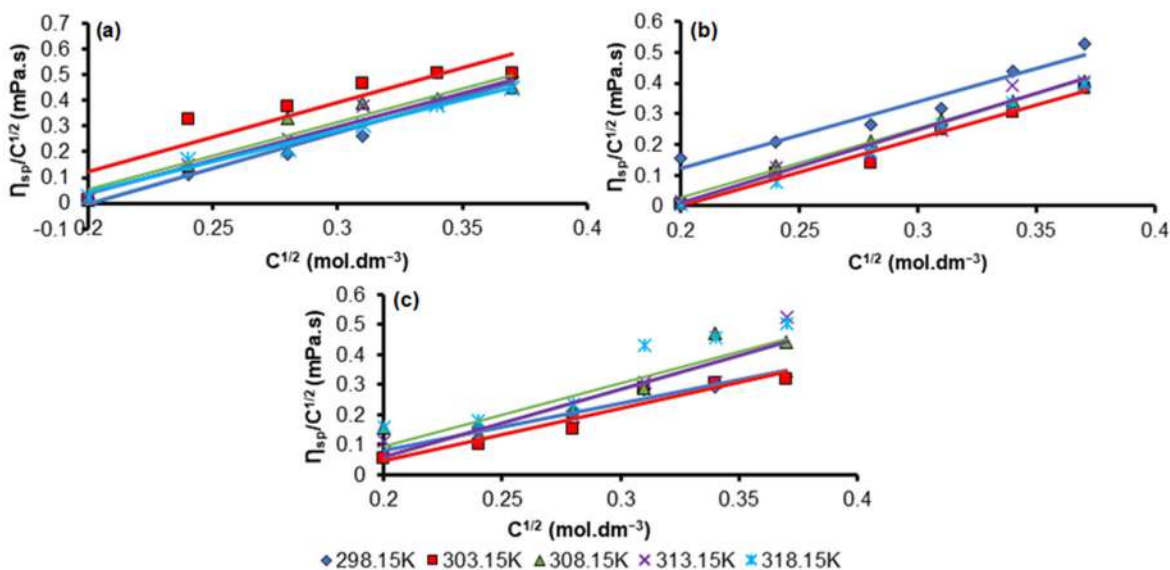
Fig 6. Plots of Jones-Dole equation for CPM in (a) aqueous, (b) aq-MeOH, (c) aq-EG system

signs of dB/dT for CPM in water corresponding structure promoting nature while positive dB/dT in aq-MeOH/EG systems shows structure breaking behavior. The $\Delta B_{(tr)}$ gives an indication about interaction patterns occurring in a solution can be manifested by using Eq. (12) [36].

$$\Delta B_{(tr)} = B_{(aq-MeOH/EG)} - B_{(water)} \qquad (12)$$

The results of $\Delta B_{(tr)}$ for CPM in studied systems arranged in Table 9, verify the supremacy of

hydrophobic-hydrophobic interactions as mentioned in the volumetric study, also illustrated in Fig. 7.

HPLC Analysis (Recovery Studies)

Chlorpheniramine maleate in the different solvent system was analyzed by a significant change in retention time (Fig. 8), the area under the curve (AUC), and % recovery as given in Table 10. In order to eradicate the
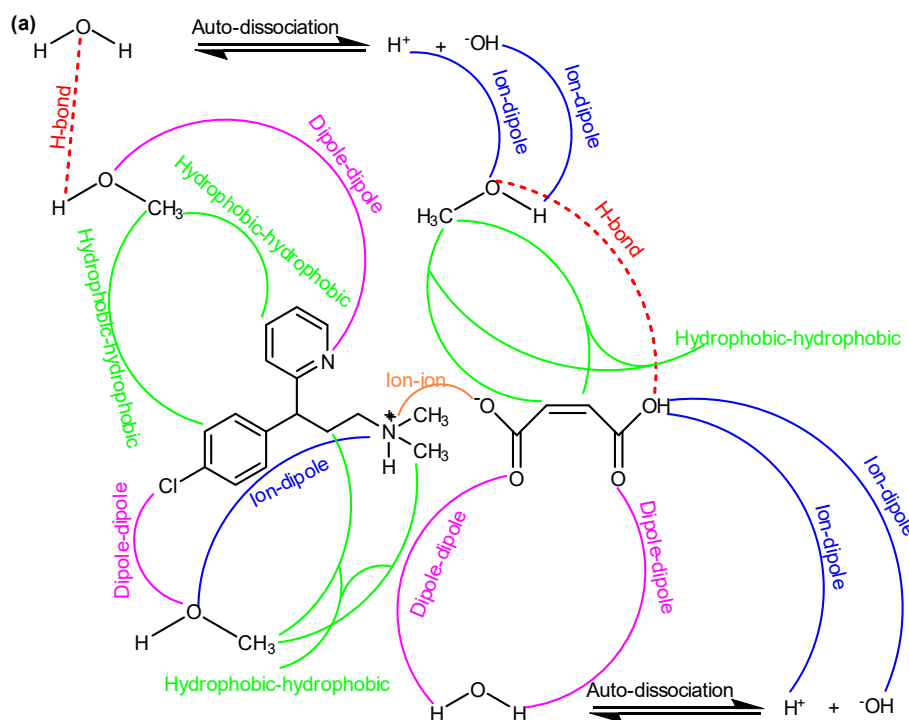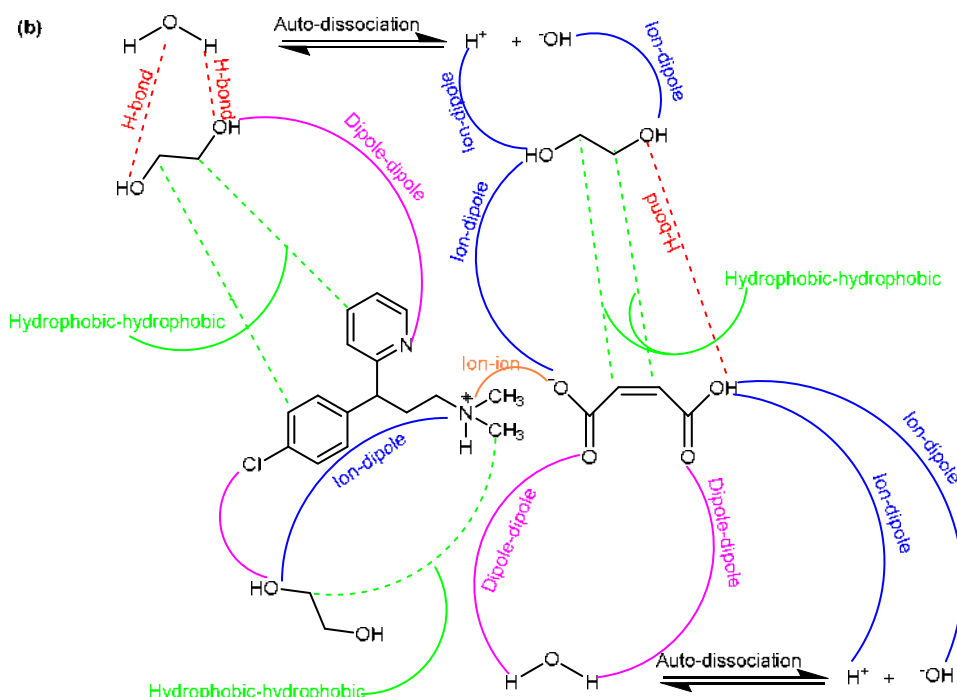
Fig 7. Different possible interactions in (a) aq-MeOH and (b) aq-EG systems

Table 9. Values of $\Delta B_{(tr)}$ for CPM in aq-MeOH and aq-EG systems at different temperatures

Solvent systems	$10 \Delta B_{(tr)}$ (kg mol^{-1}) at temperature (K)				
	298.15	303.15	308.15	313.15	318.15
aq-MeOH System (10% v/v)	-5.847±0.002[e]	-5.050±0.001[d]	-3.515±0.003[c]	-2.071±0.002[b]	-0.043±0.001[a]
aq-EG System (10% v/v)	-12.317±0.000[e]	-9.516±0.001[d]	-5.087±0.002[c]	-3.295±0.003[b]	-0.961±0.004[a]

Table 10. Retention time, recovered concentration, and percent recovery of CPM in aqueous, Aq-MeOH, and Aq-EG systems

| S. No.	Retention time (min)	Recovered conc. (M)	% Recovery
Std. CPM	1.92	-	-
CPM + water	1.89	0.024	40.72
CPM + aq-MeOH (10%, v/v)	1.89	0.021	34.83
CPM + aq-EG (10%, v/v)	1.89	0.021	34.91

effects of inactive materials (excipients) in the formulations, the interaction studies were executed by using raw materials of Active Pharmaceutical Ingredients (API) as previously reported [11].

Upon direct interaction of the API ingredients with the solvents and application of the HPLC method, the trend of recoveries clearly shows the possible interaction with the solvent system since the % recoveries of CPM is significantly affected as observed with the other techniques. In aqueous solvent, there was a decline in recoveries of CPM up to 41% while a similar decreasing trend in % recovery of CPM was observed at 35% in the case of aq-MeOH and aq-EG system. CPM is a freely soluble active pharmaceutical ingredient in the studied solvent systems (water, methanol, and ethylene glycol) [37]. Therefore, a similar retention time was observed with studied solvents (1.89 min) while a drift in retention was found comparatively with Std. CPM (1.92 min) confirms some interactions in water and aq-MeOH/EG systems.
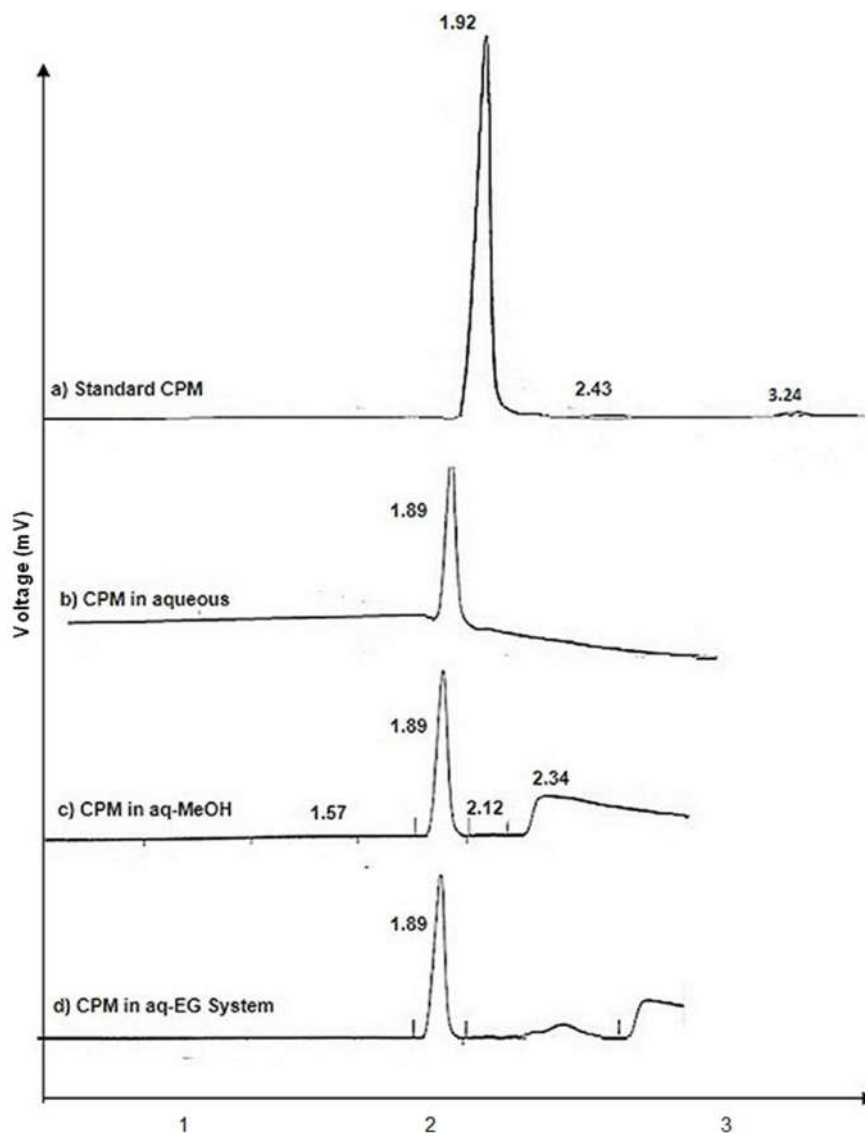
Fig 8. Chromatograms of standard (a) CPM, (b) CPM in aqueous, (c) CPM in aq-MEOH and (d) CPM in aq-EG systems

■ **CONCLUSION**

The current work provides a route to systematic information on CPM in water, mono, and dihydric alcohols (CPM+aq-MeOH/EG systems) through density and viscosity measurements at 298.15–318.15 K, which presented physicochemical properties of the drug. The results procured from the experimental data were helpful in scrutinizing drug-drug and drug-solvent interactions in the studied systems. The supremacy of hydrophobic-hydrophobic interactions over hydrophilic-hydrophilic interactions was observed in aq-MeOH/EG systems. The positive sign of the second derivative of temperature coefficient $(\partial C_P/\partial P)_T$ shows the structure-promoting property of CPM in the water, while the negative sign in aq-MeOH/EG (10%v/v) shows the structure-breaking property. The results obtained from the viscometric study also support the conclusion drawn from the volumetric study. Outcomes based on the HPLC technique proved that the recovery was affected, which also confirms the interaction behavior of CPM in water, mono, and dihydric alcohols. To study the development of structure and solvation behavior on the premise of

various kinds of interactions present in solutions, the calculated parameters are beneficial.

■ ACKNOWLEDGMENTS

■ REFERENCES

[1] Zhang, F., 2016, Physicochemical properties and mechanisms of drug release from melt-extruded granules consisting of chlorpheniramine maleate and Eudragit FS, *Drug Dev. Ind. Pharm.*, 42 (4), 563–571.

[2] Sawhney, N., Kumar, M., Sandarve, S., Sharma, P., Sharma, A.K., and Sharma, M., 2019, Structure-making behaviour of L-arginine in aqueous solution of drug ketorolac tromethamine: volumetric, compressibility and viscometric studies, *Phys. Chem. Liq.*, 57 (2), 184–203.

[3] Munir, A.Q., and Ali, M., 2014, Study of solvent and temperature effects on volumetric, viscometric and conductometric studies of amlodipine besylate, *Asian J. Biomed. Pharm. Sci.*, 4 (35), 22–29.

[4] Rajagopal, K., and Jayabalakrishnan, S.S., 2009, Volumetric and viscometric studies of 4 aminobutyric acid in aqueous solutions of salbutamol sulphate at 308.15, 313.15 and 318.15 K, *Chin. J. Chem. Eng.*, 17 (5), 796–804.

[5] Banipal, T.S., Singh, H., Banipal, P.K., and Singh, V., 2013, Volumetric and viscometric studies on L-ascorbic acid, nicotinic acid, thiamine hydrochloride and pyridoxine hydrochloride in water at temperatures (288.15–318.15) K and at atmospheric pressure, *Thermochim. Acta*, 553, 31–39.

[6] Chauhan, S., Singh, K., Kumar, K., Neelakantan, S.C., and Kumar, G., 2016, Drug–amino acid interactions in aqueous medium: Volumetric, compressibility, and viscometric studies, *J. Chem. Eng. Data*, 61 (2), 788–796.

[7] Banipal, T.S., Beri, A., Kaur, N., and Banipal, P.K., 2016, Volumetric, viscometric and spectroscopic approach to study the solvation behavior of xanthine drugs in aqueous solutions of NaCl at T = 288.15–318.15 K and at p = 101.325 kPa, *J. Chem. Eng. Data*, 62 (1), 20–34.

[8] Vercher, E., Llopis, J.F., González-Alfaro, V., Miguel, J.P., Orchillés, V., and Martínez-Andreu, A., 2015, Volumetric properties, viscosities and refractive indices of binary liquid mixtures of tetrafluoroborate-based ionic liquids with methanol at several temperatures, *J. Chem. Thermodyn.*, 90, 174–184.

[9] Jamal, M.A., Khosa, M.K., Muneer, M., Ur-Rehman, F., Zia, K.M., and Shahzad, K., 2013, Volumetric and ultrasonic studies of an antidepressant drug in aqueous and alcoholic medium over temperature range 298.15–313.15 K, *J. Chem. Soc. Pak.*, 35 (2), 276–280.

[10] Salman, T.A., and Abd, K.A., 2013, Thermodynamic properties of nicotinic acid in dilute HCl and in aqueous NaCl solutions at (293.15, 298.15, 303.15 and 308.15) K, *Baghdad Sci. J.*, 10 (2), 432–441.

[11] Shafi, N., Siddiqui, F.A., Sultana, N., and Arayne. M.S., 2015, Concurrent determination of diltiazem, lisinopril, captopril, and enalapril in dosage formulations and in human serum by liquid chromatographic technique, *J. Liq. Chromatogr. Relat. Technol.*, 38 (15), 1466–1473.

[12] Siddiqui, F.A., Sher, N., Shafi, N., Sial, A.W., Ahmad, M., Mehjebeen, M., and Naseem, H., 2014, Development of new method for simultaneous analysis of piracetam and levetiracetam in pharmaceuticals and biological fluids: Application in stability studies, *BioMed Res. Int.*, 2014, 758283.

[13] Masood, S., Khan, Z., Ashfaq, M., and Khan, S.R., 2020, Optical studies of acefylline piperazine, chlorpheniramine maleate, thiamine hydrochloride in aqueous, aqueous methanol and aqueous ethylene glycol systems, *J. Mol. Liq.*, 303, 112611.

[14] Zhu, Y., Shah, N.H., Malick, A.W., Infeld, M.H., and McGinity, J.W., 2002, Solid-state plasticization of an acrylic polymer with chlorpheniramine maleate and triethyl citrate, *Int. J. Pharm.*, 241 (2), 301–310.

[15] Sayeed, M.A., and Rana, S., 2013, In vitro and In vivo drug-drug interaction study between ketotifen fumarate and chlorpheniramine maleate at gastric and intestinal pH, *e-J. Sci. Technol.*, 2 (8), 17–25.

[16] Dhondge, S.S., Zodape, S.P., and Parwate, D.P., 2012, Volumetric and viscometric studies of some drugs in aqueous solutions at different temperatures, *J. Chem. Thermodyn.*, 48, 207–212.

[17] Mahmood, K., Shakeel, M., and Siddiq, M., 2016, Volumetric and thermodynamic study of three pharmacologically important drugs in ethanol, *Asian J. Chem.*, 28 (4), 761–764.

[18] Shakeel, M., and Mahmood, K., 2020, Use of Masson's and Jones-Dole equation to study different type of interactions of three pharmacologically important drugs in ethanol, *J. Chin. Chem. Soc.*, 67 (9), 1552–1562.

[19] Ragab, G.H., Shaleh, H.M., El-Henawee, M.M., and Elsayed, O.F., 2016, Validated ultra-high efficiency RP-HPLC and stability indicating method for determination of tranylcypromines sulphate in bulk and in tablet dosage forms, *J. Appl. Pharm. Sci.*, 6 (2), 64–71.

[20] Masood, S., Rehman, W., Begum, S., Khan, Z., and Gulnar, L., 2020, Drug-drug and drug-solvent interaction studies of Chloroquine phosphate, Acefylline piperazine and Gentamicin sulfate in polymeric systems, *Arabian J. Chem.*, 13 (7), 6221–6235.

[21] Kumar, H., and Behal, I., 2016, Thermodynamics of (solute + solute) and (solute + solvent) interactions of homologous series of amino acids with thiamine hydrochloride in aqueous medium at T = (305.15, 310.15, 315.15) K: A volumetric and acoustic approach, *J. Chem. Thermodyn.*, 102, 48–62.

[22] Singh, S., 2022, Using volumetric method the study of molecular interactions of NSAID (DP) in water and water + 1M urea at different temperatures, *Biointerface Res. Appl. Chem.*, 12 (3), 3956–3965.

[23] Frank, H.S., and Wen, W.Y., 1957, Ion-solvent interaction. Structural aspects of ion-solvent interaction in aqueous solutions: a suggested picture

of water structure, *Discuss. Faraday Soc.*, 24 (24), 133–140.

[24] Singh, J., Singh, M., Sharma, S., Sharma, S., and Sharma, M., 2021, Molecular interactions of diphenhydramine-hydrochloride with some imidazolium-based ionic liquids in aqueous media at T = 293.15–313.15 K: Volumetric, acoustic, and UV absorption studies, *ACS Omega*, 6 (35), 22655–22671.

[25] Shekaari, H., and Kazempour, A., 2011, Solution properties of ternary D-glucose + 1-ethyl-3-methylimidazolium ethyl sulfate + water solutions at 298.15 K, *J. Solution Chem.*,40 (9), 1582.

[26] Rafiee, H.R., and Frouzesh, F., 2017, The study of solute–solvent interactions in the ternary {amino acid (glycine or L-serine) + ionic liquid (1-butyl-3-methylimidazolium tetra fluoroborate [Bmim][BF$_4$]) + H$_2$O} system at different temperatures and ambient pressure: Volumetric study, *J. Mol. Liq.*, 230, 6–14.

[27] Friedman, H.L., and Krishnan, C.V., 1973, Studies of hydrophobic bonding in aqueous alcohols: enthalpy measurements and model calculations, *J. Solution Chem.*, 2 (2), 119–140.

[28] Xie, H., Zhao, L., Liu, C., Cao, Y., Lu, X., Lei, Q., and Fang, W., 2016, Volumetric property of glycine, L-serine, L-alanine and L-proline in aqueous solutions of 1-phenylpiperazinium tetrafluoro-borate, *J. Chem. Thermodyn.*, 99, 75–81.

[29] Sarkar, A., and Sinha, B., 2016, Solution properties and taste behaviour of lactose monohydrate in aqueous ascorbic acid solutions at different temperatures: Volumetric and rheological approach, *Food Chem.*, 211, 590–597.

[30] Hepler, L.G., 1969, Thermal expansion and structure in water and aqueous solutions, *Can. J. Chem.*, 47 (24), 4613–4617.

[31] Rani, R., Kumar, A., and Bamezai, R.K., 2017, Effect of glucose/lactose on the solution thermodynamics of thiamine hydrochloride in aqueous solutions at different temperatures, *J. Mol. Liq.*, 240, 642–655.

[32] Zhang, J.B., Zhang, P.Y., Ma, K., Han, F., Chen,

G.H., and Wei, X.H., 2008, Hydrogen bonding interactions between ethylene glycol and water: Density, excess molar volume, and spectral study, *Sci. China, Ser. B: Chem.*, 51 (5), 420–426.

[33] Chauhan, S., Chaudhary, P., Sharma, K., Kumar, K., and Kiran, K., 2013, Temperature-dependent volumetric and viscometric properties of amino acids in aqueous solutions of an antibiotic drug, *Chem. Pap.*, 67 (11), 1442–1452.

[34] Rehman, W., Masood, S., Begum, S., Chandio, A.D., Khan, S.R., Gulnar, L., Khattak, R., and Khan, M.S., 2021, Viscometric and FTIR studies of chloroquine phosphate, acefylline piperazine and gentamicin sulfate in aqueous-polyethylene glycol and aqueous-polyvinyl pyrrolidone at different temperatures,

Arabian J. Chem., 14 (8), 103265.

[35] Tomaš, R., Jovanović, T., and Bešter-Rogač, M., 2015, Viscosity B-coefficient for sodium chloride in aqueous mixtures of 1,4-dioxane at different temperatures, *Acta Chim. Slov.*, 62 (3), 531–537.

[36] Banipal, T.S., Kaur, J., Banipal, P.K., Sood, A.K., and Singh, K., 2011, Volumetric and viscometric studies of some amino acids in aqueous solutions of cadmium chloride at T = (288.15 to 318.15) K and at atmospheric pressure, *J. Chem. Eng. Data*, 56 (6), 2751–2760.

[37] Jafari, P., Rahimpour, E., Acee, W.E., and Jouyban, A., 2021. Prediction of drug solubility in ethylene glycol+water mixtures using generally trained cosolvency models, *J. Mol. Liq.*, 328, 115325.

Effect of Bridging Atom and Hydroxyl Position on the Antioxidant Capacity of Six Phenolic Schiff Bases

Abdelhakim Kheniche[1,2*], Imededdine Kadi[3], Abderrahim Benslama[4], Samiya Rizoug[2], Sarra Bekri[2], and Abdenassar Harrar[1]

[1]*Laboratory of Inorganic Materials, Faculty of Sciences, University of M'sila, 28000 M'sila, Algeria*

[2]*Department of Chemistry, Faculty of Sciences, University of M'sila, 28000 M'sila, Algeria*

[3]*Research Unit in Medicinal Plants (URPM. 3000, Laghouat) Attached to the Research Center of Biotechnology (CRBT. 25000, Constantine)*

[4]*Department of Biochemistry, Faculty of Sciences, University of M'sila, 28000 M'sila, Algeria*

* Corresponding author:

email:
abdelhakim.kheniche@univ-msila.dz

Abstract: *A series of new phenolic Schiff bases N,N-bis(2,3-dihydroxybenzyl-idene)-4,4'-diphenylmethane (3-DPM), and N,N-bis(2,5-dihydroxybenzylidene)-4,4'-diphenylmethane (5-DPM), for sulfide bridge N,N-bis(2,3-dihydroxybenzyl-idene)-4,4'-diphenyl sulfide (3-DPS), N,N-bis(2,5-dihydroxybenzylidene)-4,4'-diphenyl sulfide (5-DPS), N,N-bis(2,3-dihydroxybenzyl-idene)-4,4'-diphenyl disulfide (3-DPSS), and N,N-bis(2,5-dihydroxybenzylidene)-4,4'-diphenyl disulfide (5-DPSS) were synthesized by condensation of substituted 4,4'-diamino-bis-(4-aminophenyl) methane/sulfide with various substituted aldehydes. The synthesized molecules were characterized by physical data, elemental, IR and ^{1}H-NMR analyses. The antioxidant ability of compounds was determined through the use* in vitro *assays such as DPPH• scavenging, ABTS, total antioxidant capacity (TAC), hydroxyl radical OH• scavenging, and reducing power capability. The antioxidant activity of the compounds increased slightly after changing the atom bridge and hydroxyl group position. The results showed that the compound 5-DPSS exhibited superior scavenging strength against DPPH ($EC_{50} = 7.10 \pm 0.16$ µg/mL), whereas 3-DPSS showed the highest activity ($EC_{50} = 1.36 \pm 0.08$ µg/mL) when inspected by ABTS in relation to butylated hydroxyanisole (BHA) ($EC_{50} = 7.54 \pm 0.67$). The higher OH• activity was marked by the compound 5-DPS ($EC_{50} = 44.9 \pm 3.3$ µg/mL) related to BHT at ($EC_{50} = 98.73 \pm 0.3$ µg/mL). The compounds 5-DPM demonstrated remarkable activity both reducing power ($EC_{50} = 53.2 \pm 0.3$ µg/mL), and TAC assay ($EC_{50} = 620.0 \pm 2.4$ µg/mL). These results prove that the modification in hydroxyl group position affect the antioxidant ability of Schiff bases.*

Keywords: *Schiff bases; free radicals; antioxidant activity; phenolics*

■ INTRODUCTION

The free radicals are the standard sources in charge of numerous illnesses, for example, age-related maladies, rheumatoid joint inflammation, Infectious ulcer, and malignancy inception [1-5]. These medical issues are conveyed by the response of receptive oxygen species (ROS), usually known as responsive species (RSs) [6-7]. Cancer prevention agents are particles that assume a basic job in securing against oxidant-incited harm and can be displayed as hydrogen donors or electron reducers to the receptive sites in killing free radical [8-9]. It is accounted for those numerous natural atoms executed as generally amazing cell reinforcements. In this manner, it is critical to comprehend the method of activity and effectiveness of these cancer prevention agents [10]. Antioxidants are molecules that play a critical role in protecting against oxidant-induced damage and can be presented as

hydrogen donors or electron reducers to the reactive site in scavenging free radical [11]. It is reported that many organic compounds behave as very powerful antioxidants. It is therefore essential to recognize the mechanism of action and the tendency to act as antioxidants [12-13].

Schiff bases are classes of compounds that contain azomethines bond (C=N) and owe the general formulation RHC=N-R[1] (where R and R[1] may be alkyl, cycloalkyl, aryl or heterocyclic). They are attained by a condensation process of primary aromatic amines and aldehydes or ketones [14]. Schiff bases play a significant role in the biological process with various applications [15-16]. Additionally, phenolic Schiff bases are proved as efficient antioxidants and excellent free radical scavengers [17]. This radical scavenging propriety is mainly due to the transfer of hydrogen atoms from the OH, NH, and SH groups (attached to the aromatic nuclei) to the free radicals [18].

In the light of these data, we are interested in synthesizing new Schiff bases and investigating their antioxidant properties. The modification of the bridge and the position of hydroxyl groups is a useful strategy to ameliorate the antioxidant activity of Schiff bases. For that, eight compounds are synthesized by the insertion of carbon, sulfur, two sulfur atoms between two aromatic rings. The hydroxyl groups are introduced in *ortho* or *para* position to 3,3'-OH and 5,5'-OH. The aims of this work are to synthesize three series of Schiff bases and to study the effect of the atom bridging on the antioxidant capacity. In addition, the introduction of two hydroxyl groups in different positions in the Schiff bases significantly affects the scavenging efficiency of free radicals in the system, where one is fixed in position 2, and another is at different position in the aromatic ring. The effects of both the bridge and the introduction of the hydroxyl groups were studied. The contributions of the hydroxyl position structures on the antioxidant activity were also investigated.

■ EXPERIMENTAL SECTION

Materials

The chemicals utilized in this work, 4,4'-diaminodiphenylmethane (97%), bis*(4-aminophenyl)* sulfide (98%), 2,5-dihydroxybenzaldehyde (97%) and bis*(4-aminophenyl)* disulfide (98%) 2,3-dihydroxybenzaldehyde (98%), and the solvents were purchased from Sigma-Aldrich. 2,2-diphenyl-1-picrylhydrazyl (DPPH; 97%), NaOCl solution (6–14% active chlorine), 2,2-azino-bis(3-ethylbenzothiazoline-6-sulfonic acid) diammonium salt (ABTS; 98%), butylated hydroxy anisole (BHA; 99%), butylated hydroxytoluene (BHT; 99%), 1,10-phenanthroline monohydrate (99%), ascorbic acid (vitamin C; 99%), potassium ferricyanide (99%), potassium persulfate (98%) and trichloroacetic acid (99%), were obtained from Sigma Aldrich and Merck.

Instrumentation

The ^{1}H-NMR spectra were measured through Bruker AC400 spectrometer (400 MHz) using DMSO-d_6. The analysis of the elemental was taken by a Perkin Elmer 2400 (automatic elemental analyzer). The spectra of FTIR were recorded on a Bruker Vector 22 Spectrophotometer (KBr discs).

Procedure

Synthetic procedure of Schiff bases

The ligand was produced by the reported method [19]. Substituted aldehydes (2 mmol), appropriated diamine (1.0 mmol) in 20 mL of pure ethanol, two microliters of acetic acid were added into a (100 mL) round bottom flask, and the product reaction mixture was refluxed for at 78 °C for 3 h. The formed product was filtered and washed with hot ethanol and then dried. The synthesis of monosubstituted products is shown in Fig. 1.

N,N′-bis(2,3-dihydroxybenzylidene)-4,4′-diaminodiphenyl methane: (3-DPM)

2,3-Dihydroxybenzaldehyde (0.276 g, 2 mmol) 4,4′-diaminodiphenylmethane (0.198 g, 1 mmol). Yield 74%; m.p 200 °C; ^{1}H-NMR (100 MHz, CDCl$_3$) δ (ppm) = 13.28 (s, 2H, C$_2$OH, and C'$_2$OH of 2Ar-OH); 9.17 (s, 2H, C$_3$OH, and C'$_3$OH of 2Ar-OH); 8.90 (s, 2H, HC=N); 6.78–7.10 (m, 8H, ArH); 5.20 (2H, s); 4.02 (s, 2H, CH$_2$); FTIR ν (cm^{-1}) 3417 (OH, broad centered at), 1615 (C=N); Microanalysis for C$_{27}$H$_{22}$N$_2$O$_4$ (438.47), Calcd.: C, 73.96; H, 5.06; N, 6.39. Found: C, 73.85; H, 5.06; N, 6.39.
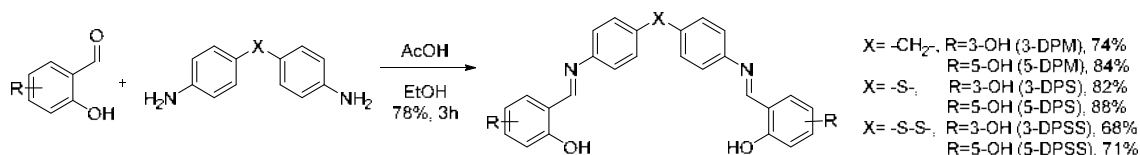
Indones. J. Chem., 2022, 22 (5), 1233 - 1245

1235

Fig 1. Synthesis of Schiff bases

N,N′-bis(2,5-dihydroxybenzylidene)-4,4′-diaminodiphenyl methane: (5-DPM)

2,5-Dihydroxybenzaldehyde (0.276 g, 2 mmol) 4,4′-diaminodiphenylmethane (0.198 g, 1 mmol). Yield 84%; m.p 210 °C; ^{1}H-NMR (25 MHz, CDCl$_3$) δ (ppm) 12.33 (s, 2H, C$_2$OH and C′$_2$OH of 2Ar-OH), 9.10 (s, 2H, C$_5$OH and C′$_5$OH of 2Ar-OH), 8.82 (s, 2H, HC=N), 6.80–7.32 (m, 8H, ArH), 5.20 (2H, s), 4.00 (s, 2H, CH$_2$); FTIR ν (cm^{-1}) 3302 (OH), 1602 (C=N); Microanalysis for C$_{27}$H$_{22}$N$_2$O$_4$ (438.47), Calcd.: C, 73.96; H, 5.06; N, 6.39. Found: C, 73.81; H, 5.04; N, 6.41.

N,N′-bis(2,3-dihydroxybenzylidene)-4,4′-diaminodiphenyl sulfide: (3-DPS)

2,3-Dihydroxybenzaldehyde (0.276 g, 2 mmol) bis(4-aminophenyl) sulfide (0.216 g, 1 mmol). Yield 82%; m.p 210 °C; ^{1}H-NMR (25 MHz, CDCl$_3$) δ (ppm) 13.78 (s, 2H, C$_2$OH and C′$_2$OH of 2Ar-OH), 9.48 (s, 2H, C$_5$OH and C′$_5$OH of 2Ar-OH), 8.88 (s, 2H, HC=N), 6.80–7.75 (m, 8H, ArH); FTIR ν (cm^{-1}) 3400 (OH), 1620 (C=N), 880 (C-S); Microanalysis for C$_{26}$H$_{20}$N$_2$O$_4$S (456.11), Calcd.: C, 68.41; H, 4.42; N, 6.14; S, 7.02. Found: C, 68.39; H, 4.40; N, 6.13; O, 14.04; S, 7.03.

N,N′-bis(2,5-dihydroxybenzylidene)-4,4′-diaminodiphenyl sulfide: (5-DPS)

2,5-Dihydroxybenzaldehyde (0.276 g, 2 mmol) bis(4-aminophenyl) sulfide (0.216 g, 1 mmol). Yield 88%; m.p > 210 °C; ^{1}H-NMR (25 MHz, CDCl$_3$) δ (ppm) 12.01 (s, 2H, C$_2$OH and C′$_2$OH of 2Ar-OH), 9.10 (s, 2H, C$_5$OH and C′$_5$OH of 2Ar-OH), 8.83 (s, 2H, HC=N), 6.82–7.60 (m, 8H, ArH), 5.20 (2H, s); FTIR ν (cm^{-1}) 3417 (OH), 1612 (C=N), 879 (C-S); Microanalysis for C$_{26}$H$_{20}$N$_2$O$_4$S (456.11), Calcd.: C, 68.41; H, 4.42; N, 6.14; S, 7.02. Found: C, 68.39; H, 4.40; N, 6.13; O, 14.04; S, 7.03.

N,N′-bis(2,3-dihydroxybenzylidene)-4,4′-diaminodiphenyl disulfide: (3-DPSS)

2,5-Dihydroxybenzaldehyde (0.276 g, 2 mmol) bis(4-aminophenyl) disulfide (0.248 g, 1 mmol). Yield 68%;

m.p > 210 °C; ^{1}H-NMR (25 MHz, CDCl$_3$) δ (ppm) 12.33 (s, 2H, C$_2$OH and C′$_2$OH of 2Ar-OH), 9.10 (s, 2H, C$_5$OH and C′$_5$OH of 2Ar-OH), 8.82 (s, 2H, HC=N), 6.80–7.32 (m, 8H, ArH), 5.20 (2H, s), 4.00 (s, 2H, CH$_2$); FTIR ν (cm^{-1}) 3425 (OH), 1620 (C=N), 881 (C-S); Microanalysis for C$_{26}$H$_{20}$N$_2$O$_4$S$_2$ (488.09), Calcd.: C, 63.92; H, 4.13; N, 5.73; O, 13.10; S, 13.12. Found: C, 63.90; H, 4.13; N, 5.72; O, 13.12; S, 13.11.

N,N′-bis(2,5-dihydroxybenzylidene)-4,4′-diaminodiphenyl disulfide: (5-DPSS)

2,5-Dihydroxybenzaldehyde (0.276 g, 2 mmol) bis(4-aminophenyl) disulfide (0.248 g, 1 mmol). Yield 71%; m.p > 210 °C; ^{1}H-NMR (25 MHz, CDCl$_3$) δ (ppm) 12.01 (s, 2H, C$_2$OH and C′$_2$OH of 2Ar-OH), 9.10 (s, 2H, C$_5$OH and C′$_5$OH of 2Ar-OH), 8.82 (s, 2H, HC=N), 6.80–7.60 (m, 8H, ArH); FTIR ν (cm^{-1}) 3340 (OH), 1604 (C=N), 879 (C-S); Microanalysis for C$_{26}$H$_{20}$N$_2$O$_4$S$_2$ (488.09), Calcd.: C, 63.92; H, 4.13; N, 5.73; O, 13.10; S, 13.12. Found: C, 63.91; H, 4.12; N, 5.73; O, 13.13; S, 13.12.

Radical scavenging capacity

Free radical scavenging capacity. The antioxidant potential of the Schiff base compounds to scavenge the 2,2-diphenyl-1-picrylhydrazyl (DPPH) free radical was assessed spectrophotometrically following the method reported by Benslama et al. [20]. Briefly, a 320 μL of DPPH methanolic solution (0.6 mg/100 mL) was added to the 80 μL of the compound prepared at various concentrations (solubilized in *N,N*-dimethylformamide). The resulting mixture was maintained in the dark at room temperature. After incubation for 30 min, the absorbance of the mixture was recorded at 517 nm, and the antiradical power was expressed as half-maximal effective concentration (EC$_{50}$) as compared to the control. The percent of antiradical capacity was then calculated according to Eq. (1):

$$\text{DPPH scavenging (\%)} = \frac{(A_c - A_s) \times 100}{A_c} \tag{1}$$

where A_c is the absorbance of control and A_s is absorbance of sample.

ABTS radical-scavenging activity. To set the antioxidant ability of the synthesized phenolic Schiff bases, we adopted the $ABTS^+$ method from [21], with a little alteration. A solution of $ABTS^+$ (7 mM) was mixed with solution of potassium persulfate (2.4 mM) to get a fresh stock solution. Thereafter, the solution used for ABTS screening was produced by combining the stock solutions of potassium persulfate and $ABTS^+$ in equal amounts for 12–14 h in the dark at room temperature. A specific absorbance of $ABTS^+$ at 0.705 ± 0.01 units at 734 nm desired for the analysis was attributed to diluting 1 mL of $ABTS^+$ solution in 60 mL of methanol. A fresh $ABTS^+$ solution was made up for each assay. The sample (50 µL) was mixed with 1 mL of the $ABTS^+$ solution, and then the absorbance at 734 nm was recorded after 6 min for each measurement. The percentage inhibitions of the synthesized SBs were calculated using Eq. (2):

$$ABS \text{ scavenging } (\%) = \frac{(A_c - A_s) \times 100}{A_c} \qquad (2)$$

where A_c is the absorbance of the ABTS free radical solution recorded without a sample and A_s is the absorbance of ABTS free radical solution with the sample. All tests and analyses were realized in triplicate and the outcomes attained were averaged. The inhibition percentage was plotted against concentration, and a straight line was generated, and the EC_{50} values of the Schiff bases were calculated from this graph, explicitly, the amount of antioxidant Schiff bases necessary to diminish the 50% of the initially ABTS radical concentration.

Hydroxyl radical (OH•) -scavenging activity. The hydroxyl radical scavenging effect of compounds was evaluated by [21]. However, 60 µL of $FeSO_4 \cdot 7H_2O$ solution (1 mM) was added to 90 mL of a 1,10-phenanthroline (1 mM) aqueous solution, and 2.4 mL of phosphate buffer (0.2 M, pH 7.8) were added to the resulting mixture following by the addition of 1.5 mL of different concentrations of the sample, then 150 µL of hydrogen peroxide (0.17 mM) in sequence. The mixture was then incubated in the water bath at 37 °C for 30 min. The decrease in the concentration of OH• was estimated spectrophotometrically by measurement of absorbance at

560 nm, and the antiradical capacity was expressed as EC_{50} the values, i.e., the concentration of the studied compound, which induces a decrease of 50% in the absorbance of 560 nm compared to the control. All readings were taken in triplicate, and Butylhydroxy toluene (BHT) was used as a positive control.

The percent inhibition was calculated according to Eq. (3).

$$\text{Hydroxyl} - \text{radical scavenging } (\%) = \frac{(A_c - A_s) \times 100}{A_c} \qquad (3)$$

where A_c is the absorbance of the control solution without the sample and A_s is the absorbance of the sample solution with the sample.

Reducing capacity

The reducing effect of the compounds was measured following the methods [22]. A volume of 20 µL of the compound at various concentrations was combined with 100 µL of potassium ferricyanide $[K_3Fe(CN)_6]$ solution (1%) and 80 µL of phosphate buffer solution (0.2 M, pH 6.6). The resulting mixture was incubated for 20 min at 50 °C. Then, 100 µL of trichloroacetic acid (10%) was also added to terminate the reaction, and the entire was centrifuged for 10 min at 2800 r/min. Finally, the supernatant solution (100 µL) of was combined with 20 µL of $FeCl_3$ solution (0.1%) and distilled water (100 µL). Then, the mixture was incubated for 10 min, and the absorbance was recorded at 700 nm. The antioxidant strength of samples was estimated using a ferrous iron standard curve, absorbance as a function of concentration, and results are expressed as Fe^{2+} concentration (µg/mL) corresponding to the half absorbance value in the standard curve $A_{0.5}$.

Total antioxidant capacity (TAC)

This assay was based on the capacity of an antioxidant agent to reduce the molybdenum (VI) to molybdenum (V) and generate a green phosphomolybdate complex (V) which to be estimated spectrophotometrically at 695 nm. Equal volumes of sodium phosphate (28 mM), sulfuric acid (0.6 M), and ammonium molybdate (4 mM) were taken in a beaker to get the phosphomolybdate reagent. To take the test, 300 µL of sample in several concentrations of Schiff bases (50–500 µg/mL in DMSO)

was mixed with phosphomolybdate reagent and incubated in a water bath for 90 min at 95 °C. The mixture was allowed to settle at room temperature, and absorbance was determined at 765 nm. Instead of the sample, DMSO was used in the blank. According to the equation obtained from the calibration curve, the total antioxidant capacity was estimated as μg/mL ascorbic acid equivalent (AAE) [23].

Statistical analyses

The experiments were performed in triplicates, and data were presented as mean ± SD. The EC_{50} (50% inhibition concentration) values were estimated using the linear regression method. The Graphpad Prism7 was determined to analyze the data. However, the statistical differences between the experimental groups and standard were analyzed using the Student t-test, and the difference were considered statistically significant where $p < 0.05$.

■ RESULTS AND DISCUSSION

Synthesis

The present work involved the preparation of the phenolic Schiff bases by condensation reaction. All the synthesized molecules were powder solids and found to be insoluble in dichloromethane and soluble in methanol and acetonitrile. The analytical data agree well with the formula of the products and were recognized through elemental analysis and spectroscopic data (UV-Vis, IR, and ^{1}H-NMR). The relevant FTIR data of the synthesized compounds presented standard features in appointed regions and characteristic bands in the other zones. In all the compounds under study, the aromatic (C–H) bond manifested in the range (3024–3082 cm^{-1}) [24], whereas the aliphatic (C–H) of 3-DPM and 5-DPM bond appeared in the range of (2924 cm^{-1}). The clear band in the range of (1604–1628 cm^{-1}) was attributed to the azomethine bond (C=N) [25]. The aromatic (C=C) bond appeared in the range of (1520–1566 cm^{-1}) [26].

The ^{1}H-NMR spectra were used in structure elucidation and identification of the synthesized phenolic Schiff bases. The ^{1}H-NMR spectra of synthesized compounds (3-DPM; 5-DPM, 3-DPS, 5-DPS, 3-DPSS, 5-DPSS) displayed the azomethine proton (-HC=N) at and 8.93, 8.77, 8.87, 8.79, 8.87, and 8.83 ppm respectively as singlet [27-28] and aromatic protons at 6.78–7.38 ppm

range as multiplets [29-30]. Furthermore, the aliphatic protons ($-CH_2$) shows a singlet at 4.02 ppm for the compound 3-DPM and 5-DPM [31]. The identified signals of all the protons of the phenolic Schiff bases were in agreement in their expected region.

Radical Scavenging Capacity

DPPH• scavenging activity

From Fig. 2, the curves of the antioxidant effect of all the Schiff base compounds appear almost the same evolutionary trend. The sharp rise in the DPPH• inhibition curve from 10 up to 180 μg/mL, taking a constant trend (stationary phase) from 200 μg/mL. The compound 5-DPSS has the best anti-free radical power with a percentage inhibition of 94.43% with a concentration threshold of 200 μg/mL. The oxidation power of the samples is related to the presence of compounds that exert actions by splitting the chain of free radicals via hydrogen atom donation [32]. The best anti-free radical activity is attributed to the compound 5-DPSS with an EC_{50} value of 7.10 ± 3.2 μg/mL, while the weak activity is recorded for the product 5-DPM (20.97 ± 0.89 μg/mL). The percentage inhibition of the DPPH• increases with increasing concentration in a dependent manner, either for the Schiff base compounds or for standards [33-35]. The inhibition efficiency of synthesized compounds was found to be in ascending order of 5-DPM < 3-DPSS < 3-DPS < 3-DPM < 5-DPS < 5-DPSS (Fig. 2). Based on the EC_{50} values (Table 1) among the six products tested, the 5-DPSS compound was noted as the most active, with an antioxidant activity equal to (7.10 ± 0.16) μg/mL. The DPPH scavenger potential increased in that order as follow: 5-DPSS (7.10 ± 0.16 μg/mL) > 5-DPS (7.20 ± 0.20 μg/mL) > 3-DPM (8.37 ± 0.34 μg/mL) > 3-DPS (8.84 ± 0.34 μg/mL) > 3-DPSS (11.34 ± 0.17 > 5-DPM (20.97 ± 0.89 μg/mL). At the same time, the positive control, BHA and BHT showed a close potential 5.73 ± 0.41 and 22.32 ± 1.19 μg/mL, respectively, than the six products. The lowest antioxidant potential was assigned for 5-DPM with 20.97 ± 0.89 μg/mL. It was clear that the compounds having sulfur bridging atom and second hydroxyl group in position 5 showed the best free radical scavenging activities in the DPPH test.
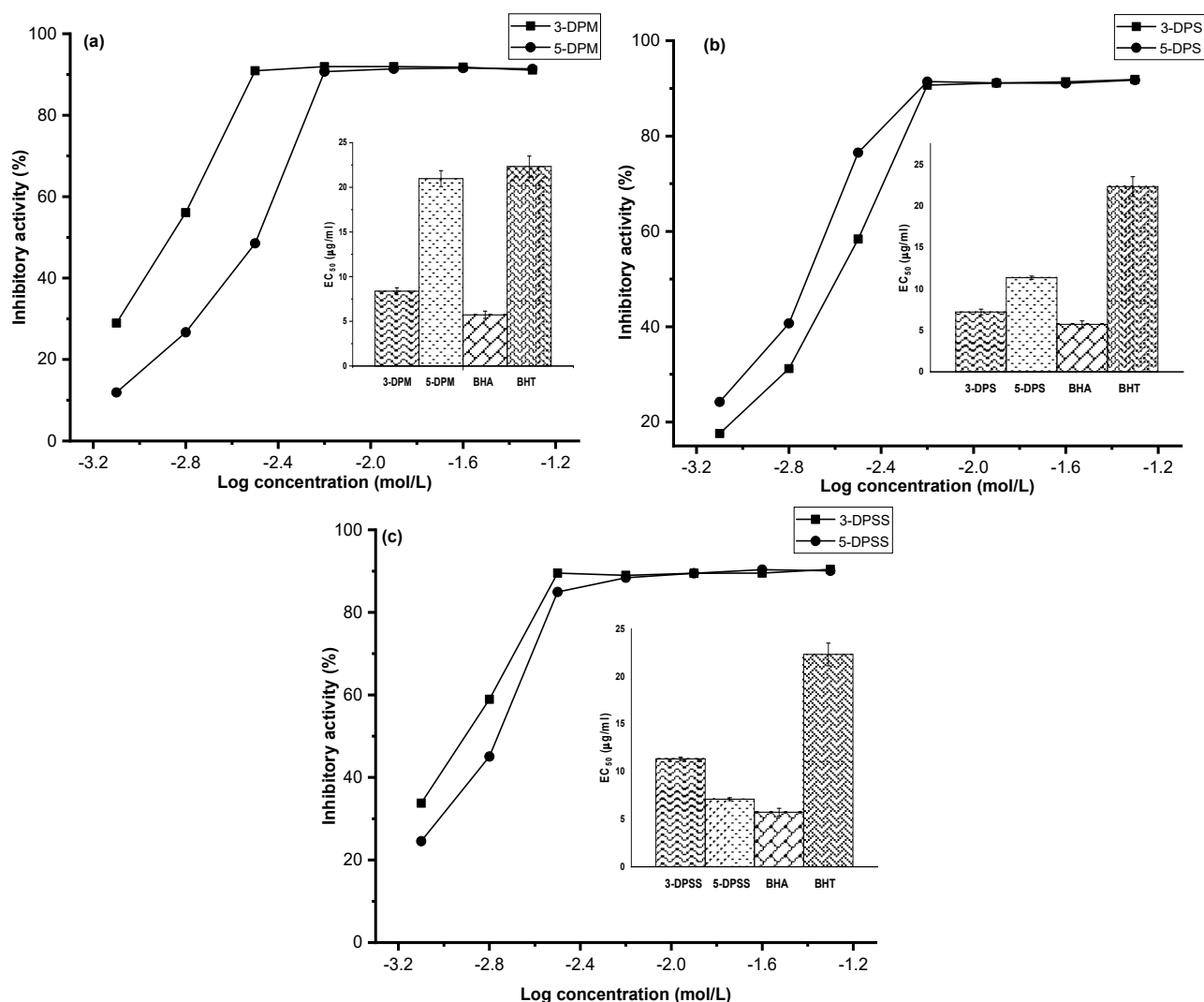
Fig 2. Free radical scavenging activity DPPH• (%) of: (a) DPM, (b) DPS, (c) DPSS. Error bar indicates SD standard deviation (n = 3)

Table 1. The antioxidant activity of the products synthesized and standards

| Product	EC_{50} values (μg/mL)			$A_{0.5}$	EAA
	DPPH	ABTS	OH•	Reducing power	TAC
3-DPM	8.37 ± 0.38	1.49 ± 0.05	227.7 ± 5.1	71.1 ± 0.1	1680.0 ± 0.01
5-DPM	20.97 ± 0.89	3.23 ± 0.01	143.2 ± 16.0	53.2 ± 0.3	620.0 ± 2.4
3-DPS	8.84 ± 0.34	1.77 ± 0.08	209.2 ± 7.3	139 ± 1.3	1153.3 ± 5.7
5-DPS	7.20 ± 0.20	1.95 ± 0.01	44.9 ± 3.3	138.9 ± 1.0	949.16 ± 1.44
3-DPSS	11.34 ± 0.17	1.36 ± 0.08	244.1 ± 16.0	75.5 ± 0.5	1193.3 ± 5.7
5-DPSS	7.10 ± 0.16	2.64 ± 0.05	232.5 ± 3 .93	68.2 ± 0.2	730.0 ± 4.6
BHA	5.73 ± 0.41	7.54 ± 0.67			
BHT	22.32 ± 1.19	1.55 ± 0.26	98.73 ± 0.3	99.2 ±0.41	100.0 ±0.21

ABTS radical scavenging activity

A significant attribute of the antioxidants is the free radical proton scavenging. A recognized protonated radical ABTS has distinctive absorbance maxima at 734 nm, which declines with the quenching of the proton free radicals [36]. The Schiff base series, with

phenyl, diphenylmethane, diphenyl sulfide, and diphenyl disulfide bridges, were powerful and impressive scavenger effect of the ABTS free radical (Fig. 3), and this capacity was consistent with those to those of BHA and BHT (Table 1) that are employed as standard drugs. The lower concentrations of the tested samples were more potent in quenching $ABTS^+$ free radicals in the system [37]. The three series of Schiff bases exhibit powerful scavenging of the $ABTS^+$ radical relative to those of the standards (BHA and BHT). 3-DPSS revealed the highest activity with an EC_{50} of about (1.36 ± 0.08 μg/mL) amongst the synthesized diphenolic Schiff bases series. The ABTS radical scavenging capacity of the tested compounds can be ranked in the order: 3-DPSS > 3-DPM > 3-DPS > 5-DPS > 5-DPSS > 5-DPM.

From the calculated values of EC_{50}, we can conclude that the compounds that have the hydroxyl group in position three present more potent scavenging effects than position 5 in the other Schiff bases series. Furthermore, the sulfur atom bridge performed well compared to that of carbon. The results of the ABTS radical test by the Schiff bases were shown to be much better than those of DPPH•. Many factors like solubility of the compounds' stereoselectivity of the radicals or the indifferent testing systems have been conveyed to affect the aptitude of compounds to react and inhibit different radicals [37-38]. Hong et al. [39] observed that some compounds that present ABTS scavenging response did not display DPPH scavenging ability. In this study, the compounds showed strong scavenging effect against
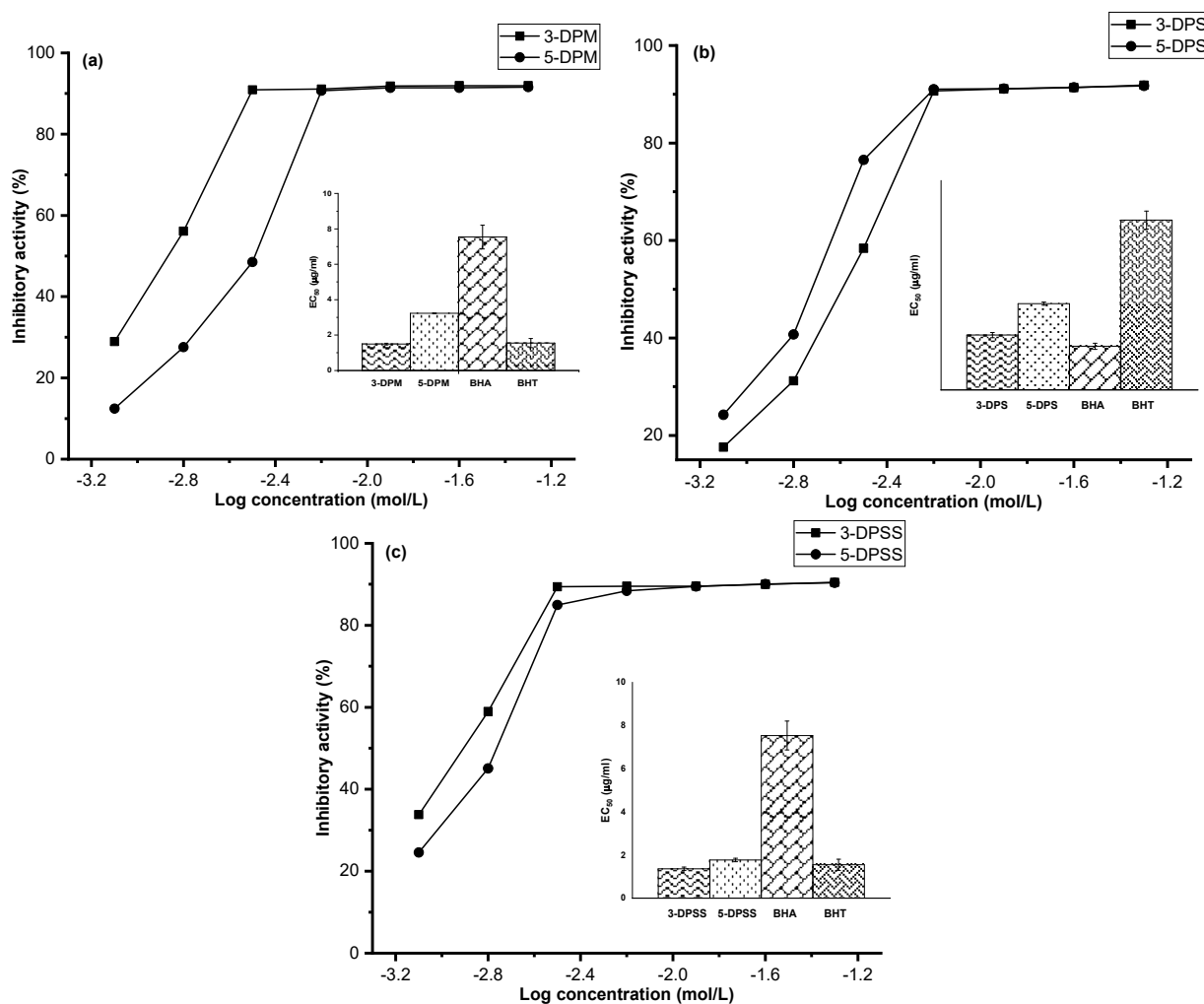
Fig 3. Free radical scavenging activity ABTS• (%). (a) DPM, (b) DPS, (c) DPSS. Error bar indicates SD standard deviation (n = 3)

DPPH and ABTS•. This supplementary showed the capacity of the extracts to quench different free radicals in different systems, signifying that they may be beneficial therapeutic agents for remedying radical-related pathological injury.

Hydroxyl radical OH• scavenging capacity

The six synthesized compounds showed different scavenging power for the OH• (Fig. 4). It is important to note that the compound which has the best inhibitory activity was 5-DPS (44.9 ± 3.3 µg/mL) among the others, which appears weak than BHT (98.73 ± 0.3 µg/mL), while the lowest was found in the compound 3-DPSS (244.1 ± 16.0 µg/mL). In addition, it is clearly seen that the compounds having two hydroxy groups at position 2-5 are more effective than the catecholic compounds (at position 2-3) in the same and the different series [40]. The

statistical results obtained show that the activity of scavenging OH• by the compound 5-DPS has a significant difference of $p < 0.05$ compared to the standard, which clearly explains the insignificant action of this compound in terms of activity and efficiency as the standard (BHT).

The results indicated that the substituents on the phenyl ring have a great influence on the antioxidant activity expressed in the activity of scavenging DPPH•. Schiff's bases carrying the 2,3-dihydroxysalicylidene fragment on the benzene ring with sulfur bridge were found to be the best scavengers of DPPH•. This result was expected since it was well known that the catechol moiety, two adjacent hydroxyl groups influence antioxidant activity [41]. Thus, the hydrogen bonds between the two adjacent hydroxyl groups involve
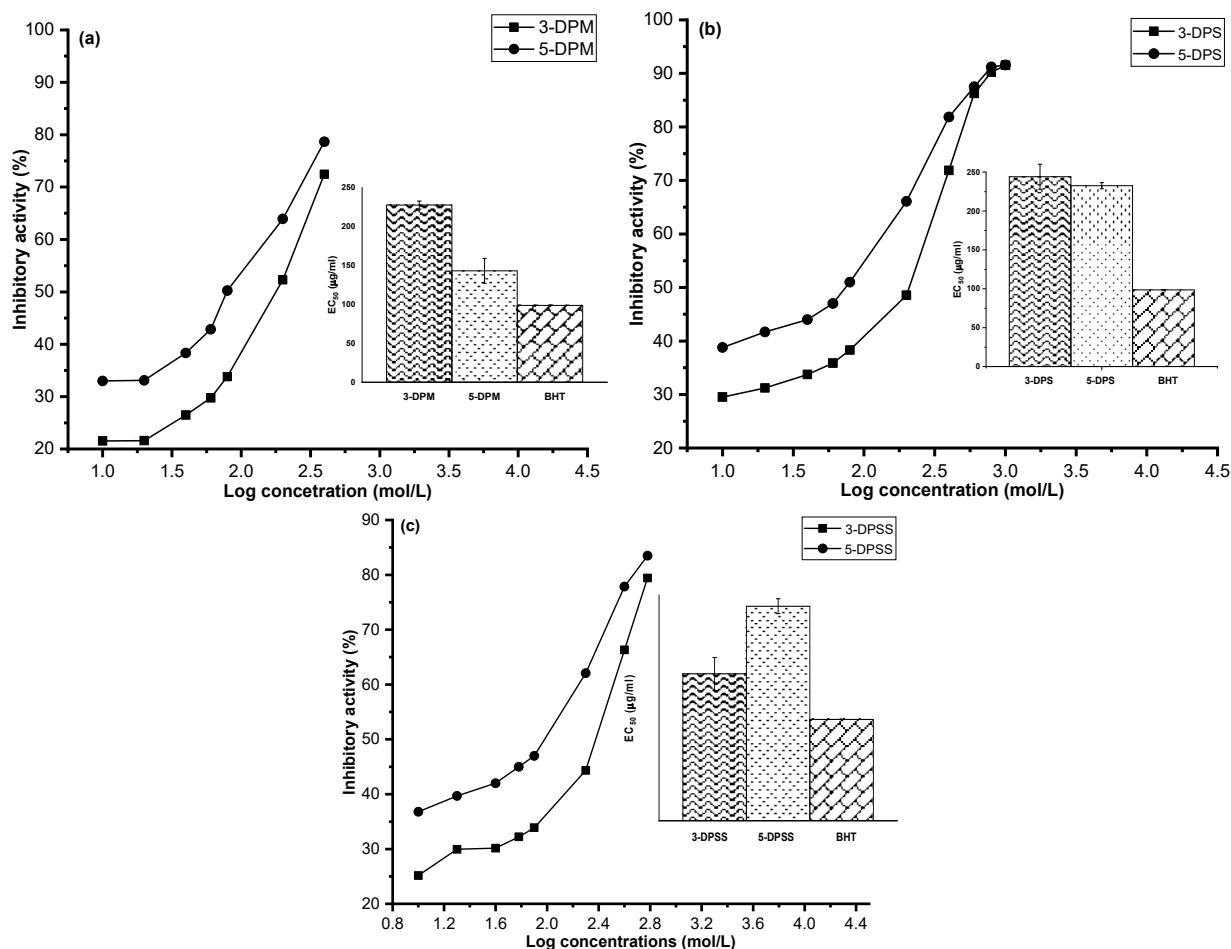
Fig 4. The OH• scavenging activity (%) of 3-DPSS and 5-DPSS. (a) DPM, (b) DPS, (c) DPSS. Error bar indicates SD standard deviation (n = 3)

electrostatical interactions between the proton of the hydroxyl in position three and the oxygen of the hydroxyl number 2. This weakens the OH bond, which consequently makes hydrogen more labile, therefore more reactive, and more ready to react with the free radical [42]. In addition, the oxidation potential of the hydroxyl group plays an important role in determining the entity responsible for the activity.

Čačić et al. [43] proved that the catecholic part 2.3-dihydroxybenzylidene (phenolic ring carrying two hydroxyl groups in *ortho* position; adjacent) is crucial for the anti-radical activity, as well as other authors [44-45], who investigated coumarin derivatives with *o*-dihydroxy phenolic groups. When two hydroxyl groups are at position 2-5 of the phenyl ring, a stable phenoxyl radical is formed, which allows an oxygen atom to share a positive charge, which causes stabilization by delocalization. When two hydroxyl groups are in position 2-4 of one of the phenyl rings, oxygen cannot share a positive charge, and this influences the scavenging DPPH activity [46].

Reducing Power

The reduction capacity is an important property of potential antioxidant activity. The antioxidant compounds can give electrons or hydrogen atoms to the reactive radicals, reducing them into more stable and unreactive species [47]. Generally, antioxidant compounds provoke the reduction of Fe^{3+}/ferricyanide complex to the ferrous (Fe^{2+}) form owing to their reductive potency [48]. According to this method, the reduction is expressed as an increasing of absorbance at 700 nm, in which higher absorbance suggests a higher ferric reducing antioxidant power. In the FRAP assay, higher $FeSO_4 \cdot 7H_2O$ equivalent signifying powerful antioxidant activity. Hence, the compound 5-DPM has relatively high ferric reducing power ability (53.2 ± 0.3 mg/mL), while compound 3-DPS (139 ± 1.3 mg/mL) exhibits inefficient ferric reducing activity (Fig. 5). As shown in Fig. 5, the reducing power of Schiff bases was augmented comparable to standard antioxidants by increasing concentration. The reducing power of samples and standard antioxidants decreased in the order of 5-DPM > 5-DPSS > 3-DPM > 3-DPSS > 5-DPS > 3-DPS. The above-cited results indicate that

compounds that have a hydroxyl group in position 5 possess powerful reductive capacity than the catechol form. The FRAP assay, overall, as the nonradical method, has been disputed to have a slight relationship with the radical scavenging method (HAT mechanism) happening in lipid systems, and it has a deprived correlation with other antioxidant activity measurements. It is, hence, advised that this assay may well be used in combination with further methods in discriminating dominant mechanisms for diverse antioxidants [49].

Total Antioxidant Capacity (TAC)

The results showed that all of the compounds tested have remarkable reducing power with values between 620 to 1680 µg EAA.mg of the product (Fig. 7). The most active compound is 3-DPM and the weakest 5-DPM. The decreasing classification of the tested is as follows: 3-DPM > 3-DPSS > 3-DPS > 5-DPS > 5-DPSS > 5-DPM.

All compounds bearing a hydroxyl group in the *para* and *ortho* position did not show significant antioxidant activity compared with the standards BHA and BHT. Compounds having two hydroxyl groups in the *para* position exhibit moderate antioxidant activity relative to the *ortho* position [50]. This indicates that the change in the position of the hydroxyl groups on the phenyl ring has a great influence on the antioxidant activity expressed in the activity of scavenging DPPH•,
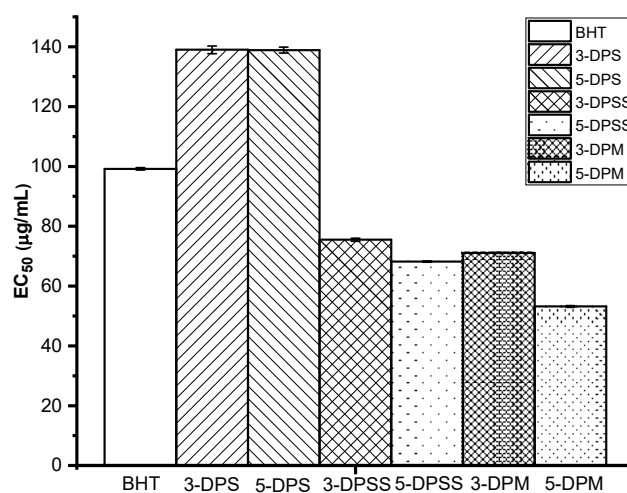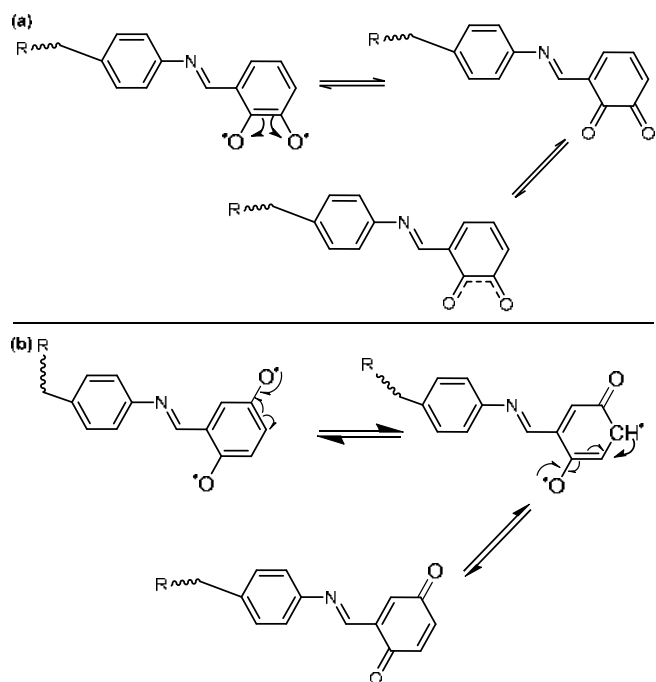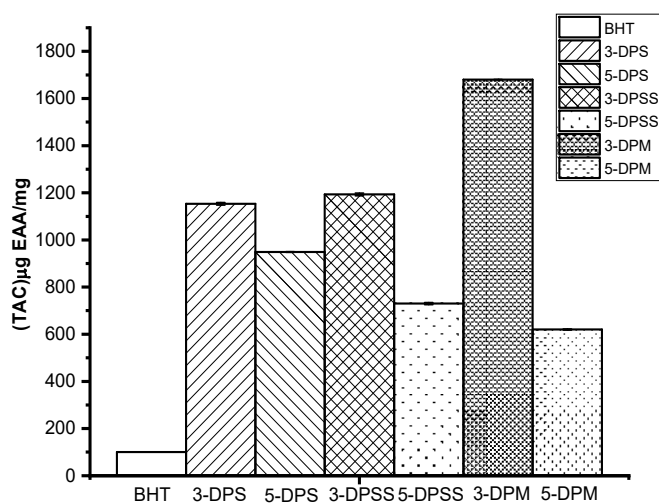

Fig 5. Reducing power of the synthesized Schiff bases

Fig 6. (a) Structure of the stable quinoid form of the compound 3-DPM stabilized by electron delocalization (b) Stable basic Schiff structure of position 2.5 with post electron/hydrogen contribution, with possibility of stabilization by delocalization

Fig 7. TAC of Schiff bases

that it carries in its structure the catecholic form. Regarding to the reducing power, the compound 5-DPM (53.2 ± 0.3) with the methylene bridge has considerable reducing power performance compared to the standards BHA (99.2 ± 0.41) (Table 1).

■ CONCLUSION

In this work, we have synthesized six phenolic Schiff bases compounds. The synthesized compounds were characterized by using various spectroscopic methods, as well as the evaluation of their antioxidant power by different methods, scavenging of the DPPH•, scavenging of the OH•, ABTS•, TAC and reducing power. Examination of the various results obtained by scavenging the DPPH• and ABTS, allowed us to conclude that Schiff bases have hydroxyl group in position 5 exhibit better antioxidant activity compared to the ones having hydroxyl group in position 3. In contrast, the ABTS assay showed that the catechol Schiff bases compounds having a hydroxyl group in position 3 reveal good antioxidant activity in comparison with their analogues having a hydroxyl in position 5. On the one hand, the antioxidant profile of the various compounds synthesized exhibits a dose-dependent power. The observation of the EC_{50} values of the ABTS method shows that the 3-DPSS compound reveals the best value by mean of EC_{50} (1.77 ± 0.08 μg/mL), the compounds: 3-DPS, 3-DPSS, 3-DPS, 5-DPSS, 3-DPM and 5-DPM, presented an inhibitory power superior to that of BHA (7.54 ± 0.67 μg/mL). Noting that all compounds have uneven results, whether OH•, reducing power, or TAC.

■ REFERENCES

[1] Poprac, P., Jomova, K., Simunkova, M., Kollar, V., Rhodes, C.J., and Valko, M., 2017, Targeting free radicals in oxidative stress-related human diseases, *Trends Pharmacol. Sci.*, 38 (7), 592–607.

[2] Archibong, A.E., Rideout, M.L., Harris, K.J., and Ramesh, A., 2018, Oxidative stress in reproductive toxicology, *Curr. Opin Toxicol.*, 7, 95–101.

[3] Hoffmann, M.H., and Griffiths, H.R., 2018, The dual role of Reactive Oxygen Species in autoimmune and inflammatory diseases: Evidence from preclinical models, *Free Radical Biol. Med.*, 125, 62–71.

[4] Phaniendra, A., Jestadi, D.B., and Periyasamy, L., 2015, Free radicals: Properties, sources, targets, and

their implication in various diseases, *Indian J. Clin. Biochem.*, 30 (1), 11–26.

[5] Gebicki, J.M., 2016, Oxidative stress, free radicals and protein peroxides, *Arch. Biochem. Biophys.*, 595, 33–39.

[6] McInnis, S.M., Desikan, R., Hancock, J.T., and Hiscock, S.J., 2006, Production of reactive oxygen species and reactive nitrogen species by angiosperm stigmas and pollen: Potential signalling crosstalk?, *New Phytol.*, 172 (2), 221–228.

[7] Hu, S., Yao, G., Wang, Y., Xu, H., Ji, X., He, Y., Zhu, Q., Chen, Z., and Sun, Y., 2014, Transcriptomic changes during the pre-receptive to receptive transition in human endometrium detected by RNA-Seq, *J. Clin. Endocrinol. Metab.*, 99 (12), E2744–E2753.

[8] Goodman, M., Bostick, R.M., Kucuk, O., and Jones, D.P., 2011, Clinical trials of antioxidants as cancer prevention agents: past, present, and future, *Free Radicals Biol. Med.*, 51 (5), 1068–1084.

[9] Khan, N., and Mukhtar, H., 2015, Dietary agents for prevention and treatment of lung cancer, *Cancer Lett.*, 359 (2), 155–164.

[10] Ghasemi, S., and Lorigooini, Z., 2016, A review of significant molecular mechanisms of flavonoids in prevention of prostate cancer, *J. Chem. Pharm. Sci.*, 9 (4), 3388–3394.

[11] Tan, H.W., Mo, H.Y., Lau, A.T., and Xu, Y.M., 2018, Selenium species: Current status and potentials in cancer prevention and therapy, *Int. J. Mol. Sci.*, 20 (1), 75.

[12] Postigo, C., and Barceló, D., 2015, Synthetic organic compounds and their transformation products in groundwater: Occurrence, fate and mitigation, *Sci. Total Environ.*, 503-504, 32–47.

[13] Gobec, M., Tomašič, T., Marković, T., Mlinarič-Raščan, I., Dolenc, M.S., and Jakopin, Ž., 2015, Antioxidant and anti-inflammatory properties of 1,2,4-oxadiazole analogs of resveratrol, *Chem.-Biol. Interact.*, 240, 200–207.

[14] Alam, M.S., Choi, J.H., and Lee, D.U., 2012, Synthesis of novel Schiff base analogues of 4-amino-1,5-dimethyl-2-phenylpyrazol-3-one and their evaluation for antioxidant and anti-inflammatory activity, *Bioorg. Med. Chem.*, 20 (13), 4103–4108.

[15] Wu, H., Pan, G., Bai, Y., Wang, H., Kong, J., Shi, F., Zhang, Y., and Wang, X., 2014, Preparation, structure, DNA-binding properties, and antioxidant activities of a homodinuclear erbium(III) complex with a pentadentate Schiff base ligand, *J. Chem. Res.*, 38 (4), 211–217.

[16] Poladian, Q., Şahin, O., Karakurt, T., İlhan-Ceylan, B., and Kurt, Y., 2021, A new zinc(II) complex with N_2O_2-tetradentate Schiff-base derived from pyridoxal-S-methylthiosemicarbazone: Synthesis, characterization, crystal structure, DFT, molecular docking and antioxidant activity studies, *Polyhedron*, 201, 115164.

[17] Adeleke, A.A., Zamisa, S.J., Islam, M., Olofinsan, K., Salau, V.F., Mocktar, C., and Omondi, B., 2021, Quinoline functionalized Schiff base silver (I) complexes: Interactions with biomolecules and *in vitro* cytotoxicity, antioxidant and antimicrobial activities, *Molecules*, 26 (5), 1205.

[18] Shahraki, S., Delarami, H.S., Mansouri-Torshizi, H., and Nouri, H., 2021, Investigation of kinetics and thermodynamics in the interaction process between two pyridine derived Schiff base complexes and catalase, *J. Mol. Liq.*, 334, 116527.

[19] Kheniche, A., Ourari, A., Dakhouche, A., Ghanem, A., Min, W., and Meguellati, K., 2018, Electrochemical and theoretical studies influencing the effect of hydroxyl position of tetraphenolic Schiff bases towards corrosion inhibition of mild steel in 1 M HCl, *J. Fundam. Appl. Sci.*, 10 (3), 209–238.

[20] Benslama, A., Harrar, A., Gul, F., and Demirtas, I., 2017, Phenolic compounds, antioxidant and antibacterial activities of *Zizyphus lotus* L. leaves extracts, *Nat. Prod. J.*, 7 (4), 316–322.

[21] Sahoo, A.K., Narayanan, N., Sahana, S., Rajan, S.S., and Mukherjee, P.K., 2008, *In vitro* antioxidant potential of *Semecarpus anacardium* L., *Pharmacologyonline*, 3 (3), 27–35.

[22] Benslama, A., and Harrar, A., 2016, Free radicals scavenging activity and reducing power of two

Algerian Sahara medicinal plants extracts, *Int. J. Herb. Med.*, 4 (6), 158–161.

[23] Aboseada, H.A., Hassanien, M.M., El-Sayed, I.H., and Saad, E.A., 2021, Schiff base 4-ethyl-1-(pyridin-2-yl) thiosemicarbazide up-regulates the antioxidant status and inhibits the progression of Ehrlich solid tumor in mice, *Biochem. Biophys. Res. Commun.*, 573, 42–47.

[24] Xing, A., Zeng, D., and Chen, Z., 2022, Synthesis, crystal structure and antioxidant activity of butylphenol Schiff bases: Experimental and DFT study, *J. Mol. Struct.*, 1253, 132209.

[25] Daravath, S., Rambabu, A., Ganji, N., Ramesh, G., and Lakshmi, P.V.A., 2022, Spectroscopic, quantum chemical calculations, antioxidant, anticancer, antimicrobial, DNA binding and photo physical properties of bioactive Cu(II) complexes obtained from trifluoromethoxy aniline Schiff bases, *J. Mol. Struct.*, 1249, 131601.

[26] Islam, M.M., Pal, T.K., Paul, S., Uddin, M.N., Sheikh, M.C., Alam, M.A., and Hossen, J., 2022, Computational, Hirshfeld surface, and molecular docking analysis of 2-(((4-methoxyphenyl)imino) methyl)-4-nitrophenol: *In-vitro* anticancer, antimicrobial, anti-inflammatory, and antioxidant studies, *Results Chem.*, 4, 100331.

[27] Çalışkan, N., Usta, A., Beriş, F.Ş., Baltaş, N., and Çelik, E., 2020, Synthesis, antibacterial and antioxidant activities of some new N substituted azachalcone, Schiff base and pyrazole derivatives, *Lett. Org. Chem.*, 17 (8), 631–638.

[28] Muğlu, H., Yakan, H., Misbah, A.G.A., Çavuş, M.S., and Bakır, T.K., 2021, Synthesis, structure characterization and quantum chemical study on relationship between structure and antioxidant properties of novel Schiff bases bearing (thio)/carbo hydrazones, *Res. Chem. Intermed.*, 47 (12), 4985–5005.

[29] Affat, S.S., 2021, Experimental and theoretical studies of new Schiff base as a corrosion inhibitor in acidic media and study antioxidant activity, *Iran. J. Chem. Chem. Eng.*, Article in Press.

[30] Prestiani, A.E., and Purwono, B., 2017, Styrene and azo-styrene based colorimetric sensors for highly selective detection of cyanide, *Indones. J. Chem.*, 17 (2), 238–247.

[31] Güngör, Ö., and Gürkan, P., 2014, Synthesis and characterization of higher amino acid Schiff bases, as monosodium salts and neutral forms. Investigation of the intramolecular hydrogen bonding in all Schiff bases, antibacterial and antifungal activities of neutral forms, *J. Mol. Struct.*, 1074, 62–70.

[32] Maduwanthi, S.D.T., and Marapana, R.A.U.J., 2021, Total phenolics, flavonoids and antioxidant activity following simulated gastro-intestinal digestion and dialysis of banana (*Musa acuminata*, AAB) as affected by induced ripening agents, *Food Chem.*, 339, 127909.

[33] Irfan, A., Imran, M., Al-Sehemi, A.G., Shah, A.T., Hussien, M., and Mumtaz, M.W., 2021, Exploration of electronic properties, radical scavenging activity and QSAR of oxadiazole derivatives by molecular docking and first-principles approaches, *Saudi J. Biol. Sci.*, 28 (12), 7416–7421.

[34] Abuelizz, H.A., Taie, H.A.A., Bakheit, A.H., Marzouk, M., Abdellatif, M.M., and Al-Salahi, R., 2021, Biological evaluation of 4-(1*H*-triazol-1-yl) benzoic acid hybrids as antioxidant agents: *In vitro* screening and DFT study, *Appl. Sci.*, 11 (24), 11642.

[35] Karkar, B., Şahin, S., and Güneş, M.E., 2021, Evaluation of antioxidant properties and determination of phenolic and carotenoid profiles of chestnut bee pollen collected from Turkey, *J. Apic. Res.*, 60 (5), 765–774.

[36] Zheng, Y.Z., Deng, G., and Zhang, Y.C., 2022, Multiple free radical scavenging reactions of flavonoids, *Dyes Pigm.*, 198, 109877.

[37] Enbaraj, E., Dhineshkumar, E., Jeyashri, K., Logeshwari, G., Mohana, V., Manikandan, H., Rajathi, V., Chakkaravarthy, J., Govindaraju, R., and Seenivasan, M., 2021, Novel synthesis, spectral characterisation and DFT calculation of (3,4-bis((*E*)-(substituted-dichlorobenzylidene)amino) phenyl)(phenyl) methanone derivatives, *Mater. Today: Proc.*, 42, 982–988.

[38] Mar, J.M., da Silva, L.S., Moreira, W.P., Biondo, M.M., Pontes, F.L.D., Campos, F.R., Kinupp, V.F., Campelo, P.H., Sanches, E.A., and Bezerra, J.A., 2021, Edible flowers from *Theobroma speciosum*: Aqueous extract rich in antioxidant compounds, *Food Chem.*, 356, 129723.

[39] Hong, Y., Wang, Z., Barrow, C.J., Dunshea, F.R., and Suleria, H.A.R., 2021, High-throughput screening and characterization of phenolic compounds in stone fruits waste by LC-ESI-QTOF-MS/MS and their potential antioxidant activities, *Antioxidants*, 10 (2), 234.

[40] Bendary, E., Francis, R.R., Ali, H.M.G., Sarwat, M.I., and El Hady, S., 2013, Antioxidant and structure–activity relationships (SARs) of some phenolic and anilines compounds, *Ann. Agric. Sci.*, 58 (2), 173–181.

[41] Hernández, J.A., Jiménez, A., Mullineaux, P., and Sevilia, F., 2000, Tolerance of pea (*Pisum sativum* L.) to long-term salt stress is associated with induction of antioxidant defences, *Plant, Cell Environ.*, 23 (8), 853–862.

[42] Marc, G., Stana, A., Oniga, S.D., Pîrnău, A., Vlase, L., and Oniga, O., 2019, New phenolic derivatives of thiazolidine-2,4-dione with antioxidant and antiradical properties: Synthesis, characterization, in vitro evaluation, and quantum studies, *Molecules*, 24 (11), 2060.

[43] Čačić, M., Pavić, V., Molnar, M., Šarkanj, B., and Has-Schön, E., 2014, Design and synthesis of some new 1,3,4-thiadiazines with coumarin moieties and their antioxidative and antifungal activity, *Molecules*, 19 (1), 1163–1177.

[44] Pele, R., Marc, G., Stana, A., Ionuţ, I., Nastasă, C., Tiperciuc, B., Oniga, I., Pîrnău, A., Vlase, L., and Oniga, O., 2022, Synthesis of new phenolic derivatives of quinazolin-4(3H)-one as potential antioxidant agents-*In vitro* evaluation and quantum studies, *Molecules*, 27 (8), 2599.

[45] Pedersen, J.Z., Oliveira, C., Incerpi, S., Kumar, V., Fiore, A.M., De Vito, P., Prasad, A.K., Malhotra, S.V., and Saso, L., 2007, Antioxidant activity of 4-methylcoumarins, *J. Pharm. Pharmacol.*, 59 (12), 1721–1728.

[46] Teran, R., Guevara, R., Mora, J., Dobronski, L., Barreiro-Costa, O., Beske, T., Pérez-Barrera, J., Araya-Maturana, R., Rojas-Silva, P., Poveda, A., and Heredia-Moya, J., 2019, Characterization of antimicrobial, antioxidant, and leishmanicidal activities of Schiff base derivatives of 4-aminoantipyrine, *Molecules*, 24 (15), 2696.

[47] Dawidowicz, A.L., Wianowska, D., and Olszowy, M., 2012, On practical problems in estimation of antioxidant activity of compounds by DPPH• method (Problems in estimation of antioxidant activity), *Food Chem.*, 131 (3), 1037–1043.

[48] Farhoosh, R., Johnny, S., Asnaashari, M., Molaahmadibahraseman, N., and Sharif, A., 2016, Structure–antioxidant activity relationships of *o*-hydroxyl, *o*-methoxy, and alkyl ester derivatives of *p*-hydroxybenzoic acid, *Food Chem.*, 194, 128–134.

[49] Martins, A.C., Bukman, L., Vargas, A.M.M., Barizão, É.O., Moraes, J.C.G., Visentainer, J.V., and Almeida, V.C., 2013, The antioxidant activity of teas measured by the FRAP method adapted to the FIA system: Optimising the conditions using the response surface methodology, *Food Chem.*, 138 (1), 574–580.

[50] Prior, R.L., Wu, X., and Schaich, K., 2005, Standardized methods for the determination of antioxidant capacity and phenolics in foods and dietary supplements, *J. Agric. Food Chem.*, 53 (10), 4290–4302.

3,4,5-Trimethoxychalcones Tubulin Inhibitors with a Stable Colchicine Binding Site as Potential Anticancer Agents

Maadh Jumaah[1], Tutik Dwi Wahyuningsih[2], and Melati Khairuddean[1*]

[1]School of Chemical Sciences, Universiti Sains Malaysia, 11800 Penang, Malaysia

[2]Department of Chemistry, Faculty of Mathematics and Natural Sciences, Universitas Gadjah Mada, Sekip Utara, Yogyakarta 55281, Indonesia

Abstract: *The development of microtubule perturbing drugs is one of the most promising anticancer therapeutic methods. Unfortunately, limitation such as drug resistance, adverse side effects, complex formulations and synthesis, and limited bioavailability of these microtubule perturbing drugs has aroused the search for a new molecule of the tubulin system. Different substituents of chalcone were designed, synthesized, and determined for inhibition of tubulin assembly and toxicity in human cancer cell lines based on conventional colchicine site ligands and a computer model of the colchicine binding site on tubulin. A molecular docking study indicated that the chalcone scaffold could fit the colchicine site on tubulin in a similar orientation to the natural product. The 3,4,5-trimethoxyphenyl ring, which occupies the same sub-cavity as the equivalent molecule in colchicine, appeared to benefit the ligand of α,β-tubulin interaction. Several 3,4,5-trimethoxychalcone compounds demonstrated improved cytotoxicity against MCF-7 cells and inhibited tubulin assembly* in vitro *as potently as colchicine. The most active chalcone 1 with the IC$_{50}$ of 6.18 ± 0.69 μM prevented the proliferation of human cell lines at micromolar concentrations, causing microtubule destabilization and mitotic arrest in humans inhibiting breast cancer cells.*

Keywords: *microtubules; 3,4,5-trimethoxychalcone; docking study; colchicine; MCF-7 cells*

■ INTRODUCTION

Microtubules (MTs) are cytoskeletal polymers made up of α,β-tubulin heterodimers that play a key role in cellular movement, division, and intracellular transport. Interfering with the assembly of MTs in dividing cells causes cell cycle arrest, resulting in apoptosis-inducing signals [1-2]. Therefore, the development of MT perturbing drugs is one of the most promising anticancer therapeutic methods [3-4]. Limitations, such as drug resistance, adverse side effects, complex formulations and synthesis, and limited bioavailability of these MT perturbing drugs [5] have continuously aroused the search for novel small molecules of the tubulin/MT system. MT-targeting drugs typically attach to one of the three primary tubulin binding sites which are taxane, vinca and colchicine sites [6] (Fig. 1). Taxanes and vinca alkaloids have made significant contributions to the treatment of human cancers, but the toxicity of colchicine and podophyllotoxin has limited their therapeutic application in the treatment of cancer [7].

In this respect, the chemically versatile chalcones are an interesting scaffold for the discovery of new colchicine site ligands that inhibit tubulin assembly [8-10]. In the ongoing attempts to develop superior tubulin polymerization inhibitors, a series of chalcones **1-7** with aromatic substitution patterns resembling those found in conventional colchicine site ligands [11] (Fig. 1) have been synthesized. The molecular modeling was built to investigate the interactions of all the chalcones **1-7** with colchicine (PDB code: 1SA0). The docking experiments and prediction of pharmacokinetic properties and toxicity were carried out using the X-ray crystallographic
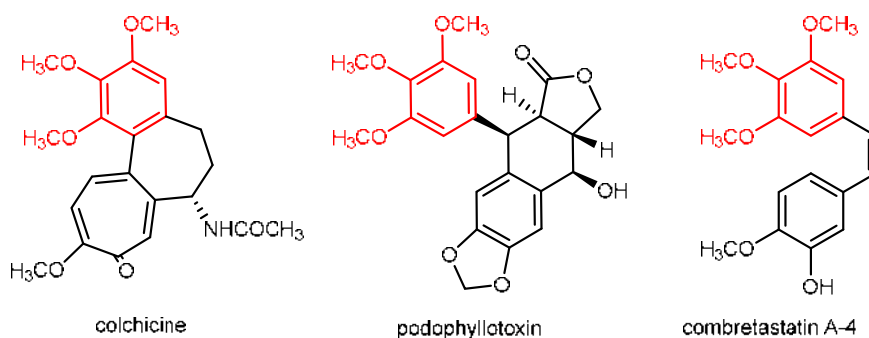
Fig 1. Microtubule-interacting agents that bind to tubulin's colchicine site

structure of colchicine in association with an inhibitor to investigate the binding affinity of these compounds at the active site.

■ EXPERIMENTAL SECTION

Materials

All the commercial chemicals and reagents in the syntheses were used without further purification; all chemicals, solvents, and materials used are as follows: QRëC, ASIA Sdn. Bhd.: acetic acid glacial, sulfuric acid (97%), hydrochloric acid (37%), acetone, chloroform, dichloromethane, diethyl ether, ethyl acetate, *n*-hexane, toluene, tetrahydrofuran, methanol (99.5%), ethanol (99.7%) and paraffin oil. Dimethyl sulfoxide-d_6 (Sigma-Aldrich, USA), sodium carbonate (99.99%, Merck, Germany), 3,4,5-trimethoxyacetophenone (97%, Sigma-Aldrich, Germany), 2-hydroxy-5-bromobenzaldehyde (98%, Sigma-Aldrich, China), 2-hydroxy-5-chlorobenzaldehyde (≥ 98%, Sigma-Aldrich, China), 2,5-dihydroxybenzaldehyde (≥ 98%, Sigma-Aldrich, China), 5-iodosalicylaldehyde (97%, Sigma-Aldrich, USA), 3-methoxy-2-hydroxybenzaldehyde (96%, Sigma-Aldrich, USA), 3-ethoxy-2-hydroxybenzaldehyde (96%, Sigma-Aldrich, USA); TLC silica gel 60 F254, aluminum sheet, 20 cm × 20 cm (Merck, Germany) and silica gel 60 (70–230 mesh).

Instrumentation

Instruments used included Thin-layer chromatography (TLC) uses a commercially available aluminum-supported silica gel 60F$_{254}$ plate, which was observed under CAMAG® Ultra Violet (UV) lamp (254 and 386 nm). The melting points were determined using the Stuart Scientific SMP1 equipment in the temperature range of 25–350 °C. The functional groups of the compounds were determined using the FTIR Perkin Elmer 2000 spectrometer. The ^{1}H and ^{13}C-NMR spectra were obtained using a 500 MHz Bruker Avance spectrometer. The CHN elemental analysis is used to determine the amount of carbon (C), hydrogen (H), and nitrogen (N) in a sample using a Perkin Elmer II, 2400 CHN analyzer.

Procedure

A mixture of 3,4,5-trimethoxyacetophenone (0.3 g) in MeOH (20 mL), LiOH• H$_2$O (0.5 g), and disubstituted benzaldehyde (0.12 g) was refluxed and the reaction progress was monitored by TLC (Scheme 1). After quenching the reaction with dilute hydrochloric acid, the solution was extracted with ethyl acetate. The organic layer was washed with aqueous NaHCO$_3$, water, and brine before it was dried over anhydrous Na$_2$SO$_4$. The crude was concentrated and purified using column chromatography with *n*-hexane/ethyl acetate (10:1) as an eluent.

(E)-3-(2-hydroxy-3-methoxyphenyl)-1-(3,4,5-trimethoxyphenyl)prop-2-en-1-one, 1. Yield: 84.8%, pine-green powder; m.p: 168–171 °C. IR (cm^{-1}): 3336 (-OH); 2946, 2839 (C-H sp^3); 1620 (C=O); 1611 and 1583 (C=C). ^{1}H-NMR (500 MHz, DMSO-d_6) δ, ppm: 8.05 (d, *J* = 15.7 Hz, 1H, H-3); 7.84 (d, *J* = 15.7 Hz, 1H, H-2); 7.45 (d, *J*=2.7, 1H, H-3"); 7.40 (s, 2H, H-6', H-2'); 6.93 (dd, J_1 = 2.7 Hz, J_2 = 8.9 Hz, 1H, H-4"); 6.91 (d, *J* = 8.9 Hz, 1H, H-6"); 6.15 (s, 1H, H-8); 3.90 (s, 6H, H-4,6); 3.77 (s, 3H, H-5); 3.76 (s, 3H, H-7). ^{13}C-NMR (125 MHz, DMSO-d_6) δ, ppm: 188.7 (C-1); 153.4 (C-5', C-3'); 152.7 (C-2"); 142.3 (C-4'); 139.7 (C-1'); 133.8 (C-3); 130.1 (C-5"); 122.2 (C-3");
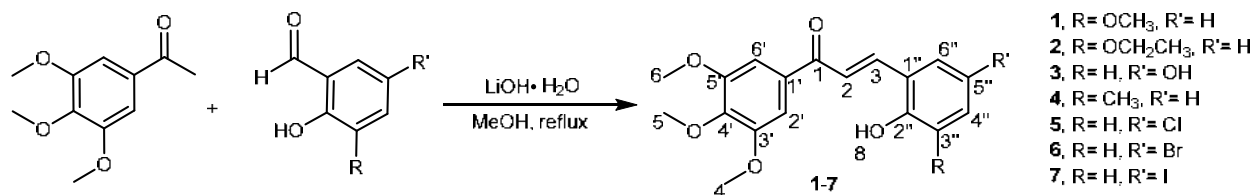
Scheme 1. Synthesis of chalcones **1-7**

121.4 (C-2); 119.1 (C-1"); 117.6 (C-4"); 112.8 (C-6"); 106.6 (C-6', C-2'); 60.7 (C-5); 56.7 (C-4, C-6); 56.1 (C-7). CHN Elemental analysis: Calculated for $C_{19}H_{20}O_6$: C, 66.27; H, 5.85. Found: C, 65.97; H, 5.57.

(*E*)-3-(3-ethoxy-2-hydroxyphenyl)-1-(3,4,5-trimethoxyphenyl)prop-2-en-1-one, 2. Yield: 65.8%, brown powder; m.p: 177–179 °C. IR (cm^{-1}): 3336 (-OH); 2946, 2839 (C-H sp^3); 1620 (C=O); 1611 and 1583 (C=C). ^{1}H-NMR (500 MHz, DMSO-d_6) δ, ppm: 8.15 (d, *J* = 15.7 Hz, 1H, H-3); 7.81 (d, *J* = 15.7 Hz, 1H, H-2); 7.55 (d, *J* = 2.7, 1H, H-3"); 7.33 (s, 2H, H-6', H-2'); 6.93 (dd, J_1 = 2.7 Hz, J_2 = 8.9 Hz, 1H, H-4"); 6.91 (d, *J* = 8.9 Hz, 1H, H-6"); 6.15 (s, 1H, H-8); 3.90 (s, 6H, H-4,6); 3.77 (s, 3H, H-5); 3.76 (s, 3H, H-7). ^{13}C-NMR (125 MHz, DMSO-d_6) δ, ppm: 189.7 (C-1); 154.4 (C-5', C-3'); 151.7 (C-2"); 142.3 (C-4'); 141.1 (C-1'); 133.8 (C-3); 130.1 (C-5"); 122.2 (C-3"); 121.4 (C-2); 120.0 (C-1"); 118.6 (C-4") 112.7 (C-6"); 108.2 (C-6', C-2'); 60.9 (C-5); 56.7 (C-4, C-6); 56.1 (C-7). CHN Elemental analysis: Calculated for $C_{19}H_{20}O_6$: C, 66.27; H, 5.84. Found: C, 65.98; H, 5.56.

(*E*)-3-(2,3-dihydroxyphenyl)-1-(3,4,5-trimethoxyphenyl)prop-2-en-1-one, 3. Yield: 78.4%, yellow powder; m.p: 195–198 °C. IR (cm^{-1}): 3238 (-OH), 2935, 2839 (C-H sp^3), 1648 (C=O), 1589 and 1552 (C=C). ^{1}H-NMR (500 MHz, 1,2-dichloroethane-d_4) δ, ppm: 11.03 (s, 1H), 8.33 (d, *J* = 16.2 Hz, 1H), 8.23 (d, *J* = 8.9 Hz, 1H), 7.60 (d, *J* = 16.2 Hz, 1H), 7.25 (d, *J* = 7.7 Hz, 2H), 7.10 (s, 2H), 4.64 (s, 3H), 4.54 (s, 3H), 4.50 (s, 6H). ^{13}C-NMR (125 MHz, 1,2-dichloroethane-d_4) δ, ppm: 195.0, 163.7, 162.9, 159.5, 159.2, 141.1, 131.1, 127.3, 115.6, 112.8, 107.6, 102.3, 92.3, 57.0, 56.7, 56.4. CHN Elemental analysis: Calculated for $C_{19}H_{20}O_6$: C, 66.27; H, 5.85. Found: C, 65.99; H, 5.56.

(*E*)-3-(2-hydroxy-3-methylphenyl)-1-(3,4,5-trimethoxyphenyl)prop-2-en-1-one,4. Yield: 72.5%, golden-yellow powder; m.p: 142–145 °C. IR (cm^{-1}): 3176 (-OH); 2943, 2836 (C-H sp^3); 1636 (C=O); 1586 and 1558

(C=C). ^{1}H-NMR (500 MHz, DMSO-d_6) δ, ppm: 10.01 (s, 1H, H-8); 8.07 (d, *J* = 15.5 Hz, 1H, H-3); 7.81 (d, *J* = 15.5 Hz, 1H, H-2); 7.70 (s, 1H, H-3"); 7.30 (s, 2H, H-6', H-2'); 7.08 (dd, J_1 = 1.8 Hz, J_2 = 8.3 Hz, 1H, H-4"); 6.85 (d, *J* = 8.3 Hz, 1H, H-6"); 3.90 (s, 6H, H-4,6); 3.77 (s, 3H, H-5); 2.27 (s, 3H, H-7). ^{13}C-NMR (125 MHz, DMSO-d_6) δ, ppm: 188.5 (C-1); 155.6 (C-2"); 153.4 (C-5', C-3'); 142.3 (C-4'); 139.8 (C-1'); 133.8 (C-3); 133.3 (C-5"); 128.8 (C-3"); 128.4 (C-1"); 121.6 (C-2); 120.8 (C-4"); 116.6 (C-6"); 106.6 (C-6', C-2'); 60.7 (C-5); 56.7 (C-4, C-6); 20.6 (C-7). CHN Elemental analysis: Calculated for $C_{19}H_{20}O_5$: C, 66.27; H, 5.85. Found: C, 66.01; H, 5.56.

(*E*)-3-(5-chloro-2-hydroxyphenyl)-1-(3,4,5-trimethoxyphenyl)prop-2-en-1-one, 5. Yield: 62.4%, yellow powder; m.p: 221–225 °C. IR (cm^{-1}): 3207 (-OH), 2937, 2839 (C-H sp^3), 1603 (C=O), 1583 and 1508 (C=C). ^{1}H-NMR (500 MHz, DMSO-d_6) δ, ppm: 10.44 (s, 1H), 7.68 (d, *J* = 2.1 Hz, 1H), 7.42 (d, *J* = 16.5 Hz, 1H),7.25 (dd, J_1 = 2.2 Hz, J_2 = 8.7 Hz, 1H), 7.00 (d, *J* = 16.5 Hz, 1H), 6.90 (d, *J* = 8.7 Hz, 1H), 6.30 (s, 2H), 3.83 (s, 3H), 3.71 (s, 6H). ^{13}C-NMR (125 MHz, DMSO-d_6) δ, ppm: 193.1, 162.4, 158.5, 155.9, 138.1, 131.6, 129.3, 128.0, 123.7, 123.3, 118.3, 111.6, 91.6, 56.3, 55.9. CHN Elemental analysis: Calculated for $C_{18}H_{17}ClO_5$: C, 61.99; H, 4.96. Found: C, 61.69; H, 4.67.

(*E*)-3-(5-bromo-2-hydroxyphenyl)-1-(3,4,5-trimethoxyphenyl)prop-2-en-1-one, 6. Yield: 67.9%, yellow powder; m.p: 171–174 °C. IR (cm^{-1}): 3154 (-OH); 2949, 2833 (C-H sp^3); 1645 (C=O); 1566 and 1507 (C=C). ^{1}H-NMR (500 MHz, DMSO-d_6) δ, ppm: 9.61 (s, 1H, H-8); 8.12 (d, *J* = 2.3 Hz, 1H, H-3"); 7.96 (d, *J* = 15.5 Hz, 1H, H-3); 7.94 (d, *J* = 15.5 Hz, 1H, H-2); 7.42 (s, 2H, H-6', H-2'); 7.40 (dd, J_1 = 2.4 Hz, J_2 = 8.7 Hz, 1H, H-4"); 6.98 (d, *J* = 8.7 Hz, 1H, H-6"); 3.90 (s, 6H, H-4,6); 3.77 (s, 3H, H-5). ^{13}C-NMR (125 MHz, DMSO-d_6) δ, ppm: 188.5 (C-1); 156.8 (C-2"); 153.4 (C-5', C-3'); 142.5 (C-

4'); 137.8 (C-1'); 134.7 (C-5''); 133.5 (C-3); 130.7 (C-3''); 124.2 (C-1''); 122.3 (C-2); 118.8 (C-4''); 111.3 (C-6''); 106.8 (C-6', C-2'); 60.7 (C-5); 56.8 (C-4,C-6). CHN Elemental analysis: Calculated for $C_{18}H_{17}BrO_5$: C, 54.98; H, 4.36. Found: C, 54.68; H, 4.06.

(*E*)-3-(2-hydroxy-5-iodophenyl)-1-(3,4,5-trimethoxyphenyl)prop-2-en-1-one, 7. Yield: 88.4%, brown powder; m.p: 197–200 °C. IR (cm^{-1}): 3218 (-OH), 2929, 2845 (C-H sp^3), 1600 (C=O), 1583 and 1500 (C=C). ^{1}H-NMR (500 MHz, DMSO-d_6) δ, ppm: 10.43 (s, 1H, H-8), 7.89 (d, J = 1.9 Hz, 1H, H-3''), 7.51 (dd, J_1 = 2.0 Hz, J_2 = 8.6 Hz, 1H, H-4''), 7.37 (d, J = 16.3 Hz, 1H, H-3), 7.00 (d, J = 16.3 Hz, 1H, H-2), 6.73 (d, J = 8.6 Hz, 1H, H-6''), 6.30 (s, 2H, H-6', H-2'), 3.83 (s, 3H, H-5), 3.71 (s, 6H, H-4,6). ^{13}C-NMR (125 MHz, DMSO-d_6) δ, ppm: 194.0 (C-1); 162.4 (C-2''); 158.5 (C-5', C-3'); 156.9 (C-4'); 140.2 (C-1'); 138.1 (C-5''); 136.9 (C-3); 129.9 (C-3''); 124.5 (C-1''); 119.2 (C-2); 111.7 (C-4''); 91.5 (C-6''); 82.1 (C-6', C-2'); 56.3 (C-5); 55.9 (C-4,6). CHN Elemental analysis: Calculated for $C_{18}H_{17}IO_5$: C, 49.11; H, 3.89. Found: C, 48.82; H, 3.58.

Cytotoxicity assay

Cell culture. The MCF-7 cell for human breast cancer was obtained from the American Type Culture Collection (ATCC, USA) in addition to 10% (v/v) of the Fetal Bovine Serum (FBS) from the Rosewell Park Memorial Institute 1640 (RPMI), (GE Healthcare HyClone, Kansas, USA). The cells were kept at 37 °C in an incubator (Memmert, Germany) with 5% CO_2 and 95% humidity. The cells were divided every two to three days or when they reached 80–90% confluency on the culture flask surface. The spent media were removed to eliminate any leftover serum that may inactivate trypsin activity and cells were washed with 1 to PBS (MediaTech, United States). Following the removal of the PBS, 2 mL of trypsin solution (SAFC Biosciences, USA) was added to the flask. Cells were incubated at 37 °C for 10 min to enable them to detach from the surface of the culture flask (Nunc, Denmark). Then, 6 mL of appropriate growth medium was added to inactivate the trypsin activity in the ratio of 1:3 (1 = trypsin; 3 = growth medium) to a Falcon tube of 15 mL. After trypsinizing the cells, they were centrifuged at 1500 rpm for 5 min, and the supernatant was discarded. The cell pellet was re-suspended in 8 mL of new growth medium before being divided into the prepared culture flasks for further usage.

Cell counting. A dye exclusion viability test in a hemocytometer was used to measure the number of cells in a particular population. The cell monolayers were unbundled by trypsinization, centrifugation, and medium re-suspension. The cell suspension (20 mL) was combined with 20 mL of a 0.08% (v/v) trypan blue dye solution (Merck, Germany) to produce a trypan blue dye solution. A capillary action distributed the solution uniformly across the counting chamber of a hemacytometer after it had been put there. The average number of viable cells in each of the four-square grid corners was determined by looking through an inverted fluorescence microscope (Nikon, Japan) at 100× magnification to count the number of unstained viable cells in each of the four-square grid corners. Each square grid represents a 0.0001 mL volume, and the cell concentration was calculated using Eq. (1) and a dilution factor of two. To measure the percentage of cell viability, both dead (stained) and viable (unstained) cells were counted individually, and the results were computed as shown in Eq. (2). Between samples and after usage, the hemocytometer slide and glass coverslip were promptly washed and cleaned with 70% (v/v) ethanol (Thermo Scientific, USA) to remove any remaining residue.

$$C = (n/v) \times D \tag{1}$$

$$\% \text{ Viability} = (Nv/Nv + ND) \times 100\% \tag{2}$$

where C: cell concentration (cells/mL), N: average number of cells, v: volume counted (mL), D: dilution factor, Nv: total number of visible cells, and ND: total number of dead cells.

MTT assay

The cytotoxicity of the compounds was determined using the MTT cell viability test. The MCF-7 cell lines were plated at a density of about 2×10^4 cells/well in a 96-well plate and incubated overnight before being treated with chalcone analogs at different doses (0–100 g) and incubated for another 24 h. Following incubation, 20 μL of MTT reagent (5 g/L) was applied to each well of the microplate, followed by 90 min in the dark at 37 °C. The spent medium was discarded, and the purple formazan precipitates were

dissolved in 200 μL of dimethyl sulfoxide (DMSO). To detect the absorbance of the solution, the optical density was measured using a microplate reader (Tecan Sunrise, Switzerland) at a test wavelength of 570 nm and a reference wavelength of 650 nm. The test was carried out in triplicate to determine the percentages of viable cells in comparison to the DMSO control. The half-maximal inhibitory concentration (IC_{50}) value was calculated from the data using the dose-response curve fitting graph at 50% cell viability.

Cytotoxic effect of the synthesized compounds on MCF-7 cells. The cell-based assays count the number of viable cells on multi-well plates and determine if a chemical affects cell growth or has direct cytotoxic effects that result in cell death. Regardless of the kind of cell-based assay employed, it is critical to know the number of viable cells left in an experiment. The antiproliferative activity was measured using 3-(4,5-dimethylthiazol-2-yl)-2,5-diphenyltetrazolium bromide (MTT) reduction assay, which is the most widely used assay and was the first homogeneous cell viability assay developed for a 96-well plate, making it suitable for high throughput screening. The viable cells with active metabolism convert the yellow tetrazolium MTT into the insoluble (E,Z)-5-(4,5-dimethylthiazol-2-yl)-1,3-diphenylformazan (formazan), a purple crystal. A dying cell lost the ability to convert MTT to formazan. When formazan is produced, it is dissolved in DMSO to give a purple solution with a distinctive absorbance at 540 nm. The intensity of the purple color is related to the cell count, showing the vitality of the cells. The antitumor efficacy of all chalcone-based drugs was determined *in vitro* against breast cancer cell lines (MCF-7) using a previously described MTT test. The IC_{50} values, which are employed as a cytotoxicity measure, relate to the proportion of cells inhibited by 3,4,5-trimethoxychalcone compounds. The inhibitory activity of drugs was determined after a 24-h exposure and was represented as the concentration needed to decrease tumor cell growth by 50% (IC_{50}). All results are expressed as means standard deviations of three separate experiments. The antiproliferative effect of paclitaxel was also evaluated using the MCF-7 cell line as a positive control.

Molecular modeling

α,β-Tubulin was chosen as the target receptor and was obtained from the Protein Data Bank. α,β-Tubulin-colchicine complex site inhibitors were developed using a structure-based approach with the reported protein crystal structure of colchicine obtained from the Protein Data Bank (http://www.rcsb.org/,PDB code: 1SA0). The potential inhibitors, trimethoxy and *ortho*-hydroxy chalcone, were designed based on the common similarities shared with those reported colchicine inhibitors by molecular docking, which was chosen based on the binding energy and inhibition constant of the chalcones. The ligand structures were drawn using Marvin-Sketch and BIOVIA to observe the ligand-protein interactions. Structure files were prepared for molecular docking by defining the number of torsion angles and hydrogen atoms. To validate the feasibility of the Autodock Vina with Chimera 1.12 programs, the docking studies were first performed on the reference compounds colchicine to predict the binding mode of the design compounds, and the calculations of AutoDock Vina were performed on a Windows Intel® Pentium® Core (TM) i5-2450M Quad CPU 4.00 GHz operating system. All structure images above were displayed using PyMOL viewer.

■ **RESULTS AND DISCUSSION**

Chemistry

The preparation of chalcones **1**-**7**, as shown in Scheme 1, was easily obtained in good yield via a Claisen-Schmidt condensation of an aromatic aldehyde with an aliphatic ketone using LiOH• H_2O as a catalyst in refluxing methanol. Purification using column chromatography with *n*-hexane/ethyl acetate (10:1) as an eluent gave the expected compounds, which were characterized using ^{1}H-NMR spectroscopy and IR spectrometry.

Antiproliferative Properties of Chalcone Compounds against Breast Cancer Cell Line (MCF-7)

Chalcones **1**-**7**, as small molecule inhibitors, were tested on MCF-7 human breast cancer cell lines.

Paclitaxel was used as a reference drug against MCF-7 in the MTT experiment. The inhibitory activity was measured after 24-h exposure to chemicals and expressed as the IC_{50} value. All data are presented as the means and standard deviations ± SDs of three independent experiments. Upon investigation of the inhibitory effects of substances, paclitaxel was also used as a positive control for the MCF-7 cell line to examine its antiproliferative efficacy.
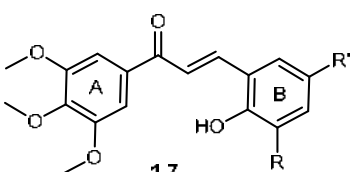
As shown in Table 1, chalcone **1** has the most potent activity with the IC_{50} of 6.18 ± 0.69 μM, compared to other chalcones, and was even more potent than the positive control, paclitaxel (IC_{50}: 15 μM). However, compounds **3**, **4**, and **5** showed moderate activity below 50 μM. Since the rest of the samples showed poor cytotoxicity, the IC_{50} values for such compounds could not be determined. The chemical structure and biological activity correlated through structure-activity relationship (SAR) analysis deduced that the trimethoxy substituents in ring A and the planar structure of fully aromatized *ortho*-hydroxy chalcones with another different substituent in ring B formed interesting cytotoxicity activities. Studies have demonstrated that the *ortho*-hydroxy chalcone or trimethoxy groups can intercalate into DNA and inhibit tubulin polymerization [12-14]. Consistent with molecular modeling expectations, chalcones inhibited MCF-7 proliferation and tubulin assembly more

effectively than the positive control paclitaxel, which retained growth inhibitory activity against MCF-7 cells. In this study, the influence of the substituents on the aromatic ring attached to the *ortho*-hydroxy position of the chalcone ring (B) system on the cytotoxic potency has also been investigated. Compounds with *ortho*-hydroxy chalcones with a variety of substituents at positions-3 and -5 have been reported to inhibit MCF-7, as shown in Table 1. Interestingly, these chalcone-based compounds possess diverse structural properties with various substituents, most of which are electron-donating functionalities, such as methoxy functional groups, at different positions of both aromatic systems. It was observed that 3-methoxy substituent displayed MCF-7 inhibition more than 3-ethoxy and 3-CH_3. The position of the substituent on the aromatic ring (*meta*, *para*, or *ortho*) has also influenced the cytotoxic activity. From data collected in Table 1, the SARs study has also revealed that compounds with another substituent, such as Cl, Br, and I, showed that the replacement of bromo substituent at position 5 to chloro has also influenced the cytotoxic activity from 60 to 46.36 μM against MCF-7.

Structure-Based Drug Design

To gain a better understanding of the efficacy of the synthesized compounds, their interactions with the

Table 1. Antiproliferative activities of chalcones **1**-**7** and docking parameters

1, R= OCH_3, R'= H
2, R= OCH_2CH_3, R'= H
3, R= H, R'= OH
4, R= CH_3, R'= H
5, R= H, R'= Cl
6, R= H, R'= Br
7, R= H, R'= I

Compound	M.W. (g/mol)	Log p	H-bond donor	H-bond acceptor	Free binding energy (kcal/mol)	IC_{50} MCF-7 (μM)[a]
1	344.36	2.62	1	6	-9.4	6.18 ± 0.69
2	358.39	2.97	1	6	-8.7	> 50
3	360.41	2.60	2	6	-8.6	38.48 ± 0.64
4	328.36	3.32	2	5	-8.4	48.62 ± 0.69
5	348.78	3.40	1	5	-8.1	46.36 ± 0.90
6	393.23	3.64	2	5	-7.5	> 60
7	440.23	3.87	1	5	-7.7	> 100
Paclitaxel	853.91	3.30	4	10	-8.9	15

[a] The data are presented as the mean ± SE from at least two separate dose-response curves

tubulin crystal structure were examined. The classical ligand of the colchicine site on tubulin (Fig. 1) contains 3,4,5-trimethoxyphenyl groups [15-17], which is linked to increased antiproliferative potency in potential inhibitors. The trimethoxy chalcones **1**-**7** were designed based on the common similarities of the reported colchicine inhibitors [18], with the conditions consistent with those described in a series of potent colchicine. For a molecule to have drug-like properties which might be pharmacologically active in humans, these compounds need to meet Lipinski's rule of five, which specifies that the number of hydrogen bond donors (5), hydrogen bond acceptors (10), molecular weight less than 500 g/mol and octanol-water partition coefficient log P less than 5 [19]. To evaluate the properties of a compound which might be pharmacological active in humans, the prediction of ADME properties was performed. Herein, the drug-likeness, solubility, and drug score values for chalcones **1**-**7** were determined to analyze their overall potential and to confirm whether they are qualified to become promising drugs. These were compared with drugs that are currently used against MCF-7, such as paclitaxel and colchicine. The drug-likeness value is calculated based on the occurrence frequency of the analyzed molecules compared to the commercial drugs and non-drug-like compounds. Potential toxicity, solubility, and drug-like properties (drug score) of the chalcones **1**-**7** were estimated by Osiris Property Explorer. According to the Osiris database, more than 80% of the traded drugs have predicted solubility values; as shown in Table 2, the synthesized chalcones **1**-**7** exhibited solubility values between −3.30 and −4.61.

In the Osiris program, the occurrence frequency of each fragment is determined within the collection created by shredding 3300 traded drugs as well as 15,000 commercially available chemicals (Fluka), yielding a complete list of all available fragments. In this case, positive values point out that the molecule contains predominantly better fragments, which are frequently present in commercial drugs but not in the non-druglike collection of Fluka compounds. The drug score combines drug-likeness and toxicity risks in one value that may be used to judge the drug potential of a compound. Interestingly, chalcones (**1**, **5**, and **7**) have positive drug-likeness (5.35–7.16) and drug score (0.38–0.71) values were similar to or even better than some of the drugs currently used in the market (Table 2). The drug score unites properties such as drug-likeness, solubility, and toxicity risks in one parameter that may be used to estimate the compound's potential to qualify as a drug.

Positive Control Docking

All chalcones **1**-**7** were docked into the binding pocket of the target protein to determine the ligand's potential poses. The root mean square deviation (RMSD) in a molecular docking study refers to the ability of docking programs to replicate the ligand binding mode to match the target protein crystal structure [20]. The docking techniques are validated only

Table 2. Estimation of toxicity, solubility, drug-likeness, and drug score for chalcones **1**-**7**

Compound	Toxicity risks[a]				Solubility	Drug-likeness	Drug score
	Mutagenicity	Tumorigenicity	Irritation	Reproductive			
1	−	−	−	−	-3.62	5.35	0.38
2	++	−	+	−	-3.92	3.90	0.75
3	−	−	+	−	-3.30	5.17	0.84
4	−	−	++	−	-3.94	5.28	0.46
5	−	−	−	−	-4.33	7.13	0.71
6	−	−	−	−	-4.43	5.00	0.66
7	−	−	−	−	-4.61	7.16	0.62
Colchicine	−	−	−	++	-3.05	1.02	0.42
Paclitaxel	−	−	−	−	-6.29	0.19	0.22

[a] −: low risk; +: moderate risk; ++: high risk
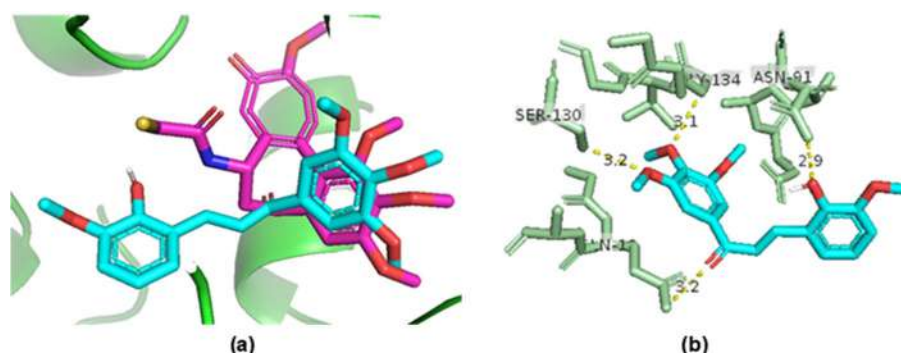
Fig 2. (a) Overview of the binding mode of chalcone **1** in the tubulin crystal structure, (b) close view of the potential binding pose of chalcone **1** in colchicine (PDB code: 1SA0)

when re-docked ligands exhibit the same docking pose as the reported protein-ligand complex, which is referred to as positive control docking. A lower RMSD value of less than 2.0 Å means higher docking accuracy, which indicates successful docking [21]. In this study, the target protein used was colchicine crystal structure (PDB code: 1SA0). Chalcone was re-docked on the active location of the same complex of colchicine and resulted in the RMSD value of 0.42. The data obtained verified that the docking experiments were highly accurate for the possible chalcone inhibitors.

In molecular docking experiments, chalcones **1**-**7** showed good free binding energy for the protein-ligand interaction in the range of −7.3 to −9.4 kcal/mol (Table 1). The binding energy is comparable with the interaction of the positive control, paclitaxel, and colchicine in the active site of the protein. Molecular docking of chalcone **1** exhibited the best anti-proliferative activity and was chosen as the optimum compound for further investigation. The amino acid residue which had interaction with tubulin was labeled. In the binding mode, compound **1** was nicely bound to the colchicine binding site of tubulin via hydrophobic interaction and binding was stabilized by a hydrogen bond. The calculated binding energies were used as the parameters for the selection of the cluster of docking posed to be evaluated, in which the binding mode of the lowest energy structure is located in the top docking cluster. The selected pose of chalcone **1** showed the interactions of methoxy oxygen (O-GLY-134; 3.1), methoxy oxygen (O-SER-130; 3.2),

carbonyl oxygen (O-GLN-10; 3.2), and hydroxy (O-ASN-91; 2.9), as observed in Fig. 2. This molecular docking result, along with the biological test results, suggests that chalcone **1** may be a tubulin inhibitor.

■ CONCLUSION

A new series of 3,4,5-trimethoxychalcone **1**-**7** were successfully synthesized and characterized. Evaluation of their cytotoxic and tubulin polymerization inhibitor activity showed significant anticancer properties, which are comparable with that of the reference drug, paclitaxel. Among these compounds, chalcone **1** exhibits the best free binding energy of −9.4 kcal/mol, which is comparable with the interaction of the positive control, paclitaxel, and colchicine in the active site of the protein. Chalcone **1** showed the most potent MCF-7 inhibitory activity (IC$_{50}$ = 6.18 ± 0.69 µM), which is a potential tubulin polymerization inhibitor. The binding of chalcone **1** with colchicine showed one protein-ligand interaction and hydrophobic interactions with the protein residues in the ASN-2 binding site, which might play essential roles in its colchicine inhibition and antiproliferative activity. Chalcones (**1**, **5**, and **7**) have been shown water solubility, ADME properties, and toxicity profile were similar to or even better than some of the drugs currently used in the market, such as paclitaxel. Thus, in search of inhibitors with potent activity, chalcone **1**, as well as other chalcone derivatives containing 3,4,5-trimethoxy and hydroxy groups, are promising compounds as potential anticancer agents.

■ REFERENCES

[1] Ilan, Y., 2019, Microtubules: From understanding their dynamics to using them as potential therapeutic target, *J. Cell. Physiol.*, 234 (6), 7923–7937.

[2] Downing, K.H., and Nogales, E., 1998, Tubulin structure: Insights into microtubule properties and functions, *Curr. Opin. Struct. Biol.*, 8 (6), 785–791.

[3] Dumontet, C., and Jordan, M.A., 2010, Microtubule-binding agents: A dynamic field of cancer therapeutics, *Nat. Rev. Drug Discovery*, 9 (10), 790–803.

[4] Arnst, K.E., Banerjee, S., Chen, H., Deng, S., Hwang, D.J., Li, W., and Miller, D.D., 2019, Current advances of tubulin inhibitors as dual-acting small molecules for cancer therapy, *Med. Res. Rev.*, 39 (4), 1398–1426.

[5] Čermák, V., Dostál, V., Jelínek, M., Libusová, L., Kovář, J., Rösel, D., and Brábek, J., 2020, Microtubule-targeting agents and their impact on cancer treatment, *Eur. J. Cell Biol.*, 99 (4), 151075.

[6] Steinmetz, M.O., and Prota, A.E., 2018, Microtubule-targeting agents: Strategies to hijack the cytoskeleton, *Trends Cell Biol.*, 28 (10), 776–792.

[7] Karahalil, B., Yardım-Akaydin, S., and Nacak Baytas, S., 2019, An overview of microtubule targeting agents for cancer therapy, *Arh. Hig. Rada Toksikol.*, 70 (3), 160–172.

[8] Dyrager, C., Wickström, M., Fridén-Saxin, M., Friberg, A., Dahlén, K., Wallén, E.A.A., Gullbo, J., Grøtli, M., and Luthman, K., 2011, Inhibitors and promoters of tubulin polymerization: Synthesis and biological evaluation of chalcones and related dienones as potential anticancer agents, *Bioorg. Med. Chem.*, 19 (8), 2659–2665.

[9] Ouyang, Y., Li, J., Chen, X., Fu, X., Sun, S., and Wu, Q., 2021, Chalcone derivatives: Role in anticancer therapy, *Biomolecules*, 11 (6), 894.

[10] Liu, W., He, M., Li, Y., Peng, Z., and Wang, G., 2022, A review on synthetic chalcone derivatives as tubulin polymerisation inhibitors, *J. Enzyme Inhib. Med. Chem.*, 37 (1), 9–38.

[11] Jumaah, M., Khairuddean, M., Owaid, S.J., Zakaria, N., Mohd Arshad, N., Nagoor, N.H., and Mohamad Taib, M.N.A., 2022, Design, synthesis, characterization and cytotoxic activity of new *ortho*-hydroxy and indole-chalcone derivatives against breast cancer cells (MCF-7), *Med. Chem. Res.*, 31 (3), 517–532.

[12] Peng, F., Meng, C.W., Zhou, Q.M., Chen, J.P., and Xiong, L., 2016, Cytotoxic evaluation against breast cancer cells of isoliquiritigenin analogues from *Spatholobus suberectus* and their synthetic derivatives, *J. Nat. Prod.*, 79 (1), 248–251.

[13] Karthikeyan, C., Narayana Moorthy, N.S.H., Ramasamy, S., Vanam, U., Manivannan, E., Karunagaran, D., and Trivedi, P., 2015, Advances in chalcones with anticancer activities, *Recent Pat. Anti-Cancer Drug Discovery*, 10 (1), 97–115.

[14] Shin, S.Y., Kim, J.H., Yoon, H., Choi, Y.K., Koh, D., Lim, Y., and Lee, Y.H., 2013, Novel antimitotic activity of 2-hydroxy-4-methoxy-2′,3′-benzochalcone (HymnPro) through the inhibition of tubulin polymerization, *J. Agric. Food Chem.*, 61 (51), 12588–12597.

[15] McLoughlin, E.C., and O'Boyle, N.M., 2020, Colchicine-binding site inhibitors from chemistry to clinic: A review, *Pharmaceuticals*, 13 (1), 8.

[16] Kumbhar, B.V., Borogaon, A., Panda, D., and Kunwar, A., 2016, Exploring the origin of differential binding affinities of human tubulin isotypes αβII, αβIII and αβIV for DAMA-colchicine using homology modelling, molecular docking and molecular dynamics simulations, *PLoS One*, 11 (5), e0156048.

[17] Salum, L.B., Mascarello, A., Canevarolo, R.R., Altei, W.F., Laranjeira, A.B., Neuenfeldt, P.D., Stumpf, T.R., Chiaradia-Delatorre, L.D., Vollmer, L.L., Daghestani, H.N., de Souza Melo, C.P., Silveira, A.B., Leal, P.C., Frederico, M.J.S., do Nascimento, L.F., Santos, A.R.S., Andricopulo, A.D., Day, B.W., Yunes,

R.A., Vogt, A., Yunes, J.A., and Nunes, R.J., 2015, *N*-(1′-naphthyl)-3,4,5-trimethoxybenzohydrazide as microtubule destabilizer: Synthesis, cytotoxicity, inhibition of cell migration and in vivo activity against acute lymphoblastic leukemia, *Eur. J. Med. Chem.*, 96, 504–518.

[18] Dong, M., Liu, F., Zhou, H., Zhai, S., and Yan, B., 2016, Novel natural product-and privileged scaffold-based tubulin inhibitors targeting the colchicine binding site, *Molecules*, 21 (10), 1375.

[19] Lipinski, C.A., Lombardo, F., Dominy, B.W., and Feeney, P.J., 2001, Experimental and computational approaches to estimate solubility and permeability in drug discovery and development settings, *Adv. Drug Delivery Rev.*, 46 (1-3), 3–26.

[20] Ramírez, D., and Caballero, J., 2018, Is it reliable to take the molecular docking top scoring position as the best solution without considering available structural data?, *Molecules*, 23 (5), 1038.

[21] Torres, P.H.M., Sodero, A.C.R., Jofily, P., and Silva-Jr, F.P., 2019, Key topics in molecular docking for drug design, *Int. J. Mol. Sci.*, 20 (18), 4574.

Optimization of Aptamer-Based Electrochemical Biosensor for ATP Detection Using Screen-Printed Carbon Electrode/Gold Nanoparticles (SPCE/AuNP)

Rahmaniar Mulyani[1,2], Nida Yumna[1], Iman Permana Maksum[1**], Toto Subroto[1], and Yeni Wahyuni Hartati[1*]

[1]Department of Chemistry, Faculty of Mathematics and Natural Sciences, Universitas Padjadjaran,
Jl. Raya Bandung-Sumedang Km. 21, Jatinangor 45363, West Java, Indonesia

[2]Department of Chemistry, Faculty of Sciences and Informatics, Universitas Jenderal Achmad Yani,
Jl. Terusan Jenderal Sudirman, Cimahi 40531, West Java, Indonesia

* Corresponding author:

tel: +62-8122132349*;
+62-82240839482**
email: yeni.w.hartati@unpad.ac.id*;
iman.permana@unpad.ac.id**

Abstract: *Electrochemical biosensors are used to detect adenosine triphosphate (ATP) levels, which are involved in a variety of biological processes, such as regulating cellular metabolism and biochemical pathways. Therefore, this research aims to develop an aptamer-based electrochemical biosensor with Screen Printed Carbon Electrode/gold nanoparticles (SPCE/AuNP) and collect data as well as information related to ATP detection. The modification of SPCE with AuNP increased the analyte's binding sensitivity and biocompatibility. The aptamer was selected based on its excellent bioreceptor characteristics. Furthermore, aptamer–SH (F1) and aptamer-NH$_2$ (F2) were immobilized on the SPCE/AuNP surface, which had been characterized using SEM, EIS, and DPV. Also, the ATP-binding aptamers were electrochemically characterized using the K$_3$[Fe(CN)$_6$] redox system and Differential Pulse Voltammetry (DPV). According to the optimization results using the Box-Behnken experimental design, the ideal conditions obtained from the factors influencing the experiment were the F1 concentration and incubation time of 4 μM and 24 h, respectively, as well as F1/F2/ATP incubation time of 7.5 min. Meanwhile, for the range of 0.1 to 100 μM, the detection (LoD) and quantification (LoQ) limits were 7.43 and 24.78 μM, respectively. Therefore, this aptasensor method can be used to measure ATP levels in real samples.*

Keywords: *adenosine triphosphate (ATP); aptamer; AuNP; electrochemistry; screen printed carbon electrode (SPCE)*

■ INTRODUCTION

Adenosine triphosphate (ATP) plays an essential role in many biological processes, such as regulating cellular metabolism and biochemical pathways [1]. Most mitochondrial diseases arise due to disturbances in the process of oxidative phosphorylation. When this process is inhibited, the important role of mitochondria in producing energy in the form of ATP is disrupted, resulting in cellular abnormalities and cell death [2].

Previous research studies have shown that diabetes mellitus and cataracts are caused by mutations that occur in the respiratory complex [3-4]. The prospect that the development of aptasensor application diagnostic methods for diagnosing mitochondrial diabetes can strengthen previous research that has studied mitochondrial DNA mutation studies both *in vitro* and *in silico* [5-7].

The function of biological ATP in biochemical studies, clinical diagnosis, and environmental analysis are essential, necessitating the development of sensitive and specific methods for its recognition and detection. Various techniques, such as fluorometric methods [8-10], high-performance liquid chromatography (HPLC) [11], mass spectrometry [12], chemiluminescence [13], and electrochemistry [14] have been used to detect ATP. However, electrochemical sensors attract more attention

due to their advantages in sensitivity, miniaturization ability, minimal power requirements, low cost, and high stability [15].

An electrochemical biosensor is an integrated receptor-transducer analytical device based on a biologically identifiable element in combination or in close contact with an electrochemical transducer [16]. The measurement is based on the observation of an active reaction that produces a measurable current, potential changes, or impedance resulting from a change in conductance, which is read using voltammetric, amperometric, potentiometric, or impedance methods [17].

The electrochemical biosensor developed in this research uses aptamer bioreceptors, also known as aptasensors. Furthermore, aptamers are short pieces of single-stranded DNA molecules that recognize specific target molecules. It was selected based on its characteristics as bioreceptors, some of which are similar to or even better than antibodies. Therefore, it generates an excellent affinity for biosensors and other applications, such as biomedical imaging, targeted drug delivery, and biomarker discovery [18].

Aptasensors, due to their advantages, have been widely used to detect ATP. For example, Mashhadizadeh et al. developed an electrochemical aptasensor for ATP with a non-enzymatic strategy using graphene oxide-modified silver nanoparticles with a detection limit of 5 nM [19]. Furthermore, Zheng et al. developed an electrochemical nanoaptasensor to monitor the continuous fluctuations of ATP at the subcellular level with a detection limit of 26 μM [20].

Aptamers were immobilized on the electrode surface for biosensor construction. Meanwhile, several aptasensor devices were developed using the Screen-Printed Carbon Electrode (SPCE), which combines a carbon working, reference, and a support electrode in one simple and easy-to-use design [21-22]. SPCE is widely used because of its small size, ease of mass production, low cost, ability to improve electrochemical performance, and ease of modification [23-24].

Modifications were made using gold nanoparticles to increase the sensitivity and conductivity of the analyte signal. Also, due to the large effective surface area and high electrocatalytic ability, gold nanoparticles (AuNP) have been widely used to modify electrode surfaces [25].

Gold nanoparticles have a high surface area, can improve the stability and immobilization of bioreceptors, and function as electron transfer between the bioreceptors and the electrode surface to produce significant signal amplification [26]. These nanoparticles, which are used as signal amplification elements, have received much attention due to their ease of synthesis, unique size, shape, and optical properties, as well as good biocompatibility [27]. Therefore, this research aims to develop an aptamer-based electrochemical biosensor with SPCE/AuNP and collect data as well as information related to the detection of ATP.

■ EXPERIMENTAL SECTION

Materials

The materials used in this study include aqua pro injection (PT Ikapharmindo Putramas), gold nanoparticles (AuNP) synthesized by the citrate reduction method at the Research Center for Biotechnology and Bioinformatics, Universitas Padjadjaran, magnesium chloride 2.0 M, sodium hydroxide 0.1 M, hydrochloric acid 0.1 M, potassium chloride 0.1 M (Merck), tris-(2 carboxyethyl) phosphine hydrochloride 0.5 mM (TCEP) (Sigma), phosphate-buffered saline pH 7.0 (PBS) (Merck), $K_3(Fe[CN]_6)$ 10 mM (Sigma), ATP 100 mM, CTP 100 mM, GTP 100 mM, UTP 100 mM (Roche Diagnostic GmbH), and amino-labeled oligonucleotides and thiol-labeled oligonucleotides (Bioneer) in the following orde': F1: 5'-HS-$(CH_2)_6$-ACCTGGGG'AGTAT-3' and F2: 5'-TGCGGAGGAAGGT-(CH_2)'$_2$-NH_2-3'.

Instrumentation

The equipment used in this study included a Zimmer Peacock potentiostat using PSTrace 5.8 software, UV-VIS Spectrophotometer (Thermo scientific), Screen Printed Carbon Electrode (SPCE) (GSI Technologies, USA), micropipette (Eppendorf), micro tube, micropipette tip, autoclave sterilizer (Hirayama).

Autoclave HVE-50), scanning electron microscope (Hitachi TM3000) used to characterize the morphology of the electrodes, as well as other general glassware available at the Research Center for Biotechnology and Bioinformatics, Universitas Padjadjaran.

Procedure

Preparation of solution AuNP on 0.76 mM

A 628.53 μL of $HAuCl_4 \cdot 3H_2O$ 55.85 mM and 19.371.47 μL of aqua pro injection were added into the Erlenmeyer flask, followed by stirring with a magnetic stirrer and heating until boiling. Then, 1.730 μL of $Na_3C_6H_5O_7 \cdot 2H_2O$ 1% were added and stirred until the color changed to red wine.

Modified SPCE preparation

The modification was performed by dripping 40 μL of colloidal AuNP solution on the SPCE surface, then allowed to dry for 24 h and rinsed with demineralized water [28]. SPCE before and after modification was characterized using DPV with a 10 mM $K_3[Fe(CN)_6]$ redox system in 0.1 M KCl at a potential range of -1 to +0.7 V and a scan rate of 0.008 V/s, E_{step} 0.004 V with E_{pulse} 0.025 V and t_{pulse} 0.05 s, EIS with 10 mM $K_3[Fe(CN)_6]$ redox system in 0.1 M KCl as well as a frequency of 0.1 to 106 Hz at 0.01 V anodic peak current potential, followed by characterization using cyclic voltammetry (CV) using 10 mM $K_3[Fe(CN)_6]$ in 0.1 M KCl with a scan rate of 0.005 V/s in a potential range of -0.6 V to +0.6 V, and SEM.

Aptamer immobilization on SPCE/AuNP surface

The disulfide bond reduction of the F1 fragment was performed by making an aliquot of 20 μL from F1 4 μM with 5 μL TCEP 0.5 mM, then incubated in the dark for 1 h. Furthermore, it was self-assembled on the SPCE/AuNP surface by dripping 15 μL of aliquot solution and 12 μL of 2 M magnesium chloride for 24 h. The electrode was then rinsed thoroughly with a phosphate buffer solution of pH 7 [29]. The electrodes that have been immobilized with aptamer F1 were characterized using DPV with 10 mM $K_3[Fe(CN)_6]$ redox system in 0.1 M KCl at a potential range of -1 to +0.7 V, the scan rate of 0.008 V/s, E_{step} of 0.004 V with an E_{pulse} of 0.025 V and a t_{pulse} of 0.05 s.

Monitoring of aptasensor response to ATP

A total of 15 μL of ATP with a certain concentration and 15 μL of F2 4 μM were simultaneously dropped on the electrodes and then incubated for various time variations. Furthermore, the modified electrodes were rinsed with a PBS solution of pH 7, making them ready for electrochemical detection [26]. Finally, the electrodes were characterized using DPV with a 10 mM $K_3[Fe(CN)_6]$ redox system in 0.1 M KCl at a potential range of -1 V to +0.7 V, the scan rate of 0.008 V/s, E_{step} of 0.004 V with E_{pulse} of 0.025 V and t_{pulse} of 0.05 s.

Optimization of factors affecting experiments

The factors to be optimized in the experiment includes aptamer F1 concentration (X1), aptamer F2 concentration (X2), and F1/F2/ATP incubation time (X3). Each of these factors is designed using 3 different levels, namely the lowest level (-1), medium (0), and the highest (+1), as shown in Table 1.

Determination of analytical parameters
Creation of calibration curves as well as detection and quantification limits. ATP solutions of various concentrations (0, 0.1, 1, 10, 100, 500, 1000, 2000, 3000) μM were tested on the aptasensor. The resulting electrochemical response was measured using DPV with a 10 mM $K_3[Fe(CN)_6]$ redox system in 0.1 M KCl at a potential range of -1 to +0.7 V and a scan rate of 0.008 V/s, E_{step} of 0.004 V with E_{pulse} of 0.025 V and t_{pulse} of 0.05 s. Furthermore, a curve is made between the concentration and the average peak current difference (ΔI) for each

Table 1. Factor and level of the analysis of experimental condition optimization

Factor	Unit	Level		
		-1	0	+1
Aptamer F1 concentration (X1)	μM	2	4	6
Aptamer F1 incubation time (X2)	hour	6	15	24
F1/F2/ATP incubation time (X3)	minute	2.5	5	7.5

resulting measurement as x and y. Hence, the resulting equation is y = bx + a. The detection and quantification limits are determined using the following equation y = yB + 3SB and y = yB + 10SB, respectively. Where yB is the response to the blank signal, SB is the blank standard deviation, and b is the slope of the regression equation y = a + bx [30].

Determination of precision and accuracy. Precision and accuracy were determined by measuring the ATP solution five times using the previously described procedure. Also, the average difference in peak current (ΔI) and the standard deviation are obtained based on the measurement results. Where $\bar{x}$ is the average measured concentration, and μ is the actual concentration. Meanwhile, the precision is expressed in terms of the coefficient of variance (KV) with the following equation [31].

$$KV = \frac{Sb}{x}100\%$$

$$Precision = 100\% - KV$$

Meanwhile, accuracy is expressed in percent relative error (%Error) with the following equation [28].

$$\%Error = \frac{\bar{x} - \mu}{\mu}100\%$$

$$Accuration = 100\% - \%Error$$

Electrochemical aptasensor selectivity test for ATP

On the electrochemical aptasensor that had been designed, the selectivity test was performed by comparing the ATP analyte solution to various nucleotide analogs, such as UTP, CTP, and GTP, each at a concentration of 3000 M. The resulting electrochemical response was measured using DPV with a 10 mM $K_3[Fe(CN)_6]$ redox system in 0.1 M KCl over a potential range of -1 to +0.7 V, the scan rate of 0.008 V/s, E_{step} of 0.004 V with E_{pulse} of 0.025 V and t_{pulse} of 0.05 s.

■ RESULTS AND DISCUSSION

Modification and Characterization of SPCE/AuNP SPCE Modification with AuNP

The metal nanoparticles exhibit unique physical and chemical properties, different from the bulk or atomic state due to the quantum size effect that produces specific electronic structures. AuNP is one of the most outstanding groups of metal nanoparticles that have attracted considerable interest by promoting various applications in biomedical fields such as biosensing, imaging, and drug delivery systems [32-33].

A UV-Vis spectrophotometer was used to identify the AuNP formation by observing the maximum wavelength value produced. Furthermore, this was indicated by the maximum wavelength on AuNP absorption at 520–530 nm [34]. The nanoparticle size influences the maximum wavelength shift [35]. The AuNP colloid used in this research has an absorption peak at a maximum wavelength of 522, implying that the size used is quite good, as shown in Fig. 1.

Electrochemical biosensors fabricated by combining biological recognition elements with electrochemical transducers modified with AuNPs have become increasingly essential in biosensor research since AuNPs provide a stable surface for the immobilization of biomolecules while retaining their biological activity. However, this is particularly useful when assembling biosensors [36]. This indicates SPCE modification with AuNP was performed to increase the sensitivity. Generally, the achievable sensitivity of an electrochemical detection scheme depends on the amount of electric charge assigned by the label or electrode. This detection sensitivity is increased by modifying the SPCE, which improves the signal element. The modification was made with gold nanomaterials because AuNPs aid in establishing an interface for direct electron transfer from redox-active probes while maintaining their bioactivity. Meanwhile, AuNP increases
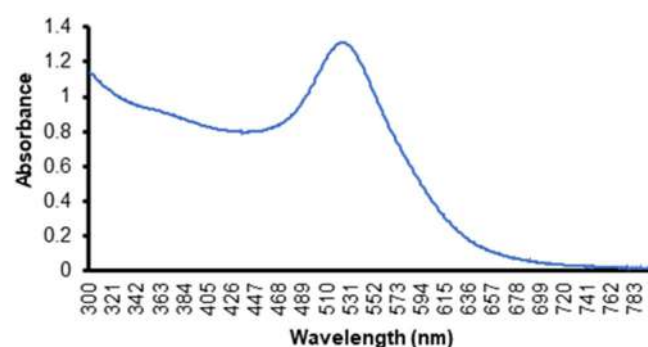

Fig 1. Characterization results of AuNP using UV/Vis spectrophotometer with the maximum wavelength of AuNP absorption at 522 nm

the sensitivity of SPCE with a relatively large surface area and high conductivity.

The modification of SPCE was conducted by dripping 40 AuNP on the surface, then was incubated for 24 h at room temperature to dry. This process takes longer because the physical adsorption method modifies AuNP on the SPCE surface.

SPCE/AuNP Characterization with Differential Pulse Voltammetry

The characterization by differential pulse voltammetry (DPV) was conducted to determine the current response in SPCE before and after modification with AuNP. Furthermore, the electrochemical measurements were performed by observing the oxidation-reduction activity of the electroactive species $[Fe(CN)_6]^{3-/4-}$. The following is an oxidation-reduction reaction in $K_3[Fe(CN)_6]$.

$[Fe(CN)_3]^{3-} + e^- \rightarrow [Fe(CN)_3]^{3-}$
$[Fe(CN)_3]^{4-} \rightarrow [Fe(CN)_3]^{3-} + e^-$
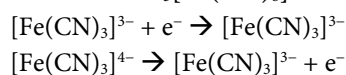
When an analyte is oxidized at the working electrode, current passes electrons to the auxiliary through the external electrical circuit, resulting in solvent reduction.

Fig. 2(a) shows the differential pulse voltammogram of the bare SPCE and AuNP modified SPCE. This shows an increase in peak current in the gold-modified SPCE of 30.979 μA compared to the bare SPCE of 11.133 μA. Furthermore, it implies that the modification provides an electrode surface with increased conductivity. Therefore,
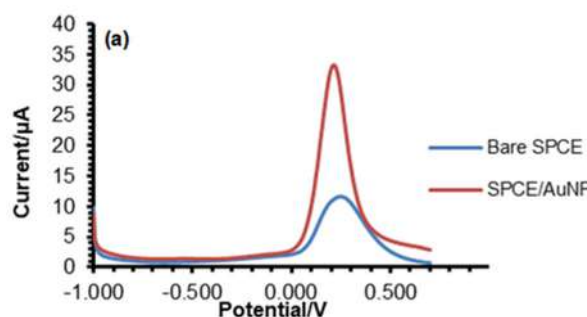
the electron transfer between the analyte and the electrode is increased. Fig. 2(b) shows the cyclic voltammogram of the bare SPCE and AuNP modified SPCE; this shows an increase in the redox peak current is associated with an increase in electrochemical activity with an increase in the active electrode area.

SPCE/AuNP Characterization by Electrochemical Impedance Spectroscopy

The characterization by electrochemical impedance spectroscopy (EIS) was conducted on SPCE before and after modification with AuNP, where the measurement was based on impedance or resistance. Fig. 3 shows the characterization results of the bare SPCE and
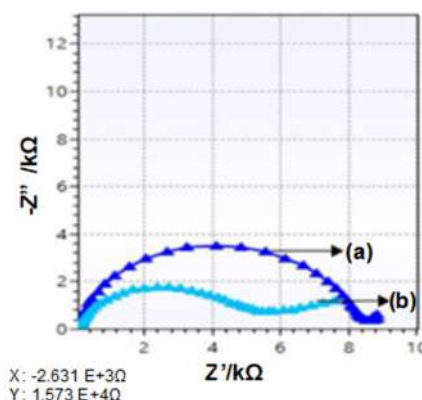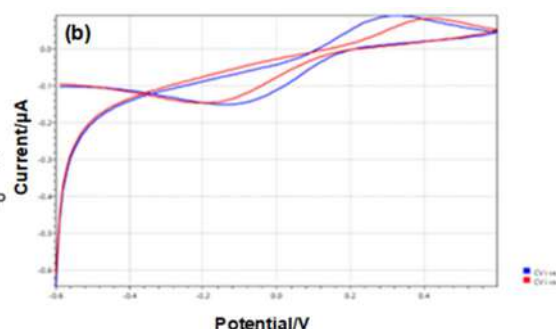

X: -2.631 E+3Ω
Y: 1.573 E+4Ω

Fig 2. SPCE characterization result spectrum using EIS; line (a) Bare SPCE and line (b) SPCE/AuNP using a redox system of 10 mM potassium ferricyanide $K_3[Fe(CN)_6]$ solution in 0.1 M KCl at a frequency of 0.1 to 10^6 Hz at an anodic peak current potential of 0.01 V

Fig 3. (a) Differential pulse voltammogram: bare SPCE (blue line) and SPCE/AuNP (red line) with 10 mM $K_3[Fe(CN)_6]$ redox system in 0.1 M KCl solution. The scan rate of 0.008 V/s was used in the potential range of -1.0 to +0.7 V. (b) Cyclic voltammograms: bare SPCE (red line) and SPCE/AuNP (blue line) with 10 mM $K_3[Fe(CN)_6]$ in 0.1 M KCl with a scan rate of 0.005 V/s over a potential range of -0.6 V to +0.6 V

AuNP-modified SPCE using EIS. The gold-modified SPCE showed a decrease when compared to the bare SPCE. The characterization results using EIS are inversely proportional to DPV because resistance and current are inversely proportional to Ohm's Law, namely V = I. R. This shows that the modification of SPCE with AuNP provides an electrode surface with increased conductivity. Therefore, there is an increase in the electron transfer between the analyte-electrodes, and the impedance value becomes lower. The measurement of the circle diameter (Rct) in the circular section of the Nyquist plot is related to the high frequency of the electron transfer process as opposed to the electron transfer current, which shows the results of surface modification of SPCE with AuNP. In Fig. 3 (line a), the unmodified SPCE has a large Rct due to the current decrease in the electron transfer process, so the resistance obtained is very large. The Rct of the gold-modified SPCE surface (line b) was smaller than that of the unmodified electrode (line a). After modification of the SPCE surface, the current increases so that the resistance is obtained, as shown in line b.

SPCE/AuNP Surface Characterization using Scanning Electron Microscopy (SEM)

SEM was used to examine the morphology of gold nanoparticles, which involves scanning the sample surface for particle shape using a high-energy radiance. Fig. 4 shows the surface morphology of SPCE before and after being modified with SEM gold nanoparticles, with a and b showing the SPCE surface before and after being modified with AuNP, respectively. Since AuNP has adhered to the SPCE surface after being changed, the final surface is more closed, thereby implying that the modification has been completed successfully.

Aptamer F1 Immobilization on Electrode Surface

Characterization of SPCE/AuNP/F1 with differential pulse voltammetry

The differential pulse voltammetry (DPV) based on electron transfer from $K_3[Fe(CN)_6]$ as the electroactive species experiencing a redox reaction was used to determine the success of aptamer F1 immobilization in SPCE/AuNP. There is a decrease in peak current due to the aptamer F1 on the electrode surface. The results of the

DPV voltammogram before and after the immobilization of the aptamer F1 are shown in Fig. 5.

After the aptamer F1 was immobilized on the SPCE surface, there was a decrease in the peak current on the DPV voltammogram to 22.619 μA. This shows that the immobilization has been conducted successfully because compounds on the SPCE surface will disrupt the electron transfer between the redox probe and the electrode.

AuNPs are particularly suitable for diagnostics because they are easily modified with thiolated ligands to detect specific molecules of interest [32]. The immobilization technique of the aptamer F1, which has modified the thiol group on SPCE/AuNP through covalent bonds, shows good stability, flexibility, and high binding strength. This procedure results in the specific binding of the aptamer to the electrode surface
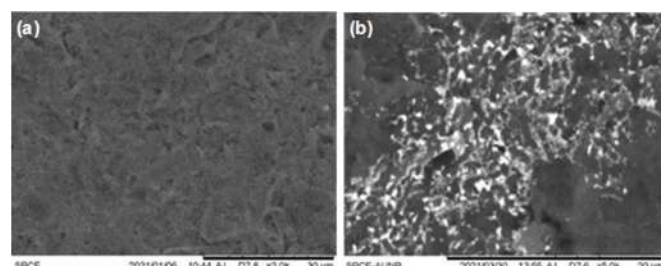

Fig 4. Characterization results of modified SPACE using SEM; (a) SPCE bare, (b) SPCE/AuNP
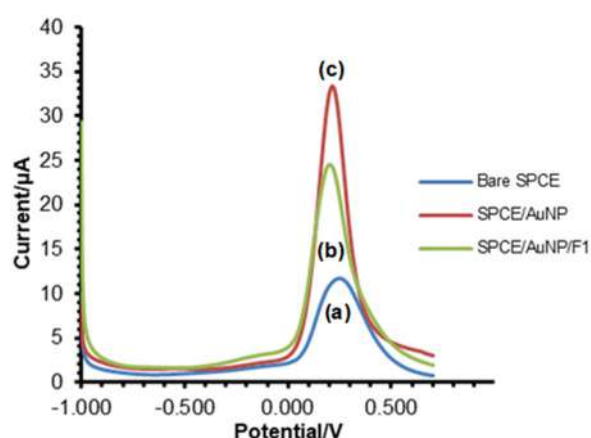

Fig 5. Differential pulse voltammogram: (a) bare SPCE, (b) SPCE/AuNP, (c) SPCE/AuNP/F1 with 10 mM $K_3[Fe(CN)_6]$ redox system in 0.1 M KCl solution. The scan rate of 0.008 V/s was used in the potential range of -1.0 V to +0.7 V

and prevents non-specific binding. Furthermore, the immobilization occurs covalently between the thiol-modified aptamer and the surface of AuNP to form a self-assembled monolayer due to the strong affinity interaction between the thiol group and the gold surface, forming an Au-SH covalent bond.

SPCE/AuNP/F1 surface characterization using scanning electron microscopy (SEM)

The efficacy of the aptamer F1 immobilization on SPCE/AuNP was tested using SEM. The characterization result of SPCE/AuNP/F1 is shown in Fig. 6, where the electrode surface is covered with a triangular shape aptamer. This implies that the immobilization of the aptamer F1 on the SPCE/AuNP surface has been conducted successfully.

Aptasensor testing on ATP and its characterization

The aptasensor test was conducted by dripping each 15 μL of aptamers F2 and ATP simultaneously on the SPCE/AuNP/F1 surface and incubated for 7.5 min at room temperature. Furthermore, the aptasensors were washed with a pH 7 PBS solution to remove nonadherent species from the SPCE/AuNP/F1 surface. Hence, it reduces errors while measuring currents that interfere with the analysis process. After adding the aptamer F2 and ATP on the SPCE/AuNP/F1 surface, there will be an association between F2 and F1 in the presence of ATP, forming a sandwich/g-quadruplex structure on the AuNP surface. The illustration of this aptasensor is shown in Fig. 7.

The aptamer layer on the electrode surface gets denser due to the association between F1 and F2, and the negative charge increases more than in the previous stage. Therefore, negatively charged ferricyanide ions will be inhibited from approaching the electrode, reducing electron transmission between the redox probe and the electrode. The current decreased to 16.775 mA, as shown in Fig. 8.
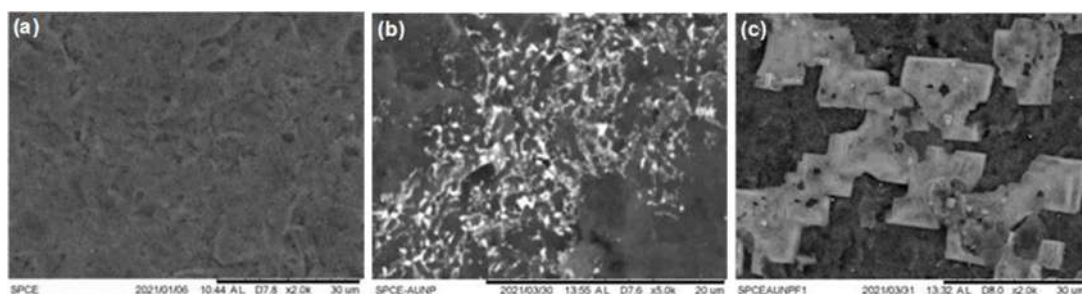
Fig 6. Characterization results of modified SPACE using SEM; (a) bare SPCE, (b) SPCE/AuNP, and (c) SPCE/AuNP/F1
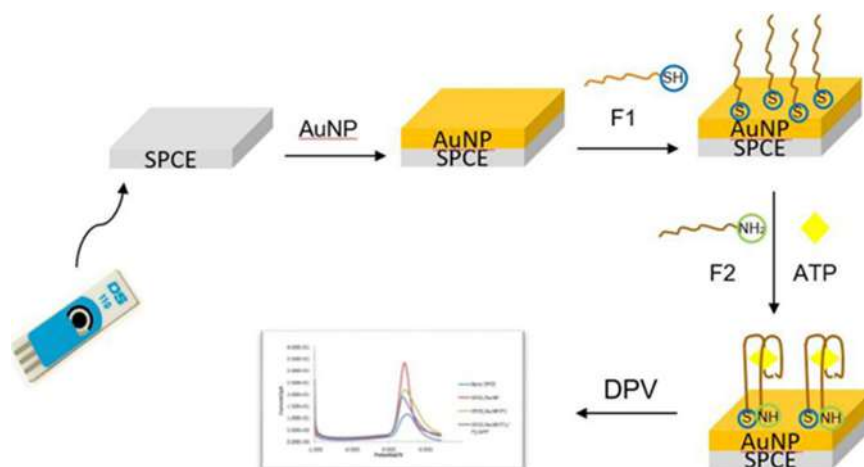
Fig 7. Illustration of an aptamer-based electrochemical biosensor for detecting ATP using APCE/AuNP
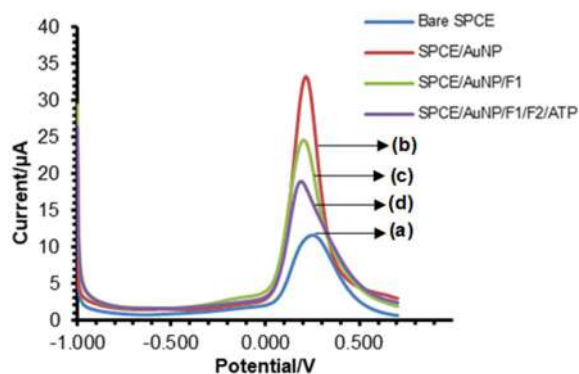
Fig 8. Differential pulse voltammogram: (a) bare SPCE, (b) SPCE/AuNP, (c) SPCE/AuNP-F1, (d) SPCE/AuNP-F1-F2-ATP with 10 mM $K_3[Fe(CN)_6]$ redox system in 0.1 M KCl solution. The scan rate of 0.008 V/s is used in the potential range of -1.0 V to +0 .7 V

Determination of Optimum Conditions with Box-Behnken Experiment Design

The factors optimized in the experiment include aptamer F1 concentration (X1), aptamer F2 concentration (X2), and F1/F2/ATP incubation time (X3). Furthermore, each of them is designed through 3 different levels, namely, the lowest level (-1), medium (0), and the highest (+1). Three experimental factors, each with three levels, produced 15 trials and were divided into two replication blocks for two repeats, yielding a total of 30 trials with the outcome in the form of current response (A), as shown in Table 2.

The response of the measurement results is processed with the Minitab 18 prog, and the coefficients

Table 2. Factor, level, and current response in the optimization analysis of experimental conditions

No.	Aptamer F1 concentration (µM)	Aptamer F1 incubation time (h)	F1/F2/ATP incubation time (min)	Current response (µA)
1	2	6	5.0	20.902
2	6	6	5.0	18.078
3	2	24	5.0	17.852
4	6	24	5.0	17.794
5	2	15	2.5	20.877
6	6	15	2.5	21.860
7	2	15	7.5	20.282
8	6	15	7.5	16.663
9	4	6	2.5	15.134
10	4	24	2.5	15.657
11	4	6	7.5	21.033
12	4	24	7.5	13.145
13	4	15	5.0	15.392
14	4	15	5.0	13.924
15	4	15	5.0	15.392
16	2	6	5.0	20.546
17	6	6	5.0	21.743
18	2	24	5.0	17.852
19	6	24	5.0	17.704
20	2	15	2.5	20.887
21	6	15	2.5	14.184
22	2	15	7.5	16.640
23	6	15	7.5	14.609
24	4	6	2.5	16.134
25	4	24	2.5	14.296
26	4	6	7.5	21.033
27	4	24	7.5	12.902
28	4	15	5.0	17.294
29	4	15	5.0	14.962
30	4	15	5.0	17.627

Table 3. P-value of ANOVA results for each factor

Factor	P-Value
Aptamer F1 concentration	0.120
Aptamer F1 incubation time	0.003
F1/F2/ATP incubation time	0.741

and response functions are obtained to determine the maximum current. Furthermore, this method is an experimental design using statistics and mathematics to discover the optimal value. Based on the results of the ANOVA output, the most significant factor affecting the experiment was the aptamer F1 incubation time because it had a P-value < 0.05, as shown in Table 2. The current response obtained is then analyzed, showing the coefficient of the response function in Eq. (1).

$$Y = 26.73 - 5.95X1 - 0.045X2 + 1.48X3 + 0.672X1^2$$
$$+ 0.00747X2^2 - 0.033X3^2 + 0.0099X1*X2 \qquad (1)$$
$$+ 0.002X1*X3 - 0.081X2*X3$$

X1: Aptamer F1 concentration, X2: Aptamer F1 incubation time, X3: F1/F2/ATP incubation time.

In the experiment, the component with negative value effects decreases the reaction, while the factor with a positive value increases the response, as shown in Eq. (1). The optimum conditions obtained from the results of the Box-Behnken experimental design for each factor include the aptamer F1 concentration of 4 μM, aptamer F1 incubation time of 24 h, and the F1/F2/ATP incubation time of 7.5 min.

**Calibration Curves, Detection Limits, and Quantification Limits**

A calibration curve is drawn after determining the optimum conditions of several factors that affect the experiment. Also, the detection and quantification limits of this electrochemical aptasensor are calculated using variations in ATP concentration. The experiment was conducted similarly to the procedure for determining the aptasensor response by using the parameters of the optimization results. ATP with various concentrations (0; 0.1; 1; 10; 100) μM was tested on an electrochemical aptasensor to describe the amount present in the sample and measured twice at each concentration. The resulting electrochemical response using DPV is shown in Fig. 9.
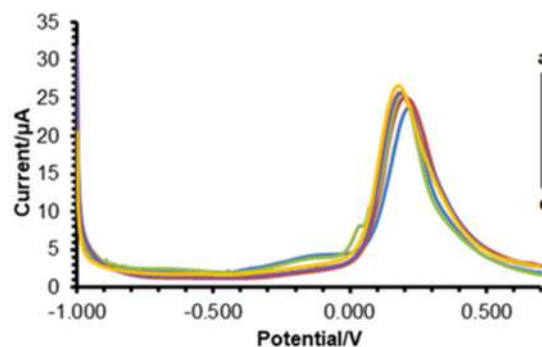
Fig 9. Differential pulse voltammogram for variations in ATP concentration a–e (0, 0.1, 1, 10, 100) μM as measured by a 10 mM $K_3[Fe(CN)_6]$ solution redox system in 0.1 M KCl solution with a scan rate of 0.008 V/s over a potential range of -1.0 V to +0.7 V, E_{step} of 0.004 V with E_{pulse} of 0.025 V and t_{pulse} of 0.05 s

Based on the characterization results using the DPV, it is known that the higher the concentration of ATP added, the lower the peak value of the current generated. As a result, the aptamer binds, crowding the SPCE surface and interrupting electron transport between the potassium ferricyanide redox probe and the electrode. A calibration curve was made by plotting the peak value of the DPV current as a result of the characterization of ATP concentration variations with concentration variations (0.1; 1; 10; 100) μM, as shown in Fig. 10. From the calibration curve, the linear regression equation y = 0.0124x + 0.8769 is obtained with R^2 of 0.9952. Based on the data processing results, the value of the detection (LoD) and quantification (LoQ) limits is 7.43 and 24.78 μM, then the accuracy and precision values are 96 and 98.69%, respectively.

The detection limit obtained on the aptasensor for ATP detection in this research is quite good compared to Zheng et al. [20], which was carried out using a conventional 3 electrode system, and Ren et al. [37] used a fluorescence aptasensor. Hence, the electrochemical aptasensor method using SPCE/AuNP is superior in sensitivity and stability. However, the detection limit is still higher when compared to Mashhadizadeh et al., that used silver nanoparticle modified graphene oxide (AgNP) nanocomposites, where graphene oxide as a substrate for binding large amounts of AgNP enhances
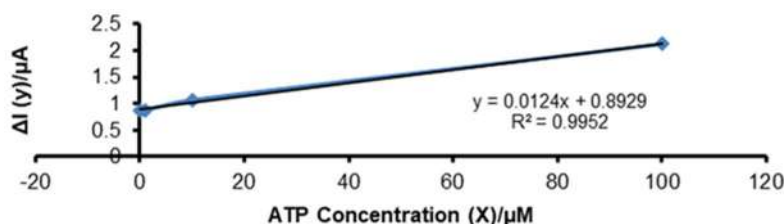
Fig 10. ATP aptasensor calibration curve with variations in concentration (0.1; 1; 10; 100) µM as measured by a of 10 mM $K_3[Fe(CN)_6]$ solution redox system in 0.1 M KCl. The scan rate is at 0.008 V/s over a potential range of -1.0 V to +0.7 V, E_{step} of 0.004 V with an E_{pulse} of 0.025 V and a t_{pulse} of 0.05 s

Table 4. Research on aptamer-based biosensors to detect ATP

	LoD	Ref.
Label-free fluorescence aptasensor based on AuNPs and CQDs for the detection of ATP	20 µM	[37]
Electrochemical nanoaptasensor for continuous monitoring ATP fluctuation at subcellular level	26 µM	[20]
Aptamer-based electrochemical biosensor for detecting Adenosine Triphosphate (ATP) using Screen Printed Carbon Electrode/Gold Nanoparticles (SPCE/AuNP)	7.43 µM	This research
A simple non-enzymatic strategy for adenosine triphosphate electrochemical aptasensor using silver nanoparticle-decorated graphene oxide	5.0 nM	[19]
A sensitive colorimetric aptasensor with a triple-helix molecular switch based on peroxidase-like	2.4 nM	[38]
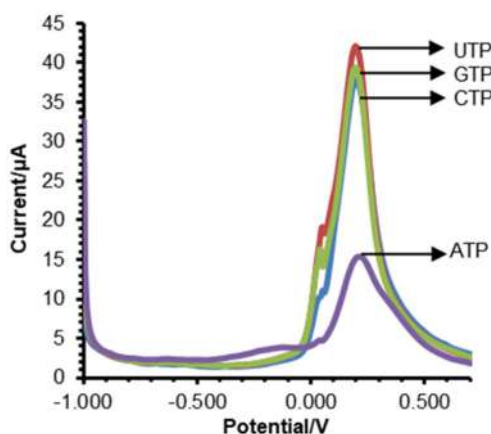
Fig 11. Electrochemical aptasensor response voltammogram for ATP in detecting ATP, UTP, GTP, and CTP at a concentration of 3 µM as measured by a 10 mM $K_3[Fe(CN)_6]$ solution redox system in 0.1 M KCl solution. The scan rate is at 0.008 V/s over a potential range of -1.0 V to +0.7 V, E_{step} of 0.004 V with E_{pulse} of 0.025 V and tp_{ulse} of 0.05 s

the amplification AgNP oxidation signals [19]. Shahsavar et al. used a colorimetric biosensor with DNAzyme [38],

as shown in Table 4.

Electrochemical Aptasensor Selectivity for ATP

The selectivity of this electrochemical aptasensor for ATP was investigated by determining the current response when the sensor was added to other nucleotide analogue analytes, which include UTP, GTP, and CTP.

The result of the voltammogram characterization in Fig. 11 shows that the peak current in ATP is 12.455 µA, while UTP, CTP, and GTP produce higher current peaks than ATP at 39.934, 35.446, and 37.034 µA, respectively. The peak DPV current in the ATP analog increases as in the analyte without ATP. Therefore, it can be seen that this electrochemical aptasensor shows a selective response to ATP.

■ **CONCLUSION**

The aptamer was successfully mobilized on the surface of the SPCE modified gold nanoparticles with the characterization results using differential pulse voltammetry, where the current decreased from 30.979

to 22.619 μA. Based on the results of SEM characterization, it is shown that the SPCE surface has been covered by aptamers. The optimum conditions obtained through the Box-Behnken experimental design were ATP concentration of 4 μM, aptamer F1 incubation time for 24 h, and F1/F2/ATP incubation time for 7.5 min. Therefore, the detection and quantification (LoD) and limits (LoQ) of the electrochemical aptasensors for ATP developed in this research were 7.43 and 24.78 μM, respectively.

■ **ACKNOWLEDGMENTS**

■ **AUTHOR CONTRIBUTIONS**

Rahmaniar Mulyani and Nida Yumna conducted the experiment, Nida Yumna conducted the calculations optimization Box-Behnken design, Rahmaniar Mulyani, Iman Permana Maksum, and Yeni Wahyuni Hartati wrote and revised the manuscript. Toto Subroto revised the manuscript. All authors agreed to the final version of this manuscript.

■ **REFERENCES**

[1] Huang, Y., Lei, J., Cheng, Y., and Ju, H., 2015, Target-assistant Zn²⁺-dependent DNAzyme for signal-on electrochemiluminescent biosensing, *Electrochim. Acta*, 155, 341–347.

[2] Frazier, A.E., Thorburn, D.R., and Compton, A.G., 2019, Mitochondrial energy generation disorders: Genes, mechanisms, and clues to pathology, *J. Biol. Chem.*, 294 (14), 5386–5395.

[3] Maksum, I.P., Farhani, A., Rachman, S.D., and Ngili, Y., 2013, Making of the A3243G mutant template through site directed mutagenesis as positive control in PASA-Mismatch three bases, *Int. J. PharmTech Res.*, 5 (2), 441–450.

[4] Maksum, I.P., Natradisastra, G., Nuswantara, S., and Ngili, Y., 2013, The effect of A3243G mutation of mitochondrial DNA to the clinical features of type-2 diabetes mellitus and cataract, *Eur. J. Sci. Res.*, 96 (4), 591–599.

[5] Hartati, Y.W., Nur Topkaya, S., Maksum, I.P., and Ozsoz, M., 2013, Sensitive detection of mitochondrial DNA A3243G tRNALeu mutation via an electrochemical biosensor using Meldola's Blue as a hybridization indicator, *Adv. Anal. Chem.*, 3 (A), 20–27.

[6] Destiarani, W., Mulyani, R., Yusuf, M., and Maksum, I.P., 2020, Molecular dynamics simulation of T10609C and C10676G mutations of mitochondrial *ND4L* gene associated with proton translocation in type 2 diabetes mellitus and cataract patients, *Bioinf. Biol. Insights*, 14, 117793222097867.

[7] Maksum, I.P., Saputra, S.R., Indrayati, N., Yusuf, M., and Subroto, T., 2017, Bioinformatics study of m.9053G>A mutation at the *ATP6* gene in relation to type 2 diabetes mellitus and cataract diseases, *Bioinf. Biol. Insights*, 11, 1177932217728515.

[8] Ning, Y., Wei, K., Cheng, L., Hu, J., and Xiang, Q., 2017, Fluorometric aptamer based determination of adenosine triphosphate based on deoxyribonuclease I-aided target recycling and signal amplification using graphene oxide as a quencher, *Microchim. Acta*, 184 (6), 1847–1854.

[9] Qu, F., Sun, C., Lv, X., and You, J., 2018, A terbium-based metal-organic framework@gold nanoparticle system as a fluorometric probe for aptamer based determination of adenosine triphosphate, *Microchim. Acta*, 185 (8), 359.

[10] Liu, X., Lin, B., Yu, Y., Cao, Y., and Guo, M., 2018, A multifunctional probe based on the use of labeled aptamer and magnetic nanoparticles for fluorometric determination of adenosine 5'-triphosphate, *Microchim. Acta*, 185 (4), 243.

[11] Khlyntseva, S.V., Bazel', Y.R., Vishnikin, A.B., and Andruch, V., 2009, Methods for the determination of adenosine triphosphate and other adenine nucleotides, *J. Anal. Chem.*, 64 (7), 657–673.

[12] Huang, Y.F., and Chang, H.T., 2007, Analysis of adenosine triphosphate and glutathione through gold nanoparticles assisted laser desorption/ionization mass spectrometry, *Anal. Chem.*, 79 (13), 4852–4859.

[13] Srivastava, P., Razi, S.S., Ali, R., Srivastav, S., Patnaik, S., Srikrishna, S., and Misra, A., 2015, Highly sensitive cell imaging "Off–On" fluorescent probe for mitochondria and ATP, *Biosens. Bioelectron.*, 69, 179–185.

[14] Chen, J.R., Jiao, X.X., Luo, H.Q., and Li, N.B., 2013, Probe-label-free electrochemical aptasensor based on methylene blue-anchored graphene oxide amplification, *J. Mater. Chem. B*, 1 (6), 861–864.

[15] Yi, Q., and Yu, W., 2009, Nanoporous gold particles modified titanium electrode for hydrazine oxidation, *J. Electroanal. Chem.*, 633 (1), 159–164.

[16] Yáñez-Sedeño, P., Villalonga, R., and Pingarrón, J.M., 2015, "Electroanalytical Methods Based on Hybrid Nanomaterials" in *Encyclopedia of Analytical Chemistry*, John Wiley & Sons, Ltd, Chichester, UK, 1–18.

[17] Goud, K.Y., Moonla, C., Mishra, R.K., Yu, C., Narayan, R., Litvan, I., and Wang, J., 2019, Wearable electrochemical microneedle sensor for continuous monitoring of levodopa: Toward Parkinson management, *ACS Sens.*, 4 (8), 2196–2204.

[18] Villalonga, A., Pérez-Calabuig, A.M., and Villalonga, R., 2020, Electrochemical biosensors based on nucleic acid aptamers, *Anal. Bioanal. Chem.*, 412 (1), 55–72.

[19] Mashhadizadeh, M.H., Naseri, N., and Mehrgardi, M.A., 2017, A simple non-enzymatic strategy for adenosine triphosphate electrochemical aptasensor using silver nanoparticle-decorated graphene oxide, *J. Iran. Chem. Soc.*, 14 (9), 2007–2016.

[20] Zheng, J., Li, X., Wang, K., Song, J., and Qi, H., 2020, Electrochemical nanoaptasensor for continuous monitoring of ATP fluctuation at subcellular level, *Anal. Chem.*, 92 (16), 10940–10945.

[21] Metters, J.P., Kadara, R.O., and Banks, C.E., 2011, New directions in screen printed electroanalytical sensors: An overview of recent developments, *Analyst*, 136 (6), 1067.

[22] Mulyasuryani, A., and Dofir, M., 2014, Enzyme biosensor for detection of organophosphate pesticide residues base on screen printed carbon electrode (SPCE)-bovine serum albumin (BSA), *Engineering*, 6 (5), 230–235.

[23] Taleat, Z., Khoshroo, A., and Mazloum-Ardakani, M., 2014, Screen-printed electrodes for biosensing: A review (2008–2013), *Microchim. Acta*, 181 (9), 865–891.

[24] Dorledo de Faria, R.A., Messaddeq, Y., Heneine, G.D., and Matencio, T., 2019, Application of screen-printed carbon electrode as an electrochemical transducer in biosensors, *Int. J. Biosens. Bioelectron.*, 5 (1), 1–2.

[25] Kanyong, P., Rawlinson, S., and Davis, J., 2016, Gold nanoparticle modified screen-printed carbon arrays for the simultaneous electrochemical analysis of lead and copper in tap water, *Microchim. Acta*, 183 (8), 2361–2368.

[26] Dridi, F., Marrakchi, M., Gargouri, M., Saulnier, J., Jaffrezic-Renault, N., and Lagarde, F., 2017, "Nanomaterial-Based Electrochemical Biosensors for Food Safety and Quality Assessment" in *Nanobiosensors*, Eds. Grumezescu, A.M., Academic Press, Cambridge, US, 167–204.

[27] Zhao, X., Mai, Z., Kang, X., and Zou, X., 2008, Direct electrochemistry and electrocatalysis of horseradish peroxidase based on clay–chitosan-gold nanoparticle nanocomposite, *Biosens. Bioelectron.*, 23 (7), 1032–1038.

[28] Bernardo-Boongaling, V.R.R., Serrano, N., García-Guzmán, J.J., Palacios-Santander, J.M., and Díaz-Cruz, J.M., 2019, Screen-printed electrodes modified with green-synthesized gold nanoparticles for the electrochemical determination of aminothiols, *J. Electroanal. Chem.*, 847, 113184.

[29] Kashefi-Kheyrabadi, L., and Mehrgardi, M.A., 2013, Aptamer-based electrochemical biosensor for detection of adenosine triphosphate using a

nanoporous gold platform, *Bioelectrochemistry*, 94, 47–52.

[30] Miller, J.N., 1991, Basic statistical methods for analytical chemistry. Part 2. Calibration and regression methods, A review, *Analyst*, 116 (1), 3–14.

[31] Skoog, D.A., Holler, F.J., and Nieman, T.A., 1998, *Principles of Instrumental Analysis*, 5th Ed., Saunders College Publishing, Philadelphia, US.

[32] Hwu, S., Garzuel, M., Forró, C., Ihle, S.J., Reichmuth, A.M., Kurdzesau, F., and Vörös, J., 2020, An analytical method to control the surface density and stability of DNA-gold nanoparticles for an optimized biosensor, *Colloids Surf., B*, 187, 110650.

[33] Zhao, P., Li, N., and Astruc, D., 2013, State of the art in gold nanoparticle synthesis, *Coord. Chem. Rev.*, 257 (3-4), 638–665.

[34] Apyari, V.V., Arkhipova, V.V., Dmitrienko, S.G., and Zolotov, Y.A., 2014, Using gold nanoparticles in spectrophotometry, *J. Anal. Chem.*, 69 (1), 1–11.

[35] Fatimah, S., Haryati, I., and Jamaludin, A., 2009, Pengaruh Uranium terhadap Analisis Thorium menggunakan Spektrofotometer UV-Vis, *Seminar Nasional V SDM Teknologi Nuklir*, 5 November 2009, Yogyakarta, 573–578.

[36] Yáñez-Sedeño, P., and Pingarrón, J.M., 2005, Gold nanoparticle-based electrochemical biosensors, *Anal. Bioanal. Chem.*, 382 (4), 884–886.

[37] Ren, L., Xu, P., Zhang, P., Qin, Z., Zhang, Y., and Jiang, L., 2021, Label-free fluorescence aptasensor based on AuNPs and CQDs for the detection of ATP, *AIP Adv.*, 11, 015316.

[38] Shahsavar, K., Hosseini, M., Shokri, E., Ganjali, M.R., and Ju, H., 2017, A sensitive colorimetric aptasensor with a triple-helix molecular switch based on peroxidase-like activity of a DNAzyme for ATP detection, *Anal. Methods*, 9 (32), 4726–4731.

Inhibition of Carbon Steel Corrosion by Some New Organic 2-Hydroselenoacetamide Derivatives in HCl Medium

Alaa Abdel Khaleq Khalib[1], Hanan Abdul Jaleel Al-Hazam[2], and Attared Fadhel Hassan[2*]

[1]*Iraqi Cement State Company, Basrah, Iraq*

[2]*Department of Chemistry, College of Science, University of Basrah, Basrah 61004, Iraq*

Abstract: *This study aims to prepare 2-hydroselenoacetamide derivatives (**5-8**) to use some of these compounds as corrosion inhibition for carbon steel in 1 M HCl. The compound $C_{10}H_{10}NO_2Cl$ **1** was prepared by reacting between* p*-aminoacetophenone with chloroacetyl chloride, and then reacted **1** with substituted benzaldehyde to obtain the corresponding derivatives as $C_{17}H_{13}N_2O_4Cl$ **2**, $C_{18}H_{16}NO_4Cl$ **3** and $C_{19}H_{18}NO_4Cl$ **4**. The last step in this study was conducted to obtain the organic hydroselenoacetamide such as $C_{10}H_{11}NO_2Se$ **5**, $C_{17}H_{14}N_2O_4Se$ **6**, $C_{18}H_{17}NO_4Se$ **7**, and $C_{19}H_{19}NO_4Se$ **8** by reacting chloroaminochalcone and sodium hydrogen selenide. All compounds were characterized by Fourier Transform Infrared Spectroscopy (FTIR), proton nuclear magnetic resonance (^{1}H-NMR), and elemental analysis (CHN). The corrosion inhibition activity of $C_{17}H_{14}N_2O_4Se$ **6**, $C_{18}H_{17}NO_4Se$ **7** and $C_{19}H_{18}NO_4Cl$ **4** for carbon steel in 1 M HCl solution was investigated by using weight loss methods and electrochemical study. The activation energy of the corrosion reaction was also calculated. The effect of different concentrations and temperatures on inhibition efficiency was investigated. The results showed that the corrosion rate decreased with the increase of the concentration of inhibitors, while the inhibition efficiency and covered area decreased with an increase in the temperature. Polarization studies demonstrated that the inhibitors were of mixed type. The purpose of this study was to prepare, characterize and evaluate the corrosion inhibition activity of hydroselenide compounds for carbon steel in 1 M HCl.*

Keywords: *corrosion inhibition; 2-hydroselenoacetamide; chalcone; acid medium*

■ INTRODUCTION

The composition of the amides has attracted considerable attention from researchers because of their importance in biochemistry and organic chemistry fields, their usage as intermediate compounds in organic synthesis, and wide range of industrial chemical applications [1]. The association of amide is significant as it plays as the main component of peptides, polymers, natural compounds products, and pharmaceuticals [2]. Many amide derivatives have been used as antifungals, antihistamines, worms, and antibacterial agents. For example, the compound *N*-aryl-2-chloroacetamides acts as an antimicrobial such as herbicides, antifungals, and disinfectants [3].

The chloroacetylation of *p*-aminoacetophenone with chloroacetyl chloride occurred in the presence of glacial acetic acid [4] or in benzene and trimethylamine [5] to give the compound no. **1** as shown in Scheme 1. The *N*-substituted chloroacetamides could be converted to chalcones through Claisen-Schmidt condensation [6]. Mostly chalcones are aromatic ketones that consist of two aromatic rings that are linked by a three-carbon α,β unsaturated carbonyl system. Chalcone has a complete delocalization π- electron system on conjugated double bond (C=C) and two phenyl rings. Therefore, the redox potential for the molecules decreases while their stability increases [7]. The Claisen-Schmidt condensation is a crossed aldol condensation reaction between ketone
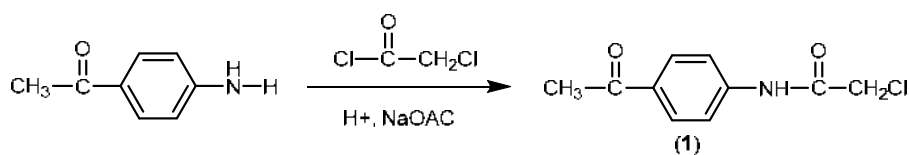
Scheme 1. Synthesis of *N*-aryl chloroacetamide (**1**)

possessing at least one α-hydrogen with the aldehyde. The reaction is proceeded via the base-catalyzed formation of enolate of the ketone. This enolate attacks the aldehyde carbon and forms the adduct. Chalcone is then formed from this adduct by the elimination of water molecule [8].

Selenium and its organic compounds are of great interest due to their various applications in some industrial fields, for example, platinum group metal complexes of seleno ligand were developed as catalysts for different reactions [9-10]. Metal selenolates exhibit as versatile single–sources of molecular precursors for the synthesis of nanoparticles and deposition of thin films of metal selenides [11-13]. Selenium and its compounds are used as oxidizing agents for organic compounds [14]. Selenium can be introduced as a nucleophile/electrophile or even as a radical in chemo–, regio– and stereo–selective manners [15].

Selenol is an organic compound that contains C-Se-H functional group, sometimes called selenothiols or selenomercaptains. Selenols are more acidic than corresponding sulfur analogous because the energy of Se-H bond is weaker than S-H bond and thus oxidized easily and serve as Hydrogen atom donors. The RSe⁻ is a good nucleophile as well as an excellent leaving group. Also, it binds metal strongly, which is used for heavy metal detoxification [16]. There are different methods for the synthesis of selenols or selenolates [17-18], one of these methods is the reaction of organic halides with sodium hydrogen selenides or sodium selenides [19], as shown in Scheme 2.

Corrosion is a process of gradual damage to material (mostly metals) through a chemical reaction with their

environment, causing the outer surface of the metal to change and breaking down the crystal structure and dissolution in the outer environment. It is a continuous process that cannot be stopped, but it can be reduced by using various preventive systems, including the use of organic compounds, which can easily be adsorbed onto the steel surface and lead to the formation of a protective organic film on the electrode surface and reduce the corrosion rate [20]. The efficiency of organic compounds as an inhibitor mainly depends on the presence of elements of groups V and VI of the periodic table, such as N, P, As, S, O, and Se, which have lone electron pairs, and the conjugated system as well as the presence of π-electrons in their structure which can strongly be adsorbed on the metal surface through to donor-acceptor process to form a protective layer [21-22]. Some organic compounds have been synthesized and evaluated as corrosion inhibition in acidic media containing heteroatoms, and the conjugated system enhances the chemical adsorption process involving electrons sharing between the vacant d-orbitals of iron and the lone electron pairs of the heteroatoms to create a strong coordinating bond which improves anti-corrosion performance [21-23]. The aim of this study is to prepare and characterize some novel organic seleno compounds and use them as corrosion inhibition for carbon steel in a 1 M HCl solution.

■ **EXPERIMENTAL SECTION**

Materials

The chemicals included *p*-amino acetophenone, 4-nitrobenzaldehyde, 3,5-dimethoxybenzaldehyde, and

X= substituents
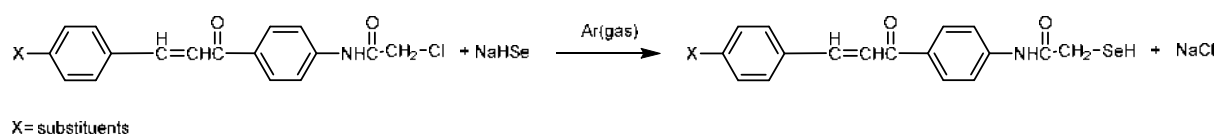
Scheme 2. Synthesis 2-hydroseleno-*N*-arylacetamide

sodium acetate were purchased from Merck. Meanwhile, glacial acetic acid, ethanol, toluene, trimethylamine (Sinopharm Chemical Reagent Co., Ltd.), chloroacetyl chloride, sodium borohydride (Sigma Aldrich), selenium powder, 3-hydroxybenzaldehyde (Alpha) were also utilized in this study. All chemicals were used as received with no purification. Carbon steel specimens were used in this work had the composition of (wt.%) [Fe:99.68, C:0.037, Mn:0.26, P:0.005, S:0.002]. The specimens were rubbed successively using emery with grade 600 to 1200 mesh/min, then washed with distilled water, cleaned with acetone then fired in a hot air blower. The working electrode was a 7.5 cm long steam for electrochemical measurement to provide an exposed surface area of 1.0 cm², while 2.5 × 2.0 × 0.2 cm³ were used in weight loss measurements. The 1 M HCl test solution was prepared from analytical grade reagent (37%) and deionized water.

Instrumentation

The elemental analysis of new synthesis compounds was done by (CE-440) Elemental Analyzer. The IR spectra were measured using FTIR-8400S SHIMADZU-Japan and ¹H-NMR was recorded on BUKER (300 MHz) with DMSO-d₆ solvent. All melting points were measured with a Gallen Kamp melting point apparatus and uncorrected. The progress of the reaction was monitored with thin-layer chromatography (TLC).

Procedure

Synthesis N-(4-acetylphenyl)-2-chloroacetamide (1)
Prepared *N*-acetylphenyl-2-chloroacetamide (1) by two methods. A solution of chloroacetyl chloride (1.13 mL) in glacial acetic acid was added to 1.35 g *p*-aminoacetophenone in 10 mL glacial acetic acid at room temperature, the solution was stirred for 30 min, and then CH₃COONa (10 mL) 0.5 M was added to the mixture with constant stirring for another 30 min. The crude product was filtered, dried, and then recrystallized by ethanol [4].

A mixture of *p*-aminoacetophenone (1.35 g) with chloroacetyl chloride (1.19 mL) in 25 mL of toluene was added 3–4 drops of triethylamine. The mixture solution was refluxed for 4 h. The progress of the reaction was monitored by TLC with the mobile phase of toluene: acetone (7:3). A buff-colored solid-state intermediate was

obtained and recrystallized by toluene [24].

Synthesis 2-chloro-N-(4-(3-(4-X-phenyl)acryloyl)phenyl) acetamide (2)

The mixture of equimolar quantities of (**1**) (2.11 g) *N*-(4-acetylphenyl)-2-chloroacetamide with substituted benzaldehyde (**2**), i.e., 4-nitrobenzaldehyde (1.51 g), (**3**) 3,4-dimethoxybenzaldehyde (1.67 g), (**4**) 3-hydroxy benzaldehyde (1.22 g) in ethanol was added by 20% sodium hydroxide solution slowly dropwise with stirring. After completing the addition, stirring continued for 6 h and then left overnight. The mixture was added to ice water, and then measured the pH of the solution. The obtained product was recrystallized from ethanol [25].

Synthesis 2-hydroseleno-N-(4-(3-(4-X-phenyl)acryloyl) phenyl)acetamide

The NaBH₄ (0.225 g: 0.0061 mol) was dissolved in 25 mL H₂O then added Se 0.23 g: 0.0029 mol while stirring and suspended in 25 mL H₂O under argon atmosphere. A severe reaction occurred in less than 10 min, and H₂ gas was immediately released. A colorless solution of sodium hydrogen selenide NaHSe was formed.

Solution of NaHSe was added to 2-chloro-*N*-(4-(3-(4-X-phenyl)acryloyl)phenyl)acetamide 2.09 g: 0.0061 mol in 50 mL absolute ethanol, after about 45 min stirred,
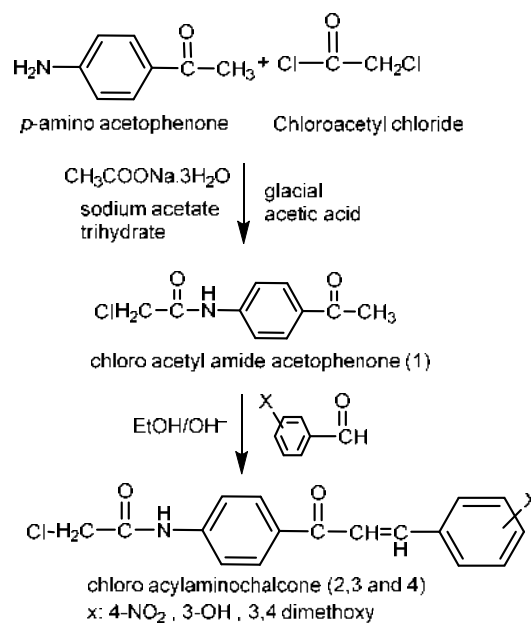
Scheme 3. Preparation of chloroaminochalcone
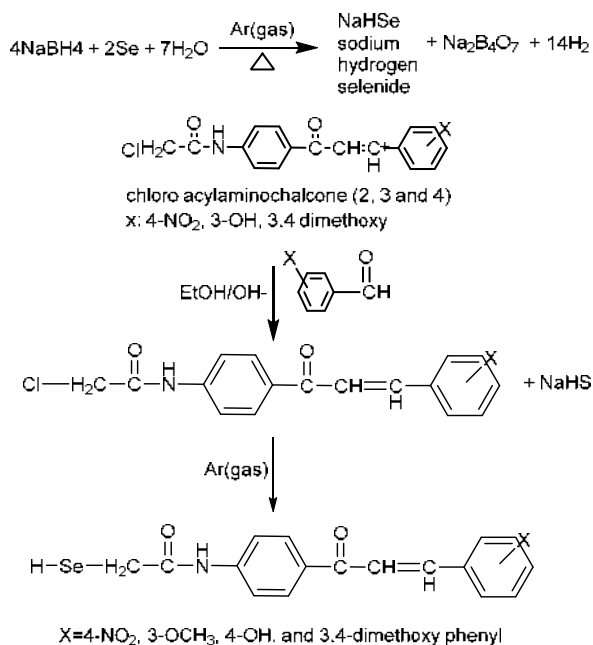
Scheme 4. Preparation of 2-hydroseleno-*N*-(X-phenyl)acryloyl)phenyl)acetamide

the reddish color precipitate was obtained, filtered, and washed several times with ethanol and dried (Schemes 3 and 4).

***N*-(4-Acetylphenyl)-2-chloroacetamide as compound 1.** Off-white. Yield: 90%. m.p 153–155 °C. IR ν cm^{-1} (KBr): 3286 (NH 2°-amide), 1654 (C=O amide), 725 (C-Cl). ^{1}H-NMR spectra (ppm) DMSO-d_6 solvent: 10.65 (1H, NH amide), 7.72 (4H aromatics), 4.34 (2H CH$_2$), 2.55 (3H CH$_3$). Anal. calc. for C$_{10}$H$_{10}$NO$_2$Cl: C, 56.75; H, 4.76; N, 6.62. Found: C, 56.16; H, 4.49; N, 6.36.

2-Chloro-I-(4-(3-(4-nitrophenyl)acryloyl)phenyl)-2-chloroacetamide as compound 2. Brown. Yield: 70%. m.p 200–202 °C. IR ν cm^{-1} (KBr): 3387 (NH amide), 1697 (C=O amide), 1635 (C=O chalcone), 632 (C-Cl). ^{1}H-NMR spectra (ppm) DMSO-d_6 solvent: 6.72 (1H NH amide), 7.69 (8H aromatics), 3.39 (2H CH$_2$), 6.54 (2H CH=CH). Anal. calc. for C$_{17}$H$_{13}$N$_2$O$_4$Cl: C, 59.23; H, 3.80; N, 8.13. Found: C, 58.96; H, 3.72; N, 7.96.

2-Chloro-*N*-(4-(3-(4-hydroxy-3-methoxyphenyl) acryloyl)phenyl)acetamide as compound 3. Brown. Yield: 40%. m.p 185–188 °C. IR ν cm^{-1} (KBr): 3394 (1H NH amide), 1681 (C=O amide), 1651 (C=O chalcone), 702 (C-Cl). ^{1}H-NMR spectra (ppm) DMSO-d_6 solvent: 9.78 (NH amide), 6.95 (8H aromatics), 2.64 (2H CH$_2$),

3.95 (3H OCH$_3$). Anal. calc. for C$_{18}$H$_{16}$NO$_4$Cl: C, 62.52; H, 4.66; N, 4.05; Found: C, 61.99; H, 4.65; N, 3.9.

2-Chloro-*N*-(4-(3-(3,4-dimethoxyphenyl)acryloyl) phenyl)acetamide as compound 4. Yellow. yield: 80%. m.p 138–140 °C. IR ν cm^{-1} (KBr): 3352 (NH amide), 1643 (C=O amide), 1600 (C=O chalcone), 721 (C-Cl). ^{1}H-NMR spectra (ppm) DMSO-d_6 solvent: 7.97 (1H NH amide), 6.13 (8H aromatics), 3.36 (2H CH$_2$), 3.83 (6H 2(OCH$_3$)). Anal. calc. for C$_{19}$H$_{18}$NO$_4$Cl: C, 3.42; H, 5.04; N,.89; Found: C, 62.96; H, 5.11; N, 3.6.

***N*-(4-Acetylphenyl)-2-hydroselenoacetamide as compound 5.** Off-white. Yield: 70%. m.p 190–192 °C. IR ν cm^{-1} (KBr): 3348 (NH amide), 1651 (C=O amide), 2370 (Se-H). ^{1}H-NMR spectra (ppm) DMSO-d_6 solvent: 10.97 (1H NH 2° amide), 7.75 (4H aromatic), 3.36 (2H CH$_2$ + 1H Se-H), 2.48 (3H CH$_3$). Anal. calc. for C$_{10}$H$_{11}$NO$_2$Se: C, 46.89; H, 4.33; N, 5.47. Found: C, 46.49; H, 3.92; N, 5.16.

2-Hydroseleno-*N*-(4-(3-(4-nitrophenyl)acryloyl) phenyl)acetamide as compound 6. Dark red. Yield: 60%. m.p 213–215 °C. IR ν cm^{-1} (KBr): 3383 (NH amide), 1635 (C=O amide), 1600 (C=O chalcone), 2470 (Se-H). ^{1}H-NMR spectra (ppm) DMSO-d_6 solvent: 9.88 (1H NH amide), 7.14 (8H aromatics), 4.38 (2H CH$_2$ + 1H Se-H), 6.54 (2H CH=CH). Anal. calc. for C$_{17}$H$_{14}$N$_2$O$_4$Se: C, 52.45; H, 3.63; N, 7.20. Found: C, 52.13; H, 4.14; N, 7.03.

2-Hydroseleno-*N*-(4-(3-(4-hydroxy-3-methoxyphenyl)acryloyl)phenyl)acetamide as compound 7. Dark red. Yield: 41%. IR ν cm^{-1} (KBr): 3406 (NH amide), 1735 (C=O amide), 1654 (C=O chalcone), 2340 (Se-H). ^{1}H-NMR spectra (ppm) DMSO-d_6 solvent: 8.66 (1H NH amide), 6.53 (8H aromatics), 4.30 (2H CH$_2$ + 1H Se-H), 3.76 (3H OCH$_3$). Anal. calc. for C$_{18}$H$_{17}$NO$_4$ClSe: C, 55.39; H, 4.39; N, 3.59. Found: C, 54.93; H, 4.55; N, 3.40.

2-Hydroseleno-*N*-(4-(3-(3,4-dimethoxyphenyl) acryloyl)phenyl)acetamide as compound 8. Dark red. Yield: 60%. IR ν cm^{-1} (KBr): 3363 (NH amide), 1658 (C=O amide), 1610 (C=O chalcone), 2340 (Se-H). ^{1}H-NMR spectra (ppm) DMSO-d_6 solvent: 8.72 (1H NH amide), 7.42 (8H aromatics), 3.36 (2H CH$_2$ + 1H Se-H), 2.52 (6H 2(OCH$_3$)). Anal. calc. for C$_{19}$H$_{19}$NO$_4$Se: C, 56.44; H, 4.74; N, 3.46. Found: C, 55.99; H, 4.69; N, 3.11.

Corrosion activity

Weight loss method. The weight loss measurements have been used to investigate the corrosion behavior of carbon steel alloy in the presence and absence of inhibitors. The inhibition efficiency (η%) and surface coverage (θ) were calculated by the Eq. (1) and (2)

$$\eta\% = \frac{C_R - C_{Ri}}{C_R} \times 100 \tag{1}$$

$$\theta = \frac{C_R - C_{Ri}}{C_R} \tag{2}$$

where C_R = Corrosion rate in absence of organic hydroselenide compounds, C_{Ri} = corrosion rate values in presence of hydroselenide compounds. The C_R of carbon steel was calculated in acidic medium by the Eq. (3)

$$C_R = \frac{\Delta W}{At} \tag{3}$$

where ΔW = weight loss for the ingot (mg), A = the area of the submerged surface of the specimen (cm^2), t = the time of immersion (h).

Electrochemical measurements (Tafel method). The potentiodynamic polarization (PDP) with computer-controlled potentiostat (model Corr Test-(5350) was used to perform electrochemical measurements. It examines the corrosion of carbon steel alloy in 0.1 M HCl solution in the absence and presence of a different concentration of inhibitor 2-chloro-*N*-(4-(3-(3,4,-dimethoxyphenyl) acryloyl)phenyl)acetamide and 2-hydroseleno-*N*-(4-(3-(4-nitrophenyl)acryloyl)phenyl)acetamide compounds at room temperature and different concentration of inhibitors, or at different temperatures and a concentration 100 ppm of inhibitors.

Electrochemical cell. In this study, an electrochemical cell consisting of three electrodes arranged as follows: The working electrode which represents alloy carbon steel with dimensions of (5 × 1.5 × 0.2) cm^3, which represents the submerged part of the alloy. Platinum Auxiliary Electrode and Saturated Calomel Electrode (SCE) with a fiber–loggin capillary represent as a Reference Electrode (RE). The device is programmed by entering information that includes the data of measurement, the thickness of the ingot, the type of operation, the equivalent weight of the metal, the type and density of the metal. The time required to conduct an examination is about 20 min, after which the cell and loggin tube is emptied, and the process is repeated three times to ensure the accuracy of the results. The examination process is carried out in the absence and presence of different concentrations of inhibitors. The corrosion rate C_{Rmpy} was evaluated from Eq. (4).

$$C_{Rmpy} = \frac{0.13 \times I_{corr} \times Eq.wt}{A \times D} \tag{4}$$

where I_{corr} is corrosion current density in μA cm^{-2}, Eq.wt is the equivalent weight of the specimen, A is the total specimen area, and D is the density of the specimen.

■ **RESULTS AND DISCUSSION**

CHN Measurement

All the prepared compounds showed agreement with the practical and theoretical results of elemental (CHN) analysis, indicating the validity of the proposed chemical structures for the prepared compounds. All results of CHN analysis are listed in Table 1.

Table 1. The CHN data of selected compounds

No.	Empirical formula	Elemental analysis found (calc)		
		% C	% H	% N
1	$C_{10}H_{10}NO_2Cl$	56.16(56.75)	4.49(4.76)	6.36(6.62)
2	$C_{17}H_{13}N_2O_4Cl$	58.96(59.23)	3.72(3.80)	7.96(8.13)
3	$C_{18}H_{16}NO_4Cl$	61.99(62.52)	4.65(4.66)	3.90(4.05)
4	$C_{19}H_{18}NO_4Cl$	62.96(63.42)	5.11(5.04)	3.69(3.89)
5	$C_{10}H_{11}NO_2Se$	46.49(46.89)	3.92(4.33)	5.16(5.47)
6	$C_{17}H_{14}N_2O_4Se$	52.13(52.45)	4.14(3.63)	7.03(7.20)
7	$C_{18}H_{17}NO_4Se$	54.93(55.39)	4.55(4.39)	3.40(3.59)
8	$C_{19}H_{19}NO_4Se$	55.99(56.44)	4.69(4.74)	3.11(3.46)

FTIR Spectra

The FTIR spectra for chalcones and their hydroselenides have been studied and analyzed in terms of functional groups. The FTIR spectrum of compounds **1**-**4** exhibited strong absorption bands that appeared at 3286–3394 and 1643–1697 cm^{-1} belonging to stretching vibration for N-H and C=O, respectively [26]. The absorption bands appear at 632–725 cm^{-1} and belong to C-Cl stretching vibration for 2-chloro-*N*-phenylacetamide derivatives [27]. The absorption bands around 1600–1651 cm^{-1} related to the carbonyl group conjugated with double bond, which indicates the formation of chalcones [28-29].

The FTIR spectrum for compounds **5**-**8** shows absorption band appears at 532–640 and 2340–2470 cm^{-1} belonging to stretching vibration for C-Se and Se-H indicating to formation 2-hydroselenide [30-31], other unsymmetrical stretching vibration for C=C aromatic, C-H aliphatic, C-H aromatic, and C=C aliphatic were found at expected positions [28-29]. Fig. 1 showed the IR-spectra of compound **6**.
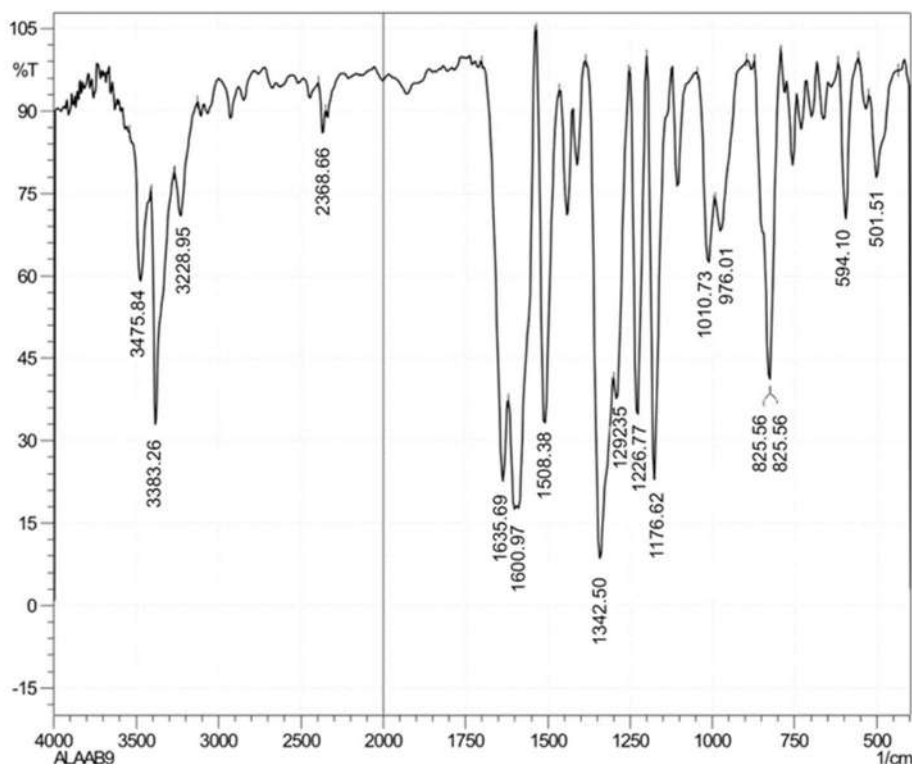
^{1}H-NMR Spectra

^{1}H-NMR spectra of compounds **1**-**4** displayed signals at 7.97–10.68 ppm belonging to NH amide [32], phenyl protons and alkene protons give multiple signals extent 6.13–8.35 ppm [30], also methylene protons appear at 3.36–4.33 ppm [34] in the low field because methylene groups attached chloride atom; high electronegativity, that increase chemical shift.

The compounds **5**-**8** displayed signals at 8.66–10.97 ppm belonging to NH amide. Methylene protons and the proton of Se-H group appears at 3.36–4.45 ppm [35] at the high field because of the disappearance chloride atom and are attached to the selenium atom, which is less electronegativity than the chloride atom. Fig. 2. The ^{1}H-NMR for compound **5**.

Weight Loss Studies

Effect of inhibitor concentration

In this study, the weight loss method was used to evaluate the effect of corrosion of carbon steel immersed in 1 M hydrochloric acid solution for 48 h at 300 K.

Fig 1. The FTIR spectra of compound **6**
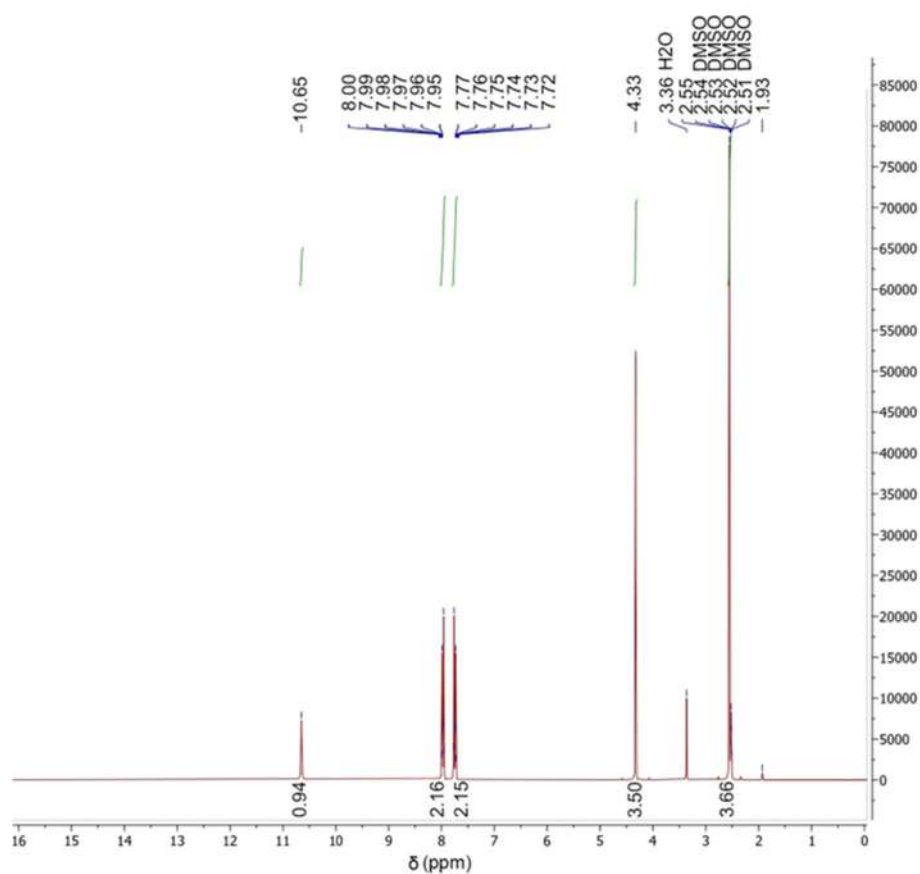
Fig 2. The ^{1}H-NMR for compound **5**

Table 2. Weight loss method results for carbon steel alloy in different concentrations at 300 K

Inhibitors	Inhibitors concentration (ppm)	C_R (mg cm^{-2} h^{-1})	θ	$\eta\%$
(0) inhibitor	0.0	0.0138	-	-
$C_{18}H_{17}NO_4Se$ (**7**)	50	0.0113	0.3864	38.64
	100	0.0106	0.4270	42.70
	150	0.0096	0.4783	47.83
	200	0.0092	0.4994	49.94
	300	0.0091	0.5081	50.81
$C_{17}H_{14}N_2O_4Se$ (**6**)	50	0.0136	0.2648	26.48
	100	0.0126	0.3189	31.89
	150	0.0111	0.4000	40.00
	200	0.0103	0.4432	44.32
	300	0.0095	0.4864	48.64

Different concentrations of selenides lead to different values of $\eta\%$, C_R, and θ were listed in Table 2. The increase of hydroselenide concentration causes the increase of $\eta\%$ at 300 K.

The obtained result showed that the hydroselenide compounds **6** and **7**, which are used as inhibitors in this study, inhibit the corrosion of carbon steel in the acidic medium. It is noted that the corrosion rate decreased, and the inhibitor efficiency increased with the increasing concentration of inhibitors, as shown in Table 2. These

results show that the presence of an inhibitor works to form a thin layer that protects the anodic and cathodic region and works to reduces oxidation reaction, and limits corrosion processes by preventing the arrival of corrosion to the surface of carbon steel [20-23].

The action of inhibitors can be explained by the molecular adsorption of inhibitors on the surface of the alloy. The effective adsorption is a result of the interact of π-electrons of multiple bonds and aromatic system of inhibitor molecules with the metal, or interaction of lone pair electron present on highly electronegative atoms (N and O) in the structure of inhibitors molecules with d-orbital of iron [21-23,33].

Referring to Table 2, we find that the inhibition efficiency of compound **7** (50.81%) is higher than that of compound **6** (48.64%) at the same concentration, 300 ppm, as shown in Fig. 3, due to the presence of electron releasing groups, –OH and –OCH$_3$, compared to the electron-withdrawing (–NO$_2$) group in compound **6**. So that the electron density on the phenyl ring in compound **7** is higher, which improves the adsorption process and increases the surface area covered by the inhibitor, unlike compound **6**, where the presence of the electron-withdrawing group reduces the electron density on the phenyl group, reducing the adsorption process and thus reducing the efficiency of the inhibitor [21-23].

Effect of temperature on inhibition efficiency

A weight-loss experiment has been performed in the temperature range between 300–320 K in the presence and absence of optimum concentration of inhibitors. Table 3 lists corrosion rate (C$_R$), inhibition efficiency (η%) and surface coverage (θ) at each temperature.
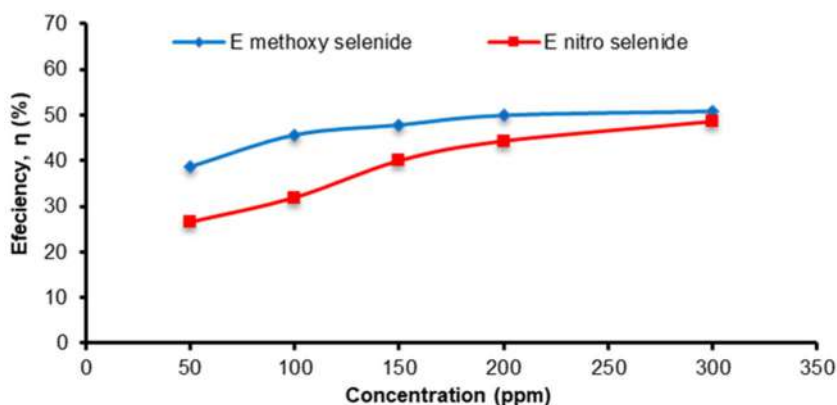
Fig 3. Relationship between inhibitor efficiency with increasing inhibitor concentration for nitro selenide (**6**) and methoxy selenide (**7**)

Table 3. Weight loss results for carbon steel alloy in different grades and at a concentration of 100 ppm of inhibitors in 1 M HCl

Inhibitors	Temperature (K)	C$_R$ (mg cm^{-2} h^{-1})	θ	η%
(0) inhibitor	300	0.0138	-	-
	310	0.0143	-	-
	320	0.0225	-	-
	300	0.0049	0.6415	64.15
C$_{18}$H$_{17}$NO$_4$Se (**7**)	310	0.0068	0.5261	52.61
	320	0.0113	0.4977	49.77
	300	0.0066	0.5171	51.71
C$_{17}$H$_{14}$N$_2$O$_4$Se (**6**)	310	0.0083	0.4216	42.16
	320	0.0156	0.3066	30.66

In general, it can be seen that the increase in the temperature leads to an increase in the corrosion rate from 0.01367 mg cm^{-1} h^{-1} at 300 K to 0.0225 mg cm^{-1} h^{-1} at 320 K in the absence of inhibitor, and from (0.0066, 0.0048) mg cm^{-1} h^{-1} at 300K to (0.0113, 0.0156) mg cm^{-1} h^{-1} at 320 K for inhibitor **6** and **7**, respectively. Also, inhibition efficiency decreased with an increase in the temperature of the corrosion medium when the concentration was fixed, as shown in Fig. 4. This behavior is because the increase in temperature in the absence of an inhibitor increases the kinetics of the anodic and cathodic reactions, and the dissolution of metal becomes more important, as shown in Table 3 [22]. In the case of the presence of the inhibitor, the corrosion rate will increase but less than in the absence of inhibitor. This is because

the high temperature leads to an increase in the kinetic energy of inhibitor molecules and an increase in their diffusion, which reduces the efficiency of adsorption of the inhibitor on the surface of carbon steel as well as reduces the surface area covered by the inhibitor molecules which may be formed by heterogeneous layer [22,34-35].

Polarization Studies (Tafel Method)

The inhibition process of inhibitors **4** and **6** for corrosion of carbon steel in HCl 1 M at 300 K was studied by polarization experiments. The electrochemical parameter values are listed in Table 4. Fig. 5 shows the relationship between the corrosion efficiency and the concentration of inhibitors.
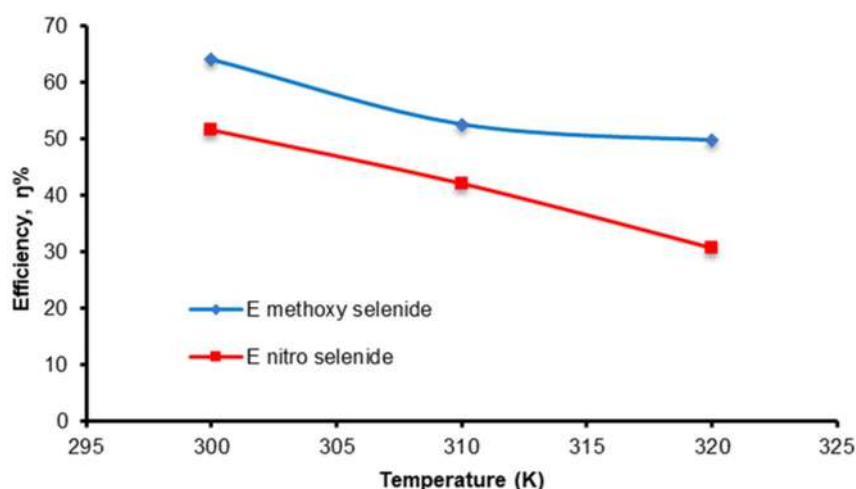

Fig 4. Relationship between the inhibition efficiency and temperature of the corrosion medium

Table 4. Tafel method results for carbon steel alloy in different concentrations of inhibitors in 1 M HCl at 300 K

| Inhibitors	Inhibitors concentration (ppm)	E_{corr} (mV)	I_{corr} (μ A cm^{-2})	C_R M_{py}	(%η)
(0) inhibitor	0.1 M	-0.54373	91.99	2.46	-
C$_{19}$H$_{18}$NO$_4$Cl (**4**)	50	-0.53325	81.44	2.18	11.38
	100	-0.50546	69.37	1.85	24.79
	150	-0.51232	77.44	2.07	15.85
	200	-0.50032	67.09	1.79	27.23
	300	-0.50677	57.15	1.52	38.21
C$_{17}$H$_{14}$N$_2$O$_4$Se (**6**)	50	-0.54465	67.55	1.80	26.82
	100	-0.50742	63.33	1.69	31.30
	150	-0.50086	55.86	1.49	39.26
	200	-0.51166	58.73	1.57	36.17
	300	-0.51200	49.37	1.32	46.34
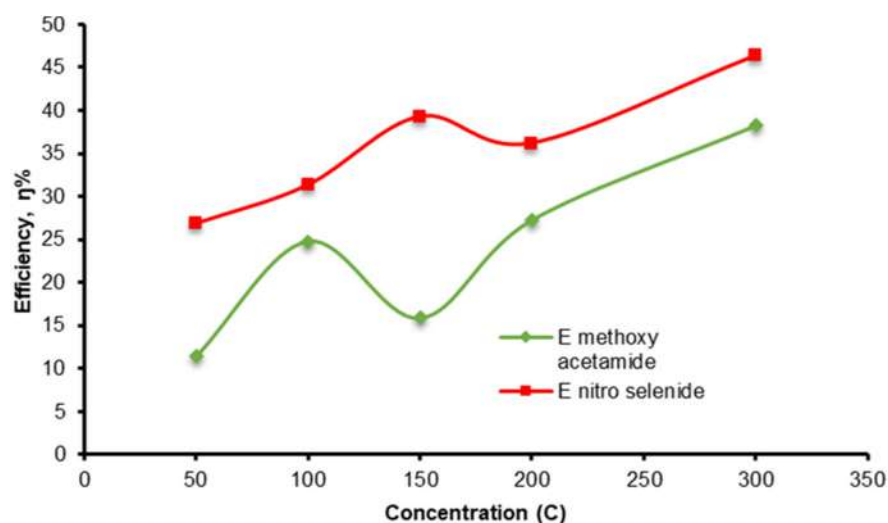
Fig 5. Relationship between the inhibition efficiency and concentration of the corrosion medium
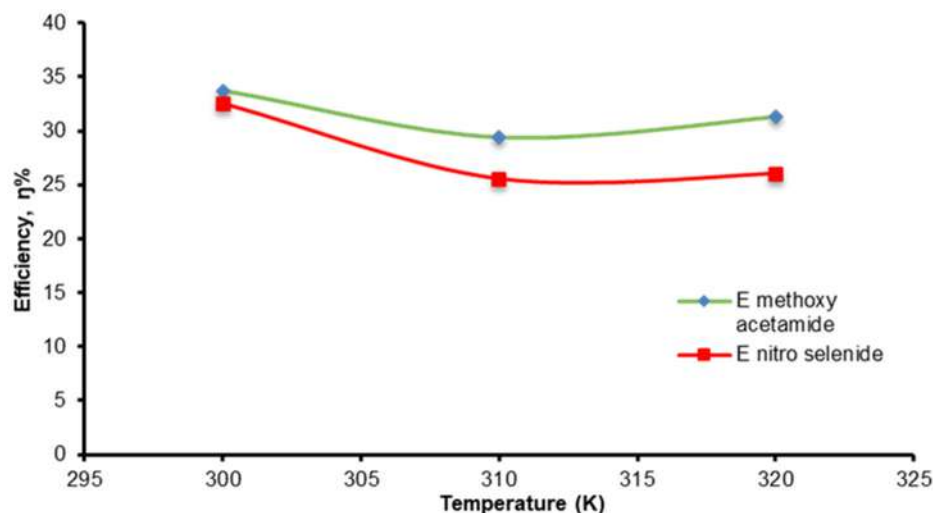

Fig 6. Relationship between the inhibition efficiency and temperature of the corrosion medium at 100 ppm

Referring to Table 4, it is evident that the value of corrosion current density is high in the absence of the inhibitor and decreases significantly with the addition of inhibitors; thus, the corrosion rate decreases. From the values of E_{corr}, it is noted that the behavior of both inhibitors is of a mixed type [36]. It shows in Fig. 5, which represents the Tafel curve for compounds **4** and **6**. The optimum concentration of both inhibitors **4** and **6** are 300 ppm, where the inhibition efficiency reached 38.21 and 46.34%, respectively.

Through the results obtained in Table 4 and Fig. 5, we note that the use of organoselenium inhibitor **6** gives a higher inhibition efficiency, 46.34%, than the chalcone (**4**)

(38.21%) at 300 ppm. The reason is due to the presence of Se heteroatoms in compound **6** which enhances the adsorption process on the surface of the alloy through the sharing between the lone electron pairs of the Se atom and empty d-orbital of iron to establish a strong coordinated bond [37].

Effect of temperature on inhibition efficiency

The effect of temperature on inhibition efficiency was studied at 300–320 K in the absence and presence of inhibitors by the Tafel method. The results are listed in Table 5. Fig. 6 shows the relationship between the inhibition efficiency and the temperature of the corrosion medium. Table 4 shows an increase in the I_{corr}

Table 5. Tafel method results for carbon steel alloy in 1 M HCl at different temperatures and 100 ppm of inhibitors

Inhibitors	Temperature (K)	E_{corr} (mV)	I_{corr} (μ A cm^{-2})	C_R M$_{py}$	(%η)
(0) inhibitor	300	-0.54373	191.99	2.46	-
	310	-0.54440	250.11	6.69	-
	320	-0.53933	290.11	7.76	-
$C_{19}H_{18}NO_4Cl$ (**4**)	300	-0.50677	127.15	3.40	33.72
	310	-0.50131	156.448	4.72	29.44
	320	-0.49248	199.16	5.33	31.31
$C_{17}H_{14}N_2O_4Se$ (**6**)	300	-0.51200	149.37	3.46	32.55
	310	-0.50121	182.14	4.87	27.20
	320	-0.50093	214.66	5.74	26.03

and, consequently, an increase in the corrosion rate with an increase in temperature from 300–320 K, which led to a decrease in the inhibition efficiency due to the dissolution of inhibitor layer adsorbed on the surface of the alloy as shown in Fig. 6.

The activation energy E_a of corrosion reaction in the absence and presence of inhibitors was calculated by the Arrhenius equation (5).

$$\ln C_R = \ln A - \frac{E_a}{RT} \qquad (5)$$

C_R is corrosion rate, A is the Arrhenius constant, T is absolute temperature, and R is the gas constant. Values of activation energy can be determined from the slope of the plots of ln C_R vs. 1/T. The values of E_a are 17.68, 20.419 and 23.75 kJ/mol in the absence, presence of inhibitors **4** and **6**, respectively. These values are less than 80 kJ/mol required for chemical adsorption. It can be concluded from the calculated E_a values that the adsorption of inhibitors is a physical type [38].

■ **CONCLUSION**

The corrosion inhibition performance of new organic hydroselenide derivatives of carbon steel in HCl 1 M solution was evaluated using weight loss technique and electrochemical studies. The result obtained showed that the inhibitors are classified as mixed-type. The corrosion rate decreases and the inhibition efficiency increases with the increase in the concentration of inhibitors. The inhibition efficiency and covered area decrease with increasing corrosion medium temperature in the absence and presence of an inhibitor. The study also showed that the inhibition efficiency of compound **7** is higher than

that of compound **6** due to the presence of –OH and –OCH$_3$ electron releasing groups on the benzene ring, which enhances the ability of adsorption of inhibitor on the surface of the alloy. From the calculated activation energy values of 17.68, 20.419, and 23.75 kJ/mol in the absence and presence of inhibitors, the adsorption process was classified as physical adsorption.

■ **REFERENCES**

[1] Olivares-Xometl, O., Likhanova, N.V., Domınguez-Aguilar, M.A., Hallen, J.M., Zamudio, L.S., and Arce, E., 2006, Surface analysis of inhibitor films formed by imidazolines and amides on mild steel in an acidic environment, *Appl. Surf. Sci.*, 252 (6), 2139–2152.

[2] Abdel-Latif, E., Fahad, M.M., El-Demerdash, A., and Ismail, M.A., 2020, Synthesis and biological evaluation of some heterocyclic scaffolds based on the multifunctional *N*-(4-acetylphenyl)-2-chloroacetamide, *J. Heterocycl. Chem.*, 57 (8), 3071–3081.

[3] Abdel-Latif, E., Fahad, M.M., and Ismail, M.A., 2020, Synthesis of *N*-aryl 2-chloroacetamides and their chemical reactivity towards various types of nucleophiles, *Synth. Commun.*, 50 (3), 289–314.

[4] Jayaramu, P.K., and Maralihalli, R.R., 2015, Synthesis and *in vitro* biological activities of chalcones and their heterocyclic derivatives, *Pharma Chem.*, 7 (8), 30–35.

[5] Shukla, M.B., Mahyavanshi, J.B., and Parmar, K.A., 2016, Synthesis and antimicrobial activities of

various *N*-phenyl-2-{[5-(3,4,5-trimethoxyphenyl)-1,3,4-oxidiazol-2-yl]sulfanyl}acetamides, *Indian J. Chem.*, 55B, 374–380.

[6] Velikorodov, A.V., Ionova, V.A., Temirbulatova, S.I., Titova, O.L., and Stepkina, N.N., 2013, Synthesis and application of chalcones to the preparation of heterocyclic structures, *Russ. J. Org. Chem.*, 49 (11), 1610–1616.

[7] Gaonkar, SL., and Vignesh, U.N., 2017, Synthesis and pharmacological properties of chalcones: A review, *Res. Chem. Intermed.*, 43 (11), 6043-6077.

[8] Gupta, J.K., Singh, S.V., and Gupta, K.R., 2017, Chalcones: A review on synthesis, chemical properties and biological activities, *Res. Pharm.*, 1 (2), 1–10.

[9] Yao, Q., Kinney, E.P., and Zheng, C., 2004, Selenium–ligated palladium(II) complexes as highly active catalysts for carbon-carbon coupling reactions: The Heck reaction, *Org. Lett.*, 6 (17), 2997–2999.

[10] Kumar, A., Rao, G.K., Saleem, F., and Singh A.K., 2012, Organoselenium ligands in catalysis, *Dalton Trans.*, 41 (39), 11949–11977.

[11] Bochmann, M., 1996, Metal chalcogenide materials: Chalcogenolato complexes as "single-source" precursors, *Chem. Vap. Deposition*, 2 (3), 85–96.

[12] Jain, V.K., 2019, Pyridyl and pyrimidyl chalcogenolates of coinage metals and their utility as molecular precursors for the preparation of metal chalcogenides, *New J. Chem.*, 43, 11034–11040.

[13] Sharma, R.K., Wadawale, A., Kedarnath, G., Manna, D., Ghanty, T.K., Vishwanadh, B., and Jain, V.K., 2014, Synthesis, structures and DFT calculations of 2-(4,6-dimethyl pyrimidyl)selenolate complexes of Cu(I), Ag(I) and Au(I) and their conversion into metal selenide nanocrystals, *Dalton Trans.*, 43 (17), 6525–6535.

[14] Waitkins, G.R., and Clark, C.W., 1945, Selenium dioxide: Preparation, properties, and use as oxidizing agent, *Chem. Rev.*, 36 (3), 235–289.

[15] Reich, H.J., and Hondal, R.J., 2016, Why nature chose selenium, *ACS Chem. Biol.*, 11 (4), 821–841.

[16] Reddy, C.C., and Massaro, E.J., 1983, Biochemistry of selenium: A brief overview, *Fundam. Appl. Toxicol.*, 3 (5), 431–436.

[17] Zhang, M., Lu, J., and Weng, Z., 2018, Copper-catalyzed synthesis of 2,2-difluoro-1,3-benzoxathioles (selenles) and their insecticidial activities: The selenium effect, *Org. Biomol. Chem.*, 16 (24), 45558–4562.

[18] Santi, C., Jacob, R.G., Monti, B., Bagnoli, L., Sancineto, L., and Lenardão, E.J., 2016, Water and aqueous mixture as convenient alternative media for organoselenium chemistry, *Molecules*, 21 (11), 1482.

[19] Klayman, D.L., and Griffin, T.S., 1973, Reaction of selenium with sodium borohydride in protic solvent. A facile method for introduction of selenium into organic molecules, *J. Am. Chem. Soc.*, 95 (1), 197–199.

[20] Ibrahim, T.H., Chehade, Y., and Abou Zour, M., 2011, Corrosion inhibition of mild steel using Potato peel extract in 2 M HCl solution, *Int. J. Electrochem. Sci.*, 6, 6542–6556.

[21] Eid, A.M., Shaaban, S., and Shalabi, K., 2020, Tetrazole-based organoselenium bi-functionalized corrosion inhibitors during oil well acidizing: Experimental, computational studies, and SRB bioassay, *J. Mol. Liq.*, 298, 111980.

[22] Sehmi, A., Ouici, H.B., Guendouzi, A., Ferhat, M., Benali, O., and Boudjellal, F., 2020, Corrosion inhibition of mild steel by newly synthesized pyrazole carboxamide derivatives and HCl acid medium: Experimental and theoretical studies, *J. Electrochem. Soc.*, 167 (15), 155508.

[23] Ma Q., Qi, S., He, X., Tang, Y., and Lu, G., 2017, 1,2,3-Triazole derivatives as corrosion inhibitors for mild steel in acidic medium: Experimental and computational chemistry studies, *Corros. Sci.*, 129, 91–101.

[24] Parikh, K., and Joshi, D., 2013, Antibacterial and antifungal screening of newly synthesized benzimidazole-clubbed chalcone derivatives, *Med. Chem. Res.*, 22 (8), 3688–3697.

[25] Shubhalaxmi, S., Pathak, L., Ananda, K., and Bhat, K.S., 2016, Synthesis of focused library of novel aryloxyacids and pyrazoline derivatives: Molecular docking studies and antimicrobial investigation, *Cogent Chem.*, 2 (1), 1141388.

[26] Behbehani, H., and Ibrahim, H.M., 2012, 4-Thiazolidinones in heterocyclic synthesis: Synthesis of novel enaminones, azolopyrimidines and 2-arylimino-5-thiazolidinones, *Molecules*, 17 (6), 6362–6385.

[27] Katke, S.A., Amrutkar, S.V., Bhor, R.J., and Khairnar M.V., 2011, Synthesis of biologically active 2-chloro-*N*-alkyl/aryl acetamide derivatives, *Int. J. Pharma Sci. Res.*, 2 (7), 148–156.

[28] Hassan, A.H., 2016, Synthesis of chalcone derivatives and evaluation their biological activities, *J. Garmian Univ.*, 1 (10), 582–593.

[29] Saleh, T.A.K., 2017, Synthesis and characterization of chalcone derivatives from furfural, *Chem. Adv. Mater.*, 2 (4), 44–52.

[30] Hassan, A.F., Abdalwahed, A.T., Al-Luaibi, M.Y., and Aljadaan, S.A., 2021, Synthesis, characterization and thermal study of some new organochalcogenide compounds containing aryl group, *Egypt. J. Chem.*, 64 (9), 5009–5015.

[31] Maru, J., Patel, G.R., and Yadav, R., 2015, Spectral and microbial studies of some newly synthesized Schiff base derivatives of 2-(1*H*-benzo[d]oxazole-2-ylthio-*N*-(4-acetylphenyl)acetamide, *Int. Lett. Chem., Phys. Astron.*, 44, 57–65.

[32] Sladek, V., Rottmannová, L., Škorňa, P., Ilčin, M., and Lukeš, V., 2012, Theoretical 1H(Se-H) NMR shift in meta substituted Ph-XH (X = O, S, Se), *Acta Chim. Slovaca*, 5 (2), 159–163.

[33] Nikpour, S., Ramezanzadeh, M., Bahlakeh, G., Ramezanzadeh, B., and Mahdavian, M., 2019, *Eriobotrya japonica* Lindl leaves extract application for effective corrosion mitigation of mild steel in HCl solution: Experimental and computational studies, *Constr. Build. Mater.*, 220, 161–176.

[34] Daoud, D., Daouadi, T., Hamani, H., Chafaa, S., and Al-Noaimi, M., 2015, Corrosion inhibition of mild steel by two new S-heterocyclic compounds in 1 M HCl: Experimental and computational study, *Corros. Sci.*, 94, 21–37.

[35] Aslam, R., Mobin, M., Zehra, S., Obot, I.B., and Ebenso, E.E., 2017, *N,N*-Dialkylcystine Gemini and monomeric *N*-alkyl cysteine surfactant as corrosion inhibitors on mild steel corrosion in 1 M HCl solution: A comparative study, *ACS Omega*, 2 (9), 5691–5707.

[36] Manssouri, M., El-Ouadi, Y., Znini, M., Bouyanzer, A., Desjobert, J.M., and Majidi, L., 2015, Adsorption properties and inhibition of mild steel corrosion in HCl solution by the essential oil from fruit of Moroccan *Ammodaucus leucotrichus*, *Mater. Environ. Sci.*, 6 (3), 631–646.

[37] Salarvand, Z., Amirnasr, M., Talebian, M., Raeissi, K., and Meghdadi, S., 2017, Enhanced corrosion resistance of mild steel in 1 M HCl solution by trace amount of 2-phenyl-benzothiazole derivatives: Experimental, quantum chemical calculation and molecular dynamics (MD) simulation studies, *Corros. Sci.*, 114, 133–145.

[38] Adeyemi, O.O., and Olubomehin, O.O., 2010, Investigation of *Anthrocleista djalonensis* stem bark extract as corrosion inhibitor for aluminium, *Pac. J. Sci. Technol.*, 11 (2), 455–462.

Microwave-Assisted Chemical Co-reduction of Pd Nanoparticles Anchored on Reduced Graphene Oxide with Different Loading Amounts

Dyah Ayu Fatmawati, Triyono Triyono*, Wega Trisunaryanti, and Uswatul Chasanah

Department of Chemistry, Faculty of Mathematics and Natural Sciences, Universitas Gadjah Mada, Sekip Utara, Yogyakarta 55281, Indonesia

Abstract: *Microwave-assisted Palladium/Reduced Graphene Oxide (Pd/RGO) synthesis was effectively carried out in this study, which looked at the effects of different Pd loading weights in Graphene Oxide (GO) on its physicochemical qualities. The Tour technique was used to make GO, with a $KMnO_4$:graphite weight ratio of 3.5. Meanwhile, Pd/RGO was synthesized utilizing the in-situ reduction method of one-pot synthesis with ascorbic acid as the green reducing agent, yielding Pd-0.5/RGO, Pd-1.0/RGO, and Pd-2.0/RGO, respectively, with variations in Pd loading weight of 0.5, 1.0, and 2.0%. XRD, FTIR, SAA, SEM-EDX, and TEM were used to examine all material characterizations. As a result, Pd-1.0/RGO had the largest surface area of 65.168 m^2/g among the Pd-based materials, with a pore volume of 0.111 cc/g, the pore diameter of 3.316 nm, Pd crystallite size of 28.29 nm, RGO nanostructure dimension of 3.37 × 28.53 nm, and reduction level (C/O) of 3.02. This material also contains specific functional groups, including O-H, C-H, CO_2, C=C, C=O, and C-O, based on FTIR spectra. Therefore, optimal weight loading of metal on the surface of the supporting material will provide a large material surface area. Increasing the surface area of the material improves its performance as a catalyst.*

Keywords: *in-situ reduction; palladium; reduced graphene oxide; microwave, Tour method*

■ INTRODUCTION

For graphene-based applications in electronics, optics, chemistry, energy storage, and biology, graphene oxide (GO) is a valuable and promising material [1]. Graphene oxide is graphite oxidized to allow oxygen molecules to intersperse between the carbon layers [2]. Although the actual structure of GO is unknown, it is evident that epoxides, alcohols, ketone carbonyls, and carboxylic groups disrupt the previously contiguous aromatic lattice of graphene [3]. Various advantages over graphene, such as more excellent solubility [4] and the ability to surface functionalize, are due to these oxygenated groups, which have opened up many possibilities for application in nanocomposite materials [5]. For GO synthesis, chemical approaches based on oxidative-exfoliation processes have been developed over time [6]. The most popular technique was developed by Hummers and employed potassium permanganate

($KMnO_4$) and sodium nitrate ($NaNO_3$). [7]. The Hummers method was additionally enhanced by omitting $NaNO_3$ to prevent the production of harmful gases, using ice in place of liquid water to prevent a high-temperature rise and thereby promoting better and easier control of the reaction, increasing yield and oxidation degree while promoting the retention of carbon rings in the basal plane by adding phosphoric acid (H_3PO^4) to the reaction medium and omitting $NaNO_3$ altogether. This approach is called Tour approach [8].

The oxidative-exfoliation procedures can yield vast amounts of GO, but a graphene-like nanosheet requires further treatment to reduce it into reduced graphene oxide (RGO) [9]. Ascorbic acid (L-AA) is an affordable and plentiful material that can reduce GO to an acceptable level as a green alternative to standard reducing agents of GO (e.g., hydrazine hydrate and

sodium borohydride) [10]. More importantly, compared to the traditional reductants employed in GO reduction, L-AA and its oxidized products are environmentally beneficial [11]. Despite the widespread use of strong reducing chemicals to reduce GO, the process is still exceedingly slow. Microwave irradiation was discovered to speed up the reduction rate [12] significantly. Microwaves heat materials directly through dielectric loss rather than heat convection, as in traditional heating methods, allowing for rapid and precise heating [13]. It is thought to be promising in reducing reaction time and producing hot spots with extremely high temperatures.

Palladium (Pd) is a platinum (Pt) group metal with numerous uses in medicine, the environment, and materials research. Pd is a unique metal with a wide range of catalytic applications in various industries at ambient temperatures [14]. Compared to Pt-based catalysts, Pd is a more effective catalyst for the Formate Oxidation Reaction (FOR) in both half-cell and fuel cell tests [15]. Because of their high surface-to-volume ratio and more active/selective surface atoms than bulk Pd catalysts, Pd nanoparticles (PdNPs) have gained much attention in organic synthesis in recent years [16]. PdNPs are a hot topic because of their high catalytic activity and the possibility of being employed as heterogeneous catalysts with unique features. As a support material of PdNPs, RGO is more commonly utilized than other carbon-based materials such as porous carbon and carbon nanotubes because of its high availability, excellent corrosion resistance, low cost, and superior dispersion in nature [17].

There are many reports regarding the synthesis of Pd/RGO compounds. Wang et al. researched the usage of reducing agents such as ethylene glycol, sodium borohydride, and hydrazine hydrate in a comparative study [18]. Kumar et al. synthesized Pd/RGO by microwave-assisted heating reduction but using GO precursor produced from the modified Staudenmaier method [19]. Ng et al. investigated the Pd/RGO using GO precursor synthesized by Tour technique, but through ultrasonic wave-assisted reduction heating type [20]. Furthermore, Li et al. made Pd/RGO under microwave irradiation but used ethylene glycol as a reducing agent [21]. Therefore, in this work, we investigated the Pd/RGO

utilizing the GO precursor obtained from the Tour method. This GO preparation was adapted from Fatmawati et al., which used a weight of oxidizing agent for graphite of 3.5 [22], which is lower than the usual value of 6. Then the Pd/RGO synthesis was carried out by microwave-assisted in-situ reduction heating using ascorbic acid. Consequently, the goal of this study is to improve on earlier research by employing a shorter and simpler reduction heating, using GO precursor with a lower ratio of oxidizing agent to graphite than recommended by the Tour method, as well as utilizing ascorbic acid as a green reducing agent. The characterization data of the XRD, FTIR, SAA, SEM-EDX, and TEM will be used to investigate further the physicochemical properties of the Pd/RGO material.

■ EXPERIMENTAL SECTION

Materials

All the ingredients used in this experiment came from commercial sources (E-Merck Germany, p.a.) and were used without being purified. Graphite powder, Potassium permanganate ($KMnO_4$, H_2SO_4 98%), Orthophosphoric acid (H_3PO_4 85%), Hydrogen peroxide (H_2O_2 30%), Hydrochloric acid (HCl 37%), absolute ethanol, L(+)-Ascorbic acid, Palladium(II) chloride ($PdCl_2$) anhydrous, Sodium hydroxide (NaOH), Silver nitrate ($AgNO_3$), Barium chloride dihydrate ($BaCl_2 \cdot 2H_2O$), deionized (DI) water, phosphate-buffered saline (PBS), and bidistilled water were among the materials utilized.

Instrumentation

The crystallinity of the materials was determined by X-Ray Diffraction (Bruker D2 Phaser) at a wide angle of 5–90°. The materials' functional groups were determined using a Fourier Transform Infrared Spectrometer (FTIR, Shimadzu Prestige 21) operating at 4000–400 cm^{-1}. The Surface Area Analyzer (SAA, JWGB Meso 112) was used to examine the textural features of materials, including specific surface area, pore volume, and pore diameter, which were determined using the BET and BJH methods. Using a Transmission Electron Microscope, the materials' structure and polycrystalline

ring pictures were captured (TEM, JEOL JEM-1400). Scanning Electron Microscope-Energy Dispersive X-ray spectroscopy was used to examine the materials' surface morphology and metal content (SEM-EDX, JSM-6510LA).

Procedure

Synthesis of graphene oxide (GO)

$KMnO_4$ 1.3125 g was mixed with 0.375 g graphite powder (weight ratio of 3.5) and placed in Beaker I [22]. Then, in Beaker II, 45 mL H_2SO_4 and 5 mL H_3PO_4 (volume ratio of 9) were added. For 1 h, the two beakers were placed in a cooler box with ice. Then, while stirring, the solution in Beaker II was transferred to Beaker I and heated for six hours at 65 °C [23]. The solution was then placed into another beaker containing 200 g DI water ice and 3 mL H_2O_2 and swirled with a stirring rod. The solids GO were left to precipitate in the solution. GO was washed with a solution of HCl (2 times), ethanol absolute (2 times), and PBS at 5000 rpm for 5 min until the pH of the solution reached 7. The solution was then tested for chloride ions using $AgNO_3$ and sulfate ions using $BaCl_2$. The washing process was repeated numerous times using hot bi-distilled water until the solution was free of both. Finally, the solid was dried for 12 h at 80 °C in an oven.

Synthesis of palladium/reduced graphene oxide (Pd/RGO)

The in-situ approach was used to deposit metal nanoparticles onto the RGO surface. First, each $PdCl_2$ salt precursor solution (with 0.5, 1.0, and 2.0 percent w/w Pd metal loading on GO) was agitated for 10 min at room temperature before being added to the GO dispersion (0.3 g in 25 mL distilled water). After stirring for 10 min, the pH of the reaction mixture was raised to 9 by adding 0.1 M NaOH solution. After 5 min of stirring, a 3 g ascorbic acid reducing agent was added to the reaction mixture (weight ratio of ascorbic acid to GO of 10). Stirring was continued for 10 min, followed by microwave-assisted heating for 4 min at 70 °C with high frequency using a microwave instrument (Electrolux, Model EMM2308X). The Pd/RGO nanostructures were rinsed numerous times with distilled water until they reached a neutral pH and then dried for 12 h at 60 °C. An illustration of the Pd/RGO synthesis procedure is briefly shown in Fig. 1.

■ RESULTS AND DISCUSSION

Analysis of Material Crystallinity

XRD measurements were used to determine the crystalline phase structure of the samples. The diffractograms of GO and Pd/RGO with various metal loading levels are shown in Fig. 2. GO material is made from graphite, which has a typical peak at about 26° and a characteristic spacing between graphene layers of 0.34 nm, according to Fatmawati et al. [24]. The expanded layer spacing after the graphite oxidation process was caused by the oxygen functional groups from oxidants
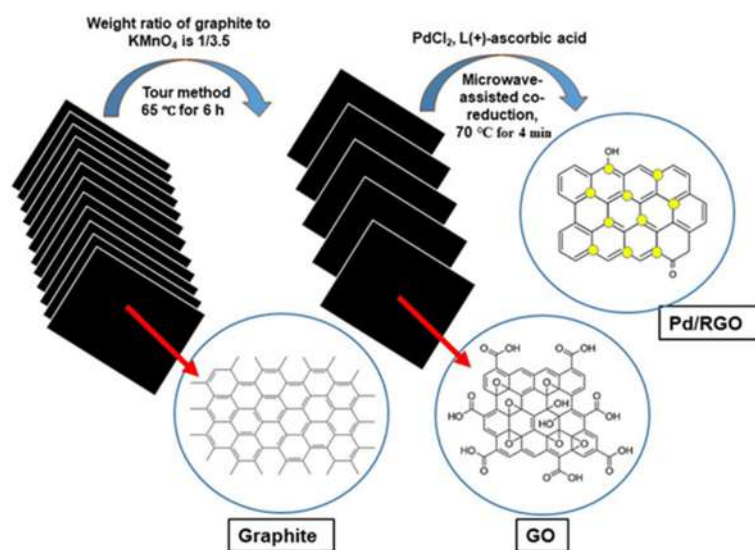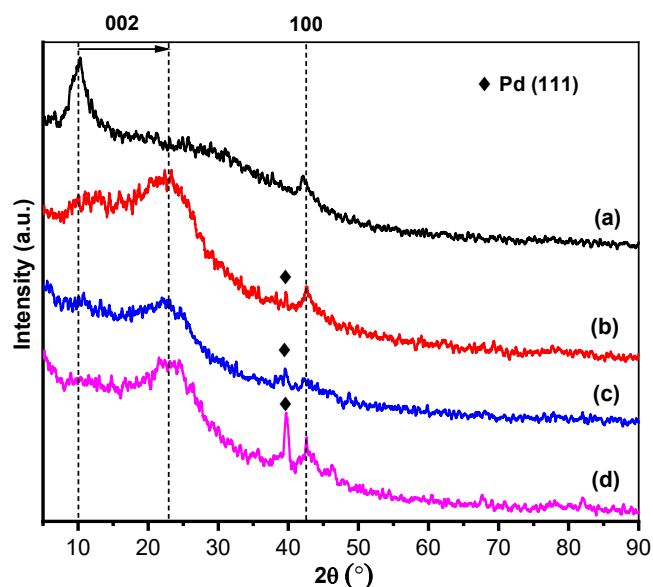

Fig 1. The illustration of the Pd/RGO synthesis procedure

Fig 2. Diffractogram of (a) GO (b) Pd-0.5/RGO (c) Pd-1.0/RGO (d) Pd-2.0/RGO

attached on both sides of the graphene sheets, as well as the resulting atomic-scale roughness to the originally atomically flat graphene sheets [25]. During the oxidation process, the d-spacing increases from 0.34 to 0.87 nm, resulting in around a 150% increase in distance between layers in GO compared to pristine graphite. The result of this study is slightly lower than that of Bera et al. [26]. This effect is owing to changes in oxidation treatment, with ultrasonic waves being used in some cases. The d value for GO, according to Prabakaran et al., is between 0.6 and 1 nm [27]. The peak of GO at 10.19° vanishes after reduction treatment, and a new peak forms at 22–23°, which belongs to RGO's C(002) planes, showing that GO sheets were successfully reduced by microwave irradiation for all samples [28]. Furthermore, each line of Pd/RGO has a large peak at 22–23°, which is attributed to the (002) planes of RGO, implying the removal of oxygen-containing functional groups from the GO [29]. The shift from a sharp to a broad peak form implies that removing oxygen groups from the graphene sheet produces crystal damage or flaws. The gap between the graphene layers was reduced from 0.87 to 0.40 nm when these groups were removed. Furthermore, the peaks near 40° could be attributed to the (111) lattice planes of Pd's face-centered cubic crystalline structure (JCPDS No. 46-1043) [20]. Due to the minimal quantity of metal loading on the support material, the crystal plane of Pd (200), (220), and (311) is missing. The diffractogram shows that increasing the amount of metal loading on the support material enhances the intensity of crystallinity while decreasing the crystallite size (CS), as reported by Ng et al. [20]. The Scherrer equation is used to obtain these values, which are based on the Scherrer constant (K = 0.9) and the height (H) of the carbon nanostructure. Following Stobinski et al., the diameter (D) of the carbon nanostructure was determined using the Warren constant (K = 1.84) [30]. As a result, the stacked carbon nanostructure has dimensions of D x H with a layer separation of d. The findings of the XRD spectra interpretation calculation are shown in Table 1.

Analysis of Material Typical Functional Groups

The rise and decrease in the spacing between layers (d) of graphite–GO–Pd/RGO are connected to the presence of oxygen functional groups, as shown in earlier XRD data in Table 1. Fig. 3 shows FTIR spectra that confirmed this type of oxygen functional group. Firm peaks in the GO spectra can be found at 3400 and 1600–1700 cm^{-1}. OH vibrations from alcohol and carboxylic acid groups, as well as water absorption, are related to these peaks, as are C=O vibrations from ketone, carboxylic acid, and ester groups. C-H vibrations from sp^3 conjugated

Table 1. Data interpretation of XRD analysis

Material	Peak characteristic of carbon material					Peak of Pd	
	2θ (002)	d (nm)	H (nm)	2θ (100)	D (nm)	2θ (111)	CS (nm)
GO	10.19	0.87	2.71	42.08	15.93	-	-
Pd-0.5/RGO	22.01	0.40	1.71	42.64	17.59	39.68	23.77
Pd-1.0/RGO	22.00	0.40	3.37	42.30	28.53	39.59	28.29
Pd-2.0/RGO	23.03	0.39	2.10	42.60	5.79	39.74	14.42
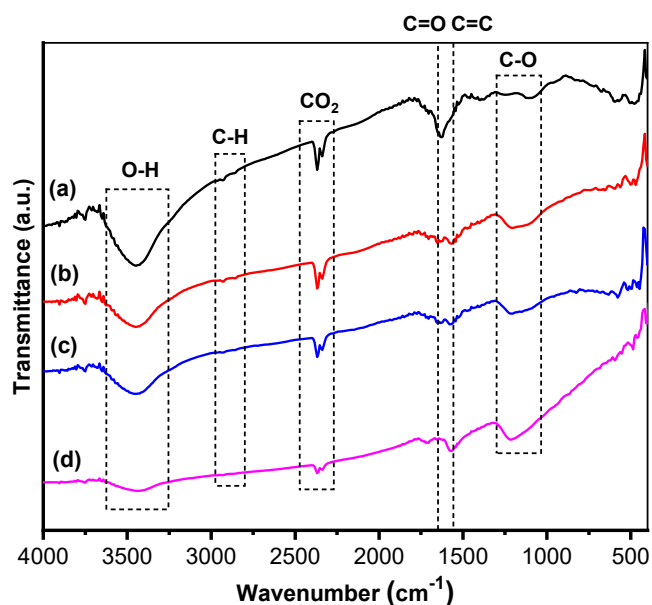
Fig 3. FTIR spectra of (a) GO (b) Pd-0.5/RGO (c) Pd-1.0/RGO (d) Pd-2.0/RGO

carbons, C=C vibrations from graphitic carbons, and C-O vibrations from alcohol, alkoxy, carboxylic, and ester groups are represented by lesser intensity peaks at 2800–2900, 1500–1600, and 1000–1300 cm^{-1} [31]. The peak at 3400 cm^{-1} reduced in strength, and the peak at 1600–1700 cm^{-1} diminished after reduction using a combination of microwave-assisted heating and a reducing agent in the form of ascorbic acid, showing carboxylic group breakdown [30]. The remaining oxygen-containing functional groups after the reduction process, according to the spectra, are hydroxyl and epoxy. Meanwhile, because metal deposition on RGO did not produce any

absorption band linked with Pd-O, the effect of metal loading cannot be substantiated using these results [32]. As a result, the three materials have pretty similar personalities. Table 2 shows the complete results of the FTIR interpretation.

Analysis of Material Elemental Composition

Furthermore, the percentage of elements present in the material, particularly oxygen functional groups, can be estimated using EDX calculations based on earlier FTIR data. The EDX data shows the investigation results with percent mass C increasing and percent mass O decreasing from GO to Pd/RGO. This finding shows that the process of reduction was successful.

The FTIR results follow the hypothesis that RGO materials primarily comprise carbon. The C/O ratio represents the reduction level, with a more excellent ratio indicating that more oxygen groups in the substance have been reduced. Due to leaching during material washing, the actual percent mass of Pd was lower than that deposited in the procedure. Another option is that the EDX spectra were only collected from the part of the sample that was photographed. Unlike the Pd concentration in the bulk chemical elemental analysis such as the ICP and AAS, therefore it is not representative of the substance. Table 3 shows the results of the data analysis of the main elements in the materials. Beyond those results, the presence of impurities such as Na of 1.041%, S of 2.307%, and K of 3.312% in the GO spectrum indicates that the washing was not optimal,

Table 2. Data analysis of FTIR functional groups of material

Material	O-H	C-H$_{sp3}$	CO$_2$	C=O	C=C	C-O
GO	3448.72	2931.80	2337.72	1627.92	1527.62	1095.57, 1249.87
Pd-0.5/RGO	3448.72	2931.80, 2862.36	2337.72	1566.20	1527.62	1203.58
Pd-1.0/RGO	3425.58	2931.80, 2862.36	2337.72	1573.91	1527.62	1149.57, 1211.30
Pd-2.0/RGO	3448.72	2931.80, 2877.79	2337.72	1705.07	1573.91	1219.01

**Table 3.** Data of the elemental composition of the material from EDX analysis

Material	% Mass C	% Mass O	% Mass Pd	C/O ratio
GO	56.76	38.94	-	1.46
Pd-0.5/RGO	73.43	26.20	0.37	2.80
Pd-1.0/RGO	74.61	24.69	0.70	3.02
Pd-2.0/RGO	75.41	24.11	0.49	3.13

leaving residues of PBS, sulfuric acid, and potassium permanganate.

Analysis of Material Textural Properties

Fig. 4A shows the nitrogen adsorption-desorption isotherm for the produced materials. According to the IUPAC classification, all materials had a type IV isotherm, which corresponded to the features of a mesoporous material. The existence of a hysteresis loop near the isotherm represents this typical mesoporous material. The N_2 sorption isotherm of GO appears to be a sizeable H3-type hysteresis loop with a BET surface area of 69.331 m^2g^{-1} from 0.5 to 1.0 relative pressure. These materials' hysteresis follows the H3 pattern, in which the desorption branch in the closure region tends to be perpendicular to the adsorption branch at lower relative pressures. The material pore pattern of the H3-type loop hysteresis,

according to theory, has a wedge or slit geometry resulting from agglomerates of parallel plate-shaped particles [33-34]. The meso- and microporosity of the GO adsorption isotherm can be attributed to the inter-layer gaps between the GO sheets and flaws in the sheets [35]. Metal impregnation, on the other hand, did not affect the overall pore structure. When Pd nanoparticles were deposited on the RGO surface, the type of hysteresis loop changed from H3 to H4, and the specific surface area and pore volume decreased (Table 4). There is a common connection between plate-like particles and the H4 hysteresis loop. The volume of nitrogen adsorption, on the other hand, fell dramatically. This decrease could be due to metal clusters obstructing the holes between the layers [36]. Pd-0.5 and Pd-2.0 have a similar isotherm pattern in that during reduction, they lose substantially all of their microporosity and most of
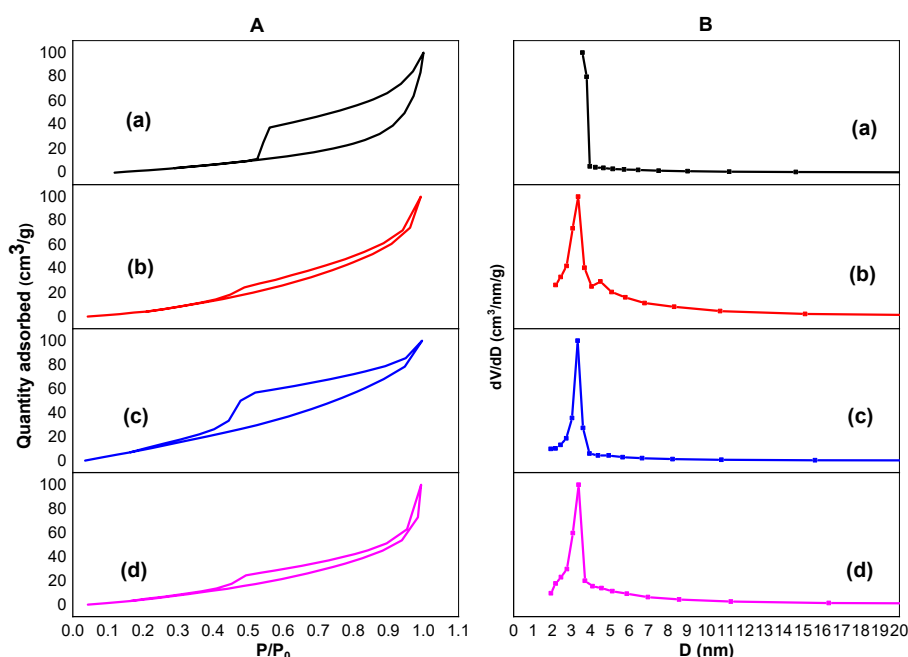
Fig 4. Nitrogen adsorption-desorption isotherm and pore distribution of (a) GO (b) Pd-0.5/RGO (c) Pd-1.0/RGO (d) Pd-2.0/RGO

Table 4. Textural properties of GO and Pd/RGO

Material	Surface area (m^2/g)	Pore volume (cc/g)	Pore diameter (nm)
GO	69.331	0.319	3.566
Pd-0.5/RGO	22.251	0.077	3.350
Pd-1.0/RGO	65.168	0.111	3.316
Pd-2.0/RGO	32.624	0.109	3.372

their mesoporosity, as evidenced by a specific surface area of 20–30 m^2/g [37]. This effect is due to the rearranging and spacing of graphene layers during the reduction process.

Fig. 4B depicts the pore distribution of the materials. The material's pores are mesoporous, ranging from 2 to 50 nm. Based on the BJH desorption method, where all of these materials have a pore diameter of roughly 3 nm, the pore diameter is selected from the highest point on each bar chart, indicating the most frequent pore diameter. Meanwhile, the BET method calculates the specific surface area of materials. Table 4 shows the results of the data analysis of the material's textural qualities. Following a series of treatments, GO transforms into curly RGO, and all Pd/RGO hybrids show a declining trend in BET surface area and pore volume when more metals are added to the hybrid system. Metal nanoparticles inhabited curved graphene surfaces, causing this tendency [38]. According to the investigation results, Pd-1.0/RGO has the most extensive surface area. This large surface area is possible because, when compared to the other two, Pd-1.0 is the most effective loading to be performed on RGO. The metal nanoparticles produced by Pd-1.0 can be distributed evenly. Pd-0.5 is regarded as too small in loading, resulting in infrequent distribution on the RGO surface and no significant increase in the material's specific surface area. Pd-2.0, due to its higher loading weight, is more prone to forming agglomerates between metal nanoparticles when placed on RGO, resulting in a small surface area. Another possibility is that the metals in Pd-0.5/RGO and Pd-2.0/RGO are mostly leached during material washing, resulting in a small surface area. This result is consistent with the percent Pd metal content of Table 3's EDX data.

Analysis of Material Surface Morphology and Nanostructures

Fig. 5 is a collection of SEM pictures. All Pd/RGO materials, including GO, have uneven, rough, wrinkled, and exfoliated sheet-like surfaces. The layered structure of graphene sheets can be seen in the SEM image of GO, according to the literature, with thin layers structured like waves or wrinkles on the surface [39]. The GO sheets had smooth surfaces, similar to what had previously been observed, whereas the RGO sheets had folded folds and wrinkles [40].

The microstructure of GO is depicted in Fig. 6(a), and it is made up of thin, stacked flakes of varied shapes
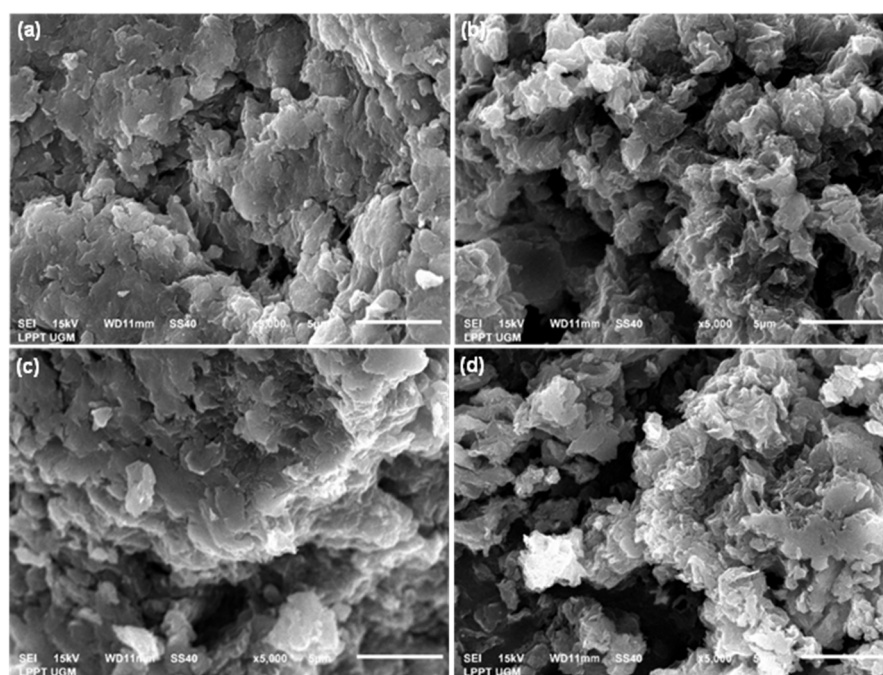
Fig 5. SEM images of (a) GO (b) Pd-0.5/RGO (c) Pd-1.0/RGO (d) Pd-2.0/RGO
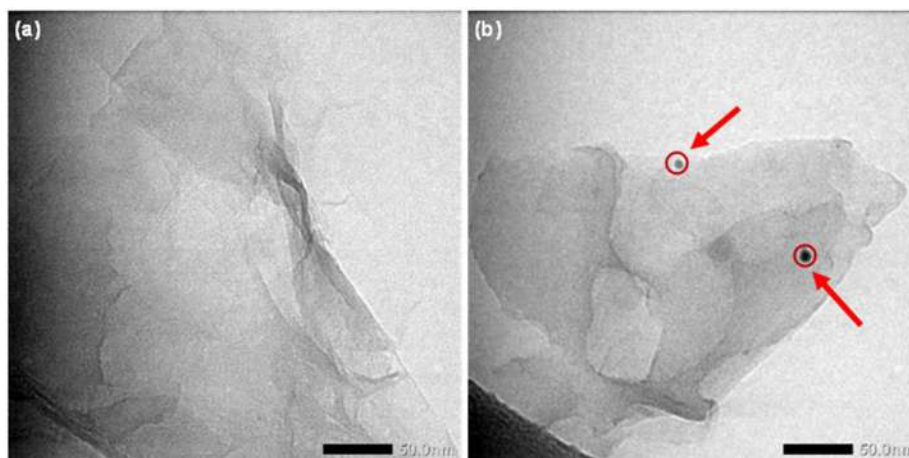
Fig 6. TEM images of (a) GO (b) Pd-2.0/RGO

that have well-defined monolayer and few-layer graphene structures at their edges [41], as well as a smooth platform surface with sporadic folds [42]. The Pd-2.0/RGO micrograph in Fig. 6(b) has a morphology similar to that of GO but with the addition of Pd nanoparticles. The percentage of Pd nanoparticles was found to be low, verified by prior EDX results. Furthermore, the size of the identified Pd-2.0/RGO nanoparticles in Fig. 6(b) is around 10–15 nm, bolstering the XRD findings in Table 1.

■ CONCLUSION

The synthesis of Pd/RGO with microwave assistance has been completed. Although material characterization results did not change significantly, the Pd loading weight on the carrier material did affect particle size, reduction level (C/O), and specific surface area. According to the analysis results, the Pd-1.0/RGO material has the most specific surface area due to the effectiveness of the loading weight towards the distribution of metal nanoparticles produced on the surface of the supporting material. The critical point is that the metal loading should not be too little or too much, as this can result in a small distribution of nanoparticles or even an agglomeration of nanoparticles. Therefore, optimal weight loading of metal on the surface of the supporting material will provide a large material surface area. Several research findings show that increasing the surface area of material improves its performance as a catalyst. Additional research to determine the performance quality of each material is possible through various electrocatalytic applications such as Direct methanol fuel cell (DMFC), Direct formic acid fuel cell (DFAFC), Direct ethanol fuel cell (DEFC), and Oxygen Reduction Reaction (ORR).

■ REFERENCES

[1] Dideikin, A.T., and Vul', A.Y., 2019, Graphene oxide and derivatives: The place in graphene family, *Front. Phys.*, 6, 149.

[2] Paulchamy, B., Arthi, G,. and Lignesh, B.D., 2015, A simple approach to stepwise synthesis of graphene oxide nanomaterial, *J. Nanomed. Nanotechnol.*, 6 (1), 253.

[3] Alam, S.N., Sharma, N., and Kumar, L., 2017, Synthesis of graphene oxide (GO) by modified hummers method and its thermal reduction to obtain reduced graphene oxide (rGO), *Graphene*, 6 (1), 1–8.

[4] Kuilla, T., Bhadra, S., Yao, D., Kim, N.H., Bose, S., and Lee, J.H., 2010, Recent advances in graphene based polymer composites, *Prog. Polym. Sci.*, 35 (11), 1350–1375.

[5] Smith, A.T., LaChance, A.M., Zeng, S., Liu, B., and Sun, L., 2019, Synthesis, properties, and applications of graphene oxide/reduced graphene

oxide and their nanocomposites, *Nano Mater. Sci.*, 1 (1), 31–47.

[6] Ranjan, P., Agrawal, S., Sinha, A., Rao, T.R., Balakrishnan, J., and Thakur, A.D., 2018, A low-cost non-explosive synthesis of graphene oxide for scalable applications, *Sci. Rep.*, 8 (1), 12007.

[7] Benzait, Z., Chen, P., and Trabzon, L., 2021, Enhanced synthesis method of graphene oxide, *Nanoscale Adv.*, 3 (1), 223–230.

[8] Marcano, D.C., Kosynkin, D.V., Berlin, J.M., Sinitskii, A., Sun, Z., Slesarev, A., Alemany, L.B., Lu, W., and Tour, J.M., 2010, Improved synthesis of graphene oxide, *ACS Nano*, 4 (8), 4806–4814.

[9] Loryuenyong, V., Totepvimarn, K., Eimburanapravat, P., Boonchompoo, W., and Buasri, A., 2013, Preparation and characterization of reduced graphene oxide sheets via water-based exfoliation and reduction methods, *Adv. Mater. Sci. Eng.*, 2013, 923403.

[10] Abdolhosseinzadeh, S., Asgharzadeh, H., and Kim, H.S., 2015, Fast and fully-scalable synthesis of reduced graphene oxide, *Sci. Rep.*, 5 (1), 10160.

[11] Habte, A.T., and Ayele, D.W., 2019, Synthesis and characterization of reduced graphene oxide (rGO) started from graphene oxide (GO) using the Tour method with different parameters, *Adv. Mater. Sci. Eng.*, 2019, 5058163.

[12] Xie, X., Zhou, Y., and Huang, K., 2019, Advances in microwave-assisted production of reduced graphene oxide, *Front. Chem.*, 7, 355.

[13] Schwenke, A.M., Hoeppener, S., and Schubert, U.S., 2015, Synthesis and modification of carbon nanomaterials utilizing microwave heating, *Adv. Mater.*, 27 (28), 4113–4141.

[14] Mallikarjuna, K., Reddy, L.V., Al-Rasheed, S., Mohammed, A., Gedi, S., and Kim, W.K., 2021, Green synthesis of reduced graphene oxide-supported palladium nanoparticles by *Coleus amboinicus* and its enhanced catalytic efficiency and antibacterial activity, *Crystals*, 11 (2), 134.

[15] Galvan, V., Glass, D.E., Baxter, A.F., and Prakash, G.K.S., 2019, Reduced graphene oxide supported palladium nanoparticles for enhanced electrocatalytic activity toward formate electrooxidation in an alkaline medium, *ACS Appl. Energy Mater.*, 2 (10), 7104–7111.

[16] Çetinkaya, Y., Metin, Ö., and Balci, M., 2016, Reduced graphene oxide supported nickel-palladium alloy nanoparticles as a superior catalyst for the hydrogenation of alkenes and alkynes under ambient conditions, *RSC Adv.*, 6 (34), 28538–28542.

[17] Anasdass, J.R., Kannaiyan, P., Raghavachary, R., Gopinath, S.C.B., and Chen, Y., 2018, Palladium nanoparticle-decorated reduced graphene oxide sheets synthesized using *Ficus carica* fruit extract: A catalyst for Suzuki cross-coupling reactions, *PLoS One*, 13 (2), e0193281.

[18] Wang, B., Yan, T., Chang, T., Wei, J., Zhou, Q., Yang, S., and Fang, T., 2017, Palladium supported on reduced graphene oxide as a high-performance catalyst for the dehydrogenation of dodecahydro-*N*-ethylcarbazole, *Carbon*, 122, 9–18.

[19] Kumar, R., da Silva, E.T.S.G., Singh, R.K., Savu, R., Alaferdov, A.V., Fonseca, L.C., Carossi, L.C., Singh, A., Khandka, S., Kar, K.K., Alves, O.L., Kubota, L.T., and Moshkalev, S.A., 2018, Microwave-assisted synthesis of palladium nanoparticles intercalated nitrogen doped reduced graphene oxide and their electrocatalytic activity for direct-ethanol fuel cells, *J. Colloid Interface Sci.*, 515, 160–171.

[20] Ng, J.C., Tan, C.Y., Ong, B.H., Matsuda, A., Basirun, W.J., Tan, W.K., Singh, R., and Yap, B.K., 2019, Nucleation and growth controlled reduced graphene oxide–supported palladium electrocatalysts for methanol oxidation reaction, *Nanomater. Nanotechnol.*, 9, 1847980419827171.

[21] Li, M., Liu, R., Han, G., Tian, Y., Chang, Y., and Xiao, Y., 2017, Facile synthesis of Pd-Ni nanoparticles on reduced graphene oxide under microwave irradiation for formic acid oxidation, *Chin. J. Chem.*, 35 (9), 1405–1410.

[22] Fatmawati, D.A., Triyono, T., Trisunaryanti, W., and Oktaviano, H.S., and Chasanah, U., 2021, The study of partially and fully oxidized ggraphene oxide prepared by green synthesis for wide-scale fabrication, *Rasayan J. Chem.*, 14, 2129–2135.

Indones. J. Chem., 2022, 22 (5), 1282 - 1292

1291

[23] Chasanah, U., Trisunaryanti, W., Triyono, T., Oktaviano, H.S., and Fatmawati, D.A., 2021, The performance of green synthesis of graphene oxide prepared by modified hummers method with oxidation time variation, *Rasayan J. Chem.*, 14 (3), 2017–2023.

[24] Fatmawati, D.A., Triyono, T., Trisunaryanti, W., Oktaviano, H.S., and Chasanah, U., 2021, The influence of permanganate enhancement to graphite on chemical structure and properties of graphene oxide material generated by improved Tour method, *Indones. J. Chem.*, 21 (5), 1086–1096.

[25] Shao, G., Lu, Y., Wu, F., Yang, C., Zeng, F., and Wu, Q., 2012, Graphene oxide: The mechanisms of oxidation and exfoliation, *J. Mater. Sci.*, 47 (10), 4400–4409.

[26] Bera, M., Chandravati, C., Gupta, P., and Maji, P.K., 2018, Facile one-pot synthesis of graphene oxide by sonication assisted mechanochemical approach and its surface chemistry, *J. Nanosci. Nanotechnol.*, 18 (2), 902–912.

[27] Prabakaran, K., Jandas, P.J., Mohanty, S., and Nayak, S.K., 2018, Synthesis, characterization of reduced graphene oxide nanosheets and its reinforcement effect on polymer electrolyte for dye sensitized solar cell applications, *Sol. Energy*, 170, 442–453.

[28] Khan, M., Al-Marri, A.H., Khan, M., Mohri, N., Adil, S.F., Al-Warthan, A., Siddiqui, M.R.H., Alkhathlan, H.Z., Berger, R., Tremel, W., and Tahir, M.N., 2014, *Pulicaria glutinosa* plant extract: A green and eco-friendly reducing agent for the preparation of highly reduced graphene oxide, *RSC Adv.*, 4 (46), 24119–24125.

[29] Zhang, J., Feng, A., Bai, J., Tan, Z., Shao, W., Yang, Y., Hong, W., and Xiao, Z., 2017, One-pot synthesis of hierarchical flower-like Pd-Cu alloy support on graphene towards ethanol oxidation, *Nanoscale Res. Lett.*, 12 (1), 521.

[30] Stobinski, L., Lesiak, B., Malolepszy, A., Mazurkiewicz, M., Mierzwa, B., Zemek, J., Jiricek, P., and Bieloshapka, I., 2014, Graphene oxide and reduced graphene oxide studied by the XRD, TEM and electron spectroscopy methods, *J. Electron. Spectrosc. Relat. Phenom.*, 195, 145–154.

[31] Johra, F.T., and Jung, W.G., 2015, Hydrothermally reduced graphene oxide as a supercapacitor, *Appl. Surf. Sci.*, 357, 1911–1914.

[32] Kujur, S., and Pathak, D.D., 2020, Reduced graphene oxide-immobilized iron nanoparticles Fe(o)@rGO as heterogeneous catalyst for one-pot synthesis of series of propargylamines, *Res. Chem. Intermed.*, 46 (1), 369–384.

[33] Thommes, M., Kaneko, K., Neimark, A.V., Olivier, J.P., Rodriguez-Reinoso, F., Rouquerol, J., and Sing, K.S.W., 2015, Physisorption of gases, with special reference to the evaluation of surface area and pore size distribution (IUPAC Technical Report), *Pure Appl. Chem.*, 87 (9), 1051–1069.

[34] Grad, O., Mihet, M., Dan, M., Blanita, G., Radu, T., Berghian-Grosan, C., and Lazar, M.D., 2019, Au/reduced graphene oxide composites: Eco-friendly preparation method and catalytic applications for formic acid dehydrogenation, *J. Mater. Sci.*, 54 (9), 6991–7004.

[35] Shruthi, T.K., Kumar, M.S., Arjunan, M., Pratap, A., and Chandrasekaran, N., 2015, Graphene oxide aided structural tailoring of 3-D *N*-doped amorphous carbon network for enhanced energy storage, *RSC Adv.*, 5 (113), 93423–93432.

[36] Singh, S.B., and De, M., 2021, Improved hydrogen uptake of metal modified reduced and exfoliated graphene oxide, *J. Mater. Res.*, 36 (15), 3109–3120.

[37] Ruiz-Garcia, C., Lei, Y., Heras, F., Elías, A.L., Terrones, M., and Gilarranz, M.A., 2019, Functional Pd/reduced graphene oxide nanocomposites: effect of reduction degree and doping in hydrodechlorination catalytic activity, *J. Nanopart. Res.*, 21 (12), 276.

[38] Wei, L., and Mao, Y., 2016, Enhanced hydrogen storage performance of reduced graphene oxide hybrids with nickel or its metallic mixtures based on spillover mechanism, *Int. J. Hydrogen Energy*, 41 (27), 11692–11699.

[39] Wanderley, K.A., Leite, A.M., Cardoso, G., Medeiros,

A.M., Matos, C.L., Dutra, R.C., and Suarez, P.A.Z., 2019, Graphene oxide and a GO/ZnO nanocomposite as catalysts for epoxy ring-opening of epoxidized soybean fatty acids methyl esters, *Braz. J. Chem. Eng.*, 36 (3), 1165–1173.

[40] Azizighannad, S., and Mitra, S., 2018, Stepwise reduction of graphene oxide (GO) and its effects on chemical and colloidal properties, *Sci. Rep.*, 8 (1), 10083.

[41] Oh, W.C., and Zhang, F.J., 2011, Preparation and characterization of graphene oxide reduced from a mild chemical method, *Asian J. Chem.*, 23 (2), 875–879.

[42] Bugárová, N., Špitálsky, Z., Mičušík, M., Bodík, M., Šiffalovič, P., Koneracká, M., Závišová, V., Kubovčíková, M., Kajanová, I., Zaťovičová, M., Pastoreková, S., Šlouf, M., Majková, E., and Omastová, M., 2019, A multifunctional graphene oxide platform for targeting cancer, *Cancers*, 11 (6), 753.

Polyvinyl Alcohol-Cellulose Nanocrystal Hydrogel Containing Anti-inflammatory Agent

Lia Amelia Tresna Wulan Asri[1*], Athiya Anindya[1], Yuni Eva Kartika[1], Dita Puspitasari[1], Untung Triadhi[2], and Husaini Ardy[1]

[1]*Materials Science and Engineering Research Group, Faculty of Mechanical and Aerospace Engineering, Institut Teknologi Bandung, Jl. Ganesha No. 10, Bandung 40132, Indonesia*

[2]*Analytical Chemistry Division, Department of Chemistry, Faculty of Mathematics and Natural Sciences, Institut Teknologi Bandung, Jl. Ganesha No. 10, Bandung 40132, Indonesia*

Abstract: *Hydrogel wound dressings were developed through cross-linking reactions of polyvinyl alcohol (PVA) with glutaraldehyde and by the addition of diclofenac sodium and rutin as anti-inflammatory agents. Cellulose nanocrystals (CNC) were added to improve mechanically and release properties. CNC was isolated from pineapple leaf fibers through the ammonium persulfate method resulting in a mixture of rod-like whisker and spherical morphology. The mechanical properties of hydrogels are increasing with the addition of CNC. Hydrogels containing 8% CNC exhibited 7.266 N/mm² tensile strength, 156.3% maximum strain, and 700.3 N/mm² elastic modulus. Drug release tests containing sodium diclofenac were done by taking incubated phosphate buffer saline samples in a pH 7.4 environment and showed that all CNC variations tested are controllable for the first 30 min compared to the sample without CNC. Sodium diclofenac is easily eluted from hydrogel due to its polar properties, and all samples almost demonstrated the same release profile. PVA hydrogels showed fluctuating concentrations of diclofenac compared to others. While hydrogels containing rutin showed a controlled release mode, the addition of CNC in PVA resulted in a slower release of rutin, possibly due to the better binding between CNC and rutin. To conclude, CNC has successfully improved the performance of PVA hydrogels, including the drug release properties.*

Keywords: *hydrogel; wound dressing; polyvinyl alcohol; cellulose nanocrystals; anti-inflammatory agents*

■ INTRODUCTION

A wound is a disorder that occurs in the integrity of the skin, mucous membranes, or skin tissue that can cause physical or thermal damage [1]. The wound healing process is a biological process that occurs in the human body, which includes four stages, namely hemostasis, inflammation, proliferation, and remodeling, that must be done sequentially and in the correct period [2]. When a skin injury occurs, microorganisms around the surrounding tissue would invade the wound and initiate an infection [3]. The presence of pathogens interferes with the inflammation stage and, as a result, delays the proliferation and remodeling stage which leads to tissue damage [4-5]. An infected wound takes longer to heal than the normal healing process [6]. External origin wounds such as those caused by falls or surgical procedures are caused by external force or trauma, resulting in a longer healing time and a higher cost of care. Therefore, the infection must be avoided to ensure a successful and accelerated healing process.

Various treatments and materials are available to treat acute and chronic wounds. Conventional wound care involves drying the area of injury with gauze and tulle by absorbing moisture. This type of dressing provided some protection from the external environment. On the other hand, advanced wound dressing promoted active healing by providing moisture and allowing therapeutic agents to be released in a

controlled manner [7-8]. Therefore, appropriate wound dressing material is necessary to ensure moisture, drug entrapment, and its release [9-10].

Hydrogels, for example, are one type of commercial wound dressing that promotes a moist environment. Hydrogels are hydrophilic polymers that help wounds stay moist while absorbing exudate and can be blended with active compounds such as antibacterial agents due to their versatility [10-13]. They also have a porous structure that holds high water content [14]. The development of hydrogels has been studied extensively, and their commercial use for biomedical applications is developing [15].

Some widely used polymers, including polyvinyl alcohol (PVA) [12,14], polyvinylpyrrolidone (PVP) [16-17], and polyethylene glycol (PEG) [18-19], have low mechanical, thermal, and barrier properties [10]. As a result, nanoparticles are frequently used to improve their properties. Nanocellulose is favored as hydrogel reinforcement because of its functional drug release capabilities, high air-holding capacity, high crystallinity, and biocompatibility [20-22]. Cellulose comprises β-1,4-linked glucopyranose monomers joined by glycosidic bonds [23]. The presence of three hydroxyl groups in each monomer contributes to forming strong hydrogen bonds.

Cellulose nanocrystals (CNCs) consist of highly crystalline regions (54–88% crystallinity) and have a rod-like shape or whisker with 2–20 nm in diameter and 100–500 nm in length [24]. Several methods are available to extract the crystalline regions of cellulose to create CNCs, including acid hydrolysis [25], an ultrasonic technique [26], and enzymatic hydrolysis [27]. Acid hydrolysis by sulfuric acid introduces sulfate groups to the surface of CNCs due to the esterification of hydroxyl groups [25]. The high density of hydroxyl groups in cellulose increases the surface modification options of CNCs. Isogai et al. [28] have demonstrated that carboxyl groups (carboxylated CNCs) can be created by the TEMPO-mediated oxidation method. The addition of carboxyl groups weakens hydrogen bonding and increases adsorption capability, allowing carboxylated CNCs to be used as drug-carrying hydrogels.

On the other hand, TEMPO-mediated oxidation requires many steps and a long oxidation time, while periodate-chlorite oxidation to make carboxylated CNCs involves a two-step procedure that needs expensive periodate. Recently, ammonium persulfate (APS) has successfully extracted CNCs with higher carboxyl content and more homogenous rod-like particles [21]. Although it is time-consuming, this method is a one-step procedure. Thus, APS hydrolysis was used to make carboxylated CNCs in this study.

Permeability to oxygen and rapid dehydration remain the main issues of hydrogel wound dressings [29]. Therefore, determining the water content is critical, and in the current research, hydrogels with various CNC concentrations and anti-inflammatory agents rutin and diclofenac sodium will be used. The modified hydrogels' functional groups, tensile properties, water content, and drug release profiles were assessed.

■ EXPERIMENTAL SECTION

Materials

PVA, diclofenac sodium, glutaraldehyde, and rutin hydrate were purchased from Sigma-Aldrich. APS 98% and sodium hydroxide (NaOH) from Merck were used. Phosphate buffer saline (PBS) pH 7.4 and sodium hypochlorite (NaOCl, technical grade 12%) were supplied by Biogear and Brataco, respectively. Pineapple leaf fiber was purchased from Inatex. All chemicals were used without further purification.

Instrumentation

Fourier-transform infrared spectroscopy (FTIR) was used to determine the functional groups of CNC and hydrogels. FTIR spectra were recorded on an FTIR spectrometer (Prestige 21, Shimadzu) using the KBr pressed-pellet method. The spectra were measured at a resolution of 4 cm^{-1} with the number of scans of 40, at wavenumber 4500 to 400 cm^{-1}.

Transmission Electron Microscopy (TEM) was used to study CNC morphology. The specimen was prepared by dispersing a small amount of CNC in ethanol on a carbon-coated Cu-grid substrate and leaving

it at room temperature for approximately 15 min. TEM images were taken using HITACHI HT7700 with an 80–100 kV acceleration voltage.

The crystal structure of the CNC was studied using X-ray Diffraction (XRD) on an X-ray diffractometer (D8 ADVANCE, Bruker) using Cu Ka X-rays ($\lambda = 0.154060$ nm) with a voltage of 40 kV and a current of 40 mA. The data were collected over the 2θ range of 10–60°. The crystallinity index (CI) was calculated using the following equation:

$$CI(\%) = \frac{I_{002} - I_{am}}{I_{002}} \times 100\% \tag{1}$$

where I_{002} is the intensity for the crystalline cellulose ($2\theta = 22.5°$) and I_{am} is the intensity for the amorphous cellulose ($2\theta = 18°$).

A tensile test was performed on a hydrogel sample shaped into dog bone. The test was conducted using Shimadzu with a maximum load of 1 kN and 10 mm/min velocity. Values of elastic modulus, maximum strain, and ultimate tensile strength were recorded.

Procedure

Isolation of CNC from pineapple leaf fiber

CNC was isolated from pineapple leaf fiber through a modified procedure [21,30]. Pineapple fibers were cut into small pieces. Fibers (40 g) were added into 600 mL NaOH 4 M solution and stirred at 80 °C for 4 h to remove lignin from the cellulosic fibers. The resulting suspension was washed with demineralized water several times until pH 7. The semi-dried fibers were left in the oven at 60 °C for 12 h, bleached using 1.3 L of 5% NaOCl, and heated at 80 °C for 4 h afterward. The resulting suspension was then rewashed with demineralized water until neutral pH. Next, semi-dried fibers were left at 60 °C for another 8 h in the oven. The fibers were then treated with 1.3 L APS 1 M at 80 °C for 16 h and washed with demineralized water several times until the filtrate reached pH 7.

Preparation of PVA-CNC hydrogel

Four hydrogel samples containing 0, 2, 4, and 8% CNC (Table 1) were prepared following Tanpichai et al. [22]. CNC suspension was diluted with distilled water to obtain a total of 100 mL colloidal solution with various concentrations of wt.% CNC. PVA powder (4 g) was added

Table 1. Composition of hydrogel samples

Hydrogel sample	Water (mL)	PVA (g)	CNC (g)
0% CNC	60	2.4	0
2% CNC	60	2.4	2
4% CNC	60	2.4	4.08
8% CNC	60	2.4	8.53

to the aqueous CNC suspension to make a 4 wt.% solid content solution and continuously stirred for 3 h at 90 °C. Glutaraldehyde (5 phr) was added dropwise to the suspension and stirred for 5 min. A small amount of HCl was added to adjust the pH to 1 to initiate a crosslink in the hydrogel solution. The suspension was poured into a petri dish and left for 24 h at room temperature to form hydrogel (Fig. 1(a)). The hydrogel was repeatedly rinsed with distilled water until reaching pH 5 and stored at 5 °C before use.

Preparation of PVA-CNC-Rutin hydrogel

PVA-CNC hydrogel was freeze-dried overnight. The dried hydrogel (50 mg) of each CNC concentration was dispersed in a 10 mL solution of rutin (5 mg/mL) for 24 h. Hydrogels were taken out of the solution and incubated in 100 mL PBS pH 7.4, stirred at 37 °C for 2 h. The solution was measured at 271 nm on a UV-Vis spectrophotometer to determine the rutin loading content.

Preparation of PVA-CNC-Diclofenac sodium hydrogel

CNC suspensions with concentrations of 0, 2, 4, 6, and 8% were prepared by dissolving CNC in distilled water. Then, PVA powder was added to CNC suspension with a concentration of 4 wt.% (4 g in 100 mL of colloidal solution). The resulting solution was stirred for 3 h at 90 °C and let sit at room temperature for about 1 h. Diclofenac sodium (0.06 g) was then added and stirred for 30 min without being heated. The hydrogel was cross-linked by adding glutaraldehyde (GA) solution (50 wt.% in water) dropwise with a content of 5 phr, then stirred for 5 min to homogenize it. A few drops of HCl were added to adjust the pH to 1. The 60 mL hydrogel solution was poured equally into a 15 cm diameter and left at room temperature for 24 h before being stored in the refrigerator to avoid dry hydrogel-forming when left at room temperature for too long.

Swelling test

PVA-CNC hydrogel samples (50 mg) were utterly soaked in distilled water at room temperature at a predetermined time (10, 20, 30, 60, 120, 240, 360, 720, and 1440 min). Each swollen sample was taken out and weighed immediately after adsorbing excess water on its surface with filter paper. The swelling ratio was calculated as follows:

$$\text{Swelling ration} = \frac{(W_t - W_o)}{W_o} \tag{2}$$

where W_t is the weight of the swollen sample, and W_o is the initial weight. The standard deviation value was determined in triplicate.

■ **RESULTS AND DISCUSSION**

Isolation of CNC

The preparation scheme of CNC from pineapple leaf fibers is shown in Fig. 1(a). Pineapple leaf fibers were treated with NaOH and NaOCl to completely remove hemicellulose and lignin. The white color of the resulting sample indicates the removal of lignin, later confirmed by

FTIR analysis. Cellulose was treated with APS 1 M to result in a colloidal solution of CNC. APS at elevated temperature generates radical ions and further forms hydrogen peroxide under acid conditions. Radical ions penetrate the amorphous area of cellulose and cleave the 1,4-β bond. Radical ions and hydrogen peroxide also undergo oxidation reactions and result in COOH groups on the surface of CNC [21].

TEM images depict rod-like whisker CNC with 17–71 nm in width and 89–1436 nm in length (Fig. 2(a-c). We also observed CNC with spherical morphology with a diameter of 13–350 nm (Fig. 2(a) and 2(d)). The stability of CNC whiskers strongly depends on particle size, size polydispersity, and surface charge. Nanocellulose dimensions, sizes, and crystallinity are influenced by the acid hydrolysis conditions and cellulose source. Cheng et al. [31]. reported that the morphology of cellulose nanoparticles would shift from whisker to spherical as APS concentration increased. In our case, besides the APS concentration, the non-uniform size of pineapple leaf fiber precursor might affect
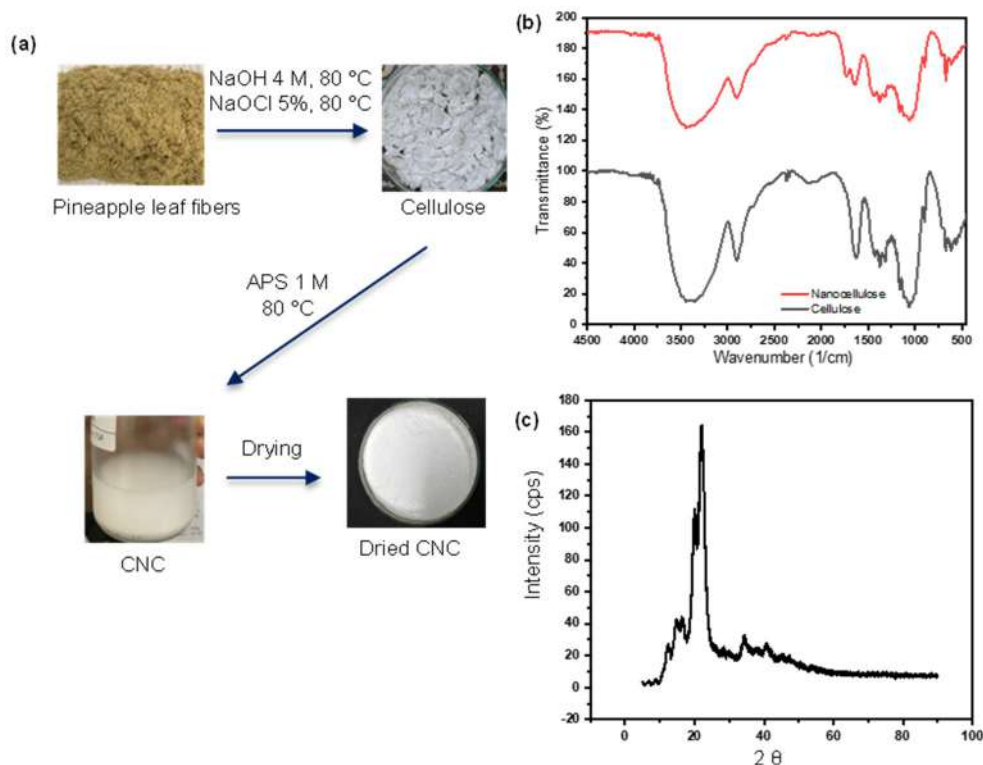
Fig 1. (a) Isolation of CNC from pineapple leaf fibers using APS method, (b) FTIR spectra and (c) XRD diffractogram of CNC
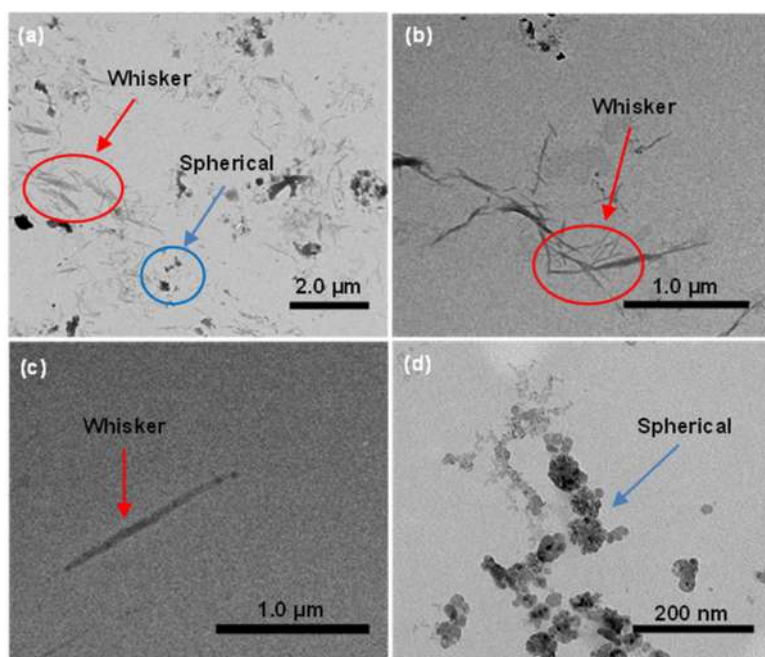
Fig 2. TEM images of CNC with (a) mixture of whisker and spherical (b, c) whisker and (d) spherical morphologies

the morphology of CNC. APS will easily react with smaller size precursors. Furthermore, the free radicals and hydrogen peroxide generated from APS not only attack the amorphous region of cellulose fibers but also hydrolyze the crystalline part. This leads to the size reduction of CNC and even morphological changes from whisker to spherical.

The FTIR spectra of CNC, as presented in Fig. 1(b), display almost similar vibrations with cellulose, as shown by vibrations at 3445 cm^{-1} (O-H hydrogen bonding), 2898 cm^{-1} (C-H asymmetric stretching), 2724 cm^{-1} (C-H symmetric stretching), 1650 cm^{-1} (O-H from adsorbed water), and 1384–1035 cm^{-1} (C-O stretching). Both cellulose and CNC show signals at 1430 cm^{-1} (CH$_2$ symmetric bending and OCH), 1162 cm^{-1} (C-O-C asymmetric stretching, β-glycosidic linkage), 1061 cm^{-1} (C-O/C-C stretching), and 896 cm^{-1} (asymmetric C-H out-of-plane stretching vibrations), attributed to the high content of cellulose I structure. A new band at 1726 cm^{-1} is observed in the CNC, originating from C=O stretching vibrations of carboxylic acid groups (COOH). This functional group was formed during the hydrolysis of cellulose fibers. APS was used to isolate CNC from pineapple fibers due to its rising prevalence as a strong oxidizing agent that can produce distributed rod-like

whiskers without pretreatments [21,32]. The fibers were dissolved in NaOH and NaOCl solutions to remove hemicellulose and lignin before being treated with APS. The peroxide bond of APS was thermally broken when heated to 80 °C, resulting in SO$_4^-$ free radicals and hydrogen peroxide. The radical ions penetrated the amorphous regions of cellulose and hydrolyzed the 1,4-β bond of the cellulose chain, allowing the formation of COOH groups [21].

The XRD pattern in Fig. 1(c) indicates the structure of cellulose I with main diffraction peaks at 15.1° (110), 16.4° (110), 20.9° (110), 22° (200) and 34.5° (004) [33]. The crystallinity of CNC accounted for 41.4% based on the ratio of crystalline area to the total scattered intensity and average crystallite size of 3.274 nm. Previously, we have reported CNC isolation with the APS method resulted in dominantly whisker morphology with 80% crystallinity [30]. The lack of ultrasound treatment and the inability of APS to dissolve amorphous cellulose resulted in low crystallinity. Besides, spherical CNC might contribute to lower crystallinity.

Synthesis of PVA-CNC Hydrogel

Fig. 3(a) depicts the visual of PVA-CNC with various concentrations of CNC. In general, all hydrogel
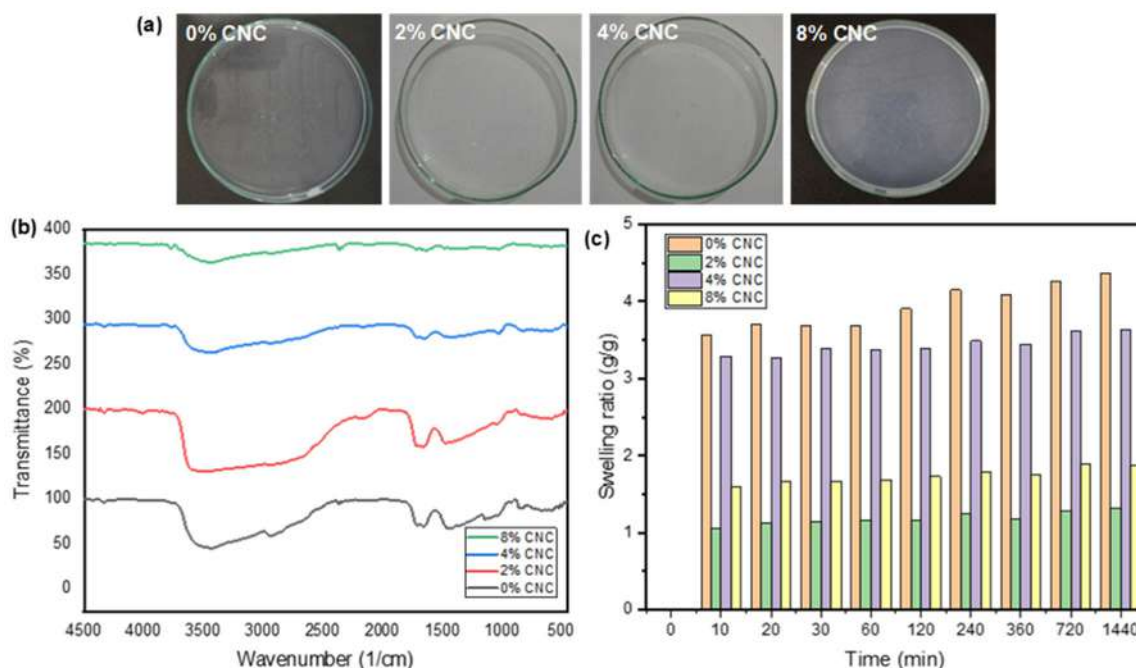
Fig 3. (a) Visual of hydrogels, (b) FTIR spectra of hydrogels and (c) Swelling ratio of PVA hydrogels with various weight concentrations of CNC

Table 2. Composition of PVA-CNC hydrogel samples loaded with diclofenac sodium

Hydrogel sample	Water (mL)	PVA (g)	CNC (g)	Diclofenac sodium (g)
Hydrogel 0% CNC	60	2.4	0	0.06
Hydrogel 2% CNC	60	2.4	2	0.06
Hydrogel 4% CNC	60	2.4	4.08	0.06
Hydrogel 8% CNC	60	2.4	8.53	0.06

variations showed no visual difference, resulting in colorless hydrogels. The FTIR spectra of various hydrogels (with and without CNCs) exhibit an almost similar profile as CNCs peaks overlap with PVA functional groups at 3430 cm^{-1} (O-H hydrogen bonding), 2935 cm^{-1} (CH$_2$ asymmetric stretching), 1653 cm^{-1} (C=O carbonyl stretching), 1440 cm^{-1} (C-H bending), 1031 cm^{-1} (C-O stretching) and 839 cm^{-1} (C-C stretching) as shown in Fig. 3(b). A small peak at 1139 cm^{-1} (C-O stretching) was present in PVA hydrogel, showing the characteristic of PVA.

A significant change was observed in the swelling ratio of hydrogels after immersion in water. The highest swelling ratio was found in the 0% CNC sample, while the lowest was found in the 2% CNC sample (Fig. 3(c)). In general, higher CNC content led to a lower swelling ratio. However, a notable deviation was observed in 2% CNC.

The combination of PVA and CNC initiates cross-linking and hydrogen bonds formation thus reducing the number of functional groups that can bond with water molecules and decreasing the swelling ratio [22]. The observable difference in 2% CNC could be attributed to uneven CNC distribution in the hydrogel matrix and the absence of pores. FTIR test of the hydrogel sample in triplicate and pore size measurement should be carried out to determine the valid reason.

Synthesis of PVA-CNC-Diclofenac Sodium Hydrogel

PVA-CNC-diclofenac sodium hydrogels were prepared as depicted in Fig. 4. The mixture of PVA, CNC, and sodium diclofenac (Table 2) was reacted with glutaraldehyde to result in a crosslink bond between hydroxyl functional groups. The crosslink can form between PVA-PVA chains, CNC-CNC or PVA-CNC. In
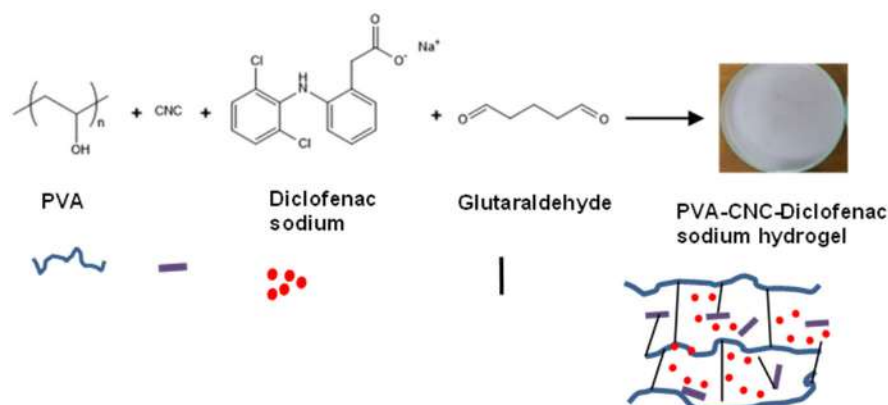
Fig 4. Synthesis of PVA-CNC-diclofenac sodium hydrogel crosslinked with glutaraldehyde

general, all hydrogel variations showed no visual difference. The white color comes from adding diclofenac sodium to the CNC solution. Due to its high water content, the hydrogel sample 0% CNC was challenging to be removed from the petri dish because the hydrogel absorbed more water during the gelling process when it was left at room temperature after mixing all materials. The hydrogel in sample 2% CNC showed a similar characteristic to the 0% CNC, which had relatively high water retention, leading it to stick to the petri dish. On the other hand, the 4, 6, and 8% CNC were more flexible and therefore, they were quickly removed from the petri dish and did not rip throughout the process.

The 8% CNC hydrogel had the highest tensile strength of 7.266 N/mm^2, while the 0% CNC hydrogel exhibited the lowest strength of 0.012 N/mm^2. Theoretically, CNC has Young's modulus value higher than microfibril cellulose (100 GPa) as CNC exhibit a higher degree of crystallinity after removal of the amorphous region [34]. CNC works as a hydrogel reinforcement, increasing the tensile strength and elastic modulus. As shown in Table 3, Young's modulus generally increased when the concentration of CNC

increased. Other than that, the material and treatment of hydrogels influence the mechanical properties.

The drug release profile of 0% CNC hydrogel, as shown in Fig. 5(a), showed a significant concentration release of about 0.009 mg/mL in the first 30 min because this hydrogel did not contain CNC and CNC controls drug release. The trend continued to peak at 0.017 mg/mL in 90 min before gradually decreasing to approximately 0.0028 mg/mL concentration in 480 min. However, after 90 min, the total weight of the hydrogel (Fig. 5(b)) increased steadily, indicating that the remaining diclofenac sodium that was not cross-linked with PVA had been dissolved. The same early bursts were present in 2% CNC hydrogel, however, the release concentration in the first 5 min was 72% lower (0.0025 mg/mL) than the 0% CNC hydrogel due to CNC content in the 2% CNC hydrogel, which played a role in controlling the release of drugs from the hydrogel. In 90 min, the release peaked at 0.022 mg/mL before declining.

However, after a 5-min incubation, the release concentration on 4% CNC hydrogel was unexpectedly greater than 0 and 2% CNC hydrogels, with approximately 0.015 mg/mL. This could be due to its

Table 3. Result of tensile test of PVA-CNC-diclofenac sodium hydrogel

Hydrogel sample	Tensile strength (MPa)	Maximum strain (%)	Young's modulus (MPa)
Hydrogel 0% CNC	0.01	76.25	191.72
Hydrogel 2% CNC	0.15	123.20	411.26
Hydrogel 4% CNC	1.53	67.48	580.03
Hydrogel 8% CNC	7.27	156.30	700.37
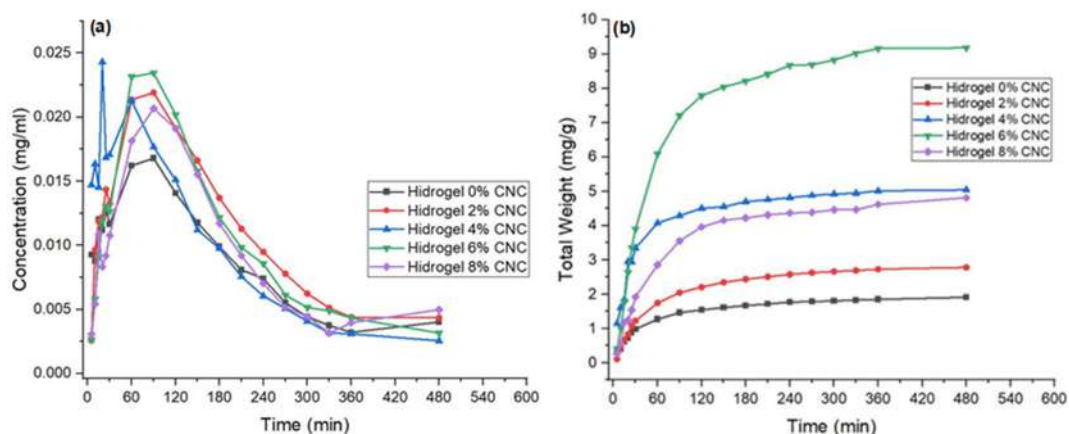
Fig 5. *In vitro* drug release of sodium diclofenac in PBS pH 7.4 (a) concentration release of rutin versus time, and (b) cumulative release ratio (mg/g) of rutin versus time

lower thickness compared to the other two hydrogels, causing more surface diclofenac sodium molecules to disperse. During the hydrogel formation process, diclofenac sodium might be trapped on the surface of the hydrogel. The concentration peaked at 0.024 mg/mL, the highest of all variants. After 60 min, the drug concentration dropped significantly, in line with the total weight profile, which remained relatively constant.

The 6% CNC hydrogel, in contrast, had a substantially lower concentration (0.002 mg/mL) than other hydrogels, indicating that CNC in the sample could effectively trap diclofenac sodium. The concentration reached a peak of 0.023 mg/mL in 90 min. As for 8% CNC hydrogel, the release concentration at the 5-min mark was slightly higher than 2% CNC hydrogel. The concentration should theoretically be lower because a higher amount of CNC should better retain drug molecules. This could be because the CNC in 8% CNC hydrogel could no longer effectively hold diclofenac sodium. Furthermore, low homogeneity of diclofenac sodium in the 8% CNC hydrogel was found.

Synthesis of PVA-CNC-Rutin Hydrogel

Hydrophobic rutin is also employed as a drug model for an anti-inflammatory agent. PVA-CNC-rutin hydrogels were prepared by crosslinking PVA and CNC with glutaraldehyde, followed by freeze-drying and drug loading in a rutin solution (Fig. 6). PVA and PVA-CNC exhibited the loading content around 4.89–4.90%.

The release profile indicates that all hydrogels performed controlled release (Fig. 7). The addition of hydrophobic rutin to 2% CNC hydrogel exhibited a significantly lower release concentration than 0% CNC hydrogel, revealing that CNC entrapment in the hydrogels affected the release of rutin. Rutin contains hydroxyl groups that can form hydrogen bonds with the hydroxyl and carboxyl groups of the hydrogel [28]. As the resulting intramolecular hydrogen bonds enhance resulting, the release concentration decrease. At the same time, the swelling ratio might also be responsible for the release behavior. A higher swelling ratio suggested that a higher rutin solution (in water) could be preserved in the hydrogel, therefore inhibiting rutin
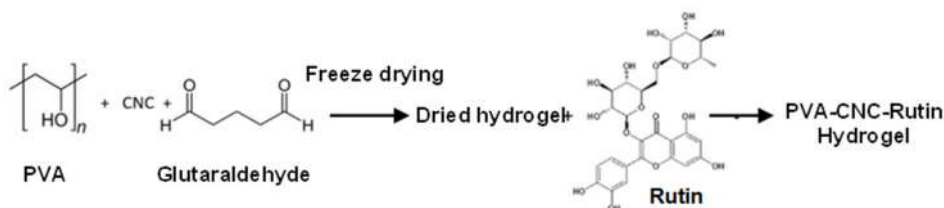
Fig 6. Synthesis of PVA-CNC-rutin hydrogel crosslinked with glutaraldehyde
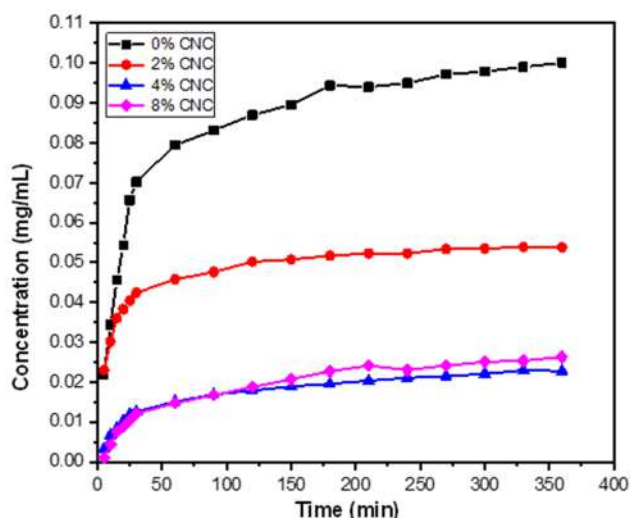
Fig 7. *In vitro* drug release of rutin in PBS pH 7.4, concentration release of rutin versus time

release from the hydrogel network. The 8% CNC showed higher release concentrations than 4% CNC after the first 120 min, and this could be due to the higher concentration of hydroxyl groups of 4% CNC, so the higher entrapment of rutin in 4% CNC was probably due to more and stronger hydrogen bonds with rutin. Further characterization should be conducted.

The *in vitro* rutin-release profiles comprised two phases. The initial one shows significant release and the later steady release. In the first 30 min, rutin was released rapidly (Fig. 7), showing release concentrations of 0.070, 0.042, 0.012 and 0.012 mg/mL for 0, 2, 4, and 8% CNC, respectively. This sudden release might be attributed to rutin near the hydrogel surface and the big difference in concentration between the hydrogel surface and PBS solution, resulting in great diffusion. The total rutin that was released from the hydrogels was 2.530, 1.376, 0.571, and 0.647 mg/mL, respectively. The low concentrations might be due to the poor solubility of rutin in water [35]. The drug release profile of hydrogel is influenced by the solubility of the drug, swelling ability of the hydrogel, and drug-hydrogel interactions [36].

Overall, all hydrogels had a similar release profile for diclofenac sodium, which was uncontrolled release behavior. Diclofenac sodium was released in high concentrations in the first 90 min, then gradually dropped. Compared to rutin, with 10 hydrogen bond

donors and 16 hydrogen bond acceptors, diclofenac sodium only has 1 hydrogen bond donor and 3 hydrogen bond acceptors [37]. Diclofenac sodium has weaker links or associations with CNC hydrogel's negatively charged carboxylate ions. Therefore, diclofenac sodium is released early and uncontrollably in PBS solution. The total weight of diclofenac sodium from the lowest to the greatest was in 0, 2, 8, 4, and 6% CNC hydrogel. This result was inversely proportional with the rutin-loaded hydrogels, where a higher CNC concentration resulted in a lower total weight of the drug released.

■ CONCLUSION

In this work, CNC reinforced PVA hydrogels containing active anti-inflammatory agents were prepared. Sodium diclofenac and rutin were employed as drug models. Hydrogels containing rutin showed controlled release properties, but hydrogel with diclofenac sodium performed non-controlled properties with high concentration release between 0 to 90-min incubation. The rutin release profile of 0% CNC showed the highest release concentration, whereas CNC containing hydrogels decreased significantly with the addition of CNC. However, 0% CNC hydrogel showed a distinct high concentration in the beginning compared with other samples comprising CNC. It was shown in this study that the addition of CNC to hydrogels can change their properties, such as tensile strength, Young's modulus, swelling ratio, loading content, and drug release behavior. Besides that, rutin and diclofenac sodium had different release profiles because rutin was better entrapped in the hydrogel. The addition of various concentrations of CNC into PVA hydrogels can result in tuneable drug release properties and potential to be applied in wound dressing. Noteworthy, the selection of active agents must be considered as it will contribute to the molecular interaction with CNC and further influence the drug release profile.

■ ACKNOWLEDGMENTS

■ **AUTHOR CONTRIBUTIONS**

LATWA: conceptualization, investigation, methodology, writing – review and editing, project administration; AA: experiment, investigation, methodology, writing; YEK: experiment, investigation, methodology; DP; writing – review and editing; UT: methodology, writing – review and editing; HA: writing – review and editing.

■ **REFERENCES**

[1] Kujath, P., and Michelsen, A., 2008, Wounds-from physiology to wound dressing, *Dtsch. Arztebl. Int.*, 105 (13), 239–248.

[2] de Oliveira Gonzalez, A.C., Costa, T.F., Andrade, Z.A., and Medrado, A.R.A.P., 2016, Wound healing - A literature review, *An. Bras. Dermatol.*, 91 (5), 614–620.

[3] Guo, S., and DiPietro, L.A., 2010, Factors affecting wound healing, *J. Dent. Res.*, 89 (3), 219–229.

[4] Zhang, J.M., and An, J., 2007, Cytokines, inflammation and pain, *Int. Anesthesiol. Clin.*, 45 (2), 27–37.

[5] Negut, I., Grumezescu, V., and Grumezescu, A.M., 2018, Treatment strategies for infected wounds, *Molecules*, 23 (9), 2392.

[6] Edwards, R., and Harding, K.G., 2004, Bacteria and wound healing, *Curr. Opin. Infect. Dis.*, 17 (2), 91–96.

[7] Heyer, K., Augustin, M., Protz, K., Herberger, K., Spehr, C., and Rustenbach, S.J., 2013, Effectiveness of advanced versus conventional wound dressings on healing of chronic wounds: Systematic review and meta-analysis, *Dermatology*, 226 (2), 172–184.

[8] Kumar, A., and Jaiswal, M., 2016, Design and *in vitro* investigation of nanocomposite hydrogel based in situ spray dressing for chronic wounds and synthesis of silver nanoparticles using green chemistry, *J. Appl. Polym. Sci.*, 133 (14), 43260.

[9] Dhivya, S., Padma, V.V., and Santhini, E., 2015, Wound dressings - A review, *Biomedicine*, 5 (4), 22.

[10] Koehler, J., Brandl, F.P., and Goepferich, A.M., 2018, Hydrogel wound dressings for bioactive treatment of acute and chronic wounds, *Eur. Polym. J.*, 100, 1–11.

[11] Wardhani, R.A.K., Asri, L.A.T.W., Rachmawati, H., Khairurrijal, K., and Purwasasmita, B.N., 2020, Physical–chemical crosslinked electrospun *Colocasia esculenta* tuber protein–chitosan–poly(ethylene oxide) nanofibers with antibacterial activity and cytocompatibility, *Int. J. Nanomed.*, 15, 6433–6449.

[12] Hanif, W., Hardiansyah, A., Randy, A., and Asri, L.A.T.W., 2021, Physically crosslinked PVA/graphene-based materials/aloe vera hydrogel with antibacterial activity, *RSC Adv.*, 11 (46), 29029–29041.

[13] Wardhani, R.A.K., Asri, L.A.T.W., Rachmawati, H., Khairurrijal, K., and Purwasasmita, B.S., 2019, Stabilization of chitosan-polyethylene oxide electrospun nanofibrous containing *Colocasia esculenta* tuber protein, *Mater. Res. Express*, 6 (11), 1150f4.

[14] Zheng, C., Liu, C., Chen, H., Wang, N., Liu, X., Sun, G., and Qiao, W., 2019, Effective wound dressing based on Poly (vinyl alcohol)/Dextran-aldehyde composite hydrogel, *Int. J. Biol. Macromol.*, 132, 1098–1105.

[15] Tavakoli, S., and Klar, A.S., 2020, Advanced hydrogels as wound dressings, *Biomolecules*, 10 (8), 1169.

[16] Wang, M., Xu, L., Hu, H., Zhai, M., Peng, J., Nho, Y., Li, J., and Wei, G., 2007, Radiation synthesis of PVP/CMC hydrogels as wound dressing, *Nucl. Instrum. Methods Phys. Res., Sect. B*, 265 (1), 385–389.

[17] Singh, D., Singh, A., and Singh, R., 2015, Polyvinyl pyrrolidone/carrageenan blend hydrogels with nanosilver prepared by gamma radiation for use as an antimicrobial wound dressing, *J. Biomater. Sci., Polym. Ed.*, 26 (17), 1269–1285.

[18] Chen, S.L., Fu, R.H., Liao, S.F., Liu, S.P., Lin, S.Z., and Wang, Y.C., 2018, A PEG-based hydrogel for effective wound care management, *Cell Transplant.*, 27 (2), 275–284.

[19] Liu, S., Jiang, T., Guo, R., Li, C., Lu, C., Yang, G., Nie, J., Wang, F., Yang, X., and Chen, Z., 2021, Injectable and degradable PEG hydrogel with antibacterial performance for promoting wound healing, *ACS Appl. Bio Mater.*, 4 (3), 2769–2780.

[20] Xu, Q., Ji, Y., Sun, Q., Fu, Y., Xu, Y., and Jin, L., 2019, Fabrication of cellulose nanocrystal/chitosan

hydrogel for controlled drug release, *Nanomaterials*, 9 (2), 253.

[21] Leung, A.C.W., Hrapovic, S., Lam, E., Liu, Y., Male, K.B., Mahmoud, K.A., and Luong, J.H.T., 2011, Characteristics and properties of carboxylated cellulose nanocrystals prepared from a novel one-step procedure, *Small*, 7 (3), 302–305.

[22] Tanpichai, S., and Oksman, K., 2016, Cross-linked nanocomposite hydrogels based on cellulose nanocrystals and PVA: Mechanical properties and creep recovery, *Composites, Part A*, 88, 226–233.

[23] George, J., and Sabapathi, S.N., 2015, Cellulose nanocrystals: Synthesis, functional properties, and applications, *Nanotechnol., Sci. Appl.*, 8, 45–54.

[24] Phanthong, P., Reubroycharoen, P., Hao, X., Xu, G., Abudula, A., and Guan, G., 2018, Nanocellulose: Extraction and application, *Carbon Resour. Convers.*, 1 (1), 32–43.

[25] Dong, S., Bortner, M.J., and Roman, M., 2016, Analysis of the sulfuric acid hydrolysis of wood pulp for cellulose nanocrystal production: A central composite design study, *Ind. Crops Prod.*, 93, 76–87.

[26] Lu, Z., Fan, L., Zheng, H., Lu, Q., Liao, Y., and Huang, B., 2013, Preparation, characterization and optimization of nanocellulose whiskers by simultaneously ultrasonic wave and microwave assisted, *Bioresour. Technol.*, 146, 82–88.

[27] Cui, S., Zhang, S., Ge, S., Xiong, L., and Sun, Q., 2016, Green preparation and characterization of size-controlled nanocrystalline cellulose via ultrasonic-assisted enzymatic hydrolysis, *Ind. Crops Prod.*, 83, 346–352.

[28] Isogai, A., and Zhou, Y., 2019, Diverse nanocelluloses prepared from TEMPO-oxidized wood cellulose fibers: Nanonetworks, nanofibers, and nanocrystals, *Curr. Opin. Solid State Mater. Sci.*, 23 (2), 101–106.

[29] Saghazadeh, S., Rinoldi, C., Schot, M., Kashaf, S.S., Sharifi, F., Jalilian, E., Nuutila, K., Giatsidis, G., Mostafalu, P., Derakhshandeh, H., Yue, K., Swieszkowski, W., Memic, A., Tamayol, A., and Khademhosseini, A., 2018, Drug delivery systems and materials for wound healing applications, *Adv. Drug Delivery Rev.*, 127, 138–166.

[30] Asri, L.A.T.W., Rahmatika, A., Fahreza, M.Z., Insanu, M., and Purwasasmita, B.S., 2018, Preparation and release behavior of carboxylated cellulose nanocrystals-alginate nanocomposite loaded with rutin, *Mater. Res. Express*, 5 (9), 095303.

[31] Cheng, M., Qin, Z., Liu, Y., Qin, Y., Li, T., Chen, L., and Zhu, M., 2014, Efficient extraction of carboxylated spherical cellulose nanocrystals with narrow distribution through hydrolysis of lyocell fibers by using ammonium persulfate as an oxidant, *J. Mater. Chem. A*, 2 (1), 251–258.

[32] Oun, A.A., and Rhim, J.W., 2018, Isolation of oxidized nanocellulose from rice straw using the ammonium persulfate method, *Cellulose*, 25 (4), 2143–2149.

[33] Santmartí, A., and Lee, K.Y., 2018, "Crystallinity and Thermal Stability of Nanocellulose" in *Nanocellulose Sustainability*, CRC Press, Boca Raton, Florida, US, 67–86.

[34] Dufresne, A., 2013, Nanocellulose: A new ageless bionanomaterial, *Mater. Today*, 16 (6), 220–227.

[35] Pivec, T., Kargl, R., Maver, U., Bračič, M., Elschner, T., Žagar, E., Gradišnik, L., and Stana Kleinschek, K., 2019, Chemical structure–Antioxidant activity relationship of water–based enzymatic polymerized rutin and its wound healing potential, *Polymers*, 11 (10), 1566.

[36] Dai, H., Zhang, H., Ma, L., Zhou, H., Yu, Y., Guo, T., Zhang, Y., and Huang, H., 2019, Green pH/magnetic sensitive hydrogels based on pineapple peel cellulose and polyvinyl alcohol: synthesis, characterization and naringin prolonged release, *Carbohydr. Polym.*, 209 (381), 51–61.

[37] National Center for Biotechnology Information, 2022, *PubChem Compound Summary for CID 5018304, Diclofenac sodium*, https://pubchem.ncbi.nlm.nih.gov/compound/Diclofenac-sodium, accessed on 10 September 2021.

Profiling of Phytochemical Compounds of East Java Red Rice Bran Has the High-Value Biological Activities as Antioxidant and Antidiabetic

Yoravika Dwiwibangga[1,2], Anna Safitri[1,2], and Fatchiyah Fatchiyah[1,3*]

[1]*Research Center of Smart Molecule of Natural Genetics Resource, Brawijaya University, Malang 65145, East Java, Indonesia*

[2]*Department of Chemistry, Faculty of Mathematics and Natural Sciences, Brawijaya University, Jl. Veteran, Malang 65145, East Java, Indonesia*

[3]*Department of Biology, Faculty of Mathematics and Natural Sciences, Brawijaya University, Jl. Veteran, Malang 65145, East Java, Indonesia*

* Corresponding author:

tel: +62-341-575-841
email: fatchiya@ub.ac.id

Abstract: *The phytochemicals contained in rice bran, mainly flavonoid compounds, are predicted to have biological activity. Flavonoids are able to counteract the free radicals and degrade insulin resistance. The East Java Red Rice Bran samples, e.g., Mentik Wangi, Aek Sibundong, and Blambangan, were used in the study. Their phytochemical profiles, functional groups, antioxidant, and antidiabetic activities were investigated. The phytochemical analysis showed that the bran of Mentik Wangi, Aek Sibundong, and Blambangan contained flavonoid, triterpenoid, phenolic, tannin, and glycoside. Based on the FTIR, some functional groups were identified in three rice bran varieties, namely, the O-H stretching, C-H aliphatic, C-H sp^3 stretching, C=C stretching aromatics, C=C stretching alkenes, CH_2 and CH_3 bonds rocking, C-H aromatic, CH-OH stretching alcohols, and C-O stretching ether or ester suggesting that rice brans are rich in phytochemical compounds. Through LC-HRMS analysis in positive ion mode, several types of flavonoids were confirmed. Pinocembrin was found in the three brands. The highest antioxidant and antidiabetic activity were observed in Blambangan rice bran with an IC_{50} value of 1.09 and 75.76 µg/mL, respectively. To conclude, the red rice bran phytochemical compounds exhibit potential biological activities as antioxidant and antidiabetic agents.*

Keywords: *antidiabetic; antioxidant; phytochemical; rice bran*

■ INTRODUCTION

Rice (*Oryza* spp.) is the most popular member of the Poaceae family [1]. Rice consists of more than 40,000 varieties worldwide and it is commonly divided into two widely cultivated types, *Oryza sativa* (Asian rice) and *Oryza glaberrima* (African rice) [2]. In developing countries, rice is an important cereal crop consumed both as a staple food as well as processed products [3]. In general, white rice dominates the rice market. Nonetheless, pigmented rice cultivars nowadays attract great interest from researchers, nutritionists, and clinicians. Attention is currently being given to the antioxidative and radical-scavenging properties of pigmented rice cultivars because

of their potential to provide and promote human health by reducing the concentration of reactive oxygen species and free radicals [1,4-6].

The pigmented rice cultivars include black rice, red rice, purple rice, and brown rice [6-7]. Red rice is suggested to contain various beneficial compounds for human health [5,8-9]. The major phytochemicals of red rice include phenolics, flavonoids, pro-anthocyanidins, and anthocyanins; which are believed to have several biological functions, such as antioxidants, antidiabetics, and anticholesterol [3,9-10].

Even though red rice and its biological capacities have been widely studied, research on red rice bran biological activities is still limited. The rice bran has been

generally used as livestock feed, although, it is potential to be explored for its contents and biological activities. The phytochemical investigations of red rice bran have shown that it contains flavonoids, phenolics, anthocyanins, proanthocyanidins, tannins, alkaloids, and some essential oils [9,11-12]. The flavonoid compounds detected in red rice bran include quercetin, apigenin, catechin, luteolin, and myricetin [9,13-14]. Moreover, several lipophilic components were identified, including γ-oryzanol, tocotrienols, and tocopherols [15-16]. These compounds have been suggested to possess high antioxidant activity [17-19].

Antioxidants are molecules that neutralize free radicals and prevent the damages that lead to degenerative diseases, such as cardiovascular, diabetes, hyperlipidemia, and other diseases. Antioxidants are substances that can protect cells from damage caused by unstable molecules known as free radicals [20-23]. Flavonoid compounds in pigmented rice are known to have a biological activity on metabolic disorders, such as cardiovascular disease, obesity, cancer, and diabetes mellitus. Flavonoid compounds act as antidiabetic agents due to their ability to regulate carbohydrate digestion, insulin signaling, insulin secretion, glucose uptake, and adipose deposition [24]. Flavonoids have been shown to decrease the pathogenesis of diabetes and its complications. Flavonoid compounds can reduce apoptosis and insulin resistance. Furthermore, flavonoids can increase insulin secretion and GLUT 4 translocation [25]. Flavonoid compounds can interact with α-amylase and α-glucosidase enzymes to form complex structures through hydrogen bonds and hydrophobic interactions. The interaction of flavonoids and enzymes causes inhibition of substrate binding to enzymes so that enzyme activity decreases [26-27].

To the best of our knowledge, exploration of biological activities from red rice bran from East Java has not been conducted. In the current study, three varieties of red rice, i.e., Aek Sibundong, Mentik Wangi, and Blambangan were studied. The study aims to identify compounds and investigate the antioxidant and antidiabetic activity of the extracts from red rice bran from East Java through phytochemical analysis, FTIR, LC-HRMS, antioxidant, and antidiabetic assays.

■ EXPERIMENTAL SECTION

Materials

The materials used were purchased from Sigma-Aldrich (Darmstadt, Germany): methanol (99.9%), sodium hydroxide (98%), sulfuric acid (99.9%), chloroform (99.5%), iron(III) chloride (97%), glacial acetic acid (99%), hydrogen chloride (37%), sodium carbonate (99%), trichloroacetic acid (99%), potassium ferricyanide (99%), and aluminium chloride (99.9%). The following materials were obtained from Merch: ascorbic acid (99%), gallic acid (97.5%), quercetin (95%), dinitrosalicylic acid reagent (98%), acarbose (95%), Wagner reagent, Folin-Ciocalteu reagent (1:1), phosphate buffer, starch, and α-amylase enzyme (from *Aspergillus oryzae*). Three varieties of rice were obtained from three regencies in East Java, Indonesia. They were Mentik Wangi from Ngawi, Aek Sibundong from South Malang, and Blambangan from Banyuwangi.

Instrumentation

The instruments used in this study were a Genesys 150 Thermo Scientific UV-Vis spectrophotometer and a Fourier Transform Infrared (FTIR) spectrophotometer (Shimadzu) IR Type Prestige 21. Identification and separation of components were performed using Liquid Chromatography-High-Resolution Mass Spectrometry (LC-HRMS) Thermo Scientific Dionex UltiMate 3000 RSLCnano in the Laboratorium Sentral Ilmu Hayati (LSIH), Brawijaya University.

Procedure

Maceration of red rice bran

The powder of three varieties of red rice bran samples, each 200 g, was macerated with 99.9% methanol for 3 × 24 h at room temperature [28]. Each extract was filtered with Whatman paper no. 42 and then evaporated by rotary evaporator vacuum with a slow speed at 95 rpm, at 45 °C. The extracts were then stored under freezing temperature (4 °C) for further analysis [8,28].

Phytochemical analysis of red rice bran

The phytochemical analysis of flavonoid, triterpenoid, phenolic, tannin, alkaloid, glycoside, and saponin was conducted based on previous studies [29-

30]. Different wavelengths were used in each test to measure the absorbance of the samples using a spectrophotometer UV-Vis, i.e., 430 nm for the flavonoid test, 544 nm for the triterpenoid test, 276 nm for the steroid test, 276 nm for the phenolic test, 725 nm for tannin test, 470 nm for alkaloid test, 600 nm for glycoside test, and 435 nm for saponin test [8].

Determination of total phenolic content

The total phenolic content in extracted red rice bran was determined by a spectrophotometric method using the Follin-Ciocalteu's reagent [31]. The 0.2 mL sample (4 mg/mL) was mixed with 0.6 mL of distilled water and 0.2 mL of Folin-Ciocalteu's reagent. After 5 min, 1 mL of saturated sodium carbonate solution (8% w/v in distilled water) was added to the mixture, and the volume was made up to 3 mL with distilled water. The final mixture was kept in the dark at ambient conditions for 30 min to complete the reaction. The absorbance was measured by a UV-Vis spectrophotometer at 745 nm. All measurements were determined in triplicate, and the data were expressed as mg Gallic Acid Equivalent (GAE)/100 g of crude extract of rice bran. The phenolic content was calculated as GAE/g of dry plant material based on a standard curve of gallic acid (5–100 mg/mL, $Y = 0.0104x - 0.0314$, $R^2 = 0.9644$). All determinations were carried out in triplicates.

Determination of total flavonoids content

The aluminium chloride colorimetric method was used for the determination of the total flavonoid content of the sample [31]. An amount of 0.6 mL extract was mixed with 0.6 mL of 2% aluminium chloride. After mixing, the solution was incubated for 60 min at room temperature. The absorbance of the reaction mixtures was measured against blank at 418 nm wavelength with a UV-Vis spectrophotometer. The concentration of total flavonoid content in the test samples was calculated from the calibration plot (5–20 mg/mL, $Y = 0.0506x + 0.0019$, $R^2 = 0.9856$) and expressed as mg quercetin equivalent (QE)/g of dried plant material. All the determinations were carried out in triplicates.

Identification of red rice bran extract using FTIR

Identification of functional groups contained in the extract of red rice bran was observed using FTIR spectrophotometer. A small amount of sample was dropped on one part of the KBr window. Then, another part of the KBr window was attached. Thus, the sample was evenly distributed on the window surface. The KBr window is placed in the holder, and the FTIR instrument is switched on. The IR spectra were recorded in the wavenumber range from 4500 to 400 cm^{-1}.

Identification of red rice bran extract using LC-HRMS

LC-HRMS was conducted in LSIH (Laboratorium Sentral Ilmu Hayati), Brawijaya University. The column used was a Hypersil GOLD aQ 50 mm × 1 mm × 1.9 μm particle size with an injection volume of 100 μL. Solvents used were solvent A = 0.1% formic acid in water and solvent B = 0.1% formic acid in acetonitrile. The elution gradient was 30 min with an analytical flow rate of 40 μL/min and the solvent ratio was set according to Table 1. Liquid chromatography was followed by mass spectrometer analysis (Thermo Scientific Q Exactive mass spectrometer) in the Electrospray ionization (ESI) method with positive ion mode detection. Experiments were set as follows: sheath gas (N_2) pressure = 50 psi, spray voltage = 4.5 kV, capillary temperature = 300 K, and m/z range = 50–750. Spectra were recorded in full mass scan condition with resolution = 70000 followed by data-dependent MS^2 scan with resolution = 17500. The compounds were determined using Compound Discoverer software version 3.2 with mzCloud MS/MS library.

Ferric reducing/antioxidant power (FRAP) assay

Various concentrations of each red rice bran extract were made with a range of 0–200 μg/mL for Mentik Wangi and Aek Sibundong; and 0–10 μg/mL for Blambangan. The solution was mixed with 2.5 mL of 0.2 M phosphate

Table 1. Gradient elution

Time (min)	%A : %B
0	95:5
2	95:5
15	40:60
22	5:95
25	5:95
25.1	95:5
30	95:5

buffer pH 6.6 and 2.5 mL of 1% potassium ferricyanide. The solution mixture was incubated at 50 °C for 20 min, and then 2.5 mL of 10% TCA was added and homogenized. An aliquot of the solution was put in a new test tube, mixed with distilled water and 0.1% ferric chloride solution. The absorbance was measured at 700 nm using a UV-Vis spectrophotometer [32]. The antioxidant activity of ascorbic acid with various concentrations of 0, 2, 4, 6, 8, and 10 μg/mL was also measured for a positive reference. The antioxidant activity was then calculated using Eq. (1).

$$\% \text{ antioxidant} = \left[\frac{\text{sample absorbance} - \text{control absorbance}}{\text{sample absorbance}} \right] \times 100\% \quad (1)$$

The IC_{50} value was determined by a linear regression equation between the sample concentration and its antioxidant activity as the X and Y-axis. The IC_{50} value of each sample was expressed as a value of Y = 50, and the value of X was obtained as IC_{50}.

α-Amylase inhibitory activity

Briefly, 250 μL of bran extracts (Mentik Wangi and Aek Sibundong (0–200 μg/mL), Blambangan (0–100 μg/mL)) and acarbose (0–10 g/mL) were put into a test tube and added 250 μL of the α-amylase enzyme (50 μg/mL). Each solution was homogenized and incubated at 37 °C for 30 min. Then, 250 μL of 1% (w/v) starch was added and incubated again at 25 °C for 10 min. After that, 500 μL of DNS reagent was added and heated in boiling water for 5 min. The solution was cooled, and 5 mL of distilled water was added. Absorbance measurements at 480 nm and the IC_{50} value were calculated [28]. The antidiabetic activity was then calculated using Eq. (2).

$$\% \text{ antioxidant} = \left[\frac{\text{control absorbance} - \text{sample absorbance}}{\text{control absorbance}} \right] \times 100\% \quad (2)$$

Statistical analysis

All values were written as means ± standard deviation (SD) of three replicates. Statistical analysis of total phenolic content, total flavonoid content, antioxidant, and antidiabetic activity was performed using one-way analysis of variance (ANOVA), followed by the Tukey test for homogeneous data. Inhomogeneous data were analyzed by Brown-Forsythe and Games-Howell in IBM Statistical Product and Service Solutions software version 23 with a 95% confidence level ($p < 0.05$).

■ RESULTS AND DISCUSSION

Phytochemical Analysis

The phytochemical constituents contained in the extracts are important for predicting the biological and pharmacological activities. The phytochemical analysis was conducted based on the color changes after extracts reacted with the standard reagents for secondary metabolite detection. Three varieties of red rice bran were subjected to phytochemical identification. Results are presented in Table 2. The phytochemical analysis revealed that the red rice bran of Mentik Wangi, Aek Sibundong, and Blambangan contained flavonoids, triterpenoid, phenolic, tannin, and glycoside. Interestingly, steroids were detected only on Aek Sibundong bran. From the measurement results of the absorbance value, the higher absorbance indicates the higher concentration of secondary metabolites contained in the bran extract. These results suggest that varieties of red rice bran are rich in secondary metabolite compounds, thus, they have high nutrition contents. Triterpenoids and flavonoids were considered as the main

Table 2. The phytochemical screening in pigmented rice

Sample	Flavonoid	Triterpenoid	Steroid	Phenolic	Tannin	Alkaloid	Glycoside	Saponin
Menthik Wangi	+++	++++	-	++	++	-	+	-
Aek Sibundong	++	++	+	++	++	-	+	-
Blambangan	++	++	-	+	+	-	+	-

-      = not detected
+   = detected phytochemical in low intensity of color
++   = detected phytochemical compound with medium color intensity
+++   = detected phytochemical compound with high color intensity
++++   = detected phytochemical compound with very high color intensity

class of secondary metabolites identified in three red rice bran based on absorbance values.

FTIR Analysis

FTIR spectra (Fig. 1) described absorbances of various chemical components in the three red rice bran extracts. The FTIR spectra of the samples visually do not show major differences demonstrating that the chemical components contained are generally similar (Table 3). Ten specific regions appeared in the three FTIR spectra. They were from O-H stretching, C-H aliphatic, C-H sp³ stretching, C=C stretching aromatic, C=C stretching alkenes, CH_2 and CH_3 rocking, C-H aromatic, CH-OH stretching alcohols, C-O stretching ether or ester, and fingerprint region. However, some specific wavenumbers shifted. The O-H stretching absorbance was found in around 3433–3217 cm⁻¹. The O-H stretching region

commonly comes from the flavonoid, phenolic, glycoside, and tannin compounds in the extracts.

FTIR results also supported the results of the phytochemical analysis. The C-H aliphatic and C-H sp³ stretching vibrations at 3000–2856 cm⁻¹ with the presence of C-H bending vibrations on CH_2 and CH_3 at 1461–1459 cm⁻¹ region indicated a dimethyl group as triterpenoid compounds [33]. The band detected in 1744–1711 cm⁻¹ indicated the presence of ester, which showed a hydrolyzed tannin compound formed from a hydroxyl group and a carboxyl group from phenolic acid. Also, the form of O-H stretching, C–H aliphatic, C=C alkenes, C=C aromatics, C-O-H, and C-O-C ethers indicated tannin groups [34]. The bands at 3433–3417, 3010–3007, 1744–1711, 1377–1370, 1268–1242, and 1169–1073 cm⁻¹ indicated the presence of phenolic compounds, glycosides, and flavonoids [35]. The absorption band in
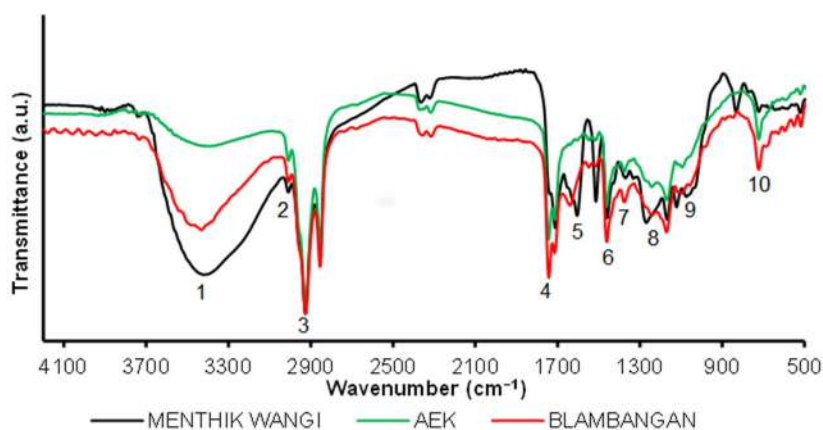
Fig 1. FTIR spectrum of red rice bran

Table 3. The wavenumber values at the FTIR absorption peaks of red rice bran and their probable functional groups

No.	Wavenumber (cm⁻¹)			Probable functional group
	Mentik Wangi	Aek Sibundong	Blambangan	
1	3417.20	3421.48	3432.89	O-H stretching
2	3009.31	3007.88	3007.88	C-H aliphatic
3	2926.59–2855.28	2925.16–2855.28	2925.16–2855.28	C-H sp³ stretching
4	1739.98–1711.45	1744.26–1712.88	1742.83–1714.31	C=C stretching aromatic
5	1605.91–1514.64	1526.05	1638.72–1548.87	C=C stretching alkenes
6	1459.01	1460.44	1460.44	CH_2 and CH_3 (the vibrational rocking of the C-H)
7	1370.59	1374.87	1376.29	C-H aromatic and carbonyl-carbonate
8	1267.90	1242.23	1243.66	CH-OH stretching alcohols
9	1168.07–1073.94	1168.07–1095.33	1170.92–1095.33	C-O stretching ether or ester
10	1000–400	1000–400	1000–400	Fingerprint region

the region 1000–400 cm^{-1} was evidenced as fingerprinting region. This region provides some information related to organic compounds that are probably present in the brans, such as carbohydrates, proteins, and organic acids.

LC-HRMS Analysis

LC-HRMS analysis aims to identify the flavonoid compounds of bran extracts. LC-HRMS analysis led to the interim identification of 20 compounds for each East Java red rice bran extract (Table 4). The results of the LC-HRMS identified many components, including flavonoids, phenolic acids, amino acids, saponin, alkaloids, vitamins, and fatty acids. The compounds that were tentatively identified in the three extracts of East Java red rice bran were pinocembrin, 4-coumaric acid, ferulic acid, hexadecanamide, 2-(methylthio)benzothiazole, 3,5-di-*tert*-butyl-4-hydroxybenzaldehyde, monoolein, methyl 9*Z*,11*E*,13*E*-octadecatrienoate, 4-methoxycinnamic acid, bis(2-ethylhexyl) phthalate, and stearamide.

Table 4. LC-HRMS results of the East Java red rice bran

Samples	Proposed Compound	RT (min)	mzCloud best match	Dm (error mass)
Mentik Wangi	4-Coumaric acid	6.74	99.3	0.66
	Ferulic acid	7.25	98.0	0.59
	Dibenzylamine	7.71	98.2	0.21
	Tricin 5-O-β-D-glucoside	7.81	98.3	0.35
	Pinocembrin	13.72	98.3	0.81
	2-(Methylthio)benzothiazole	14.37	97.9	1.88
	Bis(4-ethylbenzylidene)sorbitol	15.10	99.6	0.56
	Tributyl phosphate	17.14	99.0	0.94
	2,4-dihydroxyheptadec-16-en-1-yl acetate	17.27	98.7	0.79
	3,5-di-tert-Butyl-4-hydroxybenzaldehyde	17.37	97.9	1.07
	Dibutyl phthalate	18.43	98.6	2.05
	Linoleoyl Ethanolamide	19.34	97.2	1.52
	Methyl 9*Z*,11*E*,13*E*-Octadecatrienoate	19.72	98.3	1.70
	4-Methoxycinnamic acid	20.95	98.7	1.02
	Monoolein	21.31	98.7	2.52
	Hexadecanamide	21.95	99.0	1.92
	Bis(2-ethylhexyl) phthalate	23.18	99.8	2.70
	Bis(2-ethylhexyl) adipate	23.29	98.7	1.66
	Di(2-ethylhexyl) phthalate	23.32	99.7	2.70
	Stearamide	23.96	98.2	2.02
Aek Sibundong	Diisodecyl phthalate	5.31	98.6	0.20
	Bis(3,5,5-trimethylhexyl) phthalate	5.30	98.6	0.52
	4-Coumaric acid	6.75	99.3	0.95
	Ferulic acid	7.27	96.3	0.60
	Dibenzylamine	7.72	98.7	0.36
	12*Z*-9,10,11-trihydroxyoctadec-12-enoic acid	11.68	99.1	1.45
	Pinocembrin	13.74	97.4	0.93
	2-(Methylthio)benzothiazole	14.39	98.6	1.04
	Triisobutyl phosphate	17.15	98.1	1.40
	3,5-di-*tert*-Butyl-4-hydroxybenzaldehyde	17.37	98.3	0.87
	9-Oxo-10*E*,12*E*-octadecadienoic acid	18.32	98.2	1.45

Table 4. LC-HRMS results of the East Java red rice bran (*Continued*)

Samples	Proposed Compound	RT (min)	mzCloud best match	Dm (error mass)
Aek Sibundong	Dibutyl phthalate	18.36	96.9	1.09
	Monoolein	19.14	96.8	0.80
	Methyl 9*Z*,11*E*,13*E*-Octadecatrienoate	19.73	98.7	2.12
	1-Linoleoyl glycerol	20.03	98.3	1.27
	Palmitoyl ethanolamide	20.65	99.2	1.13
	4-Methoxycinnamic acid	20.75	98.9	0.56
	Hexadecanamide	21.92	98.9	1.09
	Bis(2-ethylhexyl) phthalate	23.17	99.7	1.37
	Stearamide	23.99	98.3	1.37
Blambangan	4-Coumaric acid	6.76	99.0	0.59
	Ferulic acid	7.28	97.5	0.65
	7-hydroxy-5-methoxy-2-phenyl-3,4-dihydro-2*H*-1-benzopyran-4-one	11.40	98.5	0.98
	Pinocembrin	13.75	97.8	0.93
	2-(Methylthio)benzothiazole	14.41	98.2	1.63
	Bis(4-ethylbenzylidene)sorbitol	15.11	99.5	1.10
	2,4-dihydroxyheptadec-16-en-1-yl acetate	17.27	98.9	0.79
	3,5-di-tert-Butyl-4-hydroxybenzaldehyde	17.38	99.2	1.26
	Diisobutyl phthalate	18.43	98.7	2.16
	Methyl 9*Z*,11*E*,13*E*-Octadecatrienoate	19.73	99.3	1.18
	1-Linoleoyl glycerol	19.86	97.9	1.08
	Palmitoyl ethanolamide	20.68	98.9	1.13
	4-Methoxycinnamic acid	20.94	98.2	0.97
	Octadec-9-ynoic acid	21.09	97.5	0.11
	Monoolein	21.54	98.4	0.88
	Oleamide	21.86	97.9	1.94
	Hexadecanamide	21.96	99.1	1.68
	Bis(2-ethylhexyl) phthalate	23.33	99.6	1.91
	Methyl palmitate	24.40	98.3	0.58
	Stearamide	24.52	98.7	2.12

Table 5. Flavonoid and phenolic components of the three bran samples

Flavonoids	Phenolics
Pinocembrin	4-Coumaric acid
Monoolein	Ferulic acid
	4-Methoxycinnamic acid

The total ion chromatogram of each bran variety is shown in Fig. 2. In Mentik Wangi bran, LC-HRMS chromatograms and mass spectra show the compound 4-coumaric acid with the molecular formula $C_9H_8O_3$, established by *m/z* 165.05453 [M+H]⁺. Tricin 5-O-β-D-glucoside has a molecular formula $C_{23}H_{24}O_{12}$, which appeared at *m/z* 493.13397 [M+H]⁺. The molecular formula of pinocembrin, 4-methoxycinnamic acid, and bis(2-ethylhexyl) phthalate is $C_{15}H_{12}O_4$, $C_{10}H_{10}O_3$, and $C_{24}H_{38}O_4$, respectively, with the *m/z*, emerged at 257.08063 [M+H]⁺, 179.06999 [M+H]⁺, and 391. 2834 [M+H]⁺ (Fig. 3). In the LC-HRMS chromatograms and mass spectra of Aek Sibundong's bran, ferulic acid, 3,5-di-tert-butyl-4-hydroxybenzaldehyde, and monoolein with the molecular formula $C_{10}H_{10}O_4$, $C_{15}H_{22}O_2$, and $C_{21}H_{40}O_4$, respectively, with the *m/z* appeared at 195.06525 [M+H]⁺,

Indones. J. Chem., 2022, 22 (5), 1304 - 1320

1311
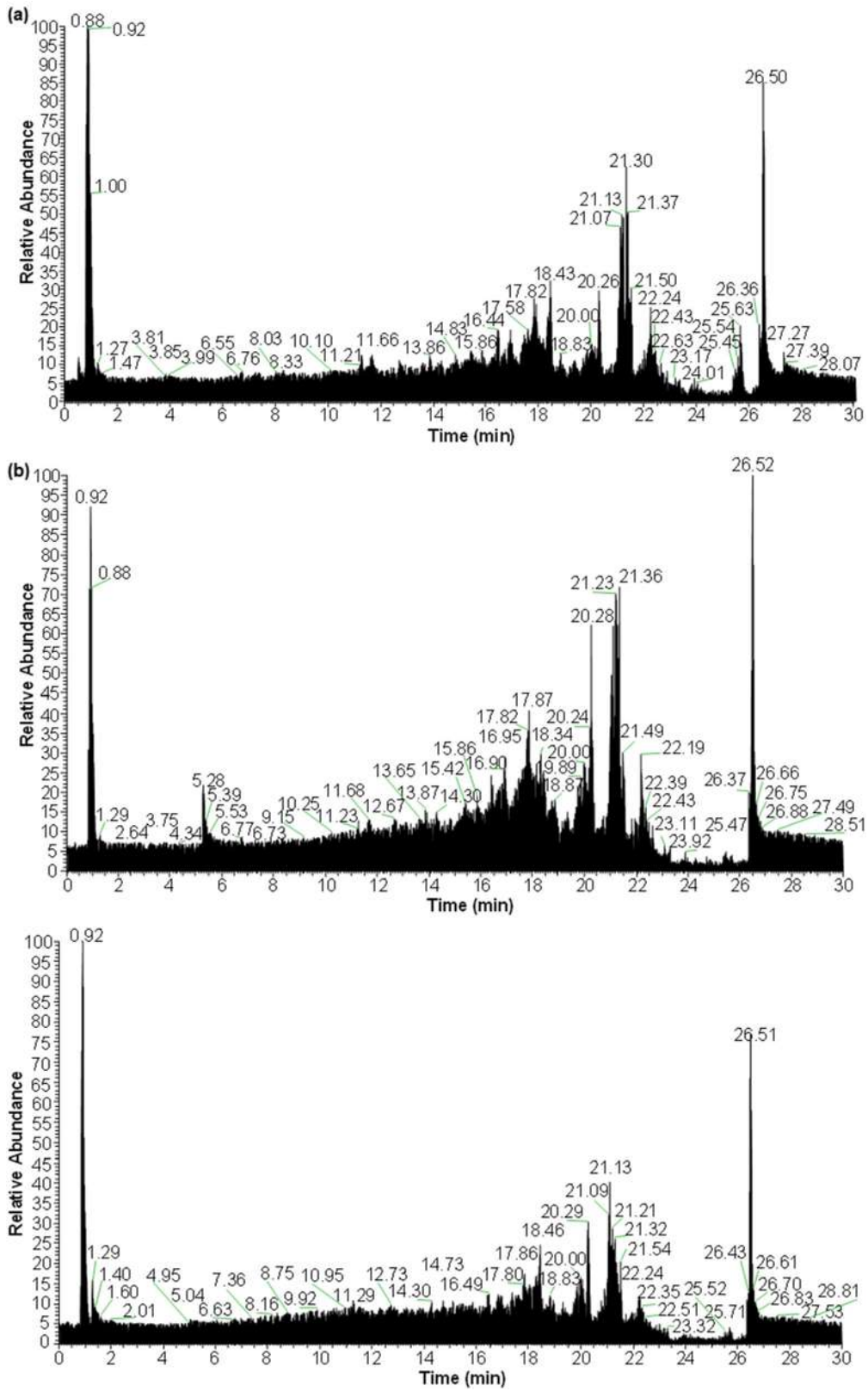
**Fig 2.** Total ion chromatograms (a) Mentik Wangi, (b) Aek Sibundong, (c) Blambangan
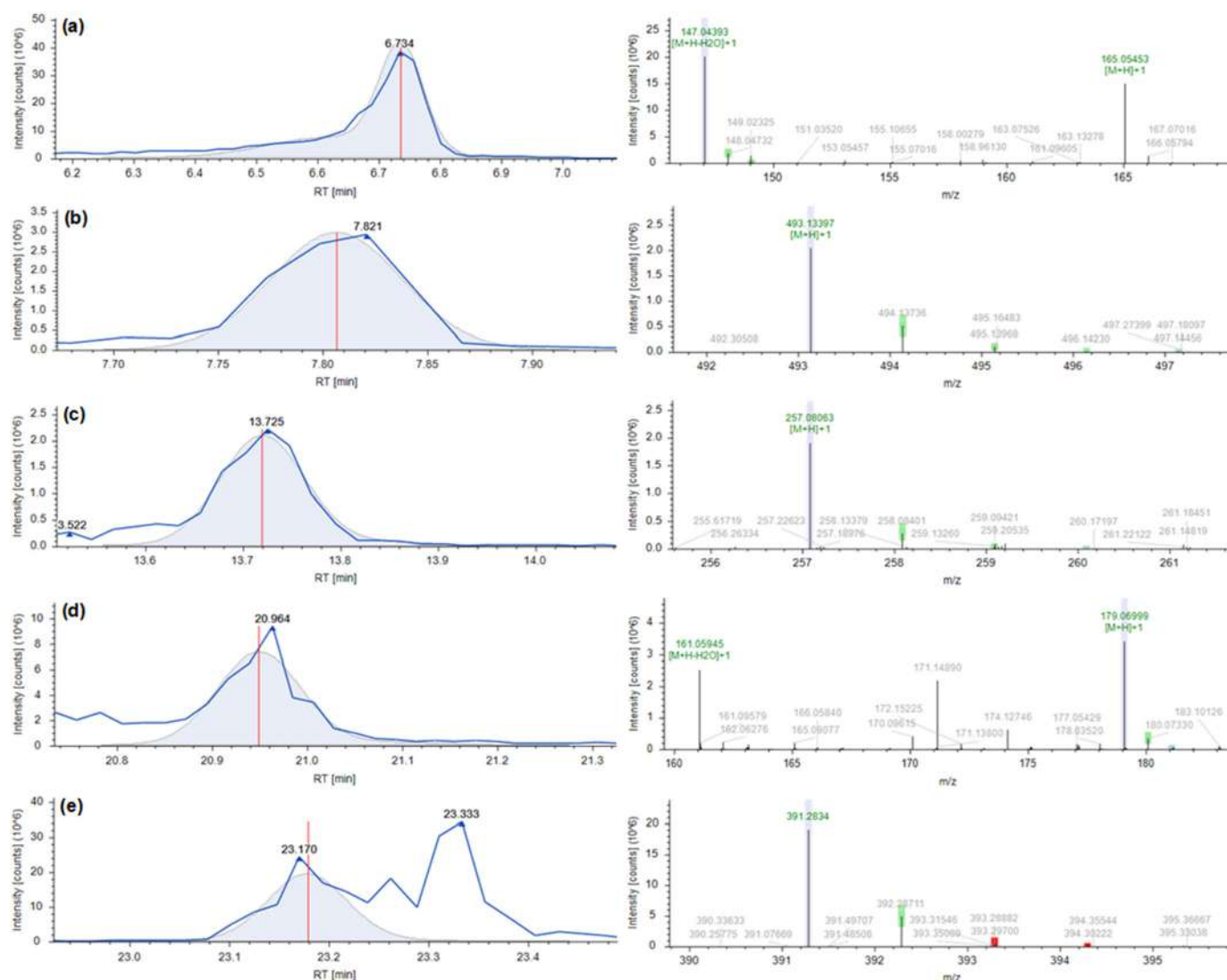
Fig 3. LC-HRMS chromatograms and mass spectra of (a) 4-Coumaric acid, (b) Tricin 5-O-β-D-glucoside, (c) Pinocembrin, (d) 4-Methoxycinnamic acid, and (e) Bis(2-ethylhexyl) phthalate from the East Java Mentik Wangi bran extract

235.16925 [M+H]$^+$, and 357.29965 [M+H]$^+$. The 1-Linoleoyl glycerol and palmitoyl ethanolamide compounds have a molecular formula $C_{21}H_{38}O_4$, and $C_{18}H_{37}NO_2$, established by m/z 355.28387 [M+H]$^+$ and 300.28937 [M+H]$^+$ were identified (Fig. 4). Furthermore, Blambangan bran identified the molecular formula for the compound 7-hydroxy-5-methoxy-2-phenyl-3,4-dihydro-2*H*-1-benzopyran-4-one, bis(4-ethylbenzylidene)sorbitol, and 2,4-dihydroxyheptadec-16-en-1-yl acetate are $C_{16}H_{14}O_4$, $C_{24}H_{30}O_6$, and $C_{19}H_{36}O_4$ with the m/z value at 271.09631 [M+H]$^+$, 415.21106 [M+H]$^+$, and 351.25052 [M+H]$^+$. Diisobutyl phthalate and methyl palmitate with

the molecular formula $C_{16}H_{22}O_4$ and $C_{17}H_{34}O_2$, recognized by m/z 279.15848 [M+H]$^+$ and 271.26312 [M+H]$^+$ (Fig. 5).

From the results of the LC-HRMS analysis, it is known that pinocembrin, tricin 5-O-β-D-glucoside, monoolein, and 7-hydroxy-5-methoxy-2-phenyl-3,4-dihydro-2*H*-1-benzopyran-4-one are part of the flavonoid compound. In addition, it's also known that 4-coumaric acid, ferulic acid, and 4-methoxycinnamic acid are part of the phenolic. In the results of the LC-HRMS, pinocembrin, monoolein, tricin 5-O-β-D-glucoside, 4-coumaric acid, 4-methoxycinnamic acid, and ferulic acid

Indones. J. Chem., 2022, 22 (5), 1304 - 1320

1313
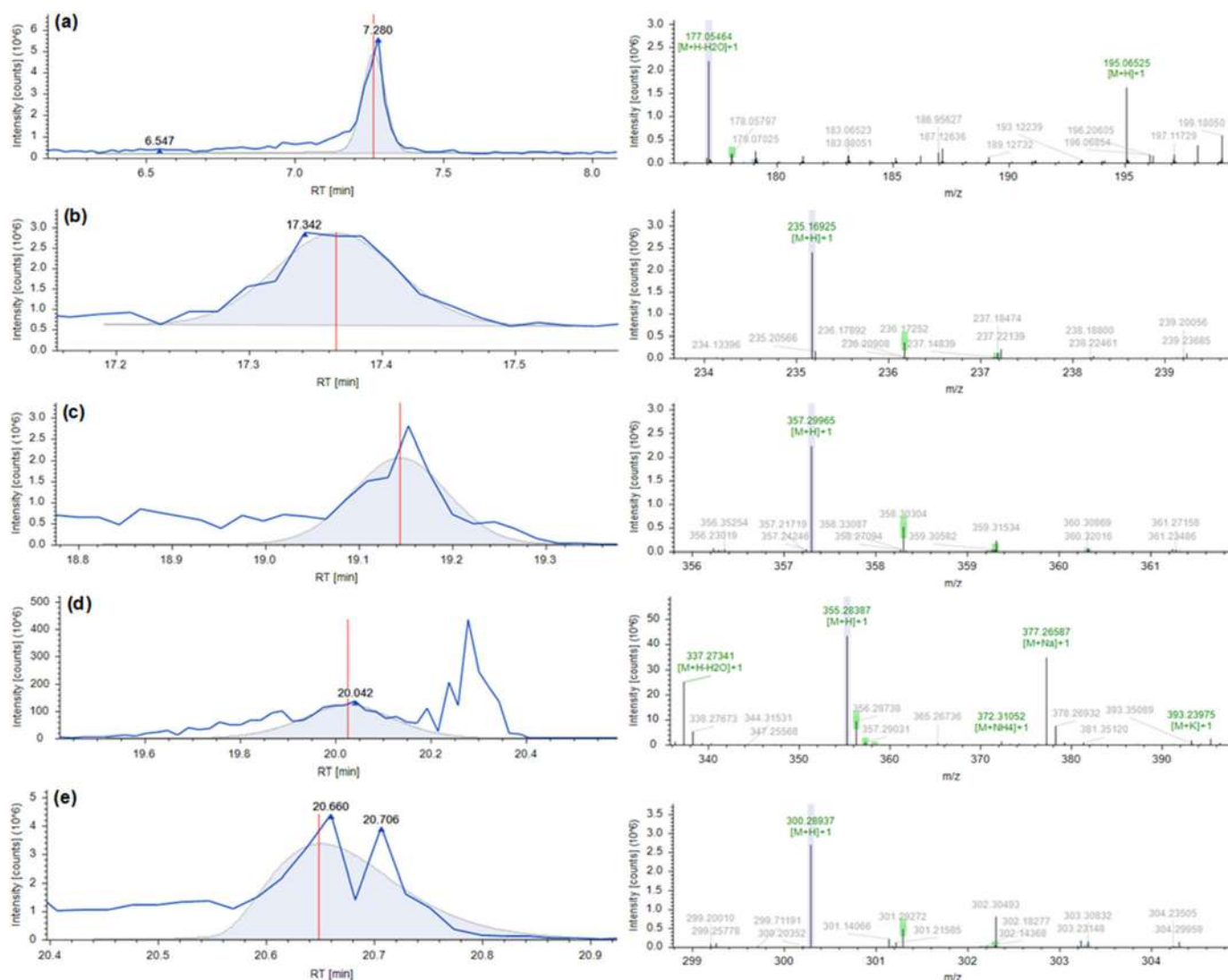
Fig 4. LC-HRMS chromatograms and mass spectra of (a) Ferulic acid, (b) 3,5-di-tert-butyl-4-hydroxybenzaldehyde, (c) Monoolein, (d) 1-Linoleoyl glycerol, and (e) Palmitoyl ethanolamide from the East Java Aek Sibundong bran extract

were found in Mentik Wangi rice were identified. In Aek Sibundong's bran, pinocembrin and monoolein were identified as flavonoid compounds. In addition, 4-coumaric acid, 4-methoxycinnamic acid, and ferulic acid were identified as phenolic compounds. In Blambangan's bran, pinocembrin, monoolein, 7-hydroxy-5-methoxy-2-phenyl-3,4-dihydro-2*H*-1-benzopyran-4-one, 4-coumaric acid, 4-methoxycinnamic acid, and ferulic acid were identified as flavonoid and phenolic compounds. The flavonoid and phenolic components in the three bran samples are shown in Table 5. Antidiabetic and antioxidant activity of each bran variety was influenced by flavonoid and phenolic compounds. Flavonoid

compounds have an important role in the health segment, such as antidiabetic, antioxidant, antiviral, anti-inflammatory, and antibacterial. Flavonoids show beneficial antioxidant activity in managing diabetes mellitus [36].

Antioxidant Activity

Investigation of flavonoid and phenolic in red rice bran continued using UV-Vis spectrophotometer to analyze total flavonoid and phenolic content. Table 6 displays the calculation of total phenolic and flavonoid content. The highest total phenolic and flavonoid content is in Mentik Wangi (2200.97 ± 0.056 mg GAE/g sample
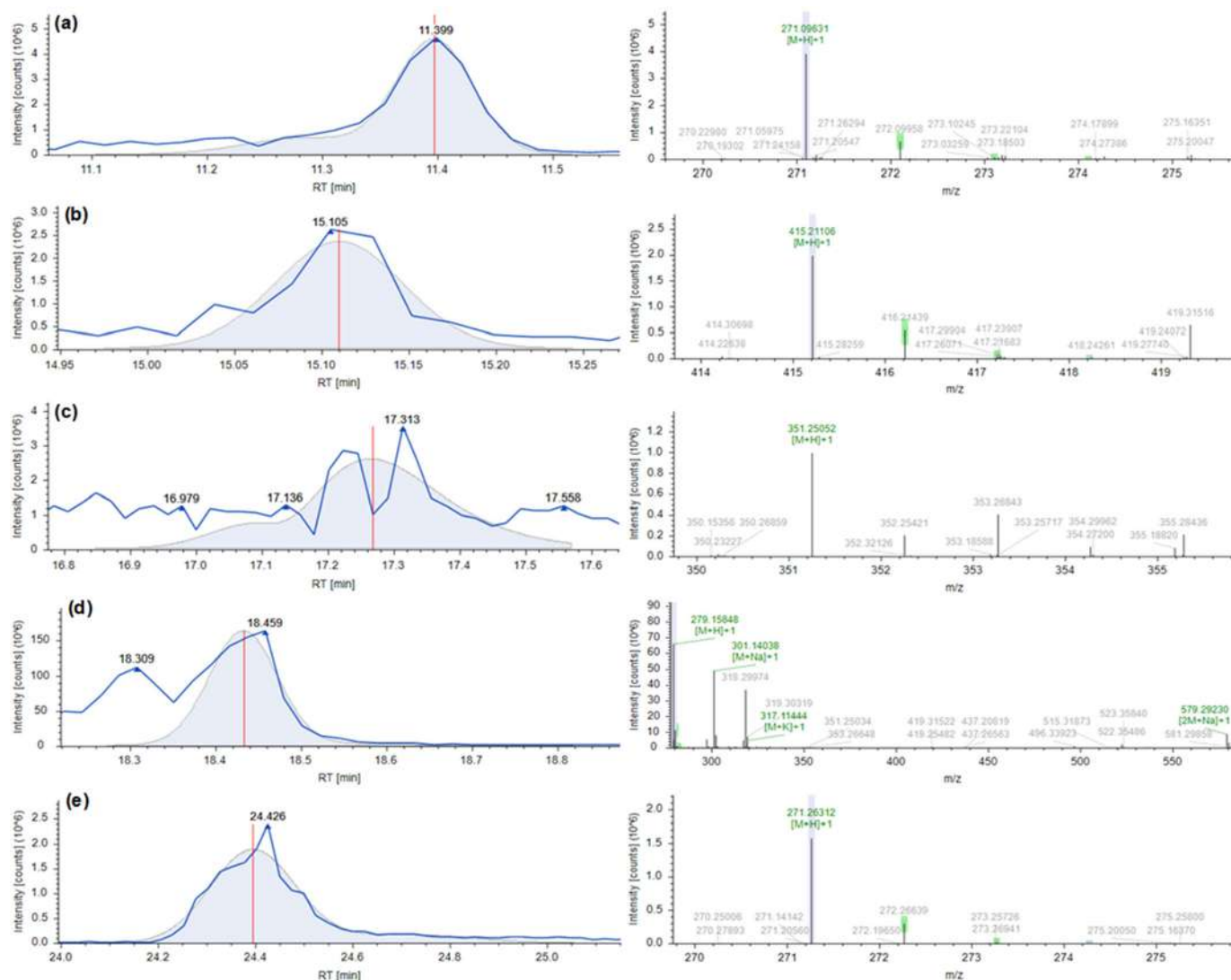
Fig 5. LC-HRMS chromatograms and mass spectra of (a) 7-hydroxy-5-methoxy-2-phenyl-3,4-dihydro-2*H*-1-benzopyran-4-one, (b) Bis(4-ethylbenzylidene)sorbitol, (c) 2,4-dihydroxyheptadec-16-en-1-yl acetate, (d) Diisobutylphthalate, and (e) Methyl palmitate from the East Java Blambangan bran extract

and 1467.96 ± 0.011 mg QE/g sample). Based on the One-Way ANOVA test, it was known that the significance value was $p > 0.05$. Therefore, it was assumed that the value of total flavonoid and phenolic content in the three varieties of red rice bran were not significantly different. Furthermore, the total flavonoid and phenolic content values also supported the results of phytochemical analysis, FTIR spectra, and LC-HRMS results. The highest total flavonoid and phenolic content were found in Mentik Wangi bran. These results indicated that the concentration of flavonoid and phenolic compounds in Mentik Wangi bran was higher than in the other two rice brans.

Ascorbic acid as the positive reference resulted in the highest antioxidant activity with the IC_{50} value of 0.28 ± 0.93 μg/mL. The reducing power activity was found in the order of ascorbic acid > Blambangan > Aek Sibundong > Mentik Wangi. The antioxidant activities of all red rice bran were lower than that of ascorbic acid. Based on the Games-Howell test, the antioxidant activity in the three varieties of red rice bran was significantly different. The lowest antioxidant activity was shown in Mentik Wangi bran with the IC_{50} value of 124.30 ± 1.27μg/mL. Both Mentik Wangi and Aek Sibundong brans resulted in an IC_{50} value of less than 250 μg/mL,

which is categorized as weak antioxidant activity; whereas Blambangan bran and ascorbic acid had an IC_{50} value of less than 10 μg/mL, which is categorized as very strong antioxidant activity (Table 6) [9]. A lower IC_{50} value represents a stronger free radical inhibitor (strong free radical inhibitors are active at low concentrations) [37].

Unpaired electrons or free radicals tend to attract electrons from other compounds to achieve atomic or molecular stability. If these free radicals are not inactivated, they can damage cell-forming macromolecules, such as proteins, carbohydrates, fats, and nucleic acids. The reducing power in the FRAP method is an indicator of the potential of antioxidant compounds [38]. Compounds that have reducing power may be able to act as antioxidants because compounds can stabilize radicals by donating electrons or hydrogen atoms. This interaction will stabilize the radical compound and stop the chain reaction of the formation of other free radicals [38-39].

Antidiabetic Activity

Inhibition of α-amylase and α-glucosidase is considered effective for controlling type 2 diabetes mellitus. The α-amylase secreted by the salivary glands and pancreas functions to break the α-1,4-glycoside bond to produce maltose and glucose. When the α-amylase enzyme is inhibited, the digestion of carbohydrates will also be blocked so as the level of glucose absorption into the blood will decrease [40]. Acarbose was used as a comparison for the α-amylase enzyme inhibition assay. The maximum potential of the sample in inhibiting α-amylase was indicated by the smallest amount of IC_{50}. Assays for the inhibitory activity of the α-amylase enzyme are shown in Table 7. Acarbose as a reference resulted in the highest antidiabetic activity with the IC_{50} value of 6.12 ± 1.68 μg/mL. The highest antidiabetic activity was shown

in Blambangan bran with the IC_{50} value of 75.76 ± 0.36 μg/mL. The antidiabetic activity was found in the order of acarbose > Blambangan > Aek Sibundong > Mentik Wangi. Based on the Games-Howell test, the antidiabetic activity in the three varieties of red rice bran was significantly different.

Flavonoids have been extensively studied as α-glucosidase and α-amylase inhibitors [41-42]. The hydroxyl group of flavonoid compounds can effectively be conjugated to the residue of the active site of α-amylase and α-glucosidase enzymes. The 4-oxo group on the C ring of flavonoids contributes to the distribution of the electron cloud by donating a hydrogen atom to form hydrogen bonds with the active site residue. This interaction will inhibit the enzyme activity [42-43].

The phytochemical profiles, total flavonoid and phenolic content values, FTIR spectra, and LC-HRMS results contained in the extracts are important for predicting the biological and pharmacological activity of plants. All phytochemical profiles detected in red rice bran have many biological activities. Flavonoid and phenolic compounds are commonly known to have high antioxidant activity [44-45]. The potential of phenolic and flavonoid compounds as antioxidants are caused by the hydroxyl groups in phenolic compounds. The hydroxyl group acts as a hydrogen atom donor when it

Table 7. The antidiabetic activity of red rice bran in inhibiting α-amylase

Sample	IC_{50} (μg/mL)
Mentik Wangi	171.82[a] ± 0.49
Aek Sibundong	157.29[b] ± 1.28
Blambangan	75.76[c] ± 0.36

*Different notations show significant differences at the α = 0.05 level

Table 6. Total phenolic, total flavonoid, and the antioxidant activity of red rice bran

Sample	Total phenolic content (mg GAE/g)	Total flavonoid content (mg QE/g)	IC_{50} (μg/mL)
Mentik wangi	2200.97 ± 0.056	1467.96 ± 0.011	124.30[a] ± 1.27
Aek sibundong	1578.00 ± 0.110	1197.00 ± 0.011	116.83[b] ± 1.42
Blambangan	949.48 ± 0.056	1122.77 ± 0.011	1.09[c] ± 0.82

*GAE = Gallic acid equivalent, QE = Quercetin equivalent.

*Different notations show significant differences at the α = 0.05 level

reacts with free radicals through an electron transfer mechanism so that the oxidation process can be inhibited [46-47]. Flavonoid and phenolic compounds are most effective at stabilizing free radicals (hydroxyl, superoxide, and peroxyl radicals) and can inhibit oxidation reactions because they can produce phenolic radicals that are stabilized by the resonance effect of aromatic rings [48]. Flavonoids and phenolic compounds are useful to stop free radicals in the body and to prevent aging factors. Flavonoids with antioxidant activity are beneficial in the management of diabetes mellitus [49-50]. The number of hydroxyl groups, hydroxyl configuration, C2-C3 double bonds, and C-4 ketonic functional groups is essential in the manifestation of flavonoid bioactivity, especially for antidiabetic effects [51-52].

The FRAP method was applied to study the antioxidant activity. The FRAP method is often used to evaluate the ability of an antioxidant to donate an electron. In this examination, the ability of extracts to reduce the ferric cyanide complex to the ferrous cyanide complex was determined [53]. Compounds with reducing power indicate that they are electron donors and can reduce the oxidized intermediates so they can act as antioxidants. Results showed that red rice bran had various antioxidant activities. Mentik Wangi and Aek Sibundong were categorized as having weak antioxidant activity, whereas Blambangan was very strong antioxidant activity. Based on previous research, Aek Sibundong bran with the IC_{50} value of 116.83 ± 1.42 g/mL had weaker antioxidant activity than Aek Sibundong red rice with the IC_{50} value of 6.65 g/mL, whereas Blambangan bran with the IC_{50} value of 1.09 ± 0.82 g/mL had stronger antioxidant activity than Blambangan red rice with the IC_{50} value of 34 g/mL [54].

The α-amylase inhibition test was used to evaluate the ability of flavonoid and phenolic compounds to inhibit enzyme activity. The results showed that red rice bran has various antidiabetic activities. The bran of Mentik Wangi, Aek Sibundong, and Blambangan had antidiabetic activity, respectively, with IC_{50} values of 171.82 ± 0.49, 157.29 ± 1.28, and 75.76 ± 0.36 μg/mL. This inhibition was influenced by the interaction of hydrogen bonds between the hydroxyl groups of flavonoids and the catalytic residues of the enzyme. The interaction between

enzymes and flavonoids can reduce starch digestion and postprandial glycemia. Flavonoids can also prevent the glucose absorption by inhibiting glucose transporters [55-56].

The results of antioxidant and antidiabetic activity were not positively correlated with the results of phytochemical analysis, total phenolic, and flavonoid content. Flavonoid and phenolic compounds were indeed responsible for the antioxidant and antidiabetic activity. However, the number and position of the –OH group in the compound were more influential. Compounds having hydroxyl groups in the 5,7-*meta* position have higher antioxidant activity. Substitution of the alkyl group at the -*ortho* or -*para* position in ring B will increase the electron density of the hydroxyl group with an inductive effect. However, long or branched alkyl chains will decrease antioxidant activity due to the influence of steric effects. In addition, the lower the dissociation energy of the –OH bond, the greater the ability of antioxidant activity because it is easier to react with free radicals [57-58].

Flavonoids have a stronger free radical scavenging ability than phenolic acids because they have a higher number of hydroxyl groups. The high antioxidant and antidiabetic activity of Blambangan bran are influenced by the flavonoid content. The highest peak area of pinocembrin and monoolein compared to other bran varieties indicated the high concentration of these compounds. Pinocembrin and monoolein are known to be effective in inhibiting the activity of the α-amylase enzyme. The conjugation of 4-oxo group on C ring plays an important role in the antioxidant and antidiabetic activities. The hydroxyl group of flavonoids enhances the interaction with enzymes, especially by forming hydrogen bonds. The hydroxyl group at the C-3 position in ring B, the C-5 position in ring A, and the carbonyl compound at the C-4 position in ring C have the potential to inhibit the activity of α-amylase enzymes. In addition, the 5,7-*meta*-dihydroxylation arrangement on the A ring also increases the antioxidant and antidiabetic capabilities of flavonoids [50,59-60]. Therefore, further *in vitro* and *in vivo* analyses are needed to elucidate the biological function of East Java red rice brans.

■ **CONCLUSION**

This study shows that each red rice bran has antioxidant activity and potential as an inhibitor α-amylase enzyme. The highest antioxidant and antidiabetic activity were found in Blambangan red rice bran with an IC_{50} value of 1.09 ± 0.82 and 75.76 ± 0.36 μg/mL, respectively. The use of phytochemical analysis, FTIR, and LC-HRMS tentatively identified many compounds contained in the rice bran extracts. The phytochemical compounds discovered in red rice bran included flavonoids, triterpenoid, phenolic, tannin, and glycoside. FTIR analysis supported the results of the phytochemical analysis. Various flavonoid and phenolic compounds found in the results of the LC-HRMS analysis affect the biological activity of the rice brans. East Java red rice bran is prospective to be used as an antioxidant and antidiabetic. Alpha-amylase inhibition has led to the discovery of new plant-based therapeutic products, specifically for diabetes. Further studies with an *in vivo* and *in silico* approach are needed to confirm the results of the current work.

■ **ACKNOWLEDGMENTS**

■ **AUTHOR CONTRIBUTIONS**

Yoravika Dwiwibangga carried out the experiment, interpretation of data, and wrote the manuscript. Fatchiyah supervised the experiment, analyzed data, and revised the manuscript. Anna Safitri analyzed data and wrote the manuscript.

■ **REFERENCES**

[1] Rathna Priya, T.S., Eliazer Nelson, A.R.L., Ravichandran, K., and Antony, U., 2019, Nutritional and functional properties of coloured rice varieties of South India: A review, *J. Ethn. Foods*, 6 (1), 11.

[2] Furuta, T., Komeda, N., Asano, K., Uehara, K., Gamuyao, R., Angeles-Shim, R.B., Nagai, K., Doi, K., Wang, D.R., Yasui, H., Yoshimura, A., Wu, J.,

McCouch, S.R., and Ashikari, M., 2015, Convergent loss of awn in two cultivated rice species *Oryza sativa* and *Oryza glaberrima* is caused by mutations in different loci, *G3: Genes, Genomes, Genet.*, 5 (11), 2267–2274.

[3] Samyor, D., Das, A.B., and Deka, S.C., 2017, Pigmented rice a potential source of bioactive compounds: A review, *Int. J. Food Sci. Technol.*, 52 (5), 1073–1081.

[4] Sari, D.R.T., Safitri, A., Cairns, J.R.K., and Fatchiyah, F., 2020, Anti-apoptotic activity of anthocyanins has potential to inhibit caspase-3 signaling, *J. Trop. Life Sci.*, 10 (1), 15–25.

[5] Agustin, A.T., Safitri, A., and Fatchiyah, F., 2020, An *in silico* approach reveals the potential function of cyanidin-3-*O*-glucoside of red rice in inhibiting the advanced glycation end products (AGEs)-receptor (RAGE) signaling pathway, *Acta Inform. Med.*, 28 (3), 170–179.

[6] Fitriana, W.D., Ersam, T., Shimizu, K., and Fatmawati, S., 2018, Antioxidant activity of *Moringa oleifera* extracts, *Indones. J. Chem.*, 16 (3), 297–301.

[7] Meera, K., Smita, M., Haripriya, S., and Sen, S., 2019, Varietal influence on antioxidant properties and glycemic index of pigmented and non-pigmented rice, *J. Cereal Sci.*, 87, 202–208.

[8] Fatchiyah, F., Sari, D.R.T., Safitri, A., and Cairns, J.R., 2020, Phytochemical compound and nutritional value in black rice from Java Island, Indonesia, *Syst. Rev. Pharm.*, 11 (7), 414–421.

[9] Ghasemzadeh, A., Karbalaii, M.T., Jaafar, H.Z.E., and Rahmat, A., 2018, Phytochemical constituents, antioxidant activity, and antiproliferative properties of black, red, and brown rice bran, *Chem. Cent. J.*, 12 (1), 17.

[10] Boue, S.M., Daigle, K.W., Chen, M.H., Cao, H., and Heiman, M.L., 2016, Antidiabetic potential of purple and red rice (*Oryza sativa* L.) bran extracts, *J. Agric. Food Chem.*, 64 (26), 5345–5353.

[11] Kubota, M., Watanabe, R., Hosojima, M., Saito, A., Sasou, A., Masumura, T., Harada, Y., Hashimoto, H., Fujimura, S., and Kadowaki, M., 2020, Rice bran protein ameliorates diabetes, reduces fatty liver, and

has renoprotective effects in Zucker diabetic fatty rats, *J. Funct. Foods*, 70, 103981.

[12] Ghasemzadeh, A., Baghdadi, A., Jaafar, H.Z.E., Swamy, M.K., and Megat Wahab, P.E., 2018, Optimization of flavonoid extraction from red and brown rice bran and evaluation of the antioxidant properties, *Molecules*, 23 (8), 1863.

[13] Moko, E.M., and Rahardiyan, D., 2020, Structure of stigmasterols in bran of red rice from Minahasa Regency, North Sulawesi, Indonesia, *Fullerene J. Chem.*, 5 (1), 16–22.

[14] Spaggiari, M., Dall'Asta, C., Galaverna, G., and del Castillo Bilbao, M.D., 2021, Rice bran by-product: From valorization strategies to nutritional perspectives, *Foods*, 10 (1), 85.

[15] Friedman, M., 2013, Rice brans, rice bran oils, and rice hulls: Composition, food, and industrial uses, and bioactivities in humans, animals, and cells, *J. Agric. Food Chem.*, 61 (45), 10626–10641.

[16] Shao, Y., and Bao, J., 2015, Polyphenols in whole rice: Genetic diversity and health benefits, *Food Chem.*, 180, 86–97.

[17] Gul, K., Yousuf, B., Singh, A.K., Singh, P., and Wani, A.A., 2015, Rice bran: Nutritional values and its emerging potential for development of functional food—A review, *Bioact. Carbohydr. Dietary Fibre*, 6 (1), 24–30.

[18] Nam, S.H., Choi, S.P., Kang, M.Y., Koh, H.J., Kozukue, N., and Friedman, M., 2006, Antioxidative activities of bran extracts from twenty one pigmented rice cultivars, *Food Chem.*, 94 (4), 613–620.

[19] Min, B., McClung, A.M., and Chen, M.H., 2011, Phytochemicals and antioxidant capacities in rice brans of different color, *J. Food Sci.*, 76 (1), C117–C126.

[20] Anand David, A.V., Arulmoli, R., and Parasuraman, S., 2016, Overviews of biological importance of quercetin: A bioactive flavonoid, *Pharmacogn. Rev.*, 10 (20), 84–89.

[21] Ho, E., Karimi Galougahi, K., Liu, C.C., Bhindi, R., and Figtree, G.A., 2013, Biological markers of oxidative stress: Applications to cardiovascular research and practice, *Redox Biol.*, 1 (1), 483–491.

[22] Renganathan, S., Srivastava, A., and Pillai, R.G., 2020, Dhanwantaram kashayam, an Ayurvedic polyherbal formulation, reduces oxidative radicals and reverts lipids profile towards normal in diabetic rats, *Biochem. Biophys. Rep.*, 22, 100755.

[23] Al-Naggar, R.A., Osman, M.T., Mohamed, I.N., Bin Nor Aripin, K.N., and Abdulghani, M.A.M., 2017, Effect of *Nigella sativa* supplementation on human lipids: Systematic review, *J. Appl. Pharm. Sci.*, 7 (4), 213–219.

[24] Abotaleb, M., Samuel, S.M., Varghese, E., Varghese, S., Kubatka, P., Liskova, A., and Büsselberg, D., 2018, Flavonoids in cancer and apoptosis, *Cancers*, 11 (1), 28.

[25] AL-Ishaq, R.K., Abotaleb, M., Kubatka, P., Kajo, K., and Büsselberg. D., 2019, Flavonoids and their anti-diabetic effects: Cellular mechanisms and effects to improve blood sugar levels, *Biomolecules*, 9 (9), 430.

[26] Takahama, U., and Hirota, S., 2018, Interactions of flavonoids with α-amylase and starch slowing down its digestion, *Food Funct.*, 9 (2), 677–687.

[27] Lo Piparo, E., Scheib, H., Frei, N., Williamson, G., Grigorov, M., and Chou, C.J., 2008, Flavonoids for controlling starch digestion: Structural requirements for inhibiting human α-amylase, *J. Med. Chem.*, 51 (12), 3555–3561.

[28] Safitri, A., Roosdiana, A., Hitdatania, E., and Damayanti, S.A., 2021, *In vitro* alpha-amylase inhibitory activity of microencapsulated *Cosmos caudatus* Kunth. extracts, *Indones. J. Chem.*, 22 (1), 212–222.

[29] Lisi, A.K.F., Runtuwene, M.R.J., and Wewengkang, D.S., 2017, Uji fitokimia dan aktivitas antioksidan bunga soyogik (*Saurauia bracteosa* DC.), *Pharmacon*, 6 (1), 53–61.

[30] Yuda, P.E.S.K., Cahyaningsih, E., and Winariyanthi, N.P.Y., 2017, Skrining fitokimia dan analisis kromatografi lapis tipis ekstrak tanaman patikan kebo (*Euphorbia hirta* L.), *JINTO*, 3 (2), 61–70.

[31] Chandra, S., Khan, S., Avula, B., Lata, H., Yang, M.H., Elsohly, M.A., and Khan, I.A., 2014, Assessment of total phenolic and flavonoid content, antioxidant properties, and yield of aeroponically

and conventionally grown leafy vegetables and fruit crops: A comparative study, *Evidence-Based Complementary Altern. Med.*, 2014, 253875.

[32] Wanyo, P., Schoenlechner, R., Meeso, N., and Siriamornpun, S., 2014, Antioxidant activities and sensory properties of rice bran with marigold tea, *Food Appl. Biosci. J.*, 2 (1), 1–14.

[33] Astuti, M.D., Kuntorini, E.M., and Wisuda, F.E.P., 2014, Isolasi dan identifikasi terpenoid dari fraksi *n*-butanol herba lampasau (*Diplazium esculentum* Swartz), *J. Kim. Valensi*, 4 (1), 20–24.

[34] Sari, P.P., Rita, W.S., and Puspawati, N.M., 2015, Identifikasi dan uji aktivitas senyawa tanin dari ekstrak daun trembesi (*Samanea saman* (Jacq.) Merr) sebagai antibakteri *Escherichia coli* (*E. coli*), *J. Kim.*, 9 (1), 27–34.

[35] Gafur, M.A., 2013, Isolasi dan Identifikasi Senyawa Flavonoid dari Daun Jamblang (*Syzygium cumini*), *Undergraduate Thesis*, Universitas Negeri Gorontalo, Gorontalo, Indonesia.

[36] Pollastri, S., and Tattini, M., 2011, Flavonols: Old compounds for old roles, *Ann. Bot.*, 108 (7), 1225–1233.

[37] Chanda, S., and Dave, R., 2009, *In vitro* models for antioxidant activity evaluation and some medicinal plants possessing antioxidant properties: An overview, *Afr. J. Microbiol. Res.*, 3 (13), 981–996.

[38] Murray, R.K., Granner, D.K., and Rodwell, V.W., 2009, *Biokimia Harper*, 27th Ed., Medical Book Publisher EGC, Jakarta, Indonesia.

[39] Wang, T., Li, Q., and Bi, K.S., 2018, Bioactive flavonoids in medicinal plants: structure, activity and biological fate, *Asian J. Pharm. Sci.*, 13 (1), 12–23.

[40] Chiang, Y.C., Chen, C.L., Jeng, T.L., and Sung, J.M., 2014, *In vitro* inhibitory effects of cranberry bean (*Phaseolus vulgaris* L.) extracts on aldose reductase, α-glucosidase and α-amylase, *Int. J. Food Sci. Technol.*, 49 (6), 1470–1479.

[41] Khalil-Moghaddam, S., Ebrahim-Habibi, A., Pasalar, P., Yaghmaei, P., and Hayati-Roodbari, N., 2012, Reflection on design and testing of pancreatic alpha-amylase inhibitors: An *in silico* comparison between rat and rabbit enzyme models, *Daru, J. Pharm. Sci.*, 20 (1), 77.

[42] Yin, Z., Zhang, W., Feng, F., Zhang, Y., and Kang, W., 2014, α-Glucosidase inhibitors isolated from medicinal plants, *Food Sci. Hum. Wellness*, 3 (3-4), 136–174.

[43] Xu, H., 2010, Inhibition kinetics of flavonoids on yeast α-glucosidase merged with docking simulations, *Protein Pept. Lett.*, 17 (10), 1270–1279.

[44] Limwachiranon, J., Huang, H., Shi, Z., Li, L., and Luo, Z., 2018, Lotus flavonoids and phenolic acids: health promotion and safe consumption dosages, *Compr. Rev. Food Sci. Food Saf.*, 17 (2), 458–471.

[45] Rukmana, R.M., Soesilo, N.P., Rumiyati, R., and Pratiwi, R., 2016, The effect of ethanolic extract of black and white rice bran (*Oryza sativa* L.) on cancer cells, *Indones. J. Biotechnol.*, 21 (1), 63–69.

[46] San Miguel-Chavez, R., 2017, "Phenolic Antioxidant Capacity: A Review of the State of the Art" in *Phenolic Compounds - Biological Activity*, Eds. Soto-Hernandez, M., Palma Tenango, M., and Garcia-Mateos, R., IntechOpen Limited, London, 59–74.

[47] Sari, B. L., Susanti, N., and Sutanto, S., 2017, Skrining Fitokimia dan aktivitas antioksidan fraksi etanol alga merah *Eucheuma spinosum*, *Pharm. Sci. Res.*, 2 (2), 59–68.

[48] Pękal, A., and Pyrzynska, K., 2014, Evaluation of aluminium complexation reaction for flavonoid content assay, *Food Anal. Methods*, 7 (9), 1776–1782.

[49] Sutjiatmo, A.B., Edriayani, N., Mulyasari, T.E., and Hermanto, F., 2020, Antioxidant and antiaging assays of *Ageratum conyzoides* L. ethanolic extract, *Pharm. Sci. Res.*, 7 (3), 145–152.

[50] Sarian, M.N., Ahmed, Q.U., Mat So'ad, S.Z., Alhassan, A.M., Murugesu, S., Perumal, V., Syed Mohamad, S.N.A., Khatib, A., and Latip, J., 2017, Antioxidant and antidiabetic effects of flavonoids: A structure-activity relationship based study, *BioMed Res. Int.*, 2017, 8386065.

[51] Semighini, E.P., Resende, J.A., de Andrade, P.,

Morais, P.A.B., Carvalho, I., Taft, C.A., and Silva, C.H.T.P., 2011, Using computer-aided drug design and medicinal chemistry strategies in the fight against diabetes, *J. Biomol. Struct. Dyn.*, 28 (5), 787–796.

[52] Jadav, P., Bahekar, R., Shah, S.R., Patel, D., Joharapurkar, A., Kshirsagar, S., Jain, M., Shaikh, M., and Sairam, K.V.V.M., 2012, Long-acting peptidomimetics based DPP-IV inhibitors, *Bioorg. Med. Chem. Lett.*, 22 (10), 3516–3521.

[53] Ferreira, I.C.F.R., Baptista, P., Vilas-Boas, M., and Barros, L., 2007, Free-radical scavenging capacity and reducing power of wild edible mushrooms from northeast Portugal: Individual cap and stipe activity, *Food Chem.*, 100 (4), 1511–1516.

[54] Agustin, A.T., Safitri, A., and Fatchiyah, F., 2021, Java red rice (*Oryza sativa* L.) nutritional value and anthocyanin profiles and its potential role as antioxidant and anti-diabetic, *Indones. J. Chem.*, 21 (4), 968–978.

[55] Cahyana, Y., and Adiyanti, T., 2021, Flavonoids as antidiabetic agents, *Indones. J. Chem.*, 21 (2), 512–526.

[56] Pascual, J.M., and Ronen, G.M., 2015, Glucose transporter type I deficiency (G1D) at 25 (1990-2015): Presumption, facts, and the lives of persons with this rare diseases, *Pediatr. Neurol.*, 53 (5), 379–393.

[57] Nsangou, M., Dhaouadi, Z., Jaidane, N., and Lakhdar, Z.B., 2008, DFT study of the structure of hydroxybenzoic acids and their reactions with $^{\bullet}OH$ and $\cdot O_2^-$ radicals, *J. Mol. Struct.*, 850 (1-3), 135–143.

[58] Wright, J.S., Johnson, E.R., and DiLabio, G.A., 2001, Predicting the activity of phenolic antioxidants: Theoretical method, analysis of substituent effects, and application to major families of antioxidants, *J. Am. Chem. Soc.*, 123 (6), 1173–1183.

[59] Şöhretoğlu, D., and Sari, S., 2019, Flavonoids as alpha-glucosidase inhibitors: Mechanistic approaches merged with enzyme kinetics and molecular modelling, *Phytochem. Rev.*, 19 (5), 1081–1092.

[60] Gonçalves, A.C., Gaspar, D., Flores-Félix, J.D., Falcão, A., Alves, G., and Silva, L.R., 2022, Effects of functional phenolics dietary supplementation on athletes' performance and recovery: A review, *Int. J. Mol. Sci.*, 23 (9), 4652.

Indones. J. Chem., 2022, 22 (5), 1321 - 1329

1321

Electrochemical Sensor of Levofloxacin on Boron-Doped Diamond Electrode Decorated by Nickel Nanoparticles

Prastika Krisma Jiwanti[1*], Irfansyah Rais Sitorus[2], Grandprix Thomryes Marth Kadja[3,4,5], Siti Wafiroh[2], and Yasuaki Einaga[6]

[1]*Nanotechnology Engineering, Faculty of Advanced Technology and Multidiscipline, Universitas Airlangga, Surabaya 60115, Indonesia*

[2]*Department of Chemistry, Faculty of Science and Technology, Universitas Airlangga, Surabaya 60115, Indonesia*

[3]*Division of Inorganic and Physical Chemistry, Faculty of Mathematics and Natural Sciences, Institut Teknologi Bandung, Jl. Ganesha No. 10, Bandung 40132, Indonesia*

[4]*Research Center for Nanosciences and Nanotechnology, Institut Teknologi Bandung, Jl. Ganesha No. 10, Bandung 40132, Indonesia*

[5]*Center for Catalysis and Reaction Engineering, Institut Teknologi Bandung, Jl. Ganesha No. 10, Bandung 40132, Indonesia*

[6]*Department of Chemistry, Faculty of Science and Technology, Keio University, 3-14-1 Hiyoshi, Yokohama 223-8522, Japan*

Abstract: *Levofloxacin (LEV) was known as one of the fluoroquinolone antibiotics that widely used as an antibacterial agent. Monitoring of LEV is important due to its negative side effect on humans. The determination of LEV was studied for the first time on nickel modified on a boron-doped diamond (NiBDD) electrode using the square wave voltammetry (SWV) method to improve the catalytic and sensitivity of the sensor. The response was linear in the range of 30–100 μM LEV. LEV sensor on NiBDD was found to be selective in the presence of urea, glucose, and ascorbic acid interferences. Good reproducibility with % a relative standard deviation of 1.45% (n = 10) was achieved. Therefore, the NiBDD electrode could be potentially applied for the real detection method of LEV.*

Keywords: *levofloxacin; electrochemical sensor; nickel; boron-doped diamond; environmental pollution*

■ INTRODUCTION

Levofloxacin (LEV), $C_{18}H_{20}FN_3O_4$, is one of the fluoroquinolone drugs which has an optical S(-) isomer of ofloxacin. This drug is commonly used as an antibacterial agent against most aerobic gram-positive and gram-negative organisms that cause respiratory, skin, and genitourinary tract infections [1]. It is also known to be more active against gram-positive organisms than other fluoroquinolone drugs, such as ciprofloxacin. LEV works by inhibiting bacterial deoxyribonucleic acid (DNA) gyrase. Thus, it is usually used as an alternative antibiotic to heal the disease if other antibiotics cannot give a positive response.

On the other hand, besides the effectiveness of LEV in treating infections, LEV may cause serious heart problems, tendon rupture, abdominal discomfort, and bacterial resistance in long-term use [2-5]. Besides that, improper waste treatment of the pharmaceutical companies of health care centers could promote environmental pollution caused by the high concentrated LEV. Therefore, it is important to monitor LEV in biological fluids and the environment. Various methods have been reported as effective methods to detect LEV, such as using HPLC [6-7], UV detection [8-9], and chemiluminescence [10]. Despite their sensitivity, these methods require expensive instrumentation, high-skilled

professionals, and are time-consuming.

One of the promising methods used is electrochemistry, which is known to have a short time analysis, and only a small amount of reagent is needed. To support the optimum analysis using the electrochemical method, a suitable electrode is mandatory. Many types of research on the detection of LEV have been reported by using various electrodes such as carbon nanotubes [11], nickel oxide porous films [12], modified screen-printed electrode (SPE) [13], and modified glassy carbon electrode (GCE) [14]. Among those electrodes, boron-doped diamond (BDD) electrode is famous for its excellent properties for sensor applications such as detecting arsenic (III) [15], neuraminidase [16], chemical oxygen demand (COD) [17], glucose [18], and many more applications such as for CO_2 reduction [19-20] and synthesis application [21]. This wide range of BDD sensor applications is known due to its low background current that supports the analysis in a very low concentration, wide potential window in aqueous solution, and high physical and chemical stability suitable for real applications [22-23].

In this report, we modified nickel nanoparticles on the surface of the BDD electrode (NiBDD) to be used as a working electrode. A previous study shows that the use of nickel oxide (NiO) modified on GCE could enhance the voltammetric signal [12]. Thereafter, we propose to use Ni NPs decorated on the BDD surface to act as a catalyst for detecting LEV in order to improve sensitivity and selectivity.

■ EXPERIMENTAL SECTION

Materials

LEV, Na_2SO_4 (99.5 %), and $NiSO_4$ (99.99%) were purchased from Sigma Aldrich. H_2SO_4 (98%), NaOH (98%), HCl (37%), and HNO_3 (65%) were purchased from SAP chemicals. Ascorbic acid (99%), D-glucose (99.8%), and ammonium sulfate (99.5%) were purchased from Merck. All solutions were used without further pretreatment and purification.

Instrumentation

The following instrumentations were used in this work are microwave plasma-assisted chemical vapor

deposition system (Model AX 5400, CORNES Technology Corp.) to synthesize BDD electrode, Potentiostat Emstat3+Blue from Palmsen, to run electrochemical methods such as cyclic voltammetry (CV), linear sweep voltammetry (LSV), and square wave voltammetry (SWV). The scanning electron microscopy-energy dispersive spectroscopy (SEM-EDS) (Hitachi SU 3500). to characterize the topography of electrode surface and metal analysis.

Procedure

Electrode preparation and characterization

One percent (B/C) BDD electrode was deposited on the surface of Si (111) using a microwave plasma-assisted chemical vapor deposition system (Model AX 5400, CORNES Technology Corp.). A detailed procedure was described by Watanabe et al. [24]. Prior experiment, the BDD electrode was ultrasonicated in ultrapure water for 5 min. Follow-up treatment was carried out by applying CV in 0.1 M H_2SO_4 in a potential range of -2.5 V to 2.5 V with a scan rate of 1 V/s for 40 times repetitions. A potential of 2.5 V for 300 s was applied using the chronoamperometry technique to prepare oxygen terminated BDD (OBDD) electrode. NiBDD electrode was prepared by depositing Ni nanoparticles on the surface of the OBDD electrode in 1 M $NiSO_4$ for 250 s at a potential of -1.2 V. OBDD and NiBDD electrodes were then characterized using CV and SEM-EDS.

Electrochemical measurement

All measurements were performed in one compartment cell (5 mL). Pt spiral and Ag/AgCl (saturated KCl) were used as counter and reference electrodes, respectively. Working electrodes, OBDD and NiBDD, were used with a geometric area of 0.04 cm^2. Prior to the electroanalytical measurement, the working and counter electrodes, including electroanalytical cells, were ultrasonicated in ultrapure water for 10 min for cleaning. The supporting electrolyte used in this experiment was 0.1 M Na_2SO_4. An electrochemical method such as CV was used to characterize the electrode, and electrochemical detection measurements were performed using LSV and SWV methods. All

measurements were performed using Emstat3+Blue potentiostat.

■ **RESULTS AND DISCUSSION**

Preparation and Characterization of NiBDD

The pretreatment of the BDD electrode was carried out before electroanalysis was performed. BDD was anodically oxidized by applying potential from 0 V to +2.5 V for 40 cycles in 0.1 M H_2SO_4. Anodic oxidation is reported to be able to convert the hydrogen functional group to an oxygen functional group on the surface of the BDD electrode [25-26]. Accordingly, it minimizes the conversion of hydrogen- to the oxygen-terminated surface during measurement, which may interfere with the LEV detection performed in positive range potentials. Fig. 1 shows the SEM image and EDS of the NiBDD electrode. The topography of the NiBDD surface was revealed, as can be seen in the white spot of Ni particles. From the EDS data, 1% Ni particles were found on the surface of the NiBDD electrode (96% C and 3% O). This result shows that Ni nanoparticles have successfully deposited on the surface of the BDD electrode.

Optimization of Electrochemical Technique for LEV Determination

The first optimization for LEV determination was carried out using LSV analytical method and then compared to SWV (Fig. 2). A significant improvement in the LEV oxidation peak was observed using the SWV method. Moreover, a correlation between LEV concentration and the current response was also conducted to know the sensitivity of measurement by using LSV and SWV methods. Linear calibration of LEV was obtained with $R^2 = 0.9927$ and sensitivity of 0.1216. Although the correlation between LEV concentration and current shows linear, the sensitivity is much lower compared to the use of the SWV analytical method, which shows a value of 1.095 with $R^2 = 0.9955$. The result was also supported by the limit of detection (LOD) value of LEV, in which 11.62 and 5.11 μM were calculated by using LSV and SWV analytical methods, respectively. In this report, this result of LOD for the SWV technique is higher compared to the report by Farias et al. using reduced graphene oxide/glassy carbon electrode [11]. This confirms that the SWV method is a sensitive analytical
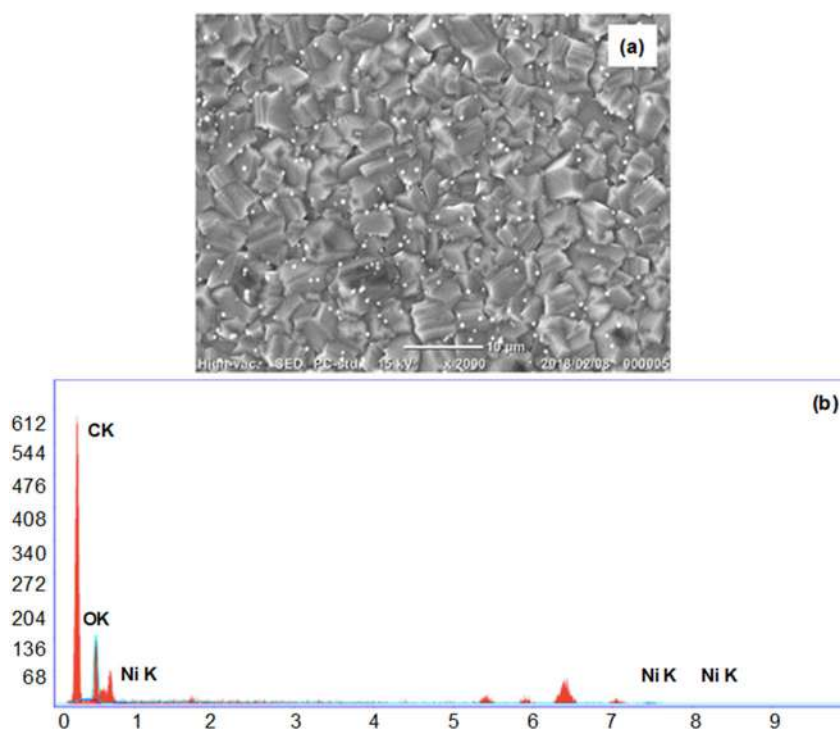
Fig 1. SEM image (a) and EDS (b) of NiBDD
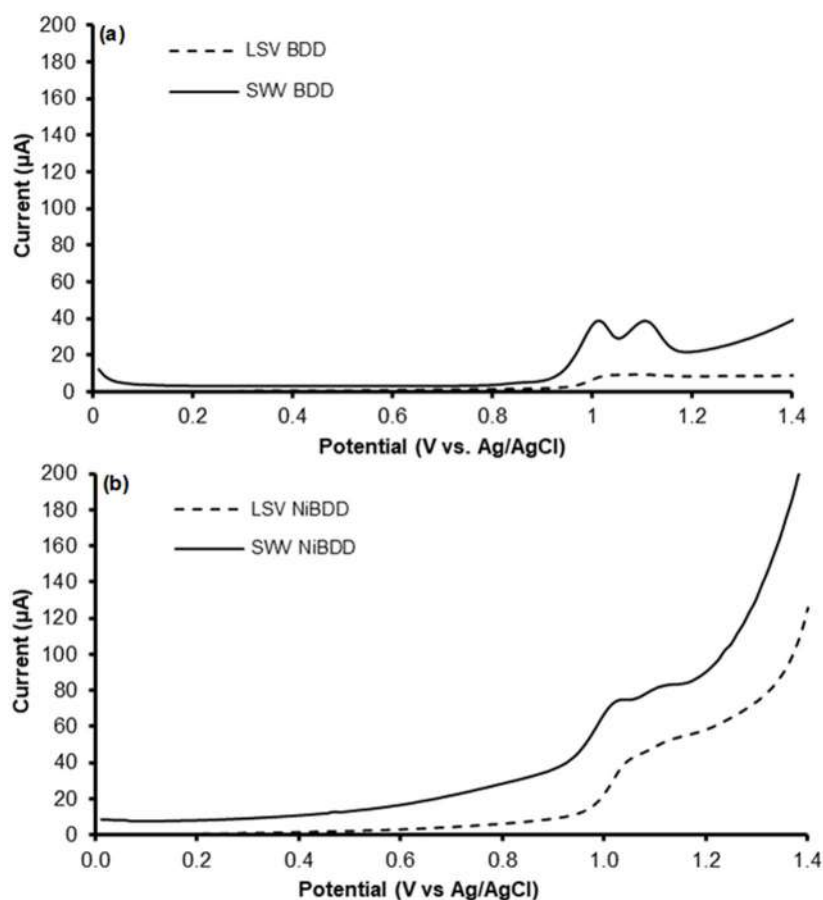
Fig 2. Voltammetric curves of potential vs. current of 50 μM LEV in 0.1 M Na_2SO_4 performed on OBDD (a) and NiBDD (b) electrodes with LSV and SWV method

method that is usually used for many sensing methods in electrochemistry, such as for environmental pollutant analysis [27]. Therefore, SWV was used for further analysis.

Optimization of SWV parameters such as frequency (Hz), pulse amplitude (mV), and step potential (mV) was performed in 0.1 M Na_2SO_4 containing 50 μM LEV. Pulse amplitude was examined by applying various amplitudes from 10 mV to 50 mV. The current response increased as the pulse amplitude increased. This trend was similar to frequency optimization. On the other hand, at step potential optimization, the current was decreased to 14 mV. The maximum step potential was 12 mV. For all these three optimizations, the peak potentials did not shift (at 1.09 V), indicating that the peak potentials were insensitive to frequency, pulse amplitude, and step potential. Therefore, for all analytical measurements in

this experiment, pulse amplitude 50 mV, frequency 50 Hz, and 12 mV step potentials were used.

Electrochemical Detection of LEV

In Fig. 3, a solid line shows the SWV of the NiBDD electrode with 50 μM LEV in 0.1 M Na_2SO_4. Two oxidation peaks at +1.0 and +1.1 V are detected and belong to the oxidation peak of LEV [28]. The oxidation of LEV occurs in two steps of electron transfer to form cation and followed by hydrolysis and deprotonation steps. This oxidation peak shows the catalytic activity of Ni nanoparticles on the detection of LEV in Na_2SO_4 solution. Ni nanoparticles increase the adsorption of LEV on the active surface of the working electrode. Thus, for further analysis, we use these oxidation peaks to study the detection of LEV on OBDD and NiBDD electrodes.

Indones. J. Chem., 2022, 22 (5), 1321 - 1329

1325
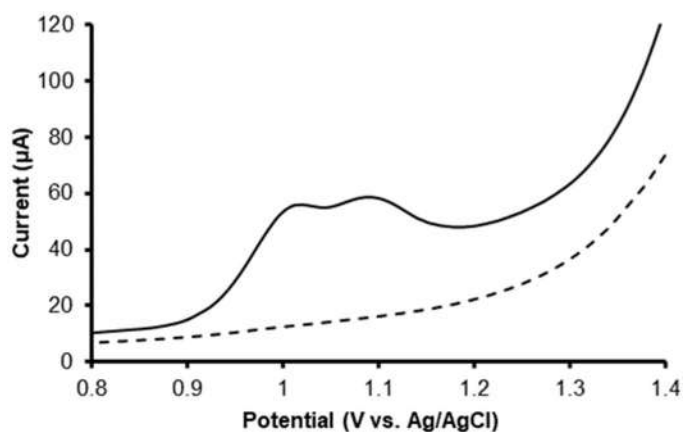
Fig 3. SWV on NiBDD electrode with (solid line) and without (dash line) 50 μM LEV in 0.1 M Na_2SO_4. The scan rate of 100 mV/s

The influence of the scan rate on the LEV determination was also studied on NiBDD electrodes. In Fig. 4(a), 50 μM LEV in 0.1 M Na_2SO_4 was measured with the CV analytical method at various scan rates ranging from 10 mV/s to 50 mV/s. The voltammogram shows the irreversible process of LEV, in which only the oxidation peak of LEV was detected. In Fig. 4, a graph of the square root of scan rate versus current at potential around +1.0 V shows a linear regression equation of y = 9.1786x + 14.485 (R^2 = 0.9927). It is suggested that the electrochemical oxidation of LEV on NiBDD was diffusion-controlled.

In addition, the influence of pH on the LEV determination was also performed. Fig. 4(b) shows the pH
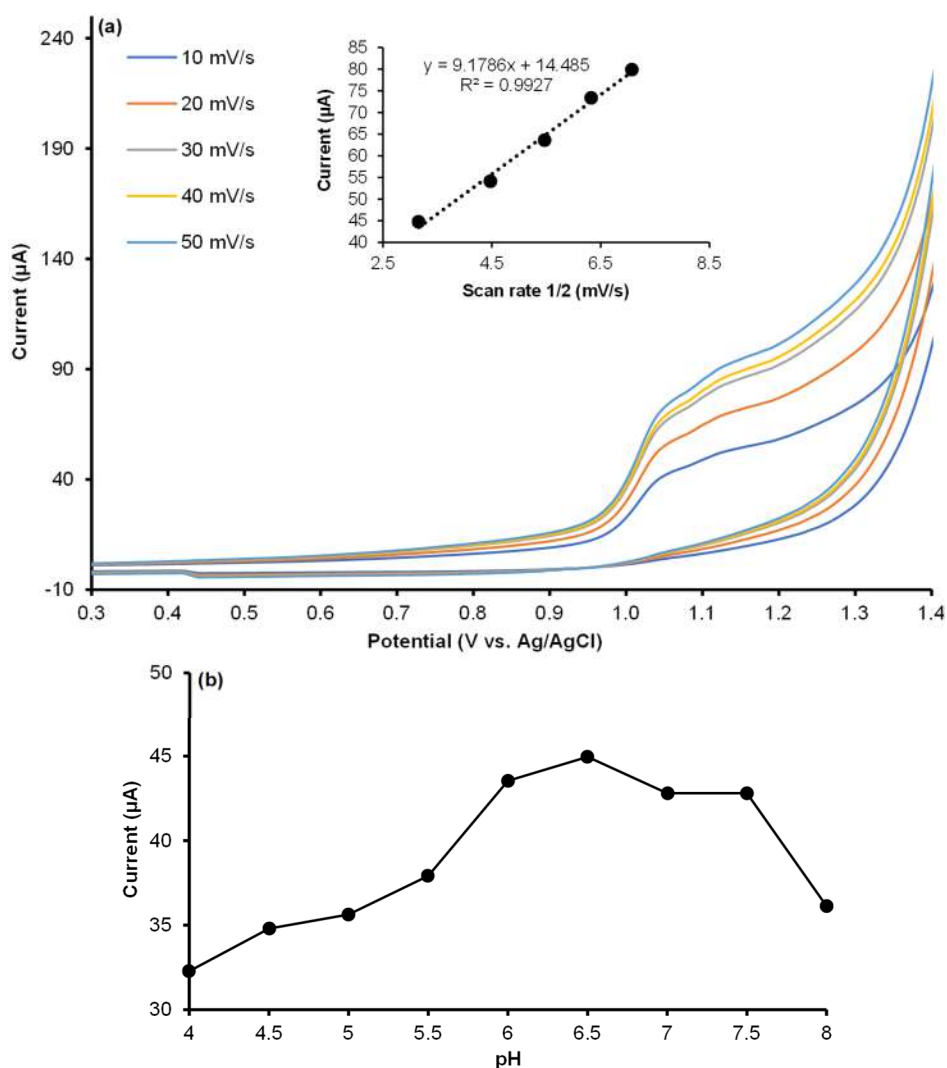
Fig 4. CV of NiBDD electrode with various scan rates. Inset: linear relationship between the square root of scan rate and current (a). Effect of pH on the anodic current (b). 50 μM LEV in 0.1 M Na_2SO_4 with a scan rate of 100 mV/s
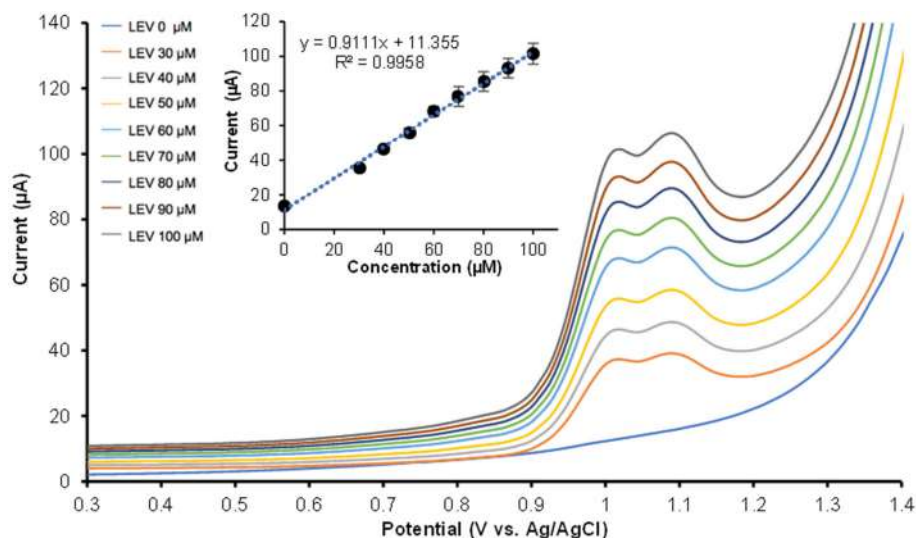
Fig 5. SWVs of LEV with various concentrations in 0.1 M Na$_2$SO$_4$ on NiBDD electrode. The scan rate was 100 mV/s. Inset: linear correlation of LEV correlation and current at a potential of +1.0 V
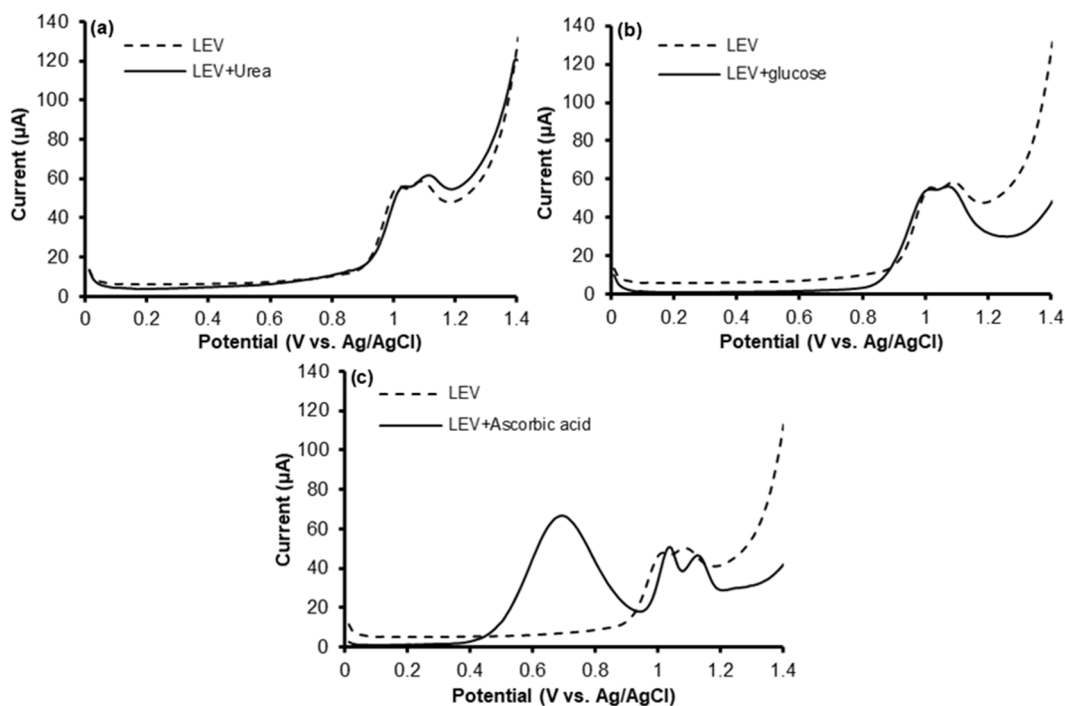
Fig 6. SWVs of 50 μM LEV with interferences of (a) urea, (b) glucose, and (c) ascorbic acid with the same concentration on NiBDD electrode

dependence on the current response of LEV oxidation studied by the SWV method. pH was varied from 4.0 to 8.0. As can be seen, the current responses increased from pH 4 to 5.5 and then decreased over 5.5. Thus, the optimal pH to measure LEV in this experiment was pH 5.5.

Determination of LEV on NiBDD using SWV was performed in optimum conditions with different LEV concentrations ranging from 0 to 100 μM (Fig. 5). Each LEV concentration was measured three times and showed the increase of current response linearly with a correlation coefficient of 0.9958. The LOD was measured and showed a value of 11.13 μM.

Selectivity, Reproducibility, and Real Sample Analysis

The selectivity of LEV measurement was evaluated. LEV with a concentration of 50 μM was measured in 0.1 M Na_2SO_4 containing the same concentration of interference (urea, glucose, and ascorbic acid). Fig. 6 shows the SWV with and without interferences. There are no significant changes in the current response, 3.06%, 4.29%, and 7.47% for the addition of urea, glucose, and ascorbic acid, respectively, according to the acceptable precision in AOAC (11%). The exception is for ascorbic acid, in which a new peak was detected at around potential +0.7 V. However, this peak does not promote a significant effect on the presence of LEV oxidation peak. Meanwhile, reproducibility is one of the important aspects to be considered in the sensor. To evaluate the reproductivity of LEV, NiBDD was fabricated, and the measurement was conducted for 10 days in the same condition, in which one measurement was carried out each day. The results show a satisfactory result, with an RSD of 1.45%, which this result is better than the report of LEV analysis (1.70%) in urine samples by Radi et al. [29] and is an acceptable % RSD value according to AOAC [30].

Determination of LEV in the real sample was conducted in a human urine sample (Fig. 7). LEV with a concentration of 50 μM was added into the urine sample and measured using the SWV method. An oxidation peal of LEV was detected at potential around +1.0 V, showing a good recovery of 93.91 ± 0.02% (acceptable limit of 80–110%) [30], indicating that this method of measurement on
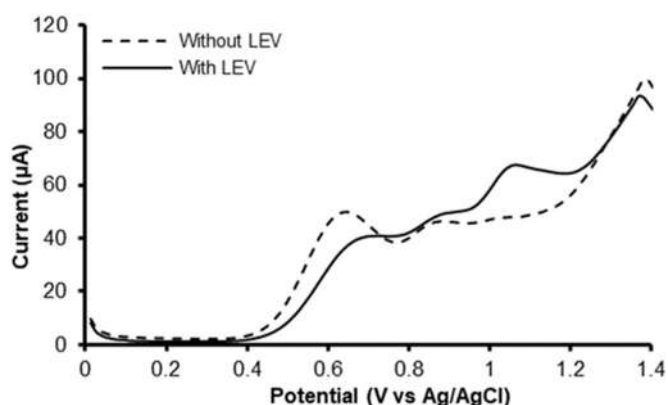
Fig 7. SWVs of LEV in urine sample on NiBDD electrode

on NiBDD electrode can be applied to detect LEV in the real sample.

■ CONCLUSION

LEV was successfully detected on the NiBDD electrode by analyzing the LEV oxidation peak at around +1 V at maximum pH of 5.5. The detection of LEV was sensitive whether in Na_2SO_4 (which contains ultrapure water) or in a real urine sample. SWV method shows a 56% lower LOD value compared to the LSV method. Optimized conditions of SWV with pulse amplitude of 50 mV, frequency of 50 Hz, and step potentials of 12 mV were used to detect LEV accurately. Analysis in real urine sample shows good antibiotic % recovery of 93.91 ± 0.02. The LEV electrochemical detection on the NiBDD electrode is fast, simple, and sensitive, which has a potential for further development in antibiotic detection.

■ ACKNOWLEDGMENTS

■ AUTHOR CONTRIBUTIONS

Prastika Krisma Jiwanti conceptualized, supervised, wrote, and revised the manuscript, Irfansyah Rais Sitorus conducted the experiment, Grandprix T.M. Kadja conducted the experiment, Siti Wafiroh supervised, and Yasuaki Einaga supervised. All authors agreed to the final version of this manuscript.

■ REFERENCES

[1] Nambasa, V., Ndagije, H.B., Serwanga, A., Manirakiza, L., Atuhaire, J., Nakitto, D., Kiguba, R., and Figueras, A., 2020, Prescription of levofloxacin and moxifloxacin in select hospitals in Uganda: a pilot study to assess guideline concordance, *Antibiotics*, 9 (8), 439.

[2] Jin, Y., Xu, G., Li, X., Ma, J., Yang, L., Li, Y., Zhang, H., Zhang, Z., Yao, D., and Li, D., 2021, Fast cathodic reduction electrodeposition of a binder-free cobalt-doped Ni-MOF film for directly sensing of levofloxacin, *J. Alloys Compd.*, 851, 156823.

[3] Borowiec, J., Yan, K., Tin, C.C., and Zhang, J., 2015, Synthesis of PDDA functionalized reduced graphene oxide decorated with gold nanoparticles and its electrochemical response toward levofloxacin, *J. Electrochem. Soc.*, 162 (3), H164–H169.

[4] Izadi, E., Afshan, G., Patel, R.P., Rao, V.M., Liew, K.B., Meor Mohd Affandi, M.M.R., Kifli, N., Suleiman, A., Lee, K.S., Sarker, M.M.R., Zaidi, S.T., and Ming, L.C., 2019, Levofloxacin: Insights into antibiotic resistance and product quality, *Front. Pharmacol.*, 10, 881.

[5] Wu, H.H., Liu, H.Y., Lin, Y.C., Hsueh, P.R., and Lee, Y.J., 2016, Correlation between levofloxacin consumption and the incidence of nosocomial infections due to fluoroquinolone-resistant *Escherichia coli*, *J. Microbiol. Immunol. Infect.*, 49 (3), 424–429.

[6] Naveed, S., Sultana, N., Saeed Arayne, M., and Dilshad, H.A., 2014, A new HPLC method for the assay of levofloxacin and its application in drug-metal interaction studies, *J. Sci. Innovative Res.*, 3 (31), 91–96.

[7] Gülfen, M., Canbaz, Y., and Özdemir, A., 2020, Simultaneous determination of amoxicillin, lansoprazole, and levofloxacin in pharmaceuticals by HPLC with UV–Vis detector, *J. Anal. Test.*, 4 (1), 45–53.

[8] Desai, V.N., Afieroho, O.E., Dagunduro, B.O., Okonkwo, T.J., and Ndu, C.C., 2011, A simple UV spectrophotometric method for the determination of levofloxacin in dosage formulations, *Trop. J. Pharm. Res.*, 10 (1), 75–79.

[9] Mohamed, S., Mvungi, H.C., Sariko, M., Rao, P., Mbelele, P., Jongedijk, E.M., van Winkel, C.A.J., Touw, D.J., Stroup, S., Alffenaar, J.W.C., Mpagama, S., and Heysell, S.K., 2021, Levofloxacin pharmacokinetics in saliva as measured by a mobile microvolume UV spectrophotometer among people treated for rifampicin-resistant TB in Tanzania, *J. Antimicrob. Chemother.*, 76 (6), 1547–1552.

[10] Shao, X., Li, Y., Liu, Y., and Song, Z., 2011, Rapid determination of levofloxacin in pharmaceuticals and biological fluids using a new chemiluminescence system, *J. Anal. Chem.*, 66 (1), 102–107.

[11] de Farias, D.M., de Faria, L.V., Lisboa, T.P., Matos, M.A.C., Muñoz, R.A.A., and Matos, R.C., 2020, Determination of levofloxacin in pharmaceutical formulations and urine at reduced graphene oxide and carbon nanotube-modified electrodes, *J. Solid State Electrochem.*, 24 (5), 1165–1173.

[12] Liu, C., Xie, D., Liu, P., Xie, S., Wang, S., Cheng, F., Zhang, M., and Wang, L., 2019, Voltammetric determination of levofloxacin using silver nanoparticles deposited on a thin nickel oxide porous film, *Microchim. Acta*, 186 (1), 21.

[13] Ganta, D., Chavez, J., and Lopez, A., 2020, Disposable chronoamperometric sensor coated with silver nanowires for detecting levofloxacin, *Anal. Lett.*, 53 (12), 1992–2001.

[14] Wong, A., Santos, A.M., and Fatibello-Filho, O., 2018, Simultaneous determination of paracetamol and levofloxacin using a glassy carbon electrode modified with carbon black, silver nanoparticles and PEDOT:PSS film, *Sens. Actuators, B*, 255, 2264–2273.

[15] Agustiany, T., Khalil, M., Einaga, Y., Jiwanti, P.K., and Ivandini, T.A., 2020, Stable iridium-modified boron-doped diamond electrode for the application in electrochemical detection of arsenic (III), *Mater. Chem. Phys.*, 244, 122723.

[16] Ivandini, T.A., Ariani, J., Jiwanti, P.K., Gunlazuardi, J., Saepudin, E., and Einaga, Y., 2017 Electrochemical detection of neuraminidase based on zanamivir inhibition reaction at platinum and platinum-modified boron-doped diamond electrodes, *Makara J. Sci.*, 21 (1), 34–42.

[17] Diksy, Y., Rahmawati, I., Jiwanti, P.K., and Ivandini, T.A., 2020, Nano-Cu modified Cu and Nano-Cu modified graphite electrodes for chemical oxygen demand sensors, *Anal. Sci.*, 36 (11), 1323–1330.

[18] Deng, Z., Long, H., Wei, Q., Yu, Z., Zhou, B., Wang, Y., Zhang, L., Li, S., Ma, L., Xie, Y., and Min, J., 2017, High-performance non-enzymatic glucose sensor based on nickel-microcrystalline graphite-boron doped diamond complex electrode, *Sens. Actuators, B*, 242, 825–834.

[19] Jiwanti, P.K., and Einaga, Y., 2020, Further study of CO_2 electrochemical reduction on palladium modified BDD electrode: Influence of electrolyte, *Chem. - Asian J.*, 15 (6), 910–914.

[20] Jiwanti, P.K., Aritonang, R.P., Abdullah, I., Einaga, Y., and Ivandini, T.A., 2019, Copper-nickel-modified boron-doped diamond electrode for CO_2 electrochemical reduction application: A preliminary study, *Makara J. Sci.*, 23 (4), 204–209.

[21] Yamamoto, T., Riehl, B., Naba, K., Nakahara, K., Wiebe, A., Saitoh, T., Waldvogel, S.R., and Einaga, Y., 2018 A solvent-directed stereoselective and electrocatalytic synthesis of diisoeugenol, *Chem. Commun.*, 54 (22), 2771–2773.

[22] Ivandini, T.A., and Einaga, Y., 2017, Polycrystalline boron-doped diamond electrodes for electrocatalytic and electrosynthetic applications, *Chem. Commun.*, 53 (8), 1338–1347.

[23] Putri, Y.M.T.A., Jiwanti, P.K, Irkham, Gunlazuardi, J., Einaga, Y., and Ivandini, T.A., 2021, Nickel cobalt modified boron-doped diamond as an electrode for a urea/H_2O_2 fuel cell, *Bull. Chem. Soc. Jpn.*, 94 (12), 2922–2928.

[24] Watanabe, T., Honda, Y., Kanda, K., and Einaga, Y., 2014, Tailored design of boron-doped diamond electrodes for various electrochemical applications with boron-doping level and sp^2-bonded carbon

impurities, *Phys. Status Solidi A*, 211 (12), 2709–2717.

[25] Kasahara, S., Natsui, K., Watanabe, T., Yokota, Y., Kim, Y., Iizuka, S., Tateyama, Y., and Einaga, Y., 2017, Surface hydrogenation of boron-doped diamond electrodes by cathodic reduction, *Anal. Chem.*, 89 (21), 11341–11347.

[26] Hoffmann, R., Obloh, H., Tokuda, N., Yang, N., and Nebel, C.E., 2012, Fractional surface termination of diamond by electrochemical oxidation, *Langmuir*, 28 (1), 47–50.

[27] Chen, A., and Shah, B., 2013, Electrochemical sensing and biosensing based on square wave voltammetry, *Anal. Methods*, 5 (9), 2158–2173.

[28] Rkik, M., Brahim, M.B., and Samet, Y., 2017, Electrochemical determination of levofloxacin antibiotic in biological samples using boron doped diamond electrode, *J. Electroanal. Chem.*, 794, 175–181.

[29] Radi, A., and El-Sherif, Z., 2002, Determination of levofloxacin in human urine by adsorptive square-wave anodic stripping voltammetry on a glassy carbon electrode, *Talanta*, 58 (2), 319–324.

[30] Taverniers, I., De Loose, M., and Van Bockstaele, E., 2004, Trends in quality in the analytical laboratory. II. Analytical method validation and quality assurance, *TrAC, Trends Anal. Chem.*, 23 (8), 535–552.

Synthesis and Characterization of 2,4-Dichlorophenoxypropanoic Acid (2,4-DP) Herbicide Interleaved into Calcium-Aluminium Layered Double Hydroxide and the Study of Controlled Release Formulation

Farah Liyana Bohari[1], Nur Aishah Mohd Noor[1], Sheikh Ahmad Izaddin Sheikh Mohd Ghazali[1*], Nur Nadia Dzulkifli[1], Is Fatimah[2], and Nurain Adam[3]

[1]*Material, Inorganic, and Oloechemistry (MaterInoleo) Research Group, School of Chemistry and Environment, Faculty of Applied Sciences, Universiti Teknologi MARA, Cawangan Negeri Sembilan, Kampus Kuala Pilah, 72000, Negeri Sembilan, Malaysia*

[2]*Department of Chemistry, Faculty of Mathematics and Natural Sciences, Universitas Islam Indonesia, Kampus Terpadu UII, Jl. Kaliurang Km 14, Sleman, Yogyakarta 55584, Indonesia*

[3]*Kontra Pharma (M) Sdn Bhd (90082-V) Kotra Technology Centre (Block B) 1, 2 &3, Industrial Estate, 75250, Jl. Ttc 12, Malacca, Malaysia*

Abstract: *The commonly used herbicide in agriculture, namely 2,4-dichlorophenoxypropanoic acid (2,4-DP), is an anionic herbicide used to interleave into the interlayer of calcium-aluminum layered double hydroxide (Ca-Al LDH) employing co-precipitation method to form a new nanohybrid labeled as CAL-2,4DP. The LDH compound serves as a host in supporting the herbicide's controlled release formulation. The effective interleave was investigated by employing a powder X-Ray Diffraction (XRD) pattern at 0.025 M nanocomposite, which revealed that the basal spacing has increased from 8.0 Å to 23.8 Å. The ATR-FTIR spectra further supported the interleaving, where the nitrate peak (NO⁻) diminished, and the carboxylate ion (COO⁻) band appeared at 1653 cm⁻¹. The percentage loading of CAL-2,4DP was 71.26%, calculated from the carbon content in the sample. The BET analysis shows that CAL-2,4DP was a mesoporous material relying on nitrogen-desorption isotherms. The release of 2,4-DP ions into the aqueous solutions followed the order of $PO_4^{3-} > CO_3^{2-} > Cl^-$ with a percentage of 83, 65, and 30%, respectively. This work indicates the successful interleaving process of the 2,4-DP anion and the potential of CAL-2,4DP as an eco-friendly agrochemical that can be beneficial for farmers in minimizing herbicide usage to the environment.*

Keywords: *2,4-dichlorophenoxypropanoic acid (2,4-DP); interleaved; co-precipitation; LDH; nanoparticles; controlled release*

■ INTRODUCTION

In the case of weed management, farmers are often concerned with the infestation of weeds that grows on a large scale. Weed infestation results in competition between the unwanted plants and the crops for resources such as water, sunlight, nutrients, and space to survive in the agrosystem. This issue needs to be tackled by farmers as their existence can reduce the crop yield, affecting its quality and marketability. As these concerns mount, farmers have used chemical herbicides directly to eradicate the weeds. Here, they usually assume that the weeds can be easily controlled at a fast rate. Farmers apply herbicide in higher concentration on the crops, which eventually affect the soil and the environment. Some chemical herbicides can evaporate into the air, contaminate the soil, and reach the surface water through running off, which threaten the aquatic organisms [1].

Layered double hydroxide (LDH) denotes the hydrotalcite-like compounds, which comprise brucite ($Mg(OH_2)$) like layers mutilated with interlayer anions [2]. The LDH general formula is $[M^{2+}_{1-x}M^{3+}_{x}(OH_2)]^{x+}(A^{n-})_{x/n}\cdot yH_2O]$, in which M^{2+} and M^{3+} denote the divalent and trivalent cations such as calcium (Ca^{2+}) and aluminum (Al^{3+}) accordingly, meanwhile A^{n-} is the interlayer anion [3]. The brucite-like sheets are positively charged, in which some part of the divalent cations can be substituted with the trivalent cations [5-8]. The negative charges reside in the hydrated interlayer to compensate for the positively charged sheets and keep the charges balanced while providing its typical stacked layered structures. The sheet's interlayer could be made up of anions and water molecules [5]. Any types of anions such as nitrate (NO_3^-), carbonate (CO_3^{2-}), and chloride (Cl^-) can be interleaved into the interlayer space due to its high anionic exchange capability and variability of chemical composition, giving rise to widespread applications of LDH in drug delivery for pharmaceutical [9-10], polymer composites [8], acting as a host and controlled release formulations in agriculture [5,11-12].

2,4-Dichlorophenoxypropanoic acid (2,4-DP) (Fig. 1) is used as a plant growth regulator commonly utilized to specifically combat broadleaf weeds in crop plantations, for instance, wheat, rice, and domestic usage [11]. However, 2,4-DP anion (Fig. 2) is highly polar and has high water solubility. Thus, the active substances can be easily released to the surface water and bioaccumulate in the water [5,13-14]. Therefore, due to the unique properties of LDH acting as a host, 2,4-DP herbicide can be interleaved into the LDH interlayer matrix. The interleaving process between the 2,4-DP herbicide and LDH host can reduce the concentration of the released agrochemicals and minimize the environmental impacts by producing the new environmentally friendly herbicide. The intercalation was synthesized using the co-

precipitation method because of its simplicity and high yield. The interaction of the 2,4-DP anion and its LDH host was analyzed using the FTIR, XRD, CHNS, and BET techniques, while the controlled release of the active substances was measured using the UV-Vis instrument.

■ EXPERIMENTAL SECTION

Materials

The reagents used in the calcium-aluminum LDH (Ca-Al LDH) interleaving and synthesis procedure were utilized without additional purification. These reagents included calcium nitrate tetrahydrate, ($Ca(NO_3)_2\cdot6H_2O$, 99%, R&M Chemicals), Aluminum nitrate nonahydrate, ($Al(NO_3)_3\cdot9H_2O$, 98.5%, R&M Chemicals), sodium hydroxide (NaOH, 99%, Merck), 2,4-dichlorophenoxypropanoic acid (2,4-DP) ($C_9H_8Cl_2O_3$, 98.5%, Sigma-Aldrich), and absolute ethanol (C_2H_5OH, 99.7%, HmbG Chemicals).

Instrumentation

X-ray powder diffraction (XRD) patterns were recorded at the 5–90° range utilizing a Bruker D8 Advance XRD diffractometer, operating under Cu Kα radiation at 40 mA and 40 kV ($\lambda = 1.54059$ Å) with a scanning step of 0.01°. The Fourier transformed infrared (FTIR) spectra were gained on a Perkin Elmer Spectrum 100 utilizing attenuated total reflectance (ATR) mode in the 4000–650 cm^{-1} range. The elemental analysis was conducted utilizing a CHNS analyzer, model CHNS-932. The pore size and surface area distribution of the Brunauer–Emmett–Teller (BET) analysis were assessed by employing nitrogen adsorption-desorption of the nanocomposites on a Micromeritics surface area and pore analyzer (ASAP 2000). The controlled release of the 2,4-DP herbicide from the Ca-Al LDH host was assessed utilizing a 0.3 mg sample into a 3.5 mL 0.01 M of various salt solutions of NaCl, Na_2CO_3, and Na_3PO_4 [13]. By
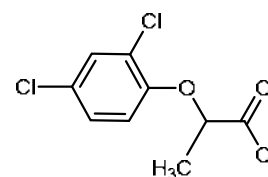

Fig 1. Molecular structure of 2,4-DP

Fig 2. Molecular structure of the 2,4-DP anion

Farah Liyana Bohari et al.

employing a Perkin Elmer UV–Vis Spectrophotometer Lambda 35, the anions produced in the aqueous solutions were monitored for 20 h at a predetermined time.

Procedure

Synthesis of calcium-aluminium layered double hydroxide host (Ca-Al LDH)

For the precursors, approximately 0.033 M $Al(NO_3)_3 \cdot 9H_2O$ as well as 0.10 M $Ca(NO_3)_2 \cdot 6H_2O$ were mixed together into 250 mL of DI water. Following from there, to avoid carbon dioxide (CO_2) contamination, the mixture pH was accustomed to 11 by adding 2 M NaOH followed by vigorous stirring under a nitrogen atmosphere. After that, the mixture went through the aging process for 18 h at 70 °C in an oil bath shaker. Precipitate could be seen in the mixture after 18 h, which was then centrifuged for 25 min at 300 rpm. After centrifugation, the precipitate was removed and washed multiple times with DI water before being dried in an oven at 80 °C for 72 h. Finally, for further usage and characterization, the material was crushed into a fine powder.

Synthesis of Ca-Al-2,4DP-LDH nanocomposite (CAL-2,4DP)

The intercalation of the 2,4-DP herbicide into the interlayer LDH was done using the co-precipitation method. The same precursors were used according to the synthesis of Ca-Al LDH, followed by adding different concentrations of 125 mL 2,4-DP herbicide in the range of 0.025–0.10 M into the conical flask filled with metal cations mixtures. Then, the solution was stirred under the nitrogen gas purge at a constant pH of 11 using NaOH solution until a white precipitate was formed. The solution was aged, followed by the centrifugation of the precipitate, and dried at 80 °C for 72 h before sample characterization.

■ RESULTS AND DISCUSSION

PXRD Analysis and Spatial Orientation of 2,4-DP

Fig. 3 portrays the PXRD patterns of both the Ca-Al LDH host and its nanocomposite, CAL-2,4DP, at various concentrations in the range of 0.025–0.1 M. The pattern of Ca-Al LDH showed high crystallinity and harmonious peaks, which is consistent with the typical LDH host [7-9, 15]. It also has a well-defined peak at 10.34° corresponding
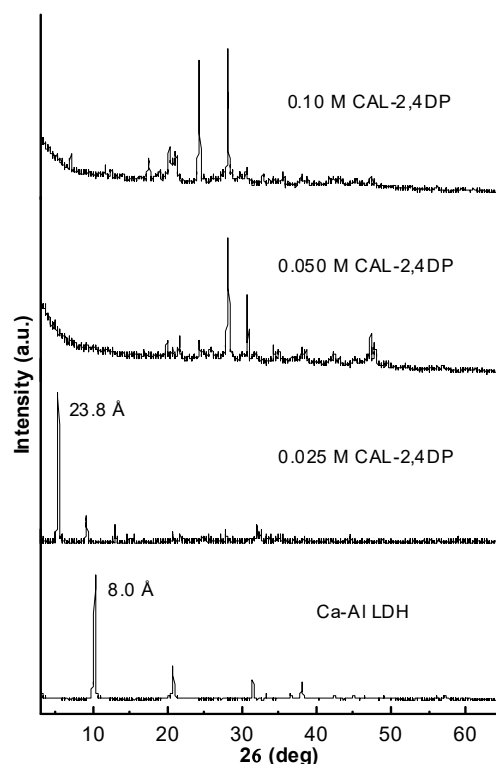
Fig 3. PXRD patterns of Ca-Al LDH and three different concentrations of CAL-2,4DP

to the basal spacing of 8.0 Å, measured utilizing Bragg's law formula. Moreover, as portrayed on 0.025 M CAL-2,4-DP, the diffraction peak of the synthesized nanohybrid can be seen shifting to the lower angle at 3.71°. The basal spacing has expanded from 8.0 to 23.8 Å, indicating that the 2,4-DP anion interleaved into the interlamellar of the LDH host. Here, the difference in the basal spacing is pronounced compared to the LDH host due to the anion size of 2,4-DP, which is larger than the nitrate ions, and the spatial orientation between the interlayers [15]. As discussed, this peak signifies the interleaving of 2,4-DP into the LDH host. However, the PXRD patterns of 0.05 M and 0.1 M CAL-2,4DP showed that the interleaving process did not complete between the guest and the host anions. The presence of carbonate and calcite can be observed near 25° and 29° due to the carbonate contamination [16]. Overall, it could be inferred that the interleaving process occurred at a lower concentration of CAL-2,4DP.

Fig. 4 shows the proposed spatial orientation of 2,4-DP within the Ca-Al LDH using ChemOffice software.
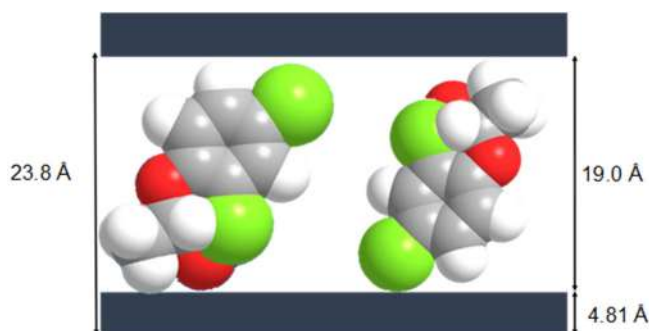
**Fig 4.** Proposed spatial orientation of 2,4-DP in the interlayer of LDH

Based on the basal spacing of CAL-2,4DP, 23.8 Å, the interlayer gallery height for the accommodation of 2,4-DP can be calculated. Taking into account that the thickness of the Ca-Al LDH layer is 4.81 Å [17] implies that the expected gallery height that the 2,4-DP anions can accommodate was 19 Å. Therefore, it can be suggested that the 2,4-DP anions were oriented in bilayer arrangement within the interlayer.

FTIR Analysis

Fig. 5 shows the FTIR-ATR spectra of the Ca-Al LDH host and its guest. Because of the O-H stretching and bending vibration of the hydroxyl groups in the interlayer water molecules, bands exist at 3460 cm^{-1} and 1631 cm^{-1} at Ca-Al LDH [18]. Note that a sharp band at 1325 cm^{-1} associates with the nitrate stretching vibration. Besides that, a peak of 1443 cm^{-1} refers to the carbonate stretching in the interlayer region that might be due to the CO_2 contamination from the air during the preparation [5]. For the FTIR spectra of pure 2,4-DP, the peak at 2912 cm^{-1} is associated with the stretching vibration of the O-H groups from COOH.

On the other hand, the sharp peak at 1732 cm^{-1} resembles the carbonyl group (C=O) functional group. Following here, another distinct peak can be seen at 1489 cm^{-1}, indicating the C=C vibrations of the aromatic ring [19]. Finally, the C-Cl vibration at the aromatic ring can be observed at 817 cm^{-1}.

The 2,4-DP herbicide was interleaved into the LDH interlayer area according to the FTIR spectra of 0.025 M CAL-2,4DP. The O-H stretching caused by the adsorbed interlayer water molecules produces a broad absorption
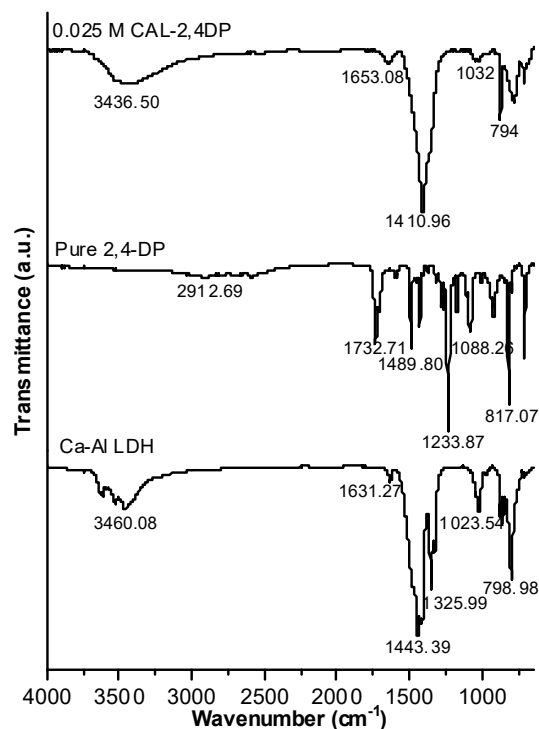
Fig 5. FTIR spectra of Ca-Al LDH and its nanocomposite

band at 3436 cm^{-1}. Moreover, the O-H bending of the COOH is shown by the emergence of a prominent absorption band at 1410 cm^{-1}, while the carbonyl group may be observed at 1653 cm^{-1}. Moreover, the interleaved process can be confirmed by vanishing the nitrate peak around 1325 cm^{-1}, signifying that 2,4-DP anion has already exchanged with the nitrate ions that initially occupied the interlayer host. On the other hand, a peak of 794 cm^{-1} attributes to the C-Cl attached to the aromatic ring. Thus, based on the spectra for CAL-2,4DP, the nanocomposite resembles the absorption bands in both LDH and 2,4-DP. The FTIR spectrum of CAL-2,4DP suggests that 2,4-DP anion can be interleaved successfully in the interlayer lamellae at a lower concentration.

Elemental Analysis

Table 1 indicates the elemental analysis of the Ca-Al LDH host and CAL-2,4DP nanocomposite obtained from the CHNS analysis. The result shows that Ca-Al LDH comprises 3.05% nitrogen. The nitrogen content aligns with the occurrence of a sharp band at 1325 cm^{-1} in the FTIR spectra of Ca-Al LDH (Fig. 5), representing

Table 1. Basal spacing and chemical composition of Ca-Al LDH host and its intercalated compound, CAL-2,4DP (0.025 M)

| Sample	d (Å)	% C (%w/w)	% H (%w/w)	% N (%w/w)	% loading
Ca-Al LDH	8.0	0.16	2.51	3.05	-
CAL-2,4DP	23.80	25.58	3.74	0.23	71.26

the nitrate group. The percentage content of C and H in the CAL-2,4DP nanocomposite increased due to the presence of a 2,4-DP anion that interleaved into the interlayer. The nitrogen content in the nanocomposite also decreases to 0.23% after the interleaving process. The percentage loading of 2,4-DP intercalated into the Ca-Al LDH interlayer is estimated to be 71.26% based on the carbon content of about 25.58 % in the CAL-2,4DP.

Surface Properties

The nitrogen adsorption-desorption isotherms and pore size distribution for Ca-Al LDH, along with its intercalated compound, 0.025 M CAL-2,4-DP, are all portrayed in Fig. 6. Depending on the IUPAC (International Union of Pure and Applied Chemistry) categorization, the isotherms resemble Type IV sorption, indicating mesopore-type material with an H3 hysteresis loop [7]. The hysteresis loop for the CAL-2,4DP observed has a broader adsorption branch than the Ca-Al LDH due to the interleaving process of the 2,4-DP anion replacing the nitrate ion. As a result, the adsorbate uptake for CAL-2,4DP increases slowly at a relative pressure of 0.0–0.5,

followed by rigorous adsorption at a relative pressure of above 0.7, with maximum uptake at 184 cm^3 g^{-1}. Nonetheless, Ca-Al LDH portrays a similar pattern of delayed adsorbate uptake at a relative pressure of 0.0–0.8, reaching an optimum uptake at 9 cm^3 g^{-1}. For the BJH desorption pore size distribution, the interleaved compound of CAL-2,4DP shows higher pore size distribution at about 200–450 Å with a pore volume of 0.07 cm^3 g^{-1}. Here, the Ca-Al LDH portrays minimal pore volume at 0.04 cm^3 g^{-1} under 620 Å. Furthermore, the difference in pore structure and distribution for both host-guest relies on the formation of interstitial pores between the size of the particles and crystallite during the interleaving process [20].

Table 2 encapsulates the porosity and surface area of Ca-Al LDH and CAL-2,4DP employing the Brunauer, Emmett, and Teller (BET) and the Barrett, Joyner, and Halenda (BJH) methods. Here, the BET surface area increased from 17.93 m^2 g^{-1} for Ca-Al LDH to 21.35 m^2 g^{-1} for CAL-2,4DP. The increase in surface area for CAL-2,4DP indicates that the interleaving process has taken place and agrees with the expansion of basal spacing in
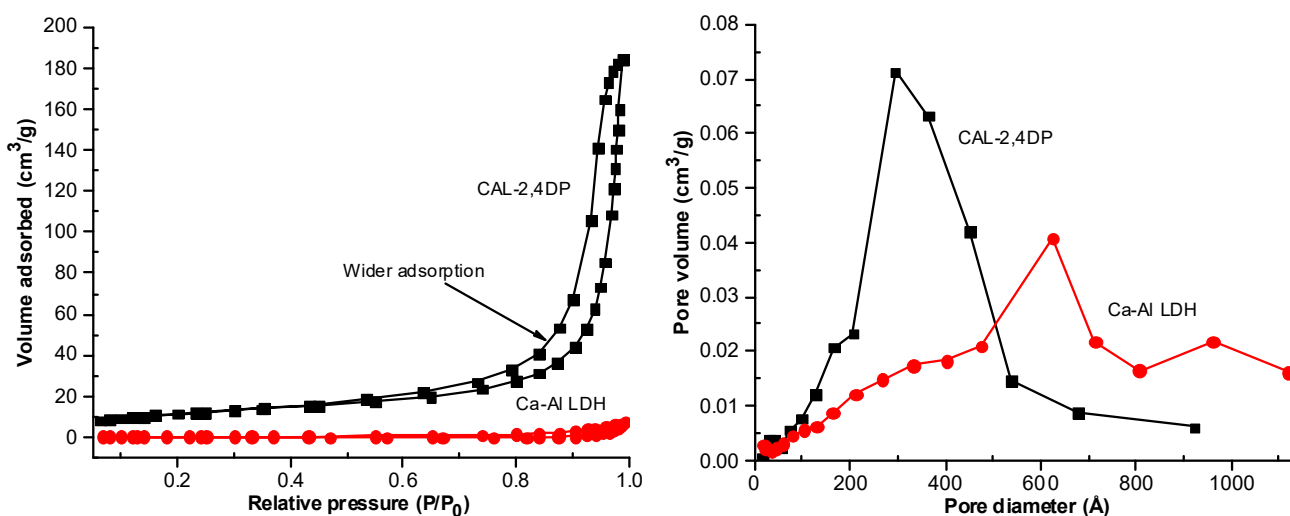
Fig 6. Adsorption-desorption isotherm and pore size distribution of Ca-Al LDH and CAL-2,4DP

Table 2. Surface properties of Ca-Al LDH and CAL-2,4DP (0.025 M)

Sample	Surface area ($m^2 g^{-1}$)	BJH desorption pore volume ($cm^3 g^{-1}$)	BET average pore diameter (Å)	BJH average pore diameter (Å)
Ca-Al LDH	17.93	180.36	94.34	156.71
CAL-2,4DP	21.35	178.59	111.14	126.90
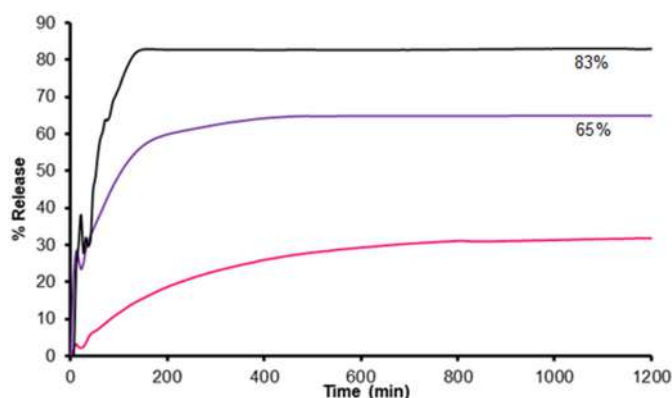
Fig 7. Release profiles of 2,4-DP anion from CAL-2,4DP into 0.01 M of various aqueous solutions

in Fig. 3. In addition, the inclusion of larger 2,4-DP anions generates more pores in the crystallites, increasing the surface area for the intercalated compound [21].

Controlled Release Studies

The release profiles of the accumulated 0.025 M CAL-2,4DP from the Ca-Al LDH interlayer into various aqueous solutions were investigated in Fig. 7. The salt solutions were observed according to their ion charges of phosphate (PO_4^{3-}), carbonate (CO_3^{2-}), and chloride (Cl^-). In the first 15 min, the release patterns of the 2,4-DP anion were rapid, followed by a much slower release upon reaching its equilibrium condition around 200 min. Here, the accumulated 2,4-DP ions depend on the availability of anion in the aqueous solutions following the order of $PO_4^{3-} > CO_3^{2-} > Cl^-$ with percentages of 83, 65, and 30%, respectively. Phosphate ions with the highest percentage confirm that a higher density charge affects a higher amount of PO_4^{3-} anion to be exchanged with 2,4-DP anion [18]. Therefore, PO_4^{3-} anions are interleaved into the Ca-Al LDH interlayer during the controlled release process, which simultaneously releases the 2,4-DP ions out from the interlayer into the aqueous solution.

■ **CONCLUSION**

In this study, a new nanohybrid LDH was successfully synthesized through the interleaving process of 2,4-DP herbicide into Ca-Al LDH interlayer via the co-precipitation method. The resulting synthesized nanohybrid, CAL-2,4DP, confirmed its interleaving process through several characterization techniques such as PXRD, FTIR, and elemental analysis. The PXRD analysis portrays the basal spacing expansion from 8.0 Å to 23.8 Å, implying that the 2,4-DP anion interleaved into the interlayer and replaced the nitrate ions. The synthesized nanohybrid of CAL-2,4DP is proven to be mesoporous material with type IV sorption according to the BET analysis. Moreover, the release of 2,4-DP anion from the Ca-Al LDH host is dependent on the available ions in the aqueous solution in the order of $PO_4^{3-} > CO_3^{2-} > Cl^-$. Therefore, this research proposes the Ca-Al LDH possibility as a host carrier for herbicide-controlled release mechanism to decrease the agrochemicals usage in agriculture.

■ **AUTHOR CONTRIBUTIONS**

Farah Liyana Bohari and Nur Aishah Mohd Noor experimented, Nur Nadia Dzulkifli analyzed the data, and Nurain Adam conducted the calculations. Is Fatimah and Sheikh Ahmad Izaddin Sheikh Mohd Ghazali wrote and revised the manuscript. All authors agreed to the final version of this manuscript.

■ **REFERENCES**

[1] Aktar, W., Sengupta, D., and Chowdhury, A., 2009, Impact of pesticides use in agriculture: Their benefits and hazards, *Interdiscip. Toxicol.*, 2 (1), 1–12.

[2] Wijitwongwan, R., Intasa-ard, S., and Ogawa, M., 2019, Preparation of layered double hydroxides toward precisely designed hierarchical organization,

ChemEngineering, 3 (3), 68.

[3] Shahabuddin, S., Sarih, N.M., Afzal Kamboh, M., Rashidi Nodeh, H., and Mohamad, S., 2016, Synthesis of polyaniline-coated graphene oxide@SrTiO₃ nanocube nanocomposites for enhanced removal of carcinogenic dyes from aqueous solution, *Polymers*, 8 (9), 305.

[4] Gonzalez Rodriguez, P., de Ruiter, M., Wijnands, T., and ten Elshof, J.E., 2017, Porous layered double hydroxides synthesized using oxygen generated by decomposition of hydrogen peroxide, *Sci. Rep.*, 7 (1), 481.

[5] Kim, G., and Park, S., 2021, Chloride removal of calcium aluminate-layered double hydroxide phases: A review, *Int. J. Environ. Res. Public Health*, 18 (6), 2797.

[6] Li, F., Jin, L., Han, J., Wei, M., and Li, C., 2009, Synthesis and controlled release properties of prednisone intercalated Mg-Al layered double hydroxide composite, *Ind. Eng. Chem. Res.*, 48 (12), 5590–5597.

[7] Jadam, M.L., Syed Mohamad, S.A., Mohd Zaki, H., Jubri, Z., and Sarijo, S.H., 2021, Antibacterial activity and physicochemical characterization of calcium-aluminium-ciprofloxacin-layered double hydroxide, *J. Drug Delivery Sci. Technol.*, 62, 102314.

[8] Zhang, Z., Chen, G., and Xu, K., 2013, One-pot green hydrothermal synthesis of stearate-intercalated MgAl layered double hydroxides, *Appl. Clay Sci.*, 72, 206–210.

[9] Bernardo, M.P., Moreira, F.K.V., and Ribeiro, C., 2017, Synthesis and characterization of eco-friendly Ca-Al-LDH loaded with phosphate for agricultural applications, *Appl. Clay Sci.*, 137, 143–150.

[10] Rebitski, E.P., Darder, M., and Aranda, P., 2019, Layered double hydroxide/sepiolite hybrid nanoarchitectures for the controlled release of herbicides, *Beilstein J. Nanotechnol.*, 10, 1679–1690.

[11] Sarijo, S.H., Sheikh Mohd Ghazali, S.A.I., and Hussein, M.Z., 2015, Synthesis of dual herbicides-intercalated hydrotalcite-like nanohybrid compound with simultaneous controlled release property, *J. Porous Mater.*, 22 (2), 473–480.

[12] Ee, G.C.L., Izzaddin, S.A., Rahmani, M., Sukari, M.A., and Lee, H.L., 2006, γ-Manggostin and rubraxanthone, two potential lead compounds for anti-cancer activity against CEM-SS cell line, *Nat. Prod. Sci.*, 12 (3), 138–143.

[13] Abdullah, A., Abd Gani, S.S., Mohd Mokhtar, N.F., Taufiq Yap, Y.H., Haiyee, Z., and Mustafa, S., 2018, Supercritical carbon dioxide extraction of red pitaya (*Hylocereus polyrhizus*) seeds: Response surface optimization, fatty acid composition and physicochemical properties, *Malays. Appl. Biol.*, 47 (2), 39–46.

[14] Mohd Nor, N., Salih, N., and Salimon, J., 2021, Optimization of the ring opening of epoxidized palm oil using D-optimal design, *Asian J. Chem.*, 33 (1), 67–75.

[15] Sarijo, S.H., Hussein, M.Z., Yahaya, A.H.J., and Zainal, Z., 2010, Effect of incoming and outgoing exchangeable anions on the release kinetics of phenoxyherbicides nanohybrids, *J. Hazard. Mater.*, 182 (1-3), 563–569.

[16] Abd Ghani, K.D., Nayan, S., Sheikh Mohd Ghazali, S.A.I., Shafie, L.A., and Nayan, S., 2010, Critical internal and external factors that affect firms strategic planning, *Int. Res. J. Finance Econ.*, 51, 50–58.

[17] Ahmad, R., Hussein, M.Z., Sarijo, S.H., Wan Abdul Kadir, W.R., and Taufiq Yap, Y.H., 2016, Synthesis and characteristics of valeric acid-zinc layered hydroxide intercalation material for insect pheromone controlled release formulation, *J. Mater.*, 2016, 1285721.

[18] Salleh, N.M., Mohsin, S.M.M., Sarijo, S.H., and Sheikh Mohd Ghazali, S.A.I., 2017, Synthesis and physico-chemical properties of zinc layered hydroxide-4-chloro-2-methylphenoxy acetic acid (ZMCPA) nanocomposite, *IOP Conf. Ser.: Mater. Sci. Eng.*, 204, 012012.

[19] Hussein, M.Z., Sarijo, S.H., Yahaya, A.H., and Zainal, Z., 2007, Synthesis of 4-chlorophenoxyacetate-zinc-aluminium-layered double hydroxide nanocomposite: Physico-chemical and controlled

release properties, *J. Nanosci. Nanotechnol.*, 7 (8), 2852–2862.

[20] Mohd Nor, N., Salih, N., and Salimon, J., 2021, Chemically modified *Jatropha curcas* oil for biolubricant applications, *Hem. Ind.*, 75 (2), 117–128.

[21] Abdullah, A., Abd Gani, S.S., Taufiq Yap, Y.H., Abdul Haiyee, Z., Zaidan, U.H., Kassim, M.A., and Effendi Halmi, M.I., 2019, Lipase-catalyzed synthesis of red pitaya (*Hylocereus polyrhizus*) seed oil esters for cosmeceutical application: Process optimization using response surface methodology, *RSC Adv.*, 9, 5599–5609.

Enhanced Drug Release of Poly(lactic-co-glycolic Acid) Nanoparticles Modified with Hydrophilic Polymers: Chitosan and Carboxymethyl Chitosan

Diah Lestari[1], Noverra Mardhatillah Nizardo[1*], and Kamarza Mulia[2]

[1]Department of Chemistry, Faculty of Mathematics and Natural Sciences, Universitas Indonesia, Depok 16424, Indonesia

[2]Department of Chemical Engineering, Universitas Indonesia, Depok 16424, Indonesia

Abstract: *The biodegradable polymer poly(lactic-co-glycolic acid) (PLGA) is a biomaterial with great potential as a drug delivery carrier and a tissue engineering scaffold. Using diclofenac sodium (DS) as a drug model, PLGA/DS nanoparticles were synthesized by modification with two hydrophilic polymers: chitosan and carboxymethyl chitosan (CMCh). The introduction of chitosan and CMCh enhances the efficiency encapsulation, capacity loading of the nanoparticles, and DS release at pH 6.8 and minimum release at pH 1.2. Synthesis of nanoparticles was carried out using a double emulsion (water/oil/water) solvent evaporation method. Characterization using an Attenuated total reflectance-Fourier transform infrared (ATR-FTIR) spectrophotometer indicates that the interaction between DS and polymer on nanoparticles is non-covalent with a spherical shape based on a transmission electron microscope (TEM) and scanning electron microscope (SEM) characterization. From the various formulation studied, nanoparticles with the ratio chitosan-PLGA-DS and CMCh-PLGA-DS of 2:20:4 proved to be the optimum model carrier with the required release profile and could be the alternative for DS delivery systems.*

Keywords: *diclofenac sodium; PLGA; chitosan; carboxymethyl chitosan; controlled release*

■ INTRODUCTION

Diclofenac sodium (DS) is a non-steroidal anti-inflammatory drug (NSAID) widely used to relieve pain and anti-inflammation in various diseases like osteoarthritis and rheumatoid arthritis [1-2]. Due to its about two hours of biological half-life, frequent administration is necessary to maintain therapeutic drug-blood levels. DS is reported to cause gastrointestinal troubles, peptic ulceration, and renal damage if large dosing is taken orally [1,3-4]. A controlled drug is required to maintain drug efficacy and reduce side effects. This can be accomplished using a drug encapsulation technique to deliver the drug to a specific target [5]. Nanoparticles are one of the most extensively exploited for drug delivery systems due to their unique properties related to their size, capacity for drug protection, and controlled drug release [6]. Encapsulation with nanoparticles is one technique for enhancing drug stability by protecting it from enzymatic degradation, controlling drug release, increasing drug solubility, absorption by target cells or tissues, and drug safety [7-8]. The biodegradable polymer poly(lactic-co-glycolic acid) (PLGA) is a biocompatible and biodegradable copolymer commonly utilized as a nanoparticle matrix [2]. Several methods to prepare PLGA nanoparticles include the single or double emulsion method, salting-out, and nanoprecipitation [9]. PLGA has been modified with other biodegradable polymeric materials to increase its use as a drug carrier.

Chitosan and its derivatives are hydrophilic polymers that can be used as a surface modification of PLGA. Chitosan has been widely applied in tissue engineering, biomedical implants, and drug delivery devices as a natural biopolymer. However, it has limitations, such as being insoluble at physiological pH

and poor mechanical stability [10]. Carboxymethyl chitosan (CMCh) is a chitosan derivative that enhances its solubility at neutral pH. The presence of a carboxyl group at C-6 of chitosan produces carboxymethyl chitosan, which is soluble in both neutral and alkaline pH solutions. CMCh can be applied as a surface coating for polymer nanoparticles in the drug encapsulation process. The pH sensitivity of CMCh can be utilized for controlled drug release in delivery systems based on gastrointestinal pH changes [11]. CMCh improves the stability of polymer nanoparticles, hence diminishing drug burst release from polymer nanoparticles [12]. Furthermore, minimizing the size of particles of the drug can increase the solubility of the drug [13-14].

In this study, PLGA nanoparticles containing different amounts of chitosan or CMCh and DS have been fabricated via a double emulsion (w/o/w) solvent evaporation technique. The effect of chitosan and CMCh on PLGA nanoparticles was studied by an *in vitro* DS release study, determining the percentage of encapsulation efficiency and loading capacity. The effect of chitosan and CMCh on PLGA nanoparticles in *in vitro* DS release study, percentage of encapsulation efficiency, loading efficiency, and morphology were compared with unmodified PLGA nanoparticles.

■ EXPERIMENTAL SECTION

Materials

The materials used in this study were diclofenac sodium (National Agency of Drug and Food Control-Republic of Indonesia) as a drug model, poly(D,L-lactic-co-glycolic acid) lactic acid-glycolic acid ratio 50:50 with carboxyl end groups, Mw = 7–17 kDa (Nomisma Healthcare, India) as a nanoparticle material, poly(vinyl alcohol) (PVA) 87–90% hydrolyzed (Sigma Aldrich) as an emulsifier, low molecular weight chitosan with a degree of deacetylation > 75%, Mw = 50–190 kDa (Sigma Aldrich), O-carboxymethyl chitosan (CMCh) with a degree of substitution > 80% (Xi'an Herben Biotech), dichloromethane (Merck, Germany) was used as a PLGA solvent. Sodium chloride (Merck, Germany), hydrochloride acid (37%, Merck, Germany), and sodium hydroxide (Merck, Germany) were used to prepare the release medium. In addition, glacial acetic acid (Merck, Germany) was used to dissolve chitosan, methanol (LC grade, Merck, Germany), and deionized water (Milli-Q, Millipore) used for analysis using High-Performance Liquid Chromatography.

Instrumentation

A probe ultrasonicator (Hielscher UP 200st, PT Petra Karunia Persada) and freeze dryer (Thermo Scientific) were used in the preparation of nanoparticles. Nanoparticles were characterized using an ATR-FTIR spectrometer (Shimadzu IRSpirit). The size of nanoparticles was analyzed by particle size analyzer (Horiba SZ 100z, Integrated Laboratory and Research Center, Universitas Indonesia), and the morphology was analyzed by using a scanning electron microscope (SEM-Quanta) and transmission electron microscope (TEM-FEI Tecnai G2, Integrated Laboratory and Research Center, Universitas Indonesia). Determination of DS was performed by high-performance liquid chromatography (HPLC Shimadzu LC-20 AD) and UV-Vis Spectrophotometer (Shimadzu UV-1800).

Procedure

Preparation of DS nanoparticles

The nanoparticles were prepared using the double emulsion solvent evaporation technique as reported by Khanal et al. [11] with modification. As much as 200 mg of PLGA was dissolved in dichloromethane, and the DS solution was added and sonicated for 30 s using a probe ultrasonicator. The mixture was added dropwise to 5 mL of 0.3% polyvinyl alcohol (PVA) solution under a constant vortex. The solution was emulsified in an ice bath for 3 min using a probe ultrasonicator (water in oil emulsion). The emulsified solution was transferred into 45 mL of 0.3% PVA solution containing CMCh or chitosan solution, and the emulsion was stirred at 500 rpm for 5 h at room temperature (water in oil in water emulsion) and centrifuged the emulsion at 8000 rpm for 30 min at 4 °C. Finally, the nanoparticles were lyophilized for 24 h. The composition of ingredients is described in Table 1 and Table 2.

Table 1. Variation of composition of CMCh and chitosan on PLGA-DS

Formulation	Code	Weight ratio CMCh-PLGA-DS
PLGA-DS	F-0	0:20:2
CMCh-PLGA-DS	F-1	1:20:2
CMCh-PLGA-DS	F-2	2:20:2
CMCh-PLGA-DS	F-3	3:20:2
CMCh-PLGA-DS	F-4	4:20:2
Chitosan-PLGA-DS	H-1	1:20:2
Chitosan-PLGA-DS	H-2	2:20:2
Chitosan-PLGA-DS	H-3	3:20:2
Chitosan-PLGA-DS	H-4	4:20:2

Table 2. Variation of composition of DS on CMCh-PLGA and chitosan-PLGA

Formulation	Code	Weight ratio PLGA-DS
CMCh-PLGA-DS*	F-A	20:1
	F-B	20:2
	F-C	20:4
Chitosan-PLGA-DS*	H-A	20:1
	H-B	20:2
	H-C	20:4

*the composition of CMCh and chitosan used was the optimum composition obtained in the optimization of Table 1

Determination of loading capacity and encapsulation efficiency

The nanoparticles loading capacity (LC) and encapsulation efficiency (EE) were determined directly using a method described in Farmakope Indonesia 6th edition as follows: Accurately weighed 5 mg of nanoparticles was put into a 20 mL volumetric flask, added 0.5 mL of dichloromethane, then shaken using a vortex mixer for 3 min. The nanoparticles were added with methanol, sonicated for 20 min, and diluted with methanol to volume. The amount of DS in lyophilized nanoparticles was analyzed using an HPLC UV detector at 254 nm. An octyl silane column was used with methanol and 0.01 M phosphate buffer pH 2.5 (7:3) as the mobile phase with a 1 mL/min flow rate. The LC and EE were given according to Eq. (1) and (2).

$$LC = \frac{\text{weight of the drug}}{\text{total weight of the drug loaded nanoparticles}} \times 100\% \quad (1)$$

$$EE = \frac{\text{weight of drug in nanoparticles}}{\text{weight of drug added}} \times 100\% \quad (2)$$

In vitro *drug release study*

In vitro release studies were conducted to determine the effect of chitosan and CMCh on PLGA/DS nanoparticles. As much as 50 mg of each formulation were immersed in 50 mL pH 1.2 solution and stirred at 100 rpm for 2 h at a temperature of 37 ± 0.5 °C. About 2 mL of filtrate was taken and replaced with preheated fresh medium at various periods. After 2 h, the pH of the release medium was increased to 6.8 by adding 2.5 M sodium hydroxide solution [15], and the release was continued for a further 24 h. About 2 mL of filtrate was taken and replaced with a preheated fresh medium within 24 h. The concentration of drug release was measured by UV-Vis spectrophotometer at wavelength 277 nm using an absorbance-drug concentration calibration curve.

■ RESULTS AND DISCUSSION

FTIR Spectroscopy Analysis

Characterization of the nanoparticles was performed by ATR-FTIR, investigating interactions between the drug and polymer (Fig. 1). Pure PLGA exhibits peaks at 1713 and 1051 cm^{-1}, corresponding to -C=O stretching and C-O-C bending [16-17]. CMCh displayed the characteristic peaks at 1547 and 1024 cm^{-1} indicating COO stretching and C-O-C bending [16,18]. A suggested COO band at 1547 cm^{-1} overlaps the NH$_2$ band at 1600 cm^{-1}. The CMCh/PLGA/DS nanoparticles spectrum displayed band at 1774 cm^{-1} indicates PLGA. The relative weak band was at 1534 and 712 cm^{-1}, indicating a typical band absorption CMCh and DS, respectively. The same profile occurred in the Chitosan/PLGA/DS nanoparticles spectrum, where the characteristic peaks of PLGA, DS, and Chitosan appeared at 1718, 1606, 1064, and 713 cm^{-1}. IR analysis showed no change in the peaks of each material which indicates there was no new absorption formed in the nanoparticle spectrum. The spectrum of nanoparticles shows a characteristic absorption band of the drug, and its polymer indicates the absence of covalent interactions between the drug and the polymer [19], suggesting the
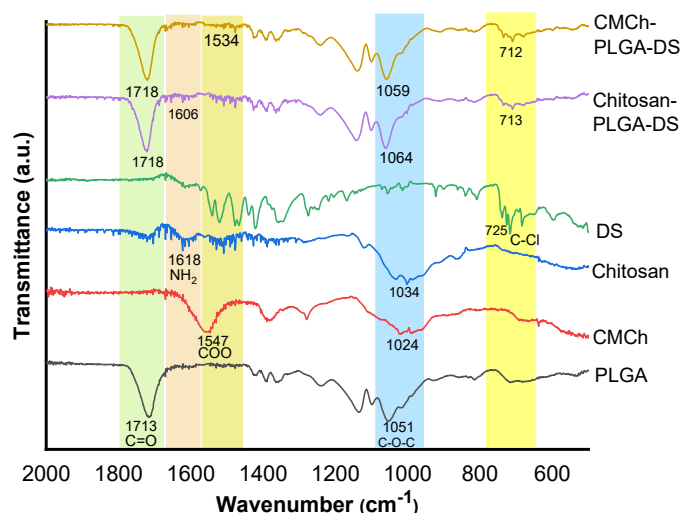
Fig 1. FTIR spectra of PLGA, CMCh, Chitosan, DS, Chitosan-PLGA-DS, and CMCh-PLGA-DS nanoparticles

interaction between PLGA and CMCh was a non-covalent bond. Non-covalent bonds on the surface of nanoparticles can occur through electrostatic interactions [20].

Particle Size, Surface Charge, and Morphology

PSA analysis

The addition of CMCh and chitosan increased the hydrodynamic diameter of the nanoparticles, according to the dynamic light scattering technique. The increase in size was due to the increased viscosity of the external phase containing CMCh or chitosan, which reduces shear stress during stirring so that larger emulsion droplets are formed [21]. The modifier composition enhanced the particle size [17,22]. Khanal et al. also reported the size increase of modified PLGA nanoparticles using chitosan

[11]. Fig. 2 shows the size distribution taken from three samples that were F-0, F-2, and H-2. Table 3 shows the hydrodynamic size for all of the nanoparticles. The size difference between the unmodified and modified nanoparticles demonstrates that carboxymethyl chitosan or chitosan was adsorbed on the PLGA surface [23].

The presence of chitosan or CMCh layer on the nanoparticle surface was caused by the electrostatic interaction between the amine group and the negatively charged surface of the PLGA. This was the dominant interaction in the formation of the first adsorption layer. The adsorption of chitosan or CMCh can continue where hydrogen bonds can be involved in the adsorption. Therefore, the chitosan or CMCh layer can be adsorbed at high concentrations on the first layer. More layers allow the chitosan or CMCh chains to repel
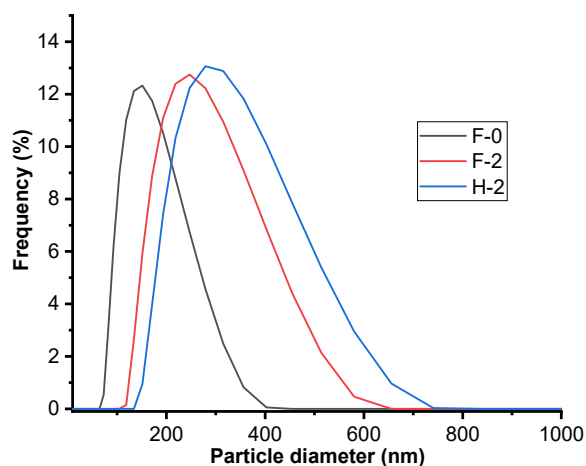
Fig 2. Size distribution of the F-0, F-2, and H-2 nanoparticles determined by dynamic light scattering measurement

Table 3. The hydrodynamic size of nanoparticles

Formulation code	Size ± SD (nm)	Polydispersity ± SD	Zeta Potential ± SD (mV)
F-0	140 ± 4	0.14 ± 0.09	-52 ± 0.7
F-1	173 ± 7	0.26 ± 0.02	
F-2	233 ± 2	0.14 ± 0.07	
F-3	238 ± 30	0.30 ± 0.17	
F-4	197 ± 2	0.23 ± 0.07	-43.4 ± 1.1
H-1	399 ± 38	0.41 ± 0.04	
H-2	267 ± 2	0.18 ± 0.07	
H-3	289 ± 5	0.35 ± 0.09	
H-4	425 ± 5	0.39 ± 0.08	24.3 ± 0.8

because they have the same charge but interact through van der Waals forces and hydrogen bonds [22]. However, in Table 3, the increase in the ratio of chitosan and CMCh to PLGA nanoparticles does not seem to give a significant difference in size increase. The small amount of chitosan or CMCh or the amount of chitosan or CMCh undergoing leaching may be due to non-optimal interactions. It is necessary to prove it by studying the addition of chitosan or CMCh with a more significant amount.

The polydispersity index (PDI) value shows the distribution of suspended particles, where the value is between 0−1. PDI values below 0.5 indicate that the nanoparticles have a homogeneous size distribution and good stability [24]. The PDI resulting from each nanoparticle formula shows good homogeneity. It can be seen from its value which is below 0.5. A large positive or negative value of zeta potential has been shown to prevent agglomeration due to electrostatic repulsion and increase colloidal stability [25-26]. We measured the zeta potential of three different formulas as representatives. It was found that the PLGA-DS nanoparticles have a zeta potential of -52 ± 0.7 mV due to carboxyl end groups on nanoparticle surfaces. The zeta-potential of the CMCh-PLGA-DS (F-4) was slightly less negative (-43.4 ± 1.1 mV) compared to the PLGA-DS nanoparticles because CMCh has an amine group and a carboxyl group, so the amine group may reduce the negative value of the nanoparticle surface, which indicates the CMCh effectively adsorbed onto the PLGA nanoparticle surfaces. In contrast to chitosan-PLGA-DS nanoparticles (H-4), a positive value for zeta potential resulted due to the presence of an amine group, which was 24.3 ± 0.8 mV.

SEM and TEM analysis

TEM measurements were conducted to investigate the morphology and size of the particle. In addition, the surface morphology of the PLGA-DS, CMCh-PLGA-DS, and Chitosan-PLGA-DS nanoparticles was observed through SEM images. Fig. 3 shows the morphology of the nanoparticles discovered to be spherical and have smooth surfaces. SEM images of the nanoparticles after the release of the drug show interparticle fusing. The morphology of
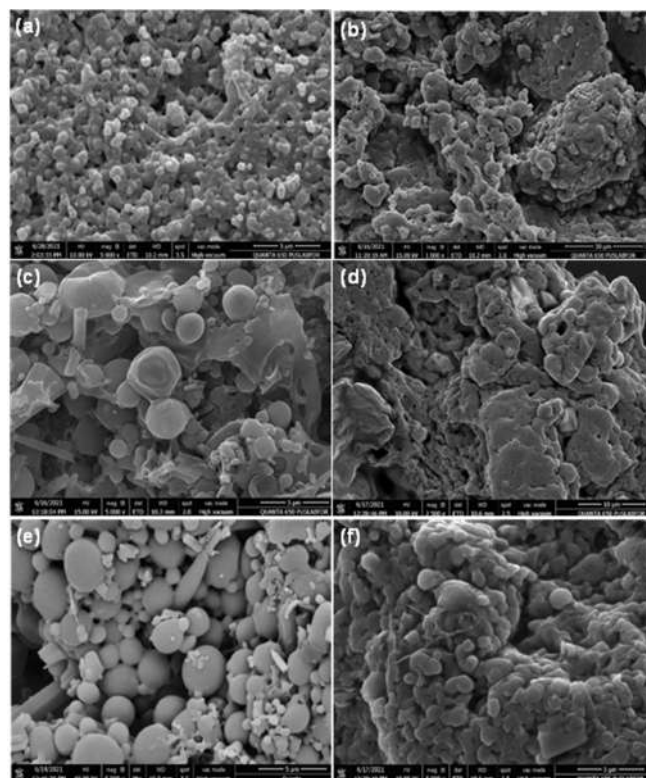
Fig 3. SEM images of nanoparticles: (a) F-0 before release; (b) F-0 after release; (c) F-2 before release; (d) F-2 after release; (e) H-2 before release (f) H-2 after release

the nanoparticles remain, suggesting that most of the release of the drug occurs through diffusion across the polymeric matrix [27].

Nanoparticles coded F-0, F-2, and H-2 were taken as samples to be measured using TEM, where the F-2 and H-2 are nanoparticles with an optimum release profile compared to other formulas. TEM images of the PLGA-DS, CMCh-PLGA-DS, and chitosan-PLGA-DS in Fig. 4 suggested that a layer of CMCh and chitosan was attached to the surface of the nanoparticles due to non-covalent interactions that may occur between CMCh with PLGA. The measurement results with TEM and PSA were only slightly different. The size of nanoparticles of F-2 based on TEM measurements was about 300 nm, and 280 nm for H-2. In general, there are differences in particle size with PSA measurements with TEM particle sizes, which can be caused by differences in the methods used. In contrast to measurements using TEM, which produces a 2D image projected from the
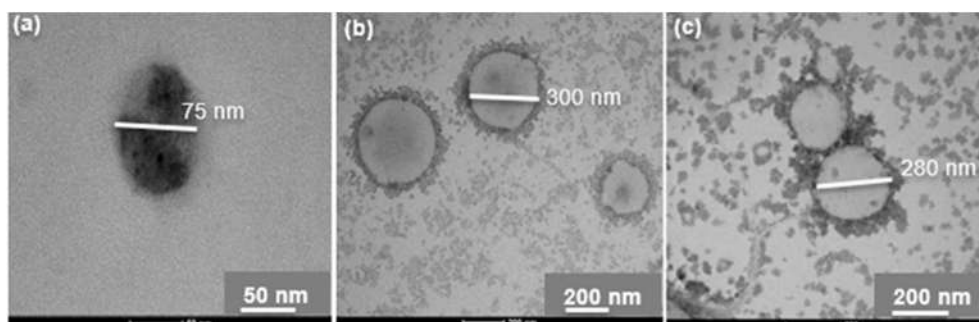
Fig 4. TEM images of nanoparticles: (a) F-0, (b) F-2, (c) H-2

nanoparticles, the dynamic light scattering (DLS) method used in PSA is based on hydrodynamic measurements of nanoparticles that produce a dispersed particle size distribution [28]. The presence of aggregation in the dispersion can encourage the distribution of particles to tend to be larger [29].

The Effect of CMCh and Chitosan Composition on EE and LC

The effect of CMCh and chitosan to PLGA weight ratio on EE of DS encapsulated in the PLGA-CMCh and PLGA-Chitosan matrix is presented in Fig. 5. This study evaluated four different weight ratios of CMCh and chitosan to PLGA. CMCh-modified PLGA (F-1 to F-4) and chitosan-modified PLGA (H-1 to H-4) nanoparticles have an encapsulation efficiency that tends to increase as the composition of CMCh and chitosan increases. As shown in Fig. 5, the EE of the PLGA nanoparticles without modification (F-0) was 59.2%. Meanwhile, the EE values of modified PLGA nanoparticles were higher. The result is higher than the optimal EE in the previous study by Khanal et al., 52% [11]. The interaction of nanoparticles with DS tends to increase with the increasing amount of chitosan and CMCh. Chitosan and CMCh have an amine group that can interact electrostatically with DS and PLGA, retaining DS in the matrix. Therefore, variations in the ratio of chitosan and CMCh to PLGA showed an increase in size, which allowed higher drug entrapment.

As shown in Fig. 6, these results have a similar trend, namely, the increasing composition of CMCh in the matrix enhances the EE and LC. These results, as observed in a previous study by Khanal et al., obtained an optimal LC of 6% [11].
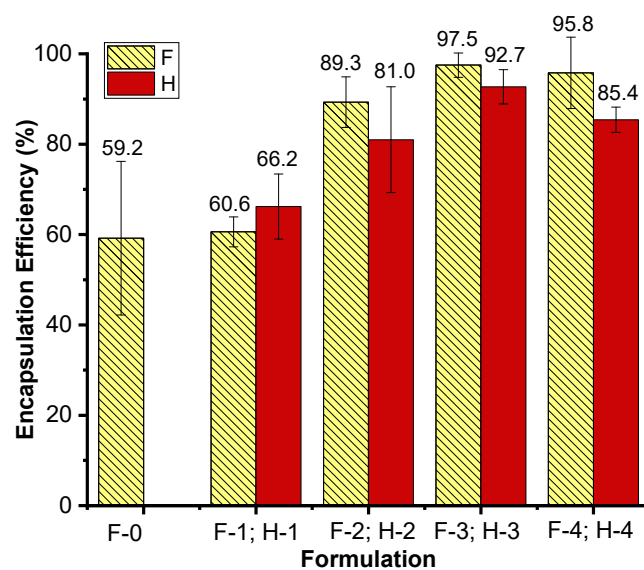
Fig 5. Effects of weight ratio of CMCh and chitosan to PLGA on encapsulation efficiency
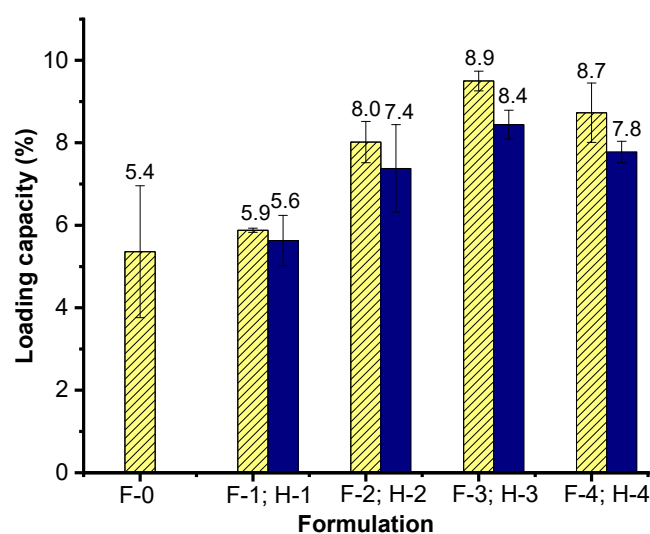
Fig 6. Effects of weight ratio of CMCh and chitosan to PLGA on loading capacity

The Effect of CMCh and Chitosan Composition on Release Drug

In vitro drug release study was performed to evaluate the release of DS from nanoparticles. Several factors influence drug release from nanoparticle-based formulations, including pH, temperature, drug solubility, desorption of surface-bound or adsorbed drugs, drug diffusion, nanoparticle matrix swelling, erosion, and the combination of erosion and diffusion processes [30]. The percentage of cumulative drug release is presented in Fig. 7(a). The results showed that DS was released from the PLGA matrix faster than from the CMCh-PLGA matrix. Approximately more than 70% of the cumulative drug release from CMCh-PLGA nanoparticles occurred in 24 h, whereas for the cumulative drug release from the PLGA matrix, only 49%. The results showed that all formulations had a biphasic release profile, characterized by an initial rapid release and continuous release [31]. As seen in Fig. 7(b), all formulas show resistance to pH 1.2. This is indicated by the low percentage of release at pH 1.2, and the highest release is only about 1.5%. The presence of CMCh was thought to play a role in protecting the surface of the PLGA matrix so that drug release could be reduced.

Compared with PLGA-DS nanoparticles, the cumulative drug release of CMCh-PLGA-DS nanoparticles was higher at pH 6.8. It was estimated that CMCh affects the release of DS in the medium. CMCh is more hydrophilic than PLGA, allowing pH 6.8 medium solution to penetrate the nanoparticle matrix more quickly and release more drug molecules [11]. The increase of CMCh concentration suggested increasing the medium penetration and hydration rate of the CMCh-PLGA matrix. The behavior of CMCh, which has a solubility at neutral pH, allows increasing the release rate at pH 6.8. At neutral pH, the carboxyl group in CMCh was deprotonated, leading to dissolution in the medium. This provides the possibility for hydration of the matrix. These factors may contribute to a higher cumulative drug release from CMCh-PLGA nanoparticles. From all formulas, the composition of CMCh to PLGA in formula F-2 seemed to have the best release profile, which resulted in low drug release at pH 1.2 was 0.2%, and sustained release up to 24 h, which reached 90.9%.

The release profile of chitosan-PLGA-DS had almost the same trend. The release study was low at pH 1.2 and relatively high at pH 6.8 for all formulas, as seen in Fig. 8. The maximum release was 1.3% at pH 1.2, while the lowest was 0.8%. Chitosan can dissolve in acidic media, so at pH 6.8, the contact of chitosan-PLGA-DS with a pH of 1.2 might cause protonation of chitosan, weakening the interaction of chitosan with PLGA to dissolve in the medium and facilitating the diffusion of DS from the matrix. The solubility of DS is known to increase at this pH. The addition of chitosan
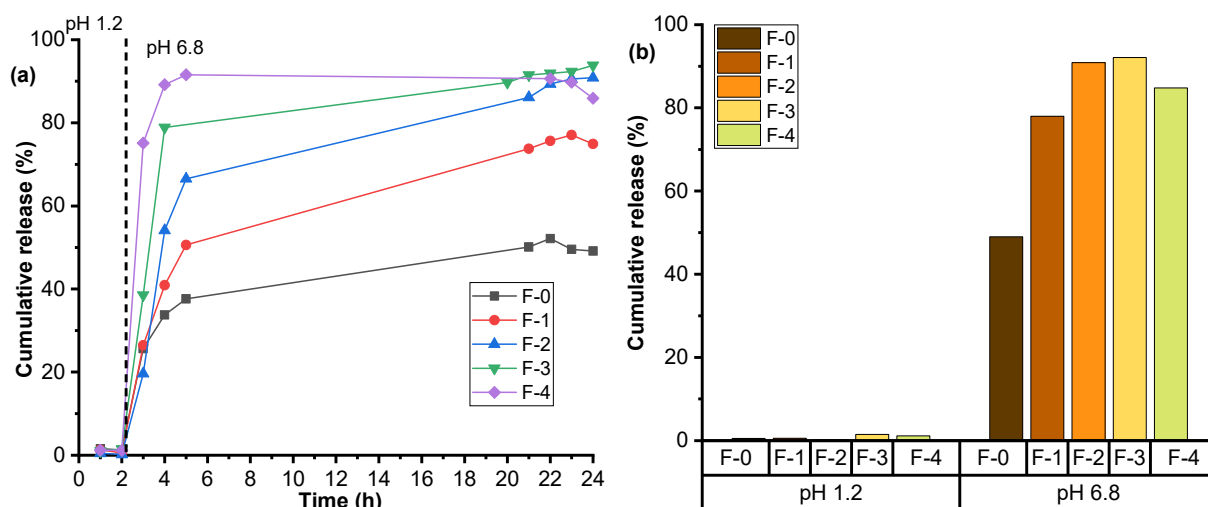
Fig 7. Effect of weight ratio of CMCh to PLGA (a) and different pH media (b) on profile release of diclofenac sodium

Indones. J. Chem., 2022, 22 (5), 1338 - 1347

1345
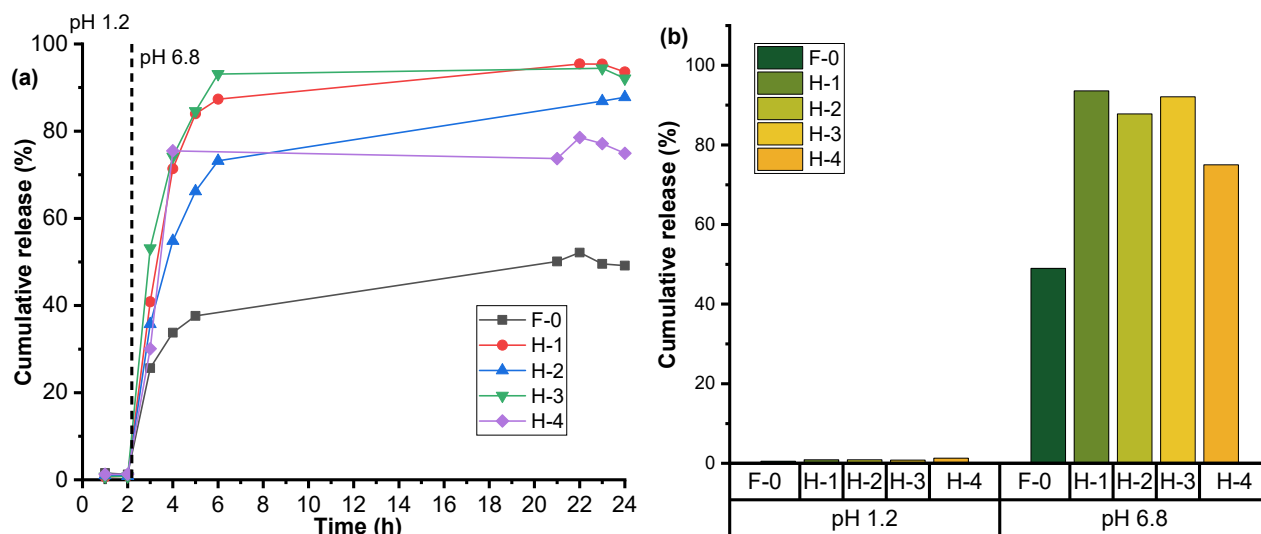
Fig 8. Effect of weight ratio of chitosan to PLGA (a) and different pH media (b) on profile release of diclofenac sodium
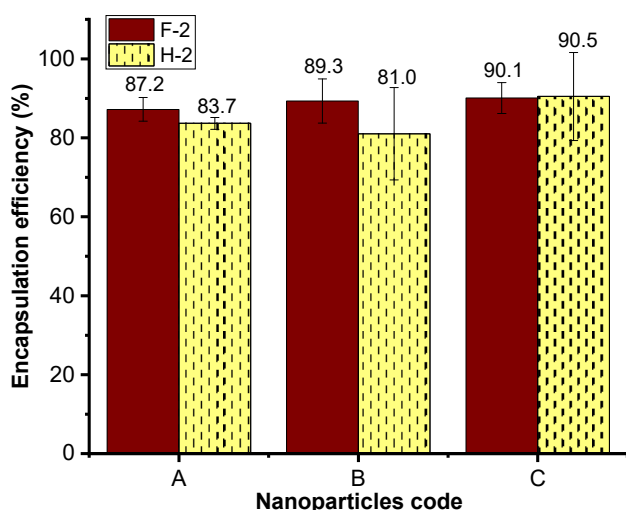

Fig 9. Effect of weight ratio of diclofenac sodium to PLGA on efficiency encapsulation
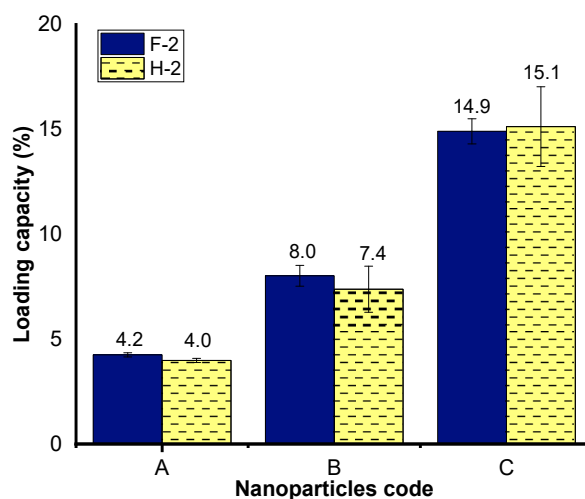

Fig 10. Effect of weight ratio of diclofenac sodium to PLGA on loading capacity

was adequate in this study to withstand the release of DS at low pH.

According to the release profile, the formula F-2 and H-2 were the optimum since they had the lowest release at pH 1.2, followed by a fairly significant release at pH 6.8. This formula is used to optimize the PLGA-DS composition.

The Effect of Diclofenac Sodium Composition on EE and LC

Fig. 9 shows the percentage of encapsulation efficiency as the mass ratio of DS to PLGA varies. All formulas, both CMCh and chitosan-modified, have excellent encapsulation efficiency. So, this suggests that

adding DS composition does not seem to influence the percentage of EE.

Fig. 10 illustrates the percentage loading capacity of the optimized DS composition. The higher the DS composition in the matrix, the higher the percentage of LC obtained. The higher percentage of LC reveals that the polymer matrix might contain drugs in a 20:4 ratio for both F-2C and H-2C, enhancing the effectiveness of nanoparticles. Although various nanoparticle systems with various characteristics have been successfully synthesized, the loading capacity of most of the nanoparticle systems is relatively low, generally less than 10%. As an outcome, developing techniques to improve

drug loading is necessary [32].

■ CONCLUSION

A modified PLGA nanoparticle was prepared successfully using carboxymethyl chitosan and chitosan to encapsulate DS. It could improve the loading capacity, efficiency encapsulation, and drug release of nanoparticles with increased size. The formula obtained the best formulation of CMCh-PLGA-DS with the best LC and EE. The minimum drug release at pH 1.2 medium and the maximum drug release at pH 6.8 with a low initial burst release, namely F-2C and H-2C.

■ ACKNOWLEDGMENTS

■ REFERENCES

[1] Hasnain, M.S., Rishishwar, P., Rishishwar, S., Ali, S., and Nayak, A.K., 2018, Isolation and characterization of *Linum usitatisimum* polysaccharide to prepare mucoadhesive beads of diclofenac sodium, *Int. J. Biol. Macromol.*, 116, 162–72.

[2] Yurtdaş-Kırımlıoğlu, G., and Görgülü, Ş., 2021, Surface modification of PLGA nanoparticles with chitosan or Eudragit® RS 100: Characterization, prolonged release, cytotoxicity, and enhanced antimicrobial activity, *J. Drug Delivery Sci. Technol.*, 61, 102145.

[3] Altman, R., Bosch, B., Brune, K., Patrignani, P., and Young, C., 2015, Advances in NSAID development: Evolution of diclofenac products using pharmaceutical technology, *Drugs*, 75 (8), 859–77.

[4] Cooper, D.L., and Harirforoosh, S., 2014, Design and optimization of PLGA-based diclofenac loaded nanoparticles, *PLoS One*, 9 (1), e87326.

[5] Yadav, H.K.S., and Shivakumar, H.G., 2012, *In vitro* and *in vivo* evaluation of pH-sensitive hydrogels of carboxymethyl chitosan for intestinal delivery of theophylline, *Int. Scholarly Res. Not.*, 2012, 763127.

[6] Sequeira, J.A.D., Pereira, I., Ribeiro, A.J., Veiga, F., and Santos, A.C., 2020, "Surface Functionalization of PLGA Nanoparticles for Drug Delivery" in *Handbook of Functionalized Nanomaterials for Industrial Applications*, Eds. Mustansar Hussain, C., Elsevier, Amsterdam, Netherlands, 185–203.

[7] Deng, Y., Zhang, X., Shen, H., He, Q., Wu, Z., Liao, W., and Yuan, M., 2020, Application of the nano-drug delivery system in treatment of cardiovascular diseases, *Front. Bioeng. Biotechnol.*, 7, 489.

[8] Bhattacharjee, S., 2019, "Polymeric Nanoparticles" in *Principles of Nanomedicine*, Jenny Stanford Publishing, Singapore, 195–240.

[9] Varga, N., Hornok, V., Janovák, L., Dékány, I., and Csapó, E., 2019, The effect of synthesis conditions and tunable hydrophilicity on the drug encapsulation capability of PLA and PLGA nanoparticles, *Colloids Surf., B*, 176, 212–218.

[10] Sharifi, F., Atyabi, S.M., Norouzian, D., Zandi, M., Irani, S., and Bakhshi, H., 2018, Polycaprolactone/carboxymethyl chitosan nanofibrous scaffolds for bone tissue engineering application, *Int. J. Biol. Macromol.*, 115, 243–248.

[11] Khanal, S., Adhikari, U., Rijal, N.P., Bhattarai, S.R., Sankar, J., and Bhattarai, N., 2016, pH-Responsive PLGA nanoparticle for controlled payload delivery of diclofenac sodium, *J. Funct. Biomater.*, 7 (3), 21.

[12] Shanavas, A., Jain, N.K., Kaur, N., Thummuri, D., Prasanna, M., Prasad, R., Naidu, V.G.M., Bahadur, D., and Srivastava, R., 2019, Polymeric core-shell combinatorial nanomedicine for synergistic anticancer therapy, *ACS Omega*, 4 (22), 19614–19622.

[13] Simonazzi, A., Cid, A.G., Villegas, M., Romero, A.I., Palma, S.D., and Bermúdez, J.M., 2018, "Nanotechnology Applications in Drug Controlled Release" in *Drug Targeting and Stimuli Sensitive Drug Delivery Systems*, Eds. Grumezescu, A.M., William Andrew Publishing, Oxford, UK, 81–116.

[14] Khadka, P., Ro, J., Kim, H., Kim, I., Kim, J.T., Kim, H., Cho, J.M., Yun, G., and Lee, J., 2014, Pharmaceutical particle technologies: An approach to improve drug solubility, dissolution and bioavailability, *Asian J. Pharm. Sci.*, 9 (6), 304–316.

[15] Wang, J., Wang, F., Li, X., Zhou, Y., Wang, H., and Zhang, Y., 2019, Uniform carboxymethyl chitosan-

enveloped Pluronic F68/poly(lactic-co-glycolic acid) nano-vehicles for facilitated oral delivery of gefitinib, a poorly soluble antitumor compound, *Colloids Surf., B,* 177, 425–432.

[16] Stuart, B.H., 2004, *Infrared Spectroscopy: Fundamentals and Applications*, John Wiley & Sons, Chichester, UK.

[17] Al-Nemrawi, N.K., Alshraiedeh, N.H., Zayed, A.L., and Altaani, B.M., 2018, Low molecular weight chitosan-coated PLGA nanoparticles for pulmonary delivery of tobramycin for cystic fibrosis, *Pharmaceuticals*, 11 (1), 28.

[18] Joshi, J.M., and Sinha, V.K., 2006, Synthesis and characterization of carboxymethyl chitosan grafted methacrylic acid initiated by ceric ammonium nitrate, *J. Polym. Res.*, 13 (5), 387–395.

[19] Javadzadeh, Y., Ahadi, F., Davaran, S., Mohammadi, G., Sabzevari, A., and Adibkia, K., 2010, Preparation and physicochemical characterization of naproxen-PLGA nanoparticles, *Colloids Surf., B*, 81 (2), 498–502.

[20] Moku, G., Gopalsamuthiram, V.R., Hoye, T.R., and Panyam, J., 2019, "Surface Modification of Nanoparticles: Methods and Applications" in *Surface Modification of Polymers: Methods and Applications*, Eds. Pinson, J., and Thiry, D., Wiley-VCH Verlag GmbH & Co. KGaA, Weinheim, Germany, 317–446.

[21] Al-Nemrawi, N.K., Okour, A.R., and Dave, R.H., 2018, Surface modification of PLGA nanoparticles using chitosan: Effect of molecular weight, concentration, and degree of deacetylation, *Adv. Polym. Technol.*, 37 (8), 3066–3075.

[22] Guo, C., and Gemeinhart, R.A., 2008, Understanding the adsorption mechanism of chitosan onto poly(lactide-co-glycolide) particles, *Eur. J. Pharm. Biopharm.*, 70 (2), 597–604.

[23] Ab El Hady, W.E., Mohamed, E.A., Soliman, O.A.E., and El-Sabbagh, H.M., 2019, *In vitro-in vivo* evaluation of chitosan-PLGA nanoparticles for

potentiated gastric retention and anti-ulcer activity of diosmin, *Int. J. Nanomed.*, 14, 7191–7213.

[24] Cerqueira, B.B.S., Lasham, A., Shelling, A.N., and Al-Kassas, R., 2017, Development of biodegradable PLGA nanoparticles surface engineered with hyaluronic acid for targeted delivery of paclitaxel to triple negative breast cancer cells, *Mater. Sci. Eng., C*, 76, 593–600.

[25] Honary, S., and Zahir, F., 2013, Effect of zeta potential on the properties of nano-drug delivery systems - A review (Part 2), *Trop. J. Pharm. Res.*, 12 (2), 265–273.

[26] Wang, Y., Li, P., and Kong, L., 2013, Chitosan-modified PLGA nanoparticles with versatile surface for improved drug delivery, *AAPS PharmSciTech*, 14 (2), 585–592.

[27] Betancourt, T., Brown, B., and Brannon-Peppas, L., 2007, Doxorubicin-loaded PLGA nanoparticles by nanoprecipitation: Preparation, characterization and in vitro evaluation, *Nanomedicine*, 2 (2), 219–232.

[28] Babick, F., 2020, "Dynamic Light Scattering (DLS)" in *Characterization of Nanoparticles*, Elsevier Inc., Amsterdam, Netherlands, 137–172.

[29] Crucho, C.I.C., and Barros, M.T., 2017, Polymeric nanoparticles: A study on the preparation variables and characterization methods, *Mater. Sci. Eng., C*, 80, 771–784.

[30] Rizvi, S.A.A., and Saleh, A.M., 2018, Applications of nanoparticle systems in drug delivery technology, *Saudi Pharm. J.*, 26 (1), 64–70.

[31] de Lima, I.A., Khalil, N.M., Tominaga, T.T., Lechanteur, A., Sarmento, B., and Mainardes, R.M., 2018, Mucoadhesive chitosan-coated PLGA nanoparticles for oral delivery of ferulic acid, *Artif. Cells, Nanomed., Biotechnol.*, 46, 993–1002.

[32] Liu, Y., Yang, G., Jin, S., Xu, L., and Zhao, C.X., 2020, Development of high-drug-loading nanoparticles, *Chempluschem*, 85 (9), 2143–2157.

Supplementary Data

This supplementary data is a part of a paper entitled "Synthesis, DFT Calculations, DNA Interaction, and Antimicrobial Studies of Some Mixed Ligand Complexes of Oxalic Acid and Schiff Base Trimethoprim with Various Metal Ions".
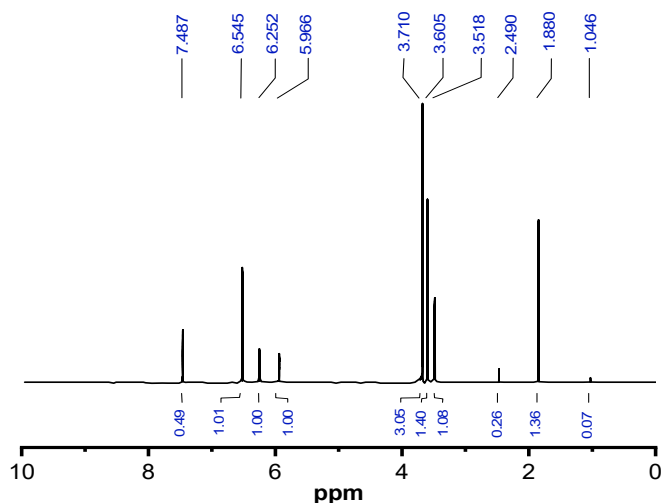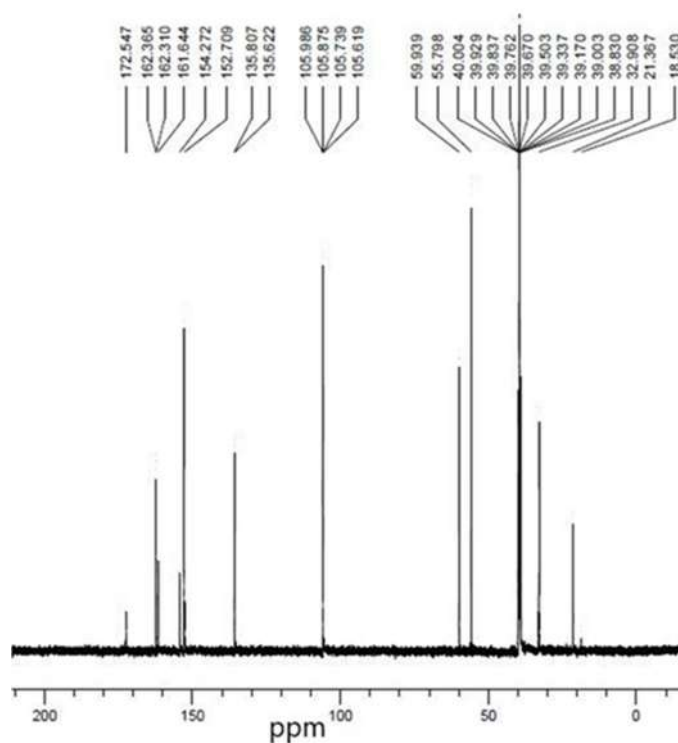

Fig S1. ^{1}H-NMR spectrum of (**L₁**) in DMSO-d_6

Fig S2. ^{13}C-NMR spectrum of **L₁** in DMSO-d_6

Synthesis, DFT Calculations, DNA Interaction, and Antimicrobial Studies of Some Mixed Ligand Complexes of Oxalic Acid and Schiff Base Trimethoprim with Various Metal Ions

Eid Abdalrazaq[1*], Abdel Aziz Qasem Jbarah[1], Taghreed Hashim Al-Noor[2], Gassan Thabit Shinain[2], and Mohammed Mahdi Jawad[3]

[1]*Department of Chemistry, College of Science, Al-Hussein Bin Talal University, Ma'an 71111, Jordan*

[2]*Department of Chemistry, Education for Pure Science College - Ibn- Al Haitham, University of Baghdad, Baghdad 10071, Iraq*

[3]*Department of Biology, Education College - Ibn- Al Haitham, University of Baghdad, Baghdad 10071, Iraq*

Abstract: *Mixed ligand metal complexes are synthesized from oxalic acid with Schiff base, and the Schiff base was obtained from trimethoprim and acetylacetone. The synthesized complexes were of the type [$M(L_1)(L_2)$], where the metal, M, is Ni(II), Cu(II), Cr(III), and Zn(II), L_1 corresponds to the trimethoprim ((Z)-4-((4-amino-5-(3,4,5-trimethoxybenzyl)pyrimidine-2-yl)imino)pentane-2-one) as the first ligand and L_2 represent the oxalate anion ($C_2O_2^{2-}$) as a second ligand. Characterization of the prepared compounds was performed by elemental analysis, molar conductivity, magnetic measurements, ^{1}H-NMR, ^{13}C-NMR, FT-IR, and Ultraviolet-visible (UV-Vis) spectral studies. The recorded infrared data is reinforced with density functional theory (DFT) calculations. Also, the recorded and calculated IR spectra of the complexes suggested that the coordination of Schiff base is a bidentate ligand with Cu and Ni complexes and a tridentate ligand with Co, Cr, and Zn complexes. The electronic structures of the complexes were investigated by DFT calculations, showing several degrees of HOMO-LUMO energy gaps between complexes. The complexes were studied for their DNA interaction activities. The synthesized ligand and its metal complexes were evaluated for antimicrobial properties against bacterial strains of* Bacillus subtilis *(G+),* Enterobacter cloacae *(G-), and* Staphylococcus aureus *(G+). These complexes considered in this study showed good antimicrobial activity.*

Keywords: *trimethoprim; oxalic acid complexes; acetyl acetone; Schiff base; antimicrobial activity*

■ INTRODUCTION

Schiff base compounds showed a unique role as ligands with transition metals and main groups in bioinorganic and coordination chemistry [1-2]. The interaction of Schiff bases with metal ions gives complexes of different geometries used as anticancer, antibacterial, antiviral, design medicinal compounds, antitumor organometallic chemistry, catalytic applications, chemical analysis, geology, and corrosion inhibition [3-4]. The complexes with mixed ligands of a Schiff base 4-dihydroxybenzylidenethiosemicarbazide (H₂L)-, Oxalic

Acid and with, M(II) = Cu, Zn, Ni and Fe(III) ions [5]. The H₂L is coordinated to the metal atom as a neutral, monoanionic, or dianionic tetradentate type (ONNO) ligand in its complexes. Chen [6] has reported the synthesis and structural characterization of a trans-(PyH)₂[Mo₂O₄(C₂O₄)₂(Py)₂] in an aqueous solution. The pyridine ligand coordinates to the Mo atom through the N atom. The oxalate ligand coordinates to each Mo atom through 2-Carboxylate Oxygen atoms in a bidentate chelating manner. Based on these observations, the present study was undertaken to synthesize and

characterize mixed ligand complexes of oxalate anion and Schiff base derived from trimethoprim and acetylacetone with one of the metal ions Cr(III), Co(II), Ni(II), Cu(II) and Zn(II). DFT calculations for molecular electrostatic potential, geometry optimization and vibrational frequencies of the synthesized molecules using the B3LYP level of theory and LANL2DZ basis set were reported.

■ **EXPERIMENTAL SECTION**

Materials

All the chemicals and solvents, trimethoprim, ethanol, acetylacetone, acetic acid, dimethyl sulfoxide, chloroform, methanol, and acetone metal chloride salts, were purchased of A.R. Grade quality obtained from Aldrich, Merck, and BDH and were used without further purification.

Instrumentation

Melting points were determined by MPA160 – Digi Melt melting point instrument. The Eager300 obtained the Elemental analysis of ligand for EA1112 Thermal Finnegan C.H.N.S 2400 instrument. The atomic absorption spectrophotometer analysis of the complexes was measured using a fair agreement method using the device from type Shimadzu (A.A 620) atomic absorption spectrophotometer. The molar conductivity values of the complexes with a concentration of 10^{-3} mol/L in dimethyl

sulfoxide (DMSO) were reached by the digital conductivity series Ino.Lab.720 device. The Magnetic susceptibility measurements of the complexes were measured using Johnson Mattey Balance. Ultraviolet-visible spectra were recorded on double-beam UV-Visible spectrophotometry of the type U.V 160A (Shimadzu) at 200 and 1100 nm with a 1 cm quartz cell, using DMSO as a solvent and a concentration of 10^{-3} mol/L. The Fourier-transform infrared spectra were measured using KBr pellets on the Shimadzu FTIR 8400S spectrophotometry instrument. The spectra FTIR are recorded in the range of 400 to 4000 cm^{-1}. The ^{1}H and ^{13}C-NMR spectra were obtained from the DMSO-d_6 solution using an Inova 500 MHz instrument.

Procedure

Synthesis of Schiff base ligand

The Schiff base ligand (**L₁**) was prepared by condensation of 1.176 g (4 mmol) of trimethoprim in 20 mL ethanol and 0.4 g (4 mmol) acetylacetone for 8 h with the addition of 4 to 5 drops of acetic acid (Scheme 1). The volume of the mixture was reduced by slow evaporation at room temperature and leave it to stand overnight. Then, the obtained off-white precipitate was washed several times with absolute ethanol, dried at room temperature, and recrystallized from ethanol to get a pure sample.
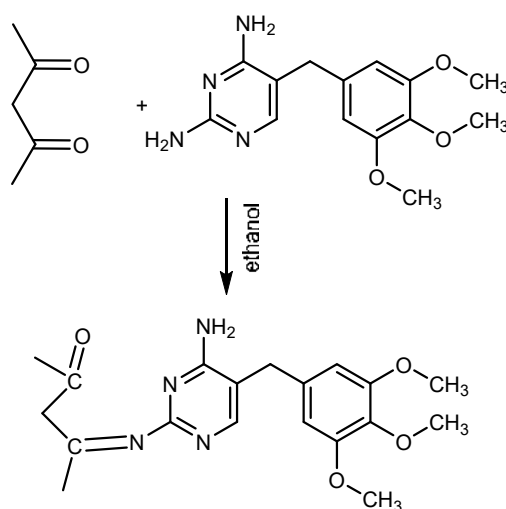
(*Z*)-4-((4-amino-5-(3,4,5-trimethoxybenzyl)pyrimidin-2-yl)imino)pentan-2-one
Scheme 1. The synthesis route of Schiff base ligand, **L₁**

$C_{19}H_{24}N_4O_4$ (**L₁**): %Yield: 86%. Anal. calc. for $C_{19}H_{24}N_4O_4$ (372.43 g/mol): C, 61.27; H, 6.50; N, 15.05. Found C, 62.06; H, 5.56; N, 13.99. Mp: 185 °C. IR (KBr, cm⁻¹): ν(C=O) 1682, ν(−C=N−) 1658. ¹H-NMR (DMSO-d_6): δ 1.880 (-N=C-C**H**₃), 2.490 ((CO)-C**H**₃), 3.518–3.605 (C**H**₂), 3.710 (O-C**H**₃), 5.966 (pyrimidine ring), 6.545–6.252 (N**H**₂), 7.487 (Ar). ¹³C-NMR (500 MHz, DMSO-d_6): δ 18.5 (-N=C-**C**H₃), 21.3 (-(CO)-**C**H₃). 55.8 (O-**C**H₃), 59.9 (**C**H₂), 105.6–135.8 (Ar), 152.7–161.6 (pyrimidine ring), 162.3 (-**C**=N), 172.5 (**C**=O).

Synthesis of the complexes of the type [M(L₁)(L₂)]

The complexes were prepared in a molar ratio of 1:1:1 (**M:L₁:L₂**). The metal chloride salts (MCl₂·nH₂O. n = 0–6, and CrCl₃·6H₂O) reacted with the two ligands according to Scheme 2 and the following proposed general equation:

$H_2C_2O_4$ +2KOH → $K_2C_2O_4$ + 2H₂O

MCl₂·nH₂O + L₁ + K₂L₂ → [M(L₁)(L₂)] + 2KCl + nH₂O
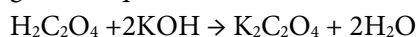
where **L₁** = Schiff base (the first ligand), **L₂** = $C_2O_4^{2-}$ (Oxalate anion as a second ligand) and **M** = the corresponding metal.

Dissolving 0.23793, 0.23769, 0.17048, 0.17228 and 0.26635 g (1 mmol) of CoCl₂·6H₂O, NiCl₂·6H₂O, CuCl₂·2H₂O, ZnCl₂, and CrCl₃·6H₂O, respectively, in 10 mL of ethanol. A 0.372 g (1 mmol) of **L₁** in 10 mL of ethanol and the solution of potassium oxalate were added at the same time to the metal chloride solution. The mixture was stirred for 4 h at room temperature and left for 24 h. The precipitate was filtered and washed with ethanol before recrystallizing and drying at room temperature. The percentage yield range is 79 to 85%.

CoC₂₁H₂₄N₄O₈ (**1**): %Yield: 83%. Anal. calc. for CoC₂₁H₂₄N₄O₈ (519.38 g/mol): C, 48.56; H, 4.66; N, 10.79. Found C, 49.02; H, 4.44; N, 11.13. Mp: 223–255 °C. IR (KBr, cm⁻¹): ν(C=O) 1670 (carbonyl of **L₁**), ν(−C=N−) 1645, ν(C-O) 1238 (oxalate), ν(Co-N) 524, ν(Co-O) 480 (oxygen of **L₂**), ν(Co-O) 459 (oxygen of **L₁**).

CrC₂₁H₂₄N₄O₈ (**2**): %Yield: 82%. Anal. calc. for CrC₂₁H₂₄N₄O₈ (512.44 g/mol): C, 49.22; H, 4.72; N, 10.93. Found C, 48.78; H, 4.36; N, 10.61. Mp: 285 °C. IR (KBr, cm⁻¹): ν(C=O) 1671 (carbonyl of **L₁**), ν(−C=N−) 1643, ν(C-O) 1235 (oxalate), ν(Cr-N) 526, ν(Cr-O) 475 (oxygen of **L₂**), ν(Cr-O) 448 (oxygen of **L₁**).

ZnC₂₁H₂₄N₄O₈ (**3**): %Yield: 79%. Anal. calc. for ZnC₂₁H₂₄N₄O₈ (525.82 g/mol): C, 47.97; H, 4.60; N, 10.66. Found C, 48.11; H, 4.98; N, 10.85. Mp: 216–220 °C. IR (KBr, cm⁻¹): ν(C=O) 1674 (carbonyl of **L₁**), ν(−C=N−) 1643, ν(C-O) 1242 (oxalate), ν(Zn-N) 542, ν(Zn-O) 484 (oxygen of **L₂**), ν(Zn-O) 438 (oxygen of **L₁**).

CuC₂₁H₂₄N₄O₈ (**4**): %Yield: 83%. Anal. calc. for CuC₂₁H₂₄N₄O₈ (523.99 g/mol): C, 48.14; H, 4.62; N, 10.69. Found C, 49.03; H, 4.86; N, 10.93. Mp: 253–255 °C. IR (KBr, cm⁻¹): ν(C=O) 1681 (carbonyl of **L₁**), ν(−C=N−) 1642, ν(C-O) 1240 (oxalate), ν(Cu-N) 513, ν(Cu-O) 479 (oxygen of **L₂**).

NiC₂₁H₂₄N₄O₈ (**5**): %Yield: 85%. Anal. calc. for NiC₂₁H₂₄N₄O₈ (519.14 g/mol): C, 48.59; H, 4.66; N, 10.79. Found C, 47.82; H, 4.92; N, 10.41. IR (KBr, cm⁻¹): ν(C=O) 1680 (carbonyl of **L₁**), ν(−C=N−) 1643, ν(C-O) 1245 (oxalate), ν(Ni-N) 532, ν(Ni-O) 472 (oxygen of **L₂**).

DNA binding properties

DNA was extracted from human blood samples without any health problems in the city of Baghdad/Iraq
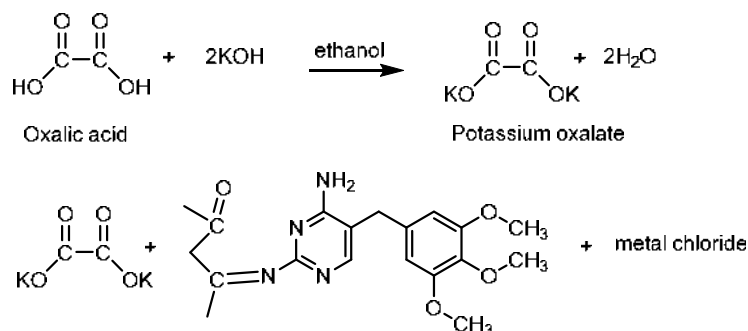
Scheme 2. The synthesis route of the complexes contains Schiff base ligand and metal ion

using unique extraction from Promiga USA. The steps mentioned in the protocol were followed. The DNA concentration and the purity of the extracted DNA were obtained using the spectrophotometer of 1.6 to 1.8 ng/mL. The purity and concentration were measured using the subject standards. The samples were initially extracted on the 1% agarose gel to confirm their quality and to see if there was any breakage during extraction. The studied materials were then mixed with the extracted DNA by 2:1 v/v and put in a water bath for one hour at 37 °C and then transported in 1.5% agarose gel for 1 h and 75 V, then treated with Red safe fluorescent dye and under the UV source using the gel documentation system.

Computational details

All the DFT calculations were performed with the Gaussian09 program [7]. The geometries of the complexes were fully optimized at B3LYP (Becke's, three-parameter exchange functional, in combination with Lee-Yang-Parr correlation function) [8-10] with the 6-311G* basis set for C, H, O and N atoms and LANL2DZ (Los Alamos National Laboratory 2 double-zeta) [11-13] basis set for metal atom. LANL2DZ is an effective core potential (ECP) type and has been widely used for studies of transition metals (TM) containing systems. The computational cost is decreased with the chemically inactive core electrons represented by an ECP since the cost formally increases as ~N4, where N is the number of explicitly treated electrons. The program GaussView 6 [14] was used to inspect the input and output files generated by Gaussian09 for pre-processing, structure modification, and post-processing analyses of structures, frequencies, and forces. A frequency analysis was performed for each stationary point to identify the minima's most stable structure. All minima have no imaginary frequencies in the vibrational mode calculations. The molecular electrostatic potential, V(r), at a given point r(x,y,z) in the vicinity of a molecule, to determine the reactive sites of the complexes, was calculated at the B3LYP functional with the 6-311G* basis set for C, H, O and N atoms and LANL2DZ basis set for the metal atom of the optimized geometry. The definition, description, and calculation of V(r) were reported in

many reports [15]. The B3LYP level of theory with the 6-311G* basis set for C, H, O, and N atoms and the LANL2DZ basis set for metal atoms is used to calculate the energies and electron densities of the frontiers molecular orbitals. The PDOS (Projected density of states) has been obtained via the calculated orbital populations for all synthesized complexes at the same level of theory, using GAUSSSUM 3.0 program [16].

■ RESULTS AND DISCUSSION

The solubility of the compounds was tested using various solvents. The synthesized complexes are non-hygroscopic solids, varying colors and soluble in water and dimethyl sulfoxide, whereas insoluble in ethanol, chloroform, methanol, and acetone. Also, they are air-stable at room temperature. The molecular weight, melting point, and Flame-AAS analysis of the synthesized complexes were carried out by the literature methods [17]. The experimental and calculated values of a metal content percent (M%) in all complexes are in fair agreement. The chloride ions test in all complexes was done with the $AgNO_3$ solution, and a negative result was obtained [18]. The molar conductance values of the complexes in DMSO solvent indicated that $[ML_1L_2]$ complexes are non-electrolytes, while complex **2** is a 1:1 electrolyte [19-20]. These results support the proposed formula of the complexes (Fig. 1). The physical and analytical data of Schiff base ligand **L₁**, and its metal complexes are listed in Table 1.

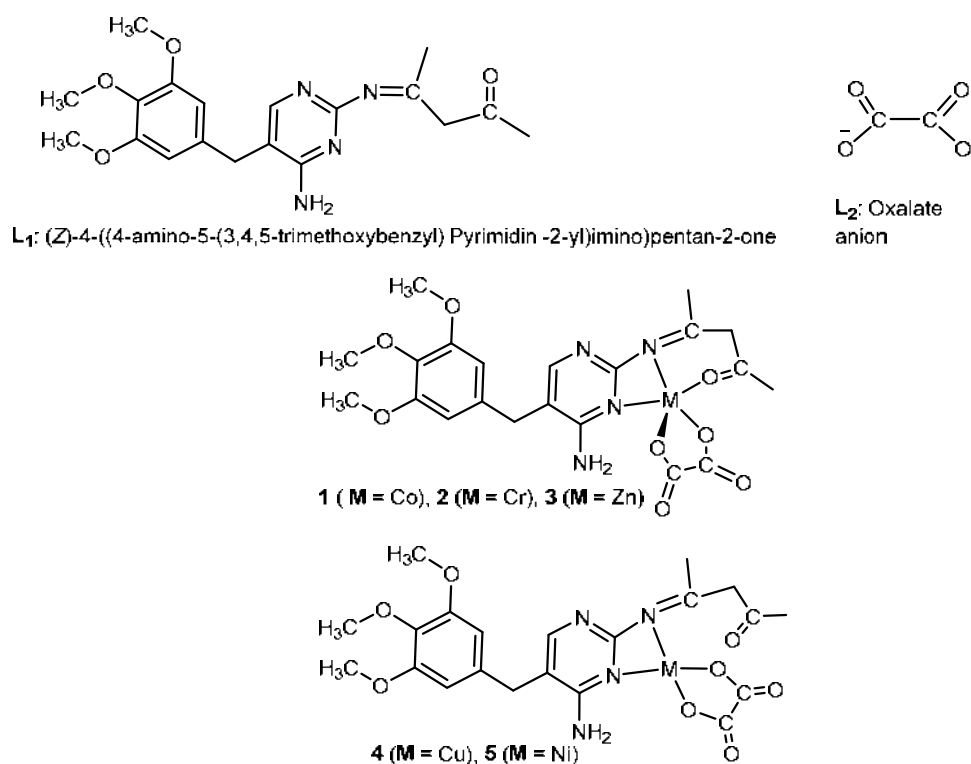### ¹H-NMR Result

The ¹H-NMR in the DMSO-d_6 solvent of the ligand (**L₁**) is shown in S1. In S1, two signals appeared at 3.605 and 3.518 ppm, which were assigned to the protons of the CH_2 groups. The previously reported values of the CH_2 group signals in the ¹H-NMR spectrum are in the range of 3.59–3.52 ppm [20]. The spectrum of the ligand, S1, also showed a peak at 3.710 ppm. This peak is attributed to the methoxy protons (O-CH_3 group). The chemical shifts of the protons of the O-CH_3 group are reported in the range of 3.65–3.8 ppm [21-23]. The chemical shift of the benzene ring protons is found at 7.487 ppm. It was reported that the chemical shift of the

Table 1. Analytical data and some physical measurements of the Schiff base ligand and the complexes

Compound	Molecular weight (g/mol)	Color	Melting point (°C)	M%	Molar conductance Λ ($\Omega^{-1}cm^2mol^{-1}$)
L_1	372.43	Yellow	185	-	-
1	519.38	Pink	223–255	11.35[a] 10.85[b]	25.88[c]
2	512.44	Dark green	285	10.15[a] 10.20[b]	37.88[c]
3	525.82	White	216–220	12.43[a] 11.93[b]	17.18[c]
4	523.99	Off white	253–255	12.13[a] 11.13[b]	16.55[c]
5	519.14	Light green	216	11.31[a] 10.20[b]	18.6[c]

[a]: theoretical value, [b]: experimental value, [c]: measured in DMSO

L_1: (Z)-4-((4-amino-5-(3,4,5-trimethoxybenzyl) Pyrimidin -2-yl)imino)pentan-2-one

L_2: Oxalate anion

1 (M = Co), 2 (M = Cr), 3 (M = Zn)

4 (M = Cu), 5 (M = Ni)

Fig 1. The suggested structure of the complexes [$M(L_1)(L_2)$]) and ligands

benzene ring protons displayed in 6.75–8.01 ppm [23-24]. The chemical shift of the proton of the pyrimidine ring is observed at 5.966 ppm. The protons of the amine group (NH_2) showed two peaks at 6.545 and 6.252 ppm. The reported values for the pyrimidine ring proton and the protons of the amine group are 5.8 and 6.9, respectively [25]. The chemical shifts of the methyl protons of the (-N=C-C$\underline{H}_3$) and ((CO)-C$\underline{H}_3$) groups were observed at 1.880 and 2.490 ppm, respectively [26].

^{13}C-NMR Results

The ^{13}C-NMR spectrum of the ligand L_1 in DMSO-d_6 solvent is shown in S2. The spectrum of the ligand, S2, exhibits a chemical shift at 18.53 ppm, which is assigned

to the carbon atom of the methyl group, which is attached to the azomethine group (-N=C-**C**H₃). It was reported that the chemical shifts of the carbon atom in the methyl group of C-**C**H₃ in the range 19.09–19.87 [22]. The chemical shift at 21.3 ppm is attributed to the carbon atom of the methyl group, which is attached to the carbonyl group (-(CO)-**C**H₃). It was reported that the carbon atom of the methyl group displayed chemical shifts at 21.06 and 21.4 ppm [27]. The signals appeared in the range 40.0–32.9 ppm concerning the DMSO solvent. The chemical shift at 55.8 ppm is assigned to the carbon atom of the O-**C**H₃ group. This assignment is based on the previously reported chemical shifts of the carbon atom of this group [21-22]. The chemical shift at 59.9 ppm is due to the carbon atom of the **C**H₂ group. The reported values of the carbon atom of the CH₂ group of the mono- and diphenyl tin(IV) complexes were 59.9–60.46 ppm [28]. The chemical shift of the carbon atoms of the aromatic ring appeared in the range of 105.6–135.8 ppm [26]. The carbons of the pyrimidine ring showed three signals at 152.7, 154.3, and 161.6 ppm [26]. The peak that appeared at 162.3 ppm can be assigned to the carbon atom of the azomethine group (-**C**=N). In a previous work reported by Saheb et al., the carbon atom of the azomethine group showed a chemical shift at 162.79 ppm [21]. The signal

appeared at 172.5 ppm concerning the carbon atom of the carbonyl group. The carbon atom of the carbonyl group showed chemical shifts in the reported value of 167.3–170.0 ppm [22].

Vibration Frequencies Results

Table 2 displays the selective vibrational frequencies of infrared spectra of the synthesized complexes and ligands. The assignments for the observed infrared bands were made primarily based on the vibration modes as calculated (theoretically) and on the literature data [27-32]. The infrared spectrum of the free ligand **L₁** exhibits a sharp band at 1658 cm⁻¹, which is assigned to $\nu(-C=N-)$. This vibrational band appears at a lower frequency, in the range 1642–1645 cm⁻¹, in the infrared spectra of all complexes. The shifting of the $\nu(-C=N-)$ to the lower frequency after complexation indicates coordination with the metal ion through the nitrogen atom of the $-C=N-$ group. The vibrational frequency of the **L₁** ligand at 1682 cm⁻¹, which is assigned to the $\nu(C=O)$ of the acetyl group, is shifted to lower frequencies in the infrared spectra of complexes **1**, **2**, and **3** and appears in the range of 1670–1674 cm⁻¹ indicating the coordination is through the oxygen atom of the acetyl group of the **L₁** ligand. In the cases of complexes **4** and **5**,

Table 2. Experimental and calculated infrared absorption (cm⁻¹) data of the free ligand and complexes

Compounds	$\nu(C=O)^b$	$\nu(-C=N-)$	$\nu(C-O)^c$	$\nu(M-N)$	$\nu(M-O)^c$	$\nu(M-O)^b$
L₁	1682	1658	-	-	-	-
	(1693)ᵃ	(1665)ᵃ				
L₂	-	-	1277	-	-	-
			(1310)ᵃ			
1	1670	1645	1238	524	480	459
	(1689)ᵃ	(1643)ᵃ	(1273)ᵃ	(565)ᵃ	(488)ᵃ	(443)ᵃ
2	1671	1643	1235	526	475	448
	(1680)ᵃ	(1651)ᵃ	(1272)ᵃ	(536)ᵃ	(470)ᵃ	(422)ᵃ
3	1674	1643	1242	542	484	438
	(1677)ᵃ	(1651)ᵃ	(1270)ᵃ	(551)ᵃ	(473)ᵃ	(401)ᵃ
4	1681	1642	1240	513	479	-
	(1694)ᵃ	(1638)ᵃ	(1265)ᵃ	(553)ᵃ	(447)ᵃ	
5	1680	1643	1245	532	472	-
	(1694)ᵃ	(1650)ᵃ	(1270)ᵃ	(533)ᵃ	(463)ᵃ	

ᵃ: Calculated value at the B3LYP level of theory with the 6-311G* basis set for C, H, O, and N atoms and LANL2DZ basis set for metal atom., ν: stretching, **M**: the corresponding metal, ᵇ: oxygen of the carbonyl of **L₁** ligand, ᶜ: Oxygen of **L₂** ligand

the ν(C=O) of the acetyl group appeared at 1681 and 1680 cm^{-1}, respectively. These peaks are similar to that of the free ligand **L₁**, indicating that the acetyl group in **L₁** does not participate in the coordination with the metal in complexes **4** and **5**. It is interesting to note that the frequency of the ν(C-O) band of the free **L₂** ligand appears at 1277 cm^{-1}, while in the infrared spectra of complexes **1**, **2**, **3**, **4**, and **5**, this band is downshifted and located at 1238, 1235, 1242, 1240, and 1245 cm^{-1}, respectively. This result suggested the coordination of the oxygen atoms of the hydroxyl group, the **L₂** ligand, with the metal ion. The downshifting of the frequency values of the ν(−C=N−), ν(C=O), and ν(C-O) bands of the complexes as compared to the free ligands are further supported by the calculated vibrational frequencies (Table 2). In the lower frequencies region of the infrared spectra of all complexes, new bands observed in the range 513–542 cm^{-1} and 472–480 cm^{-1} were ascribed to the ν(M-N) and ν(M−O) vibrations, respectively. Also, in the infrared spectra of complexes **1**, **2**, and **3**, another new band was observed at 459, 448, and 438 cm^{-1}, respectively, and assigned to the ν(M-O). Accordingly, the primary ligand **L₁** binds to the metal ion in a tridentate fashion through two nitrogen atoms and

one oxygen atom in complexes **1**, **2**, and **3** and as a bidentate ligand fashion through two nitrogen atoms in the case of complexes **4** and **5** (Fig. 1). In the case of the **L₂** ligand, it binds the metal ion as bidentate donors via an oxygen atom in all complexes.

Geometry Optimization

The optimized geometry around the central metal ion in complex **1** is trigonal bipyramid, where **2** and **3** adopted a distorted square pyramid configuration. These results are based on the observation obtained from the calculated geometries according to the B3LYP level of the theory of these complexes (Fig. 2, Table 3). The distorted square pyramid of the optimized geometry around the metal ion in these complexes is due to the tension in N6-M-N8 and N8-M-O46 angles. Accordingly, we can deduce that the Schiff base ligand (**L₁**) binds to the metal ion as tridentate fashion (NNO) donors, Fig. 2, and as bidentate ligand fashion (NN) donors, Fig. 3, while the (oxalate anion) binds to the metal ion as bidentate donors through oxygen atoms. The optimized geometries for complexes **4** and **5** (Fig. 3, Table 4) showed a slight N6-M-N8 angle and indicated a distorted square planar geometry.

Table 3. Selected bond angles (°) and bond distances (Å) of the optimized structures of **1**, **2**, and **3** at the B3LYP level of theory with the 6-311G* basis set for C, H, O, and N atoms and LANL2DZ basis set for metal atom

| Bond lengths (Å) of complex **1**		Bond lengths (Å) of complex **2**		Bond lengths (Å) of complex **3**	
Co(52)-O(46)	1.927	Cr(58)-O(46)	1.968	O(46)-Zn(58)	2.196
Co(52)-N(8)	1.926	Cr(58)-O(52)	1.921	N(6)-Zn(58)	2.125
Co(52)-N(6)	1.910	Cr(58)-O(53)	1.940	N(8)-Zn(58)	2.275
O(54)-Co(52)	1.849	N(6)-Cr(58)	2.071	Zn(58)-O(52)	1.949
O(53)-Co(52)	1.836	N(8)-Cr(58)	2.067	Zn(58)-O(53)	2.005
Angles (°) of complex **1**		Angles (°) of complex **2**		Angles (°) of complex **3**	
N(6)-Co(52)-N(8)	69.3	O(52)-Cr(58)-O(46)	101.9	O(52)-Zn(58)-N(6)	138.9
N(6)-Co(52)-O(46)	159.8	O(52)-Cr(58)-N(6)	131.3	O(52)-Zn(58)-O(46)	94.8
N(6)-Co(52)-O(54)	99.4	O(52)-Cr(58)-N(8)	98.9	O(52)-Zn(58)-N(8)	114.6
N(6)-Co(52)-O(53)	99.7	O(52)-Cr(58)-O(53)	83.6	O(52)-Zn(58)-O(53)	85.8
N(8)-Co(52)-O(46)	93.0	O(46)-Cr(58)-N(6)	116.8	N(6)-Zn(58)-O(46)	120.2
N(8)-Co(52)-O(54)	168.7	O(46)-Cr(58)-N(8)	79.1	N(6)-Zn(58)-N(8)	60.3
N(8)-Co(52)-O(53)	93.6	O(46)-Cr(58)-O(53)	132.6	N(6)-Zn(58)-O(53)	89.3
O(46)-Co(52)-O(54)	98.2	N(6)-Cr(58)-N(8)	63.5	O(46)-Zn(58)-N(8)	76.4
O(46)-Co(52)-O(53)	90.8	N(6)-Cr(58)-O(53)	90.2	O(46)-Zn(58)-O(53)	126.5
O(54)-Co(52)-O(53)	87.9	N(8)-Cr(58)-O(53)	147.2	N(8)-Zn(58)-O(53)	149.5
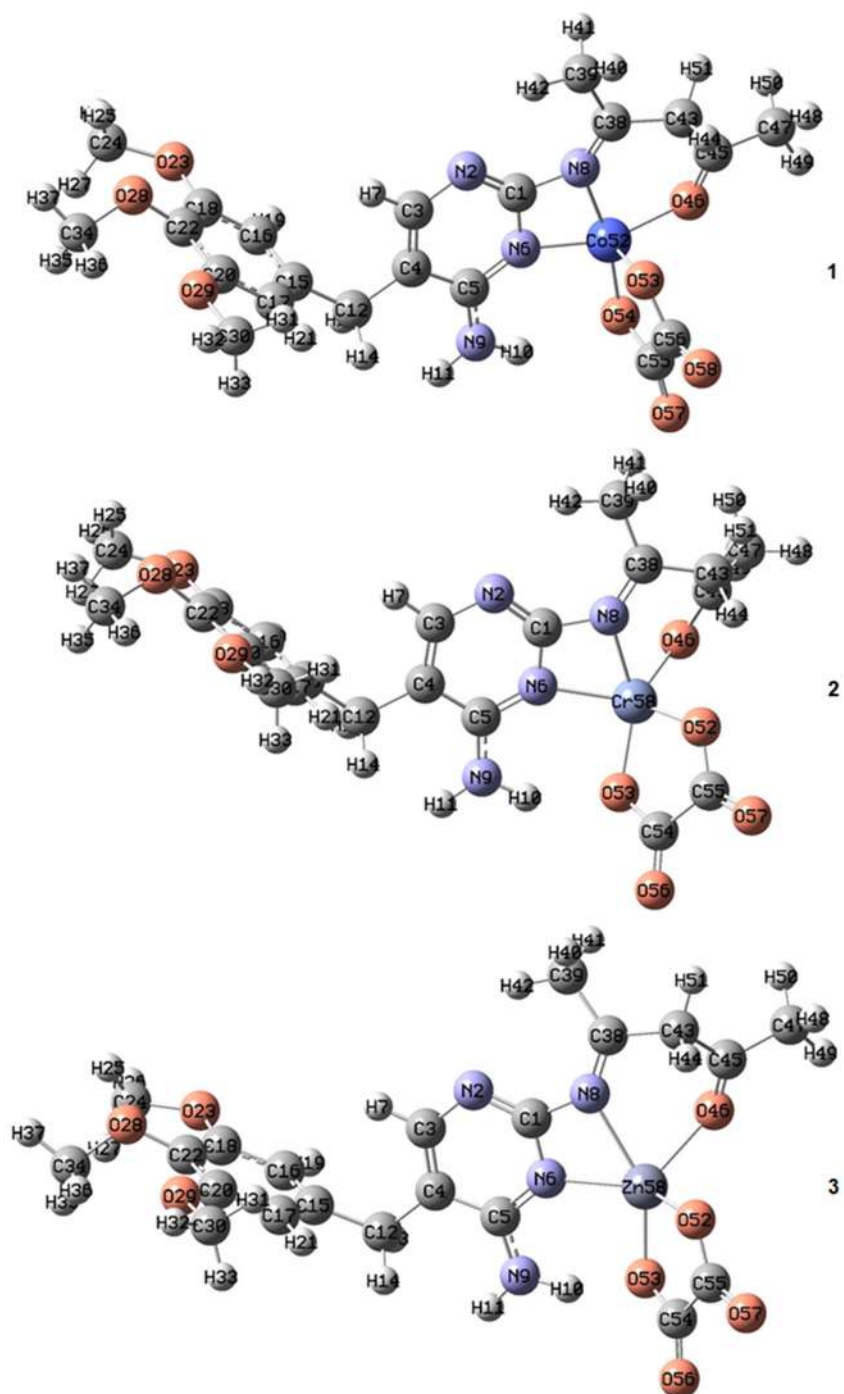
Fig 2. The optimized structures of **1**, **2,** and **3** complexes at the B3LYP level of theory with the 6-311G* basis set for C, H, O, and N atoms and LANL2DZ basis set for metal atom

The μ_{eff} value for complex **1** is 4.86, complex **2** is 3.52, and complex **4** is 1.98 BM, respectively, while the μ_{eff} values for complex **3** and **5** are approximately zero (diamagnetic).

The electronic spectral studies of compounds were carried out in DMSO (10^{-3} M) solution [33-36]. Oxalic acid in the DMSO solvent showed two high intensive bands at 262 nm (38167 cm^{-1}) attributed to $\pi \rightarrow \pi^*$ and at 310 nm (28490 cm^{-1}) attributed to $n \rightarrow \pi^*$, respectively. The spectrum of the free ligand (**L$_1$**) showed a strong band
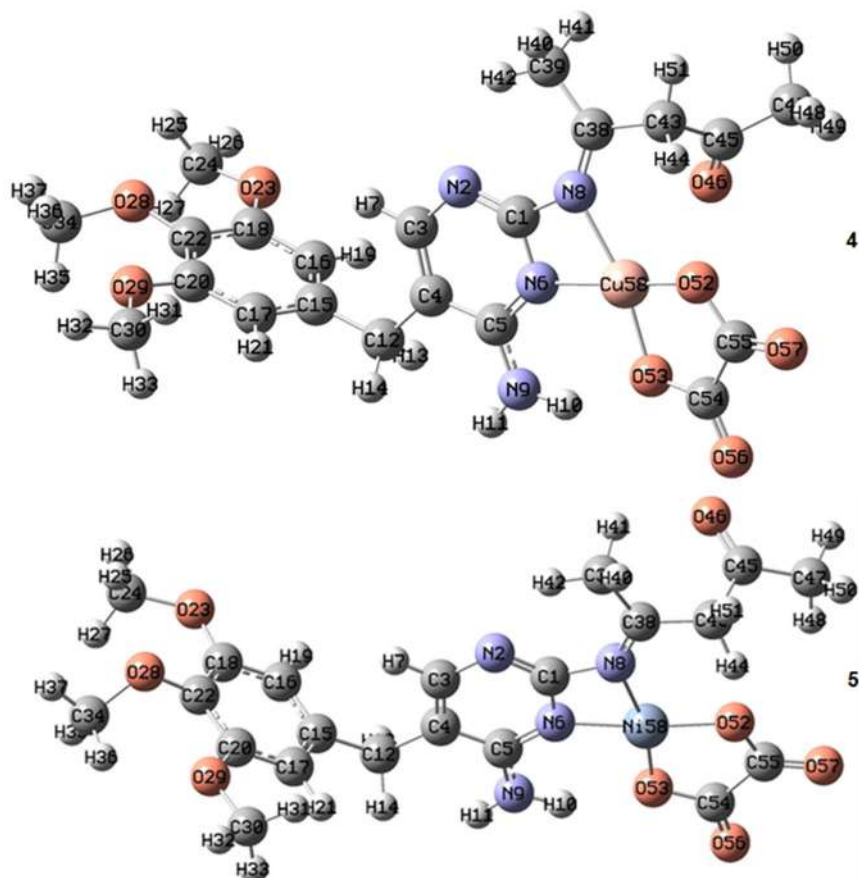
Fig 3. The optimized structures of **4** and **5** complexes at the B3LYP level of theory with the 6-311G* basis set for C, H, O, and N atoms and LANL2DZ basis set for metal atom

Table 4. Selected bond angles and bond distances (Å) of the optimized structure of **4** and **5** at the B3LYP level of theory with the 6-311G* basis set for C, H, O, and N atoms and LANL2DZ basis set for metal atom

Bond lengths (Å) of complex **4**		Bond lengths (Å) of complex **5**	
Cu(58)-O(52)	1.877	Ni(58)-O(52)	1.844
Cu(58)-N(8)	2.026	Ni(58)-N(8)	1.987
Cu(58)-O(53)	1.876	Ni(58)-O(53)	1.846
Cu(58)-N(6)	1.949	Ni(58)-N(6)	1.886
Angles (°) of complex **4**		Angles (°) of complex **5**	
N(6)-Cu(58)-N(8)	67.0	N(6)-Ni(58)-N(8)	68.5
N(6)-Cu(58)-O(52)	168.3	N(6)-Ni(58)-O(52)	173.8
N(6)-Cu(58)-O(53)	98.6	N(6)-Ni(58)-O(53)	97.7
N(8)-Cu(58)-O(52)	107.6	N(8)-Ni(58)-O(52)	105.4
N(8)-Cu(58)-O(53)	165.6	N(8)-Ni(58)-O(53)	166.2
O(52)-Cu(58)-O(53)	86.3	O(52)-Ni(58)-O(53)	88.3

at 281 nm (35587 cm^{-1}), which may be ascribed to $\pi \to \pi^*$ electronic transition within the organic ligand.

Complex **1** is considered distorted trigonal bipyramidal, and the electronic spectrum might be assigned in the "regular" geometry. In a trigonal-bipyramidal ligand field, the ground term is split into the states $^4A_2'$, $^4A_1''$, $^4A_2''$, $^4E'$, and $^4E'$; the ^4P term is split into $^4A_2'$ and $^4E''$. The electronic spectrum of complex **1** (d^7,

Term symbol of ^4F) exhibits four bands, the first band at 279 nm (35842 cm^{-1}) assigned to the charge transfer transition. The other three bands are due to d-d transitions at 526 nm (19011 cm^{-1}), 672 nm (14880 cm^{-1}), and 826 nm (12106 cm^{-1}), which are assigned to $^4A_2'(F) \to ^4A1''(F)$, $^4A_2'(F) \to ^4A_2''(F)$, $^4A_2'(F) \to ^4E''(F)$ transitions, respectively [36-40].

The electronic spectral data of the chromium complex (complex **2**) reveal four bands at 604 nm (16556 cm^{-1}), 509 nm (19646 cm^{-1}), 425 nm (23529 cm^{-1}), and 277 nm (36101 cm^{-1}), (Table 3 and 4) [29-30]. The intense high band appearing at 277 nm is assigned to the $\pi \to \pi^\star$ transition of the benzene ring. Furthermore, the band at 425 nm is assigned to the $n \to \pi^\star$ transitions of the azomethine group. The electronic spectrum of the Cr(III) complex showed two bands at 509 and 604 nm. The spectral band is consistent with that of five coordinated Cr(III) complexes (Cr(III), d^3, Term symbol of ^4F), so a "regular" square-pyramidal geometry may be assigned for this complex [34-35,41]. However, distorted geometry is observed in this instance. The zinc(II) complex (complex **3**) displays multiple intense absorption bands in the UV region at 281 nm (35587 cm^{-1}) that we assume result from metal-ligand charge-transfer and ligand internal transitions, which is compatible with this complex having distorted square pyramid structures [35-36].

The electronic spectrum of complex **4** displays a broad single d-d band that appeared at 859 nm (11641 cm^{-1}) which implies the three allowed spin transitions, $^2B_{1g} \to ^2A_{1g}(\nu_1)$, $^2B_1 \to ^2B_{2g}(\nu_2)$ and $^2B_1 \to ^2E_g$, may be due to square planar (slightly distorted) geometry around the copper(II) ion and 281 nm (35587 cm^{-1}) which assigned to ligand to metal charge transfer (LMCT) [37].

The (UV-Vis) spectrum of complex **5** exhibits four bands; the first band at 279 nm (35842 cm^{-1}) is assigned to the $\pi \to \pi^*$ transition of the aromatic ring. The second band appeared at 419 nm (23866 cm^{-1}), which is attributed to the charge transfer from ligand, azomethine, to metal. From the electronic spectrum, the observed peak at (628 nm) 15923 cm^{-1} is assigned to the $^1A_1 \to ^1B_1$ band and 778 nm (12853 cm^{-1}), which is attributed to the $^1A_1 \to ^1A_2$ band. These transitions suggest the square planar geometry around Ni(II). The 10 Dq = 2853 cm^{-1}, and

ν_1/ν_2 = 80 (or ν_2/ν_1 = 1.23 are in the usual range reported for a distorted square planar of the Ni(II) complexes [38].

Electronic Structures

The calculated electron densities and energies of the frontiers' molecular orbitals (HOMO and LUMO) were investigated to explain the electronic properties of the prepared complexes. Fig. 4 and 5 summarize the calculated absolute energies of the HOMO and LUMO orbitals together with the HOMO-LUMO energy gap values. Complex **5** has a more significant HOMO-LUMO energy gap. The calculated orbital energy levels and percent composition of particular chosen frontier inhabited and virtual molecular orbitals of the prepared compounds, expressed in terms of composing fragments (L_1, L_2, and metal ion), are listed in Table 5. As shown in Table 5, the HOMO of complex **1** is wholly localized on the L_1 ligand, and its LUMO complex is mainly localized on the metal ion. The HOMO and LUMO of complex **2** are mainly localized on the metal ion, as shown in Fig. 4 and presented in Table 5. The percent composition of frontier occupied and virtual molecular orbitals of complex **3** differ from those of complexes **1** and **2**, as shown in Table 5. The ligands L_1 and L_2 of complex **3** contribute 100% of LUMO and 99% of HOMO, respectively. The LUMO orbital of complex **4** is distributed over metal ions, L_1 and L_2, with almost equal percent, while its HOMO orbital is almost localized on the metal ion (Fig. 5, Table 5). The percent composition of HOMO and LUMO molecular orbitals of complex **5** are very similar to those of complex **3** (Fig. 5, Table 5).

Molecular Electrostatic Potential

The generated molecular electrostatic potential in the space around a molecule, including the charge distribution, is very helpful in understanding the sites for electrophilic attacks and nucleophilic reactions. Also, exploring the charge distribution around the molecule is essential for studying biological recognition processes and hydrogen bonding interactions [42-45]. Hence, the molecular electrostatic potentials for complexes **2** and **5** were calculated from the optimized geometry (Fig. 6). The
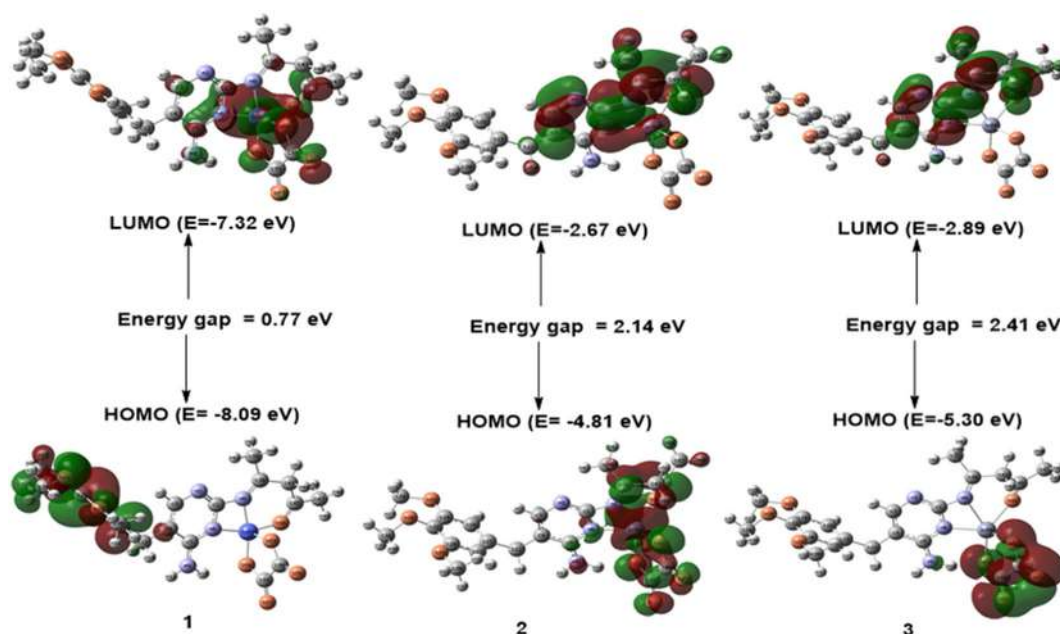
Fig 4. The frontier orbitals, HOMO, and LUMO of the complexes **1**, **2**, and **3** were calculated at the B3LYP level of theory with the 6-311G* basis set for C, H, O, and N atoms and LANL2DZ basis set for metal atom, with the surface isovalue of 0.02
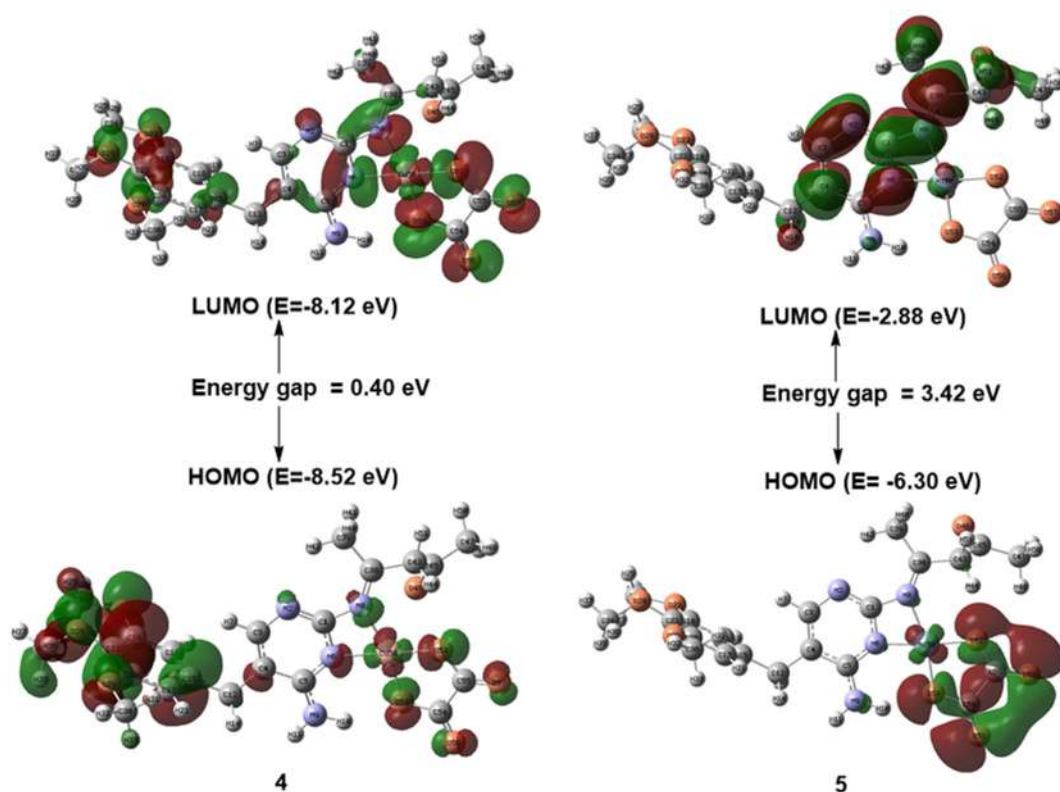

Fig 5. The frontier orbitals, HOMO, and LUMO of complexes **4** and **5** were calculated at the B3LYP level of theory with the 6-311G* basis set for C, H, O, and N atoms and LANL2DZ basis set for metal atoms, with the surface isovalue is 0.02

Table 5. Energies and percent composition of HOMO and LUMO molecular orbitals of complexes, expressed in terms of composing fragments, calculated at the B3LYP level of theory with the 6-311G* basis set for C, H, O, and N atoms and LANL2DZ basis set for metal atom

Compound	Molecular orbital	Orbital energy (eV)	Fragment		
			Metal	L_1 ligand	L_2 ligand
1	LUMO	-7.32	62	12	26
	HOMO	-8.09	0	100	0
2	LUMO	-2.67	63	17	20
	HOMO	-4.81	83	8	9
3	LUMO	-2.89	0	100	0
	HOMO	-5.30	0	1	99
4	LUMO	-8.12	30	31	39
	HOMO	-8.52	5	88	7
5	LUMO	-2.88	1	99	0
	HOMO	-6.30	3	1	96

electrophilic reactive sites of the molecule are concerned with the negative (red) regions of molecular electrostatic potential (Fig. 6). The nucleophilic reactive sites are regarded by the positive (blue) regions of molecular electrostatic potential. For complex **2**, the negative electrostatic potential regions are mainly localized over the O57, O56, O23, O28, and N2 atoms (Fig. 6). The V(r) values are -0.092, -0.085, -0.032, -0.037 and -0.022 a.u. for O57, O56, O23, O28 and N2 atoms of complex **2**, respectively. According to these results, complex **2** has five possible sites for the electrophilic attack. The most positive electrostatic potential is localized on the C47−H50 (V(r) = 0.045 a.u.) region of complex **2**. Therefore, the C47−H50 region represents the most reactive site toward nucleophilic attack within complex **2**. For complexes **1** and **3**, the most positive and negative electrostatic potentials are similar to those observed for complex **2**. For the complex **5**, the negative electrostatic potential regions are mainly localized over the O57 (V(r) = -0.080 a.u.), O56 (V(r) = -0.079 a.u.), O46 (V(r) = -0.028 a.u.), and O29 (V(r) = -0.036 a.u.) atoms (Fig. 6). Accordingly, the O57, O56, O46, and O29 atoms represent the possible sites for the electrophilic attack of the complex **5**. The most positive electrostatic potential region is localized on the N9−H11 (V(r) = 0.049 a.u.) of the complex **5**. Therefore, the region N9−H11, in complex **5**, is an electrophilic site and represents the most reactive site toward nucleophilic attack. For complex **4** the most
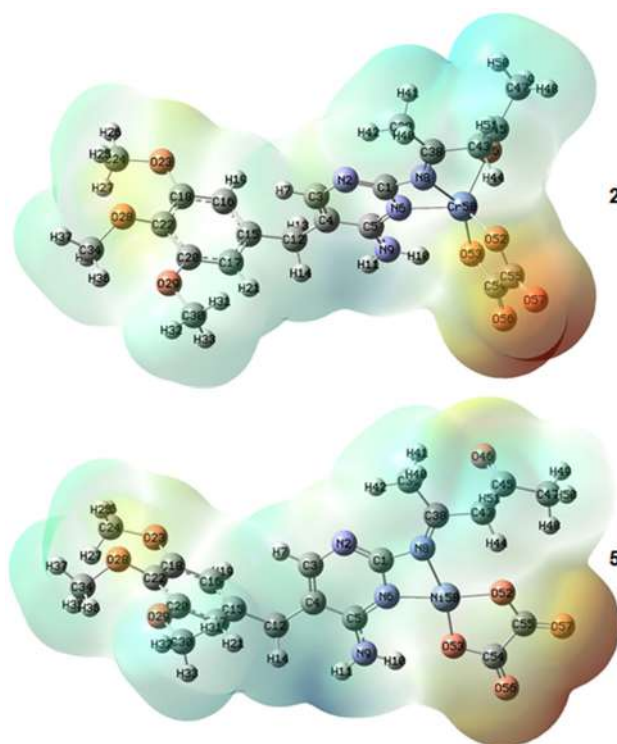
Fig 6. The Molecular electrostatic potential map of complexes **2** and **5**

positive and negative electrostatic potentials are similar to those observed for complex **5**.

Antibacterial Activities

The comparative study of the biological effects of the ligands and their complexes is listed in Fig. 7. The synthesized complexes have been tested against the
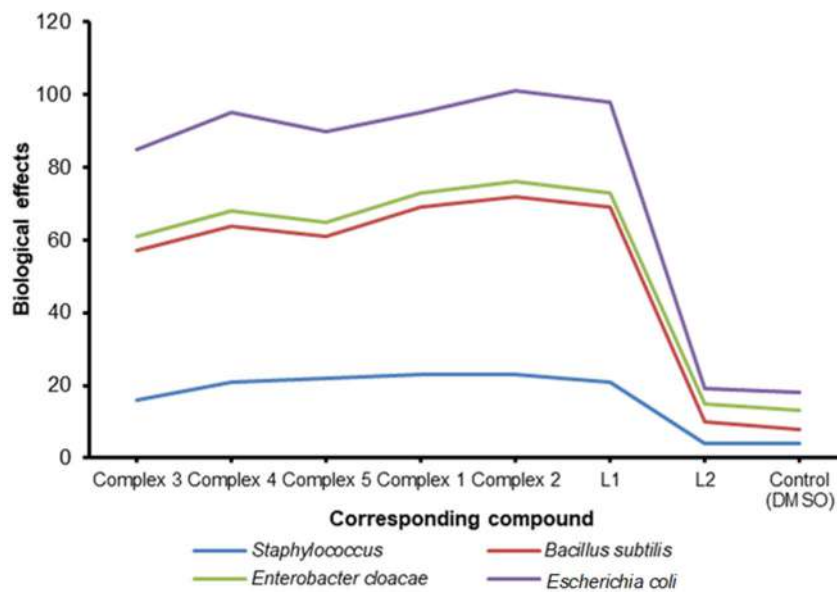
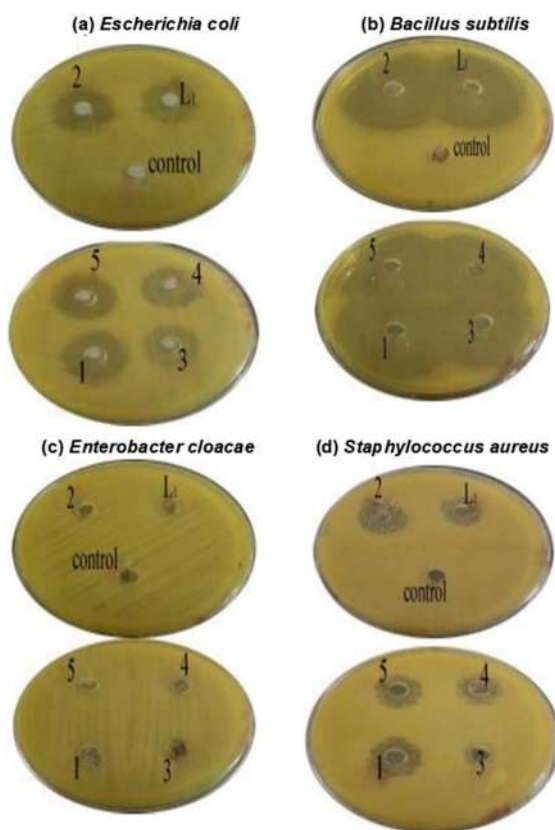**Fig 7.** The biological effect of compounds

Fig 8. Photograph of the zone of inhibition in mm antibacterial activity of compounds

growth of *Escherichia coli*, *Enterobacter cloacae*, *Staphylococcus aureus*, and *Bacillus subtilis*. Generally, the antibacterial activities were in the order: Complex **2** > L_1

> complex **5** > complex **4** ≈ complex **1** > complex **3** > L_2 = DMSO. This finding means that complexes significantly affect the antimicrobial activity of the organic ligand. Fig. 8. The antibacterial activity (ZI) of all the complexes >> Oxalic acid ≈ DMSO. The DMSO was used as a solvent and negative control. It did not show any activity against bacteria. All tests lacked antibacterial activity against *Enterobacter cloacae*. All complex tests had anti-bacterial activity against test bacteria (*Escherichia coli*, *Staphylococcus aureus*, and *Bacillus subtilis*). The results showed that the nature of the metal ion (M(II), Cr(III)) in complexes plays a significant role in the ZI activity [46]. Also, the structure of L_1 due to the presence of the (C=N) group, which is significant in the mechanism reactions in biological reactions, and ligands with (N) and (O) donor systems might inhibit enzyme production and possibly (π-e) delocalization through the whole (chelate ring) system thus include through coordination [46].

DNA Binding Properties

The electrophoresis diagram of compounds is in Fig. 9. In comparison to control samples 1 and 2, there was a complete breakage in samples 3 and 10, which represented CrA and DMSOA, respectively, and the number 5 (lane 5), which represented NiA, was not found to be broken, and in samples 4 (lane 4), 6 (lane 6),
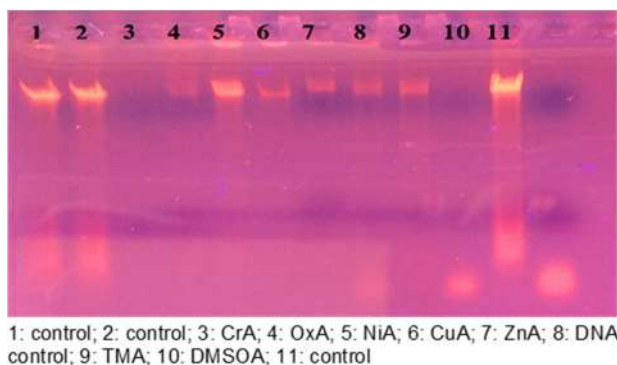
Fig 9. Agarose gel electrophoresis pattern for the DNA binding studies of oxalic acid and Schiff base trimethoprim with various metal ions

7 (lane 7), 8 (lane 8), and 9 (lane 9), representing OxA, CuA, ZnA, DNA control 3, and TMA, respectively. The most influential sample on DNA was sample 8 (lane 8), which represents DNA control, where a long haze streak showed DNA breaking along the gel transfer line. In the DNA cracking that was detected by the weak radiation of the sample and the use of Red safe stain at the examination under the source of ultraviolet compared to the control sample. The intensity of the metal-DNA bands is also reduced when compared to the DNA control [39,46].

■ **CONCLUSION**

The new mixed ligand complexes are synthesized from the reaction of Schiff base ligand, L_1, and oxalate anion, L_2, with metal salts. The synthesized Schiff base ligand, L_1, was prepared from the reaction of trimethoprim and acetylacetone. The general formula of the synthesized complexes is $[M(L_1)(L_2)]$, where **M** represents one of the following metals Co(II), Ni(II), Cu(II), Zn(II), and Cr(III), L_1 represents the trimethoprim ((*Z*)-4-((4-amino-5-(3,4,5-trimethoxybenzyl)pyrimidine-2-yl)imino)pentane-2-one) as the first ligand and L_2 represent the oxalate anion ($C_2O_2^{2-}$) as a second ligand. The analytical and conductivity measurements support the proposed formulae and indicate that the complexes are non-electrolytes except complex **2**, which is a 1:1 electrolyte. The results obtained from measurements of UV, IR, and NMR are in good agreement with the optimized structures of these complexes, which are calculated at the B3LYP level of theory with the 6-311G* basis set for C, H, O, and N atoms and LANL2DZ basis set for metal atom. The Schiff base, L_1, coordinated to the metal ion in a tridentate fashion through two nitrogen atoms and one oxygen atom in the case of complexes **1**, **2**, and **3**, which adopted highly distorted trigonal bipyramid for complex **1**, and distorted square pyramid configuration for **2** and **3**, and as bidentate ligand fashion through two nitrogen atoms in the case of complexes **4** and **5** which adopted a highly distorted square planar geometry. The molecular electrostatic potential of the complexes is explored. The results show that the negative electrostatic potential regions are mainly localized over the oxygen atoms in most cases. The electronic structures of the complexes are investigated in terms of the energies of the HOMO and LUMO orbitals and the electron density distribution of these orbitals over the composing fragments (L_1, L_2, and metal ions) of the complexes. The antibacterial activities of the prepared compounds were in the order: complex **2** > L_1 > complex **5** > complex **4** ≈ complex **1** > complex **3** > L_2. In the DNA cracking that was detected by the weak radiation of the sample and the use of a Red safe stain, it is observed that the intensity decreased for the metal-DNA bands compared to DNA control.

■ **AUTHOR CONTRIBUTIONS**

All authors contributed to the study's conception and design. Material preparation, data collection, and analysis were performed by Eid Abdalrazaq, Abdel Aziz Qasem Jbarah, Tagreed H. Al-Noor, G.T. Shinain, and M.M. Jawad. Tagreed H. Al-Noor wrote the first draft of the manuscript, and all authors commented on previous versions. All authors read and approved the final manuscript.

1362

Indones. J. Chem., 2022, 22 (5), 1348 - 1364

■ REFERENCES

[1] El-Sawaf, A.K., El-Essawy, F., Nassar, A.A., and El-Samanody, E.S.A., 2018, Synthesis, spectral, thermal and antimicrobial studies on cobalt(II), nickel(II), copper(II), zinc(II) and palladium(II) complexes containing thiosemicarbazone ligand, *J. Mol. Struct.*, 1157, 381–394.

[2] Muralisankar, M., Haribabu, J., Bhuvanesh, N.S.P., Karvembu, R., and Sreekanth, A., 2016, Synthesis, X-ray crystal structure, DNA/protein binding, DNA cleavage and cytotoxicity studies of *N*(4) substituted thiosemicarbazone based copper(II)/nickel(II) complexes, *Inorg. Chim. Acta*, 449, 82–95.

[3] Mathan Kumar, S., Rajesh, J., Anitha, K., Dhahagani, K., Marappan, M., Indra Gandhi, N., and Rajagopal, G., 2015, Synthesis, characterization, crystal structure and cytotoxic properties of thiosemicarbazide Ni(II) and Zn(II) complexes, *Spectrochim. Acta, Part A*, 142, 292–302.

[4] Pahonţu, E., Julea, F., Chumakov, Y., Petrenco, P., Roşu, T., and Gulea, A., 2017, Synthesis, characterization, crystal structure and antiproliferative activity studies of Cu(II), Ni(II) and Co(II) complexes with 4-benzoyl-5-pyrazolones derived compounds, *J. Organomet. Chem.*, 836-837, 44–55.

[5] Pu, L.M., Zhao, Q., Liu, L.Z., Zhang, H., Long, H.T., and Dong, W.K., 2018, Synthesis and fluorescence properties of a new heterotrinuclear Co(II)-Ce(III)complex constructed from a bis(salamo)-type tetraoxime ligand, *Molecules*, 23 (4), 804.

[6] Chen, Q.L., 2016, Synthesis and structural characterization of a pyridine oxalato molybdenum(V) complex, *Int. J. New Technol. Res.*, 2 (1), 40–43.

[7] Frisch, M.J., Trucks, G.W., Schlegel, H.B., Scuseria, G.E., Robb, M.A., Cheeseman, J.R., Scalmani, G., Barone, V., Mennucci, B., Petersson, G.A., Nakatsuji, H., Caricato, M., Li, X., Hratchian, H.P., Izmaylov, A.F., Bloino, J., Zheng, G., Sonnenberg, J.L., Hada, M., Ehara, M., Toyota, K., Fukuda, R., Hasegawa, J., Ishida, M., Nakajima, T., Honda, Y., Kitao, O., Nakai, H., Vreven, T., Montgomery, J.A., Jr., Peralta, J.E., Ogliaro, F., Bearpark, M., Heyd, J.J., Brothers, E., Kudin, K.N., Staroverov, V.N., Kobayashi, R., Normand, J., Raghavachari, K., Rendell, A., Burant, J.C., Iyengar, S.S., Tomasi, J., Cossi, M., Rega, N., Millam, J.M., Klene, M., Knox, J.E., Cross, J.B., Bakken, V., Adamo, C., Jaramillo, J., Gomperts, R., Stratmann, R.E., Yazyev, O., Austin, A.J., Cammi, R., Pomelli, C., Ochterski, J.W., Martin, R.L., Morokuma, K., Zakrzewski, V.G., Voth, G.A., Salvador, P., Dannenberg, J.J., Dapprich, S., Daniels, A.D., Farkas, Ö., Foresman, J.B., Ortiz, J.V., Cioslowski, J., and Fox, D.J., 2009, *Gaussian-09 Revision E.01*, Gaussian, Inc., Wallingford, CT.

[8] Makkonen, I., Ervasti, M.M., Kauppila, V.J., and Harju, A., 2012, Exchange-correlation potentials for inhomogeneous electron systems in two dimensions from exact diagonalization: Comparison with the local-spin-density approximation, *Phys. Rev. B*, 85, 205140.

[9] Becke, A.D., 2019, Dependence of the virial exciton model on basis set and exact-exchange fraction, *J. Chem. Phys.*, 150, 241101.

[10] Chen, H., Nusspickel, M., Tilly, J., and Booth, G.H., 2021, Variational quantum eigensolver for dynamic correlation functions, *Phys. Rev. A*, 104 (3), 032405.

[11] Wang, G., Annaberdiyev, A., Melton, C.A., Bennett, M.C., Shulenburger, L., and Mitas, L., 2019, A new generation of effective core potentials from correlated calculations: 4s and 4p Main group elements and first row additions, *J. Chem. Phys.*, 151, 144110.

[12] Hill, J.G., and Shaw, R.A., 2021, Correlation consistent basis sets for explicitly correlated wavefunctions: Pseudopotential-based basis sets for the group 11 (Cu, Ag, Au) and 12 (Zn, Cd, Hg) elements, *J. Chem. Phys.*, 155, 174113.

[13] Hassan, S.S., Shoukry, M.M., and Jbarah, A.A.Q., 2020, Cordination compound of dimethyltin(IV) with *N,N,N',N'*-tetraethylethylenediamine: speciation and theoretical approach, *J. Mex. Chem. Soc.*, 64 (2), 24–43.

[14] Dennington, R., Keith, T.A., and Millam, J.M., 2016, *GaussView, Version 6*, Semichem Inc., Shawnee Mission, KS.

[15] Abu-Yamin, A.A., Jbarah, A.A.Q.M., AlKhalyfeh, K., Matar, S., Alqasaimeh, M., Rüffer, T., and Lang,

H., 2022, Crystal structure, spectroscopic studies, DFT calculations, and biological activity of 5-bromosalicylaldehyde–based Schiff bases, *J. Mol. Struct.*, 1262, 132976.

[16] O'boyle, N.M., Tenderholt, A.L., and Langner, K.M., 2008, Cclib: A library for package-independent computational chemistry algorithms, *J. Comput. Chem.*, 29 (5), 839–845.

[17] Mary Juliet, B.M., and Amaladasan, M., 2014, Preparation and properties of macrocyclic ligand, *Int. J. Recent Innovation Trends Comput. Commun.*, 2 (8), 2102–2105.

[18] Jeffery, G.H., Bassett, J., Mendham, J., and Denney, R.C., 1989, *Vogel's Textbook of Quantitative Chemical Analysis*, 5th Ed., John Wiley & Sons Inc., New York, US.

[19] Orekhov, M.A., 2021, Coordination numbers of bivalent ions in organic solvents, *Russ. J. Phys. Chem. A*, 95 (10), 2059–2064.

[20] Marcus, R.A., 1964, Chemical and electrochemical electron-transfer theory, *Annu. Rev. Phys. Chem.*, 15 (1), 155–196.

[21] Saheb, V., Sheikhshoaie, I., and Stoeckli-Evans, H., 2012, A novel tridentate Schiff base dioxo-molybdenum(VI) complex: Synthesis, experimental and theoretical studies on its crystal structure, FTIR, UV–visible, ^{1}H NMR and ^{13}C NMR spectra, *Spectrochim. Acta, Part A*, 95, 29–36.

[22] Agrwal, A., Verma, A., Chantola, N., Verma, S., and Kasana, V., 2022, Synthesis, molecular docking and extensive structure activity relationship of substituted DHP derivatives: A new class of herbicides, *J. Environ. Sci. Health, Part B*, 57 (5), 379–420.

[23] Odion, E.E., Enadeghe, D.O., and Usifoh, C.O., 2021, Synthesis, characterization and antibacterial assessment of 3,4,5-trimethoxy-3',4'-dimethoxychal cone and 2,4,6-trimethoxy-3',4'-dimethoxychalcone, *Niger. J. Pharm. Appl. Sci. Res.*, 10 (2), 1–5.

[24] Jin, R.Y., Sun, X.H., Liu, Y.F., Wong, W., Lu, W.T., and Ma, H.X., 2014, Synthesis, crystal structure, IR, ^{1}H NMR and theoretical calculations of 1,2,4-triazole Schiff base, *J. Mol. Struct.*, 1062, 13–20.

[25] Aparna, E.P., and Devaky, K.S., 2018, Microwave assisted solid phase synthesis of trisubstituted pyrimidines, *J. Chem. Pharm. Res.*, 10 (8), 67–72.

[26] Jacobsen, N.E., 2017, *NMR Data Interpretation Explained: Understanding 1D and 2D NMR Spectra of Organic Compounds and Natural Products*, John Wiley & Sons, Inc., Hoboken, New Jersey, US.

[27] Ebrahimi, H.P., Hadi, J.S., Abdulnabi, Z.A., and Bolandnazar, Z., 2014, Spectroscopic, thermal analysis and DFT computational studies of salen-type Schiff base complexes, *Spectrochim. Acta, Part A*, 117, 485–492.

[28] Adeyemi, J.O., Olasunkanmi, L.O., Fadaka, A.O., Sibuyi, N.R.S., Oyedeji, A.O., and Onwudiwe, D.C., 2022, Synthesis, theoretical calculation, and biological studies of mono- and diphenyltin(IV) complexes of *N*-methyl-*N*-hydroxyethyldithio carbamate, *Molecules*, 27 (9), 2947.

[29] Al-Noor, T.H., Karam, N.H., Ghanim, F.H., Kindeel, A.S., and Al-Dujaili, A.H., 2017, Synthesis, characterization and liquid crystalline properties of novel benzimidazol-8-hydroxyquinoline complexes, *Inorg. Chim. Acta*, 466, 612–617.

[30] Nakamoto, K., 2009, *Infrared and Raman Spectra of Inorganic and Coordination Compounds, Part B: Applications in Coordination, Organometallic, and Bioinorganic Chemistry*, 6th Ed., John Wiley & Sons, Inc., Hoboken, New Jersey, US.

[31] Mezey, R.Ş., Máthé, I., Shova, S., Grecu, M.N., and Roşu, T., 2015, Synthesis, characterization and antimicrobial activity of copper(II) complexes with hydrazone derived from 3-hydroxy-5-(hydroxymethyl)-2-methylpyridine-4-carbaldehyde, *Polyhedron*, 102, 684–692.

[32] Bellamy, L.J., 1975, *The Infra-Red Spectra of Complex Molecules*, Springer, Dordrecht, Netherlands.

[33] Housecroft, C.E., and Sharpe, A.G., 2018, *Inorganic Chemistry*, 5th Ed., Pearson Education Limited, Harlow, UK.

[34] Jamil, Y.M.S., Al-Qadasy, J.M.K., Al-Azab, F.M., and Al-Maqtari, M.A., 2018, Synthesis, characterization and antibacterial study of some 3d-metal complexes

of paracetamol and 1,10-phenanthroline, *Jordan J. Chem.*, 13 (4), 203–212.

[35] Fleming, G.R., Lewis, N.H.C., Arsenault, E.A., Wu, E.C., and Oldemeyer, S., 2019, "Two-Dimensional Electronic Vibrational Spectroscopy" in *Coherent Multidimensional Spectroscopy*, Eds. Cho, M., Springer, Singapore, 35–49.

[36] Galić, N., Dijanošić, A., Kontrec, D., and Miljanić, S., 2012, Structural investigation of aroylhydrazones in dimethylsulphoxide/water mixtures, *Spectrochim. Acta, Part A*, 95, 347–353.

[37] Abbas, S.H., 2017, Synthesis, characterization and biological activity of some nickel(II) mixed ligands complexes of dithiocarbamate and 1,10-phenanthroline, *Eur. J. Chem.*, 8 (4), 367–370.

[38] Yallur, B.C., Krishna, P.M., and Challa, M., 2021, Bivalent Ni(II), Co(II) and Cu(II) complexes of [(*E*)-[(2-methyl-1,3-thiazol-5-yl)methylidene]amino]thio urea: Synthesis, spectral characterization, DNA and *in-vitro* anti-bacterial studies, *Heliyon*, 7 (4), e06838.

[39] Rajendran, N., Periyasamy, A., Kamatchi, N., and Solomon, V., 2020, Synthesis and efficacy of copper(II) complexes bearing *N*(4)-substituted thiosemicarbazide and diimine co-ligands on plasmid DNA and HeLa cell lines, *J. Serb. Chem. Soc.*, 85 (3), 321–334.

[40] Dance, I.G., Gerloch, M., Lewis, J., Stephens, F.S., and Lions, F., 1966, High-spin five-coordinate cobalt (II), *Nature*, 210 (5033), 298.

[41] Kafi-Ahmadi, L., and Shirmohammadzadeh, L., 2017, Synthesis of Co(II) and Cr(III) salicylidenic

Schiff base complexes derived from thiourea as precursors for nano-sized Co_3O_4 and Cr_2O_3 and their catalytic, antibacterial properties, *J. Nanostruct. Chem.*, 7 (2), 179–190.

[42] Bendjeddou, A., Abbaz, T., Gouasmia, A., and Villemin, D., 2017, Determination of reactive properties of a series of mono-functionalized bis-tetrathiafulvalene employing DFT calculations, *ASRJETS*, 29 (1), 308–326.

[43] Politzer, P., and Murray, J.S., 2021, "Molecular Electrostatic Potentials: Significance and Applications" in *Chemical Reactivity in Confined Systems: Theory, Modelling and Applications*, Eds. Chattaraj, P.K., and Chakraborty, D., John Wiley & Sons Ltd, Hoboken, New Jersey, US.

[44] Gadre, S.R., Suresh, C.H., and Mohan, N., 2021, Electrostatic potential topology for probing molecular structure, bonding and reactivity, *Molecules*, 26 (11), 3289.

[45] da Silva, G.C.Q., Cardozo, T.M., Amarante, G.W., Abreu, C.R.A., and Horta, B.A.C., 2018, Solvent effects on the decarboxylation of trichloroacetic acid: Insights from *ab initio* molecular dynamics simulations, *Phys. Chem. Chem. Phys.*, 20 (34), 21988–21998.

[46] Muthukkumar, M., Malathy, M., and Rajavel, R., 2015, Antimicrobial and DNA cleavage activities of macrocyclic Cu(II), Ni(II), Co(II), and Zn(II) Schiff base complexes, *Chem. Sci. Rev. Lett.*, 4 (16), 1227–1236.

Indones. J. Chem., 2022, 22 (5), 1365 - 1375

Suppl. **1**

Supplementary Data

This supplementary data is a part of a paper entitled "Synthesis, Characterization, and Antibacterial Activity of Lanthanide Metal Complexes with Schiff Base Ligand Produced from Reaction of 4,4-Methylene Diantipyrine with Ethylenediamine".
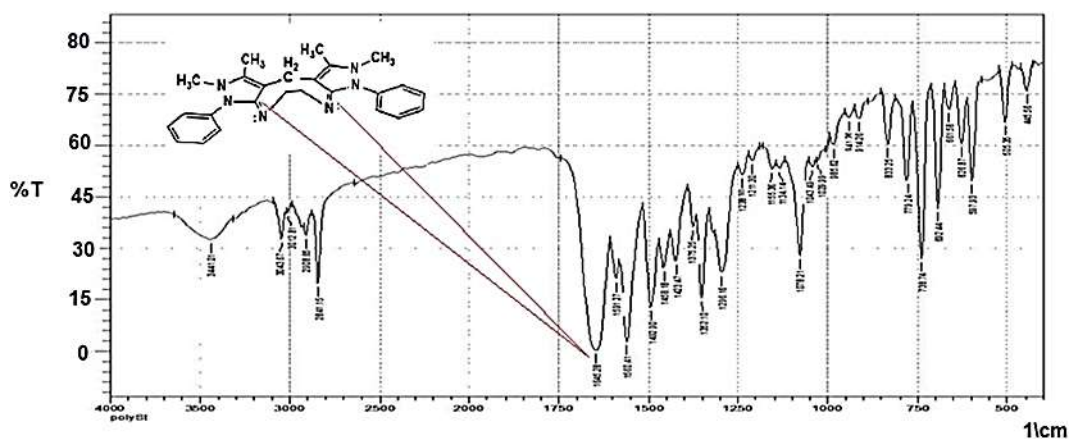

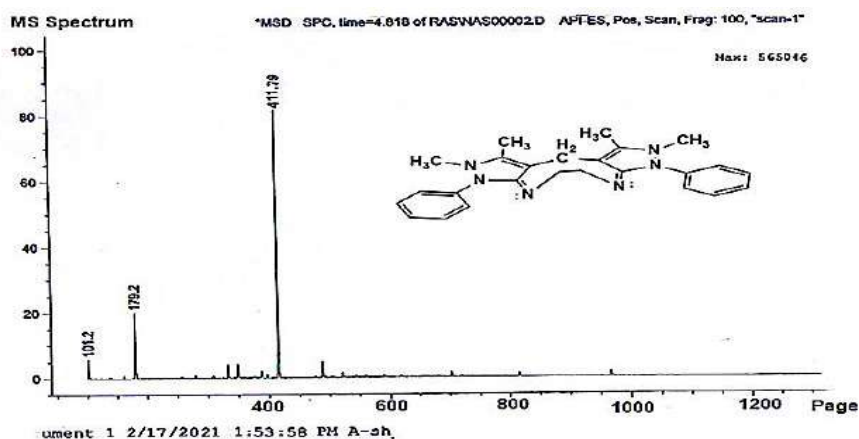**Fig S1.** FT-IR spectra of Schiff base ligand
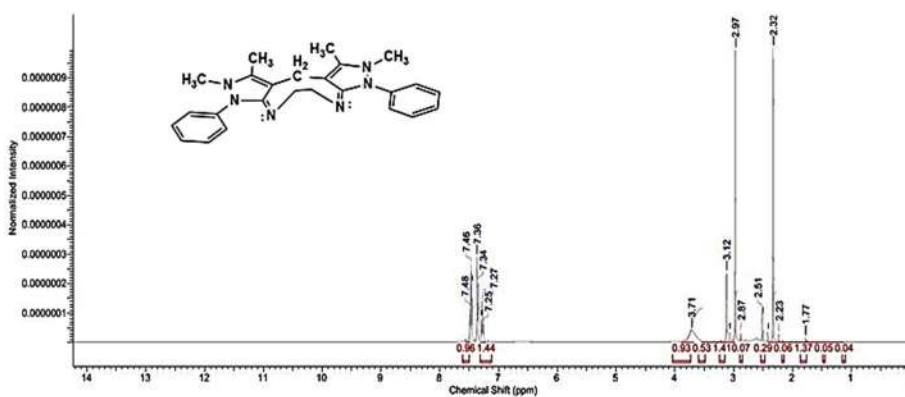

Fig S2. LC-MS spectra of Schiff base ligand
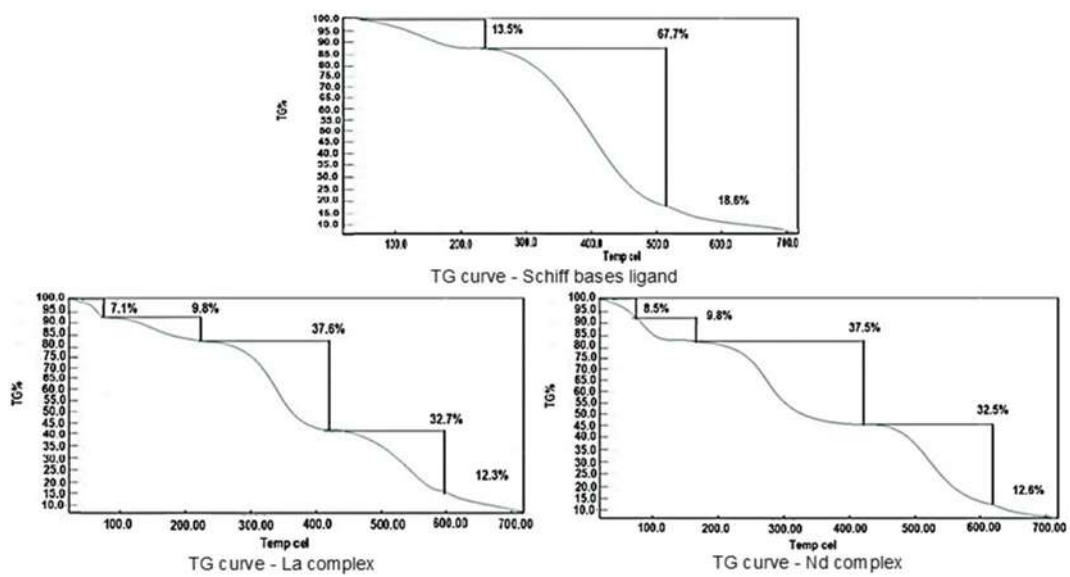

Fig S3. ^{1}H-NMR Spectrophotometer of Schiff base ligand

Fig S4. ^{13}C-NMR Spectrophotometer of Schiff base ligand

Fig S5. FT-IR spectra of lanthanide complexes

Fig S6. UV-Visible of Schiff bases and lanthanide complexes

Indones. J. Chem., 2022, 22 (5), 1365 - 1375

Suppl. **3**

Fig S7. TG curve - Schiff bases ligand and lanthanide complexes

Synthesis, Characterization, and Antibacterial Activity of Lanthanide Metal Complexes with Schiff Base Ligand Produced from Reaction of 4,4-Methylene Diantipyrine with Ethylenediamine

Kawther Adeeb Hussein* and Naser Shaalan

Department of Chemistry, College of Science for Women, University of Baghdad, Iraq

Abstract: *An environmentally friendly method for the synthesis of Schiff bases was described by combining 4,4-methylenediantipyrine with ethylenediamine. The complex was prepared in a classical way, the usual condensation reaction method. A series of metal complexes were prepared from reactions of lanthanide nitrate salts [Nd^{+3}, La^{+3}, Er^{+3}, Gd^{+3}, and Dy^{+3}] with a Schiff base ligand. The structures of the complexes were confirmed by analytical studies, spectral measurements, and thermal studies, and the prepared ligand was characterized using microanalysis technique, UV-Visible, infrared, nuclear magnetic resonance ^{1}H-NMR and ^{13}C-NMR, mass spectrometry, and thermogravimetric analysis (TGA), and the addition of conductivity measurement and magnetic moment of complexes. The results showed that these complexes have a consistency of 10 in which the elements are bonded with the ligand through the two nitrogen atoms at C=N and that the bonding ratio between the metal:ligand is in 1:2 ratio. By using agar disc-spreading, we tested several* in vitro *compounds for their antibacterial activity against four pathogenic bacteria, including* Staphylococcus aureus, Bacillus subtilis, Escherichia coli, *and* Klebsiella pneumoniae. *The majority of the complexes demonstrated antibacterial activity.*

Keywords: *Schiff's bases; lanthanide complexes; biological activity; 4,4-methylenediantipyrine*

■ INTRODUCTION

The lanthanide (III) ions (rare earth metal ions) coordination chemistry field is rapidly expanding because of its application in fundamental and applied research in a variety of fields ranging from chemistry to material science and biology [1-3]. The chemistry of Schiff base complexes with lanthanide has gained importance recently because of the vast range of applications of lanthanide complexes, such as in photochemistry and medicine [4-5]. The lanthanides are a series of 15 rare earth elements starting from cerium to lutetium in the Periodic Table with atomic numbers 58 through 71. Some scientists have added to them the element lanthanum 57, which precedes them in the Periodic Table, and the name of the lanthanide series is due to the element lanthanum [6-7]. The lanthanide series consists of a series of successive elements in which the f orbital is partially or filled with electrons, and the outer orbital is empty [8].

These elements overcome in their compounds the oxidation state +3, and in some of them, the +2 and +4 states appear, and the +3 state is the only stable state in lanthanum, gadolinium, and lutetium because it corresponds to the vacancy of the 4f orbital in it and its half-filling, and then it is completely filling [9-11]. While these metals can be considered transitional elements, they have properties that distinguish them from the rest of the elements [12].

One of the properties of the lanthanides that affect how they interact with other elements is the alkalinity property, which is the extent to which the atom can lose electrons [13]. Schiff base compounds are azomethine-containing compounds formed through a condensation reaction between primary amine and carbonyl compounds, and they were first reported by Hugo Schiff in 1864 [14-16]. Schiff base compounds are a significant and well-studied class due to their wide variety of

biological uses, simplicity of manufacturing, chelating properties, and stability [17-19]. In addition to their unique properties and practical uses, Schiff bases are also particularly fascinating compounds that shield metal ions from the chemical environment by creating kinetically inert complexes. Additionally, they have a remarkable ability to organize lanthanide ions, and antipyrine derivatives possess certain scientific advantages [20-22]. Several lanthanide coordination compounds have been demonstrated to contain ligands containing nitrogen donor atoms that serve as good building blocks for creating other lanthanide coordination compounds. As a linkage in metal coordination chemistry, Schiff bases continue to play a significant role [23-24]. Schiff base metal complexes have played a significant role in the history of coordination chemistry, resulting in a wide range of articles ranging from pure synthetic efforts to contemporary studies of metal complexes on a physical, chemical, and biological level [25-26]. The objectives of this study are synthesizing a new Schiff base ligand from antipyrine derivatives which is (4,4-methylene diantipyrine), characterizing it by spectroscopic methods, synthesizing some complexes using salts of rare earth metal ions (Nd^{+3}, La^{+3}, Er^{+3}, Gd^{+3}, and Dy^{+3}), characterizing them by physical and spectral analytical methods, and studying their biological activity [27].

■ EXPERIMENTAL SECTION

Materials

All reagents and chemicals used in this study are in the analytical grade and purchased from Sigma-Aldrich such as 4,4-methylenediantipyrine (97%), ethylenediamine (99%), absolute ethanol (99%), and lanthanide nitrate $[Ln(NO_3)_3]\cdot6H_2O$ whereas Ln^{+3} = La, Nd, Er, Gd, and Dy.

Instrumentation

The microanalysis element of the studied ligand and complexes was carried out with a Thermo Finnegan flash device in Syria Energy Centre. Infrared spectra of ligands and their complexes were recorded within the range 4000–250 cm^{-1} using a device of the type Shimadzu FTIR-spectrometer and using a KBr disk for ligands and CsI for

complexes at the Department of Chemistry, College of Science, Baghdad University. Also, the ^{1}H-NMR and ^{13}C-NMR spectra of the prepared ligand were recorded by using a Bruker 400 MHz AVANCE spectrometer after dissolving it with DMSO-d_6 solvent and using $Si(CH_3)_4$ (TMS) as a reference for measurement at room temperature in Ankara, Turkey, and the mass spectra of the prepared compounds were recorded by a Network Mass Selective device at the University of Ankara, Turkey. The melting point of the prepared ligand and their complexes using a device from the English company Stuart with a temperature range of 300 °C at the Department of Chemistry, College of Science, Baghdad University.

### Procedure

Synthesis Schiff base of ligand

Schiff's base ligand was prepared by dissolving 1 g (1 mol) of 4,4-methylenediantipyrine in (20 mL) of ethanol absolute 99.9% in a round-bottom flask with a capacity of 100 mL. An amount of 0.154 g (1 mmol) of ethylenediamine in a separating funnel was added dropwise into the mixture, followed by 3–5 drops of glacial acetic acid with continuous stirring until the components were homogenous. The mixture was heated and refluxed for 4–6 h, at 100 °C. After the precipitation was completed, the white crystals were collected by filtration, washed with absolute ethanol, dried for 24 h, and then recrystallized in absolute hot ethanol. The re-crystallized powder was collected by filtration and then dried for 12 h. It had 75% yield and a melting point (m.p) 189–191 °C. The ligand was characterized by several techniques [28].

Preparation of lanthanide complexes

Lanthanide complexes are prepared by dissolving 0.1 g of Schiff bases ligand in 5 mL of methanol absolute in a 25 mL round bottom flask. An amount of 5 mL of methanol absolute at a time was added with lanthanides salts. The mixture was refluxed, stirred for 4 to 7 h, and then left to precipitate. Then the precipitate was collected and purified with water and ether and let dry to obtain a pure precipitate; the molar ratio was fixed at 1:2 [29].
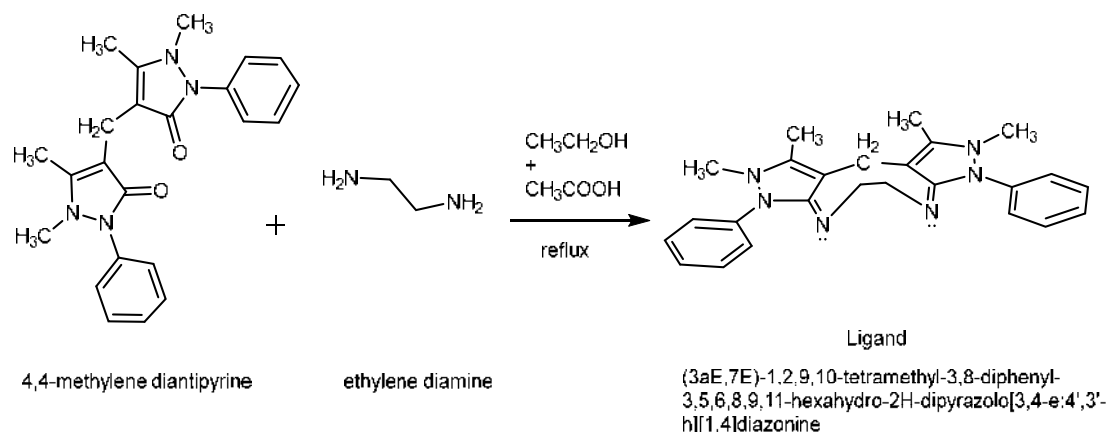
Scheme 1. The prepared Schiff base ligand
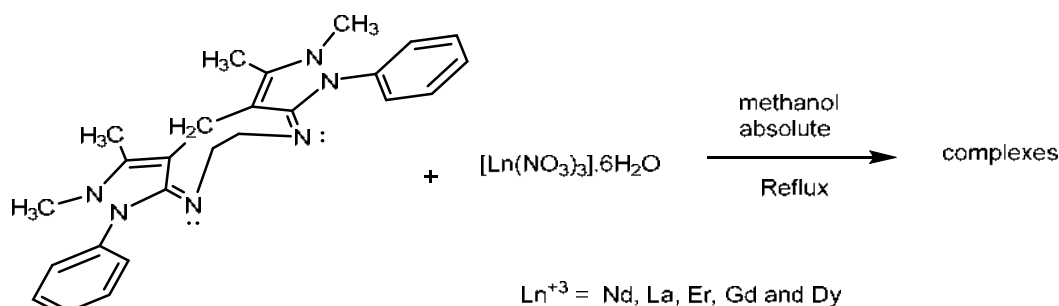
Scheme 2. Preparation of lanthanide complexes

Table 1. Microanalysis elements C, H, N, and O and physical data for ligand as well as its lanthanide complexes

Compound	M.wt	Yield%	Analysis (calculated)			
			C%	H%	N%	O%
L/[$C_{25}H_{28}N_6$]	412.54	75%	72.79 (73.02)	6.84 (6.79)	20.37 (19.95)	--
$C_{50}H_{56}N_{15}NdO_9$	1155.34	65%	51.98 (52.34)	4.89 (4.92)	18.19 (17.95)	12.46 (12.53)
$C_{50}H_{56}N_{15}LaO_9$	1150.00	60%	52.22 (52.34)	4.91 (4.82)	18.27 (17.95)	12.52 (12.67)
$C_{50}H_{56}N_{15}ErO_9$	1178.35	68%	50.97 (51.23)	4.79 (4.58)	17.83 (17.92)	12.22 (12.40)
$C_{50}H_{56}N_{15}GdO_9$	1168.34	65%	51.40 (52.13)	4.83 (3.97)	17.98 (17.89)	12.32 (12.72)
$C_{50}H_{56}N_{15}DyO_9$	1173.62	65%	51.17 (51.42)	4.81 (4.63)	17.90 (17.57)	12.27 (12.59)

■ RESULTS AND DISCUSSION

The reaction of the Schiff base ligand with the lanthanide nitrate [Ln(NO$_3$)$_3$]·6H$_2$O, Ln = La^{+3}, Nd^{+3}, Er^{+3}, Gd^{+3}, and Dy^{+3} produced good yields of complexes. The analytical data, along with some physical properties of the ligand and its metal complexes, are listed in Table 1.

FTIR Spectra of Schiff Bases Ligand

The Schiff bases ligand [$C_{25}H_{28}N_6$] was characterized using an FTIR spectrum as shown in Fig. S1, which revealed bands 3441, 3043, 2908, 1643, and 1589 cm^{-1} that

are attributed to ν(O-H), hydrated water [30], ν(C-H) Aromatic, ν(C-H) (Aliph), ν(C=N), and ν(C=C) [31].

Mass Spectrum of Ligand

In coordination chemistry, mass spectroscopy is increasingly being used as a potent structural characterization tool. Mass spectra fragmentation patterns for free Schiff base ligand [$C_{25}H_{28}N_6$] were in good agreement with the structure in Fig. S2. The mass spectrum was characterized by an intense peak at 412.54 *m/z*, which corresponds to its molecular weight computed

at 411.79 *m/z* [32].

Nuclear Magnetic Resonance Spectrum

^{1}H-NMR spectrum of ligand

The ^{1}H-NMR of protons was studied in DMSO-d_6 as the solvent and TMS as the standard reference. The spectrum of ligand showed a chemical shift at δ = 1.77, 2.23, and 2.51 ppm, which appeared to return to -CH$_2$-, -CH$_3$, and –CH$_2$- proton, respectively, in the 4-amino antipyrine and ethylenediamine compounds. The spectrum displayed various signals at δ = 7.34 and 7.48 ppm assigned into aromatic protons. In comparison, the beam appeared to return to N-CH$_3$ at the chemical shift at δ = 3.12 ppm; the chemical shift of the azomethine group C=N is not observable from ^{1}H-NMR because no proton is present related to the carbon azomethine group, the signals at δ = 2.32 and 2.97 ppm indicated into DMSO-d_6 and water (H$_2$O), respectively [33-34]. The ligand ^{1}H-NMR spectrum is shown in Fig. S3.

^{13}C-NMR spectrum of ligand

The ^{13}C-NMR was studied in DMSO-d_6 as the solvent. The spectrum of ligand showed CH$_2$ aliphatic at 11.48 ppm, -CH$_3$ at the 15.52 ppm, CH$_3$ and CH$_2$ at the aliphatic, N-CH$_3$ and N-CH$_2$ at 35.39, 40.02 at the CH. CH$_2$ at the aliphatic, CH-N-N at the 135.97 ppm, and the C-CH$_3$ at 155.33 ppm, while C=N at the 165.76 ppm [35], as shown in Fig. S4.

FTIR Spectra of Complexes

Infrared spectra were recorded for the ligand (C$_{25}$H$_{28}$N$_6$) in the range of 4000–400 cm^{-1} and its complexes in the range of 4000–200 cm^{-1}. The absorbance peaks of the IR spectra are summarized in Table 2, and representative IR spectra of the La complex are shown in

Fig. S5. There was a distinct difference between the spectra of the complexes and the spectrum of the ligand due to its intensity and location. Further to that, it appeared that new bands emerged as a result of coordination between the ligand and the ions of the internal elements (lanthanides). It was also noted that the spectra of the complexes are similar among themselves due to the presence of the same effects in the vibrations of the ligand, and the infrared spectrum indicates the presence of a band at 3441–3439 cm^{-1}; which is attributed to the stretching frequencies of the O-H bond of the moisture that appeared in the spectra of each of the ligands and its lanthanide complexes.

The spectrum of the ligand also showed a medium-intensity absorption band located at a frequency of 3043 cm^{-1} due to the vibration of the aromatic C-H band stretching and the aliphatic absorption band at the frequency of 2908 cm^{-1}. The spectrum of the ligand similarly showed a medium-intensity band at the frequency 1492 cm^{-1}, which is generated from the vibration of the stretch band C=C of episode 4-aminoantipyrene. The spectrum of the ligand likewise showed a band at the frequency 1589 cm^{-1} belonging to the frequencies of the azomethine group C=N, 1591, 1583, 1593, 1581, 1577, and 1578 cm^{-1}, respectively, due to their participation in the coordination process with the lanthanide ions and forming complexes C$_{50}$H$_{56}$N$_{15}$NdO$_9$, C$_{50}$H$_{56}$N$_{15}$LaO$_9$, C$_{50}$H$_{56}$N$_{15}$ErO$_9$, C$_{50}$H$_{56}$N$_{15}$GdO$_9$, and C$_{50}$H$_{56}$N$_{15}$DyO$_9$ bond through the free electron pair of one of the atoms of this group. Bands appeared in the spectra of complexes 565, 530, 574, 572, and 572 cm^{-1} back to frequencies (M-O), 503, 412, 505, 503, and 435 cm^{-1} back to frequencies (M-N),

Table 2. The infrared spectrum of the prepared ligand and lanthanide complexes

Ligand\Complexes	ν(O-H) H$_2$O	ν(C=N)	ν(C=C)	ν(NO$_3$)	ν(NO$_3$)	ν(NO$_3$)	ν(M-O)	ν(M-N)
L/[C$_{25}$H$_{28}$N$_6$]	3458	1643	1589	---	---	--	---	---
C$_{50}$H$_{56}$N$_{15}$NdO$_9$	3481	1643	1525	1490	1456	1311	582	453
C$_{50}$H$_{56}$N$_{15}$LaO$_9$	3477	1620	1585	1492	1458	1304	588	458
C$_{50}$H$_{56}$N$_{15}$ErO$_9$	3446	1618	1575	1490	1458	1303	592	459
C$_{50}$H$_{56}$N$_{15}$GdO$_9$	3448	1616	1566	1490	1440	1300	590	435
C$_{50}$H$_{56}$N$_{15}$DyO$_9$	3446	1616	1560	1496	1458	1303	592	424

respectively, which is the result of forming coordination bonds between the donating atoms O and N with the central lanthanide ions [36-37].

Measurements with UV-Visible Spectroscopy

In Table 3, the UV-Vis spectra of the Schiff base ligand and its lanthanide complexes dissolved in DMSO (1×10^{-3} M) are listed. The absorption bands of ligand and two representative ions are shown in Fig. S6. The first high-intensity pack observed at λ_{max} = 283 was likely caused by the $\pi \rightarrow \pi^*$ transition of aromatic rings. The second absorption pack that appeared at λ_{max} = 290 nm corresponds to the $n \rightarrow \pi^*$ transition of the carbonyl group (C=O), and the last band at λ_{max} = 328 nm could be attributed to the $n \rightarrow \pi^*$ transition of the azomethine group (C=N). The absorption spectra of all investigated lanthanide complexes differ from the free Schiff base ligand in intensity and pattern [38], indicating that the Schiff base ligand is coordinated with Ln^{+3} ions. Evidence of complexes is revealed with different absorption bands around 450–1100 nm [39] (Table 3). In spectral terms with the same configuration 4f, a transition occurs (f→f). As a result, there are very sharp spectral bands that are similar to those observed with free ions. This is related to the possibility of such transitions. As a consequence of the valence selection rule (Laporte), electrical dipole transitions are not allowed when the lanthanide ion is subjected to a ligand field. As a result of the center asymmetric interactions, the dipole transition becomes partially permissible [40].

Magnetic Measurements of Lanthanide Complexes

The response of the transition elements to magnetism increases with the increase in the number of single electrons in the shell. As for the response of the

lanthanide ions, it is related to how the electrons move in the orbit, as it is in the depth of the atom, and thus the lanthanide elements depend on the 4f shell electrons, especially the single electrons. Among the direct results, $\mu_{eff} = \sqrt{4S(S + 1) + L(L + 1)}$, where the magnetic effect resulting from the movement of the electron in its orbit contributes to paramagnetic, next to the spinning movement of the electron S, while the transitional elements, the participation of the orbital movement, is neglected due to the interference with the electric field of the ocean. The effective magnetic moment (μ_{eff}) of the created complexes has demonstrated that all the prepared complexes, except lanthanum complexes, are paramagnetic. The findings were compared with the real values and were closely related to the calculated values [41], as shown in Table 3.

Molar Conductivity Measurement of Lanthanide Complexes

Table 3 shows that all the lanthanide complexes are non-conductive in dimethylformamide (DMF) solvent at a concentration of 1×10^{-3} M. It was revealed that nitrate ions do not exist outside the coordination sphere.

Thermogravimetric Analysis (TGA)

The results of TGA of La^{+3}, Nd^{+3}, Er^{+3}, Gd^{+3}, and Dy^{+3} complexes are given in Fig. S7 and Table 4. The thermograms have been carried out in the range of up to 700 °C at a heating rate of 10 °C/min in a nitrogen atmosphere. They show an agreement in weight loss between the results obtained from the thermal decomposition and the calculated values. It was observed that the ligand undergoes two stages of decomposition. In the range of 45–240 °C, the estimated mass loss was 13.5% (calculated at 13.8%). Due to the decomposition

Table 3. The physical data, molar conductivity, and electronic spectra for Schiff base ligand and lanthanide complexes

Compound	Dec Point (°C)	Color	Conductivity DMF (Cm^2.ohm^{-1}.mol^{-1})	Absorption bonds (nm)	Assigned transition	Magnetic moment (B.M)
L/[C$_{25}$H$_{28}$N$_6$]	189–191	White crystals	---	283, 290, 328	$\pi \rightarrow \pi^*$, $n \rightarrow \pi^*$	----
C$_{50}$H$_{56}$N$_{15}$NdO$_9$	280	White	20	---	$^1S_0$	Dia
C$_{50}$H$_{56}$N$_{15}$LaO$_9$	> 300	Light yellow	30	584, 738, 803, 981	$^4I_{9/2} \rightarrow {}^4G_{5/2}$, $^4I_{9/2} \rightarrow {}^2P_{1/2}$, $^4I_{9/2} \rightarrow {}^2D_{7/2}$	2.67
C$_{50}$H$_{56}$N$_{15}$ErO$_9$	270	Misty rose	20	488, 521, 542, 652, 974	$^3H_4 \rightarrow {}^4I_{15/2}$, $^4I_{15/2} \rightarrow {}^4G_{11/2}$	7.54
C$_{50}$H$_{56}$N$_{15}$GdO$_9$	280	Sea shell	20	757, 806, 909	$^8S_{7/2} \rightarrow {}^6I_{7/2}$	2.46
C$_{50}$H$_{56}$N$_{15}$DyO$_9$	260	Light yellow	30	650, 982	$^5I_{11} \rightarrow {}^6H_{5/2}$, $^6H_{15/2} \rightarrow {}^6P_{5/2}$	3.84

**Table 4.** TGA data of Schiff bases ligand and its lanthanide complexes

| Sample step	Temperature range °C	TG weight mass loss		Reaction	Sample step	Temperature range °C	TG weight mass loss		Reaction
		Calc%	Found %				Calc%	Found %	
L(I)	45–240	13.8	13.5	$C_2H_4N_2$	Er (I)	25–75	7.5	7.3	$5H_2O$
L(II)	240–510	67.5	67.7	$C_{17}H_{19}N_4$	Er (II)	80–230	10.0	9.6	$2NO_3$
--	--	--	--	--	Er (III)	230–415	35.6	36.8	$NO_3 + C_{25}H_{28}N_6$
--	--	--	--	--	Er (IV)	415–590	32.3	32.1	$C_{25}H_{28}N_6$
Final residual		18.5	18.6	C_6H_6	Final residual		14.5	14.2	ErO
Nd (I)	25–75	8.0	8.5	$6H_2O$	Gd (I)	30–75	7.4	7.0	$6H_2O$
Nd (II)	75–180	10.1	9.8	$2NO_3$	Gd (II)	75–225	9.9	9.7	$2NO_3$
Nd (III)	180–430	36.9	37.5	$NO_3 + C_{25}H_{28}N_6$	Gd (III)	225–440	37.2	37.1	$NO_3 + C_{25}H_{28}N_6$
Nd (IV)	430–620	33.0	32.5	$C_{25}H_{28}N_6$	Gd (IV)	440–575	32.5	32.3	$C_{25}H_{28}N_6$
Final residual		12.5	12.6	NdO	Final residual		13.0	13.5	GdO
La (I)	25–70	6.9	7.1	$5H_2O$	Dy (I)	25–70	5.4	5.6	$4H_2O$
La (II)	70–225	10.2	9.8	$2NO_3$	Dy (II)	70–215	10.0	9.6	$2NO_3$
La (III)	225–430	37.5	37.6	$NO_3 + C_{25}H_{28}N_6$	Dy (III)	215–420	37.2	37.0	$NO_3 + C_{25}H_{28}N_6$
La (IV)	430–595	32.5	32.7	$C_{25}H_{28}N_6$	Dy (IV)	420–590	32.4	32.5	$C_{25}H_{28}N_6$
Final residual		12.4	12.3	LaO	Final residual		15.0	15.2	DyO

of $C_2H_4N_2$ in the first step, the range 240–510 °C, the estimated mass loss was 67.7% (calculated 67.5%) due to the decomposition of the $C_{17}H_{19}N_4$ molecule. In the final stage, an estimated mass loss of 18.6% (calculation of 18.5%) was due to the loss of the C_6H_6 molecule with a complete analysis. The data supports the results of elemental analysis and confirms the suggested formula. The complexes shown in Scheme 3 showed common behavior as in the following steps to the lanthanide complexes, respectively, as shown in Table 4 and Fig. S7. The analysis of the lanthanide complexes showed that the dissociation process of the loss goes through several stages, and the process occurs through 3 steps, as in Scheme 3, and this is proof of good thermal stability, where the loss in the first step is hydrated water not coordinated, and this means that the water is out of

coordination, in each stage losing part of its weight and liberating a specific compound of the complexes that have been prepared. The temperature ranges are different among them, causing these differences to disintegrate the ions formed by the complexes after the dissolution, the material remaining after the complex has been formed may belong to lanthanide oxide [42-43]. Based on the characterization, the complex structure of lanthanide ions may be presented in Fig. 1.

Study of Antibacterial Activity

The findings showed that the produced ligand and its constituents were biologically efficient since the experiment was conducted in aerobic circumstances at 37 °C. Drilling was used to expose Schiff base ligand and lanthanide complexes to every pathogenic active of
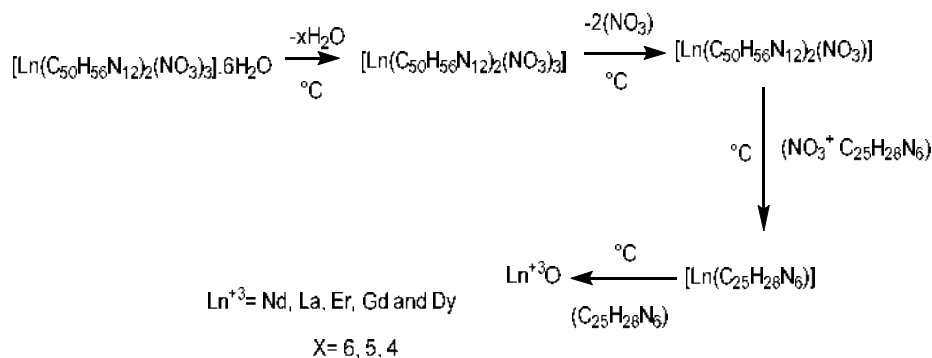
Scheme 3. TGA-analyses of lanthanide complexes

Kawther Adeeb Hussein and Naser Shaalan
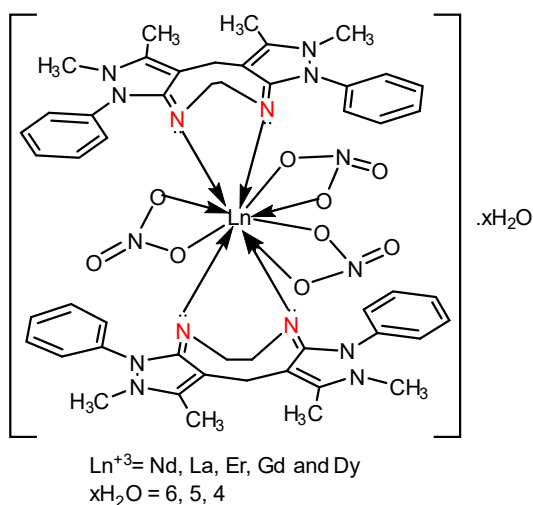
Fig 1. Suggested lanthanide complex structure with a coordination number of ten

pathogenic bacteria to four different types of pathogenic bacteria, i.e., two types of gram-negative bacteria: *Escherichia coli* and *Klebsiella pneumoniae*, and two gram-positive bacteria: *Staphylococcus aureus* and

Bacillus subtilis. The complex was dissolved in DMF at 1×10^{-3} M concentration and they showed different efficacy to the negative and positive stain-bacteria of the complexes. The data is shown in Table 5, Fig. 2 and 3.

We conclude from the bacterial dishes that the ligand has variable biological activities, as it shows its activity for some types of bacteria and not for others, where it was found that the lanthanide complexes are

Table 5. The antibacterial activity of the prepared Schiff bases ligand and lanthanide compound

Sample	*S. aureus*	*B. subtilis*	*E. coli*	*K. penumoniae*
DMSO	−	−	−	−
L/[$C_{25}H_{28}N_6$]	++	+	−	+++
$C_{50}H_{56}N_{15}NdO_9$	++++	+	−	+++
$C_{50}H_{56}N_{15}LaO_9$	++++	+	−	+++
$C_{50}H_{56}N_{15}ErO_9$	++++	+++	++	−
$C_{50}H_{56}N_{15}GdO_9$	++++	++++	+	−
$C_{50}H_{56}N_{15}DyO_9$	++++	+++	−	−
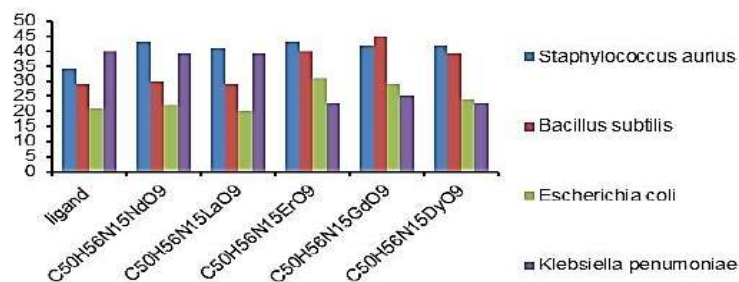
Fig 2. The chart shows the results of antibacterial biological activity of ligand and lanthanide complexes
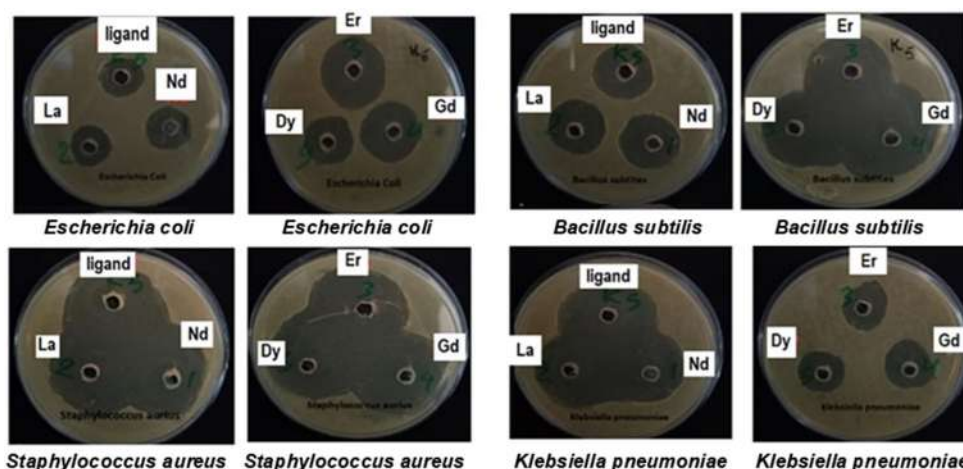
Fig 3. Biological activity of investigated compounds against *Escherichia coli, Klebsiella pneumoniae, Staphylococcus aureus*, and *Bacillus subtilis* for Schiff base ligand and its lanthanide complexes

1372

Indones. J. Chem., 2022, 22 (5), 1365 - 1375

more biologically active than the ligand due to the effect of the lanthanide elements, where the complexes showed more effective towards Gram-positive bacteria (*S. aureus*), followed by Gram-positive bacteria (*B. subtilis*), while Gram-negative bacteria show less activity than Gram-positive bacteria, especially (*E. coli*) where it shows less biological activity than (*K. pneumoniae*).

The created complexes are more efficient against Gram-positive bacteria (*S. aureus*). Gram-negative bacteria are more resistant due to the presence of a double membrane in each bacterial cell. Although all bacteria have an inner cell membrane, Gram-negative bacteria have a separate outer membrane. Some medicines and antibiotics are prevented from entering the cell by this outer layer [44]. Also, it turned out that the prepared compounds are antibacterial, positive, and negative for the Gram stain. We found that the prepared ligand is less effective than its complexes, and this is due to the small invasion that bacterial species show for such ions. The demise of bacterial species or the cessation of their growth can be through damage to the cell walls or prevention of the formation of the cell wall, or a decrease in the permeability of the cytoplasmic membranes, the physical and chemical composition of the protein, and nucleic acids in the cell, or cellular enzymatic activity, as well as through the prevention of manufacture of proteins and nucleic acids [45-47].

■ CONCLUSION

The Schiff-base ligand ((3a*E*,7*E*)-1,2,9,10-tetramethyl-3,8-diphenyl-3,5,6,8,9,11-hexahydro-2*H*-dipyrazolo[3,4-e:4',3'-h] [1,4]diazonine) obtained by condensation of 4,4-methyleneantipyrine with ethylenediamine and followed by the reaction with lanthanide(III) nitrate salts to form mononuclear complexes. The Schiff base ligand, on interaction with La^{+3}, Nd^{+3}, Er^{+3}, Gd^{+3}, and Dy^{+3}, yields compounds corresponding to the general formula $[Ln(L)_2(NO_3)_3]\cdot XH_2O$. $[Ln^{+3} = La, Nd, Er, Gd, and Dy, (X = 6, 5, 4)]$. The analytical data showed that the metal-to-ligand ratio of the complexes is 2:1. At room temperature, spectroscopic studies, element microanalysis CHNO, molar conductivity, and magnetic moment measurements

were used to describe these complexes. The compounds are crystalline complexes that disintegrate in four steps when heated in N_2 gas to 700 K. One of the results of thermal decomposition was that water is located outside the coordination field. As is the case in the structural complexes that were seen by four nitrogen atoms azomethine group and six oxygen from nitrate. The peaks of the infrared spectrum also support these findings. Furthermore, the thermal decomposition results support the assumptions we make about the complexes' structural features. The molecular ion peaks found in the ligand's mass spectra and peaks can be traced back to the products of possible ligand cleavage, which supports the structural formula of the ligand. There is no effect of the Schiff bases ligand on the 4f electrons of the lanthanide ions. The ligand and its metal complexes act as good effective biological activity using four types of bacteria which are two types of Gram-negative bacteria (*E. coli* and *K. pneumoniae*) and two Gram-positive bacteria (*S. aureus* and *B. subtilis*).

■ REFERENCES

[1] Paderni, D., Giorgi, L., Fusi, V., Formica, M., Ambrosi, G., and Micheloni, M., 2021, Chemical sensors for rare earth metal ions, *Coord. Chem. Rev.*, 429, 213639.

[2] Bünzli, J.C.G., 2014, Review: Lanthanide coordination chemistry: From old concepts to coordination polymers, *J. Coord. Chem.*, 67 (23-24), 3706–3733.

[3] Atwood, D.A., 2013, *The Rare Earth Elements: Fundamentals and Applications*, John Wiley & Sons, Hoboken, New Jersey, US.

[4] Alghool, S., Zoromba, M.S., and Abd El-Halim, H.F., 2013, Lanthanide amino acid Schiff base complexes: Synthesis, spectroscopic characterization, physical properties and *in vitro* antimicrobial studies, *J. Rare Earths*, 31 (7), 715–721.

[5] Chundawat, N.S., Jadoun, S., Zarrintaj, P., and Chauhan, N.P.S., 2021, Lanthanide complexes as anticancer agents: A review, *Polyhedron*, 207, 115387.

[6] Vernon, R.E., 2021, The location and composition of Group 3 of the periodic table, *Found. Chem.*, 23 (2), 155–197.

[7] Wedal, J.C., and Evans, W.J., 2021, A rare-earth metal retrospective to stimulate all fields, *J. Am. Chem. Soc.*, 143 (44), 18354–18367.

[8] Zasimov, P., Amidani, L., Retegan, M., Walter, O., Caciuffo, R., and Kvashnina, K.O., 2022, HERFD-XANES and RIXS Study on the electronic structure of trivalent lanthanides across a series of isostructural compounds, *Inorg. Chem.*, 61 (4), 1817–1830.

[9] Cotton, S., 2013, *Lanthanide and Actinide Chemistry*, John Wiley & Sons, Chichester, UK.

[10] Nehra, K., Dalal, A., Hooda, A., Bhagwan, S., Saini, R.K., Mari, B., Kumar, S., and Singh, D., 2022, Lanthanides β-diketonate complexes as energy-efficient emissive materials: A review, *J. Mol. Struct.*, 1249, 131531.

[11] Pari, G., Mookerjee, A., and Bhattacharya, A.K., 2005, First-principles electronic structure calculations of $R_3Al_5O_{12}$ (R being the rare-earth elements Ce–Lu), *Phys. B*, 365 (1-4), 163–172.

[12] Prats, H., and Stamatakis, M., 2022, Atomistic and electronic structure of metal clusters supported on transition metal carbides: Implications for catalysis, *J. Mater. Chem. A*, 10 (3), 1522–1534.

[13] Al-Qahtani, S.D., Alzahrani, S.O., Snari, R.M., Al-Ahmed, Z.A., Alkhamis, K., Alhasani, M., and El-Metwaly, N.M., 2022, Preparation of photoluminescent and photochromic smart glass window using sol-gel technique and lanthanides-activated aluminate phosphor, *Ceram. Int.*, 48 (12), 17489–17498.

[14] Malik, M.A., Dar, O.A., Gull, P., Wani, M.Y., and Hashmi, A.A., 2018, Heterocyclic Schiff base transition metal complexes in antimicrobial and anticancer chemotherapy, *MedChemComm*, 9 (3), 409–436.

[15] Patil, C.J., Patil, M.C., and Patil, M.C., 2019, Reduction of azomethine bond of organic compound: Part-2. Formation of aldimine and ketimine and their catalytic hydrogenation, *Int. J. Pharm. Biol. Arch.*, 10 (2), 134–137.

[16] Xu, Y., Shi, Y., Lei, F., and Dai, L., 2020, A novel and green cellulose-based Schiff base-Cu(II) complex and its excellent antibacterial activity, *Carbohydr. Polym.*, 230, 115671.

[17] Panda, J., Raiguru, B.P., Mishra, M., Mohapatra, S., and Nayak, S., 2022, Recent advances in the synthesis of imidazo[1,2-a]pyridines: A brief review, *ChemistrySelect*, 7 (3), e202103987.

[18] Soleimani, E., Taheri, S.A.N., and Sargolzaei, M., 2017, Synthesis, characterization, theoretical and biological studies of a new macrocycle Schiff base with Co(II), Ni(II), Cu(II) and Zn(II) complexes, *J. Chil. Chem. Soc.*, 62 (4), 3731–3740.

[19] Jirjees, V.Y., Suleman, V.T., Al-Hamdani, A.A., and Ahmed, S.D., 2019, Preparation, spectroscopic characterization and theoretical studies of transition metal complexes with 1-[(2-(1*H*-indol-3-yl)ethylimino)methyl]naphthalene-2-ol ligand, *Asian J. Chem.*, 31 (11), 2430–2438.

[20] Rasheed, A.M., Al-Bayati, S.M.M., Al-Hasani, R.A.M., and Shakir, M.A., 2021, Synthesizing, structuring, and characterizing bioactivities of Cr(III), La(III), and Ce(III) complexes with nitrogen, oxygen, and Sulpher donor bidentate Schiff base ligands, *Baghdad Sci. J.*, 18 (4), 1545–1551.

[21] Ajlouni, A.M., Abu-Salem, Q., Taha, Z.A., Hijazi, A.K., and Al Momani, W., 2016, Synthesis, characterization, biological activities and luminescent properties of lanthanide complexes with [2-thiophenecarboxylic acid, 2-(2-pyridinylmethylene)hydrazide] Schiff bases ligand, *J. Rare Earths*, 34 (10), 986–993.

[22] Al Zoubi, W., Mohamed, S.G., Al-Hamdani, A.A.S., Mahendradhany, A.P., and Ko, Y.G., 2018, Acyclic and cyclic imines and their metal complexes: Recent progress in biomaterials and corrosion applications, *RSC Adv.*, 8 (41), 23294–23318.

[23] El-Ansary, A.L., and Abdel-Kader, N.S., 2012, Synthesis, characterization of La(III), Nd(III), and Er(III) complexes with Schiff bases derived from benzopyran-4-one and thier fluorescence study, *Int. J. Inorg. Chem.*, 2012, 901415.

[24] Raczuk, E., Dmochowska, B., Samaszko-Fiertek, J., and Madaj, J., 2022, Different Schiff bases—Structure, importance and classification, *Molecules*, 27 (3), 787.

[25] Yusuf, T.L., Oladipo, S.D., Zamisa, S., Kumalo, H.M., Lawal, I.A., Lawal, M.M., and Mabuba, N., 2021, Design of new Schiff-base copper(II) complexes: Synthesis, crystal structures, DFT study, and binding potency toward cytochrome P450 3A4, *ACS Omega*, 6 (21), 13704–13718.

[26] Raman, N., Johnson Raja, S., and Sakthivel, A., 2009, Transition metal complexes with Schiff-base ligands: 4-Aminoantipyrine based derivatives–A review, *J. Coord. Chem.*, 62 (5), 691–709.

[27] Shaalan, N., Abed, A.Y., Alkubaisi, H.M., and Mahde, S., 2019, Synthesis, spectroscopy, biological activities and thermodynamic studies for new complexes of some lanthanide metals with Schiff's bases derived from [2-acetylth-iophene] with [2,5-dihydrazino-1,3,4-thiadiazole], *Res. J. Chem. Environ.*, 23, 181–187.

[28] Shaalan, N., Khalaf, W.M., and Mahdi, S., 2022, Preparation and characterization of new tetra-dentate N_2O_2 Schiff base with some of metal ions complexes, *Indones. J. Chem.*, 22 (1), 62–71.

[29] Shaalan, N.D., and Abdulwahhab, S.M., 2021, Synthesis, characterization and biological activity study of some new metal complexes with Schiff's bases derived from [*o*-vanillin] with [2-amino-5-(2-hydroxy-phenyl)-1,3,4-thiadiazole], *Egypt. J. Chem.*, 64 (8), 4059–4067.

[30] Martinez-Gomez, N.C., Vu, H.N., and Skovran, E., 2016, Lanthanide chemistry: From coordination in chemical complexes shaping our technology to coordination in enzymes shaping bacterial metabolism, *Inorg. Chem.*, 55 (20), 10083–10089.

[31] Akram, E., Shaalan, N., Rashad., A.A., Hasan, A., Al-Amiery, A., and Yousif, E., 2016, Study of structural and optical properties of new films derived PVC-2-[5-phenyl-1,3,4-thiadiazol-2-ylimino-methyl]-benzoic acid, *Res. J. Pharm., Biol. Chem. Sci.*, 7 (5), 2836–2844.

[32] Kareem, M.J., Al-Hamdani, A.A.S., Jirjees, V.Y., Khan, M.E., Allaf, A.W., and Al Zoubi, W., 2021, Preparation, spectroscopic study of Schiff base derived from dopamine and metal Ni(II), Pd(II), and Pt(IV) complexes, and activity determination as antioxidants, *J. Phys. Org. Chem.*, 34 (3), e4156.

[33] Obaid, S.M.H., Sultan, J.S., and Al-Hamdani, A.A.S., 2020, Synthesis, characterization and biological efficacies from some new dinuclear metal complexes for base 3-(3,4-dihydroxy-phenyl)-2-[(2-hydroxy-3-methylperoxy-benzylidene)-amino]-2-methyl propionic acid, *Indones. J. Chem.*, 20 (6), 1311–1322.

[34] Halli, M.B., and Sumathi, R.B., 2017, Synthesis, physico-chemical investigations and biological screening of metal (II) complexes with Schiff base derived from naphthofuran-2-carbohydrazide and citral, *Arabian J. Chem.*, 10, S1748–S1759.

[35] Sönmez, M., Sogukomerogullari, H.G., Öztemel, F., and Berber, İ., 2014, Synthesis and biological evaluation of a novel ONS tridentate Schiff base bearing pyrimidine ring and some metal complexes, *Med. Chem. Res.*, 23 (7), 3451–3457.

[36] Fouad, R., 2020, Synthesis and characterization of lanthanide complexes as potential therapeutic agents, *J. Coord. Chem.*, 73 (14), 2015–2028.

[37] Jawad, S.A.A., and Ahmed, H.A., 2021, Synthesis, characterization and study of amide ligand type N_2S_2 and metal complexes with di valance manganese, zinc and tri valance iron, *Ann. Rom. Soc. Cell Biol.*, 25 (3), 8511–8520.

[38] Kohale, R.L., Pawade, V.B., Dhoble, S.J., and Deshmukh, A.H., 2020, *Optical Properties of Phosphate and Pyrophosphate Compounds*, Woodhead Publishing, Sawston, UK.

[39] Al Zoubi, W., Kim, M.J., Yoon, D.K., Al-Hamdani, A.A.S., Kim, Y.G., and Ko, Y.G., 2020, Effect of organic compounds and rough inorganic layer formed by plasma electrolytic oxidation on photocatalytic performance, *J. Alloys Compd.*, 823, 153787.

[40] Hussein, K.A., and Shaalan, N., 2021, Synthesis, spectroscopy and biological activities studies for new complexes of some lanthanide metals with Schiff's bases derived from dimedone with 4-aminoantipyrine, *Chem. Methodol.*, 6 (2), 103–113.

[41] Satten, R.A., 1953, Analysis of the spectrum of the Nd^{+++} ion in the bromate crystal, *J. Chem. Phys.*, 21 (4), 637–648.

[42] Pallares, R.M., and Abergel, R.J., 2020, Transforming lanthanide and actinide chemistry with nanoparticles, *Nanoscale*, 12 (3), 1339–1348.

[43] Wanja, D.W., Mbuthia, P.G., Waruiru, R.M., Bebora, L.C., Ngowi, H.A., and Nyaga, P.N., 2020, Antibiotic and disinfectant susceptibility patterns of bacteria isolated from farmed fish in Kirinyaga county, Kenya, *Int. J. Microbiol.*, 2020, 8897338.

[44] Obaid, S.M., Jarad, A.J., and Al-Hamdani, A.A.S., 2020, Synthesis, characterization and biological activity of mixed ligand metal salts complexes with various ligands, *J. Phys.: Conf. Ser.*, 1660, 012028.

[45] Tavares, T.D., Antunes, J.C., Padrão, J., Ribeiro, A.I., Zille, A., Amorim, M.T.P., Ferreira, F., and Felgueiras, H.P., 2020, Activity of specialized biomolecules against gram-positive and gram-negative bacteria, *Antibiotics*, 9 (6), 314.

[46] Delcour, A.H., 2009, Outer membrane permeability and antibiotic resistance, *Biochim. Biophys. Acta, Proteins Proteomics*, 1794 (5), 808–816.

[47] Sherif, S.H., Kure, D.A., Moges, E.A., and Argaw, B., 2021, Synthesis, characterization, and antibacterial, activity, evaluation of 4-amino antipyrine derivatives and their transition metal complexes, *Am. J. Biosci. Bioeng.*, 9 (1), 8–12.

Supplementary Data

This supplementary data is a part of a paper entitled "Synthesis, Thermal Analysis, and Thermodynamic Properties Study of New Quinoline Derivative and Their V(IV), Co(II), and Cu(II) Complexes".

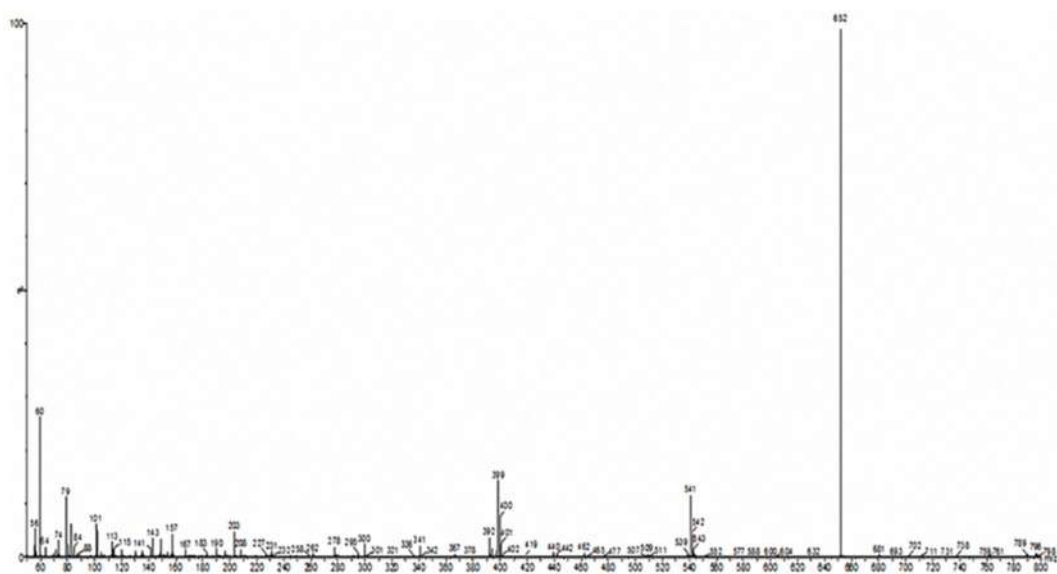**Fig S1.** ^{1}H-NMR spectra of QH

Fig S2. ^{13}C-NMR spectra of QH
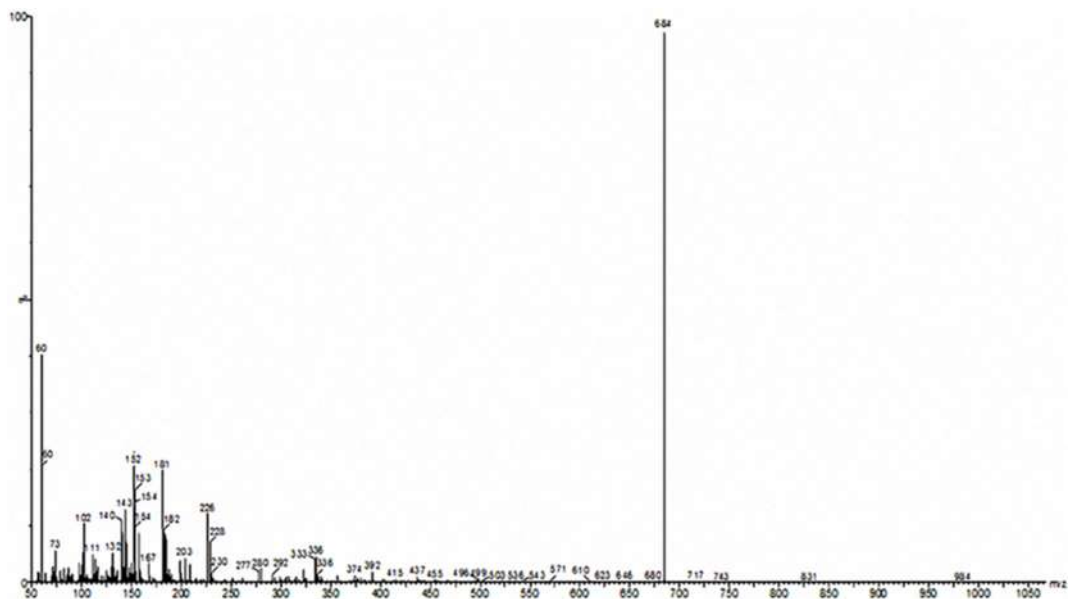
Fig S3. The Electrospray Ionization (ESI) spectra of the compound QCo

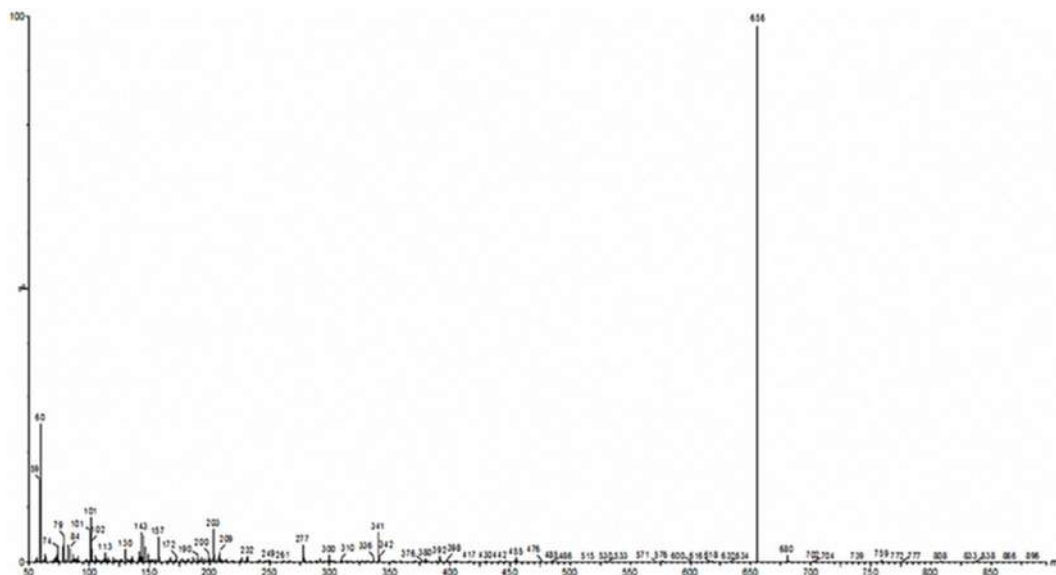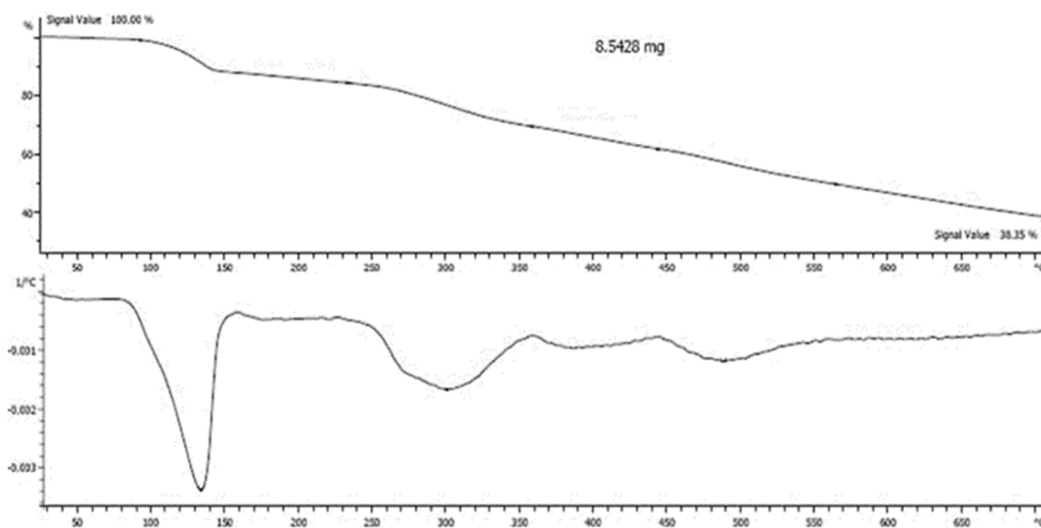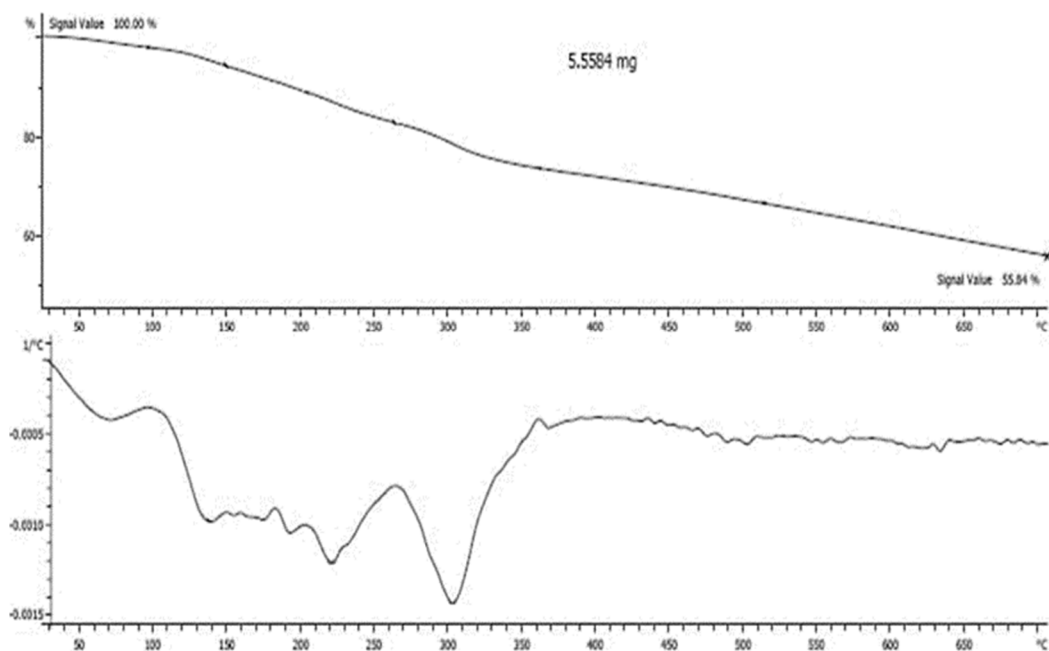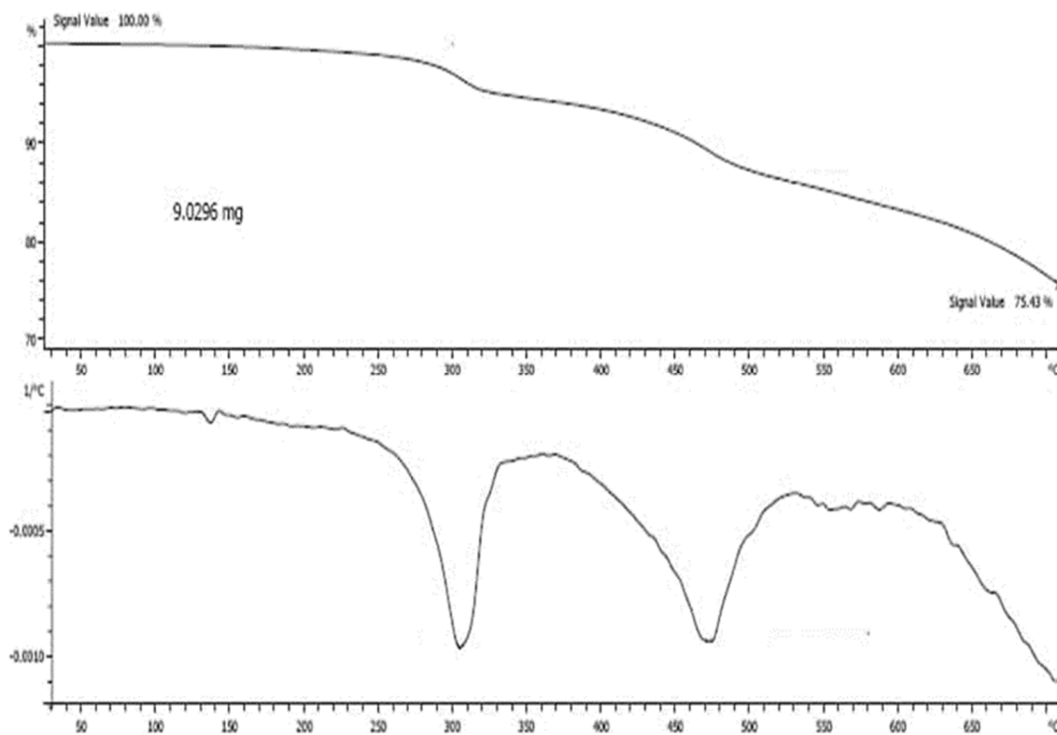**Fig S4.** The Electrospray Ionization (ESI) spectra of the compound QCu

Fig S5. The Electrospray Ionization (ESI) spectra of the compound QV

Fig S6. TG and DTG of the QCo complex

Fig S7. TG and DTG for the QCu complex

Fig S8. TG and DTG for the QV complex

Synthesis, Thermal Analysis, and Thermodynamic Properties Study of New Quinoline Derivative and Their V(IV), Co(II), and Cu(II) Complexes

Raghad Jawad Kadhim Aldoghachi[1], Faris Abdulridha Jassim Aldoghachi[2*], Tahseen Abdul Qader Alsalim[3], and Mohd Lokman Ibrahim[4]

[1]*Department of Pharmaceutical Chemistry, University of Basrah, 61004, Basrah, Iraq*

[2]*Department of Chemistry, Faculty of Science, University of Basrah, 61004, Basrah, Iraq*

[3]*Department of Chemistry, Faculty of Education, University of Basrah, 61004, Basrah, Iraq*

[4]*School of Chemistry and Environment, Faculty of Applied Sciences, Universiti Teknologi MARA, Shah Alam, Selangor 40450, Malaysia*

Abstract: *A new ligand (E)-2-((2-chloro-6-methylquinoline-3-yl)methylene)-N'-((E)-(2-chloro-6-methylquinoline-3-yl)methylene)hydrazine-1-carbothiohydrazide (QH) was prepared by reacting hydrazine hydrate with carbon disulfide to yield thiocarbohydrazide. The thiocarbohydrazide in the second step was treated with a quinoline derivative 2-chloro-6-methylquinoline-3-carbaldehyde to yield the ligand. The ligand was identified by spectroscopic techniques FTIR, ^{1}H-NMR, and ^{13}C-NMR. Next, vanadium (V), cobalt (Co), and copper (Cu) complexes were prepared in the [M:L] ratio of 1:1 (QV, QCo, QCu). The complexes were characterized using FTIR, ESI, magnetic susceptibility, and molar conductivity. The thermal analysis (TGA) of V(IV), Co(II), and Cu(II) complexes were studied. The activation thermodynamic parameters, such as the energy of activation, enthalpy, entropy, and free energy change of the complexes, were evaluated, and the stabilities of the thermal decomposition of the complexes were discussed.*

Keywords: *quinoline derivative; thiocarbohydrazide; metal complexes; thermodynamic parameters*

■ INTRODUCTION

Thiocarbohydrazide, $H_2N–NH–(C=S)–NH–NH_2$, is a promising unit for synthesizing new polyfunctional organic compounds following condensation with a ketone or an aldehyde. Both hydrazine groups of thiocarbohydrazide are very reactive and predominantly form bis-derivatives with aldehydes and ketones [1]. Although ligands with donor atoms, nitrogen, and oxygen, are by far the most thoroughly studied, interest in sulfur donor chelating agents has grown over time, and chemical studies in this area have increased significantly [2]. The coordination of a metal cation with a prepared ligand indicates that it has two azomethine nitrogen as donor atoms, which are the two terminal nitrogen atoms and, in most cases, the sulfur donor atom [3-4]. Interest in these ligand system complexes now includes numerous areas, ranging from general considerations of the effect of sulfur and electron delocalization in transition metal complexes to potential biological activity and practical application [5-7].

Thiocarbohydrazones are a class of vital compounds in the pharmaceutical and medical fields. They possess several biological activities based on their parent aldehyde or ketone moiety. Among their biological activities are antibacterial, anticancer, antifungal, anti-inflammatory, antimycobacterial, antioxidative, antituberculosis, and herbicidal activities. Furthermore, thiocarbohydrazones are utilized as starting materials in the synthesis of industrial and biological compounds with the potential of developing a new class of antileishmanial compounds

[8-10]. The fungicidal activity of thiocarbohydrazones has been tested on textile fabrics [11], and recently, the synthesis and investigation of a series of 2-acetylpyridine thiocarbohydrazones as inactivators of Herpes simplex virus-1 (HSV-1) ribonucleotide reductase showed better results compared to analogous 2-acetylpyridine thiosemicarbazone derivatives [12]. The antifungal and antimicrobial properties of thiosemicarbazones and their transition metal complexes have been studied widely. However, little is known about the biological properties of thiocarbohydrazones [13]. Hence, the purpose of the present work was to synthesize a new thiocarbohydrazone ligand and determine its transition metal complexes with V(IV), Co(II), and Cu(II) ions that can potentially function as an antiviral agent.

■ EXPERIMENTAL SECTION

Materials

The o-aminophenol, chloroform, sulfuric acid, and p-toluidine were purchased from BDH, UK. Dimethylformamide, cyclohexane, diethyl ether, ethanol, hexane sulfuric acid, and glacial acetic acid were purchased from Sigma-Aldrich, Germany. Carbon disulfide, vanadyl sulfate pentahydrate, acetic anhydride, 4-bromoaniline, copper dichloride hexahydrate, cobalt dichloride, and hexahydrate were purchased from Fluka, Switzerland. Hydrazine and phosphoryl chloride were purchased from Merck, Germany. Acetone and dioxane were purchased from Fischer, UK. All materials and reagents were used without further purification, following the manufacturer's protocol.

Instrumentation

The studied compounds' infrared spectra were measured using FTIR spectrophotometer model FTIR Affinity 1, as KBr disks at room temperature and a range of 4000–400 cm^{-1}. ^{1}H-NMR spectra of the studied compounds were scanned on a Bruker Vance 500 MHz spectrometer, whereas the ^{13}C-NMR spectra were scanned on 125 MHz. TMS, as the internal standard, was used as a reference to determine the 0.0 ppm. DMSO-d_6 was used as a solvent.

TGA studies were conducted using Mettler Toledo

with a 10 °C/min heat rate and a range of 0–700 °C. The Electrospray Ionization (ESI) of the compounds was measured by Waters Alliance 2695 HPLC-Micromass Quattro micro-API Mass Spectrometer.

The magnetic susceptibility of the complexes was measured at room temperature using the Gouy Method Model with a device manufactured from Auto Magnetic Susceptibility (Sherwood scientific). The correction factor for the prepared complexes was calculated using Pascal's constants for the atoms constituting the complexes. The molar conductivity of the complexes was measured using a conductivity device manufactured by a Switzerland company at a temperature of 25 °C using dimethylformamide (DMF) as a solvent at 1×10^{-3} M.

Procedure Preparation of the Ligand (QH)

Preparation of thiocarbohydrazide

Thiocarbohydrazide was prepared by adding (0.5 mol, 24 mL) of hydrazine hydrate to (75 mL) of distilled water in a flask. Next, (0.25 mol, 15 mL) of carbon bisulfide was added dropwise with continuous stirring for 1 h at room temperature. The mixture was then heated for 2 h, cooled in an ice bath, and filtered. The precipitate was recrystallized from water, with a yield of 95% (0.836 g), m.p. (171–174 °C) [14].

Synthesis of the ligand (E)-2-((2-chloro-6-methylquinoline-3-yl)methylene)-N'-((E)-(2-chloro-6-methylquinoline-3-yl)methylene)hydrazine-1-carbothiohydrazide (QH)

2-Chloro-6-methylquinoline-3-carbaldehyde (2.5 mmol) 0.5 g and (1 mmol) 0.106 g thiocarbohydrazide were mixed in a round flask with 10 mL ethanol and a few drops of acetic acid as catalyst. The mixture was heated with reflux for 2 h, and the reaction mixture was monitored by TLC using ethanol: chloroform (2:8 v/v). The mixture was cooled, filtered, dried, and recrystallized from dioxane [15]. The pale yellow powder was obtained with a yield of 75 % (0.879 g) m.p. (190–193 °C).

Synthesis of the complexes
Vanadyl complex: Diaqua [((E)-2-((2-chloro-6-methylquinoline-3-yl)methylene)-N'-((E)-(2-chloro-6-methylquinoline-3-yl)methylene)hydrazine-1-carbothiohydrazide)

Vanadium(IV) chloride] (QV). The vanadyl complex was prepared by reacting (1 mmol, 0.18 g) $VOSO_4 \cdot 5H_2O$ and (1 mmol, 0.481 g) of the ligand (QH) with 50 mL of dioxane followed by 2 h reflux to obtain the vanadyl complex QV filtrate. The filtrate was then washed twice with diethyl ether and dioxane to produce a dried brown powder with a yield of 90% (0.589 g).

Cobalt complex: Tetra-aqua ((E)-2-((2-chloro-6-methylquinoline-3-yl)methylene)-N'-((E)-(2-chloro-6-methylquinoline-3-yl)methylene)hydrazine-1-carbothiohydrazide) Cobalt(II) chloride (QCo). Cobalt complex was prepared by reacting (1 mmol, 0.237 g) cobalt chloride, $CoCl_2 \cdot 6H_2O$, and (1 mmol, 0.481 g) ligand (QH) with 50 mL Dioxane and reflux for 2 h to yield brown powder cobalt complex, the yield of 98% (0.670 g).

Copper complex: Diaqua ((E)-2-((2-chloro-6-methylquinoline-3-yl)methylene)-N'-((E)-(2-chloro-6-methylquinoline-3-yl)methylene)hydrazine-1-carbothiohydrazide) Copper(II) chloride (QCu). The copper complex was prepared by reacting (1 mmol, 0.170 g) of copper chloride, $CuCl_2 \cdot 2H_2O$, and (1 mmol, 0.481 g) of ligand (QH) with 50 mL dioxane and reflux for 2 h to yield dark green powder, the yield of 95% (0.618 g)

m.p. dec. < 250 °C. Table 1 lists the physical properties of the new complexes.

■ RESULTS AND DISCUSSION

The present study focused on the synthesis of transition metal complexes V(IV), Co(II), and Cu(II) with the ligand QH (Fig. 1). Scheme 1 demonstrates the synthesis path of ligand QH.
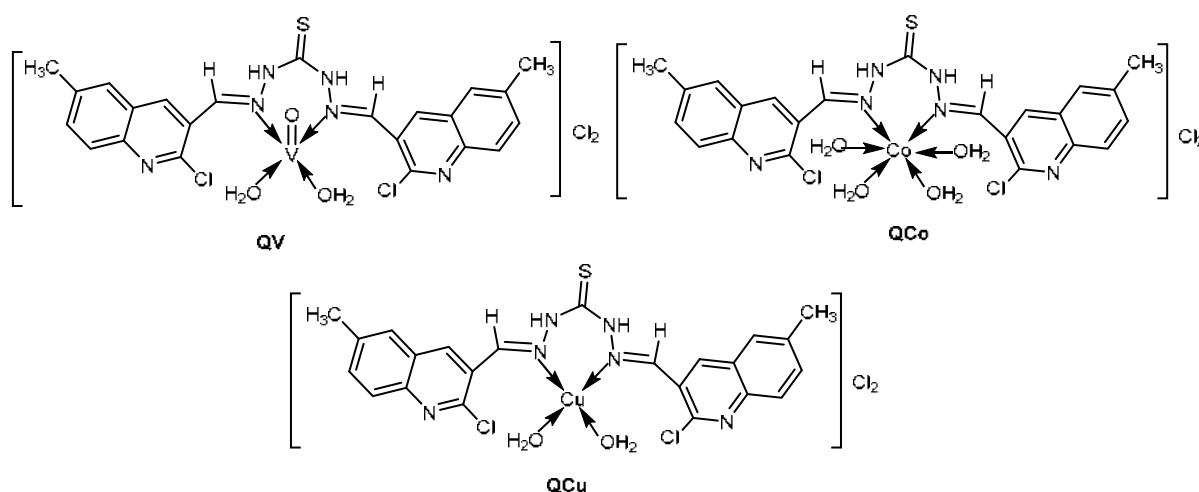
FTIR Spectra of the Complex (QV, QCo, and QCu)

The IR spectrum of the ligand (QH) displays the H-N group's stretching vibration band at 3450 cm^{-1} and stretching bands at 3051 and 2954 cm^{-1}, attributed to the aromatic and aliphatic C-H, respectively. The appearance of the stretching band at 1691 cm^{-1} was due to azomethine C=N. The band at wavenumber 1581 cm^{-1} was attributed to the stretching vibration of the aromatic C=C, whereas the band at 1303 cm^{-1} was due to the bending vibration of the C-N group. The band at 1176 cm^{-1} was attributed to C=S, as displayed in Table 2.

The FTIR spectra of the studied complexes are shown in Fig. 2, and the data is in Table 2. All the spectra

Table 1. Physical properties of the new complexes

Complex	Molecular formula	M.wt (g/mol)	Color	Yield (%)
QH	$C_{23}H_{18}Cl_2N_6S$	481.40	Yellow pale	75
QV	$C_{23}H_{18}Cl_2N_6SV$	655	Brown	90
QCo	$C_{23}H_{20}Cl_2CoN_6O_2S$	684	Brown	98
QCu	$C_{23}H_{18}Cl_2CuN_6S$	651	Dark green	95

Fig 1. Structure of complexes QV, QCo, and QCu

Indones. J. Chem., 2022, 22 (5), 1376 - 1385

1379
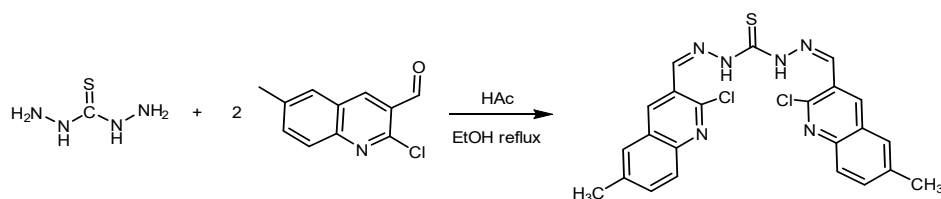
Scheme 1. The synthesis path of ligand OH

Table 2. IR spectra data of the complexes

Complex	Stretching									
	O-H	N-H	Ar-H	C-H	C=N	C=C	C-N	C=S	C-Cl	Other
QH	-----	3450	3051	2922	1691	1581	1303	1176	736	-----
QCu	3446	3358	3053	2926	1620	1558	1375	1195	823	N-Cu 561
QV	3421	3344	3051	2921	1614	1554	1333	1265	761	N-V 522
QCo	3400	3261	3060	2902	1656	1566	1377	1220	750	N-Co 550
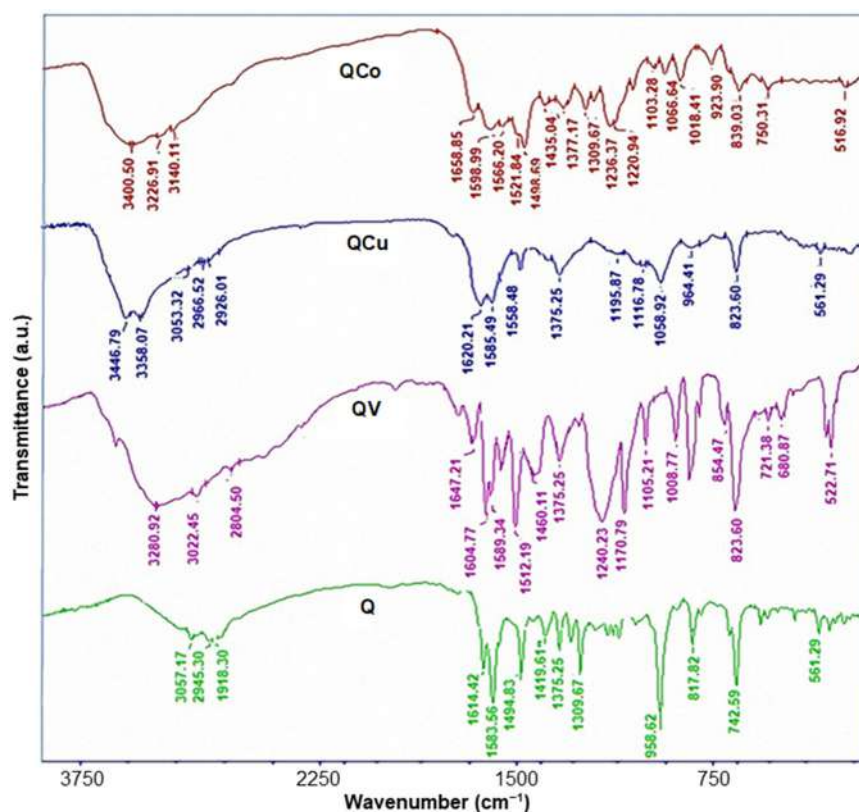
Fig 2. FTIR spectra of the ligands and their complexes

displayed bands of stretching vibration of the O-H group within the range of 3400–3446 cm^{-1}, whereas the bands of stretching vibration of the N-H group were observed in the region of 3261–3358 cm^{-1}. The stretching vibration band of the Ar C-H group was seen within the range of 3053–3060 cm^{-1}. Whereas those in the range of 2902–2926 cm^{-1} were due to the aliphatic C-H group. The bands

related to the C=N group were observed in 1614–1656 cm^{-1}. The IR spectrum of all complexes showed bands of stretching vibration of the C=C group within the range of 1554–1566 cm^{-1}, whereas the bands of C-N stretching vibration were seen in the range of 1333–1377 cm^{-1}. The bands related to the C=S group were observed in the range of 1195–1265 cm^{-1}, and the bands

1380

Indones. J. Chem., 2022, 22 (5), 1376 - 1385

of stretching vibration within the region of 750–823 cm^{-1} were attributed to the C-Cl group. As for the bonding of the ligands with transition metals, the bands showed a stretching vibration in the region of 522–561 cm^{-1} [16-17]. However, no broad band of stretching vibration of the O-H group was observed for the ligand QH, indicating the formation of complexes.

^{1}H-NMR and ^{13}C-NMR Spectrum of QH

The ^{1}H-NMR spectra of the synthesized ligand were recorded on a Bruker Avance 500 MHz spectrometer used to confirm the proposed structure of QH in DMSO-d_6, with tetramethylsilane (TMS) as the internal standard. The peaks at 2.5 and 3.3 ppm were attributed to DMSO and water solution, respectively [18]. The main peaks appear in Table 3 (Supplementary Fig. S1).

The ^{13}C-NMR spectrum of the new compound data is summarized in Table 4 (Supplementary Fig. S2). The spectra showed a heptate signal at 39 ppm due to the DMSO-d_6 solvent [19].

Magnetic Susceptibility

Magnetic susceptibility is one of the methods for single electrons used to study the complex's properties. Paramagnetic properties are obtained when the central atom contains single electrons, whereas diamagnetic properties are obtained when double electrons are present. This method is successfully implemented for studying the complex's geometry, shape, hybridization, and oxidation number [20].

The magnetic properties of complexes are due to the orbital and perchance motion. The theoretical magnetic moment of the first transition series of metal ions is defined by the following equation (Eq. (1)):

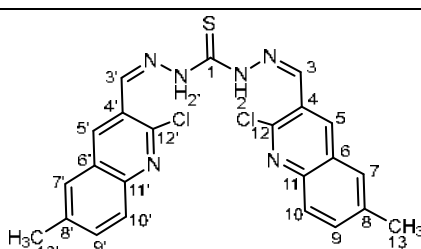$$\mu = \sqrt{4S(S+1)+(L+1)B.M}$$ (1)

Most of the paramagnetic materials consist of paramagnetic centers and diamagnetic groups. Hence, the obtained values for the magnetic susceptibility need to be corrected based on Pascal's constants to calculate the value of the correction factor (D) and reduce the error rate arising from the magnetic influences.

In this study, we relied on Faraday's method for forbidden complexes and the magnetic moment values were calculated based on the following equations:
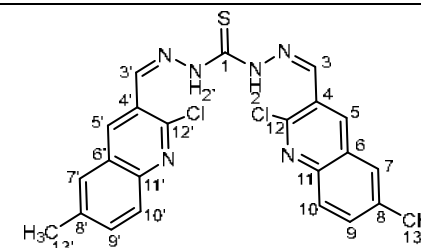
$$\mu_{eff} = 2.82 \times (X_A \times T)^{1/2}$$
$$X_A = X_m - (-D)$$ (2)
$$X_m = X_g * M$$

where X_g: weight susceptibility, M: molecular weight of the complex, X_m: molar susceptibility, X_A: atom's susceptibility,

Table 3. The ^{1}H-NMR data of the ligand QH

Structure	Chemical shift (ppm)
	(13.13') 2.43 (s, 6H, CH₃)
	(10.10') 7.30 (d, 2H, Ar-H)
	(9.9') 7.72 (d, 2H, Ar-H)
	(5,5') 7.80 (s, 2H, Ar-H)
	(7.7') 8.08 (s, 2H, Ar-H)
	(3.3') 8.64 (s, 2H, CH=N)
	(2.2') 10.96 (s, 2H, N-H)

Table 4. The ^{13}C-NMR data of the ligand QH

Structure	Chemical shift (ppm)
	169.3: C=N (C3, C3')
	151-149: C=N ring
	143-141: C-Cl, (C12, C12')
	134-121: Aromatic carbon
	21.06: CH₃, (C13, C13')

Table 5. Magnetic properties of the prepared complexes

Complex	$X_g * 10^{-4}$	X_M	X_A	$D * 10^{-6}$	μ_{eff} B.M
QCo	0.099	0.0067617	0.00692425	-162.65	4.09
QCu	0.018	0.001178	0.00130836	-136.56	1.78
QV	0.021	0.0013755	0.00151206	-136.56	1.9

D: diamagnetic correction, μ_{eff}: effective magnetic momentum, T: absolute temperature, X_g: given from the device by the practical measurement of the solid model

The magnetic moment calculated for the QCo was 4.09 M.B (Table 5), indicating a paramagnetic character due to the presence of three single electrons in the outer shell. The geometrical shape was octahedral due to the sp^3d^2 hybridization [21]. The complexes, QV and QCu, had a paramagnetic character due to the presence of one single electron in the outer shell. The value of the magnetic moment of the QCu demonstrated that the geometrical shape of the complex was a square planer due to the dsp^2 hybridization, while based on the value obtained for the QV, the geometrical shape was square pyramidal due to the dsp^3 hybridization [22].

Molar Conductivity

Molar conductivity is extensively used in the field of coordination chemistry to investigate the ionic formula of compounds in the solution when in the solid-state [23]. The greater number of ions released by the complex in the solution, the higher degree of molar conductivity. The complexes with low molar conductivity due to difficult ionization can be neglected. and can be calculated the conductivity by using the following relationship

$$\Lambda_m = \Lambda_\infty - K_c C^{1/2} \,(\text{mol}^{-1}.\text{cm}^2.\Omega^{-1}) \tag{3}$$

Λ_m: molar conductivity, Λ_∞: electrical conductivity at the final dilution

$$\Lambda = 10^3 \, K_c / C \tag{4}$$

Therefore, based on the values presented in Table 6, it was concluded that the solutions were electrolytes.

The Electrospray Ionization (ESI)

The soft ionization mass spectrum is a valuable instrument for obtaining the molecular structure of the molecules by the appearance of a molecular ion signal

Table 6. Molar conductivity of the complexes

Complex	Molar conductivity ($\text{mol}^{-1}.\text{cm}^2.\Omega^{-1}$)
QCo	140.8
QCu	93.38
QV	132.6

corresponding to the compound's molecular weight. The spectra data can be seen in Table 7 (Supplementary Fig. S3-5). The protonation ion of the analyst $[M+H]^+$ can normally be used to identify the molecular weight of the compound. Although fragmentation is possible due to ESI-MS experimental conditions, it yields less intense fragment ion peaks as compared to electron impact (EI). The ESI mass spectra of complexes gave a molecular ion peak equal to $[M+1]^+$. The mass spectra confirmed the proposed chemical structure of these complexes. As can be observed in Table 7, the molecular weight of QCo was 683, while the $[M+H]^+$ was 684. The molecular weight of the QCu was 651, while the $[M+H]^+$ was 652. The molecular weight of the QV was 655, while the $[M+H]^+$ was 656.

Thermal Analysis

Thermal analysis (TG and DTG) was utilized to determine the thermal stability of these complexes and to confirm whether water molecules were inside or outside the central metal ion's inner coordination sphere. The complexes were heated to 700 °C in a nitrogen environment at a rate of 10 °C/min for TG analysis. The mass losses calculated using TG curves were very close to the calculated values. All complex degradation paths, which differ from one to the next, confirm the postulated structures [7].

Table 8 represents the thermal breakdown data of the complexes and reveals that the complexes' remaining components were more stable [24]. The thermal curve of the QCo at the first stage of 90–150 °C represents the loss of water of crystallization molecules with a practical loss

1382

Indones. J. Chem., 2022, 22 (5), 1376 - 1385

Table 7. The ESI of the complexes

Complex	Structure	M.wt	[M+H]⁺
QV		655	656
QCo		683	684
QCu		651	652

Table 8. Thermogravimetric analysis of the prepared complexes

Complex	Decom. temp. (°C)			Char. content at 600 °C	Mass loss (%) theoretical	Assignment
	T_i	T_{max}	T_f			
QCo	90	133	150	38.35%	10.5 (10.7)	H_2O crystallization
	150	300	320		10.5 (10.6)	$4H_2O$ coordination
	320	420	600		40.35	Survival of parts of the ligand
QCu	100	140	170	55.84%	5.5 (5.51)	H_2O crystallization
	170	220	270		11 (10.4)	$2H_2O$ coordination
	270	300	600		25.15	Survival of parts of the ligand
QV	90	130	150	75.43%	5.49 (5.51)	H_2O crystallization
	150	305	350		10.98 (11.8)	$2H_2O$ coordination
	350	470	600		7.26	Survival of parts of the ligand

of 10.7% and a theoretical ratio of 10.5% (DTG$_{max}$ 133 °C). As for the second stage of 150–320 °C, which represents the loss of four molecules of coordinated water ($4H_2O$), the percentage of practical loss was 10.6%, the theoretical percentage was 10.5%, and the DTG$_{max}$ was at 300 °C. As for the third stage, which appears clearly in the spectrum of TG, DTG at 320–600 °C, the results revealed loss of parts of the ligand with a percentage of 40.35%, and the residual percentage was 38.35%, indicating the survival of parts of the ligand at the end of the stage, which exceeds the proportion of cobalt oxide (CoO) with a theoretical

ratio of 10.9%. The results show that the complex has high thermal stability and intensity of bonding of the ligand with the metal (Supplementary Fig. S6).

As for the QCu, the thermal analysis curve demonstrates several stages of loss. The first stage is represented by 100–170 °C (DTG$_{max}$ 140 °C), demonstrating a practical loss of 5.51% and a theoretical ratio of 5.5% (loss of crystallization water molecules). As for the second stage of 170–270 °C (DTG$_{max}$ 220 °C), the results revealed the loss of two molecules of coordinated water ($2H_2O$), and the third stage of 270–600 °C

(DTG$_{max}$ 300 °C) showed the loss of parts of the ligand with a percentage of loss of 25.15% and a residual percentage of 55.84%. This percentage exceeds the percentage of copper oxide (CuO) as we relate it to the theory (12.1%), and this explains the presence of organic parts of the ligand connected to the metal (Supplementary Fig. S7).

With regards to the QV, the thermal curve of the complex where the first stage starts from 90–150 °C (DTG$_{max}$ 130 °C) represents the loss of a molecule of crystallization water (H_2O), whereby the practical loss ratio was 5.51%, and the theoretical ratio was 5.49%. At the second stage of 150–350 °C (DTG$_{max}$ 305 °C), the practical loss ratio was 11.8%, and the theoretical ratio was 10.98%, representing the loss of a molecule of coordinated water ($2H_2O$). Furthermore, the third stage was clear in the spectrum (TG, DTG) at 350–600 °C (DTG$_{max}$ 470 °C) due to the loss of parts of ligand at a percentage of 7.26% with a residual ratio of 75.43%, indicating the survival of parts of the ligand at the end of the process which exceeded the percentage of vanadium oxide (VO_2) (theoretical part of 12.28%). This is explained by the fact that the complex has thermal stability and strong bonding of the ligand with the metal (Supplementary Fig. S8).

In summary, it is evident that the shapes of the proposed complexes were accurately correct, as demonstrated in the analyzed results. The mass spectrum revealed the proposed molecular weight of each complex, and the thermal analysis of the complexes demonstrated that they contain water of coordination, both according to their composition. Also, the molar conductivity showed that the complexes were ionic due to the presence of chlorine ions outside of the coordination sphere. The study of the magnetic susceptibility showed the hybridization and geometrical shapes of the molecules through the number of single electrons for each metal ion.

Calculation of the Thermodynamic Functions of the Prepared Complexes

The thermodynamic functions of the complexes prepared in this study were calculated in a range of different temperatures of 150–600 °C (Table 9). The data indicate a gradual increase in the values of stability constants at higher temperatures. The increase in the values of the stability constants in this study with the increase in temperature enabled us to study this interaction from a thermodynamic point of view, i.e., extracting the thermodynamic variables, each of which has a change in enthalpy (ΔH), a change in free energy (ΔG), and a change in entropy (ΔS), from the Coats-Redfern equation at all the temperatures mentioned above, represented by the Eq. (5) [25]:

$$\log\left[\frac{\log\frac{W_f}{W_f - W_t}}{T^2}\right] = \log\left[\frac{AR}{\theta E}\left(1 - \frac{2RT}{E}\right)\right] - \frac{E}{2.303RT} \quad (5)$$

where, W_f = weight loss at the end of stage; W_t = weight loss at temp (t); E = activation energy; A= constant; θ = constant; R = gas constant = 8.314 $M^{-1}.J^{-1}.K$; T = absolute temperature.

$$\Delta G = \Delta H - T\Delta S \quad (6)$$

After calculating the thermodynamic functions based on the above equation, what follows is evident. The negative ΔS values meant that all the processes took place at a low rate and that the activated complex was more ordered than either of the reactants. Furthermore,

Table 9. Kinetic parameters of the complexes using the Coats–Redfern equation

Complex	Stage	A (s^{-1})	E (kJ.mol^{-1})	ΔH (kJ.mol^{-1})	ΔS (kJ.mol^{-1}.K^{-1})	ΔG (kJ.mol^{-1})
QCo	I	2.19×10^4	6.25×10^1	59.12	-0.16	1.25×10^5
	II	5.20×10^{13}	1.52×10^{12}	147.20	0.01	1.54×10^2
QCu	I	2.18×10^5	5.97×10^1	56.79	-0.14	1.06×10^2
	II	7.21×10^{22}	1.20×10^2	196.38	0.19	-1.18×10^1
	III	8.51×10^9	1.19×10^2	114.45	-0.06	1.44×10^2
QVO	I	1.01×10^6	1.80×10^1	13.16	-0.14	9.12×10^1
	II	1.00×10^{11}	1.98×10^2	191.80	-0.04	2.23×10^2

the values of ΔH of activation were positive for all the complexes, indicating the endothermic nature of the process. In addition, all the ΔG values were positive, demonstrating that all steps were nonspontaneous (Table 9).

■ CONCLUSION

We have synthesized new V(IV), Co(II), and Cu(II) complexes with quinoline-thiocarbohydrizide ligands containing different steric and electronic properties in good yields. The new complexes have been well-characterized by FTIR, ^{1}H-NMR,^{13}C-NMR, ESI-MS, TGA, molar conductance, magnetic susceptibility, and calculating the thermodynamic function. The studied complexes were found to be more stable at 700 °C. Findings from this study provide insight into the potential role of the synthesized thiocarbohydrazone ligand and its transition metal complexes as potential virotherapy.

■ ACKNOWLEDGMENTS

■ AUTHOR CONTRIBUTIONS

Faris A.J. Aldoghachi and Tahseen A. Alsalim were involved in supervision, funding provision, conceiving the experimental design of the study, and reviewing and editing the manuscript. Raghad J.K. Aldoghachi was involved in conducting the experiment, data collection and analysis, and writing the manuscript. Mohd Lokman Ibrahim was involved in the provision of resources, analysis, and revision of the paper.

■ REFERENCES

[1] Kaya, Y., Erçağ, A., and Kaya, K., 2018, Synthesis, characterization and antioxidant activities of dioxomolybdenum(VI) complexes of new Schiff bases derived from substituted benzophenones, *J. Coord. Chem.*, 71 (20), 3364–3380.

[2] Kareem, M.J., Al-Hamdani, A.A.S., Ko, Y.G., Al Zoubi, W., and Mohammed, S.G., 2021, Synthesis, characterization, and determination antioxidant activities for new Schiff base complexes derived from 2-(1H-indol-3-yl)-ethylamine and metal ion complexes, *J. Mol. Struct.*, 1231, 129669.

[3] Burrows, A.D., Menzer, S., Mingos, D.M.P., White, A.J., and Williams, D.J., 1997, The influence of the chelate effect on supramolecular structure formation: Synthesis and crystal structures of zinc thiourea and thiosemicarbazide complexes with terephthalate, *J. Chem. Soc., Dalton Trans.*, 22, 4237–4240.

[4] Shaalan, N., Khalaf, W.M., and Mahdi, S., 2022, Preparation and characterization of new tetra-dentate N_2O_2 Schiff base with some of metal ions complexes, *Indones. J. Chem.*, 22 (1), 62–71.

[5] Al-Saadawy, N.H., 2022, Synthesis, characterization, and theoretical study of some new organotellurium compounds derived from camphor, *Indones. J. Chem.*, 22 (2), 437–445.

[6] Al-Saadawy, N.H., 2021, Synthesis, characterization, and theoretical studies of new organotellurium compounds based on (4-(((1S,E)-1,7,7-trimethylbicyclo[2.2.1]heptan-2-ylidene)amino) phenyl)mercury(II) chloride, *Indones. J. Chem.*, 21 (6), 1443–1453.

[7] Jirjees, V.Y., Al-Hamdani, A.A.S., Wannas, N.M., Farqad, A.R., Dib, A., and Al Zoubi, W., 2021, Spectroscopic characterization for new model from Schiff base and its complexes, *J. Phys. Org. Chem.*, 34 (4), e4169.

[8] Božić, A.R., Bjelogrlić, S.K., Novaković, I.T., Filipović, N.R., Petrović, P.M., Marinković, A.D., Todorović, T.R., and Cvijetić, I.N., 2018, Antimicrobial activity of thiocarbohydrazones: Experimental studies and alignment-independent 3D QSAR models, *ChemistrySelect*, 3 (7), 2215–2221.

[9] Božić, A., Marinković, A., Bjelogrlić, S., Todorović, T.R., Cvijetić, I.N., Novaković, I., Muller, C.D., and Filipović, N.R., 2016, Quinoline based mono-and bis-(thio)carbohydrazones: Synthesis, anticancer activity in 2D and 3D cancer and cancer stem cell models, *RSC Adv.*, 6 (106), 104763–104781.

[10] Mojallal-Tabatabaei, Z., Foroumadi, P., Toolabi, M., Goli, F., Moghimi, S., Kaboudanian-Ardestani, S., and Foroumadi, A., 2019, 2-(Bipiperidin-1-yl)-

5-(nitroaryl)-1,3,4-thiadiazoles: Synthesis, evaluation of *in vitro* leishmanicidal activity, and mechanism of action, *Bioorg. Med. Chem.*, 27 (16), 3682–3691.

[11] Neunhoeffer, H., and Wiley, P.F., 2009, *The Chemistry of Heterocyclic Compounds: Chemistry of 1,2,3-Triazines and 1,2,4-Triazines, Tetrazines, and Pentazin*, Vol. 33, Wiley-Interscience, Hoboken, US.

[12] Obaid, S.M.H., Sultan, J.S., and Al-Hamdani, A.A.S., 2020, Synthesis, characterization and biological efficacies from some new dinuclear metal complexes for base 3-(3,4-dihydroxy-phenyl)-2-[(2-hydroxy-3-methylperoxy-benzylidene)-amino]-2-methyl propionic acid, *Indones. J. Chem.*, 20 (6), 1311–1322.

[13] Shaalan, N., Abed, A.Y., Alkubaisi, H.M., and Mahde, S., 2019, Synthesis, spectroscopy, biological activities and thermodynamic studies for new complexes of some lanthanide metals with Schiff's bases derived from [2-acetylthiophene] with [2,5-dihydrazino-1,3,4-thiadiazole], *Res. J. Chem. Environ.*, 23, 181–187.

[14] Shaalan, N.D., and Abdulwahhab, S.M., 2021, Synthesis, characterization and biological activity study of some new metal complexes with Schiff's bases derived from [*o*-vanillin] with [2-amino-5-(2-hydroxy-phenyl)-1,3,4-thiadiazole], *Egypt. J. Chem.*, 8 (8), 4059–4067.

[15] Al-Obaidy, G., Ibraheem, K.R., and Mesher, M.F., 2020, Synthesis and characterization of some new Cu II, Co II, Ni II, Au III potassium 2-(2,4-dinitrophenyl) hydrazine-1-carbodithioate complexes and evaluation of their biological activity, *Int. J. Pharm. Res.*, 12 (1), 1025–1032.

[16] Obaid, S.M.H., Jarad, A.J., and Al-Hamdani, A.A.S., 2020, Synthesis, characterization and biological activity of mixed ligand metal salts complexes with various ligands, *J. Phys.: Conf. Ser.*, 1660, 012028.

[17] Abdulnabi, Z.A., Al-doghachi, F.A.J., and Abdulsahib, H.T., 2021, Synthesis, characterization and thermo gravimetric study of some metal complexes of

selenazone ligand nanoparticles analogue of dithizone, *Indones. J. Chem.*, 21 (5), 1231–1243.

[18] Deligeorgiev, T., Gadjev, N., Vasilev, A., Kaloyanova, S., Vaquero, J.J., and Alvarez-Builla, J., 2010, Green chemistry in organic synthesis, *Mini-Rev. Org. Chem.*, 7 (1), 44–53.

[19] Jasim, A.M., 2011, Preparation and characterization of novel 3-(4-chloro phenyl)-1-nitro phenyl-5-(substituted phenyl)-formazans, *J. Basrah Res.*, 37 (5), 90–98.

[20] Morrison, M.D., Hanthorn, J.J., and Pratt, D.A., 2009, Synthesis of pyrrolnitrin and related halogenated phenylpyrroles, *Org. Lett.*, 11 (5), 1051–1054.

[21] Tiekink, E.R.T., 2018, Competing supramolecular interactions in crystals of heavy-element compounds–a consideration of the energies of association between molecules, *2nd Southeast Asian Conference on Crystal Engineering (SEACCE-2)*, Sunway University, Selangor, August 6-8th, 2018.

[22] Alsalim, T.A., Hadi, J.S., Ali, O.N., Abbo, H.S., and Titinchi, S.J.J., 2013, Oxidation of benzoin catalyzed by oxovanadium (IV) Schiff base complexes, *Chem. Cent. J.*, 7 (1), 3.

[23] Zajdel, P., Partyka, A., Marciniec, K., Bojarski, A.J., Pawlowski, M., and Wesolowska, A., 2014, Quinoline- and isoquinoline-sulfonamide analogs of aripiprazole: Novel antipsychotic agents?, *Future Med. Chem.*, 6 (1), 57–75.

[24] Shim, J.O., Jeong, D.W., Jang, W.J., Jeon, K.W., Jeon, B.H., Kim, S.H., Roh, H.S., Na, J.G., Han, S.S., and Ko, C.H., 2016, Bio-diesel production from deoxygenation reaction over $Ce_{0.6}Zr_{0.4}O_2$ supported transition metal (Ni, Cu, Co, and Mo) catalysts, *J. Nanosci. Nanotechnol.*, 16 (5), 4587–4592.

[25] Ebrahimi, H.P., Hadi, J.S., Abdulnabi, Z.A., and Bolandnazar, Z., 2014, Spectroscopic, thermal analysis and DFT computational studies of salen-type Schiff base complexes, *Spectrochim. Acta, Part A*, 117, 485–492.

Characterization of Lignin Peroxidase from the Suspected Novel Strain *Phanerochaete chrysosporium* ITB Isolate

Evi Susanti[1,2*], Tri Ardyati[3], Suharjono Suharjono[3], and Aulani'am Aulani'am[4]

[1]*Department of Chemistry, Faculty of Mathematics and Natural Sciences, Universitas Negeri Malang, Jl. Semarang No. 5, Malang 65145, East Java, Indonesia*

[2]*Department of Biotechnology, Faculty of Mathematics and Natural Sciences, Universitas Negeri Malang, Jl. Semarang No. 5, Malang 65145, East Java, Indonesia*

[3]*Department of Biology, Faculty of Mathematics and Natural Sciences, Brawijaya University, Jl. Veteran, Malang 65145, East Java, Indonesia*

[4]*Department of Chemistry, Faculty of Mathematics and Natural Sciences, Brawijaya University, Jl. Veteran, Malang 65145, East Java, Indonesia*

Abstract: *This study was aimed to characterize lignin peroxidase (LiP) obtained from* Phanerochaete chrysosporium *ITB isolate. The characterizations included molecular weight, the pH and optimum working temperature of the crude extract of the enzyme, the temperature stability, the effect of metal ions and inhibitors, their precipitation with ethanol, and the storage stability. The LiP of* P. chrysosporium *ITB isolates was 34 kDa. The crude extract of LiP displays high activity at pH between 3 until 5 and 26–32 °C, has good thermal stability at 26–32 °C for 20 h. The activity is affected by Pb^{2+}, K^+, Co^{2+}, Fe^{2+}, Cd^{2+}, Mg^{2+}, and Cu^{2+} EDTA, Na^+, Cr^{3+}, Hg^{2+}, NaN_3, Ni^{2+}, and Ca^{2+} ions, is not affected by Mn^{2+} and Zn^{2+} ions, precipitated with the optimum ethanol at 64% ethanol saturation which results in an increase in specific activity of 2.3 times. The crude extract storage at 0 °C is more stable than the precipitate resulting from ethanol precipitation and resuspension from ethanol precipitation. These results strengthen that LiP from* P. chrysosporium *is another LiP isoenzyme that can be used for bioremediation processes. Unfortunately, the concentration using the ethanol precipitation method has not been effective, so further studies using other methods should be required.*

Keywords: *lignin peroxidase;* Phanerochaete chrysosporium*; ITB isolate; characterization*

■ INTRODUCTION

Phanerochaete chrysosporium is known to degrade lignin and various aromatic pollutants during secondary metabolism in the stationary phase. Peroxidases (manganese peroxidase and lignin peroxidase) and the extracellular H_2O_2-producing enzyme system of oxidase produced by these organisms are the main enzymes involved in the metabolism of lignin degradation, synthesized in response to the limited levels of nitrogen, carbon, and sulfur; also adopted various metabolic strategies to degrade complex polymeric substrates [1-5]. Many studies have shown that the type of strain and medium culture conditions affected the type of isoenzyme of LiP produced. *Phanerochaete chrysosporium* has multiple LiP-encoding genes and secretes the enzyme as numerous isozymes (H1, H2, H6, H7, H8, and H10), where H8 has been well characterized. It is an extracellular globular glycoprotein of approximately 343 amino acid residues with a molecular size of 38–42 kDa. Lignin peroxidases have unique properties, such as a low optimum pH of 3.0–4.5 and a theoretical isoelectric point (pI) of 3.3–4.7, depending on the isozyme [6]. However, LiP of *P. chrysosporium* Karnataka India isolates was 55 kDa [7].

Phanerochaete chrysosporium ITB isolate is a group of white rot fungus owned by the Microbiology Laboratory of the Bandung Institute of Technology since 1999. Although this strain has been widely used for various studies, such as improving the quality of pulp from kapok wood [8] and improving the quality of animal feed from lignocellulosic waste [9-10], neither its ligninolytic enzyme, especially LiP, has been investigated. In fact, the application of LiP in various industrial fields is intensively being developed, including for delignification of feedstock for ethanol production, textile effluent treatment, dye decolorization, coal depolymerization, treatment of hyperpigmentation, skin-lightening through melanin oxidation and catalytic elimination of pharmaceutical and endocrine-disrupting compounds [11-12].

The phylogenetic analysis using the ITS sequence showed that *P. chrysosporium* ITB isolate had the highest similarity of 99.6% with *P. chrysosporium* BKM-F-1767, RP78, PV1, KCTC 6728, SF-4, ATCC MYA-476, FCL208, FCL236, and Gold-9-419-4 and it was suspected as a new strain of *P. chrysosporium* [13]. This was reinforced by the fact that the ability of this strain to produce MnP lowest than LiP even in specific media for production MnP whereas *P. chrysosporium* BKMF-1767 (ATCC 24725), which had been widely studied, can generate MnP with high activity. On the other side, it was also known that the highest specific activity of LiP from *P. chrysosporium* ITB isolate in modified Kirk's medium containing sawdust 1% (w/v), ammonium sulfate 20 mM, Tween-80 0.025%, and veratryl alcohol 300 ppm in aqua demineralized, cultivated to 1×10^5 spore/mL, and were grown at 37 °C and 50 rpm for five days was 77.4 ± 13.1 U/mg [14]. The activity was high enough that this isolate had a high potential to be used as a source of LiP. It was essential to observe and determine the characteristics of the LiP enzyme from *P. chrysosporium* ITB isolate. The characterizations included molecular weight, the pH and the optimum working temperature of the crude extract of the enzyme, the temperature stability, the effect of metal ions and inhibitors, their precipitation with ethanol, and the storage stability.

■ EXPERIMENTAL SECTION

Materials

Chemicals used were of analytical grade, purchased from Merck including Tween-80, glasswool, KH_2PO_4, $MgSO_4 \cdot 7H_2O$, $CaCl_2$, $MgSO_4 \cdot 7H_2O$, NaCl, $FeSO_4 \cdot 7H_2O$, $CoCl_2$, $ZnSO_4 \cdot 7H_2O$, $CuSO_4 \cdot 5H_2O$, $AlK(SO_4)_2 \cdot 12H_2O$, nitriloacetate, thiamine-HCl, CH_3COOH, CH_3COONa, $(NH_4)_2SO_4$, veratryl alcohol, Tween-80, HCl, KCl, citric acid, sodium citrate, Folin Ciocalteu, NaCl, $MnSO_4$, Pb-acetate, $ZnSO_4$, $Cd(NO_3)_2$, $CaCl_2$, $HgCl_2$, $Cr(NO_3)_3$, EDTA, NaN_3, ethanol absolute, bovine serum albumin (BSA), $Na_3C_6H_5O_7 \cdot 2H_2O$, sodium carbonate, NaOH, K_2HPO_4, and KH_2PO_4. Potato dextrose agar was purchased from Difco, while the demineralized water and sawdust were obtained from a local brand.

Instrumentation

The equipment used in this study included glass apparatus, analytical balance (Precisa XT 120 A), thermo scientific water bath shaker incubator, vortex laboratory shaker (Dragon Lab MX-5), shaking water bath (Medfuture), soft incubator (Eyela SLI-600ND), drying oven (Memert UNB 400), autoclave (Tomy), universal indicator (Merck), amicon ultrafiltration, laminar airflow, microcentrifuge (Tomy MX-105), and magnetic stirrer (B -One). The used instrument for analysis was Vis 50 DA spectrophotometer.

Procedure

Production of crude extract of lignin peroxidase (LiP)

The *P. chrysosporium* ITB isolate was obtained from the Culture Collection of Microbiology Laboratory of Institut Teknologi Bandung, Indonesia. This strain was purified with monospore technique on potato dextrose agar (Difco) and was cultured on potato dextrose refers to [14]. As many as 1×10^6 spores/mL of suspension spore were inoculated to the production medium of LiP, were modified from Kirk's Medium (Basal medium 1 X, sawdust 1%, trace element solution 1 X, Thiamine-HCl 0.01%, 20 mM acetate buffer pH 4.5, ammonium sulfate 20 mM, Tween-80 0.025%, and veratryl alcohol 300 ppm in aqua demineralized), were

grown at 37 °C and 50 rpm for 5 d. The mixture was centrifuged at 10000 rpm at 4 °C for 10 min. The filtrate obtained was the crude extract of the LiP enzyme and was determined for its protein level and LiP activity. The protein levels were determined by referring to the Lowry assay [14].

Lignin peroxidase assay

Determination of the activity of the LiP enzyme in this experiment was carried out by a modified method referring to [3,14] as follows: 800 μL of 10 mM veratryl alcohol, 1,000 μL of 0.2 M tartaric acid, and 1,680 μL of aquaDM and 200 μL of enzyme solution were mixed in a test tube. The mixture was incubated for 2 min, and then the reaction was initiated by the addition of 320 μL H_2O_2 5 mM. The absorbance was measured at a wavelength of 310 nm at the 0th and 1st min. The activity of the LiP enzyme in this experiment was calculated using Eq. (1).

$$\text{Activity of LiP (U/mL)} = \frac{(At - Ao) \times V_{total}(mL).10^6}{\varepsilon_{max} \times d \times V_{enzym}(mL) \times t} \quad (1)$$

where ε_{max} = veraryl aldehyde molar extension coefficient (9300 M^{-1} cm^{-1}), d = cuvette width (1 cm), V_{total} = 4 mL, V_{enzym} = 0.2 mL, t = 1 min

Characterization of LiP peroxidase from **Phanerochaete chrysosporium** *ITB isolate*

The activity of the LiP enzyme was determined at various pH by replacing the tartaric acid in the LiP assay with 0.2 M HCl-KCl buffer (pH = 1 and 2), 0.2 M citrate buffer (pH = 3), 0.2 M acetate buffer (pH = 4 and 5), 0.2 M phosphate buffer (pH = 6 and 7).

The temperature was optimized at, 32, 38, 50 and 58 °C, whereas the other conditions were remained the same.

The thermal stability assay of LiP was carried out by incubating the crude extract of LiP for 0, 20, 24, and 30 h at various temperatures.

The effect of metal ions and inhibitor was observed by measuring the LiP activity in the reaction mixture containing 10 mM metal ions. The tested inhibitor that were K^+, Na^+, Mn^{2+}, Pb^{2+}, Zn^{2+}, Mg^{2+}, Cd^{2+}, Ca^{2+}, Hg^{2+}, Co^{2+}, Cu^{2+}, Fe^{2+}, Cr^{3+}, EDTA and NaN_3. The enzymes that were not added with metal ions and inhibitors were used as controls.

The thermal stability of the LiP enzyme was expressed as the relative activity of LiP or the activity remaining after incubation for the n th hour according to Eq. (2).

Relative activity of LiP (%)

$$= \frac{\text{LiP activity at } n - \text{hour}}{\text{LiP activity at 0}} \times 100\% \quad (2)$$

The effect of metal ions and inhibitors on the activity of the LiP enzyme was expressed as the relative activity of LiP which was determined using Eq. (3).

Relative activity LiP (%)

$$= \frac{\text{Activity of LiP with addition compounds}}{\text{Activity LiP as control}} \times 100\% \quad (3)$$

The crude extract was precipitated by adding ethanol until the ethanol saturation was 33, 50, 55, 60, 64, and 67%. The mixture was stored in the refrigerator (4 °C) overnight. The mixture was centrifuged at 0 °C at 10000 rpm for 30 min. The pellets obtained were air-dried at room temperature for 2 h and resuspended in 1.5 mL acetate buffer pH 4.5 for approximately 3 h. Each measured protein content, LiP activity, and storage stability for 0, 2, 9, 16, and 23 days at 0 °C. The protein profile of each treatment was traced by SDS-PAGE to identify the molecular weight of LiP.

Data analysis

All treatments were repeated in triplicate. The results were expressed as mean ± standard deviation of three repetitions. The statistical analysis was conducted using the Statistical Package for The Social Science (SPSS) v.16 software. The one-way analysis of variance (ANOVA) followed by Tukey's HSD test was used to determine the real difference from each variation. The differences at $p < 0.05$ were considered statistically significant.

■ RESULTS AND DISCUSSION

Optimum pH of LiP from *P. chrysosporium* ITB Isolate

The results showed that the LiP of *P. chrysosporium* ITB isolate was affected by the pH of the reaction (the farther away the alphabetical differences are, the more significant the difference due to the treatment). At very acidic pH (pH 1.0), the activity was low. The activity was

increased with increasing of the reaction pH until it reached pH 5.0. However, the LiP activity dramatically decreased at pH 6, and no LiP enzyme activity was detected at pH = 7 and 8 (Fig. 1). The optimum pH value for the oxidation reaction of veratryl alcohol by LiP from *P. chrysosporium* ITB isolate was in the pH range of 3–5 because the high activity of the LiP enzyme at this pH range did not statistically differ. These results were in line with previous studies, which stated that the most dominant LiP isoenzyme, LiPH8, from *P. chrysosporium* BKMF-1767 wildtype, had the highest catalytic ability at pH 3.0, and low at pH < 3.0, but differed at pH 4.0 and 5.0 [15]. In that study, the activity of LiPH8 at pH 4.0 and 5.0 tended to decrease although was still considered stable, while in this study, it tended to increase. This study was in line with the purified LiP of immobilized *P. chrysosporium* Indian Karnataka isolate, which has high activity at pH 3.0 and was still stable up to pH 5.0, then decreased at high pH [7]. The high activity of LiP at low pH was in line with the computational studies showing that at low pH, the heme redox potential value of LiP was higher so that LiP can oxidize veratryl alcohol at that pH [15]. Based on this comparison, LiP from *P. chrysosporium* ITB isolates offered the advantage that the crude extract had a fairly wide pH working range of 3.0 to 5.0.

The Optimum Temperature of LiP from *P. chrysosporium* ITB Isolate

Temperature is a factor that greatly affects enzyme activity. Certain temperatures (generally more than 40 °C) can change the conformation of the three-dimensional structure of the enzyme because the heat breaks some of the noncovalent bonds that stabilize the three-dimensional structure of the enzyme [16]. The LiP enzyme from *P. chrysosporium* ITB isolates had high activity and did not differ significantly at 26 and 32 °C, while at temperatures higher than 32 °C the activity of the LiP enzyme decreased, as shown in Fig. 2. These results were not in line with the optimum temperature of LiP production [14]. The production of LiP at 37 °C was much higher than at 30 °C.
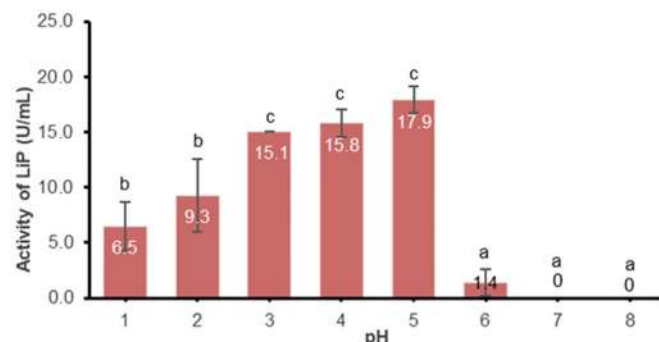
Fig 1. LiP activity at various pH of enzymatic reactions (the farther away the alphabetical differences are, the more significant the difference due to the treatment)
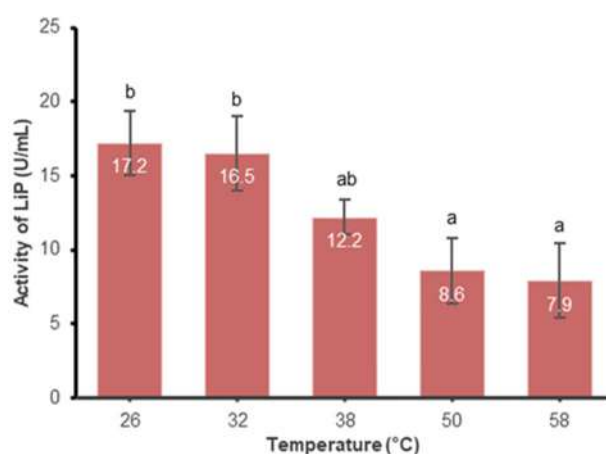
Fig 2. LiP activity at various temperatures of enzymatic reactions

On the contrary, these results showed that the activity of the LiP enzyme decreased at 38 °C, indicating that the growth temperature for LiP enzyme production did not automatically reflect the optimum reaction temperature carried out by the LiP enzyme. However, the results of this study were in line with the optimum reaction temperature of LiP enzymes from various other fungi, namely *P. chrysosporium* ATCC-24725 (26 °C), *Penicillium citrinum* (30 °C), *Gloeophyllum sepiarium* (25 °C), and *Pycnoporus sanguineus* (25 °C) as summarized in [17], also in line with [2] and [7] which stated that the LiP enzyme from *P. chrysosporium* BKM-F-1767 and *P. chrysosporium* Karnataka India isolate had optimum activity at 30 °C.

Thermal Stability of LiP from *P. chrysosporium* ITB Isolate

The thermal stability profile of LiP from *P. chrysosporium* ITB isolate was shown in Fig. 3. The LiP enzyme was stable at 26 and 32 °C after 20 h of incubation and decreased slightly after 24 and 30 h of incubation. The thermal stability of the enzyme at a temperature of more than 32 °C decreased by varying degrees after 20, 24, and 30 h of incubation. The LiP enzyme activity after incubation for 20, 24, and 30 h at the highest temperature of 58 °C still displayed the activity of 58, 53, and 42%, respectively, indicating that LiP from *P. chrysosporium* isolate ITB was a moderate thermostable enzyme. The results were better than the LiP enzyme from *P. chrysosporium* BKMF-1767, which had an activity of only 38% after 24 h of incubation at 60 °C [2], and much better than the purified LiP from *P. pulmonarius*, where the activity became 25 and 20% after 2 h incubation at 40 and 60 °C [18].

Effect of Metal Ions and Inhibitors on LiP from *P. chrysosporium* ITB Isolates

Lignin peroxidase (LiP) is expected to be applied for the bioremediation of xenobiotic compounds in the environment. The waste in the environment certainly contains various metal ions and some enzyme inhibitors. Actually, it is necessary to have information about the effect of these compounds, which may also be present in the waste, on LiP activity. The results obtained indicated that the data distribution was not normal because the significance value is < 0.05. Therefore, the Kruskal Wallis test was performed. The results of the analysis showed that the addition of metal ions and inhibitors affected the decolorization ability of the LiP enzyme. The Pb^{2+} ion eliminated the activity of the LiP enzyme; EDTA, Na^+, Cr^{3+}, and Hg^{2+} ions decreased LiP enzyme activity to less than 40%; K^+, Co^{2+}, Fe^{2+}, Cd^{2+}, Mg^{2+}, and Cu^{2+} ions decreased the activity of the LiP enzyme to 78–90%; Mn^{2+} and Zn^{2+} ions did not affect LiP enzyme activity, while Ni^{2+}, NaN_3, and Ca^{2+} ions increased LiP enzyme activity (Fig. 4). These results were similar to those [2] in the case that Ca^{2+} ions increased LiP activity and Hg^{2+}, K^+, Fe^{2+}, and Mg^{2+} ions decreased LiP activity, while Na^+ and Co^{2+} ions in this study increased LiP activity. These results were also in line with [18] in case of K^+, Na^+, Hg^{2+}, Mn^{2+}, and Zn^{2+} ions, but opposite to the effect of Fe^{2+}, EDTA, Cu^{2+}, and Mg^{2+} [18]. These results were presumably because the LiP isoenzyme produced in this experiment was different from the LiP isoenzyme. The LiP enzyme had a protoporphyrin heme group at its active center, so it was suspected that the presence of other metal ions affected the stability of the Fe^{2+} ion in the heme group. The stability of the heme group greatly affected the activity of LiP.

Fractionation Profile of Crude Extract of LiP Enzyme from *P. chrysosporium* ITB Isolate with Ethanol Precipitation

Although the crude extract of the LiP enzyme has a relatively high specific activity (± 77 U/mg) but the protein content is very low (± 150 ug/mL). Concentration
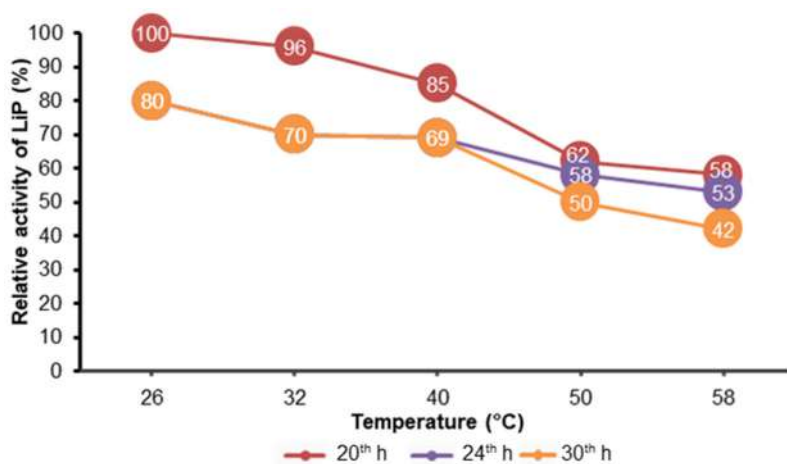

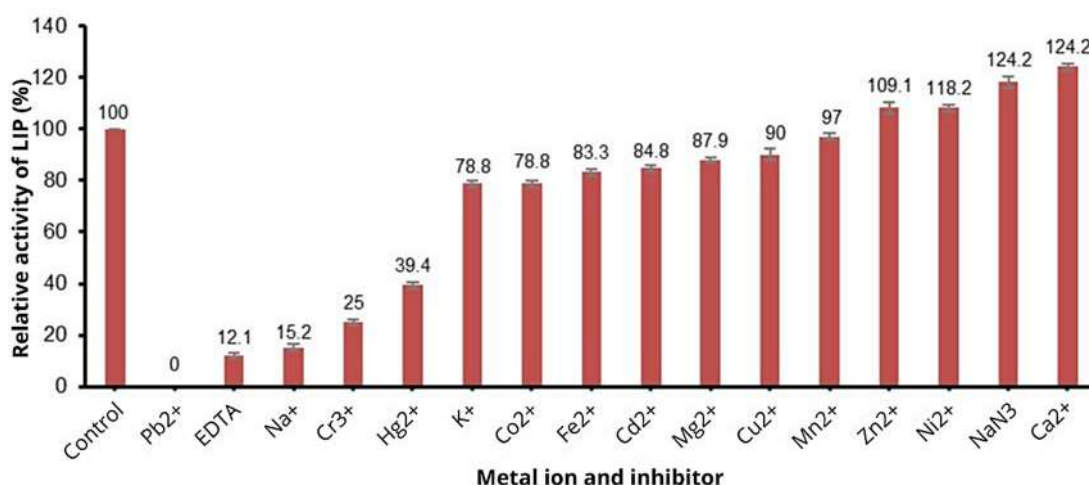**Fig 3.** Thermal stability of LiP from *P. chrysosporium* ITB isolate

Fig 4. The effect of metals ion and inhibitor on LiP of *P. chrysosporium* ITB isolate

of the sample will reduce the volume of the sample, making it easier for packaging and storage. Concentration is the first step in enzyme purification as an effort to increase enzyme activity and stability, and it is also required for molecular analysis of enzymes such as SDS-PAGE. The addition of organic solvents will reduce the interaction between proteins and water molecules because water will immediately surround the organic solvent molecules through hydrogen bonds. This situation encourages electrostatic interactions between protein molecules so that they form aggregations and precipitate [19].

In this study, it appeared that the concentration of the added ethanol affected the deposition of the LiP, which was indicated by changes in the specific activity value of LiP produced at each concentration of ethanol used (Fig. 5). The greater the concentration of ethanol added, the higher the specific activity of LiP produced because more LiP enzymes were deposited. Although the use of ethanol at concentrations of 55, 60, 64, and 67% did not statistically and significantly affected the value of specific LiP activity, the use of 64% ethanol produced the highest specific activity value of LiP. Under these conditions, from five milliliters of the sample, which has a specific activity of 48.36 U/mg, precipitated with 64% ethanol, then the precipitate obtained was resuspended in 1.5 mL of acetate buffer pH 5.0, the specific activity of LiP was 112.82 U/mg on average. It indicated that there was a volume concentration of 3.3 times and an increase in specific activity of 2.3 times.

The storage stability test was carried out on three samples of LiP enzyme, namely LiP enzyme in the form
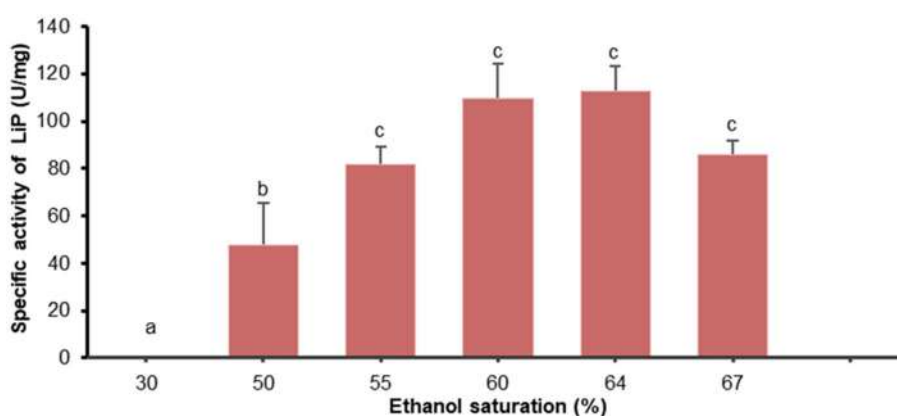
Fig 5. Effect of ethanol concentration on crude extract fractionation of LiP with ethanol precipitation method

of crude extract of LiP, resuspension of ethanol fractionated precipitate, and ethanol fractionated precipitate, which were stored at 0 °C. On day of 0, 2, 9, 16, and 23, each sample was placed at room temperature, allowed to melt, and the activity of the LiP enzyme was measured. The timing was chosen to observe the stability of the enzyme in short (2 d), medium (8 and 16 d), and long-term (23 d) storage. So far, no similar research had been found, whereas for large-scale applications, information on enzyme stability during storage was very necessary. Fig. 6 shows the crude extract has the best enzyme stability compared to the precipitate resulting from the fractionation of ethanol and the resuspension of the precipitate from the fractionated ethanol. The crude extract had LiP enzyme activity which remained high until the 23rd day. At the same time, the ethanol fractionated precipitate started to gradually decrease since the 9th day, and the resuspension of the ethanol fractionated precipitate experienced a sharp decrease in LiP enzyme activity since the 2nd day and lost its activity on the 16th day of storage. The decreased activity of the LiP in the ethanol fractionated precipitate and the loss of LiP enzyme activity in the resuspension of the ethanol fractionated precipitate during storage at 0 °C were unexpected results. This was presumably because, during the deposition process with ethanol, there was a change in the dielectric constant of the medium, which led to changes in protein conformation so that the structure was

less stable. Before being stored, the precipitate resuspended in acetate buffer pH 5.0 might experience a change in the dielectric constant of the medium. It allowed a change in protein conformation again so that when the sample was thawed or subjected to freeze-thaw, it triggers denaturation so that the enzymes in the sample lose their activity. Buffering in protein solution will result in dramatic changes in pH during the freezing process, which can result in protein denaturation [20]. The LiP enzyme in the precipitate resuspended in acetate buffer pH 5.0 was not only denatured due to conformational changes due to changes in the dielectric constant of the medium but it was also thought to be due to drastic changes in pH during freezing so that there was no LiP activity after 16 d of storage. On the other hand, the crude enzyme extract sample remained stable because denaturation did not occur before and during the freezing process at 0 °C, so when the sample was thawed, the LiP activity remained high. Therefore, it was suggested that it was not necessary to concentrate the sample with ethanol precipitation methods, to maintain the stability and activity of the crude extract of the LiP from *P. chrysosporium* ITB isolates. However, this suggestion should be further studied, considering that the higher the concentration of purified protein, the higher its stability of protein. Unfortunately, there was no similar research that can be used as a comparison. Recent studies have used the filtration method at the
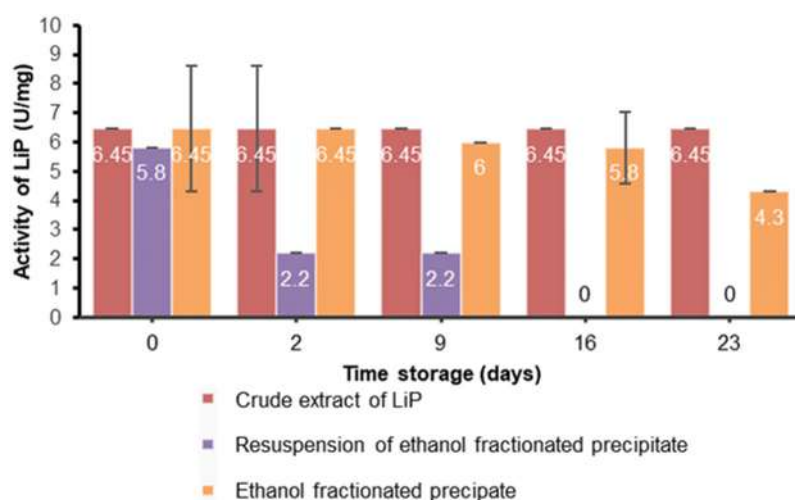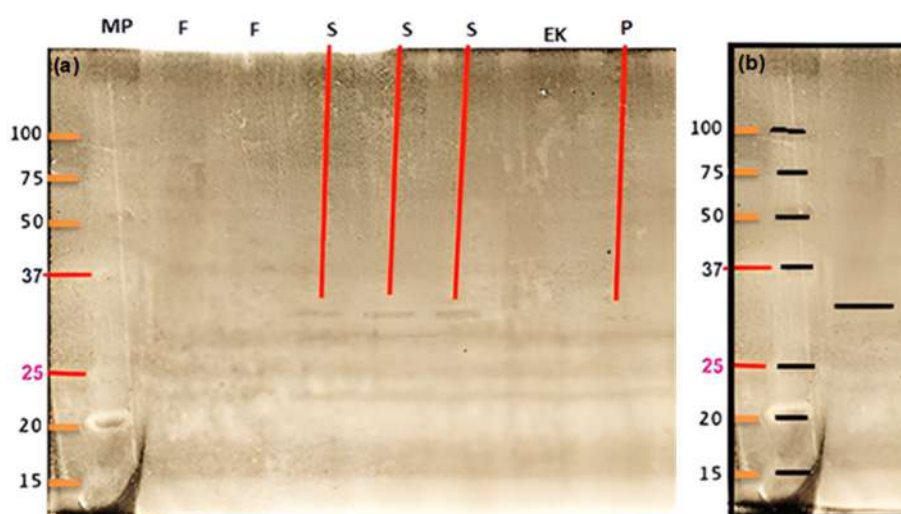

Fig 6. Stability of the storage of LiP

Fig 7. SDS-PAGE profile of LiP enzymes from *P. chrysosporium* ITB isolate. Electropherogram photo from SDS-PAGE with MP: standard protein, F: filtrate before ultrafiltration, S: filtrate from ultrafiltration, EK: crude extract of LiP enzyme, P: result of concentration with ethanol fraction (a). Illustration of LiP enzyme band versus standard protein band (b)

stage of concentration of crude LiP extract [18]. The use of this method minimized the occurrence of denaturation due to changes in the dielectric constant of the medium as happened in this study. But the ultrafiltration technique was still quite expensive for large-scale enzyme purification.

The Molecular Size of LiP from *P. chrysosporium* ITB Isolate

Electropherogram of SDS-PAGE shows that the MP well (which were the standard protein bands used, ranging from 15 kDa to 100 kDa), the F well (containing the filtrate before ultrafiltration) and the EK well (containing the crude extract of the LiP enzyme) did not show any bands, while the S well (containing the filtrate from ultrafiltration) and the P well (as the result of concentration by ethanol fractionation) showed a thin band measuring ± 34 kDa. This band was suspected to be the LiP enzyme because both the filtrate and the ethanol fractionation results showed LiP activity. Although the crude extract measured the activity of the LiP enzyme, there was no visible bands because the concentration was too small. These results were slightly different from previous studies. The pure LiP enzymes from *P. chrysosporium* ATCC 20696, namely LiP1 and LiP2 measuring 38 and 40 kDa [21], displayed three bands measuring between 35–45 kD in the extracellular protein of *P. chrysosporium* RP28, which was

thought to be an H1-ligninase isoenzyme. The H5 LiP isoenzyme [22] and the pure LiP enzyme from *P. chrysosporium* BKMF-1767 measuring at 36 kDa [2]. This confirmed that *P. chrysosporium* isolate ITB was a different strain from the previous *P. chrysosporium* strains, namely *P. chrysosporium* ATCC 20696, *P. chrysosporium* RP28, and *P. chrysosporium* BKMF-1767.

■ CONCLUSION

The LiP was suspected to be a LiP isoenzyme with a molecular weight of 34 kDa. The crude extract of LiP displayed high activity at pH 3–5, at 26–32 °C, had good thermal stability at 26–32 °C as long as 20 h. The activity was lost due to the presence of Pb^{2+} ion, decreased to 78–90% due to K^+, Co^{2+}, Fe^{2+}, Cd^{2+}, Mg^{2+}, and Cu^{2+} ions, decreased to less than 40% due to EDTA, Na^+, Cr^{3+}, and Hg^{2+} ions, was not affected by Mn^{2+} and Zn^{2+} ions, but increased in the presence of NaN_3, Ni^{2+}, and Ca^{2+} ions. The crude extract precipitated with the optimum ethanol at 64% ethanol saturation which resulted in an increase in specific activity of 2.3 times. The storage of the crude at 0 °C was more stable than the precipitate resulting from ethanol precipitation and resuspension from ethanol precipitation. With these characteristics, the crude extract of LiP from *P. chrysosporium* ITB isolate has good potential to be used as industrial enzymes.

■ **AUTHOR CONTRIBUTIONS**

The authors confirm contribution to the paper as follows: study conception, design, data collection and draft manuscript preparation: ES; analysis and interpretation of data: ES and A. All authors reviewed the results and approved the final version of the manuscript.

■ **REFERENCES**

[1] Khatoon, N., Jamal, A., and Ali, M.I., 2019, Lignin peroxidase isoenzyme: A novel approach to biodegrade the toxic synthetic polymer waste, *Environ. Technol.*, 40 (11), 1366–1375.

[2] Zeng, G.M., Zhao, M.H., Huang, D.L., Lai, C., Huang, C., Wei, Z., Xu, P., Li, N.J., Zhang, C., Li, F.L., and Cheng, M., 2013, Purification and biochemical characterization of two extracellular peroxidases from *Phanerochaete chrysosporium* responsible for lignin biodegradation, *Int. Biodeterior. Biodegrad.*, 85, 166–172.

[3] Coconi-Linares, N., Magaña-Ortíz, D., Guzmán-Ortiz, D.A., Fernández, F., Loske, A.M., and Gómez-Lim., M.A., 2014, High-yield production of manganese peroxidase, lignin peroxidase, and versatile peroxidase in *Phanerochaete chrysosporium*, *Appl. Microbiol. Biotechnol.*, 98 (22), 9283–9294.

[4] Matityahu, A., Sitruk, A., Hadar, Y., and Belinky, P.A., 2015, Factors affecting the induction of lignin peroxidase in manganese-deficient cultures of the white rot fungus *Phanerochaete chrysosporium*, *Adv. Microbiol.*, 5 (2), 83–92.

[5] da Silva Vilar, D., Bilal, M., Bharagava, R.N., Kumar, A., Kumar Nadda, A., Salazar-Banda, G.R., Eguiluz, K.I.B., and Romanholo Ferreira, L.F., 2022, Lignin-modifying enzymes: A green and environmental responsive technology for organic compound degradation, *J. Chem. Technol. Biotechnol.*, 97 (2), 327–342.

[6] Biko, O.D., Viljoen-Bloom, M., and van Zyl, W.H., 2020, Microbial lignin peroxidases: Applications, production challenges and future perspectives, *Enzyme Microb. Technol.*, 141, 109669.

[7] Vandana, T., Kumar, S.A., Swaraj, S., and Manpal, S., 2019, Purification, characterization, and biodelignification potential of lignin peroxidase from Immobilized *Phanerochaete chrysosporium*, *BioResources*, 14 (3), 5380–5399.

[8] Istikowati, W.T., and Marsoemb, S.N., 2012, *Phanerochaete chrysosporium* Burds inoculation to improve the physical properties of kapok pulp, *Jurnal Sains dan Terapan Kimia*, 6 (1), 87–92.

[9] Imsya, A., Laconi, E.B., Wiryawan, K.G., and Widyastuti, Y., 2014, Biodegradasi lignoselulosa dengan Phanerochaete chrysosporium terhadap perubahan nilai gizi pelepah sawit, *Jurnal Peternakan Sriwijaya*, 3 (2), 12–19.

[10] Dewi, F., 2016, Pemanfaatan Hasil Biodelignifikasi Pelepah Sawit menggunakan Kapang *Phanerochaete chrysosporium* sebagai Pengganti Hijauan Pakan pada Ternak Kambing, *Dissertation*, Faculty of Animal Husbandry, Andalas University, Padang, Indonesia.

[11] Falade, A.O., Nwodo, U.U., Iweriebor, B.C., Green, E., Mabinya, L.V., and Okoh, A.I., 2017, Lignin peroxidase functionalities and prospective applications, *MicrobiologyOpen*, 6 (1), e00394.

[12] Singh, A.K., Bilal, M., Iqbal, H.M.N., and Raj, A., 2021, Lignin peroxidase in focus for catalytic elimination of contaminants — A critical review on recent progress and perspectives, *Int. J. Biol. Macromol.*, 177, 58–82.

[13] Susanti, E., Suharjono, S., Ardyati, T., and Aulani'am, A., 2015, Phylogenetic analysis of *Phanerochaete chrysosporium* ITB isolate using internal transcribed spacer (ITS) sequence, *Int. J. ChemTech Res.*, 8 (6), 654–658.

[14] Susanti E., Ardyati, T., Suharjono, S., and Aulani'am, A., 2016, Optimizing of lignin

peroxidase production by the suspected novel strain of *Phanerochaete chrysosporium* ITB isolate, *Int. J. ChemTech Res.*, 9 (11), 24–33.

[15] Pham, L.T.M., Deng, K., Northen, T.R., Singer, S.W., Adams, P.D., Simmons, B.A., and Sale, K.L., 2021, Experimental and theoretical insights into the effects of pH on catalysis of bond-cleavage by the lignin peroxidase isozyme H8 from *Phanerochaete chrysosporium*, *Biotechnol. Biofuels*, 14 (1), 108.

[16] Robinson, P.K., 2015, Enzymes: Principles and biotechnological applications, *Essays Biochem.*, 59, 1–41.

[17] Sharma, J.K., Yadav, M., Singh, N.P., and Yadav, K.D.S., 2011, Purification and characterisation of lignin peroxidase from *Pycnoporus sanguineus* MTCC-137, *Appl. Biochem. Microbiol.*, 47 (5), 532.

[18] Giap, V.D., Duc, H.T., Huong, P.T.M., Hanh, D.T., Nghi, D.H., Duy, V.D., and Quynh, D.T., 2022, Purification and characterization of lignin peroxidase from white-rot fungi *Pleurotus pulmonarius* CPG6 and its application in decolorization of synthetic textile dyes, *J. Gen. Appl. Microbiol.*, advpub, 2022.05.005.

[19] Liu, S., Li, Z., Yu, B., Wang, S., Shen, Y., and Cong, H., 2020, Recent advances on protein separation and purification methods, *Adv. Colloid Interface Sci.*, 284, 102254.

[20] Ugwu, S.O., and Apte, S.P., 2004, The effect of buffers on protein conformational stability, *Pharm. Technol.*, 28 (3), 86–109.

[21] Wang, P., Hu, X., Cook, S., Begonia, M., Lee, K.S., and Hwang. H.M., 2008, Effect of culture conditions on the production of ligninolytic enzymes by white rot fungi *Phanerochaete chrysosporium* (ATCC 20696) and separation of its lignin peroxidase, *World J. Microbiol. Biotechnol.*, 24 (10), 2205–2212.

[22] Ghasemi, F., Tabandeh, F., Bambai, B., and Rao, K.R.S., 2010, Decolorization of different azo dyes by *Phanerochaete chrysosporium* RP78 under optimal condition, *Int. J. Environ. Sci. Technol*, 7 (3), 457–464.

Synthesis and Characterization of ZnO Nanoparticles via Thermal Decomposition for Zn(II) Schiff Base Complex

Hadeer Mohammed Subhi, Ali Taleb Bader*, and Hazim Yahya Al-Gubury

Department of Chemistry, College of Sciences for Women, University of Babylon, Hilla, Iraq

Abstract: *Zinc(II) oxide (ZnO) nanoparticles were easily produced in this research by thermal decomposition of the Zn(II) Schiff base complex. The ligand was synthesized via condensation of benzylamine with 2-hydroxybenzaldehyde. The Zn(II) Schiff base complex was prepared by the reaction between zinc salt and Schiff base with the molar ratio of 1:1 (metal:ligand). The binary complex powder was calcined at 700 °C to produce ZnO nanoparticles. Various methods were used to characterize the Schiff base, complexes, and nanoparticles, including ^1H and ^{13}C-NMR, FTIR, TGA, DTA thermal analysis, XRD, TEM, SEM, EDX, BET, UV-Vis Diffuse Reflectance, atomic absorption, melting point, and UV-Vis spectrophotometer. ZnO nanoparticles had an average crystallite size of 48.2 nm.*

Keywords: *Schiff base; Zn(II) Schiff base complex; ZnO nanoparticles*

■ INTRODUCTION

Schiff bases are compounds that contain the azomethine group (C=N) in their structure and are often formed via the reaction of primary amines and carbonyl groups Schiff bases are a type of ligand; these ligands, as well as their metal complexes, are important [1-2] because of their capacity to stabilize metal ions in a variety of oxidation states, as well as their use in a variety of catalytic and industrial applications [3]. Because of their unique topologies, structural lability, and sensitivity to molecular environments as a functional material, metal complexes with oxygen and nitrogen donor Schiff bases are of special interest [4]. Zinc complexes of bidentate Schiff-base ligands have recently become popular in several disciplines of research due to their potential uses in biomolecules, catalysts, and optoelectronics [5-6]. There was also a study on the synthesis of numerous salicylaldehydes and benzylamine derivatives Schiff base from simple condensation and their complex [7-10]. Nanoparticles have gotten a lot of interest lately because of their wide range of uses, such as photocatalysis [11]. Zinc(II) oxide is an n-type semiconductor with a 3.37 eV large and direct band gap that can be used in dye-sensitized solar cells [12], gas sensors [13], electric and optical devices [14],

and chemical absorbance [15]. ZnO exists in a range of morphologies, including rode, nanoplate, tube, and its prepared from difference methods such as Microwave-assisted thermal methods, electrochemical methods, and sol-gel procedures are all used to make ZnO nanoparticles [16-19]. The thermochemical decomposition of zinc(II) complexes has attracted a lot of interest in recent years [7,11,20-21]. The process of manufacturing ZnO nanoparticles is straightforward, solvent-free, and effective. In this study, the structure of a compound was described using ^{13}C, ^1H-NMR, FTR, and UV-Vis. Additionally, ZnO nanoparticles were successfully synthesized using the complex's combustion synthesis approach (Scheme 1). SEM, TEM, XRD, BET, and FT-IR spectroscopy were used to examine the shape and structure of the as-prepared ZnO.

■ EXPERIMENTAL SECTION

Materials

The salicylaldehyde, benzylamine, absolute ethanol, acetic acid, diethyl ether, and zinc acetate dihydrate ($Zn(CH_3COO)_2 \cdot 2H_2O$) were bought (99% purity; Merck company Germany). All compounds were taken without being purified further.
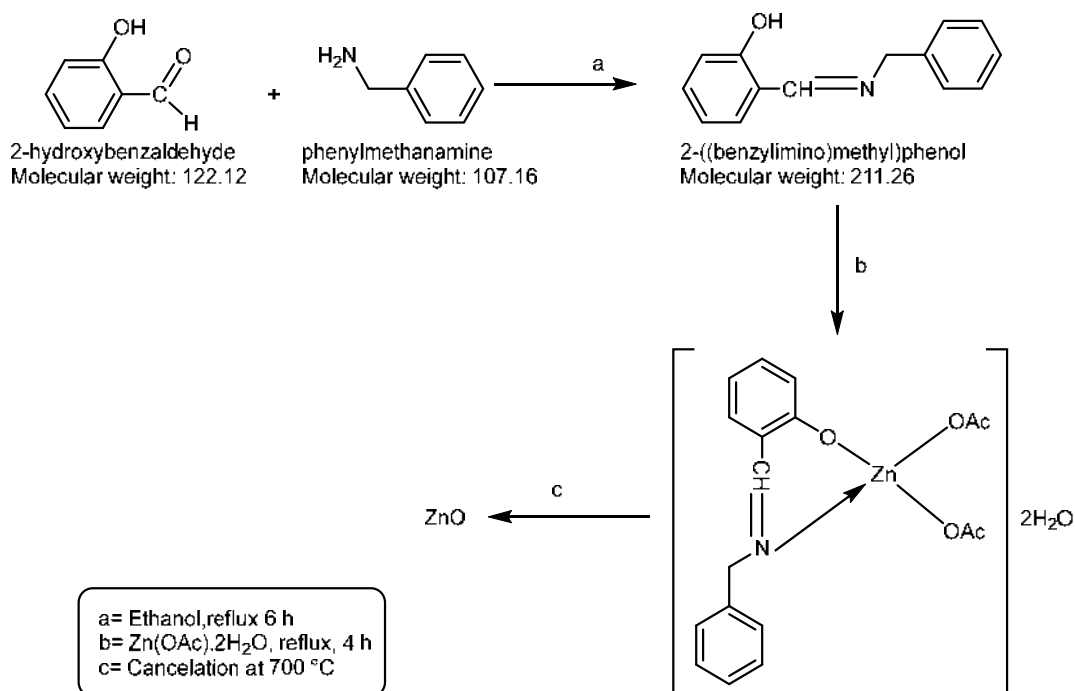
Instrumentation

The Fourier-transform infrared spectroscopy (FTIR) measurements of the prepared compounds were performed at 4000–400 cm^{-1} using a KBr disc by using an 8400 FT-IR SHIMADZU spectrophotometer. The UV–Vis spectra were measured on (UV-1700) SHIMADZU spectrophotometer in the range of 300–800 nm. The UV-visible spectrophotometer with Labspher diffuse reflectance was recorded on the UV-2600 SHIMADZU spectrophotometer (Japan). The thermal analysis for the ligand and complex was conducted by using thermos gravimetric analysis (TGA) on DTG-60. The melting point was conducted using Stuart SMP30 (UK). The molar conductivity measurements were obtained using WTW cond 720 (Germany). The cancellation of compounds was done by using furnace Carbolite S336RB (England). The above instruments were obtained at the University of Babylon, College of Science for Women. The produced compounds were measured by nuclear magnetic resonance (NMR) at 400 MHz in DMSO-d_6 at 25 °C and tetramethylsilane (TMS) as the internal standard on a Bruker spectrometer (Germany) in Isfahan University of Technology (IUT, Iran). The images of ZnO nanoparticles were recorded using a scanning electron microscope (SEM; Zeiss Germany), and a transmission electron microscope (TEM; 912AB, Germany) at the University of Tehran. The X-ray diffractometer (XRD 6000, SHIMADZU, Japan) was conducted in the Ministry of Science and Technology, Baghdad, Iraq. Atomic absorption measurements were obtained by using GBC Avanta Ver 1.33.

Procedure

Synthesized of 2-((benzylimino)methyl)phenol ligand

The ligand was prepared by condensation, as shown in Scheme 1. In a 250 mL round bottom flask was placed a mixture of 2-hydroxybenzaldehyde 0.095 mol, 10 mL) and benzylamine (0.095 mmol, 8.93 g) dissolved in 20 mL of ethanol and 2–3 drops of acetic acid with heated to reflux for 6 h. The precipitate obtained was filtered under reduced pressure, dried, and purified by recrystallization from ethanol. The solvent was removed under reduced pressure to yield the ligand as a yellow solid and recrystallization in ethanol m.p. at 35–38 °C [22-23].

Scheme 1. Synthesized Schiff base, Zn (Schiff base) complex and of ZnO nanoparticles

a= Ethanol,reflux 6 h
b= Zn(OAc).2H$_2$O, reflux, 4 h
c= Cancelation at 700 °C

2-hydroxybenzaldehyde
Molecular weight: 122.12

phenylmethanamine
Molecular weight: 107.16

2-((benzylimino)methyl)phenol
Molecular weight: 211.26

ZnO

2H$_2$O

The chelation complex, as shown in Scheme 1, was made in a 1:1 (M:L) ratio by adding an ethanolic ligand solution (5.00 g, 0.023 mol) to an aqueous solution of metal salts (5.04 g, 0.023 mol) ($Zn(OAC)_2 \cdot 2H_2O$). For 6 h, the mixture was refluxed at 75 °C and stirred. After cooling to room temperature, a yellow solid precipitant was formed, and the product was filtered, dried, and then recrystallized from hot ethanol m.p. 110–115 °C.

Synthesis ZnO nanoparticle

ZnO nanoparticles (NPs) were obtained by directly calcining the yellow powders of Zinc Schiff base complex. Approximately 2 g were poured into a platinum crucible, placed in an electrical furnace, and heated at 10 °C/min in the air to 700 °C for 5 h. The ZnO NPs yielded in Scheme 1 were washed in ethanol to remove any remaining contaminants and then dried in the air [24].

■ RESULTS AND DISCUSSION

FTIR Spectra of Schiff Base Ligand

The Schiff base (L) ligand's FTIR spectra in Fig. 1 showed an appearance of a band at 3061 cm^{-1} due to ν(O-H) of the phenol group, proving the existence of a strong intramolecular hydrogen bonding [25]. The synthesis of

Schiff base ligand (L) was confirmed by the assignment of a new stretching vibration band to the ν(C=N) group at 1636 cm^{-1} [8]. The bands at 2888 and 2842 cm^{-1} were due to asymmetric and symmetric stretching of ν(CH$_2$). Other bands of 3032, 1578, and 1486 cm^{-1} were due to ν(C-H aromatic) st and (C=C) st. The FTIR of the Zinc (Schiff base) complex was recorded as KBr discs. The ν(C=N) group at 1636 cm^{-1} stretching frequency for free ligands (L) was shifted to 1619 cm^{-1} due to the coordination with the azomethine function to the metal. In the spectra of the complexes, upon metal complexation, the ν(OH) phenolic band arising at 3105 cm^{-1} in the ligand spectrum vanished, and the ν(C-O) phenolic underwent a bathochromic shift [8]. The major stretching vibrations of ligands and their complexes are listed in Table 1.

Nuclear Magnetic Resonance ¹H and ¹³C-NMR for Schiff Base (2-((Benzylimino)methyl)phenol

The signal assignments for the ¹H-NMR spectra of Schiff base (ligand L) in DMSO-d_6 are shown in Fig. 2. The Schiff base proton was detected as a key singlet (s, ¹H, CH=N), 8.2 ppm (1H). The aromatic protons exhibited chemical shifts at 7.2–7.4 ppm (m, 7H, ArH)
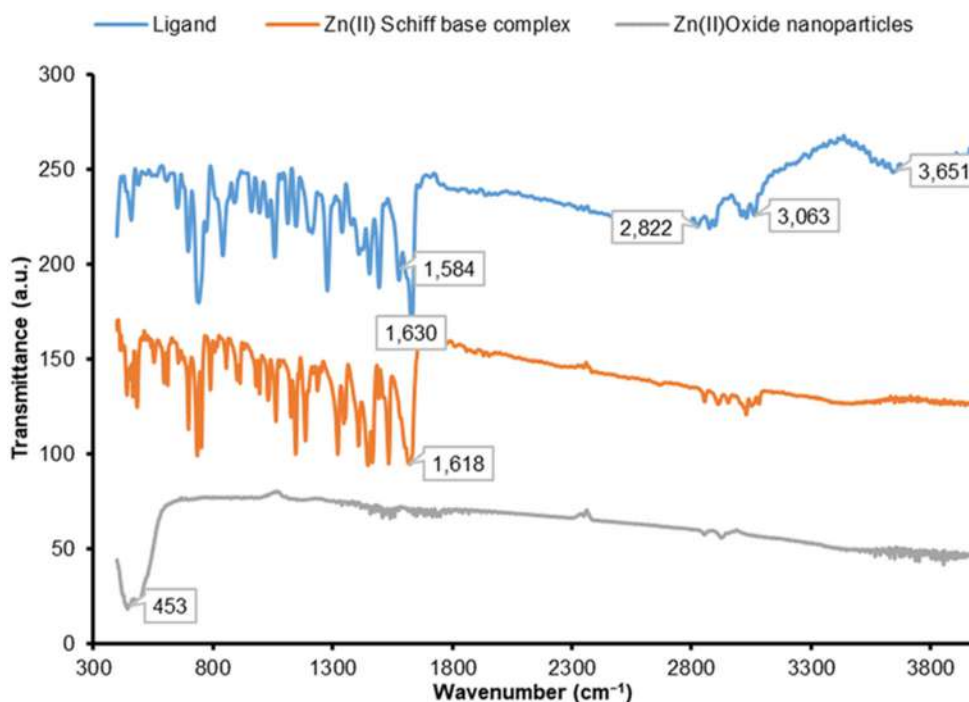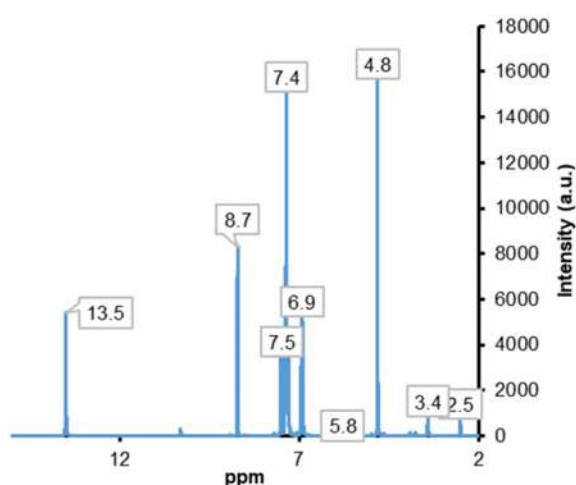

Fig 1. FTIR spectra for Schiff base (ligand), Zn (Schiff base) complex and ZnO nanoparticles

Table 1. FTIR data for Schiff base (ligand), Zn (Schiff base) complex, and ZnO

Band	Wavenumber (cm^{-1})		
	Schiff base	Zn (Schiff base)	ZnO
ν(O-H)	3061	3105	-
ν(C=N)	1636	1619	-
ν(CH_2) asymmetric and symmetric	2888 and 2842	-	-
-C=C (aromatic)	1578 and 1486		
-C-H (aromatic)	3032		
ν(C-O)	1135	1120	
Zn-O	-	-	474

Fig 2. ^{1}H-NMR spectra for Schiff base (2-((benzylimino)methyl)phenol

and 6.8–6.9 ppm (m, 1H, ArH). The O-H proton singlet had a significant peak at 13.48 ppm (s, 1H) in the spectra (1H) and the methylene group at 4.5 ppm (s, 2H) [23,25].

The ligand's ^{13}C-NMR spectra are shown in Fig. 3. A distinguishing feature of the ligand's spectra was the presence of the (N=CH) azomethine group, which appeared at 166 ppm. The carbon of the hydroxyl group was at 153.49 ppm (C-OH). The carbons in aromatic compounds were at 149.88 ppm (C Ar), 139.28 ppm (CH Ar), 129.03 ppm (CH Ar), 128.23 ppm (2C, CH Ar), 127.60 ppm (CH Ar), 120.48 ppm (2C, CH Ar), 119.12 ppm (C Ar), 117.37 ppm (CH Ar), 117.06 ppm (CH Ar) and 62.83 ppm (CH_2).
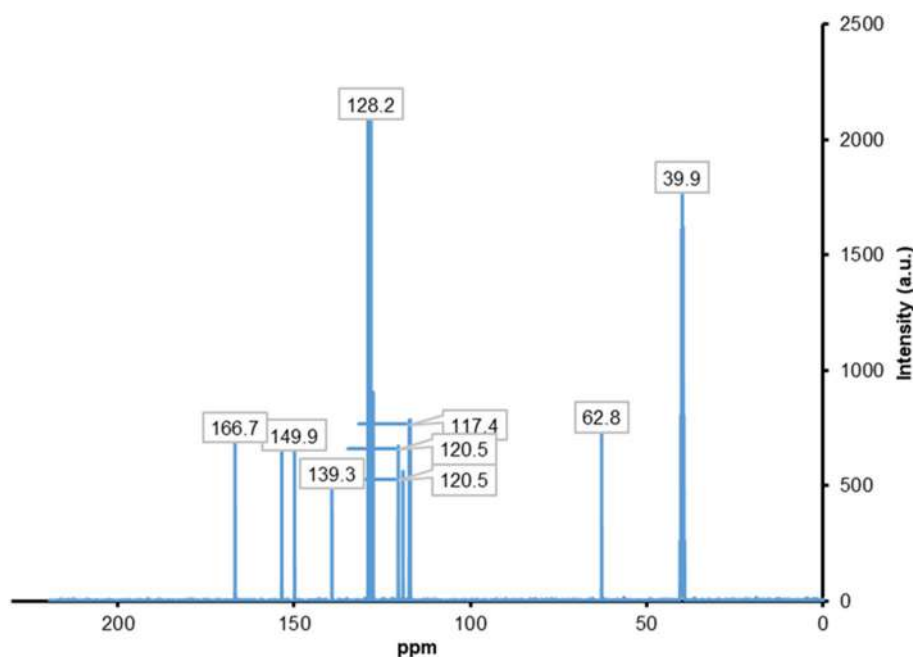
Fig 3. ^{13}C-NMR spectra for Schiff base (2-((benzylimino)methyl)phenol

1400

Indones. J. Chem., 2022, 22 (5), 1396 - 1406

Electronic Spectra of Schiff Base (L) and Zinc Complex

The UV-Visible absorption spectra of ligand L in a DMF solution are presented in Fig. 4 and reported in Table 2. The transitions were allocated in two bands at 267 nm, 37453.18 cm^{-1} and 316 nm, 31645.56 cm^{-1} due to the π-π* and the n−π* transition. The spectrum of the ZnL complex in DMF solution exhibited three bands at 288 nm, 34722.20 cm^{-1}, 300 nm, 33333.30 cm^{-1}, and 345 nm, 28986 cm^{-1}, which were assigned to π-π* and Zn→L$_{CT}$ transitions in a tetrahedral.

Thermal Analysis

TGA and DTA for Schiff base (ligand) and its Zn(II) complex

Under nitrogen at a rate of 20 °C/min, Fig. 5 and 6 illustrate TG and DTA trends for the Schiff base (ligand) and its metal ion complexes [26]. The first step, endothermic, is caused by the loss of two adsorbed water and two acetate molecules as indicated in the temperature of 30–323 °C. The second endothermic reaction, which is observed in the temperature range of 323–490 °C, is triggered by the removed of one benzene ring. The third exothermic process, which occurs in the
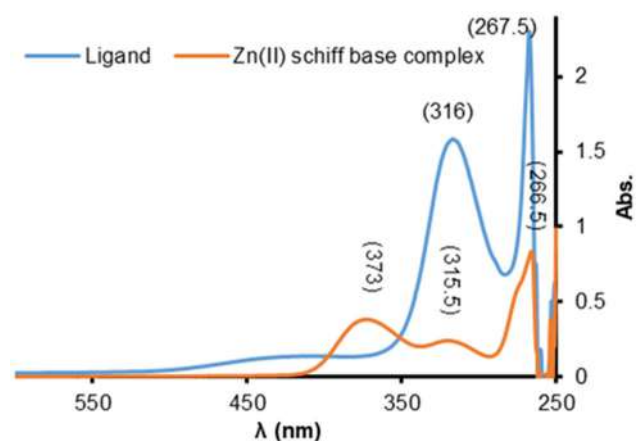
Fig 4. Electronic spectra of Schiff base (L) and zinc complex

Table 2. Electronic spectra of Schiff base (L), zinc complex

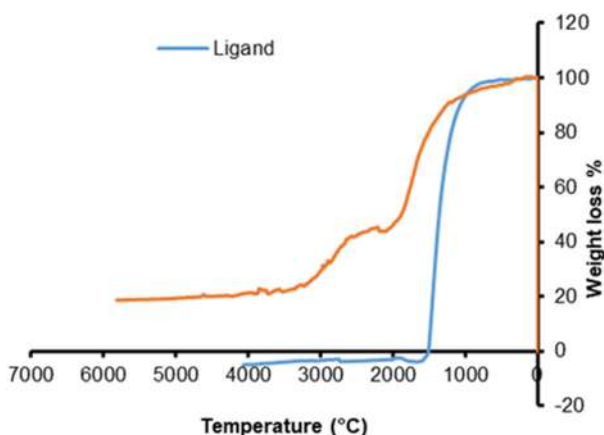| Compound	λ$_{max}$ nm (ν cm^{-1})	Assignment	Suggested geometry
Schiff base (L)	267 (37453.18), 316 (31645.56)	(n−π*) (π-π*)	-
ZnL	288, (34722.20) 300, (33333.30) 345, (28986)	(n−π*) (π-π*) CTML	Tetrahedral geometry

Fig 5. TGA analysis for Schiff base (Ligand) and its zinc complex
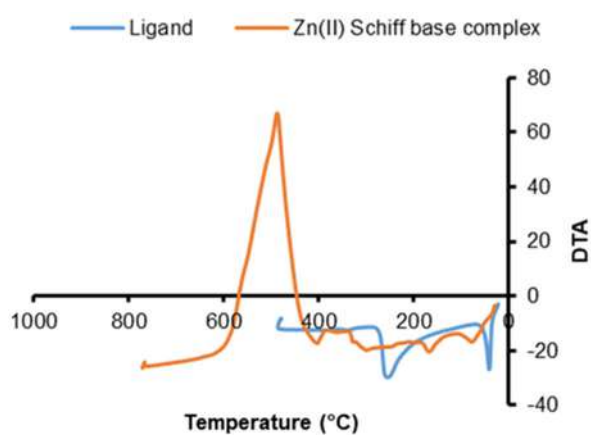

Fig 6. DTA analysis for Schiff base (Ligand) and its zinc complex

temperature range of 490–650 °C, is caused by the breaking up of the organic reduction. Finally, the metal (Zn) oxidized at temperature between 650 and 800 °C, resulting in ZnO [27].

Characterization of ZnO Nanoparticle

The ZnO NPs were made by calcining a typical complex for 5 h at 700 °C. The nature of the obtained ZnO was validated using FTIR, UV-Vis Diffuse Reflectance, XRD, SEM, TEM, EDX, and BET pattern analysis.

FTIR of the ZnO nanostructure

The FTIR pattern of the produced ZnO NPs is shown in Fig. 1 on a scale of 4000 to 400 cm^{-1}. The absorption bands of ZnO NPs at 474 cm^{-1} were due to ν(Zn–O). The FTIR spectra obtained clearly showed that ZnO NPs were synthesized [24,28].

UV-Vis diffuse reflectance for ZnONps

The Tauc method is a practical and basic approach for measuring a thin film material's characteristic optical band gap [29]. The UV-Vis reflectance spectra of ZnO nanoparticles are shown in Fig. 7. The band gap energy could then be calculated using the Tauc's relation. The UV-Vis reflectance spectrum had a lower scattering effect than absorption. The optical band gap, which corresponded to a sharp reduction in reflectance at a certain wavelength, indicated that the particles in the sample were nearly evenly spread. The direct band gap energy (Eg) for ZnO nanoparticles was obtained by fitting the reflection data to the direct transition, as shown in Eq. (1).

$$(\alpha h\nu)^{\gamma} = A(h\nu - Eg) \tag{1}$$

where α is the absorption coefficient, $h\nu$ is the photon energy, and Eg is the direct band gap. The direct band gap was 3.2 eV when plotting $(h\nu)^2$ as a function of photon energy and projecting the linear component of the curve to absorption equal to zero [30-31].

X-Ray diffraction (XRD) analysis for the ZnO nanoparticles

The X-Ray beam incident on a sample and diffracted by the crystalline phases based on Bragg's law, as shown by Eq. (2), is the fundamental approach used to estimate the solid crystalline structures and crystallite size [32].
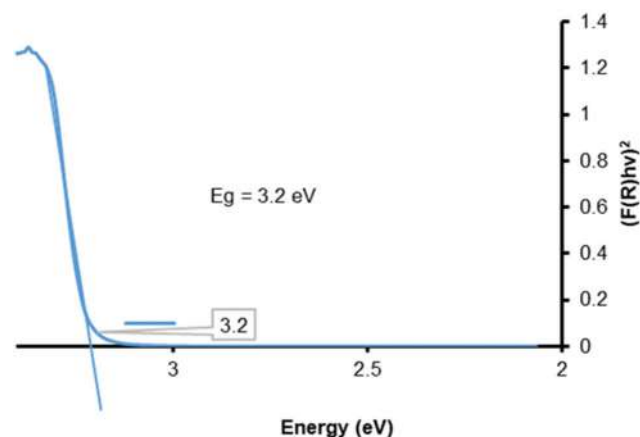

Fig 7. Energy band gap for ZnO Nps

$$n\lambda = 2d\sin\theta \tag{2}$$

where n is the order of reflection, λ is the wavelength of X-Rays, and θ is the Bragg angle. Then, d spacing was calculated, allowing for easy identification of material structure in the interplanar spacing. The shape, position, and intensity of the peak are the most important aspects of a diffraction pattern. The structure of the investigated material can be moduled after assigning Miller indices (h,k,l) to each unit cell and comparing peak positions to standard patterns published by the International Center for Diffraction Data (ICDD). Sherrer's formula Eq. (3) can also be applied to the XRD data to determine the crystallite size [33].

$$L(D) = \frac{K.\lambda}{B.\cos\theta} \tag{3}$$

where L or (D) is the crystal size, K (0.94) is a constant that depends on the crystal type, λ (1.54180 Å) is the wavelength of X-Ray, B is FWHM (full width at half maximum), and θ is Bragg's angle [34].

Fig. 8 compares the X-Ray diffraction data of ZnO NPs to the JCPDS 01-076-0205 standard reference for ZnO. Diffraction peaks (100), (002), (101), (102), (110), (103), and (112) were found and were confirmed by the hexagonal ZnO (Wurtzite) according to the standard reference. Through the figure, three very clear zinc oxide peaks were noted at the angles 31.96°, 34.84°, and 36.42° compared to the JCPDS card.

SEM for synthesized ZnO

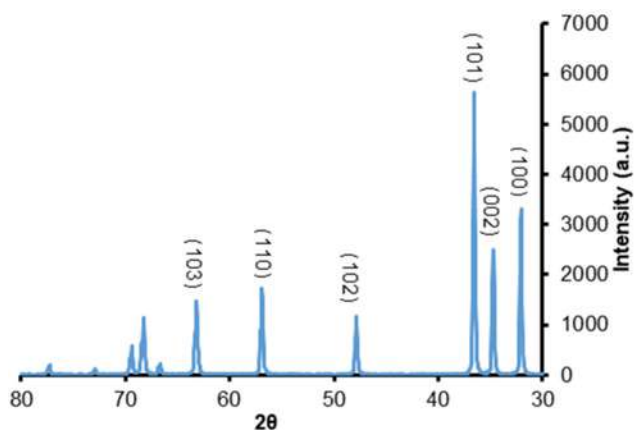The morphology of ZnO nanoparticles sintered at 700 °C in Fig. 9 was studied using SEM techniques to

Fig 8. XRD for ZnO nanoparticles

collect useful information about the structure of the produced nanoparticles. Gaussian and SEM picture

micrograph investigations showed irregular aggregated distribution and aspherical shape. According to the histogram, the average grain size was between 40 and 190 nanometers.

EDX analysis of ZnO nanoparticles

The production of ZnO NPs was studied using EDX analysis. Various locations were concentrated during the EDX measurement. The relevant peaks are shown in Fig. 10. The EDX spectrum revealed the presence of ZnO in the produced nanostructure. The atomic percent values of Zn and O in the spectrum were 86.7 and 13.3, respectively. In the synthesized samples, there was a presence of Zn and O dopants. There was no significant quantity of impurities found.
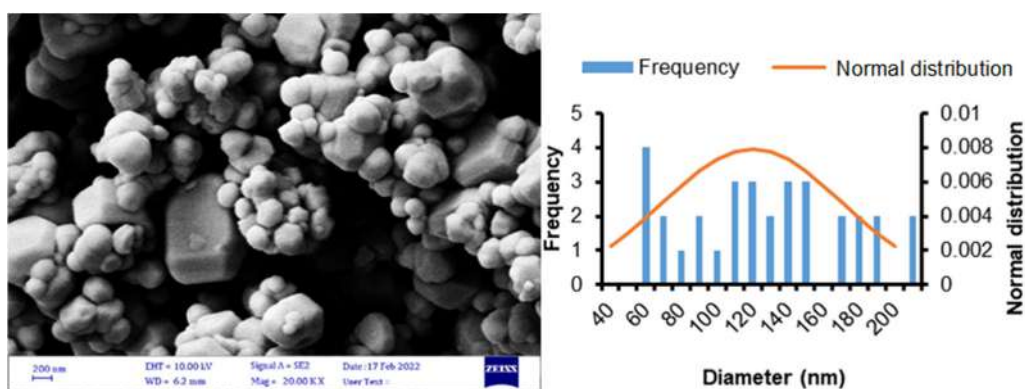
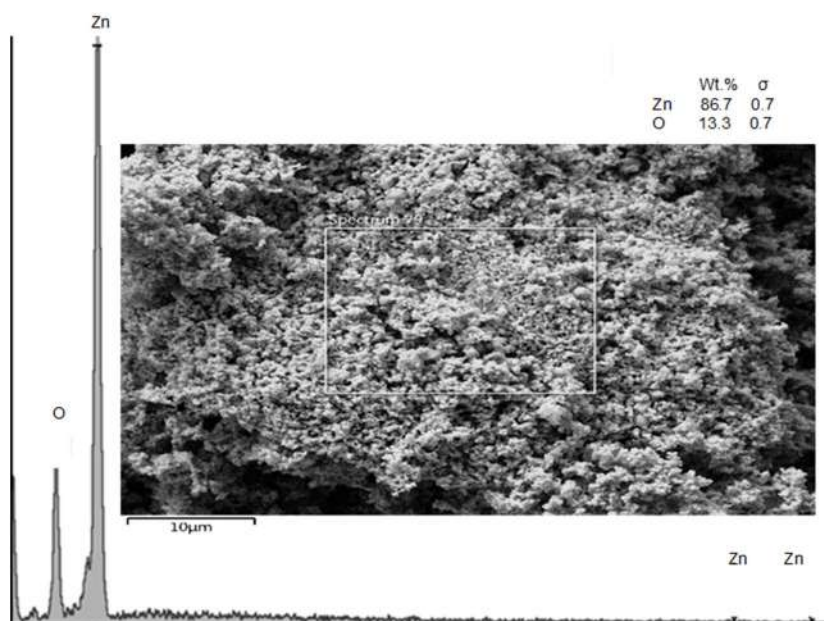**Fig 9.** SEM and Histogram for ZnO nanoparticles

Fig 10. EDX analysis for ZnO nanoparticles

TEM of ZnO nanoparticles

Fig. 11 shows the TEM images of ZnO. The TEM investigation was held to better understand the nanoparticles' crystalline properties and size. The TEM images of ZnO showed that the particles were virtually hexagonal with a minor thickness variation, confirming the SEM findings [35]. Fig. 11 shows that TEM morphology surface analysis is used to analyze the morphology of the surface of ZnO nanoparticles.

Surface area analyzer

The nitrogen isothermal adsorption technique shown in Fig. 12 was used to determine the surface area and pore structure of the ZnO nanoparticles. The isotherm profiles of ZnO showed a minor hysteresis loop, which could be classified as type IV. The surface area, average pore diameter, and total pore volume for ZnO are listed in Table 3. The high surface energy of ZnO nanoparticles is thought to be the source of nanoparticle aggregation or the creation of bigger nanoparticles [36]. From the nitrogen adsorption/desorption studies, the BET

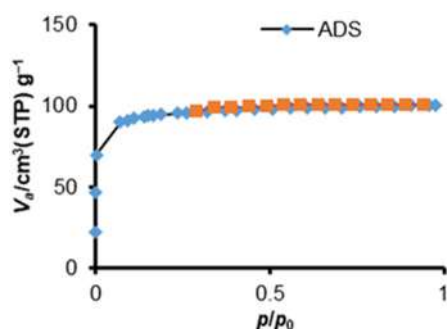**Fig 11.** Transmittance electron microscopy for ZnO NPs

Fig 12. Nitrogen adsorption-desorption isotherms for ZnO NPs

Table 3. Surface physical characteristics of ZnO

Surface physical parameters	Value
Surface area	363.61 [$m^2\ g^{-1}$]
Average pore diameter	83.54 [$cm^3(STP)\ g^{-1}$]
Total pore volume	0.1558 [$cm^3\ g^{-1}$]

method was utilized to compute the S_{BET} of ZnO nanoparticles. Prior to analysis, the material was degassed for two hours at 100 °C. The following equation was used to determine the diameter of ZnO nanoparticles:

$$d_{BET} = \frac{6000}{\rho\ sample * S_{BET}} \tag{4}$$

where the sample is the density of ZnO powder (5.60 g/cm^3), S_{BET} is the BET-specific surface area (m^2/g), and d_{BET} is the mean crystalline size (nm). d_{BET} Values of 5.72 nm for ZnO nanoparticles annealed at 700 °C were found using Eq. (4). The difference between the XRD Scherrer formula and the BET methods for determining the mean crystalline size of ZnO nanoparticles suggested that there were agglomerations in the ZnO nanoparticles.

■ CONCLUSION

Salicylaldehyde, phenylmethanamine, and zinc acetate were used to create a binary Zn Schiff-base complex. FTIR, ^{1}H-NMR, ^{13}C-NMR, TGA, DTA, and UV-Vis were utilized to determine the structure of the new Zn(II) complex produced and describe the formation of Schiff base ligand and metal with a molar ratio of 1:1. These observations led to the suggestion of deformed tetrahedral molecular geometries for the metal complex. Thermal decomposition was employed to make ZnO NPs with a 3.2 eV bandgap energy and particle sizes of 48 nm. The results of XRD, EDX, SEM, TEM, and BET revealed that single-phase ZnO NPs with particle sizes of less than 100 nm were produced via solid-state thermochemical decomposition of binary Zn-Schiff base complex. These findings might be utilized to predict the behavior of ZnO NPs, to serve as a foundation for future research at the *in vitro* and *in vivo* levels of experiments, and in the photodegradation of dye.

■ REFERENCES

[1] Mahmoud, W.H., Omar, M.M., Sayed, F.N., and Mohamed, G.G., 2018, Synthesis, characterization, spectroscopic and theoretical studies of transition metal complexes of new nano Schiff base derived from L-histidine and 2-acetylferrocene and evaluation of biological and anticancer activities, *Appl. Organomet. Chem.*, 32 (7), e4386.

[2] Sahin, M., Kocak, N., Arslan, U., Sahin, O., and Yilmaz, M., 2013, Bis-Schiff base derivatives of 2,5-dihydroxybenzaldehyde: Synthesis, characterization and antimicrobial activity of their Cu(II), Co(II) and Zn(II) complexes, *J. Macromol. Sci., Part A: Pure Appl. Chem.*, 50 (8), 821–827.

[3] El-Sonbati, A., Mahmoud, W., Mohamed, G.G., Diab, M., Morgan, S.M., and Abbas, S.Y., 2019, Synthesis, characterization of Schiff base metal complexes and their biological investigation, *Appl. Organomet. Chem.*, 33 (9), e5048.

[4] Dey, D., Kaur, G., Patra, M., Choudhury, A.R., Kole, N., and Biswas, B., 2014, A perfectly linear trinuclear zinc–Schiff base complex: Synthesis, luminescence property and photocatalytic activity of zinc oxide nanoparticle, *Inorg. Chim. Acta*, 421, 335–341.

[5] Turk, P., Singh, K., and Dhanda, A., 2022, Synthesis, spectroscopic, electrochemical, thermal and antimicrobial studies of Ni(II), Zn(II), Cu(II) and Co(II) metal complexes of novel bidentate Schiff base ligand, *J. Iran. Chem. Soc.*, 19 (9), 3797–3813.

[6] Saeednia, S., Iranmanesh, P., Ardakani, M.H., Mohammadi, M., and Norouzi, G., 2016, Phenoxo bridged dinuclear Zn(II) Schiff base complex as new precursor for preparation zinc oxide nanoparticles: Synthesis, characterization, crystal structures and photoluminescence studies, *Mater. Res. Bull.*, 78, 1–10.

[7] Gharagozlou, M., Naghibi, S., and Ataei, M., 2018, Water-based synthesis of ZnO nanoparticles via decomposition of a ternary zinc complex containing Schiff-base, chelating, and Phen ligands, *J. Chin. Chem. Soc.*, 65 (10), 1210–1217.

[8] Keerthi, K.D., Santra, B.K., and Lahiri, G.K., 1998, Ruthenium(II) bipyridine complexes with modified phenolic Schiff base ligands. Synthesis, spectroscopic characterization and Redox properties, *Polyhedron*, 17 (8), 1387–1396.

[9] Demetgül, C., Deletıoğlu, D., Karaca, F., Yalçinkaya, S., Tımur, M., and Serın, S., 2010, Synthesis and characterization of a Schiff base derived from 2-aminobenzylamine and its Cu (II) complex: Electropolymerization of the complex on a platinum electrode, *J. Coord. Chem.*, 63 (12), 2181–2191.

[10] Makal, A., Schilf, W., Kamieński, B., Szady-Chelmieniecka, A., Grech, E., and Woźniak, K., 2011, Hydrogen bonding in Schiff bases – NMR, structural and experimental charge density studies, *Dalton Trans.*, 40 (2), 421–430.

[11] Gharagozlou, M., Baradaran, Z., and Bayati, R., 2015, A green chemical method for synthesis of ZnO nanoparticles from solid-state decomposition of Schiff-bases derived from amino acid alanine complexes, *Ceram. Int.*, 41 (7), 8382–8387.

[12] Wang, Y.X., Shen, Z.C., Huang, D.D., and Yang, Z.S., 2018, High-performance ZnO nanosheets/nanocrystalline aggregates composite photoanode film in dye-sensitized solar cells, *Mater. Lett.*, 214, 88–90.

[13] Meng, L., Xu, Q., Sun, Z., Li, G., Bai, S., Wang, Z., and Qin, Y., 2018, Enhancing the performance of room temperature ZnO microwire gas sensor through a combined technology of surface etching and UV illumination, *Mater. Lett.*, 212, 296–298.

[14] Saleem, S., Jameel, M.H., Akhtar, N., Nazir, N., Ali, A., Zaman, A., Rehman, A., Butt, S., Sultana, F., Mushtaq, M., Zeng, J.H., Amami, M., and Althubeiti, K., 2022, Modification in structural, optical, morphological, and electrical properties of zinc oxide (ZnO) nanoparticles (NPs) by metal (Ni, Co) dopants for electronic device applications, *Arabian J. Chem.*, 15 (1), 103518.

[15] Khalaji, A.D., 2019, Preparation and characterization of ZnO nanoparticles via thermal decomposition from zinc(II) Schiff base complex as new precursor, *Chem. Methodol.*, 3 (5), 571–579.

[16] Li, Q., Cao, W., Lei, J., Zhao, X., Hou, T., Fan, B., Chen, D., Zhang, L., Wang, H., Xu, H., Zhang, R.,

and Lu, H., 2014, Synthesis and growth mechanism of ZnO rod-like nanostructures by a microwave-assisted low-temperature aqueous solution route, *Cryst. Res. Technol.*, 49 (5), 298–302.

[17] Zhang, X.L., Dai, H.T., Zhao, J.L., Wang, S.G., and Sun, X.W., 2014, Surface-morphology evolution of ZnO nanostructures grown by hydrothermal method, *Cryst. Res. Technol.*, 49 (4), 220–226.

[18] Li, T., Cao, Z., You, H., Xu, M., Song, X., and Fang, J., 2013, Controllable growth of ZnO mesocrystals using a facile electrochemical approach, *Chem. Phys. Lett.*, 555, 154–158.

[19] Salavati-Niasari, M., Gholami-Daghian, M., Esmaeili-Zare, M., and Sangsefidi, F.S., 2013, Solid state synthesis and characterization of zinc oxide (ZnO) microflakes by [bis(acetylacetonato)zinc(II)] and sodium hydroxide at room temperature, *J. Cluster Sci.*, 24 (4), 1093–1101.

[20] Galini, M., Salehi, M., Kubicki, M., Bayat, M., and Malekshah, R.E., 2020, Synthesis, structural characterization, DFT and molecular simulation study of new zinc-Schiff base complex and its application as a precursor for preparation of ZnO nanoparticle, *J. Mol. Struct.*, 1207, 127715.

[21] Shahraki, S., and Heydari, A., 2017, New zinc(II) N4 tetradentate Schiff base complex: A potential cytotoxic metallodrug and simple precursor for the preparation of ZnO nanoparticles, *Colloids Surf., B*, 160, 564–571.

[22] Ortegón-Reyna, D., Garcías-Morales, C., Padilla-Martínez, I., García-Báez, E., Aríza-Castolo, A., Peraza-Campos, A., and Martínez-Martínez, F., 2013, NMR structural study of the prototropic equilibrium in solution of Schiff bases as model compounds, *Molecules*, 19 (1), 459–481.

[23] Vaz, P.A.A.M., Rocha, J., Silva, A.M.S., and Guieu, S., 2018, Aggregation-induced emission enhancement of chiral boranils, *New J. Chem.*, 42 (22), 18166–18171.

[24] Alothman, A.A., and Albaqami, M.D., 2020, Nano-sized Cu(II) and Zn(II) complexes and their use as a precursor for synthesis of CuO and ZnO nanoparticles: A study on their sonochemical synthesis, characterization, and DNA-binding/cleavage, anticancer, and antimicrobial activities, *Appl. Organomet. Chem.*, 34 (10), e5827.

[25] Silverstein, R.M., and Bassler, G.C., 1962, Spectrometric identification of organic compounds, *J. Chem. Educ.*, 39 (11), 546.

[26] Bader, A.T., Al-qasii, N.A.R., Shntaif, A.H., El Marouani, M., AL Majidi, M.I.H., Trif, L., and Boulhaoua, M., 2022, Synthesis, structural analysis and thermal behavior of new 1,2,4-triazole derivative and its transition metal complexes, *Indones. J. Chem.*, 22 (1), 223–232.

[27] Katouah, H.A., 2021, Facile synthesis of Co_3O_4 and ZnO nanoparticles by thermal decomposition of novel Co(II) and Zn(II) Schiff base complexes for studying their biological properties and photocatalytic degradation of crystal violet dye, *J. Mol. Struct.*, 1241, 130676.

[28] Muthukumaran, S., and Gopalakrishnan, R., 2012, Structural, FTIR and photoluminescence studies of Cu doped ZnO nanopowders by co-precipitation method, *Opt. Mater.*, 34 (11), 1946–1953.

[29] Viezbicke, B.D., Patel, S., Davis, B.E., and Birnie III, D.P., 2015, Evaluation of the Tauc method for optical absorption edge determination: ZnO thin films as a model system, *Phys. Status Solidi B*, 252 (8), 1700–1710.

[30] Talam, S., Karumuri, S.R., and Gunnam, N., 2012, Synthesis, characterization, and spectroscopic properties of ZnO nanoparticles, *Int. Scholarly Res. Not.*, 2012, 372505.

[31] Sales Amalraj, A., Christina Joycee, S., and Natarajan, G., 2022, Investigation of the properties of tungsten doped ZnO thin films synthesised by SILAR method, *Mater. Res. Innovations*, 26 (5), 263–269.

[32] Doustkhah, E., Esmat, M., Fukata, N., Ide, Y., Hanaor, D.A.H., and Assadi, M.H.N., 2022, MOF-derived nanocrystalline ZnO with controlled orientation and photocatalytic activity, *Chemosphere*, 303, 134932.

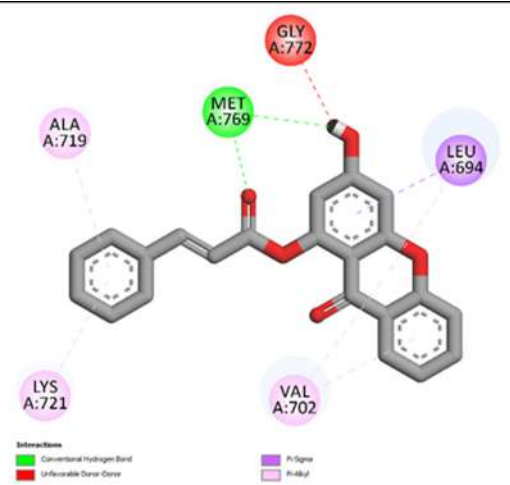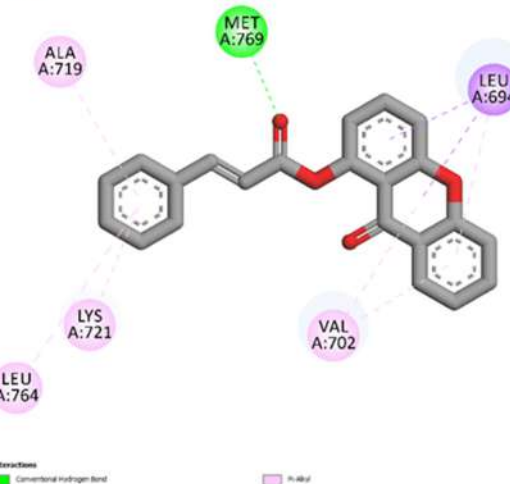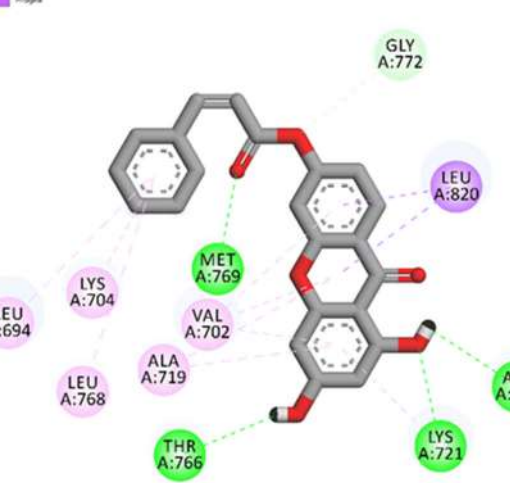[33] Kinra, S., Ghosh, M.P., Mohanty, S., Choubey, R.K., and Mukherjee, S., 2022, Manganese ions

substituted ZnO nanoparticles: Synthesis, microstructural and optical properties, *Phys. B*, 627, 413523.

[34] Sa'aedi, A., Akl, A.A., and Hassanien, A.S., 2022, Effective role of Rb doping in controlling crystallization, crystal imperfections, microstructural, and morphological features of ZnO-NPs synthesized by sol-gel approach, *CrystEngComm*, 24 (26), 4661–4678.

[35] Geetha, M.S., Nagabhushana, H., and Shivananjaiah, H.N., 2016, Green mediated synthesis and characterization of ZnO nanoparticles using *Euphorbia Jatropa* latex as reducing agent, *J. Sci.: Adv. Mater. Devices*, 1 (3), 301–310.

[36] Jin, S.E., Hwang, S.J., and Jin, H.E., 2022, Hierarchical tetramodal-porous architecture of zinc oxide nanoparticles microfluidically synthesized via dual-step nanofabrication, *Mater. Des.*, 215, 110486.

Indones. J. Chem., 2022, 22 (5), 1407 - 1417

Suppl. **1**

Supplementary Data

This supplementary data is a part of a paper entitled "Synthesis, Cytotoxicity Evaluation and Molecular Docking Studies of Xanthyl-Cinnamate Derivatives as Potential Anticancer Agents".

Table S1. 2D structure of ligand interaction with EGFR amino acid residues

Compound	2D structure of ligand interaction with EGFR amino acid residues	Interaction
3a		Hydrogen bond: MET769, GLN767, THR766 Hydrophobic bond: ALA719, LEU694, LEU820
3b		Hydrogen bond: MET769, GLN767, THR766 Hydrophobic bond: ALA719, VAL702, LEU694, LEU820
3c		Hydrogen bond: MET769, GLN767, THR766, LYS721 Hydrophobic bond: ALA719, VAL702, LEU820

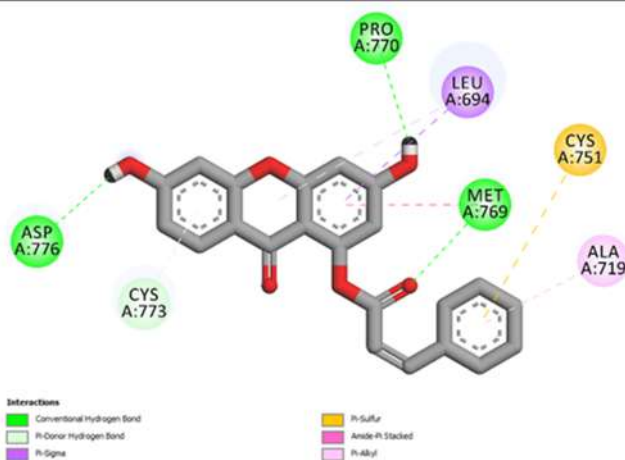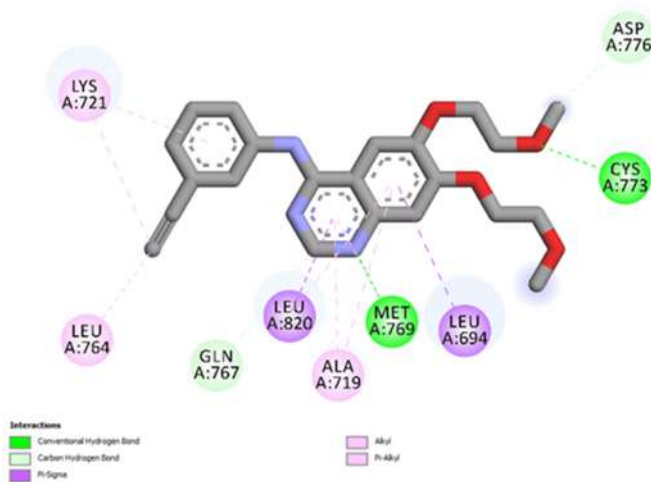| Compound	2D structure of ligand interaction with EGFR amino acid residues	Interaction
4a		Hydrogen bond: MET769 Hydrophobic bond: ALA719, VAL702, LYS721, LEU694 Unfavorable donor-donor: GLY772
4b		Hydrogen bond: MET769 Hydrophobic bond: ALA719, VAL702, LYS721, LEU764, LEU694
4c		Hydrogen bond: MET769, THR766, LYS721, ASP831 Hydrophobic bond: ALA719, VAL702, LEU694, LYS704, LEU768, LEU820 Carbon hydrogen bond: GLY772

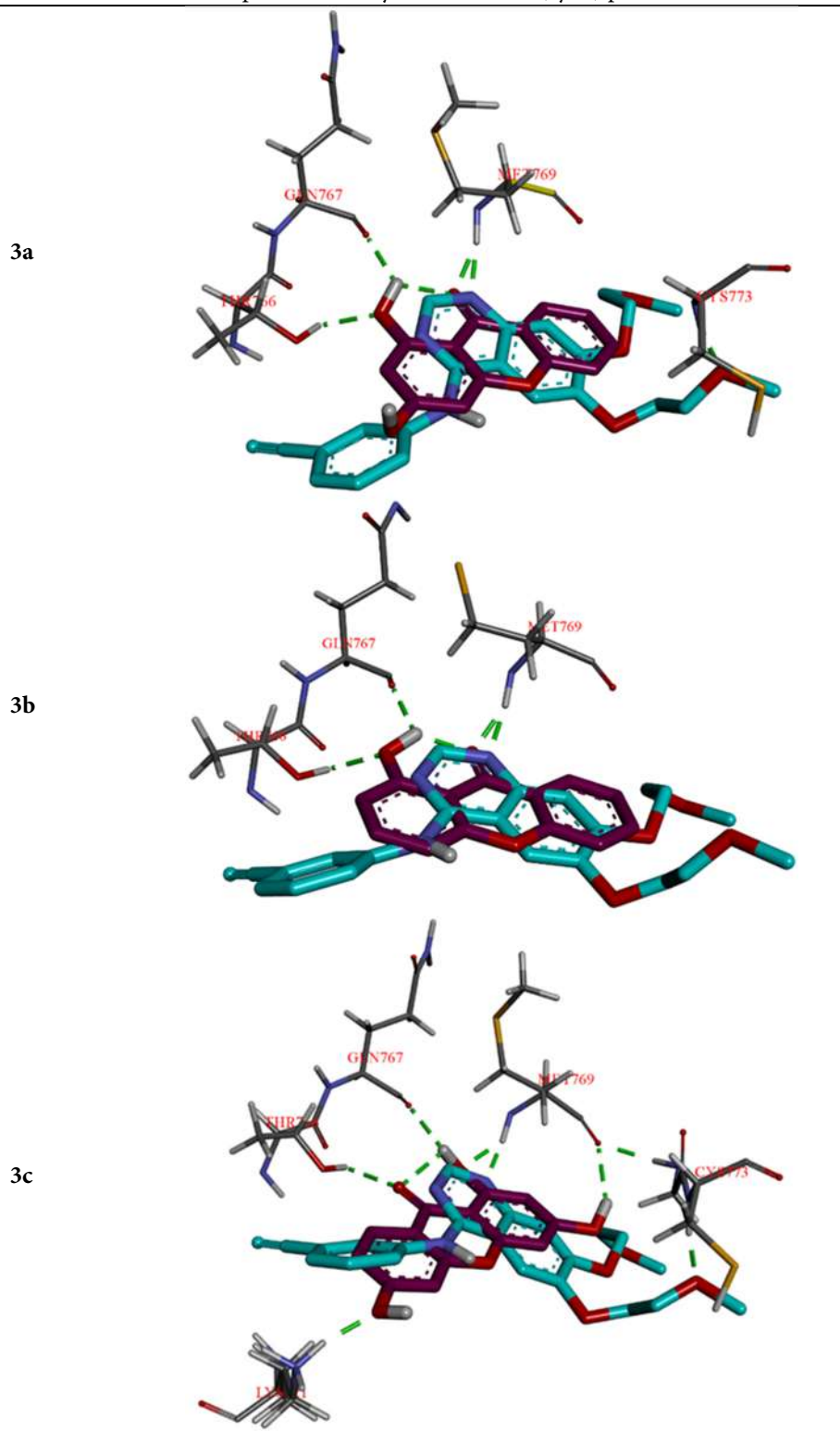| Compound	2D structure of ligand interaction with EGFR amino acid residues	Interaction
4d		Hydrogen bond: MET769, ASP776, PRO770 Hydrophobic bond: ALA719, LYS721, LEU764, LEU820, LEU694 π-sulfur: CYS751 π -donor hydrogen bond: CYS773
erlotinib		Hydrogen bond: MET769, CYS773 Hydrophobic bond: ALA719, LYS721, LEU764, LEU820, LEU694 Carbon hydrogen bond: GLN767, ASP776

Suppl. **4**

Indones. J. Chem., 2022, 22 (5), 1407 - 1417

Table S2. 3D structure molecular docking results of ligand molecule in EGFR protein overlay with erlotinib position

Compound	3D structure molecular docking results of ligand molecule (magenta) in EGFR protein overlay with erlotinib (cyan) position
3a	
3b	
3c	

Indones. J. Chem., 2022, 22 (5), 1407 - 1417

Suppl. **5**

Compound	3D structure molecular docking results of ligand molecule (magenta) in EGFR protein overlay with erlotinib (cyan) position
4a	
4b	
4c	